SEISMIC STUDIES OF LATERALLY HETEROGENEOUS STRUCTURES

INTERPRETATION AND MODELLING OF SEISMIC DATA

Edited by
ERNST R. FLUEH

Proceedings of the 8th Workshop Meeting
Commission on Controlled Source Seismology

CCSS

held at Kiel - Fellhorst (Germany)

August 27 - 31, 1990

GEOMAR
Forschungszentrum
für marine Geowissenschaften
der Christian-Albrechts-Universität
zu Kiel

Kiel 1991

GEOMAR REPORT 6

GEOMAR
Research Center
for Marine Geosciences
Christian Albrechts University
in Kiel

Herausgeber: Jörn Thiede

GEOMAR REPORT
ISSN 0936 - 5788

GEOMAR
Forschungszentrum
für marine Geowissenschaften
D-2300 Kiel
Wischhofstr. 1-3
Telefon (0431) 7202-0
Telefax (0431) 72 53 91, 7 20 22 93, 72 56 50

Editor: Jörn Thiede

GEOMAR REPORT
ISSN 0936 - 5788

GEOMAR
Research Center
for Marine Geosciences
D-2300 Kiel / Germany
Wischhofstr. 1-3
Telephone (49) 431 / 7202-0
Telefax (49) 431 / 72 53 91, 7 20 22 93, 72 56 50

Contents

PROLOGUE

The 8. Workshop meeting of the Commission on Controlled Source Seismology (CCSS) was held from 27-31 August 1990 at the beautiful Tagungs- und Sporthotel in Fellhorst, located between the Baltic Sea and the North Sea in northernmost Germany. The main topic was "Seismic studies of laterally heterogeneous structures - interpretation and modelling of seismic data". Altogether 29 participants representing nine countries attended the workshop. As was done for previous workshops, four different datasets had been distributed to the participants about six months prior to the meeting; the main emphasize of the meeting was to discuss, compose and evaluate the different approaches of processing and interpretation methods presented by the participants during the meeting.

The individual datasets covered a broad spectrum of major research problems in deep crustal seismic studies. The datasets distributed were previously collected and interpreted by different research groups and generously made available to the workshop participants. Included were tasks such as:

(i) an evaluation of pre- and poststack processing of a high fold Vibroseis line (dataset I),

(ii) exploring the value of coincident near-vertical and high-density wide-angle data (dataset II),

(iii) investigating a closely spaced three-component observation (dataset III) from marine airgun shots, and

(4) forward modelling of a complex crustal scale model of the kind frequently shown in modern literature (dataset IV).

This volume puts together the individual contributions for all datasets. The contributions follow an introduction, describing the material distributed to the participants, a summary and comparison of the results, and the discussions during the workshop. It is aimed at providing the reader with a concise overview of the results, the inherent problems encountered, and suggestions for future research activities. As far as possible, all results for a specific dataset are presented at identical scales, so that a direct comparison can be easily achieved. Datasets I and III (6 contributions each) attracted the greatest interest, but datasets II and IV (4 contributions each) were also well analyzed.

In addition to editorial review each contribution was evaluated by at least two external reviewers. Besides workshop participants T. Dahl-Jensen, D. Gajewski, R. Hobbs, I. Psencik, T. Reston, and R. Roberts provided profound and helpful comments.

Financial support towards the travel costs of some participants and for organizational expenses during the workshop were received from IASPEI, ICL, the University of Kiel and GEOMAR, which are greatly appreciated. The data used during the workshop were provided for reproduction by DEKORP (Deutsches Kontinentales Reflexions-seismisches Programm), BIRPS (British Institutions Reflection Profiling Syndicate), the Department of Geological Sciences of Durham University, U. K., and the GRÖKORT Study Group (Grönland Kolbeinsey-Rücken Traverse). The organizer thanks all participant for their efforts towards a successful workshop, and especially those who contributed to this volume. During the workshop valuable technical assistance was provided by Cristel Hansen and Frauke Klingelhöfer from GEOMAR. Special thanks go to Alexander Stavenhagen for his patience and skills in retyping this volume over and over again.

Ernst R. Flueh

Kiel 1991

INTRODUCTION TO DATASET I

Ernst R. Flueh

GEOMAR, Kiel, Germany

Dataset I aimed at comparing different pre- and poststack processing techniques applied to deep reflection data. The profile chosen was the BELCORP / DEKORP 1A Profile, traversing the northwestern rim of the Rhenish Massif and its forelands. This 93.3 km long line starts near Maastricht at the Dutch/Belgian border and extends in an ESE-direction towards the town of Adenau (Figure 1). It is part of the network of deep reflection lines collected by DEKORP (Deutsches Kontinentales Reflexions-seismisches Programm) within Germany. The field work was carried out in a joint cooperation with BELCORP (Belgian Continental Reflection Seismic Program) in 1987. A detailed description of the profile, the field-techniques, the data-processing and its interpretation is given by DEKORP Research Group (1991). Additional information can be found in the DEKORP-Atlas (Meissner and Bortfeld, 1990) and in DEKORP Research Group (1990). Since the workshop focussed on the technical details of data-processing, the reader is referred to DEKORP Research Group (1991) for details on the geological background and the geological/tectonic interpretation.

The field work was contracted to Prakla Seismos AG, and the Vibroseis method was used to collect the data. A 400 channel Sercel SN368 recording system with a VFTT-02 noise reduction system was operated. Group spacing was 40 m, with 24 SM4 (10 Hz) geophones per group, and the records of 36s listening time, sampled at 4ms were field correlated and stacked. As sources five VVEA vibrators were used, they transmitted five sweeps of 20s each from 12 to 48 Hz at a source interval of 40 m and a source length of 48 m. Of the nominal fold of 200 per 20 m CDP an average coverage of 80% (thus 160 fold) was achieved. An asymmetric split spread geometry with a 120 m gap to each side of the source was used throughout the survey, the offsets being 12080 - 120 - 120 - 4080 m.

Data processing was carried out at the DEKORP Processing Center in Clausthal-Zellerfeld (Germany), closely following the routine procedure as described by Stiller and Thomas (1989). The processing sequence is outlined by Klöckner and Stiller (this volume). For the final migration the data were resampled to 8ms after stacking, and an FD-Migration using smoothed stacking velocities was applied.

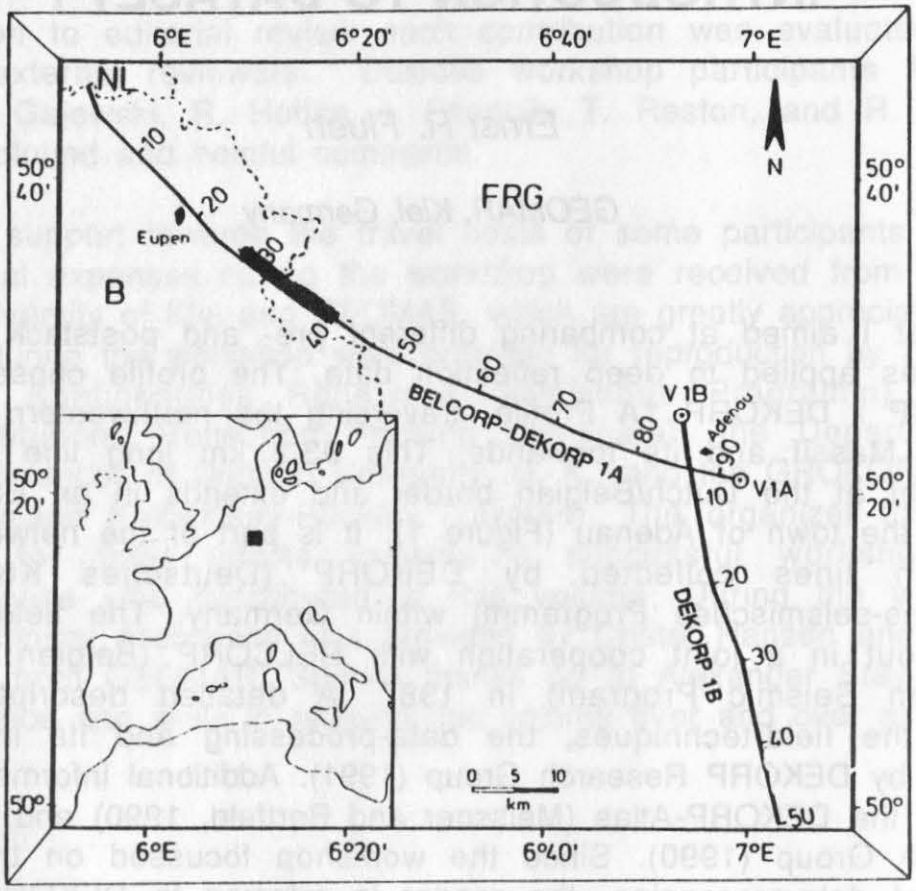

Figure 1: Location map of profiles BELCORP/DEKORP 1A and DEKORP 1B (modified after DEKORP Research Group, 1990). Thick line marks the area to which dataset 1 c corresponds.

After migration a two trace summation was applied. Further details and several test panels can be found in DEKORP Research Group (1991). From both the stacked and the migrated section automatic line drawings were made. The stacked and migrated section, and the line drawings of both of them, are reproduced in the accompanying contribution by Klöckner and Stiller (this volume). In Figure 2 a manual line drawing and a geological cross section along the profile is shown (DEKORP Research Group, 1990).

The material distributed to the participants working on dataset I consisted of three parts:

(a) paper copies of the record sections of the final stack and final migration, as processed by the DEKORP Processing Center, at a scale of 1:50000. Also included were the processing sequences and velocities used for stacking. This package was meant for additional and independent interpretation of the crustal structure and its geological and tectonic implications.

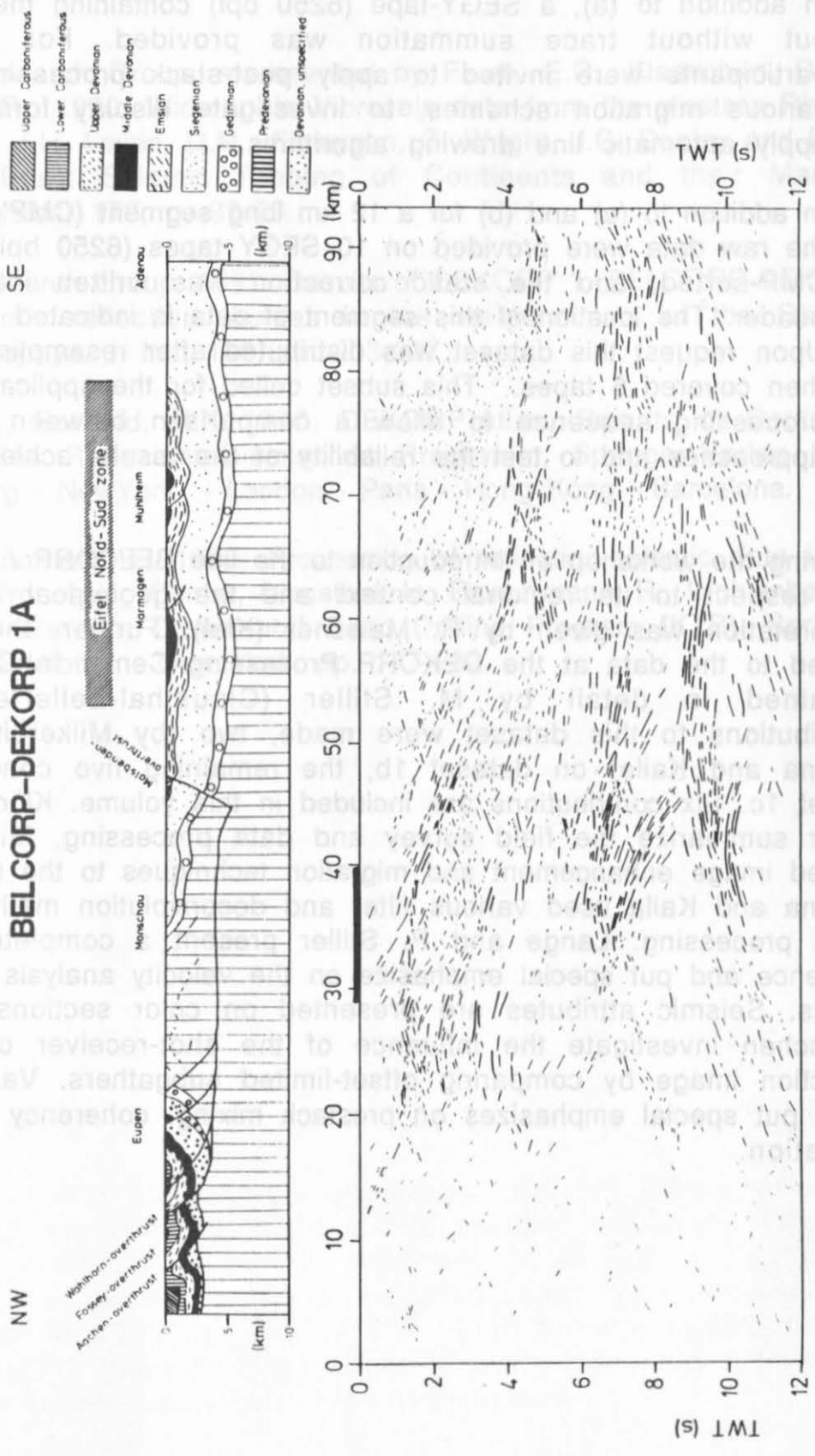

Figure 2: Interpretative line drawing of the final stack of the profile BELCORP/DEKORP 1A (after DEKORP Research Group, 1990). Thick bar mark the area to which dataset 1 c corresponds.

(b) In addition to (a), a SEGY-tape (6250 bpi) containing the final stack, but without trace summation was provided. For these data participants were invited to apply post-stack processing, such as various migration schemes, to investigate display formats and to apply automatic line drawing algorithms.

(c) In addition to (a) and (b) for a 12 km long segment (CMP's 3366-3964) the raw data were provided on 10 SEGY tapes (6250 bpi). Data were CMP-sorted, and the static correction was written into the trace header. The location of this segment of data is indicated in Figures 2. Upon request this dataset was distributed after resampling to 8ms, it then covered 6 tapes. This subset called for the application of a full processing sequence to allow a comparison between the various approaches and to test the reliability of the results achieved.

During the workshop an introduction to the line BELCORP / DEKORP 1A with respect to its regional context and the geological and tectonic interpretation was given by R. Meissner (Kiel). Further, the processing applied to the data at the DEKORP Processing Center in Clausthal was explained in detail by M. Stiller (Clausthal-Zellerfeld). Seven contributions to this dataset were made, two (by Milkereit et al. and Krishna and Kaila) on dataset 1b, the remaining five concentrated on subset 1c. Six contributions are included in this volume. Klöckner and M. Stiller summarize the field survey and data processing. Milkereit et al. applied image enhancement and migration techniques to the stacked data. Krishna and Kaila used various filter and deconvolution methods in post-stack processing. Lange and P. Stiller present a complete processing sequence and put special emphasize on the velocity analysis and residual statics. Seismic attributes are presented on color sections. Flueh and Klaeschen investigate the influence of the shot-receiver offset on the reflection image by comparing offset-limited subgathers. Vasudevan and Clark put special emphasizes on prestack mixing, coherency analysis and migration.

References

DEKORP Research Group, represented by Flueh, E.R., Klaeschen, D. and Meissner, R., 1990: Wide-angle Vibroseis data from the western Rhenish Massiv; In: J.H. Leven, D.M., Finlayson, C. Wright, J.C. Dooley and B.L.N. Kennett (Eds): Seismic Probing of Continents and their Margins; Tectonophysics, 173, p. 83-93.

DEKORP Research Group, 1991: Results of DEKORP 1 (BELCORP-DEKORP) deep seismic reflection studies in the western part of the Rhenish Massif; Geophys. J. Int., 106, pp. 203-227.

Meissner, R., Bortfeld, R.K 1990: DEKORP-Atlas, Results of Deutsches Kontinentales Reflexionsseismisches Programm; Springer-Verlag Berlin - Heidelberg - NewYork - London - Paris - Hong Kong - Barcelona.

Stiller, M., Thomas, R., 1989: Processing of reflection-seismic data in the DEKORP Processing Center, Clausthal; In: Emmermann, R., Wohlenberg, J. (Eds.): the German Continental Deep Drilling Program (KTB); Springer, Berlin - Heidelberg - New York, pp. 177-232.

FIELD SURVEY AND DATA PROCESSING OF LINE DEKORP 1A

Margret Klöckner and Manfred Stiller

DEKORP Processing Center, Institut für Geophysik,
TU Clausthal

Introduction

The near vertical reflection Line DEKORP 1A is located west of the Rhein river and consists of three parts: BELCORP/ DEKORP 1A, 1B, 1C.

Line 1A starts near Maastricht at the Dutch/ Belgian border, crosses the North Variscan Deformation Front and the Eifel Nord- Süd Zone (see location map of Figure 1).

The processing of the deep seismic data of DEKORP 1A was carried out in the DEKORP Processing Center (DPC) at the Geophysical Institute of the Technical University in Clausthal. The two proceeding systems (Phoenix DPU, VAX 11/750 and Phoenix 1, Raytheon RDS 500) have been used with the SSC/ SSL software package for analysis, processing and display for seismic data.

A generalized processing scheme for deep seismics used in the DPC is already discussed and illustrated extensively by Stiller and Thomas (1989).

Data Processing

A very efficient, three phase processing sequence developed at the DPC involves production of a single-fold section, raw stack, and final stack. The single-fold section is generated in the processing center directly from shot gathers. In these unstacked shots, dominant events are already visible after scaling, filtering and rough dynamic corrections. For further processing, information on where to place the analysis points for the raw stack is also taken from these seismograms.

The first raw stack of all traces, which only a few velocity and muting functions, gives a quick overview of the whole profile. Major geological units, structures, and boundaries can now be recognized and evaluated for an initial interpretation. Proceeding on this basis, a large number of analyses (amplitude, velocity, frequency, noise) are then performed to

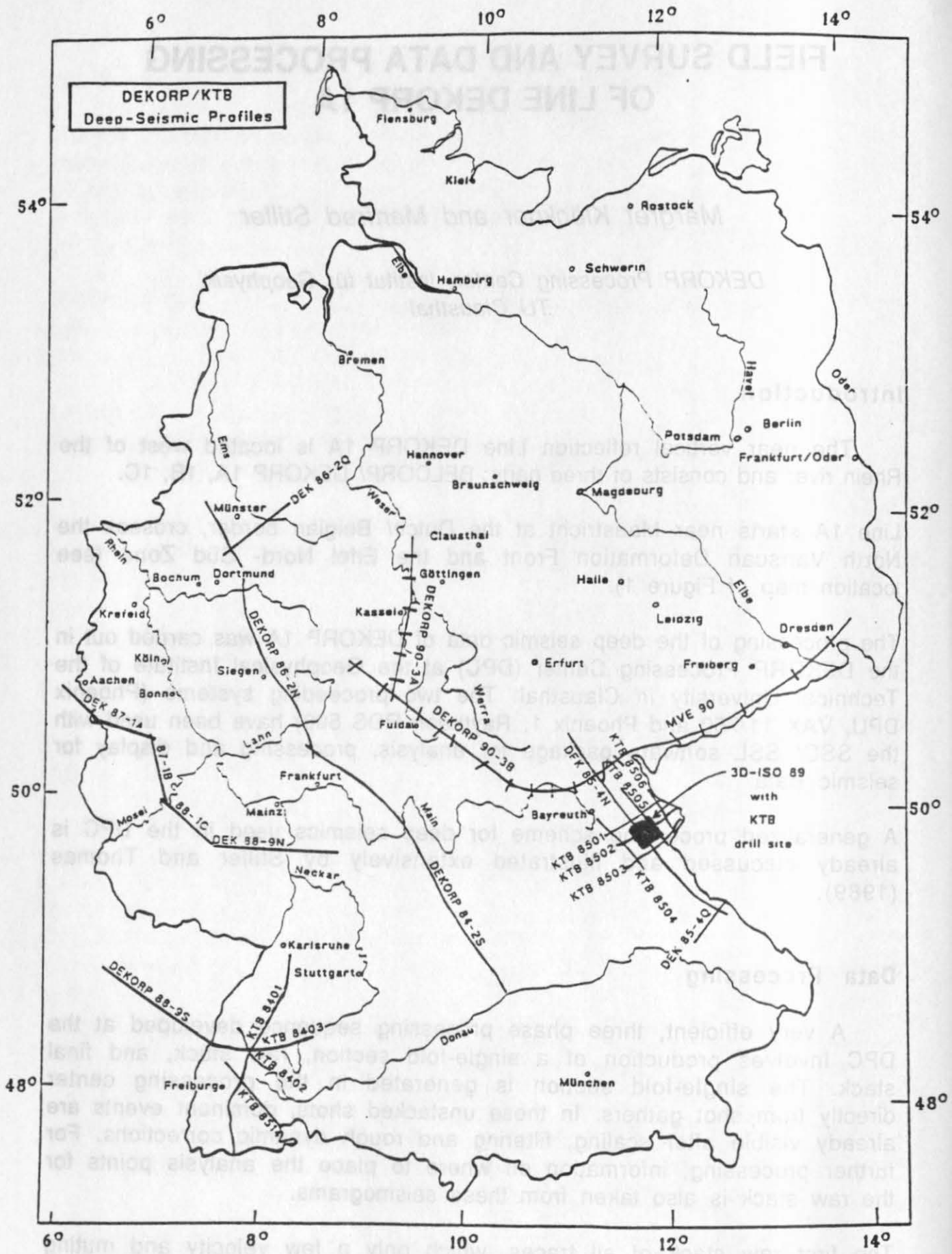

Figure 1: Location map of deep-seismic profiles DEKORP/KTB.

Data Description

Table 1:

Date:	August 1987
Contractor:	Prakla Seismos AG
Profile length:	93 km
Method:	Vibroseis
Equipment:	Sercel SN 368/ MTC-01
Channels/ Record:	400
Sampling rate:	4 ms
Sweep:	12-48 Hz upsweep
Sweep length:	20 s
Listening time:	36 s
Record length:	16 s
Filter:	Lo 12.5 Hz/18 dB
	Hi 62.5 Hz/72 dB
Geophone:	SM 4/10 Hz
Geophones/ Group:	24 (In-Line Array)
Group length:	40 m
Group spacing:	40 m
Geometry:	asymmetric split-spread -12/4 km
Number of shots:	1915
Vibrator:	VVEA
Vertical stack:	5-fould
Source spacing:	40 m
Coverage (theor./real):	200/167
Number of CMP's:	4666

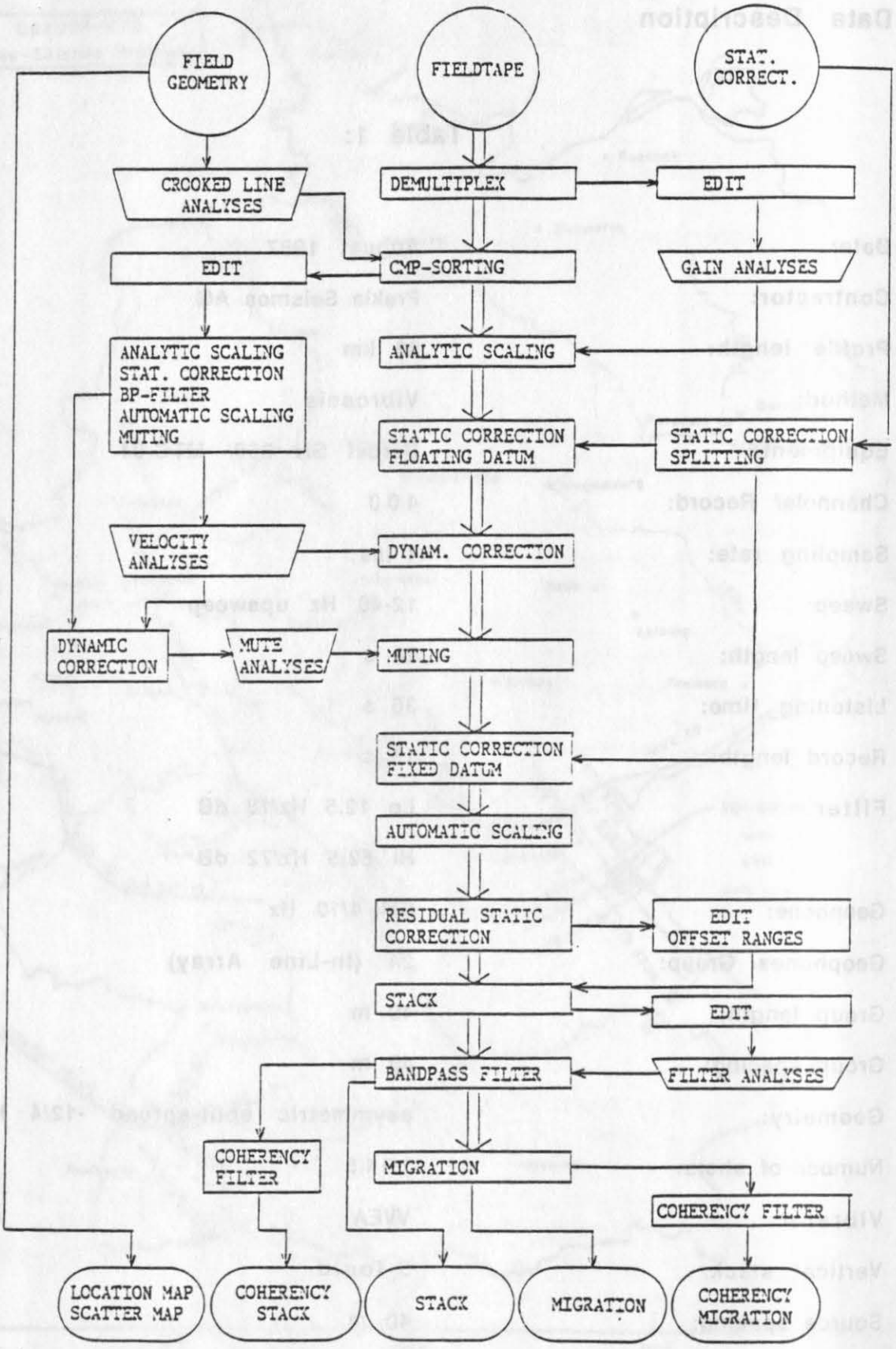

Figure 2: Generalized flowchart for deep-seismic Vibroseis processing.

determine the individual processing parameters for the more time-consuming final stack. Additional processes (e.g. determining and applying residual static corrections) involve extensive calculations. A generalized flowchart of the final processing is shown in Figure 2. It is not rigid and must frequently be modified depending on the data (omitting, adding, or ex-changing processing steps). The individual processing sequence can be taken from the side labels of the sections.

For structural interpretation automatic line-drawings have been generated from both unmigrated and migrated zero-distance sections (Figures 3-6). This method has been developed and successfully tested at the DPC in Clausthal. It automatical carries out the evaluation, i.e. correlating events are attenuated according to a mathematical procedure. A description of the automatical line-drawing algorithm is presented in Meissner and Bortfeld (1990).

References

Meissner, R., Bortfeld, R.K., 1990: DEKORP-Atlas: Results of Deutsches Kontinentales Reflektionsseismisches Programm; Springer-Verlag, Berlin -Heidelberg -New York -London -Paris -Hong Kong -Barcelona

Stiller, M., Thomas, R., 1989: Processing of reflection-seismic data in the DEKORP Processing Center, Clausthal; In: Emmermann, R., Wohlenberg, J. (Eds.): The German Continental Deep Drilling Programm (KTB); Springer-Verlag, Berlin -Heidelberg -New York -Barcelona, pp. 177-232.

Figures 3-6, see the next pages.

Figure 3: DEKORP 87 1A Final stack.

Figure 4: DEKORP 87 1A Final migration.

Figure 5: DEKORP 87 1A Final stack, automatical line drawing.

Figure 6: DEKORP 87 1A Final migration, automatical line drawing.

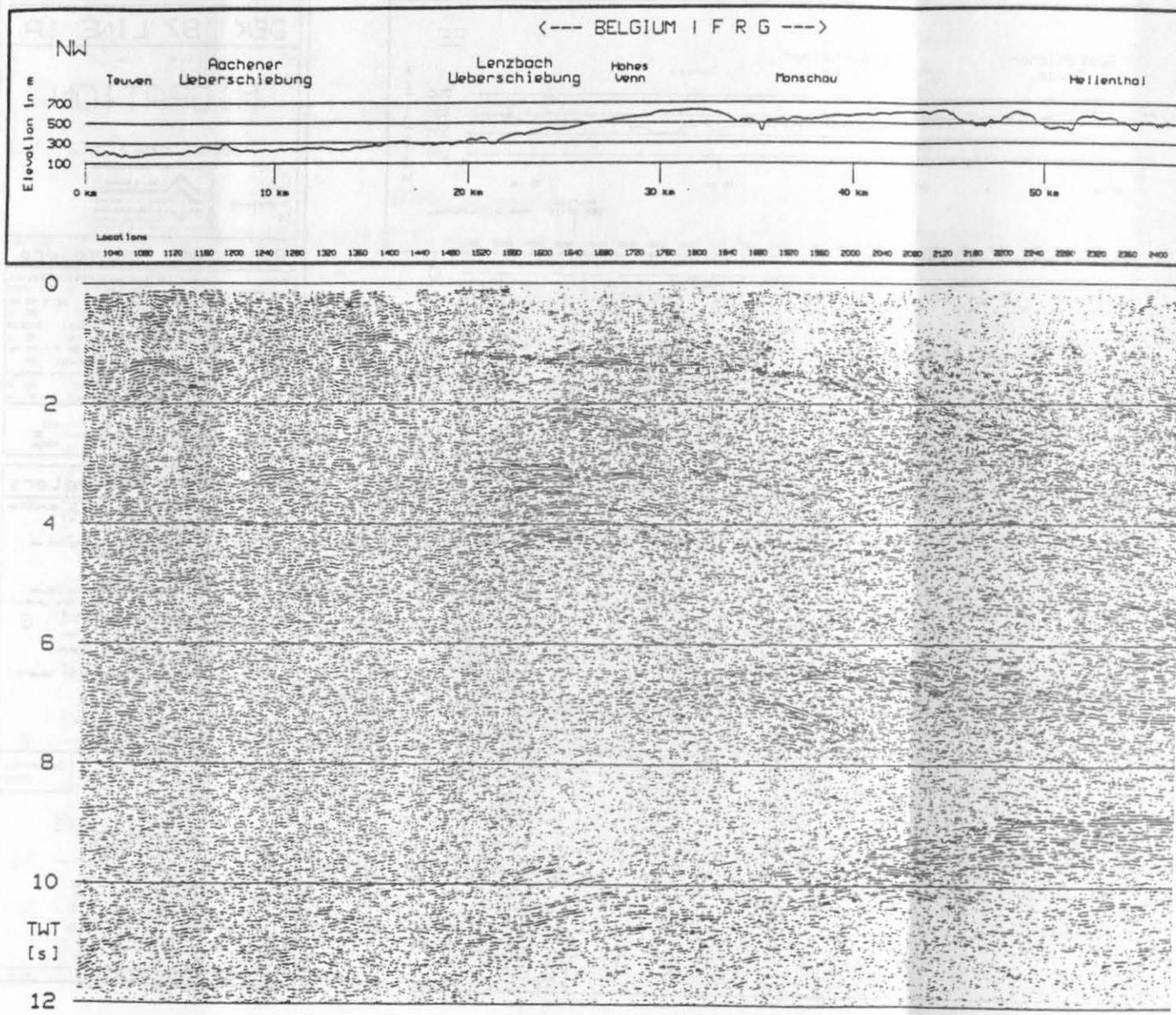
<--- BELGIUM I F R G --->
NW
Teuven
Aachener Ueberschiebung
Lenzbach Ueberschiebung
Hohes Venn
Monschau
Hellenthal
Elevation in m
700
500
300
100
0 Km
10 Km
20 Km
30 Km
40 Km
50 Km
Locations
0
2
4
6
8
10
TWT [s]
12

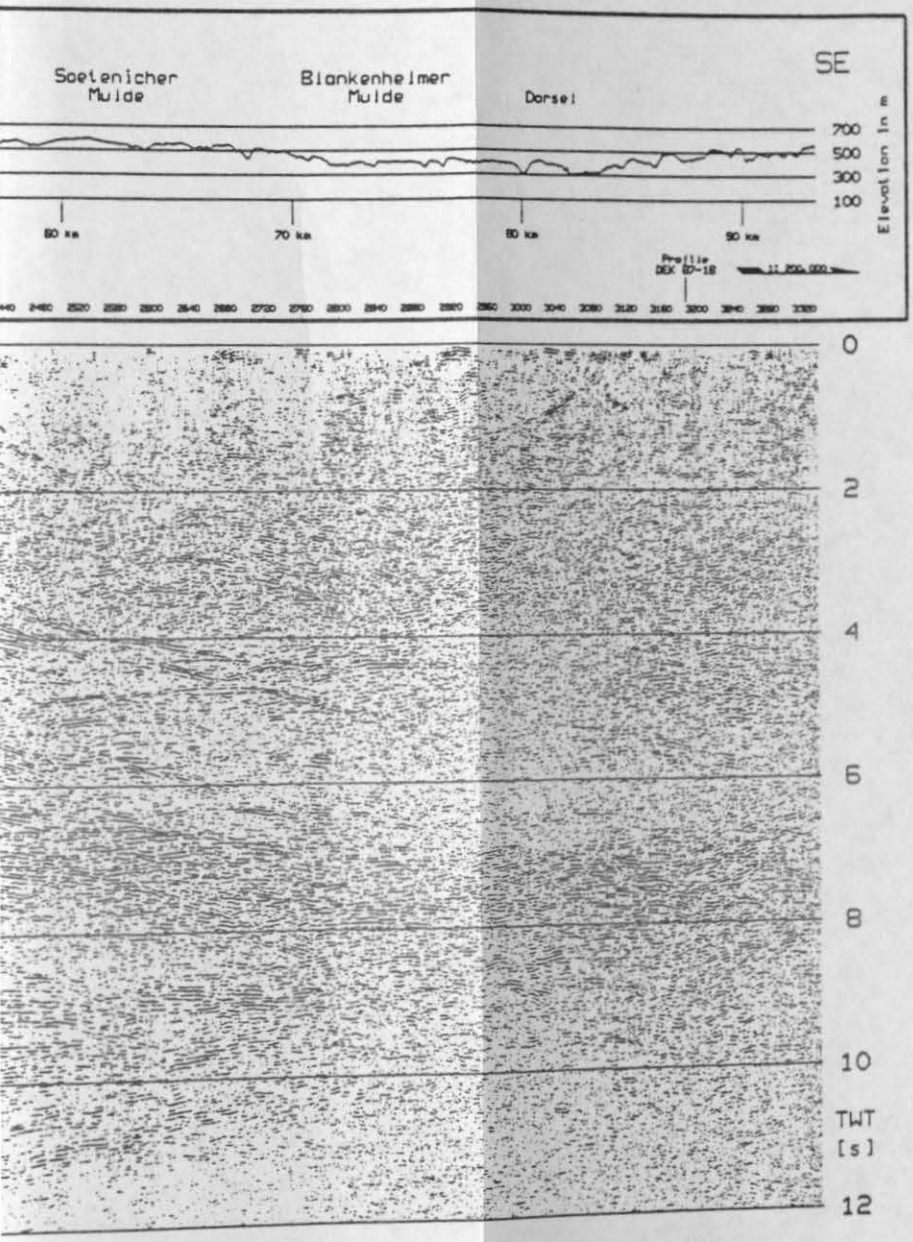
Soetenicher Mulde
Blankenheimer Mulde
Dorsel
SE
700
500
300
100
Elevation in m
80 km
70 km
80 km
90 km
Profile DEK 87-1A
0
2
4
6
8
10
TWT [s]
12


DEK '87 LINE 1A
FINAL STACK
Loc's: 1003 - 3332
Data Processed by:
Recording Parameters
Date: August 87
Contractor: Prakla-Seismos AG
Instrument: Sercel SN 388 / MTC-01
Channels/Record: 400
Sampling Rate: 4 ms
Record Length: 16 s
Filter: Lo 12.6 Hz/18 dB
Hi 62.5 Hz/72 dB
Theor. Coverage: 200
Energy Source: Vibrosels
Vibrator: 5 x VAE
Sweep: 12 - 48 Hz
Sweep Length: 20 s
Vertical Stack: 5-fold
Source Spacing: 40 m
Geophone: SM 4 / 10 Hz
Geophones/Group: 24 (In-Line Array)
Group Length: 40 m
Group Spacing: 40 m
Cable Configuration
1 Channel 300 305 400
NW SE
-1206m Offset -120m 120m 408m
Processing Parameters
1. Demultiplexing and Bad Trace Elimination
2. CMP Sorting (CMP-Spacing: 20 m)
3. Analytical Gain
4. Static Corrections to Floating Datum
5. Normal Moveout Corrections
6. Initial Muting
7. Automatical Scaling
8. Static Corrections to Constant Datum (Reference Plane 500 m above Sea Level)
9. Stacking (coverage ca. 160-fold)
10. Bandpass Filtering
11. Summation of Two Adjacent Traces
12. Coherency Filtering
13. Variable Area Display (Black = Positive = Compression Upward)
General Map
N
Belgium
FRG
Luxembourg
DEK 87-1A
0 10 20 km

Figure: 3

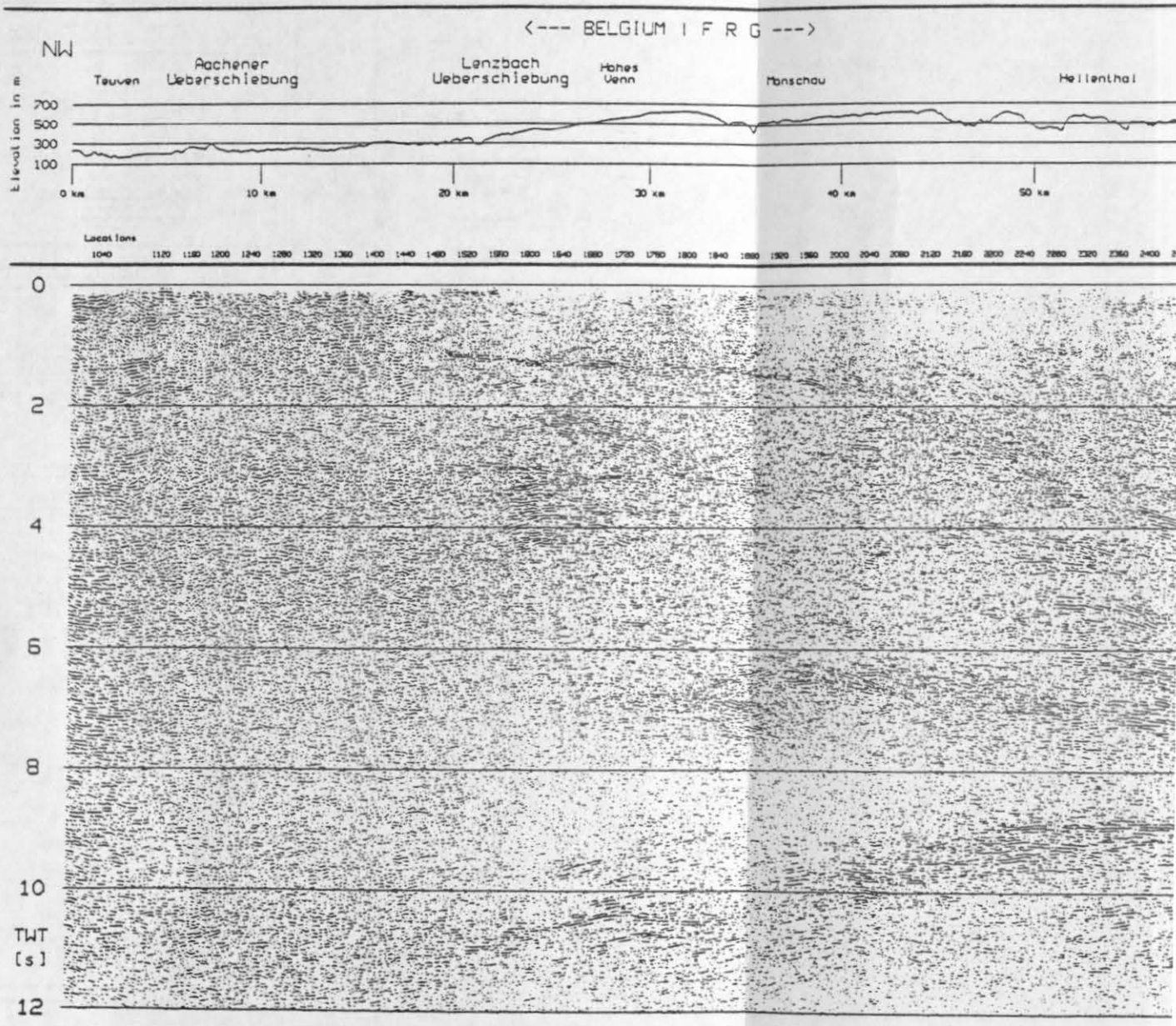
<--- BELGIUM I F R G --->
NW
Elevation in m
700
500
300
100
Teuven
Aachener Ueberschiebung
Lenzbach Ueberschiebung
Hohes Venn
Monschau
Hellenthal
0 km
10 km
20 km
30 km
40 km
50 km
Locations
1040
1120
1160
1200
1240
1280
1320
1360
1400
1440
1480
1520
1560
1600
1640
1680
1720
1760
1800
1840
1880
1920
1960
2000
2040
2080
2120
2160
2200
2240
2280
2320
2360
2400
0
2
4
6
8
10
TWT [s]
12

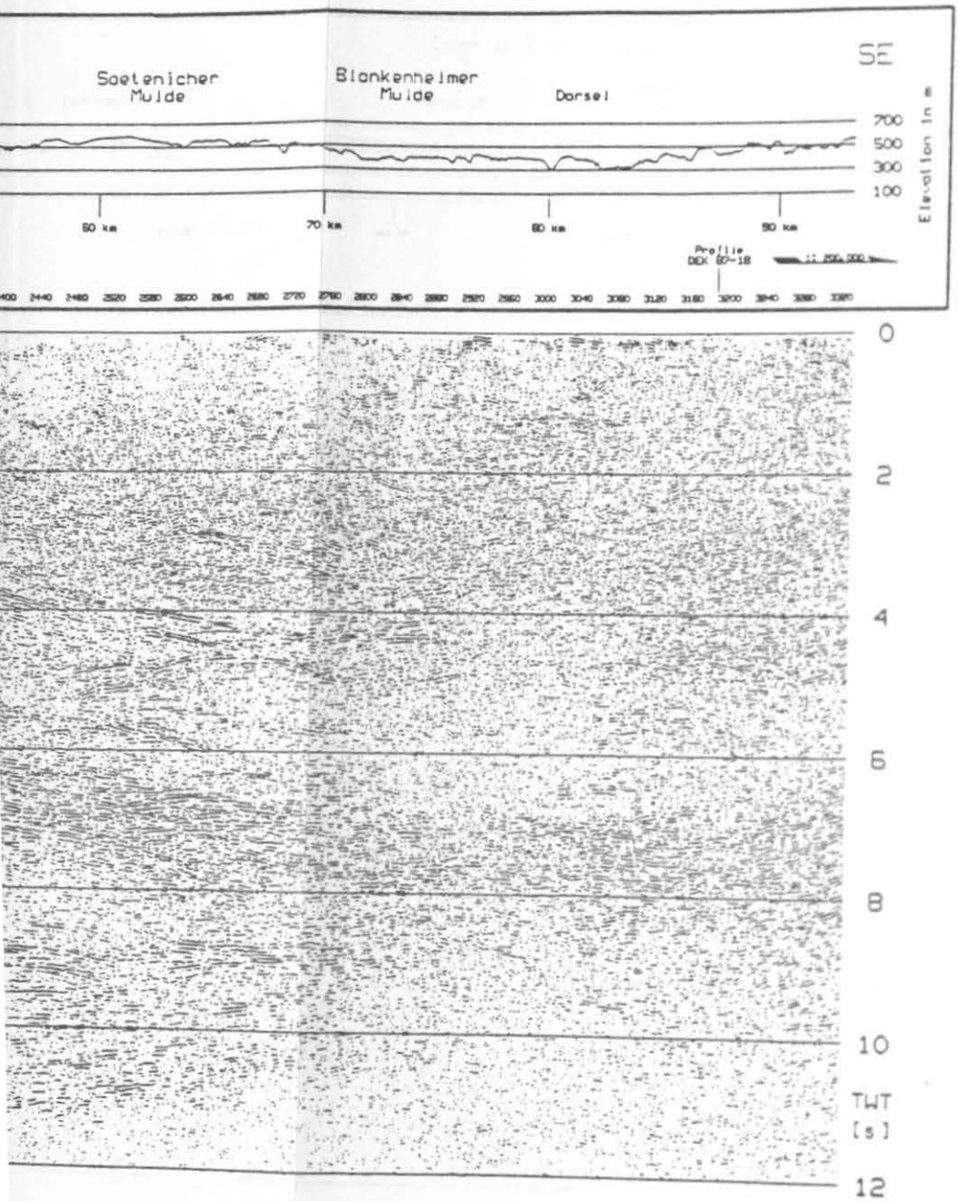
SE
Soetenicher Mulde
Blankenheimer Mulde
Dorsel
700
500
300
100
Elevation in m
50 km
70 km
80 km
90 km
Profile DEK 87-1A
0
2
4
6
8
10
TWT [s]
12


DEK '87 LINE 1A
MIGRATION
Loc's: 1003 - 3332
Data Processed By:
Recording Parameters
Processing Parameters
1. Demultiplexing and Base Trace Elimination
2. CMP Sorting (CMP-Spacing: 20 m)
3. Analysis: Semi
4. Static Corrections to Floating Datum
5. Normal Moveout Corrections
6. Initial Muting
7. Horizontal Scaling
8. Static Corrections to Constant Datum (Reference Plane 500 m above Sea Level)
9. Stacking (coverage 6fo 1600-fold)
10. Bandpass Filtering
11. Migration
12. Summation of Two Adjacent Traces
13. Variable Area Display (Black = Positive = Compression Waves)
General Map
N
FRG
Belgium
DEK 87-1A


NW
Elevation in m
700
500
300
100
0 km
0
2
4
6
8
10
TWT [s]
12

Figure: 4

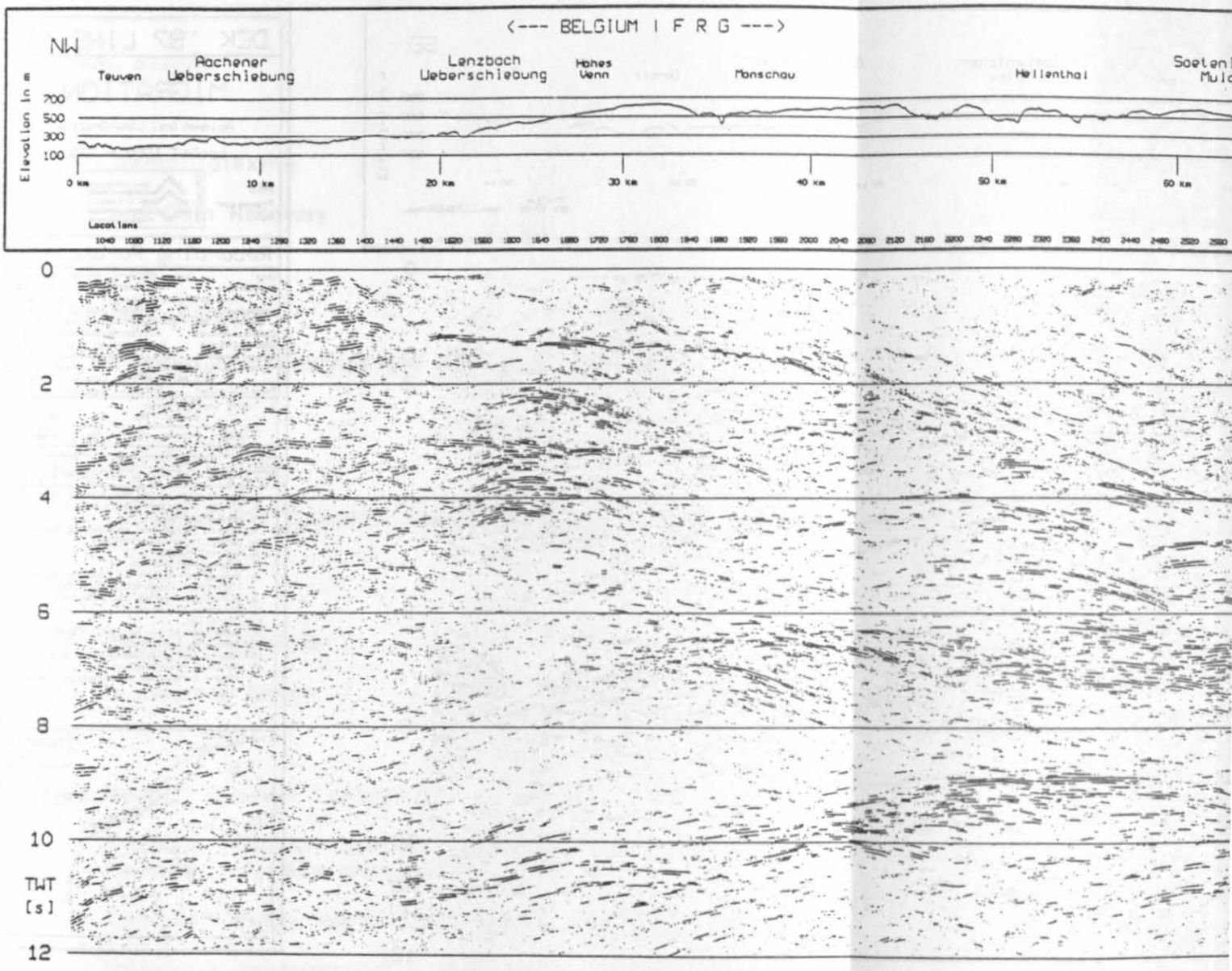
<--- BELGIUM I F R G --->
NW
Teuven
Aachener Ueberschiebung
Lenzbach Ueberschiebung
Hohes Venn
Monschau
Hellenthal
Elevation in m
700
500
300
100
0 km
10 km
20 km
30 km
40 km
50 km
60 km
Locations
0
2
4
6
8
10
TWT [s]
12

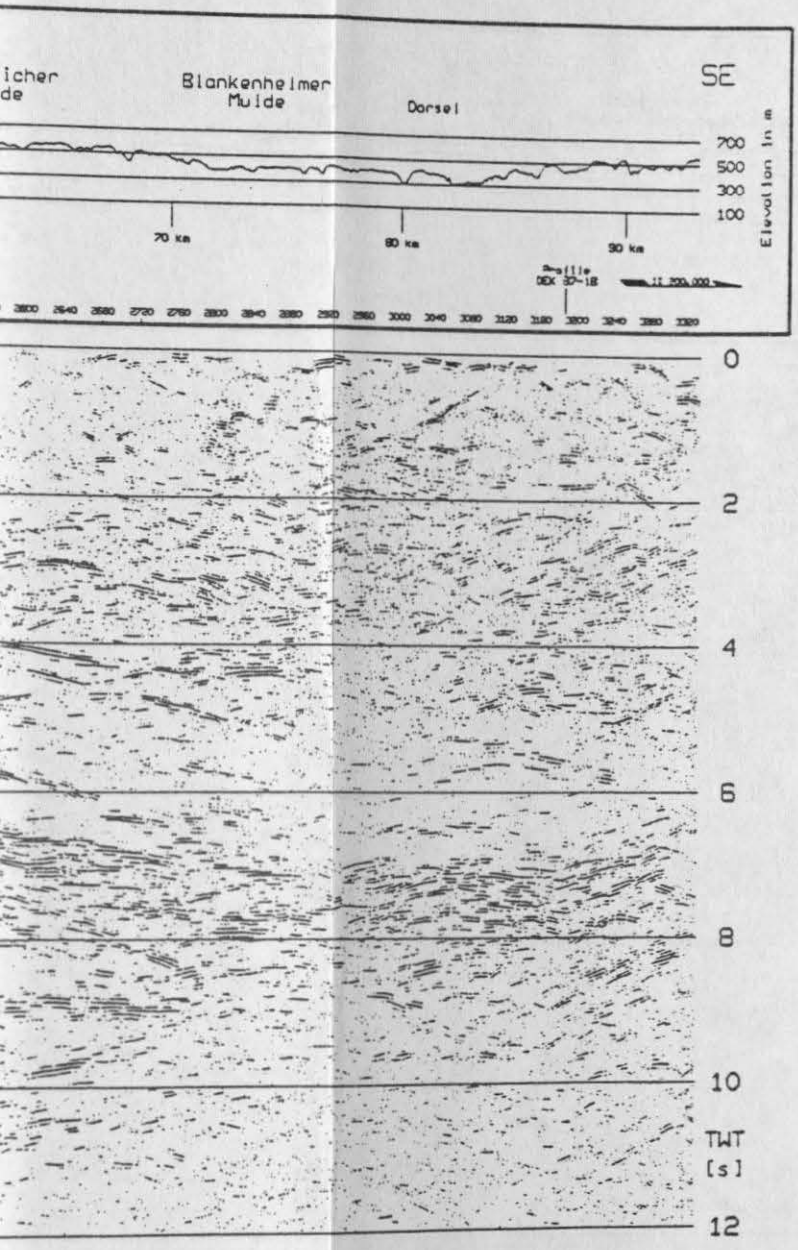

DEK '87 LINE 1A

FINAL STACK

Automatical Line-Drawing

Loc's: 1003 - 3332

Data Processed by: DEKORP Processing Center

Recording Parameters

Date:	August 87	Energy Source:	Vibroseis
Contractor:		Vibrator:	5 x IAVER
	Prakla-Seismos AG	Sweep:	12 - 48 Hz
Instrument:		Sweep Length:	20 s
	Sercel SN 388 / MTC-01	Vertical Stack:	5-fold
Channels/Record:	400	Source Spacing:	40 m
Sampling Rate:	4 ms	Geophone:	SM 4 / 10 Hz
Record Length:	16 s	Geophones/Group:	24
Filter:	Lo 12.5 Hz/18 dB		(In-Line Array)
	Hi 62.5 Hz/72 dB	Group Length:	40 m
Theor. Coverage:	200	Group Spacing:	40 m

Cable Configuration

1 Channel 300 301 400

NW |——| up |——| SE

-12060m Offset -120m 120m 4080m

Processing Parameters

1. Demultiplexing and Bad Trace Elimination
2. CMP Sorting (CMP-Spacing: 20 m)
3. Analytical Gain
4. Static Corrections to Floating Datum
5. Normal Moveout Corrections
6. Initial Muting
7. Automatical Scaling
8. Static Corrections to Constant Datum (Reference Plane 500 m above Sea Level)
9. Stacking (coverage ca. 160-fold)
10. Bandpass Filtering
11. Summation of Two Adjacent Traces
12. Coherency Enhancement
13. Automatical Clip-Scaling and Bias
14. Variable Area Display (Black = Positive = Compression Upward)

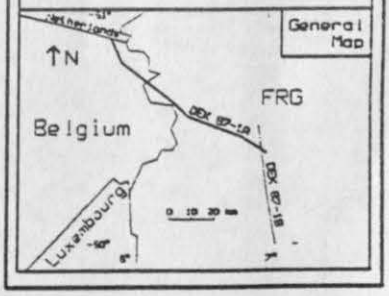

Figure: 5

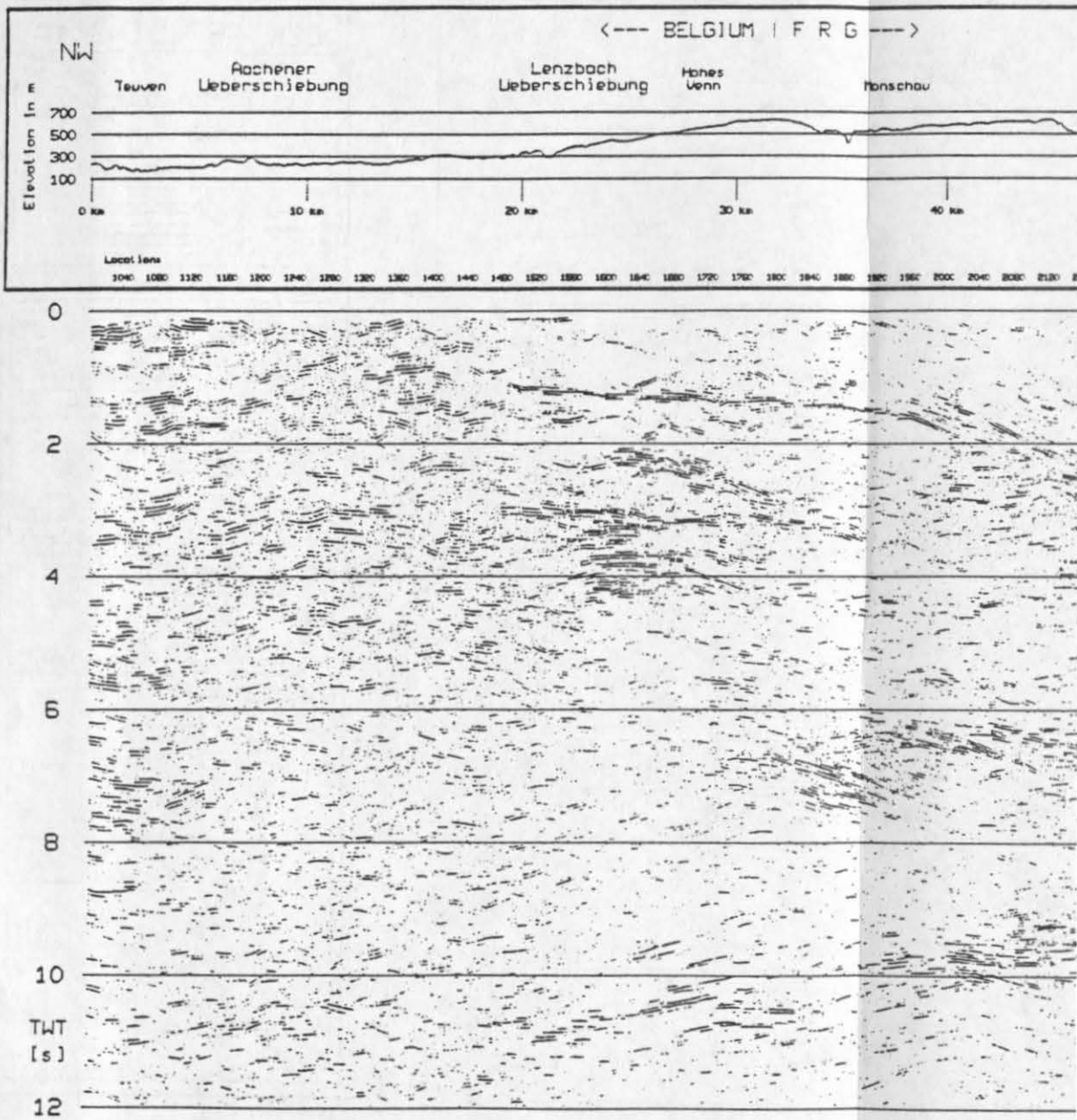
<--- BELGIUM | F R G --->
NW
Teuven
Aachener Ueberschiebung
Lenzbach Ueberschiebung
Hohes Venn
Monschau
Elevation in m
700
500
300
100
0 km
10 km
20 km
30 km
40 km
Locations
0
2
4
6
8
10
TWT [s]
12

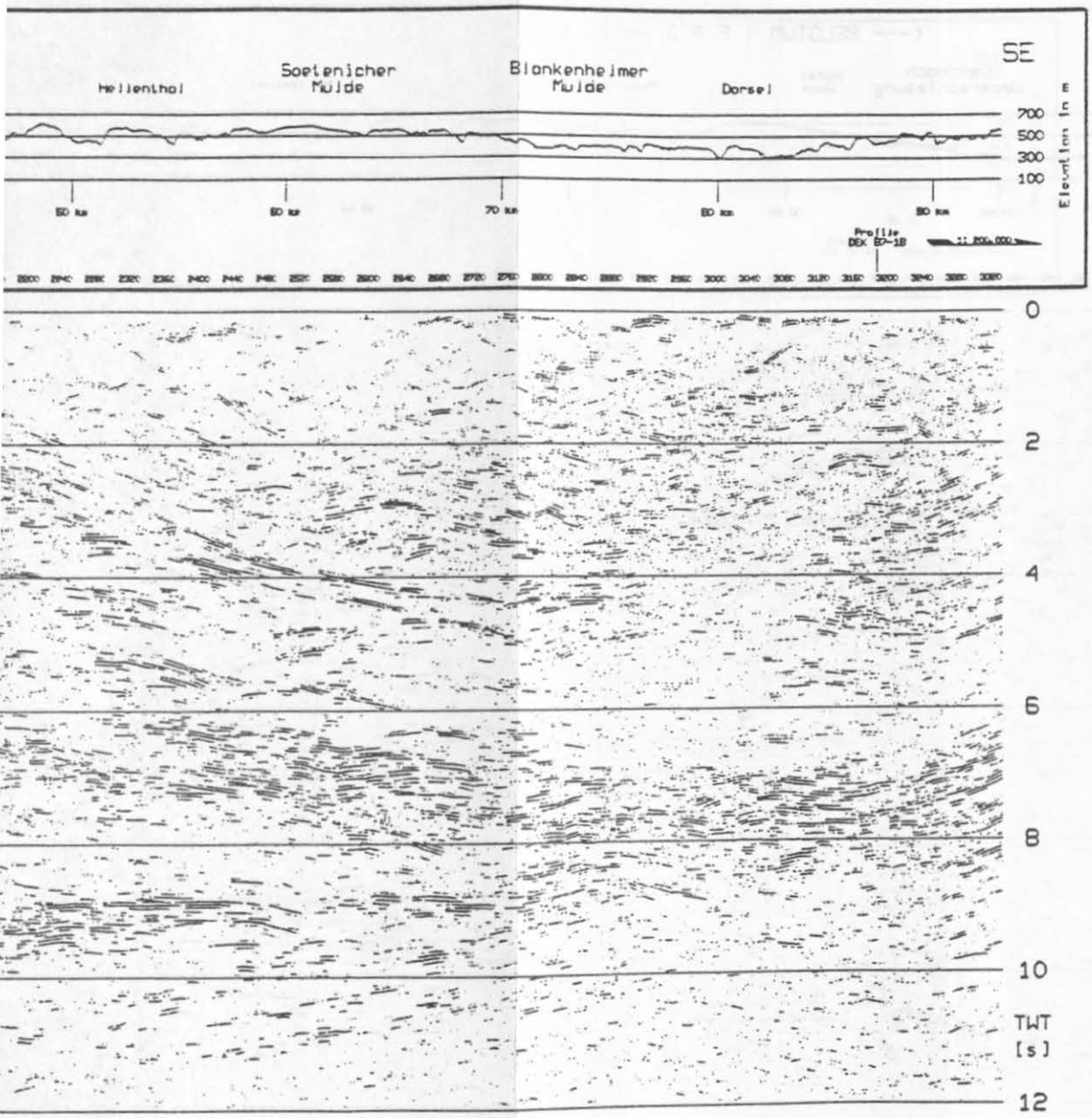
SE
Hellenthal
Soetenicher Mulde
Blankenheimer Mulde
Dorsel
700
500
300
100
Elevation in m
80 km
80 km
70 km
80 km
80 km
Profile DEX 87-1A
0
2
4
6
8
10
12
TWT [s]

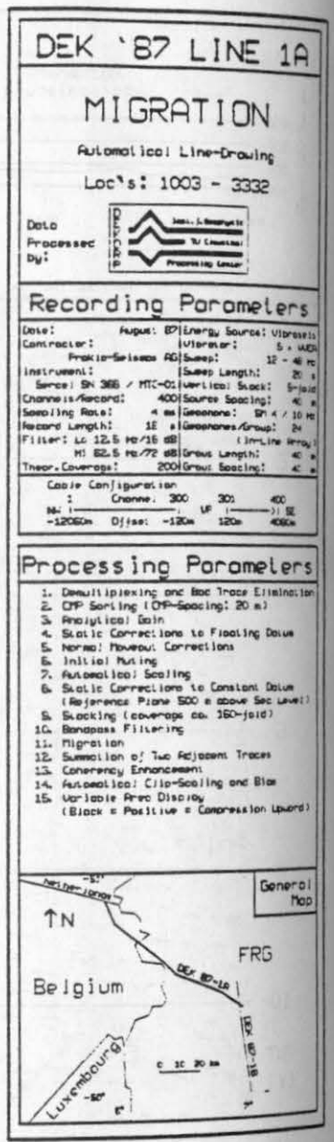
DEK '87 LINE 1A
MIGRATION
Automatical Line-Drawing
Loc's: 1003 - 3332
Data Processed by:
Recording Parameters
Processing Parameters
1. Demultiplexing and Bad Trace Elimination
2. CMP Sorting (CMP-Spacing: 20 m)
3. Analytical Gain
4. Static Corrections to Floating Datum
5. Normal Moveout Corrections
6. Initial Muting
7. Automatical Scaling
8. Static Corrections to Constant Datum
(Reference Plane 500 m above Sea Level)
9. Stacking (coverage ca. 160-fold)
10. Bandpass Filtering
11. Migration
12. Summation of Two Adjacent Traces
13. Coherency Enhancement
14. Automatical Clip-Scaling and Plot
15. Variable Area Display
(Black = Positive = Compression Upward)
General Map
N
FRG
Belgium
Luxembourg
DEK 87-1A

Figure: 6

Processing Sequence

Table 2:

FINAL STACK

(1) Demultiplexing

and Gain Recovery

(2) CMP Sorting

Crooked Line Analysis and Bad Trace Elimination

(3) Analytical Gain

Correction for Spherical Divergence and Absorption with T^2 down to ca. 3 s.

(4) Static Corrections

to Floating Datum

(5) Normal Moveout Corrections

Stacking velocities from 29 analyses, a combination of two different methods of analysis was used:

Constant Velocity Stacks each with 21 CMPs and 42 velocities

Semblance Analyses with 9 CMPs and 67 velocity functions

(6) Initial Muting

Offset-dependent, picked from 7 analyses

Mute max. 4.2 s at 12 km offset

(7) Automatical Scaling

500 ms window (AGC)

(8) Static Corrections

to Constant Datum (Reference Plane 500 m above Sea Level)

(9) Residual Static Corrections

Automatical/Subsurface-oriented

(10) Stacking

all traces, offset range from -12 to 4 km

coverage ca. 160-fold

(11) Bandpass Filtering

3 Windows **1: 13/18 Hz down to 3.2 s**

2: 11/16 Hz down to 8.5 s

3: 10/15 Hz down to 16.0 s

COHERENCY FILTERING of FINAL STACK

(12a) Coherency Filtering

11 Traces, Window 400 ms, max. Dip 7 ms/Trace

(13a) Summation (optional)

of two adjacent traces

MIGRATION of FINAL STACK

(12b) Scaling

Horizontal Trace Equalization

(13b) Resampling

from 4 ms to 8 ms

(14b) Migration

Finite-Difference (FD) Migration

Vmig from smoothed Vrms

Depth Step 40 ms

(15b) Summation (optional)

of two adjacent traces

PROCESSING AND INTERPRETATION OF DEEP SEISMIC REFLECTION DATA IN THE RHENISH MASSIF ALONG THE LINE BELCORP/DEKORP 1A (CCSS DATASET 1a AND 1b)

V.G. Krishna and K.L. Kaila

National Geophysical Research Institute, Hyderabad-500 007, India

Abstract

We present the results of poststack processing and interpretation of near-vertical reflection data in the western and central parts of the Rhenish Massif along the 93 km long line BELCORP/DEKORP 1A. The main objective of this data processing exercise is to improve the seismic image and study the deep crustal and uppermost mantle structure in this region. The processed seismic section clearly reveals a very strong and continuous reflective structure, extending over the central 60 km stretch of the line, in the upper crust. This southeast dipping reflector, starting at 0.5 s on the northwestern end and eventually bending into the subhorizontal at 5 s TWT, represents the well known shallow-angle Aachen Thrust in this region. The upper crust is otherwise generally less reflective up to about 6 s TWT, although a few bands of discontinuous reflector segments, possibly disturbed by the Aachen Thrust, are recognizable. The lower crust is highly reflective and is marked by an abrupt increase in reflectivity at 6-7 s TWT. However, an important feature of the lower crustal reflectivity in this region is a 1.5-2.0 s gap in the reflectivity, separating the two strong bands especially in the central and southeastern parts of the section. This feature represents a typical model of 'multiple finger type' reflectivity of the lower crust recognized by Meissner and Kusznir (1987) and may be indicative of rheological stratification of the crustal lithosphere. The Moho reflection in the central 55 km stretch of the section is well depicted by a marked increase of reflectivity at 9-10 s TWT, although it is weak on the northwestern and southeastern ends. There is a clear shift of 0.5 s in the Moho reflection time in the central part of the line (near CDP 4300), which may imply a faulting at the Moho boundary or an abrupt lateral velocity change. Coinciding with the region of strong Moho reflection, another band of weak, but well correlatable reflection event is observable at 10.5-11.0 s. We interpret this deep continuous event as a reflection from an interface within the uppermost mantle at relatively shallow depths.

Introduction

As a contribution to the CCSS workshop, the deep seismic reflection data in the western and central parts of the Rhenish Massif, along the NW-SE trending line BELCORP/DEKORP 1A (Figure 1), has been processed by application of poststack processing techniques with an objective to improve the seismic image and study the structure of the deep crust and uppermost mantle in this region. The deep reflection data on this 93 km long profile, acquired by the DEKORP group in 1987 using the Vibroseis method with 20 m CMP interval and 4 ms sample interval, has a maximum reflection time of 16 s after correlation. This profile runs from the Variscan foreland in Belgium across the Aachen Thrust (Faille du Midi) that is part of the North Variscan Deformation Front, across the Stavelot-Venn Anticline, and then arcs across the axial depression of the Eifel Nord-Sued Zone. The details of field techniques, data acquisition parameters and interpretation results are described by the DEKORP RESEARCH GROUP (1990,1991). This dataset was initially processed by the DEKORP PROCESSING CENTER at the Institute for Geophysics, Clausthal, Germany. The staked reflection data was made available in SEG-Y format on a magnetic tape (dataset 1b) for application of poststack processing techniques as well as in the form of plotted sections (dataset 1a) for interpretation of the deep structure along this line.

Data processing

Poststack processing of deep reflection data on the line BELCORP/DEKORP 1A has been carried out on the recently established seismic data processing system at the National Geophysical Research Institute, Hyderabad. The hardware configuration of this system consists of a CDC CYBER 180/850A host computer running the dual operating systems NOS and NOS/VE, a MAP IV array processor, a versatec plotter, large capacity disk storage units, high speed tape drive units and printers. The seismic data processing software package GEOMASTER of the Compagnie Generale de Geophysique, Masse, France, is running with its VOS Control system under the NOS operating system. The stacked reflection data is resampled to 8 ms for application of poststack processing sequence. The poststack processing sequence for the line BELCORP/DEKORP 1A consisted of frequency-wavenumber (f-k) dip filtering for attenuating steeply dipping coherent noise, followed by predictive deconvolution for suppressing the multiples, time variant band pass frequency filtering to readjust the spectrum, finally the amplitude equalization and display of the final stack section. Parameter optimization for each of these processes has been achieved by making a number of trial runs over a representative sample section in the central part of the line. We, however, show here only the final plots obtained after application of this processing sequence.

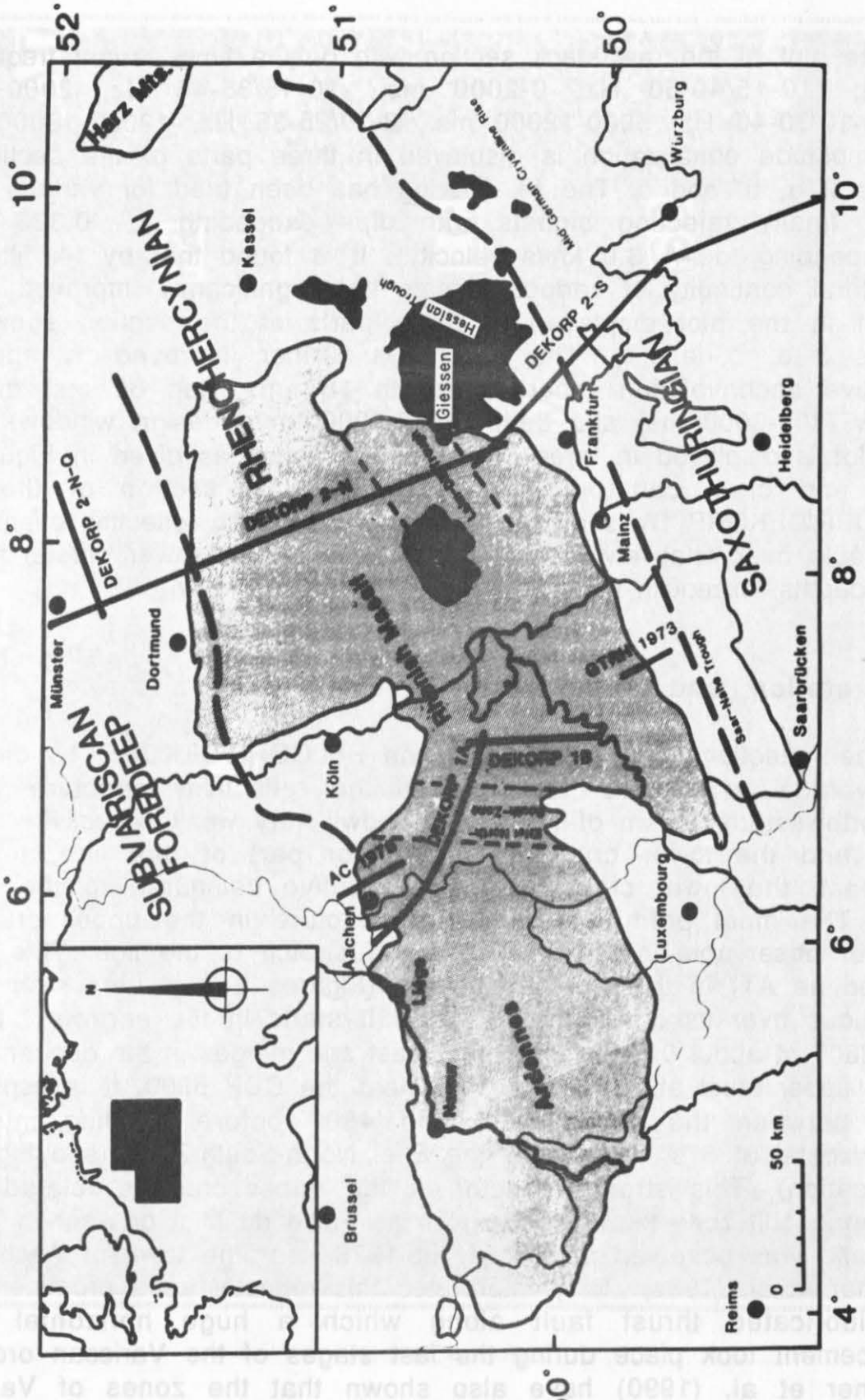

Figure 1: Map of DEKORP deep seismic reflection profiles in the Rhenish Massif (after DEKORP RESEARCH GROUP, 1990).

The plot of the raw stack section with only a time variant frequency filtering (10-15/40-50 Hz, 0-2000 ms., 10-15/35-45 Hz, 2000-5000 ms., 8-10/30-40 Hz, 5000-12000 ms., 8-10/25-35 Hz, 12000-16000 ms) and amplitude equalization is displayed in three parts of the section in Figures 2 a, b, and c. The f-k filtering has been tried for various pass bands, finally rejecting signals with dips exceeding +/- 0.333 s/km (corresponding to +/- 3.0 km/s velocity). It is found that by f-k filtering, the lateral continuity of various signals has significantly improved as is evident in the plot displayed in three parts of the section shown in Figures 3 a, b, and c. The section is further improved by applying predictive deconvolution (operator length 180 ms, gap 60 ms) on the shallow (300-6000 ms) and deep (5000-12000 ms) design windows. The final plot is displayed in three parts of the section as given in Figures 4 a, b, and c. It can be seen from the final section of the line BELCORP/DEKORP 1A, shown in Figure 4, that strong reflection events are observable over relatively long distances even at the lower crustal to the Moho depths, except in the northwestern 20 km of the line.

Interpretation and discussion

The reflection section along the line BELCORP/DEKORP 1A displays both vertical and lateral variations of the reflectivity structure. While the northwestern 20 km of the profile shows very weak reflectivity in the upper and the lower crust, on the major part of this line, towards southeast, the lower crust is highly reflective compared to the upper crust. The most prominent reflective structure in the upper crust, is however observable in the middle 60 km stretch of the line. This event (marked as AT) in the seismic sections (Figures 2-4) is very strong and continuous over its considerable length. It starts in the northwest at the CDP 2800 at about 0.5 s dipping southeast and merges in the deeper levels of the upper crust at about 5 s TWT near the CDP 5800. It is especially steep between the CDPs 4000 and 4800 before bending into the subhorizontal at 5 s TWT below the Eifel North-South-Zone (see Figure 1 for location). This strong reflector in the upper crust is related to a prominent fault zone known in Belgium as Faille du Midi or Aachen Thrust (AT), and was observed seismically in 1978 near the town of Aachen by Meissner et al. (1981). They interpreted this reflector as a prominent and well lubricated thrust fault along which a huge horizontal nape displacement took place during the last stages of the Variscan orogeny. Meissner et al. (1990) have also shown that the zones of Variscan compression are well preserved by shallow-angle thrust zones in the upper crust in the older massifs.

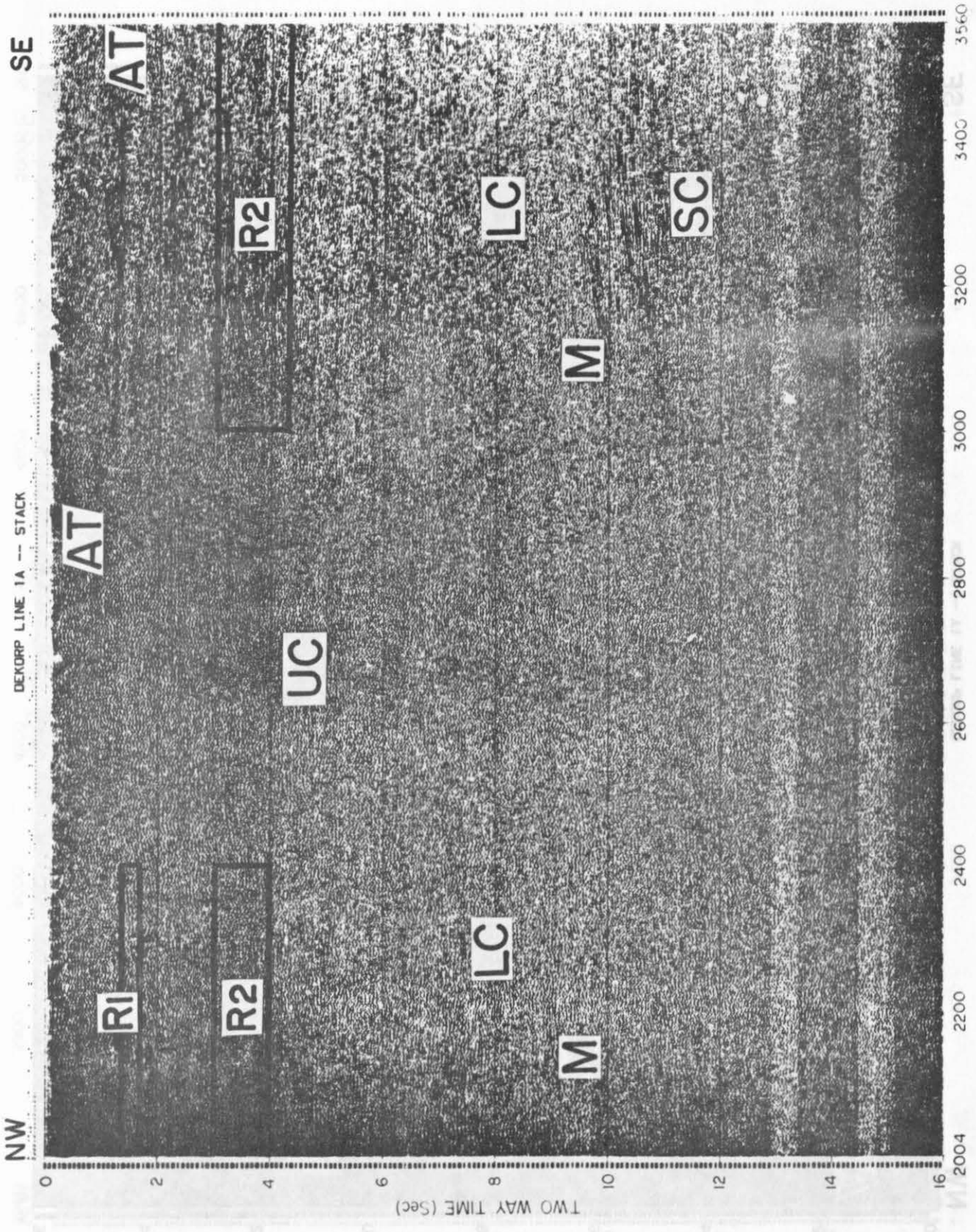

Figures 2 (a,b,c): Stack section (Two way time versus CDP locations) plotted with a time variant frequency filtering and amplitude equalization.

Figures 2b and 2c, see next pages.

NW
SE
DEKORP LINE 1A — STACK
AT
R2
UC
AT
R3
LC
M
SC
LC
M
SC
AT
TWO WAY TIME (Sec)
0
2
4
6
8
10
12
14
16
3561
3800
4000
4200
4400
4600
4800
5000
5115

Figure 2b:

NW
SE
DEKORP LINE 1A — STACK
R3
UC
R4
LC
AT
AT
LC
M
SC
5116
5400
5600
5800
6000
6200
6400
6670
0
2
4
6
8
10
12
14
16

Figure 2c:

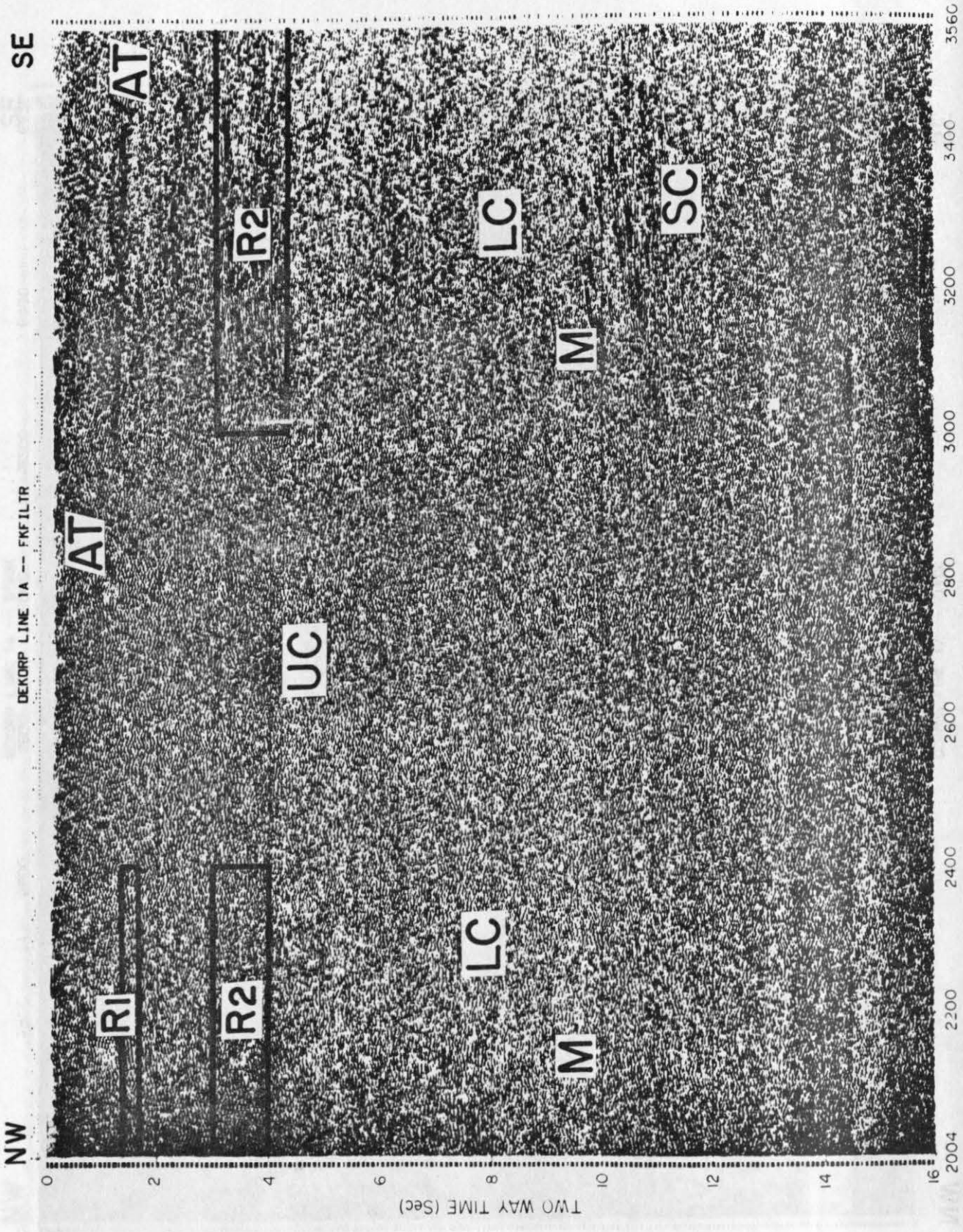

Figures 3 (a,b,c): Same as Figures 2, after application of the f-k filtering rejecting slopes exceeding +/- 0.333 s/km).

Figures 3b and 3c, see next pages.

NW
SE
DEKORP LINE 1A -- FKFILTR
AT
R2
UC
LC
M
SC
R3
AT
LC
M
SC
0
2
4
6
8
10
12
14
16
TWO WAY TIME (Sec)
3561
3800
4000
4200
4400
4600
4800
5000
5115

Figure 3b:

NW
SE
DEKORP LINE 1A -- FKFILTR
AT
R3
UC
R4
AT
LC
LC
M
SC
0
2
4
6
8
10
12
14
16
TWO WAY TIME (Sec)
5116
5400
5600
5800
6000
6200
6400
6670

Figure 3c:

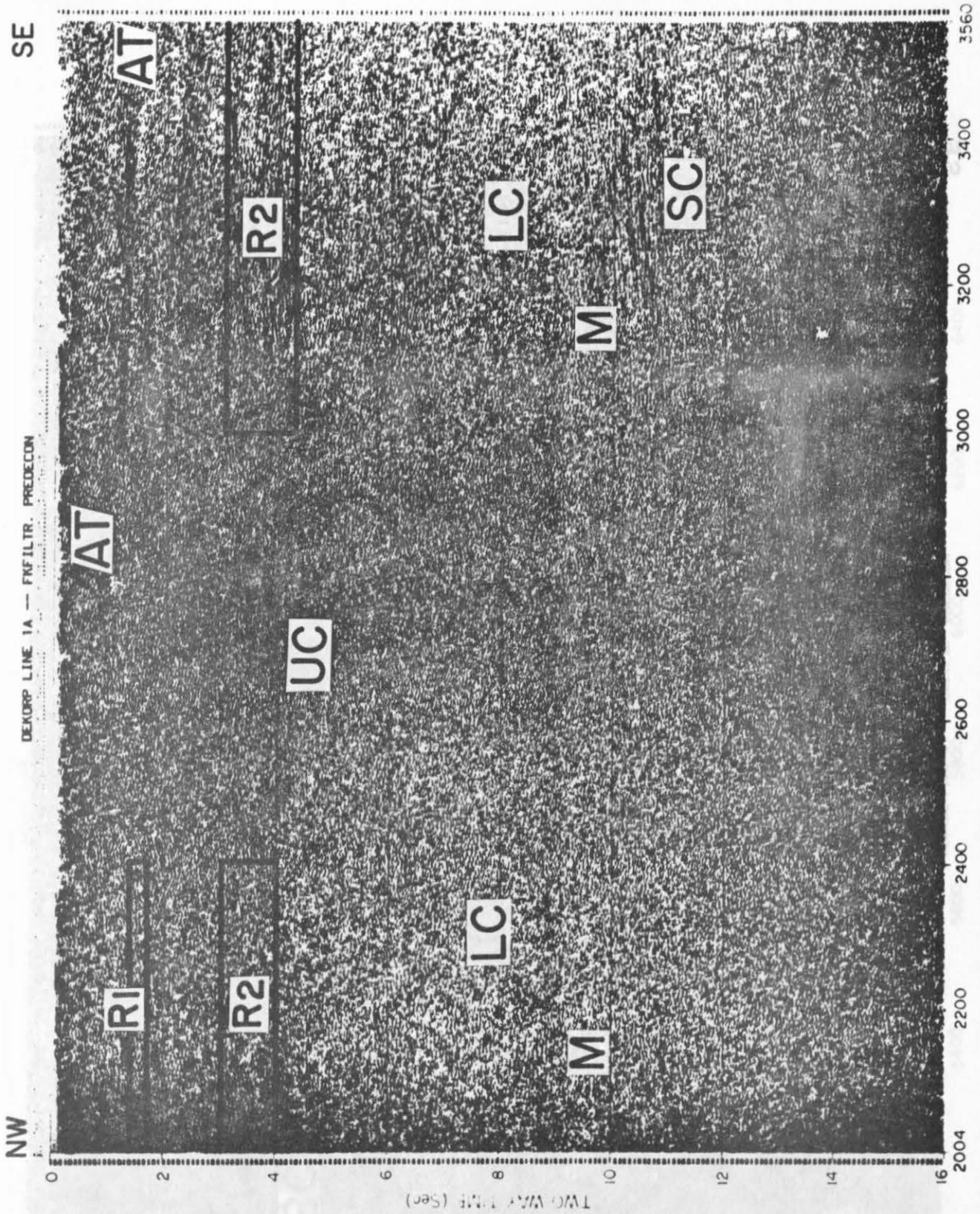

Figures 4 (a,b,c): Same as Figures 3, after predictive deconvolution. Various symbols in Figures 2-4 are: R1-R4 (bands of weak discontinuous reflector segments in the upper crust), AT (Aachen Thrust), UC (upper crust), LC (lower crust), M (Moho reflector), SC (subcrustal reflector).

Figures 4b and 4c, see next pages.

NW
SE
DEKORP LINE 1A -- FKFILTR. PREDECON
AT
R2
LC
SC
UC
M
AT
R3
LC
M
SC
AT
TWO WAY TIME (Sec)
0
2
4
6
8
10
12
14
16
3800
4000
4200
4400
4600
4800
5000
3561

Figure 4b:

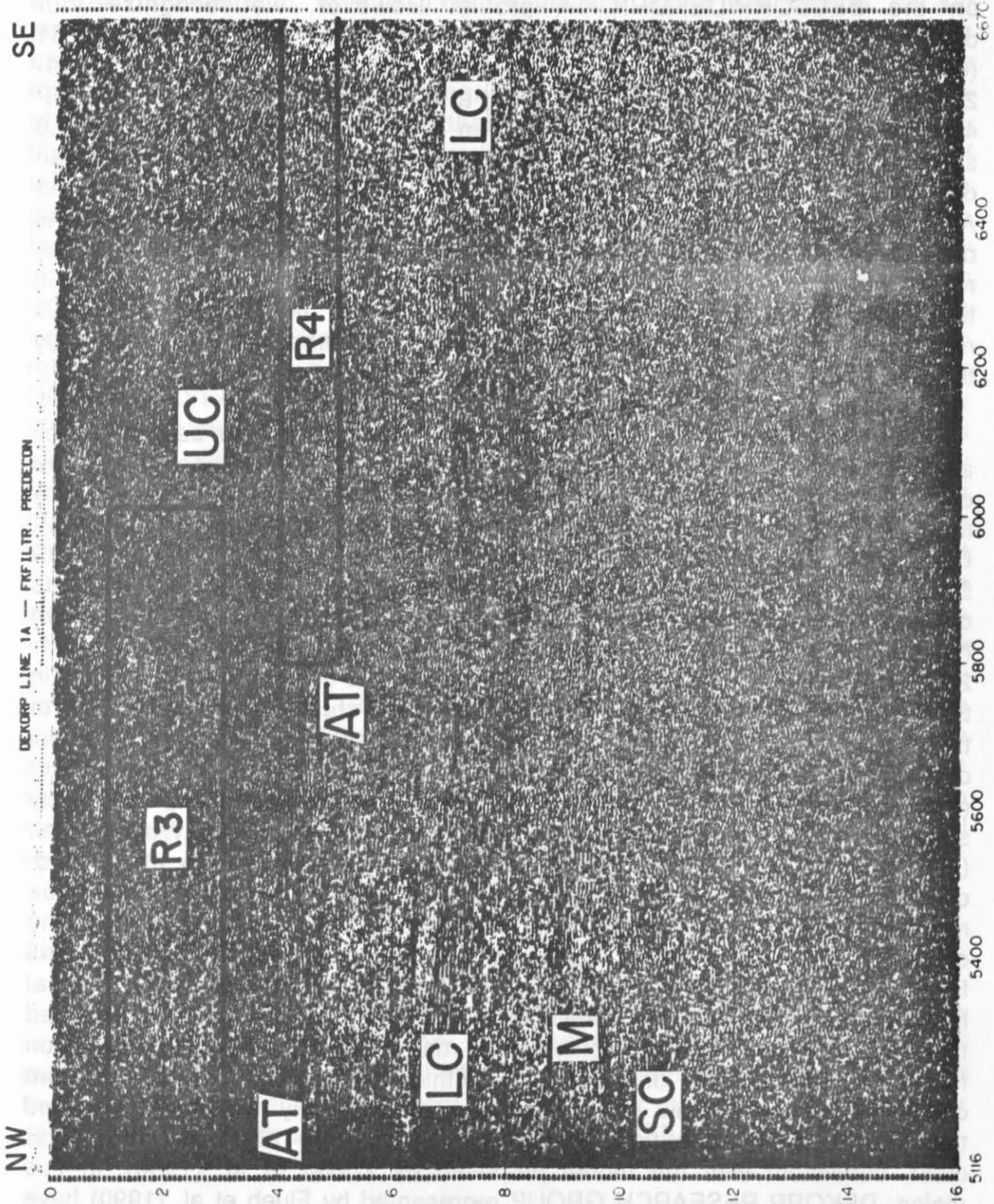
NW
SE
DEKORP LINE 1A — FKF ILTR. PREDECON
R3
UC
R4
AT
LC
AT
LC
M
SC
TWO WAY TIME (Sec.)
0
2
4
6
8
10
12
14
16
5116
5400
5600
5800
6000
6200
6400
6670

Figure 4c:

The upper crust (UC), up to about 6 s TWT, is generally less reflective on the BELCORP/DEKORP 1A profile. However, we recognize four discontinuous bands of weak reflections in the upper crust: marked as R1 (8 km long, CDP 2004-2400, at 1.3-1.7 s), R2 (28 km long, CDP 2004-2400, at 3.0-4.0 s, and CDP 3000-4000, at 3.0-4.3 s), R3 (26 km long, CDP 4700-6000, at 1.0-3.0 s), and R4 (17 km long, CDP 5800-6670, at 4.0-5.0 s). The reflectors corresponding to the band R2 appear to have been disturbed by the extensive activity that would have taken place on the Aachen Thrust and thus got abruptly terminated at about the CDP 4000. As described above, the Aachen Thrust merges into the R4 band of weak reflections at the base of the upper crust. It is possible that the events in the reflection bands R2 and R3 may represent the same contiguous reflector in the upper crust that probably got disturbed and separated by the Aachen Thrust.

The top of the lower crust (LC) in this region seems to be marked by an abrupt increase in the reflectivity at 6-7 s TWT. Especially in the central and the southeastern parts of this line very strong and relatively long horizontal reflector segments from CDP 3560-4300 (at 6.0-7.5 s), CDP 4300-5115 (at 5.0-7.5 s), CDP 5115-5800 (at 6.5-8.0 s) and CDP 5800-6670 at (7.0-8.5 s) represent the top of the lower crust. Its continuation on the northwestern end of the line, although weak, can however be correlated with reflection events at 7.0-7.5 s (CDP 2004-2400) and 6.0-7.5 s (CDP 3000-3560). There is a clear gap of 1.5-2.0 s in the reflectivity in the deeper part of the lower crust, before the onset of the strong Moho reflectivity. This feature corresponds to a typical model of the 'multiple finger type' reflectivity proposed by Meissner and Kusznir (1987) and Wever et al. 1987). The model consistent with this reflectivity structure of the lower crust has recently been interpreted by Wever et al. (1990), as having a strong P wave velocity and viscosity jump at the mid-crustal discontinuity. According to them, the brittle regime may be reached again between the two ductile regions thus explaining the occurrence of the 'finger type' reflectivity in the lower crust. This feature is indicative of rheological stratification of the crustal lithosphere in this region. Meissner and Kusznir (1987) also suggested that the 'multiple finger reflection type' may be generated by a transition from wet to partially dry rheology within the lower crust giving two distinct relatively narrow low viscosity zones. It may further be inferred that the P wave velocities should substantially be higher in the lower crust, consistent with the model proposed by Wever et al. (1990), in this region. DEKORP RESEARCH GROUP represented by Flueh et al. (1990) have also found quite high P wave velocities of the order of 7.0 km/s in the lower crust in the Rhenish Massif region from the wide-angle Vibroseis data, consistent with this inference.

The reflection 'Moho' (M) is also well depicted by an abrupt increase of the reflectivity at 9-10 s TWT, especially along the central 55 km stretch of the profile. However, at the northwestern and southeastern ends, each 18-20 km long, the Moho reflection is very weak although some discontinuous events may be observable at 9-9.5 s. This lateral variation of the reflectivity may indicate that the Moho is not a sharp boundary throughout but probably more gradational especially at the two ends of the line. We observe a clear shift of 0.5 s at the CDP 4300 in the Moho reflection time, which may imply a real shift of the Moho boundary due to faulting or an abrupt lateral velocity change. The Moho reflection is very clearly correlatable at 9.5-10.0 s from CDP 3000-4300 and at 9.0-9.5 s from CDP 4300-5800. In the region of the strong Moho reflectivity (i.e. from CDP 3000-5800) we recognize a rather weak, but well correlatable reflection event at 10.5-11.0 s TWT. The preliminary interpretation by the DEKORP RESEARCH GROUP (1990) suggests that this band of energy below the Moho reflection might indicate a crust-mantle transition rather than a crust-mantle discontinuity. In our opinion, however, this deep event may be representing a reflection boundary below the Moho in the uppermost mantle. This is because a number of explosion seismic experiments on long range profiles, in the western Europe and other regions, brought out new results on the vertical velocity structure at subcrustal depths. These models clearly reveal regions of alternating high and low velocity layers with velocity contrasts at their boundaries as large as those found at the Moho at relatively shallow depths below the Moho (Fuchs et al., 1987). As pointed out by Fuchs (1986), when the velocity contrasts are so large then, it is possible to observe near-vertical reflections from these shallow velocity discontinuities at subcrustal depths. Therefore the reflection section on this profile may serve as a good example to substantiate observations of near-vertical reflections from subcrustal reflectors.

Acknowledgements

We are grateful to the Director, National Geophysical Research Institute, for providing necessary facilities to undertake this study and permission to publish the paper. We are also grateful to the organizers of this workshop, especially to Ernst R. Flueh, for providing the necessary datasets for this study and a reprint of DEKORP RESEARCH GROUP (1990).

References

DEKORP RESEARCH GROUP 1990: Results of deep-seismic reflection investigations in the Rhenish Massif; Tectonophysics, 173, 507-515.

DEKORP Research Group, represented by Flueh, E.R., Klaeschen, D., and Meissner, R., 1990: Wide-angle Vibroseis data from the western Rhenish Massif; In: Leven, J.H., Finlayson, D.M., Wright, C., Dooley, J.C., and Kennett, B.L.N. (Eds.); Seismic Probing of Continents and their Margins; Tectonophysics, 173, p. 83-93.

DEKORP Research Group 1991: Results of DEKORP 1 (BELCORP-DEKORP) deep seismic reflection studies in the western part of the Rhenish Massif; Geophys. J. Int., 106, pp. 203-227.

Fuchs, K. 1986: Reflections from the subcrustal lithosphere; In: Reflection Seismology: The continental Crust, Geodynamics Series, AGU, Washington, D.C., 14, 67-76.

Fuchs, K., Vinnik, L.P., and Prodehl, C. 1987: Exploring heterogeneities of the continental mantle by high resolution seismic experiments; In: Composition, Structure and Dynamics of the Lithosphere-Asthenosphere-system, Geodynamics Series, AGU, Washington, D.C., 16, 137-154.

Meissner, R. and Kusznir, N.J. 1987: Crustal viscosity and the reflectivity of the lower crust; Annales Geophysicae, 5B, 365-374.

Meissner, R., Wever, Th., and Sadowiak, P. 1990: Reflectivity patterns in the variscan mountain belts and adjacent areas: an attempt for a pattern recognition and correlation to tectonic units; Tectonophysics, 173, 361-378.

Meissner, R., Bartelsen, H. and Murawski, H. 1981: Thin-skinned tectonics in the northern Rhenish Massif; Germany, Nature, 290, 399-401.

Wever, Th., Meissner, R., and Sadowiak, P.1990: Comparative investigations of continental reflectivity; Tectonophysics, 173, 199-206.

Wever, Th., Trappe, H. and Meissner, R. 1987: Possible relations between crustal reflectivity, crustal age, heat flow and viscosity of the Continents; Annales Geophysicae, 5B, 255-266.

APPLICATION OF IMAGE ENHANCEMENT AND MIGRATION TECHNIQUES TO DEKORP DATA.

Bernd Milkereit[1], Carl Spencer[1], and Ernst R. Flueh[2]

[1] *Geological Survey of Canada, Ottawa, Canada, K1A 0Y3*
[2] *Geomar, Wischhofstr. 1-3, 2300 Kiel, F.R. Germany*

Summary

New image enhancement techniques and migration schemes are applied to assist in the interpretation of DEKORP 1A multichannel seismic reflection data. Results of a computerefficient noise suppression and coherency enhancement scheme based upon the combination of multi-trace localized slant stacking and median filtering are presented. Enhanced data are weighted versions of the input data and no data mixing or smearing of information is required. In addition, results of multi-attribute analysis will be presented as color overlays to the conventional seismic section allowing correlation with subsurface structure and the easy identification of features such as lateral changes in the wavefield.

Coherency enhancement

In order to separate the signal and noise components of seismic data u(x,t) the following assumptions are made: (a) background noise has no spatial coherency, thus phase-coherent signal can be separated from background noise on the basis of coherency estimates; and (b) coherent noise can be separated from coherent signal on the basis of different dips (slowness).

Here we apply a semblance-based filter in the time domain that has been designed to enhance coherent seismic energy by simply suppressing incoherent background noise. A detailed description of the coherency filter can be found in Milkereit and Spencer (1990a).

The coherency enhanced data U(x,t) are given by multiplying the observed image u(x,t) with the coherency weight image C(x,t):

$$U(x,t)=u(x,t)C(x,t)^{y}+d \quad , \qquad (1)$$

where y is a scaling factor and d corresponds to a dc shift.

It is worth emphasizing that the enhanced data U(x,t) are weighted versions of the input data u(x,t) and that no data mixing or smearing are involved.
Data from the DEKORP transect are shown in variable area display in Figure 1-A (11 s, 1:1 display for 6 km/s, 5% bias for variable area display). The stacked section exhibits a significant background noise level.The coherency enhanced section is shown in Figure 1-B. Processing and display are based on a -0,35 to 0,35 s km^{-1} dip, an exponent of y=1,5 for scaling the coherency weights C(x,t), and dc shift (bias) of 5 per cent of the overall rms-amplitude.

Post stack depth migration

We have investigate the effects of various interval velocity models on poststack migration. The velocity functions are shown in Figure 2. Velocity model A is a simple gradient model, model B accounts for steep velocity gradients or fist order discontinuities, and model C by the DEKORP Research Group (1990) represents a `realistic´ velocity model´for the DEKORP profile. Migration results are shown in Figure 3. None of the velocity models provides superior migrated images and diffracted energy is focused equally well by each of the three velocity models.

Multi-attribute analysis

Attributes of seismic data can be grouped into single- or multi-trace attributes, based on their method of calculation. For example, coherency estimates can be obtained from semblance or cross-correlation analyses. In addition, there are a number of attributes such as stacking velocities, interval velocities, multiple identification, polarisation, and variation of Poisson´s ratio, that can be obtained from the interactive processing of seismic data. Once a seismic attribute has been assigned to each sample of a seismic section, the attribute data themselves can be considered as a two dimensional image. Attributes are calculated for each sample of the wavefield from two-dimensional subsets of the input data (see Figure 4-a). Details of this process are given by Milkereit and Spencer (1990b).

Here we use a combination of single-trace attributes (such as reflection strength and instantaneous frequency) and multi-trace attributes (such as dip and coherency) to analyze DEKORP data. For display we use the HLS-scheme that is best suited to those cases where there is a hierarchical relationship between attributes (in which one attribute is considered of primary importance).

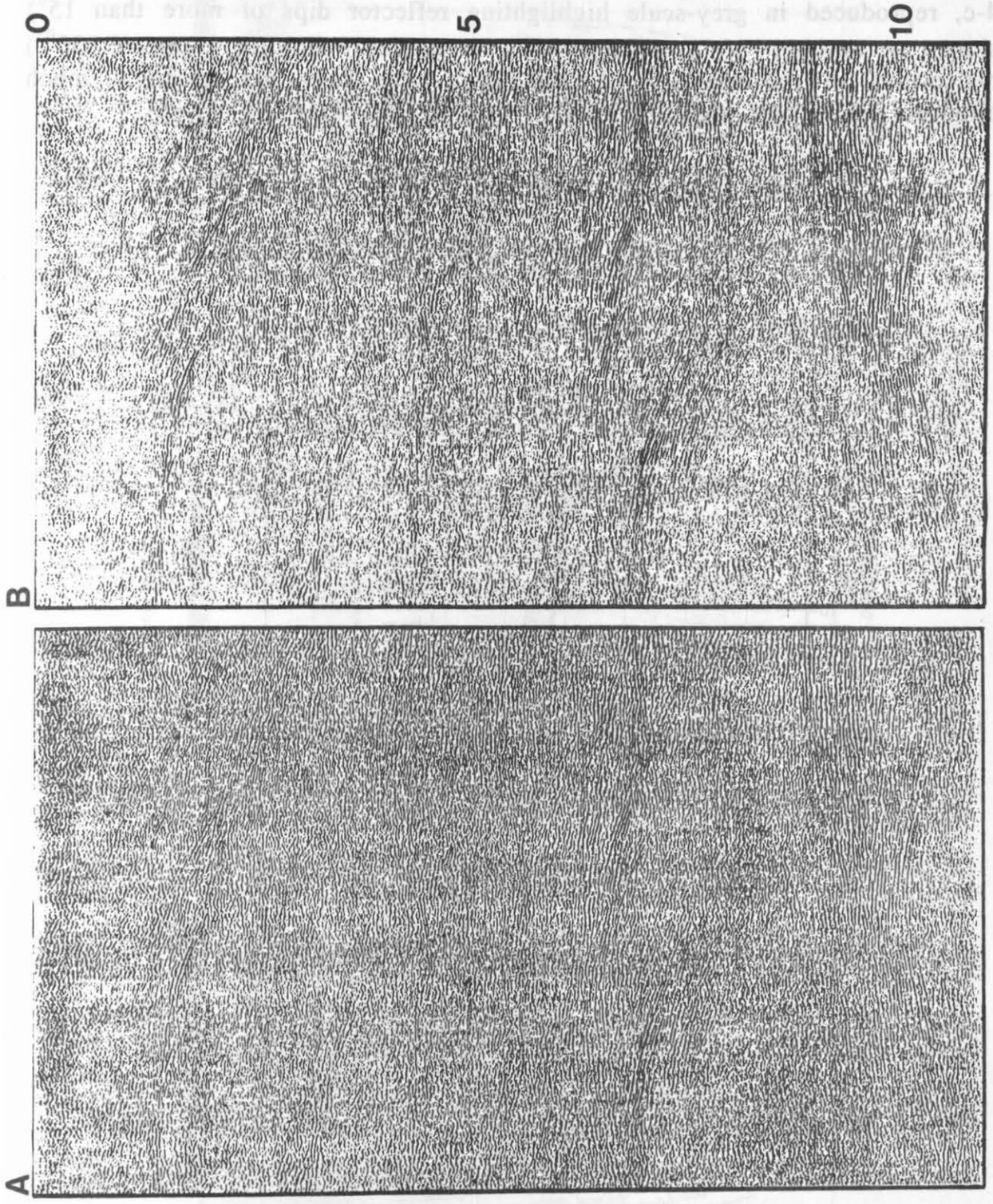

Figure 1 A: Data example from the DEKORP profile. B: Display of coherency enhanced DEKORP data. Variable area display with 5% bias applied to both data sets.

An example of the application of multi-attribute composite colour images to a real data set is shown in Figure 4. The multi-attribute display (Figure 4-c, reproduced in grey-scale highlighting reflector dips of more than 15^0) shows a number of low amplitude, southward dipping (approx. 30^0) reflections in the Eifel Nord-Sued Zone that have not received much attention in earlier interpretations.

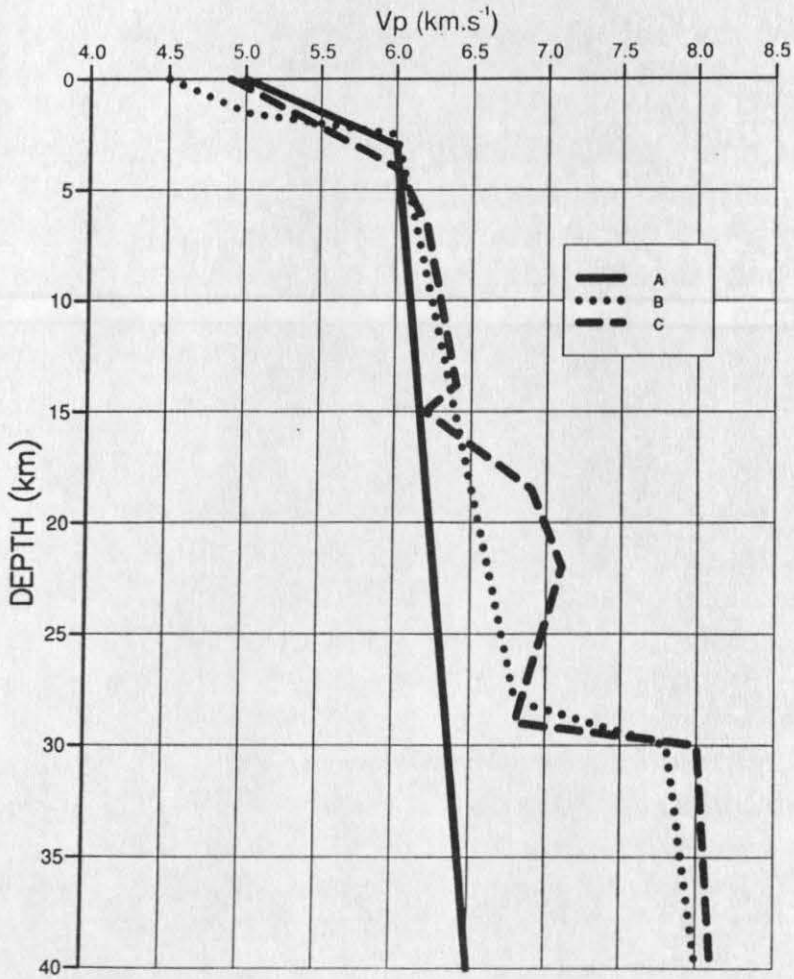

Figure 2 Velocity models for poststack depth migration of DEKORP profile. A: Simple gradient model, B: Model with steep velocity gradients, C: Model presented by the DEKORP Research Group (1990).

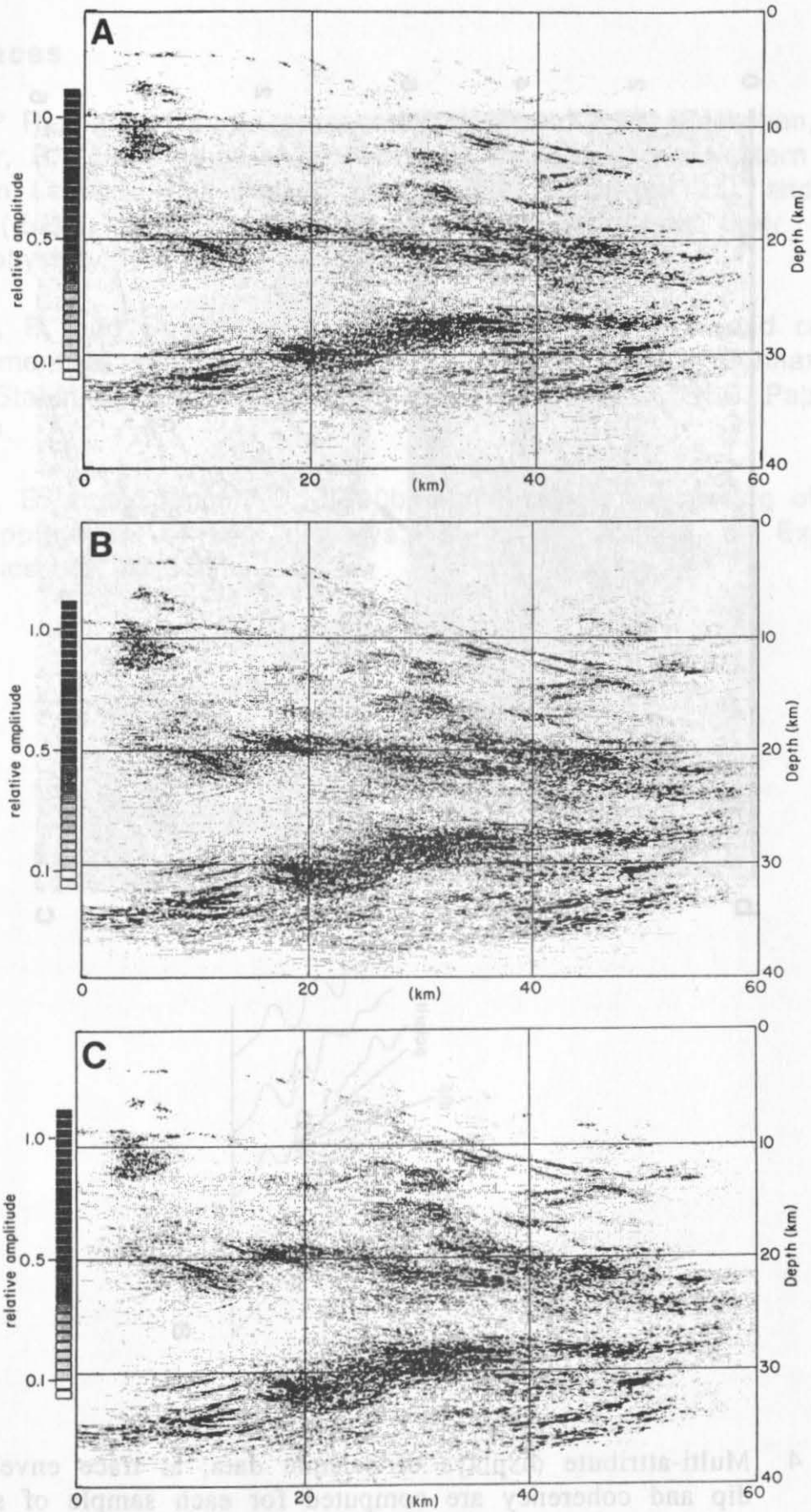

Figure 3 Trace envelope display of the depth migrated DEKORP data for velocity models A, B and C.

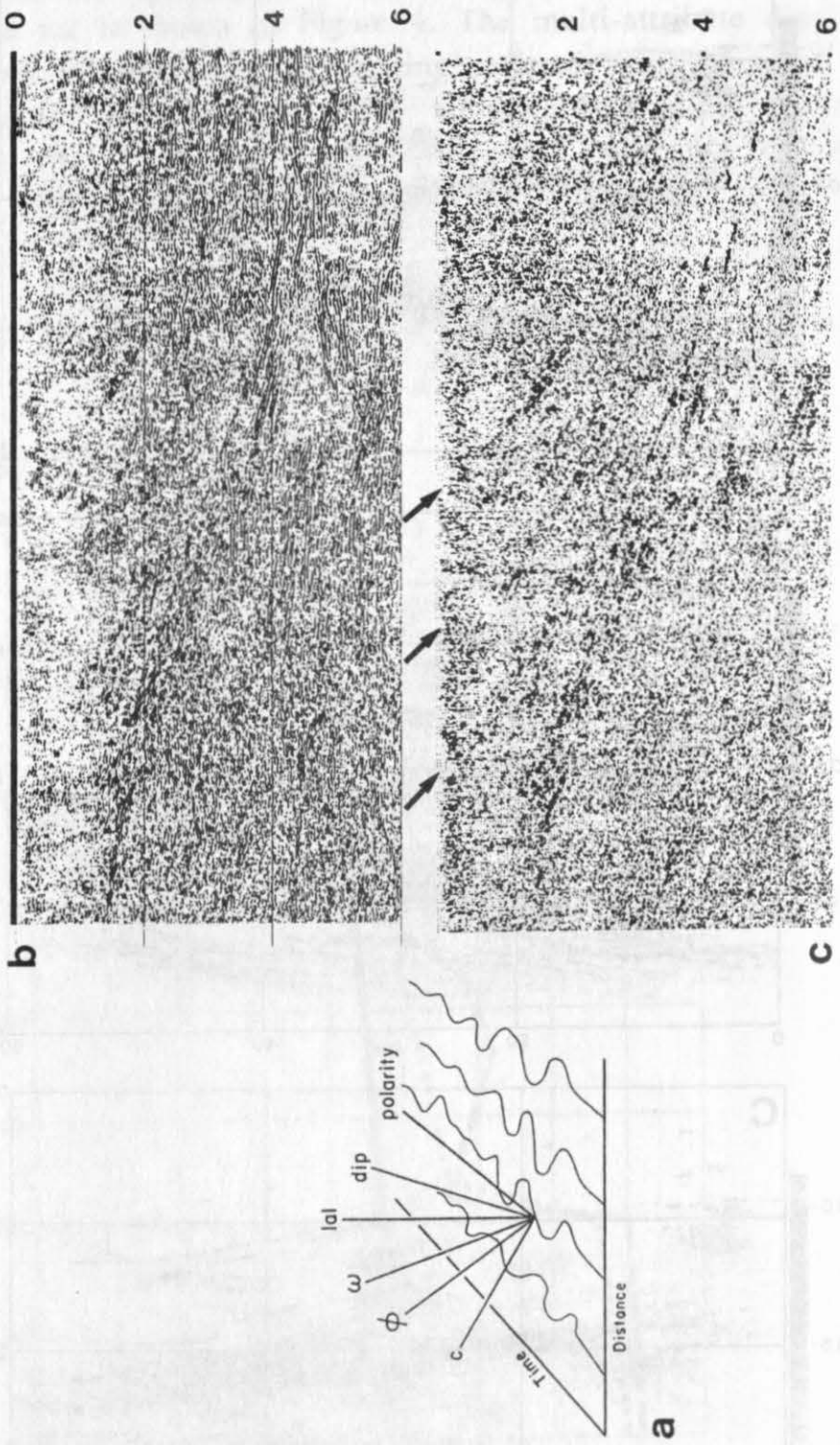

Figure 4 Multi-attribute displays of seismic data; a: trace envelope, dip and coherency are computed for each sample of stacked section; b: data example from the DEKORP profile; c: multiattribute display (reproduced in grey scale) highlighting coherent southdipping reflections in the Eifel Nord-Sued Zone.

References

DEKORP Research Group, represented by Flueh, E.R., Klaeschen, D., and Meissner, R., 1990: Wide-angle Vibroseis data from the western Rhenish Massif; In: Leven, J.H., Finlayson, D.M., Wright, C., Dooley, J.C., and Kennett, B.L.N. (Eds.); Seismic Probing of Continents and their Margins; Tectonophysics, 173, p. 83-93.

Milkereit, B. and Spencer, C., 1990a: Noise suppression and coherency enhancement of seismic data; In: F. Agterberg and G. Bonham-Carter, (Eds.); Statistical Applications in the Earth Sciences, GSC Paper 89-9, 243-248.

Milkereit, B. and Spencer, C., 1990b: Multi-attribute processing of seismic data: Application of dip displays; Canadian Journal of Exploration Geophysics, 26, 47-53.

RE-PROCESSING OF LINE BELCORP/DEKORP 1A (CMP 3366-3965) CCSS DATA SET 1C

Claus W. Lange and Peter K. Stiller

PREUSSAG Leibniz-Rechenzentrum GmbH, Hannover, Germany

Abstract

A re-processing of a part of the Line BELCORP/DEKORP 1A (Meissner and Bortfeld, 1990) was carried out on CMP sorted "raw" data provided by CCSS. The following processing sequence was applied: Automatic gain control, predictive deconvolution, narrow spaced velocity analyses, CMP consistent residual static correction, CMP stacking, frequency filtering, gain control, coherency filtering, FD-migration after stack, and instantaneous amplitude of the final stacked and final migrated section.

The final results show correlating reflections of good quality in three time zones: 1.0 s through 3.5 s, 6.0 s through 7.5 s and 9.5 s through 11.0 s. Improvements of the quality were achieved by carefully determined stacking velocities, mainly in the upper part, by CMP consistent residual static corrections and by coherency filtering.

The instantaneous amplitude sections and additionally the final stacked section are displayed in color. The color makes events better visible and the correlation of reflections easier, i.e. color aids in interpretation of the sections.

Introduction

The re-processing has been carried out as a contribution to the CCSS workshop in Kiel-Fellhorst, FRG on "Seismic Studies of Laterally Heterogeneous Structures - Interpretation and Modelling of Seismic Data".

The data to be re-processed cover a small part of BELCORP/DEKORP line 1a: CMP 3366 through CMP 3965 (Meissner and Bortfeld, 1990). The line was recorded in August 1987 by PRAKLA-SEISMOS using Vibroseis (20 s sweep, 12-48 Hz), with 400 traces per seismogram, 40 m geophone group spacing and 40 m VP-interval resulting in a subsurface coverage of max. 200 fold. One geophone layout - asymmetric split spread - covers 16.160 m with shot farthest traces of 12.080 m NW and 4.080 m SE.

The FINAL STACK of a part of the line, processed by DEKORP PROCESSING CENTER at the Institute of Geophysics at Clausthal, FRG, (Fig. 1) shows good reflecting events down to 13 s. The part to be re-processed is indicated by heavy lines in the upper part of the section. The aim of the reprocessing is to improve the quality of the results and to compare various processing approaches.

Re-Processing

The input data for the re-processing were provided by CCSS on magnetic-tape in form of CMP sorted "raw" traces. This pre-processing was done by the DEKORP PROCESSING CENTER, Clausthal. The field statics to datum level of 500 m were supplied in the trace headers.

The re-processing was carried out by PREUSSAG Leibniz-Rechenzentrum GmbH, Hannover, on a PHOENIX-VPU System (Volumetric Processing Unit, VAX 11/785, CSPI MAP 300 Array Processor) of Seismograph Service Ltd., England.

1. Re-Processing Sequence

Starting from CMP sorted "raw" data the following processing steps were applied using standard processing technics:

STACKING

(1) Bandpass Filter : 8/12-70/90 Hz

(2) Scaling AGC : Window 1000 ms

(3) Static Corrections
Datum Statics : 500 m NN

(4) Predictive Deconvolution
Pred. Distance : 24 ms
Operator Length : 200 ms
Design Window : 200 ms - 10.000 ms

(5) Muting

(6) Velocity Analyses spaced every km
12 CMPs
Velocity Range : 2500 m/s - 8800 m/s

(7) Dynamic Correction

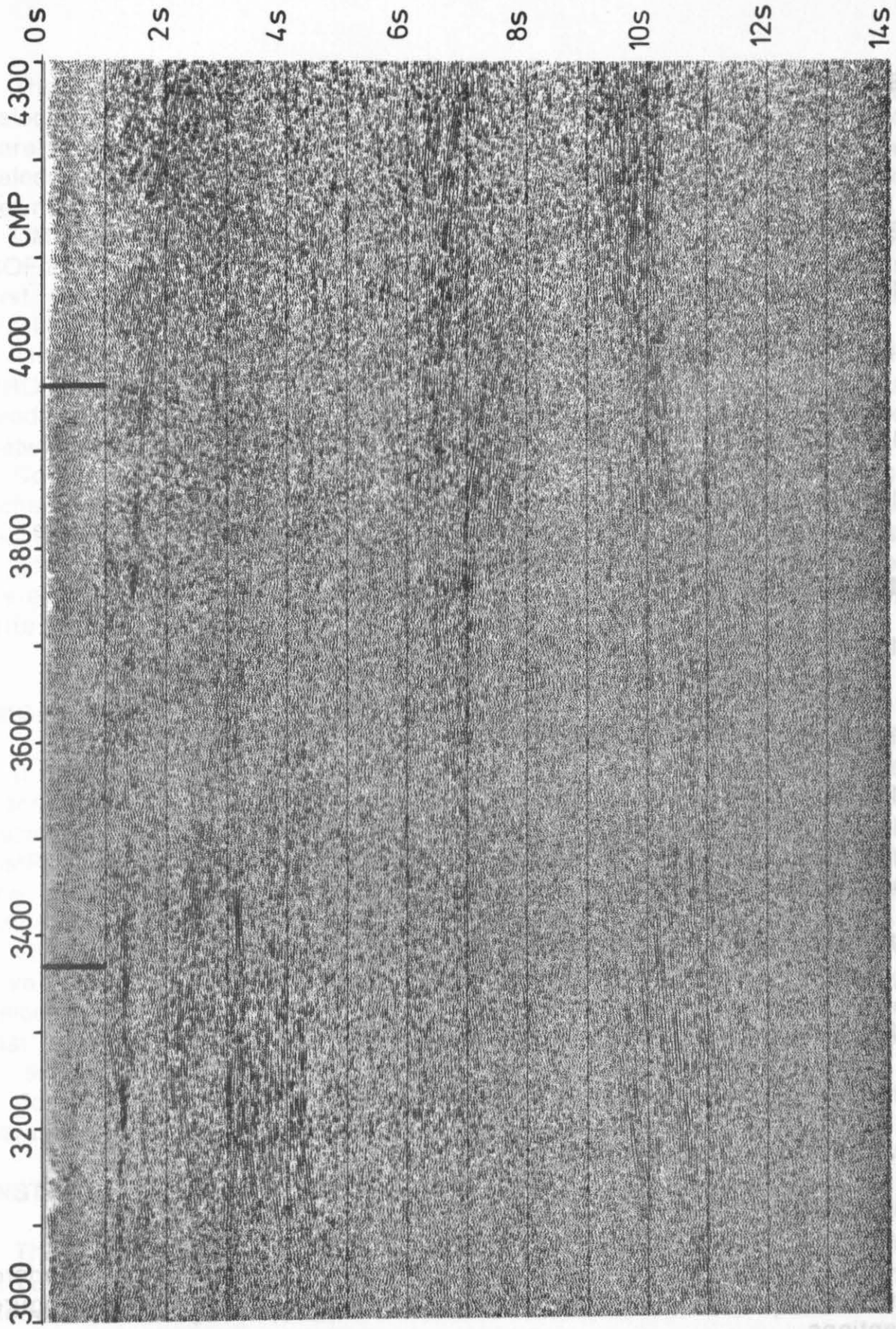

Figure 1: STACK-FILTER
Part of BELCORP/DEKORP line 1a, processed by DEKORP PROCESSING CENTER at the Institute for Geophysics at Clausthal, FRG. The data to be reprocessed are marked by heavy lines.

(8) Residual Static Corrections
CMP consistent (COST)
Window : 500 ms - 11 000 ms
Pilot Traces : STACK-COFILT

(9) Stacking : 160fold

(10) Bandpass Filter
0 - 3200 ms : 10/17-37/47 Hz
3200 - 8500 ms : 10/15-37/47 Hz
8500 - 16000 ms : 10/15-35/44 Hz

(11) Scaling AGC : Window 5000 ms

(12) Coherency Filtering : Scan 15 traces
Dip Range +- 7 ms/trace

MIGRATION

(13) FD-Migration with smoothed Stacking Velocities
Input Stacking (9)

(14) Bandpass Filter as given in (10)

(15) Scaling AGC : Window 5000 ms

ANALYTICAL SIGNAL

(16) Instantaneous Amplitude (Envelope)
Input Coherency Filter (12)

(17) Instantaneous Amplitude (Envelope)
Input Migration (15)

2. Re-Processing Remarks

STACKING

The processing sequence is set up straight forward using standard processing procedures. The processing steps are given in the figure captions.

The predictive deconvolution was mainly applied to suppress coherent noise. Therefore, a 24 ms prediction distance was chosen to cope with the none minimum phase Vibroseis data without minimum delay transformations and to prevent the blow up of high frequencies.

The main effort was put on the dynamic corrections, i.e. on the stacking velocities. Thus, velocity analysis were computed every one kilometer and carefully interpreted. Each analysis contains 12 CMPs stacked in the velocity range from 2500 m/s through 8800 m/s. The results were good down to 7 s, but very poor below 7 s.

CMP consistent static corrections were computed using the STACK-COFILT section (12) as pilot traces. Therefore, the processing was run in a first pass without residual static corrections (8) and then, for the final stacking, in a second pass with residual statics.

The bandpass filter (10) is the filter which was used by DEKORP PROCESSING CENTER. The data were finally scaled using an AGC with a window of 5000 ms. The large window was chosen to scale down the noise between the time zones with strong reflections.

Coherency filtering (12), named COFILT, uses a simple form of coherency measurement. An odd number of traces is used to scan the data along different dips within a given dip range for coherency maxima. Thus, a coherency trace is calculated, which is used to scale the center trace. Here, 15 traces and a dip range of +- 7 ms/trace were used for coherency filtering.

MIGRATION

In order to avoid edge effects from the migration process, about 300 traces from the DEKORP processing were added on both sides of the section. The migrated part of the line therefore covers CMP 3000 through CMP 4300, as shown in Figure 1. The line was migrated three times with the following velocity distributions: Smoothed stacking velocities, smoothed stacking velocities reduced by 10% and by 20%.

The velocity distribution for the migration is shown in Figure 11. The given interval velocities are derived from the smoothed stacking velocities, reduced by 10%, using the DIX/KREY formula (Krey, 1954). The last two digits of the interval velocities are numeric results and do not reflect actual accuracy of the data.

For final display the migrated data are filtered and scaled with parameters used on the stacked data.

INSTANTANEOUS AMPLITUDE (ENVELOPE)

The instantaneous amplitude or reflection strength (Taner et al., 1979) is computed from the STACK-COFILT and the MIGRATION (-10%) section. Reflection strength represents the amplitude of the envelope and is independent of phase.

Results

1. Stacking Results (Figures 2 through 5)

All sections as well as the DEKORP processing (Figure 1) show good and correlating events in three time zones: 1.0 s through 3.5 s, 6.0 s through 7.5 s and 9.5 s through 11.0 s. There is an obvious improvement of the quality from RAW-STACK (Figure 2) up to the final results COST-STACK-FILTER-COFILT (Figure 4). The color display (Figure 5) of the final section even makes the reflecting horizons better visible.

Comparing these sections with the section from DEKORP processing (Figure 1) results in the following findings: improvements of the quality in the upper time zone were mainly achieved by careful determination of dynamic corrections, e.g. on the horizon at approximately 1.5 s; in the middle and lower time zones the quality is rather similar, however, coherency filtering after stack improves the quality of the results remarkably and aids in interpretation.

2. Migration (Figures 7 through 9)

The section generated with smoothed stacking velocities (Figure 7) seems to be "over" migrated, especially in the lower part. For that reason the migration process was run again using velocities reduced by 10% and 20%. It seems, that velocities reduced by 10% give the best migration results (Figure 8).

This finding is in accordance with our experience in processing oil exploration data down to 5 s. In cases, where no well controlled velocities exist, best migration results are achieved by using smoothed stacking velocities reduced by 10%.

3. Instantaneous Amplitude (Figures 6 and 10)

Instantaneous amplitude or reflection strength is the composite of several reflections generated by an acoustic impedance contrast. Thus, the main inhomogeneities are emphasized. The instantaneous amplitude sections (ENVELOPE) demonstrate this effect quite clearly.

4. Remarks on the velocity distribution for migration (Figure 11)

Stacking velocities and migration velocities are determined as processing parameters rather than as formation velocities. A plausible time migration result is not necessarily a proof that the geologic model

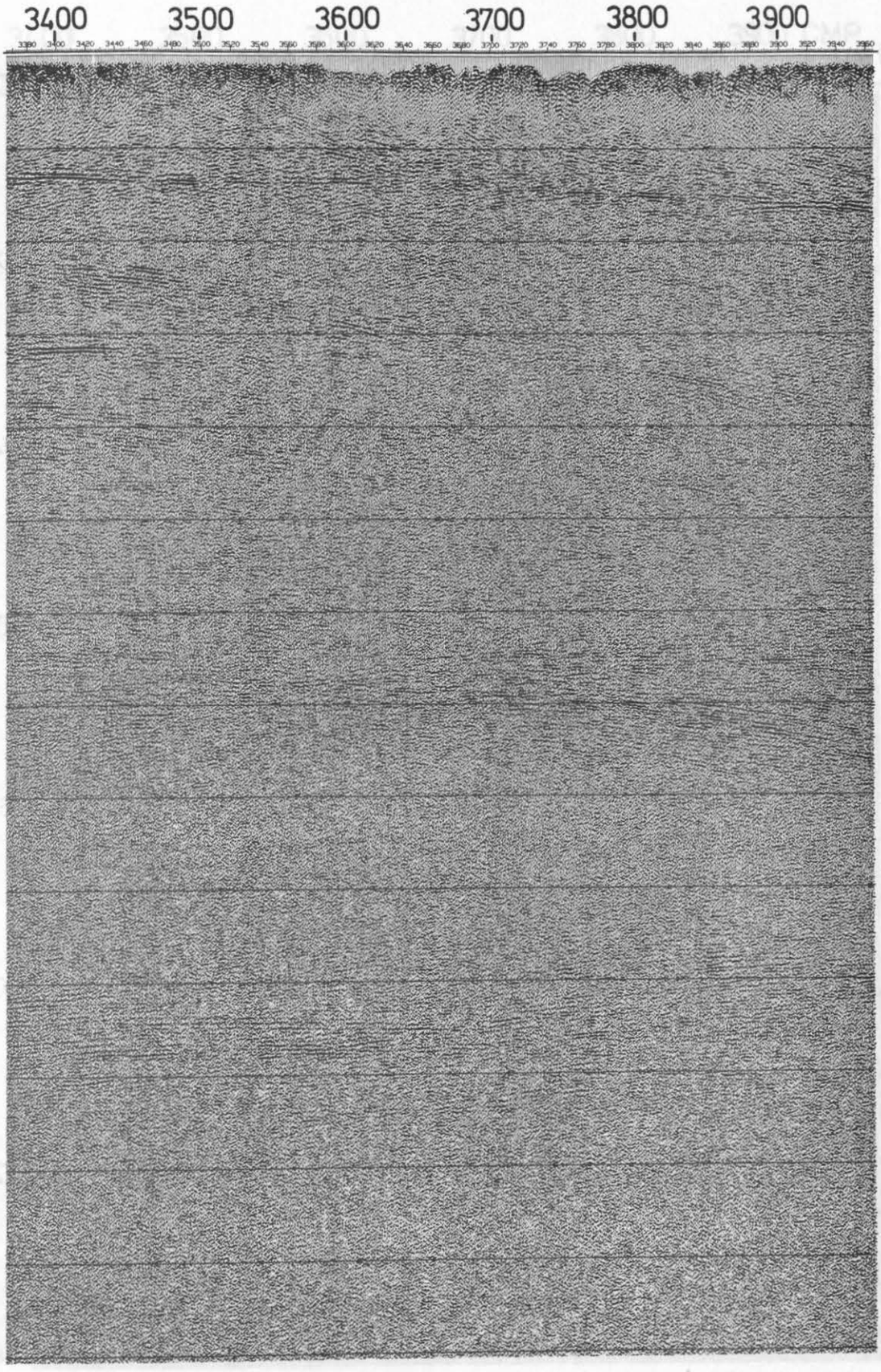

Figure 2: RAW-STACK-FILTER
Raw stacked section without residual static corrections.
Processing steps: (1) through (7), (9) through (11).

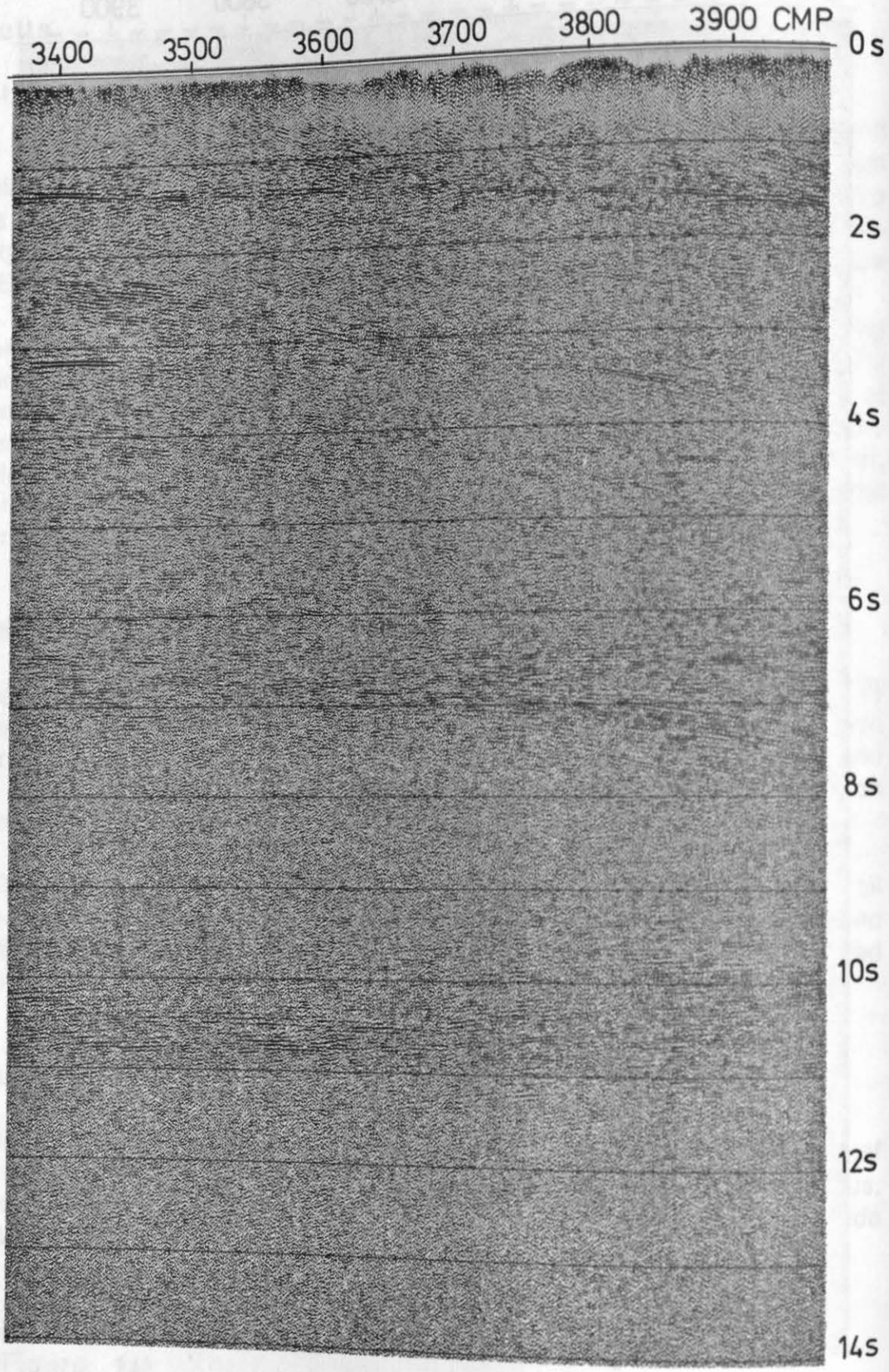

Figure 3: COST-STACK-FILTER
Final stacked section. Processing steps: (1) through (11).

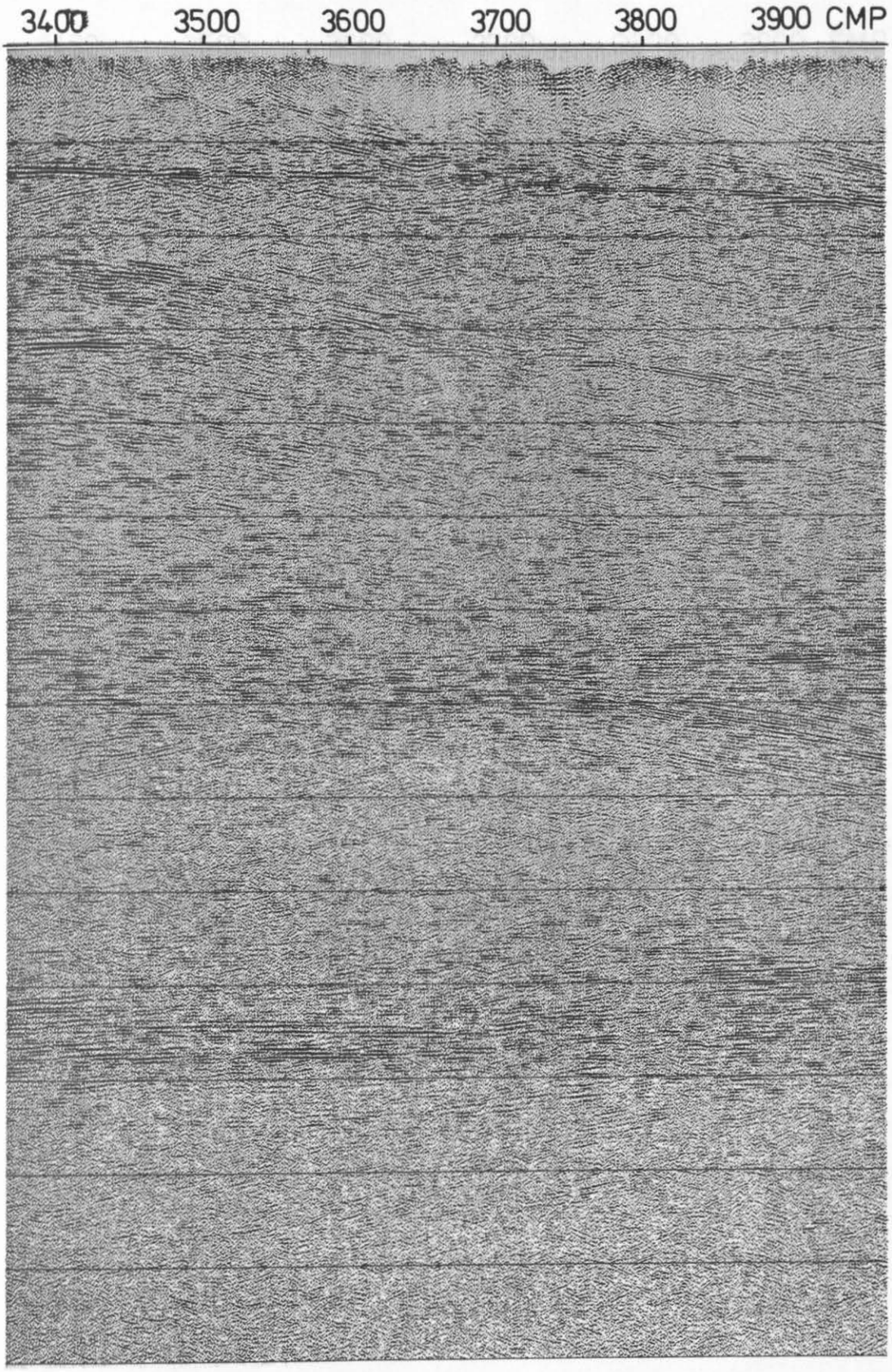

Figure 4: COST-STACK-FILTER-COFILT
Final stacked section with coherency filter after stack.
Processing steps: (1) through (12)

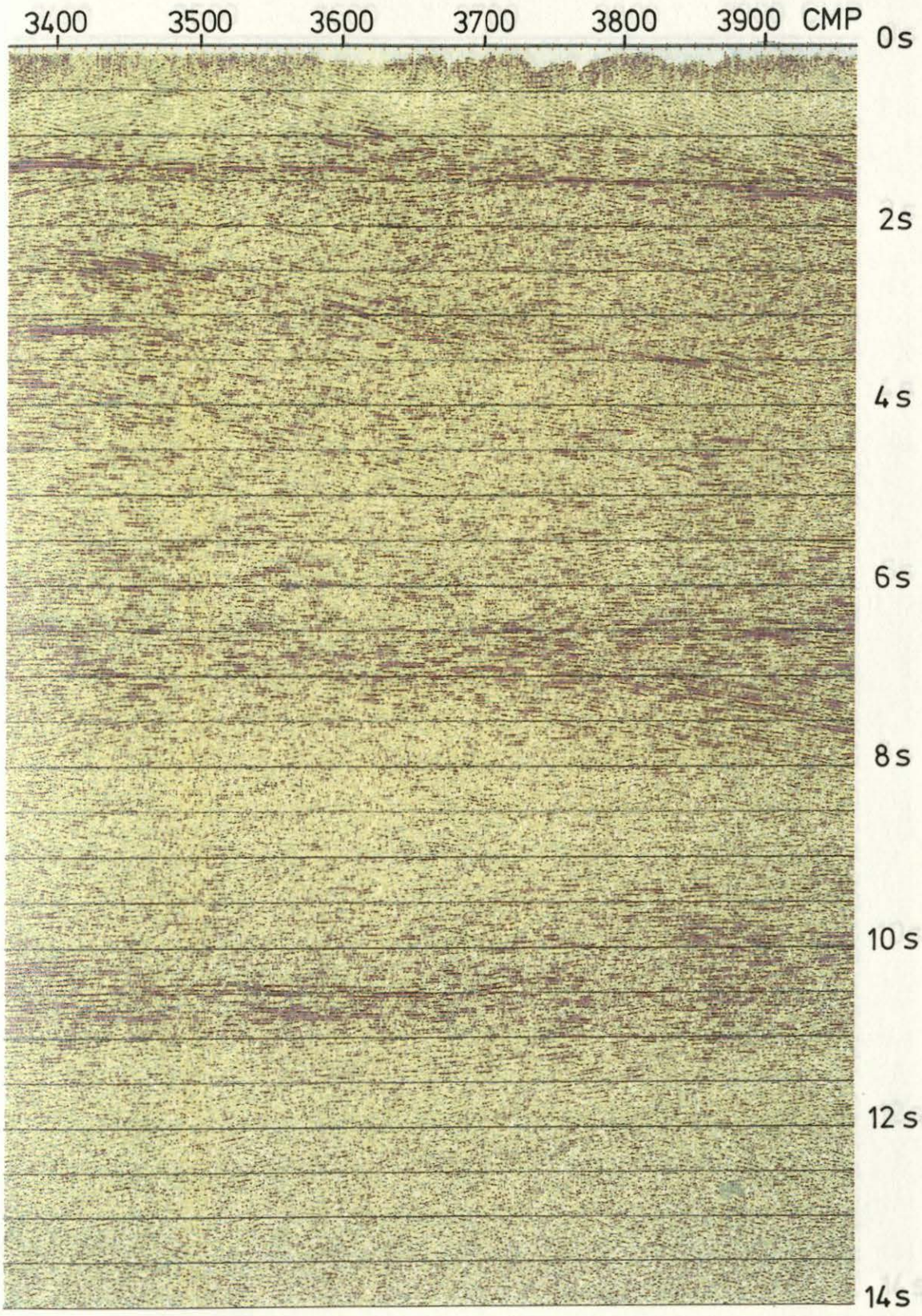

Figure 5: COST-STACK-FILTER-COFILT
Color display of the final stacked section of Figure 4.

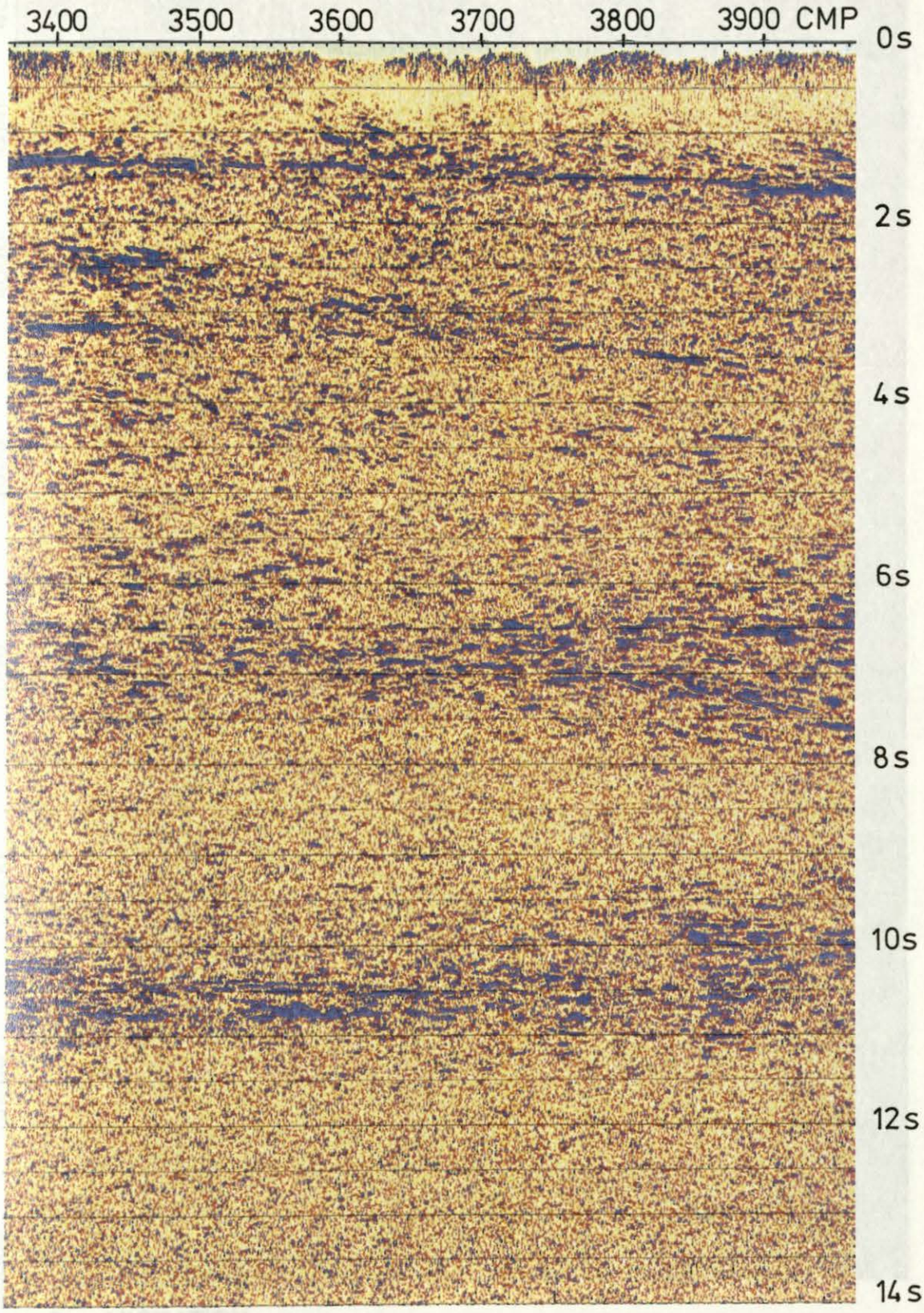

Figure 6: ENVELOPE
Instantaneous amplitude (Envelope) of the final stacked section of Figure 4. Processing steps: (1) through (12), (16).

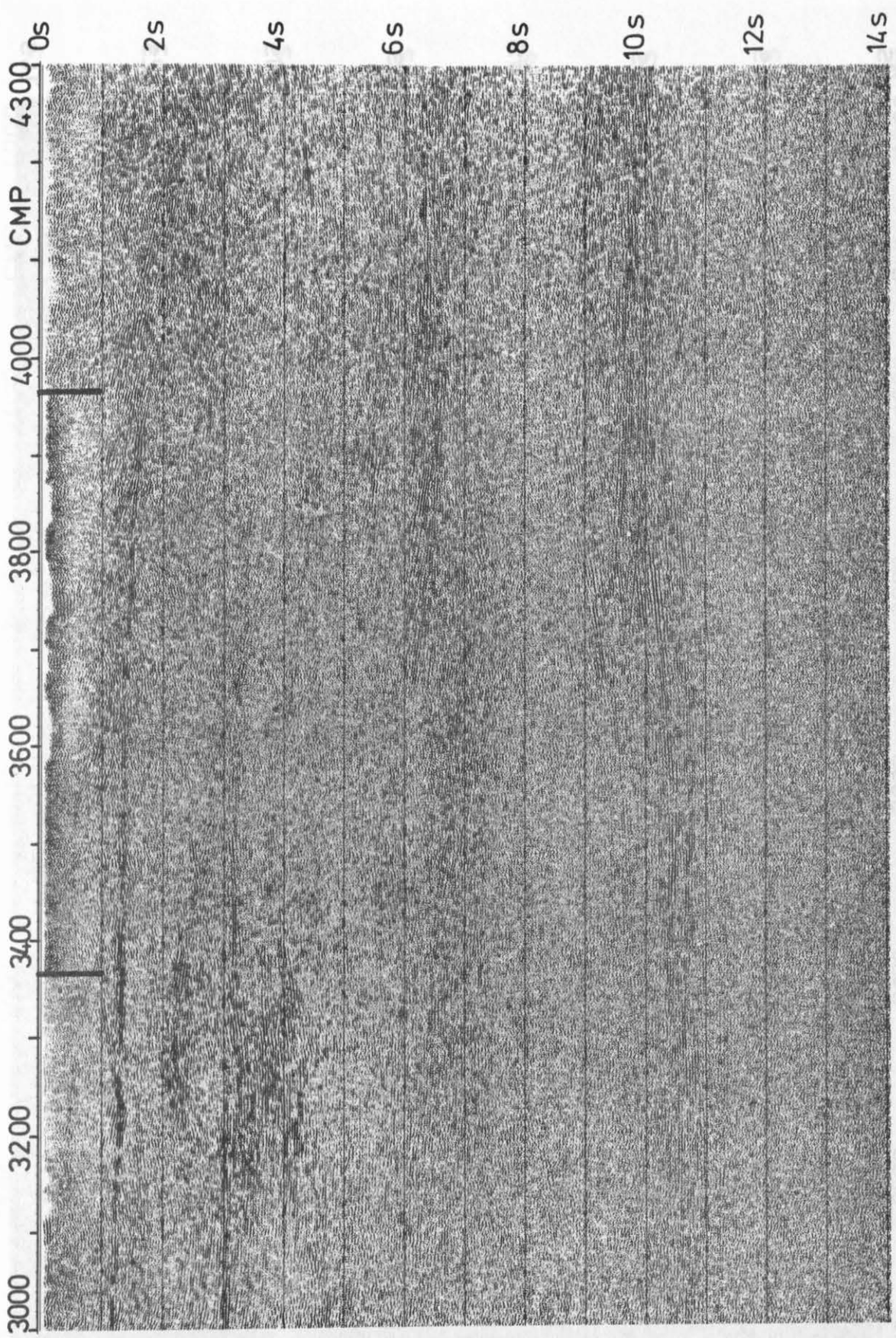

Figure 7: MIGRATION
FD-Migration of the final stacked section of Figure 3 with smoothed stacking velocities. Processing steps: (1) through (9), (13) through (15). In order to avoid edge effects by the migration process, about 300 traces from the DEKORP processing are added on both sides of the section.

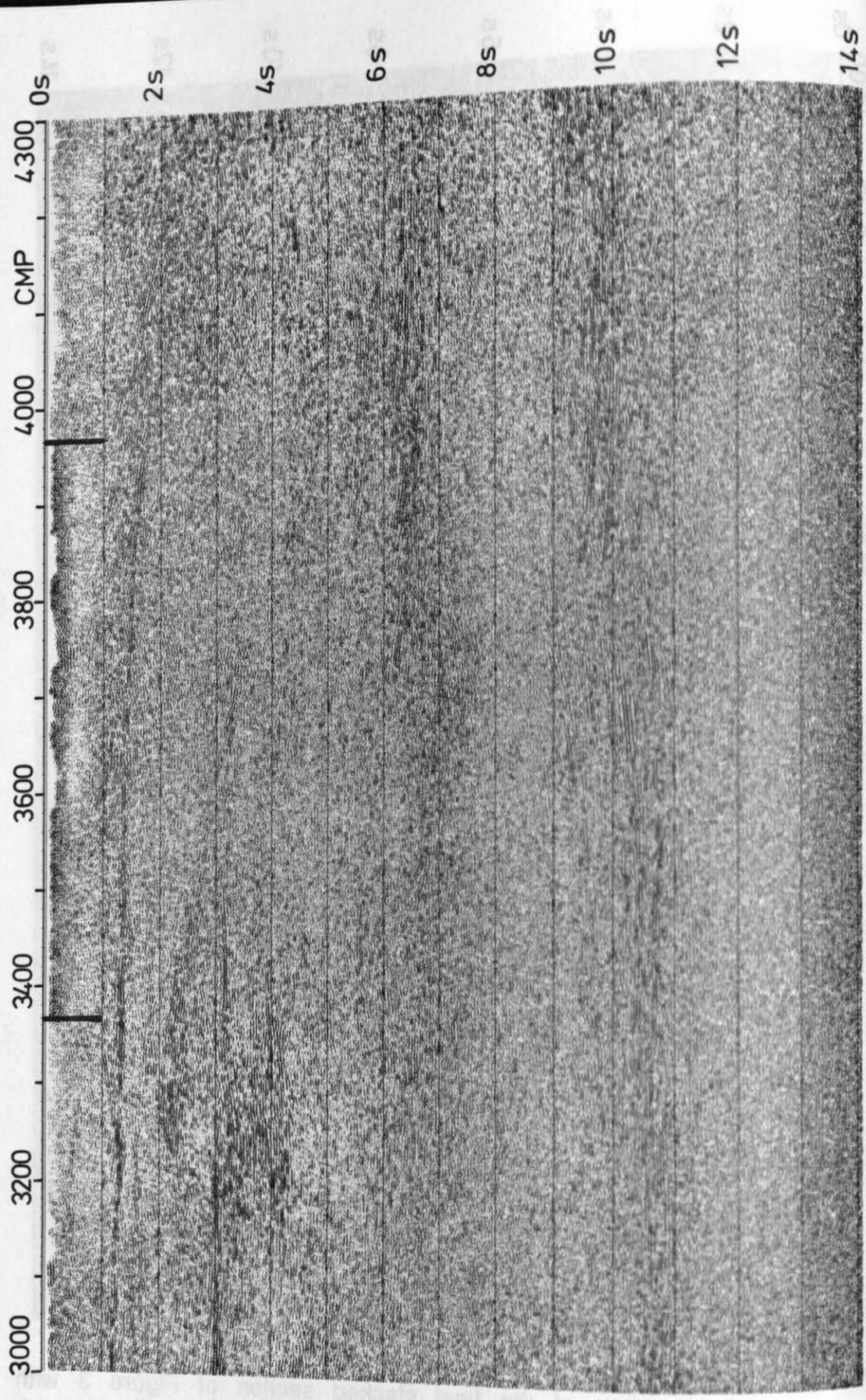

Figure 8: MIGRATION
FD-Migration as for Figure 7, but with velocities reduced by 20%.

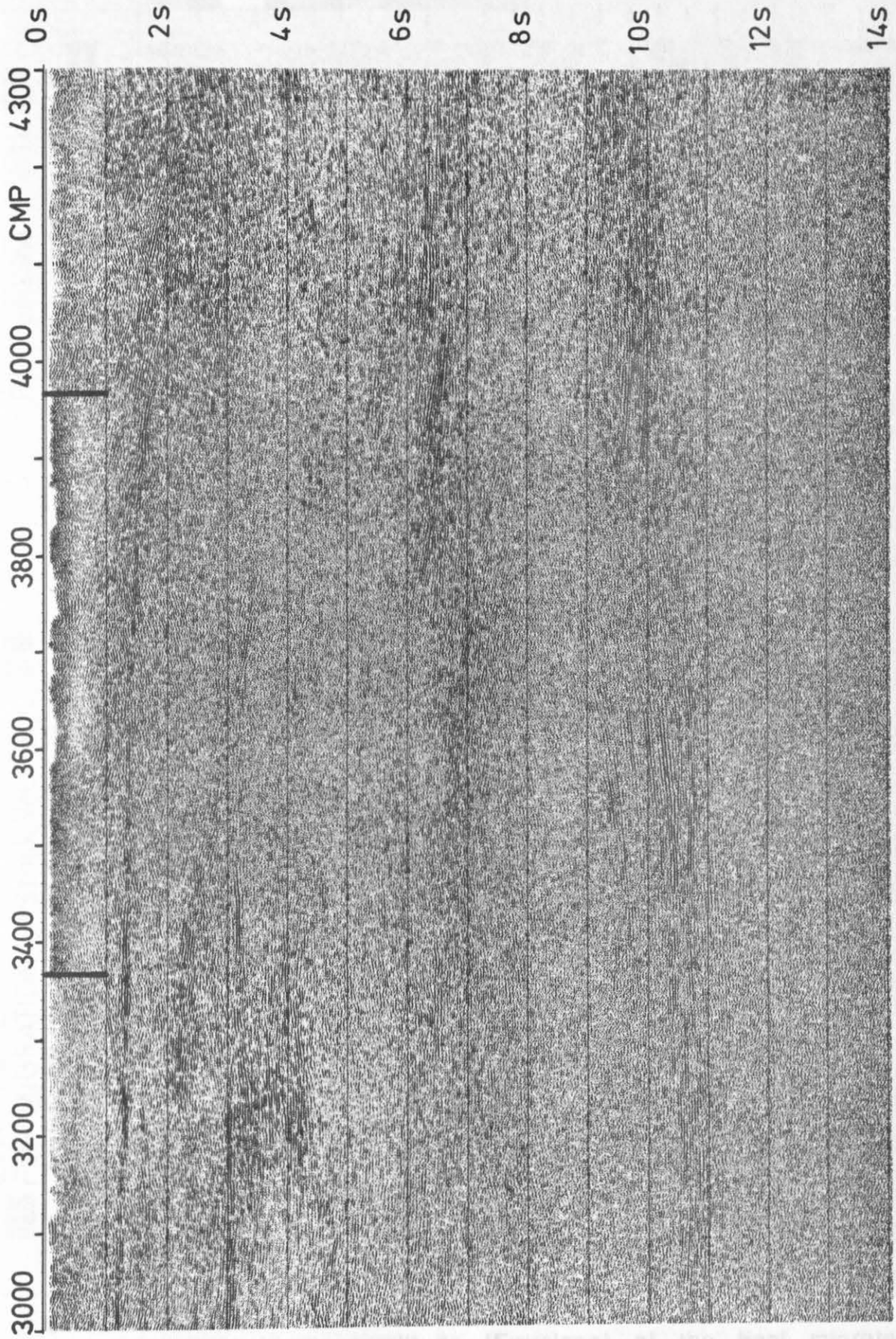

Figure 9: MIGRATION
FD-Migration as for Figure 7, but with velocities reduced by 10%.

Figure 10: ENVELOPE
Instantaneous amplitude (Envelope) of the final migrated section of Figure 8. Processing steps: (1) through (9), (13) through (15), (17),

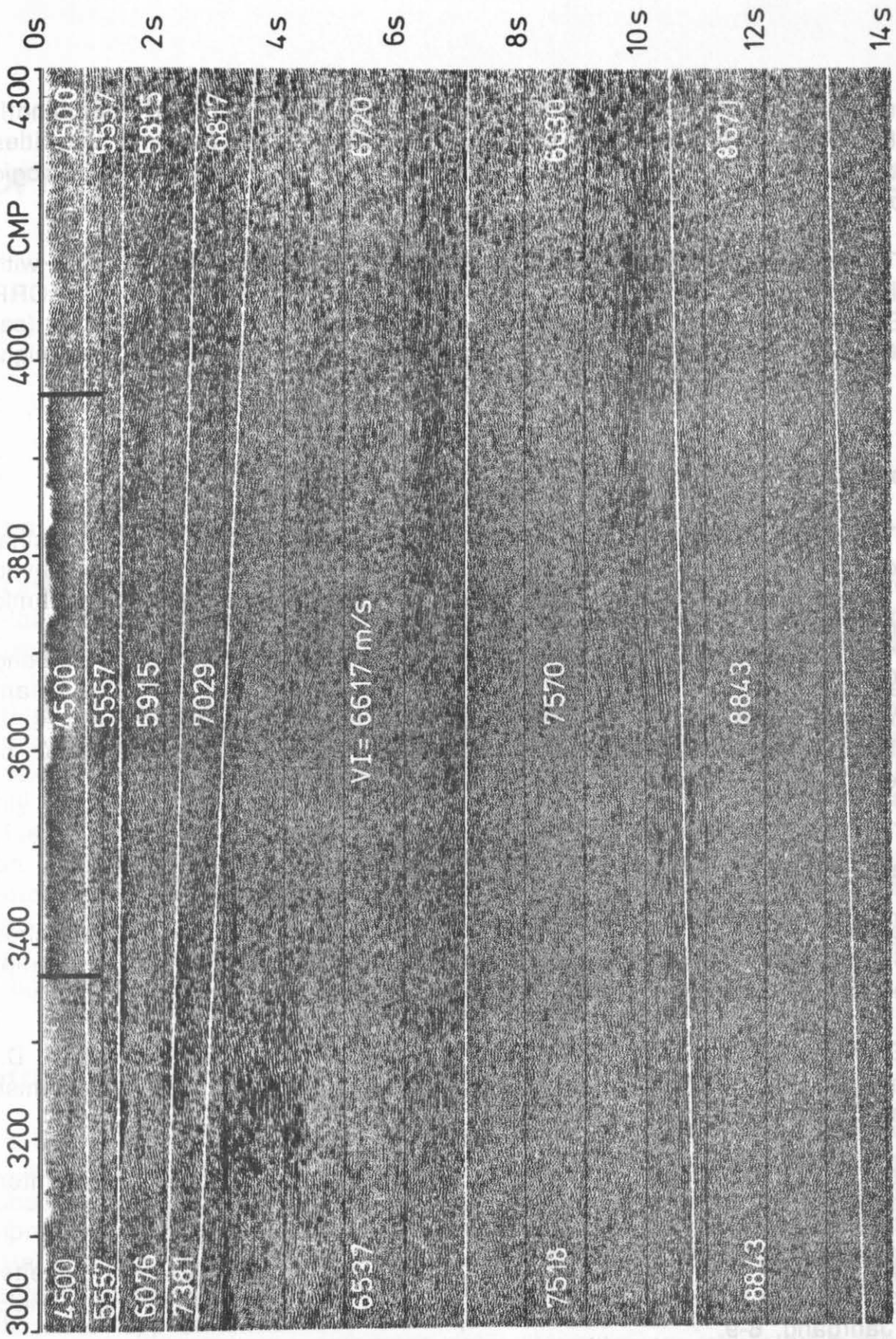

Figure 11: INTERVAL VELOCITIES
Interval velocities used for the migration of the final migrated section of Figure 8. The interval velocities are derived from smoothed stacking velocities, reduced by 10%, using the DIX/KREY formula (Krey, 1954).

derived from the migration velocities is correct (Diet and Golubinoff, 1987). This finding and the fact, that the accuracy of stacking velocities decrease with increasing depth have to be considered in deriving geologic models from migration velocity distributions.

The migration velocities given in Figure 11 correspond rather good with velocity models derived from wide-angle and refraction data (DEKORP RESEARCH GROUP, 1990). The only exception is a high velocity layer (ca. 7000 m/s) in the upper part between 2 and 3 s. The high velocities might be caused by inaccuracies of the stacking velocities.

Conclusion

The results of the processing by DEKORP PROCESSING CENTER, Clausthal show all the main reflecting horizons. Improvements have been achieved in detail, mainly in the upper part, by carefully determined dynamic corrections, and by coherency filtering after stack.

The instantaneous amplitude sections emphasize the main reflecting elements. Such sections may aid in correlation of the main inhomogeneities and in the interpretation of the main geologic features.

Display in color makes reflections better visible and the correlation of events easier. Thus, color aids in interpretation of sections.

References

Meissner, R., Bortfeld, R.K., 1990: DEKORP-Atlas, Results of Deutsches Kontinentales Reflektionsseismisches Programm; Springer Verlag Berlin-Heidelberg- New York- London- Paris- Hong Kong- Barcelona.

DEKORP RESEARCH GROUP, represented by Flueh, E.R., Klaeschen, D., Meissner, R., 1990: Wide-angle vibroseis data from the western Rhenish Massif; Tectonophysics, 173 , 83-93.

Diet, J.P., Coloubinoff, 1987: Geschwindigkeiten als Processing-Paramter; Sonderdruck 7., MINTROP-Seminar über seismische Geschwindigkeiten.

Krey, Th., 1954: Bemerkung zu einer Formel für Geschwindigkeits-bestimmungen aus seismischen Messungen von C.H. Dix; ERDÖL und KOHLE, 7. Jahrgang, 8-9.

Taner, M.T., Koehler, F., Sheriff, R.E., 1976: Complex seismic trace analysis; Geophysics, Vol. 44, 1041-1063.

REPROCESSING OF BELCORP/DEKORP DEEP REFLECTION DATA: OFFSET DEPENDENCY OF STACKING VELOCITIES AND CMP-STACKED SECTIONS

Ernst R. Flueh and Dirk Klaeschen

GEOMAR, Kiel , Germany

Abstract

Offset limited stacks of the dataset 1c were produced using stacking velocities determined from the individual subsets. Four datasets were analyzed, the full dataset (200 fold), and three subsets (0-4, 4-8, and 8-12 km offset). Constant velocity stacks were used to define stacking velocities, determined at 10 locations (appr. every 1000 m). The individual stacking velocities differ locally by more than 15%, and the stacks show pronounced differences. A strong reflection at 3.2 s TWT is only mapped on the short offset (0-4 km) data and is not visible on the far offsets. Although the general pattern is similar, individual reflections can seldom be correlated between the different stacks. It is therefore concluded that diffractions and out of plane reflections contribute significantly to the observed pattern. This is further confirmed by using high (7.0 km/s) and low (5.8 km/s) constant velocity stacks for the subgathers.

Introduction

It has long been recognized that AVO (Amplitude versus offset) analysis is a valuable tool for determining the elastic properties of the subsurface. This is especially clear in sedimentary strata, where large impedance contrast do exist. However, for deep continental reflection data probing the crystalline crust and upper mantle, the reflection coefficients are usually too small and individual events are too short to allow the application of this technique. In addition, the spreadlengths employed are too small and lateral inhomogeneities too severe to enable AVO-analysis.

Even more, the meaning of the stacking velocity is controversially debated, with opinions ranging from "totally useless" to "physically significant". They are generally best defined by visual interpretation of constant velocity stack panels.

Most of the controversy about stacking velocities centers around the processors attitude to allow only "reasonable" events to be picked or if every high amplitude event should be considered. Both approaches are acceptable.

One method to avoid the ambiguity is to use large offsets. However, this increases the field expenses considerably and introduces additional problems, such as long wavelength statics and lateral inhomogeneities which further complicate the processing. As a compromise between a desired large offset and cost efficiency the DEKORP-surveys were shot using an asymmetric split spread geometry from -4 to 12 km (Meissner and Bortfeld, 1990). Although this is not sufficient to determine accurate interval velocities, the stacks are highly sensitive to stacking velocities.

For the CCSS-workshop we have analyzed the stacking velocities and the stacks by subdividing the data into offset limited subgathers (0-4, 4-8, and 8-12 km). Theoretical considerations, that are discussed demonstrate that out-of-plane reflections and diffractions can show considerable variation in stacking velocities when compared to a lateral homogeneous crust. The results of our reprocessing confirm these theoretical considerations.

Travel times of diffractions in CMP domain

If diffractions, that may be arbitrarily oriented with respect to the seismic line, interfere with primary reflections, their apparent velocities in the CMP-gather, which must be regarded as the optimum stacking velocities to highlighte the diffractions, can range from infinity to a minimum value which is much less than for a reflection at identical two-way time. This is demonstrated in Figures 1a and 1b. Figure 1a shows the geometry considered. Along a CMP-line three CMP-gathers (*a, b* and *c*), separated by 5 km each are investigated. Each CMP-gather has an aperture of 30 km. Perpendicular to the CMP-line at four positions (1, 2, 3 and 4) diffraction elements are located. Location 1 lies on the CMP-line, while 2, 3 and 4 are 2.5, 5 and 10 km off the line. For each of these locations four diffraction elements at depths of 2, 4, 6 and 8 s TWT are considered. A realistic crustal velocity model with a constant velocity gradient from 4.5 km/s at the surface to 6.5 km/s at 30 km depth is assumed. A three-dimensional two point raytracing algorithm was used to determine the travel times of the diffraction hyperbolae within the CMP-gathers. The results are shown in Figure 1b. Each diffraction hyperbola is compared to the reflection hyperbola from a horizontal interface that has an identical t_0-time, and thus not necessarily the same depth. In fact, the reflection would generally be at larger depth, since it has no lateral offset. This reflection hyperbola also corresponds to the correct stacking velocity, as generated by the model.

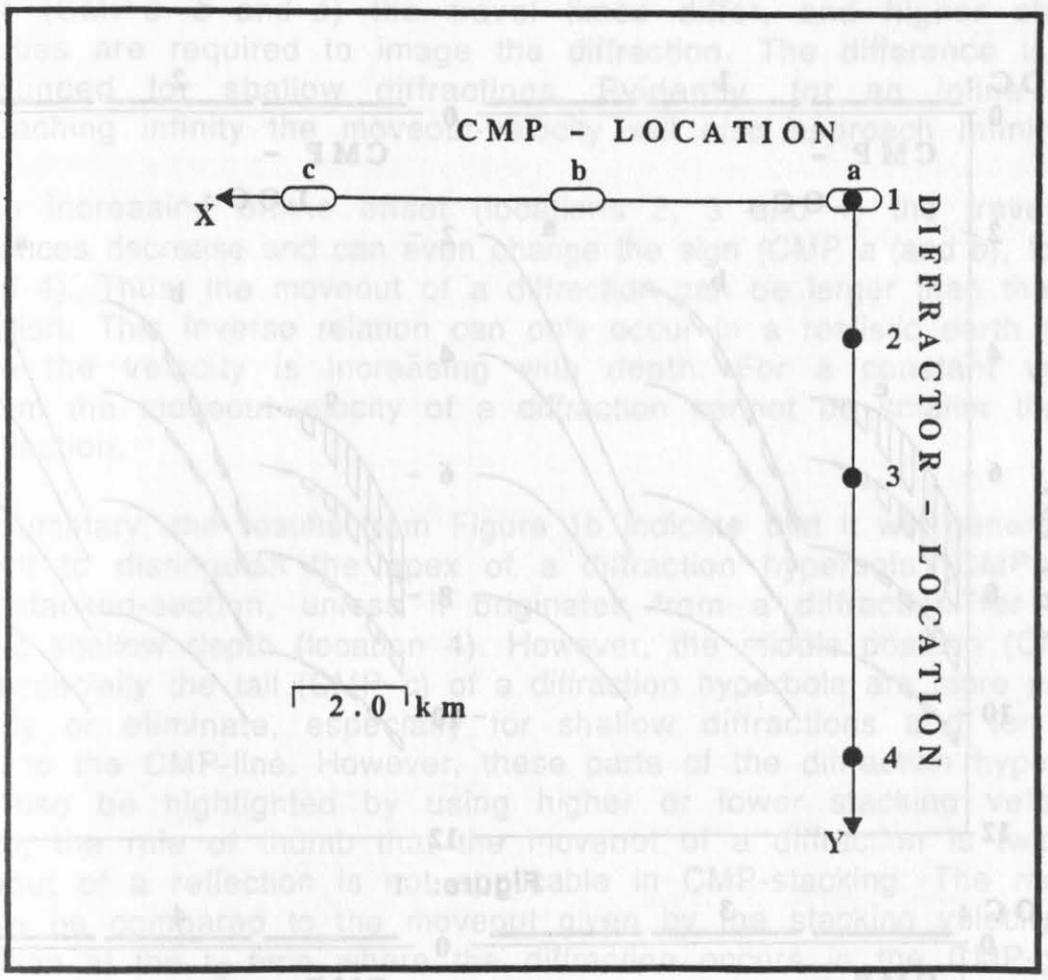

Figure 1a: Map of common midpoint (a, b, and c) and diffractor locations (1, 2, 3, and 4) used for the calculation of travel times. The depths of the diffractors at each of the locations are at 2, 4, 6, and 8 s TWT each.

Figure 1b, see next page.

Figure 1b: Travel times of diffractions (solid lines) from location 1, 2, 3, and 4 in CMP-gathers a, b, and c for different vertical depths (2, 4, 6, and 8 s TWT) of the diffractors. The CMP-aperture is 30 km. A reflection hyperbolae for a plane horizontal reflector at a depth such that the zero offset times are identical is calculated for comparison. Where these two hyperbola diverge, the area enclosed is hatched. Open bars indicate that the reflection hyperbola is delayed, whereas solid bars indicate that the reflection hyperbola will be faster than the corresponding diffraction hyperbola. A linear velocity gradient with 4.5 km/s at the surface to 6.5 km/s at 30 km depth was assumed.

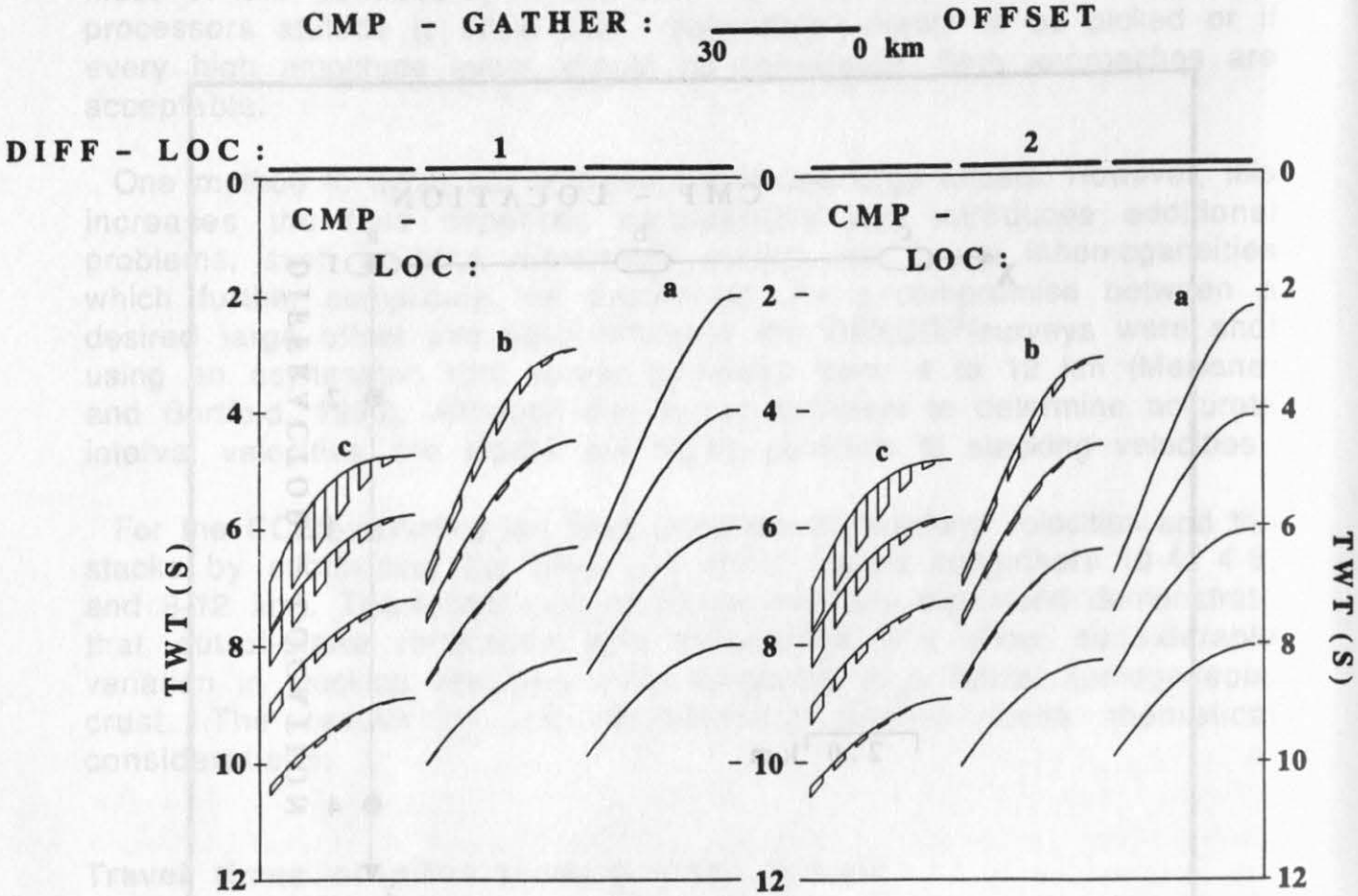
CMP - GATHER :
30
0 km
OFFSET
DIFF - LOC :
1
2
CMP -
LOC :
a
b
c
TWT (S)
0
2
4
6
8
10
12

Figure: 1

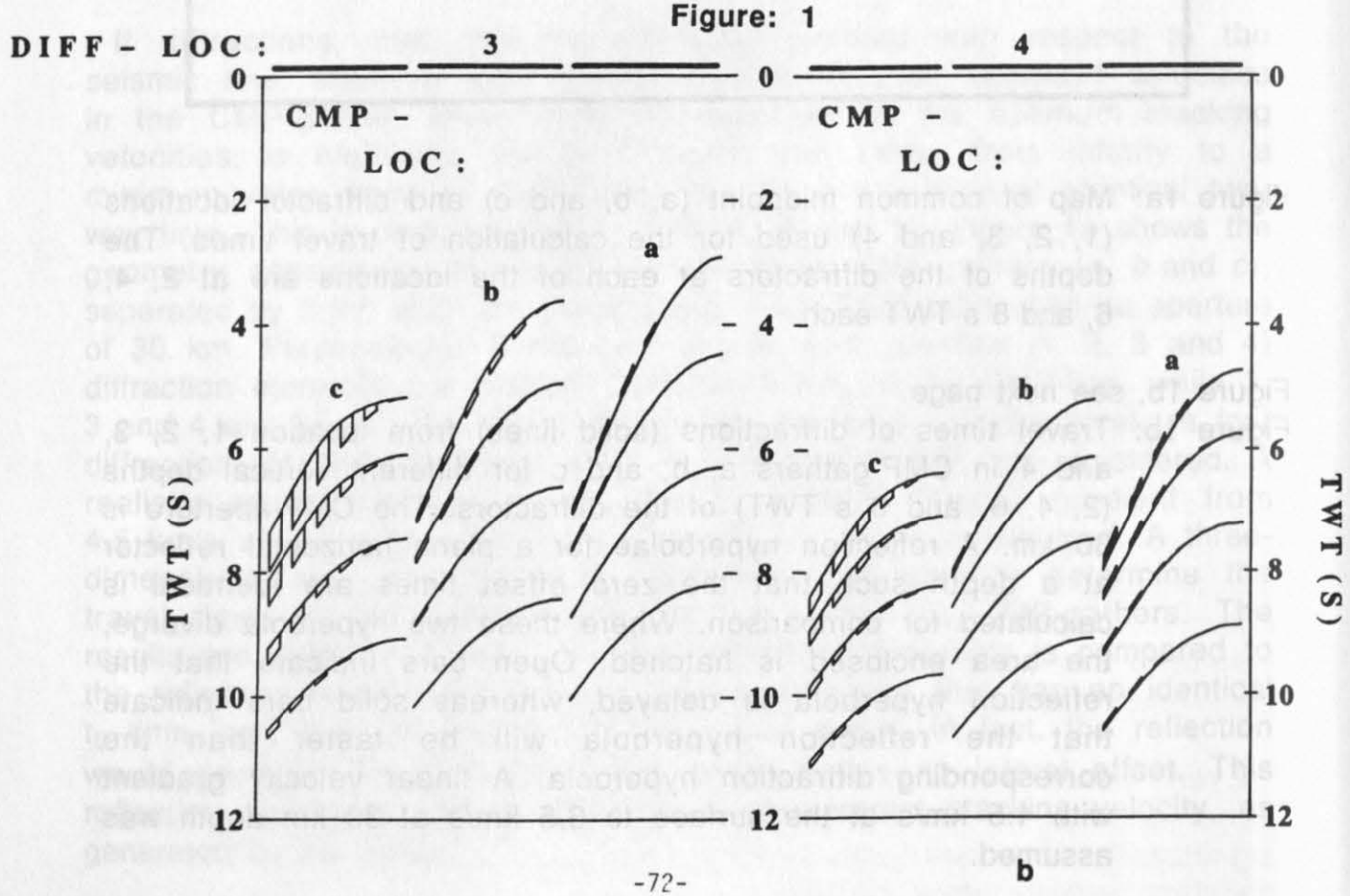
DIFF - LOC :
3
4
CMP -
LOC :
a
b
c
TWT (S)
0
2
4
6
8
10
12

Obviously, at the CMP-location *a*, hyperbolae from location 1 and the corresponding reflection hyperbolae coincide. With increasing inline offset (CMP's *b* and *c*) the travel times differ, and higher stacking velocities are required to image the diffraction. The difference is most pronounced for shallow diffractions. Evidently, for an inline offset approaching infinity the moveout-velocity will also approach infinity.

With increasing offline offset (locations 2, 3 and 4) the travel time differences decrease and can even change the sign (CMP *a* (and *b*), location 3 and 4). Thus, the moveout of a diffraction can be larger than that of a reflection. This inverse relation can only occur in a realistic earth model, where the velocity is increasing with depth. For a constant velocity medium the moveout-velocity of a diffraction cannot be smaller than for a reflection.

In summary, the results from Figure 1b indicate that it will generally be difficult to distinguish the apex of a diffraction hyperbola (CMP*a*) in a CMP-stacked-section, unless it originates from a diffraction far offline and at shallow depth (location 4). However, the middle position (CMP *b*) and especially the tail (CMP *c*) of a diffraction hyperbola are more easy to identify or eliminate, especially for shallow diffractions and for those close to the CMP-line. However, these parts of the diffraction hyperbolae can also be highlighted by using higher or lower stacking velocities. Hence, the rule of thumb that the moveout of a diffraction is twice the moveout of a reflection is not applicable in CMP-stacking. The moveout has to be compared to the moveout given by the stacking velocity of a reflection at the t_0-time where the diffraction occurs in the CMP-gather. Consequently, offset limited subgathers should provide a means of suppressing or highlighting diffractions, which are a common feature of many deep crustal reflection data. Further considerations and applications to real data can be found in Klaeschen (1988).

Processing sequence of data

The processing that we applied to dataset 1c is rather similar to the sequence used at the DEKORP Processing Center (DEKORP Research Group, 1991; Klöckner and Stiller, this volume). However, no emphasis was put on the first two seconds of the data volume. This was done mainly to avoid spending time on careful analysis of the mute and near surface velocity variations. Further, for the intermediate (4-8 km) and large (8-12 km) offset subgathers the fold is dramatically reduced in the upper part of the section, and therefore a comparison can only be made for the deeper parts. The complete processing sequence is shown in Table 1. In addition to the standard processing a prestack deconvolution was applied, mainly to achieve a spectral whitening. Velocity analysis was carried out using constant velocity stacks for each of the subgathers. The four velocity

Table 1

Processing sequence

Input-Pre-Stack

despike
statics from header
mute (offset [km]/time[s]: 0/0-4/1-12/2.8)
spherical divergence (time [s]/V_{rms} [km/s]: 1/5.1-2/5.8-3/6.1-7/6.3-10/6.4-16/6.5
predictive deconvolution (operator length-gap length-%noise added) 128-32-3
two design gates (offset [km]/start-end [s]: 0/0.3-6 // 12/2.9-7
0/5-12 // 12/5.9-12.9
filter 10-48 Hz pass, 24db slope

Output

Input

AGC (time [s]/length [km]: 1.5/0.6-14/2)
velocity analysis at 10 CDP's: constant velocity stack (21 CDP's)
CDP-gather
energy
velocity analysis of offset limited subsets of data
full offset, 0-4 km, 4-8 km, 8-12 km

best velocity fields for: full offset
0-4 km offset
4-8 km offset
8-12 km offset

Input

NMO for 6 velocity fields: 5.8 km/s
full offset
0-4 km offset
4-8 km offset
8-12 km offset
7.0 km/s
mute 2.0 s
AGC 0.6 s
3 iterations of surface consistent statics, determined in time window from 3 to 12 s
statics
6 stacks each for full offset // 0-4 km offset // 4-8 km offset // 8-12 km offset
filter (time [s]/passband [Hz]: 2/10-50 // 5/10-30 // 12/10-25; 24 db slope)
tracemix (3 traces weighted 0.25-0.5-0.25)
sum 2 traces
predictive deconcolution (operator length-gap length-%noise added) 256-64-3
two design gates [s] (2-6, 5-12)
resample 8 ms
filter (time [s]/passband [Hz]: 2/10-50 // 5/10-30 // 12/12-25; 24 db slope)
AGC 4 s

Output

Plot

6 velocity fields/4 subsets; 24 sections to compare

fields obtained are shown in Figures 2a through 2d. Three iterations of surface consistent statics were applied in a time window from 3 to 12 s, using the procedure described by Kirchheimer (1990).

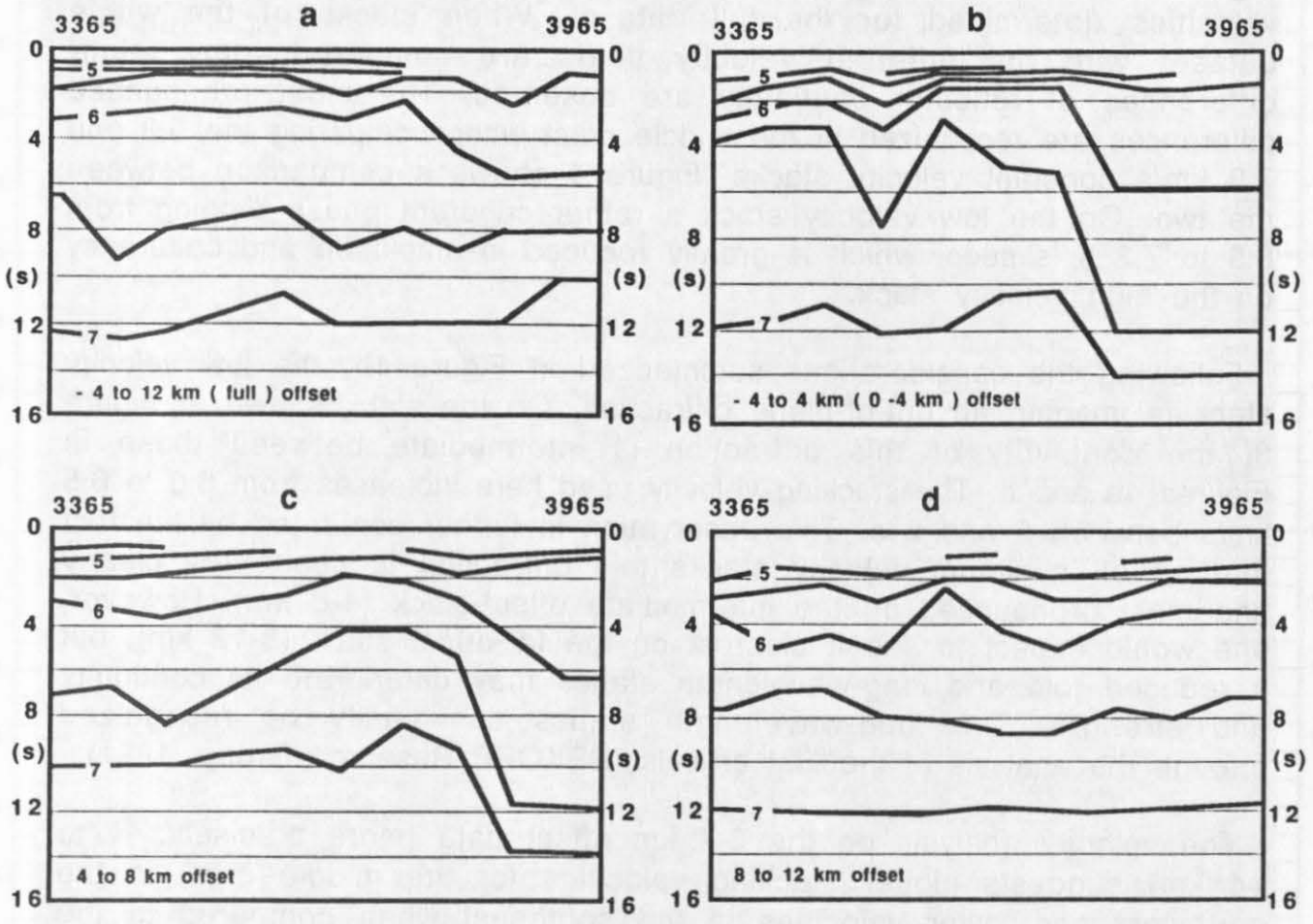

Figure 2: Stacking velocities determined using constant velocity stacks for the full dataset (a) and the offset-limited subgathers (b, c, and d). Contour interval 0.5 km/s.

Stacks were subsequently produced for each of the four subgathers and each of the four velocity fields, and in addition a constant high (7.0 km/s) and a low (5.8 km/s) velocity field, thus a total of 24 different stacks were made. The post stack processing is also straightforward. A weighted three trace mix followed by a two trace sum was applied to enhance lateral coherency. Time dependent bandpass filtering and scaling was applied for cosmetic reasons.

Discussion

The resulting 24 stacks produce similar overall pictures, which compare well with the results obtained in the original processing. Two strong bands of reflections, one centered at about 7 s, the second between 9.5 and 11.5 s, are visible on each section. In the northwest a high amplitude event at 3.2 s and southeast dipping reflection between 2 and 4 s are seen. Figure 3 shows the section derived from the full dataset using the velocities determined for the full dataset. When stacks of the whole dataset with the different velocity fields are compared, only minor differences of reflector continuity are observed. The most pronounced differences are recognized in the middle crust when comparing the 5.8 and 7.0 km/s constant velocity stacks. Figure 4 shows a comparison between the two. On the low velocity stack a rather coherent phase dipping from 6.9 to 7.2 s is seen, which is greatly reduced in amplitude and coherency on the high velocity stack.

Following the considerations summarized in Figure 1b, the low velocity stack is imaging an out-of-plane diffraction. On the stack shown in Figure 3, the continuity of this diffraction is intermediate between those in Figures 4a and b. The stacking velocity used here increases from 6.0 to 6.5 km/s between 5 and 8 s. This observation is further confirmed by the fact that on all minimum velocity stacks this diffraction is seen very clearly and most pronounced on the intermediate offset-stack (4-8 km). However, one would expect to see it clearest on the far-offset stack (8-12 km), but a reduced fold and long-wavelength statics may deteriorate its continuity and strength. The long-wavelength statics can easily be recognized through the analysis of the first arrivals (DEKORP Research Group, 1991).

The velocity analysis on the 0-4 km offset data (more precisely: -4 to +4 km) suggests higher stacking velocities for the middle crust in the northwest and lower velocities in the southeast when compared to the full offset data. The stacked section is shown in Figure 5, and when compared to the full offset data (Figure 3) several of the horizontal reflections are seen to extend over longer distances. Two portions are shown for comparison with the full offset data in Figure 6. When stacking the 0-4 km offset data using the other velocity fields, only minor differences occur. Major differences should not be expected, since small offsets are not sensitive to velocity changes at greater depth. The differences seen between the full offset and the short offset data may indicate a poor or improper treatment of long-wavelength statics. This is confirmed by the results of the iterative computations of residual statics, which converged more rapidly on the subgathers than on the full offset.

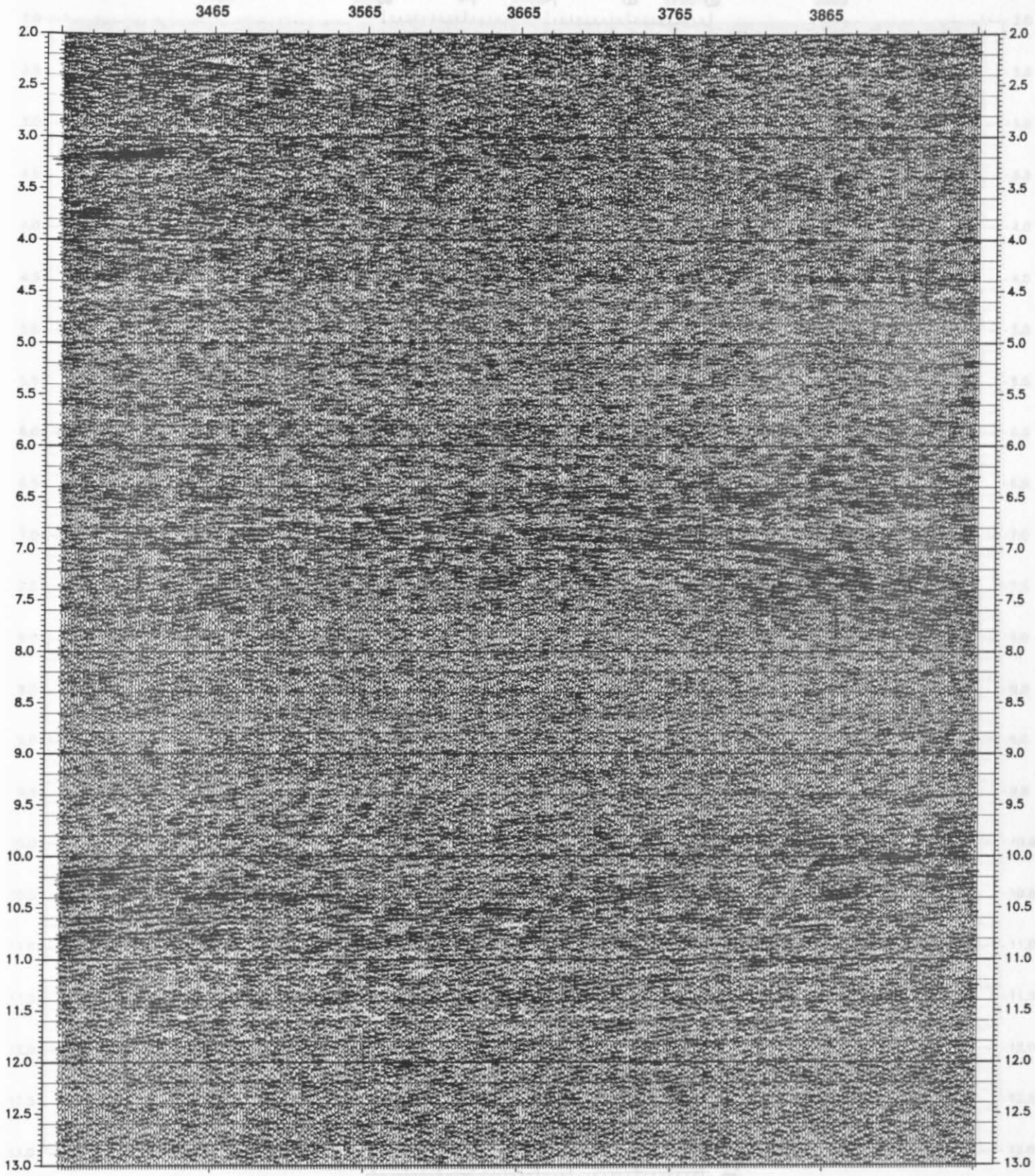

Figure 3: Final Stack of the full dataset; the processing sequence is summarized in Table 1. Stacking velocities as in Figure 2a.

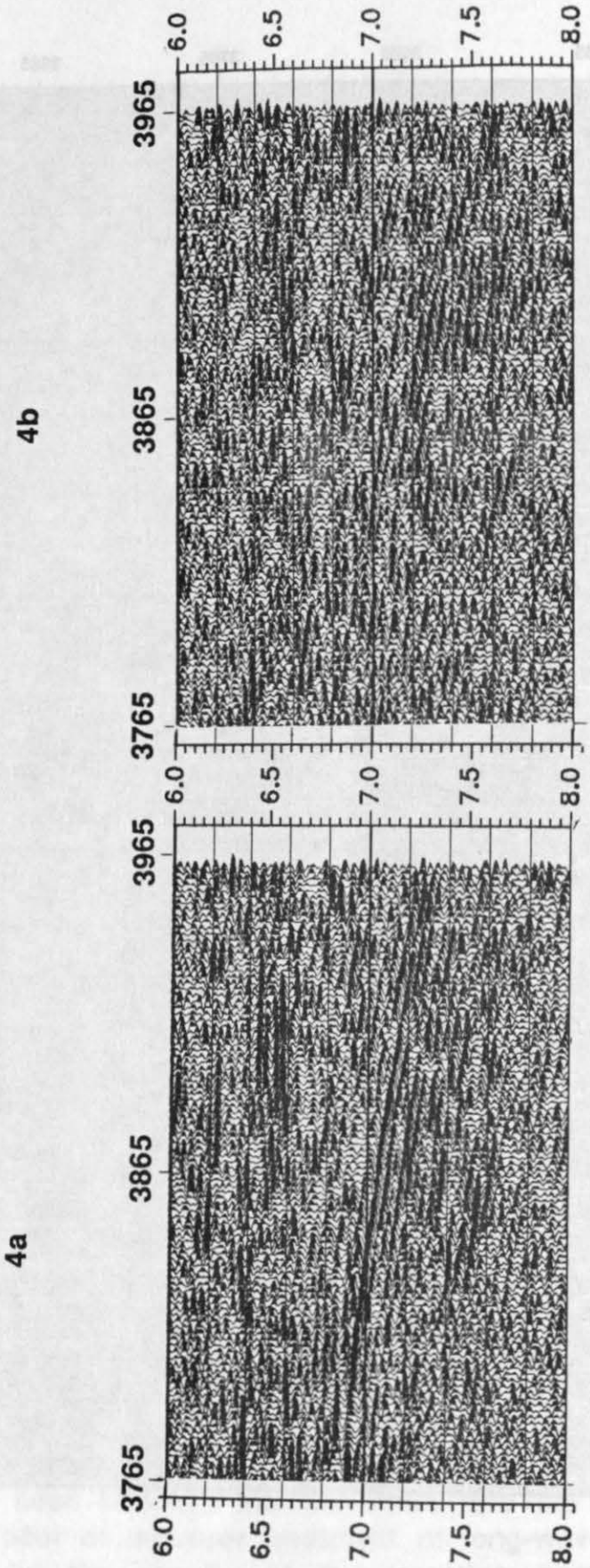

Figure 4: Comparison of a part of the full offset dataset, stacked with constant velocities. Left: V_{Stack} = 5800 m/s; right: V_{Stack} = 7000 m/s.

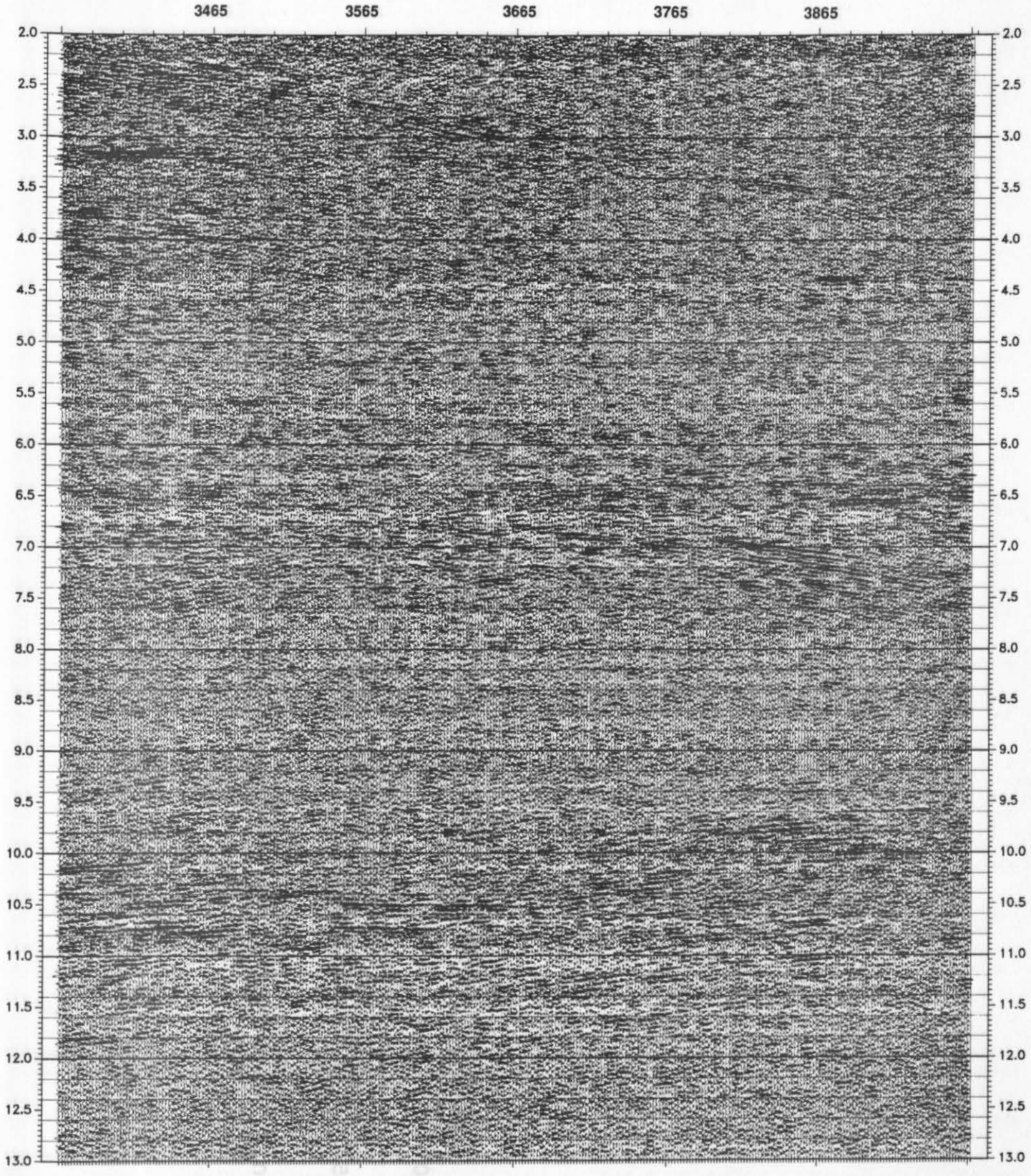

Figure 5: Final stack of the 0-4 km offset subgather. Stacking velocities as in Figure 2b.

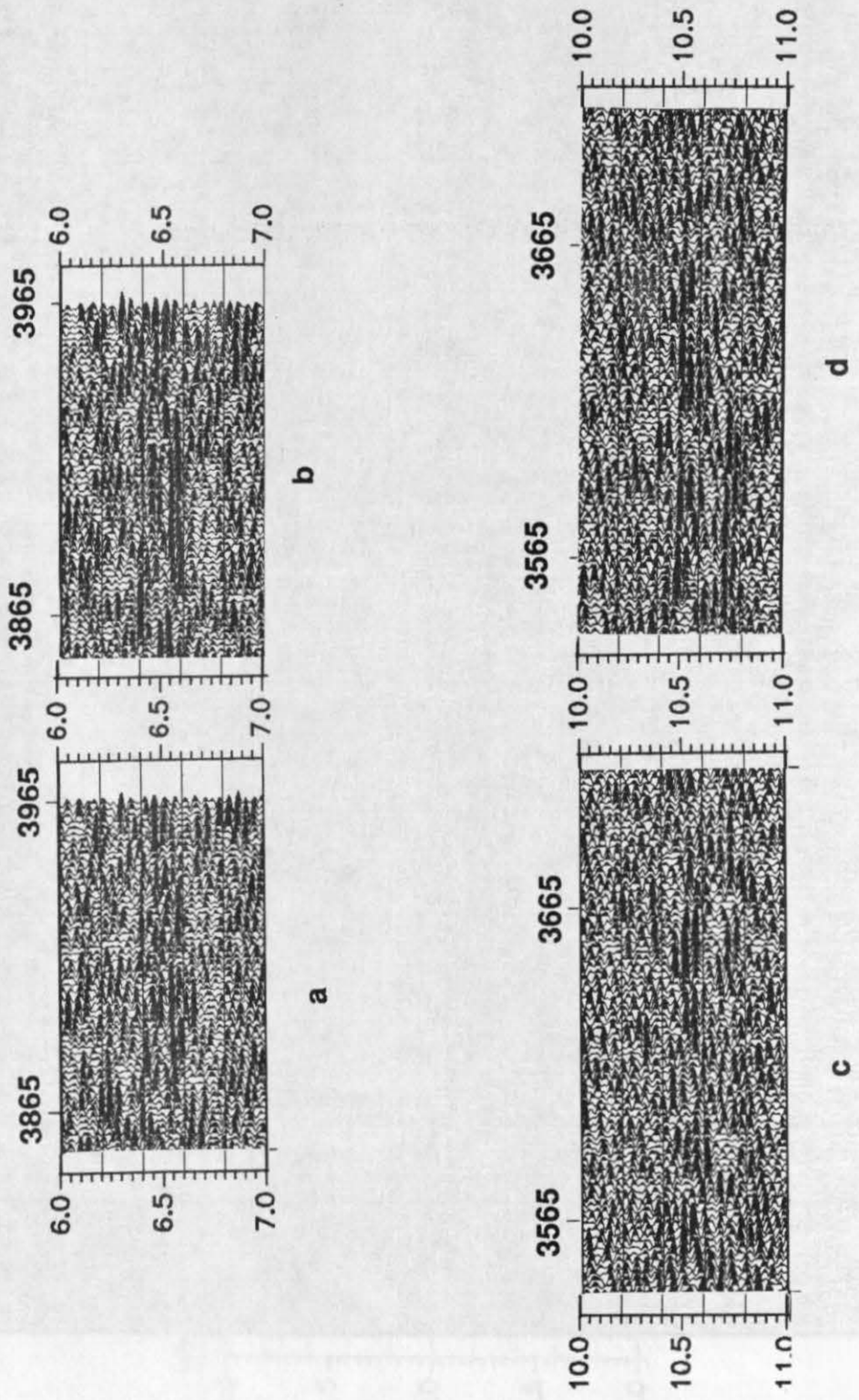

Figure 6: Comparison of parts of the full offset (a and c) and 0-4 km offsets (b and d).

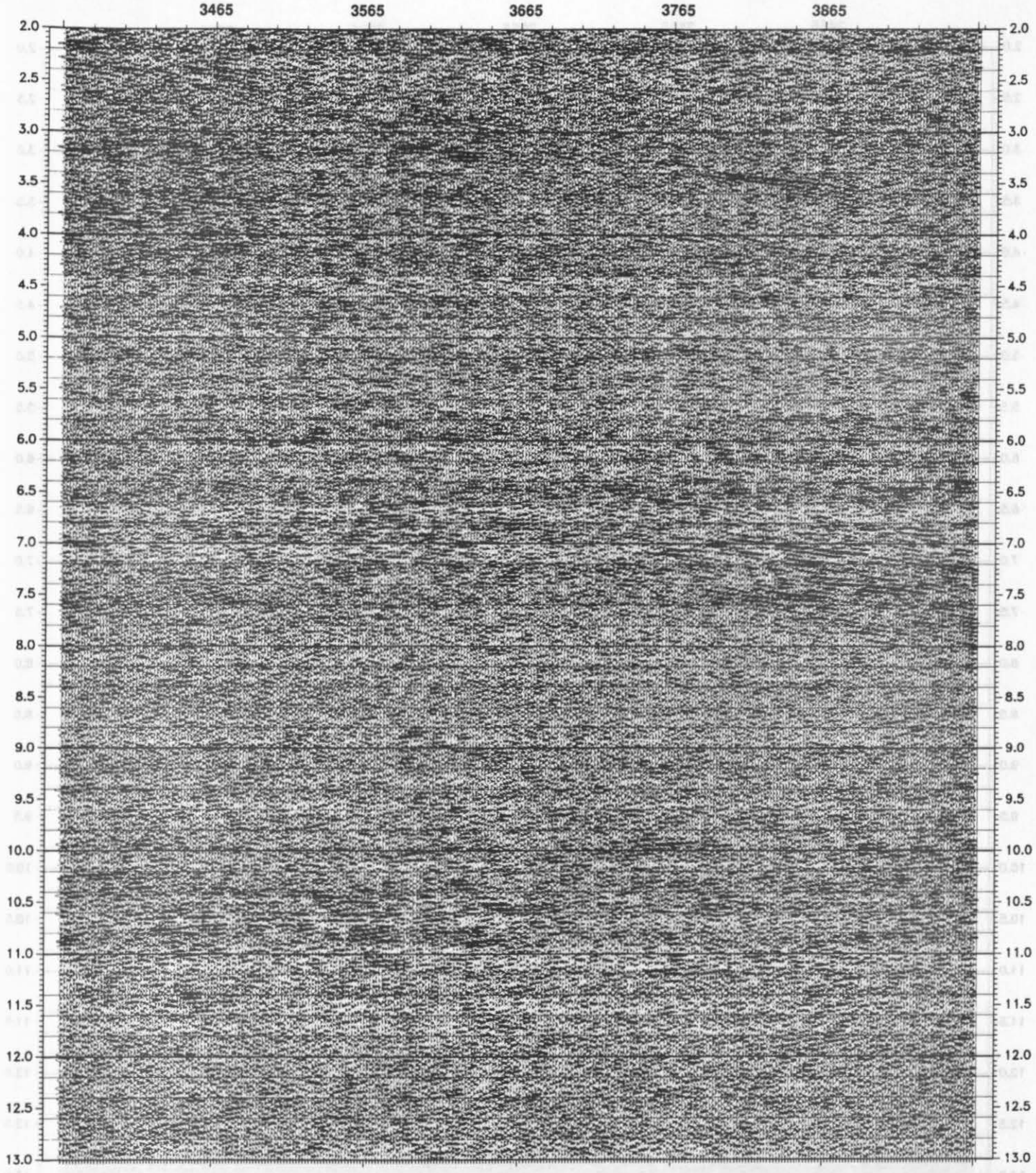

Figure 7: Final stack of the 4-8 km offset subgather. Stacking velocities as in Figure 2c.

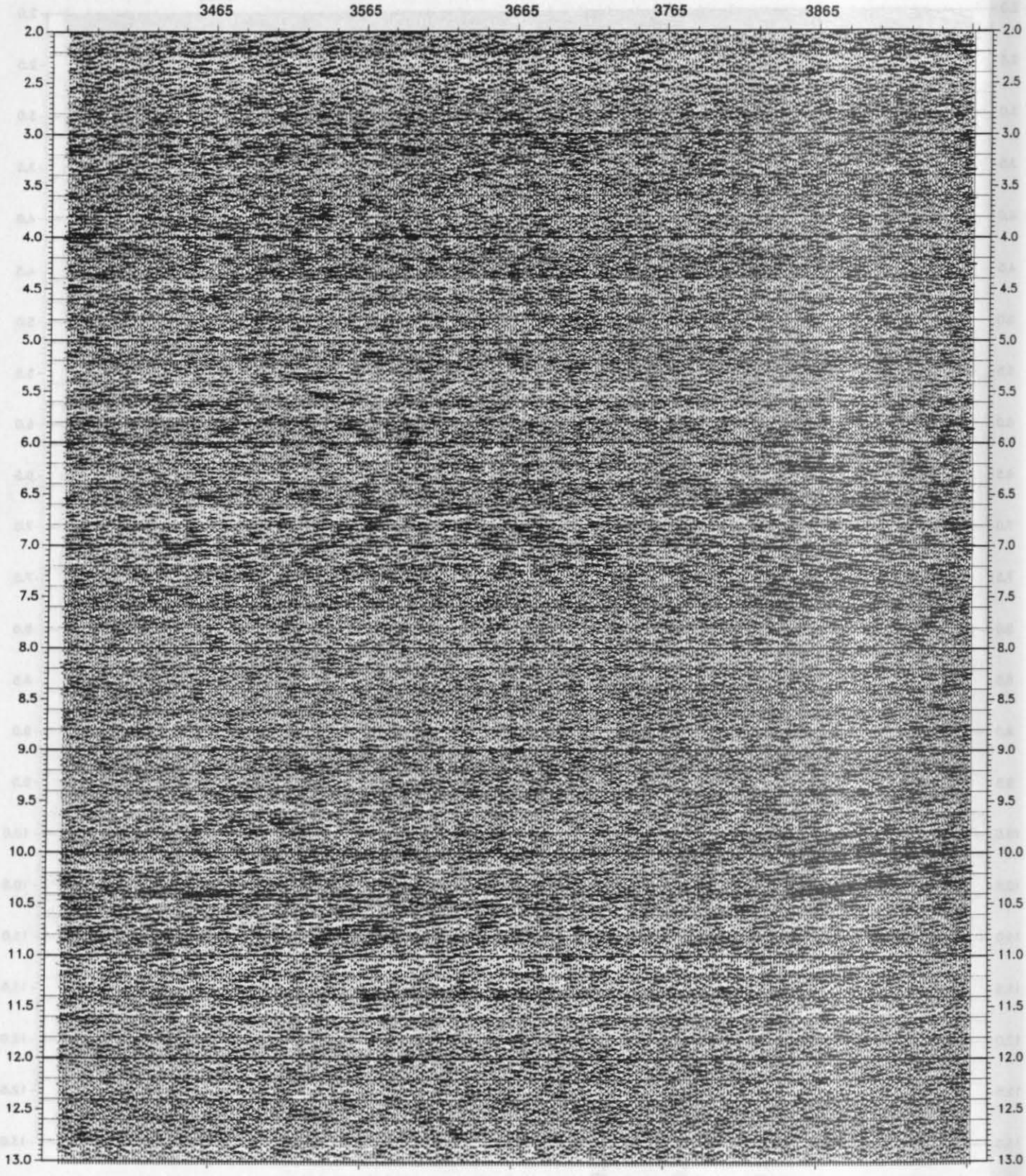

Figure 8: Final stack of the 8-12 km offset subgather. Stacking velocities as in Figure 2d.

The stack of the 4-8 km subgather, which has only half the fold as the 0-4 km subgather, is shown in Figure 7. The stacking velocities determined (Figure 2c) show rather high velocities in the center. The main differences compared to the sections described above are the absence of the bright reflection at 3.2 s in the northeast, and a generally much reduced reflectivity at middle and lower crustal levels. Only the dipping events between 7.0 and 7.5 s in the southeast show some continuity. This subgather is much more sensitive to velocity variations compared to the 0-4 km offset subgather. However, the bright reflection at 3.2 s is not imaged, independent of the velocities used. This remarkable observation suggests a strong decrease of reflection amplitudes at 4 km offset. Since it is at a depth of about 9.5 to 10 km, the angle of incidence is about 12° at 4 km offset, assuming a velocity as found from the velocity analysis. It is impossible to explain this decrease of amplitude by a first order velocity discontinuity, which would require velocity increase of a factor around 3 to 4 (see Telford et al., 1976, p. 254). We therefore suggest a tuning effect from a thin layer to be the most probable explanation.

On the 8-12 km subgather stacks similar observations to the 4-8 km subgather can be made. As seen in Figure 8, the 3.2 s event is missing, and in addition the southeastward dipping events between 2 and 4 s are not imaged. However, middle and lower crustal reflectivity is more pronounced, and a set of strong northwest dipping events at Moho depths in the southeast are prominent. This subgather is sensitive to velocity changes. The northwest dipping Moho reflections mentioned above seem to be independent of velocity changes, but they are only observed in the 8-12 km subgather data. In Figure 9 reflections are compared using the high and the low velocity stack. On the high velocity stack the wave field is more simple and seems to be better focussed. This should then be taken as evidence that we are imaging the tail of an inline diffraction. The middle crustal image between 6 and 8 s is also markedly different when the minimum and maximum velocity stacks of the 8-12 km subgather are compared, as shown in Figure 10.

Figures 9 and 10, see next pages.

Figure 9: Comparison of a part of the 8-12 km offset data, stacked with constant velocities.
Top: V_{Stack} = 5800 m/s; Bottom: V_{Stack} = 7000 m/s.

Figure 10: Comparison of a part of the 8-12 km offset data, stacked with constant velocities.
Top: V_{Stack} = 5800 m/s; Bottom: V_{Stack} = 7000 m/s.

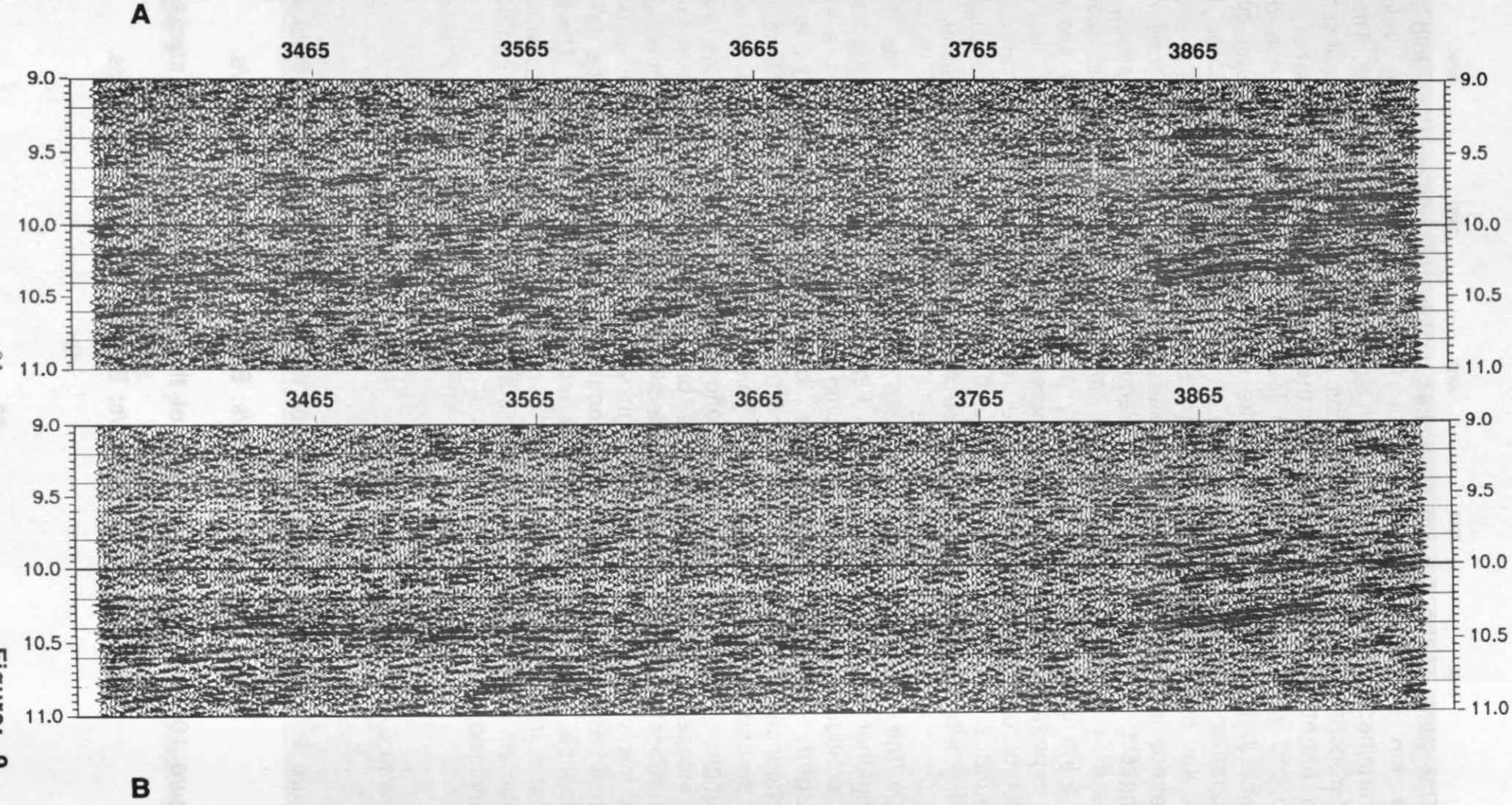
A
3465
3565
3665
3765
3865
9.0
9.5
10.0
10.5
11.0
3465
3565
3665
3765
3865
9.0
9.5
10.0
10.5
11.0
B

Figure: 9

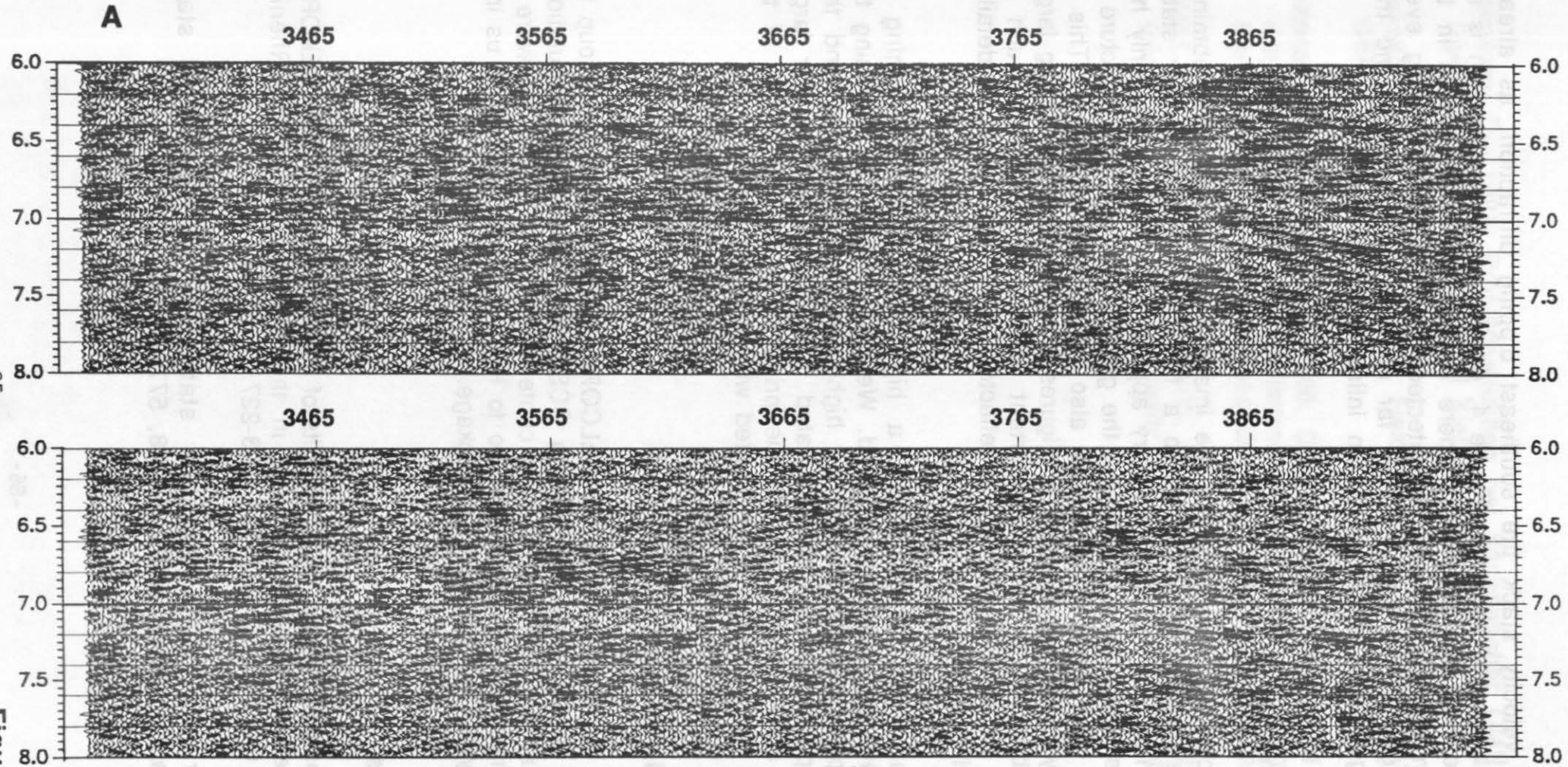
A
3465
3565
3665
3765
3865
6.0
6.5
7.0
7.5
8.0
3465
3565
3665
3765
3865
6.0
6.5
7.0
7.5
8.0
B

Figure: 10

In the low velocity stack the southeast dipping diffraction, as already discussed above and shown in Figure 4, dominates. This diffraction is not seen on the high velocity stack, where northwest dipping events in the northwestern part can clearly be detected. This northwest dipping event is best imaged on the high velocity far offset subgather stack and thus indicates again that is represents an inline diffraction tail.

Conclusions

This exercise demonstrates that the image of crustal structure obtained by deep seismic investigations is to a first approximation rather stable and independent of the field geometry applied. If for the survey only half the channels would have been used, the general outline of the structure of the middle and lower crust could also have been obtained. This is confirmed by comparing the data in Figures 3 and 5. However, using larger offsets enables us to extract important additional information, such as the curious behavior of the 3.2 s reflector, which still awaits a detailed and convincing answer.

In addition, with larger offsets a high amount of fine tuning of individual reflections can be achieved. We have shown that by using the "right" velocities diffractions can be highlighted or illuminated, and that also out-of-plane events can be treated in a similar fashion. For larger offset data stacking velocities are the primary key for this tuning of the section and should therefore be treated with greatest care.

Acknowledgements

We thank our colleagues of the BELCORP/DEKORP Research Group for making this dataset available for the CCSS Workshop. Our computations were made at GEOMAR's processing center using the GEOSYS software of Prakla Seismos AG. Special thanks go to Hans Vosberg for guiding us into the deep mystery of the software package.

References

DEKORP Research Group, 1991: Results of DEKORP 1 (BELCORP-DEKORP) deep seismic reflection studies in the western part of the Rhenish Massif; Geophys. J. Int., 106, 203-227.

Kirchheimer, F., 1990: Residual statics by CDP-localized stack optimization; Geophys. Prosp., 38, 577-606.

Klaeschen, D., 1988: Profilkonstruktion bei flächenhafter CMP-Verteilung; Diploma Thesis, University of Kiel, 85 pp.

Klöckner, M. and Stiller, M., 1991: Field Survey and Data Processing of Line DEKORP 1A; This volume.

Meissner, R., Bortfeld, R.K., 1990: DEKORP-Atlas, Results of Deutsches Kontinentales Reflexionsseismisches Programm; Springer Verlag, Berlin-Heidelberg-New York-London-Paris-Hong Kong-Barcelona.

Telford, W.M., Geldart, L.P., Sherift, R.E., and Keys, D.A., 1976: Applied Geophysics; Cambridge University Press, Cambridge, 860 pp.

REPROCESSED RESULTS OF DEEP-SEISMIC REFLECTION PROFILE, LINE BELCORP/DEKORP 1A [1)]

Kris Vasudevan and Todd Clark

LITHOPROBE Seismic Processing Facility, Department of Geology and Geophysics
The University of Calgary, Calgary, Alberta T2N 1N4, CANADA

ABSTRACT

The DEKORP RESEARCH GROUP provided the LITHOPROBE Seismic Processing Facility two data sets, CCSS data set 1b and CCSS data set 1c for both post-stack and pre-stack processing. The data sets are part of BELCORP-DEKORP line 1A. Dataset 1b contains the final stack of the deep seismic reflection profile for line 1A. Pre-stack common mid-point gathers for a portion of the line, CMPs 3366-3964, represent the dataset 1c.

In this paper, the results of post-stack processing of the final stack (CCSS 1b) including migration and coherency analysis, and the pre-stack processing of the CMPs (CCSS 1c) are presented. The coherency analysis in conjunction with the appropriate choice of plotting parameters of the migrated sections affords a mechanism to generate coherent reflections without random noise. This minimizes bias in selection of events and permits reporting of selection criteria as tunable parameters.

Two slightly different pre-stack processing schemes were used for the data set 1c. The difference lies in the pre-stack mixing of the traces within each CMP ensemble. The final stacks from the two schemes were subjected to several migration and coherency analysis tests. Stacking velocities as well as refraction velocities derived by Mechie, Prodehl and Fuchs were used for the migrations.

Results show that pre-stack mixing of the traces within each CMP ensemble brings more detail into the shallow part of the seismic reflection profile, indicate that migration velocities are crucial in elucidating the crustal structure, and they lend support to the automated line drawing of the crustal data for display and interpretation purposes.

---

1) LITHOPROBE contribution number: 257

INTRODUCTION

The BELCORP-DEKORP line 1A (Figure 1) starts close to the Belgian-Dutch border southeast of Maastricht. It traverses the Stavelot Venn Massif and finally crosses the volcanic Eifel north-south zone in Germany. Initial results of deep-seismic reflection investigations in the Rhenish Massif pertaining to line 1A (DEKORP Research Group, 1990a, 1990b) reveal lower and mid crustal reflections over long distances in the central and southeastern portion of the line, a band of reflections below the perceived Moho reflections in the same part of the line, and very little crustal reflectivity from 1 s to 9 s in the northwestern part of the profile.

In this study, the results of post-stack migration and coherency analysis of the final stack (CCSS 1b) are presented. Also considered are results of pre-stack processing of CMP gathers (CMPs 3366 to 3964) representing the portion of the profile with reflectivity from all parts of the crust. The processed results confirm earlier interpretations made by the DEKORP Research Group (1990a, 1990b). They also show the importance of the automated line diagrams in presenting crustal reflection data and the sensitivity of velocities on the migration of steeply dipping events in the middle and lower crusts. All the processing at the LITHOPROBE Seismic Processing Facility (LSPF) was carried out with the CYBER/DISCO^{TM} [2] processing system.

PRE-STACK PROCESSING OF CCSS 1c

Two pre-stack processing schemes, SCHEME 1 and SCHEME 2 (Figures 2a and 2b) were applied to the CCSS 1c. As the necessary geometry information such as CMP number, shot station number, and receiver station number did not come with the data set, the processing was restricted to examining the results of two processing schemes and studying the offset-dependency of the final stack. In both processing schemes, velocity functions used for normal move-out corrections were derived from constant velocity stack procedure. This was used in preference to semblance analysis since picking semblance was found to be extremely difficult and unreliable because of the noise content of the data set. For display purposes, coherency analysis was used. In SCHEME 1, 1-3-1 weighted running-mix of three traces within each NMO-corrected CMP ensemble was carried out.

---

[2] DISCO^{TM} : Trademark of CogniSeis Development Limited.

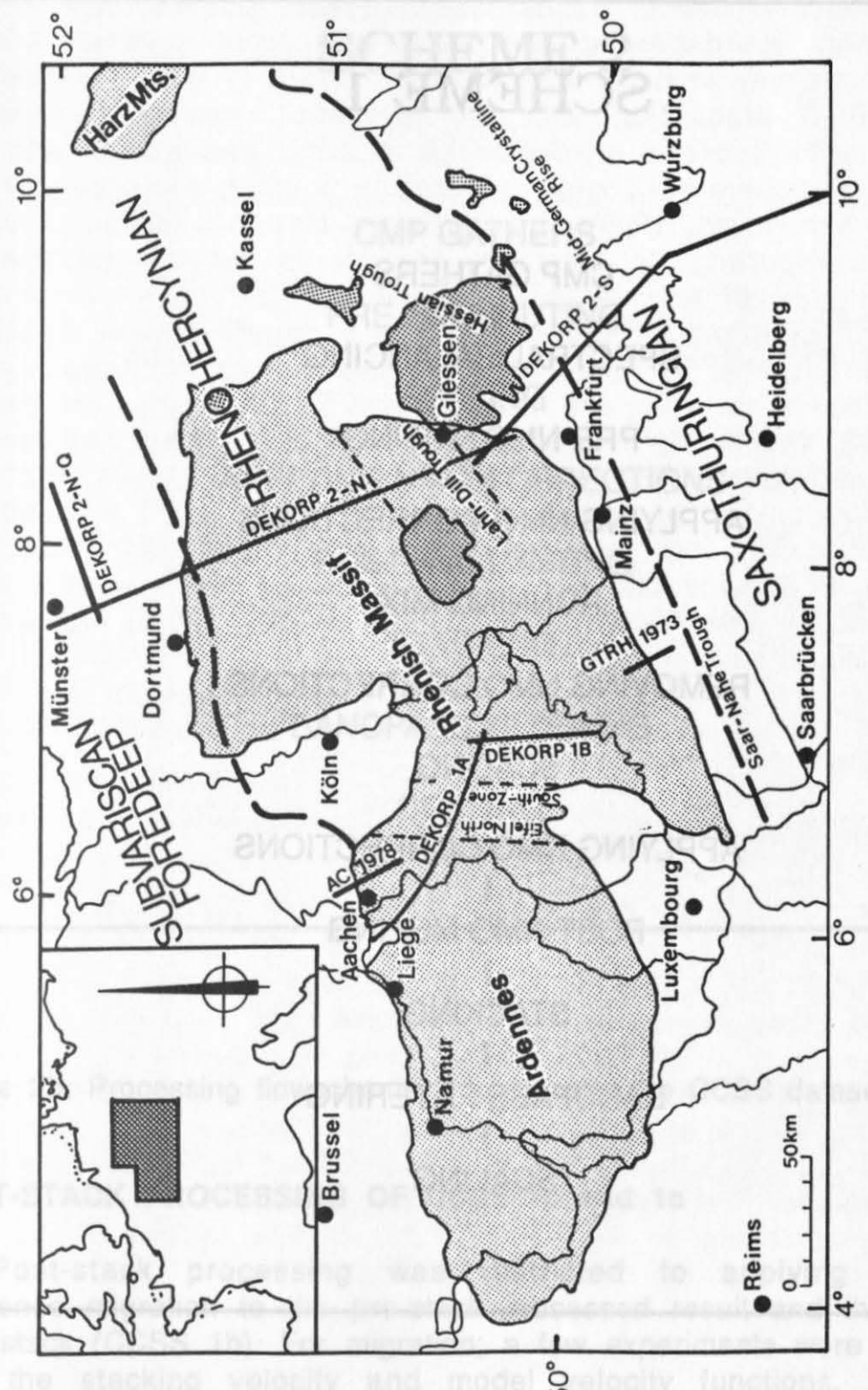

Figure 1: Location map of the DEKORP lines in the Rhenish Massif (Courtesy of DEKORP Research Group).

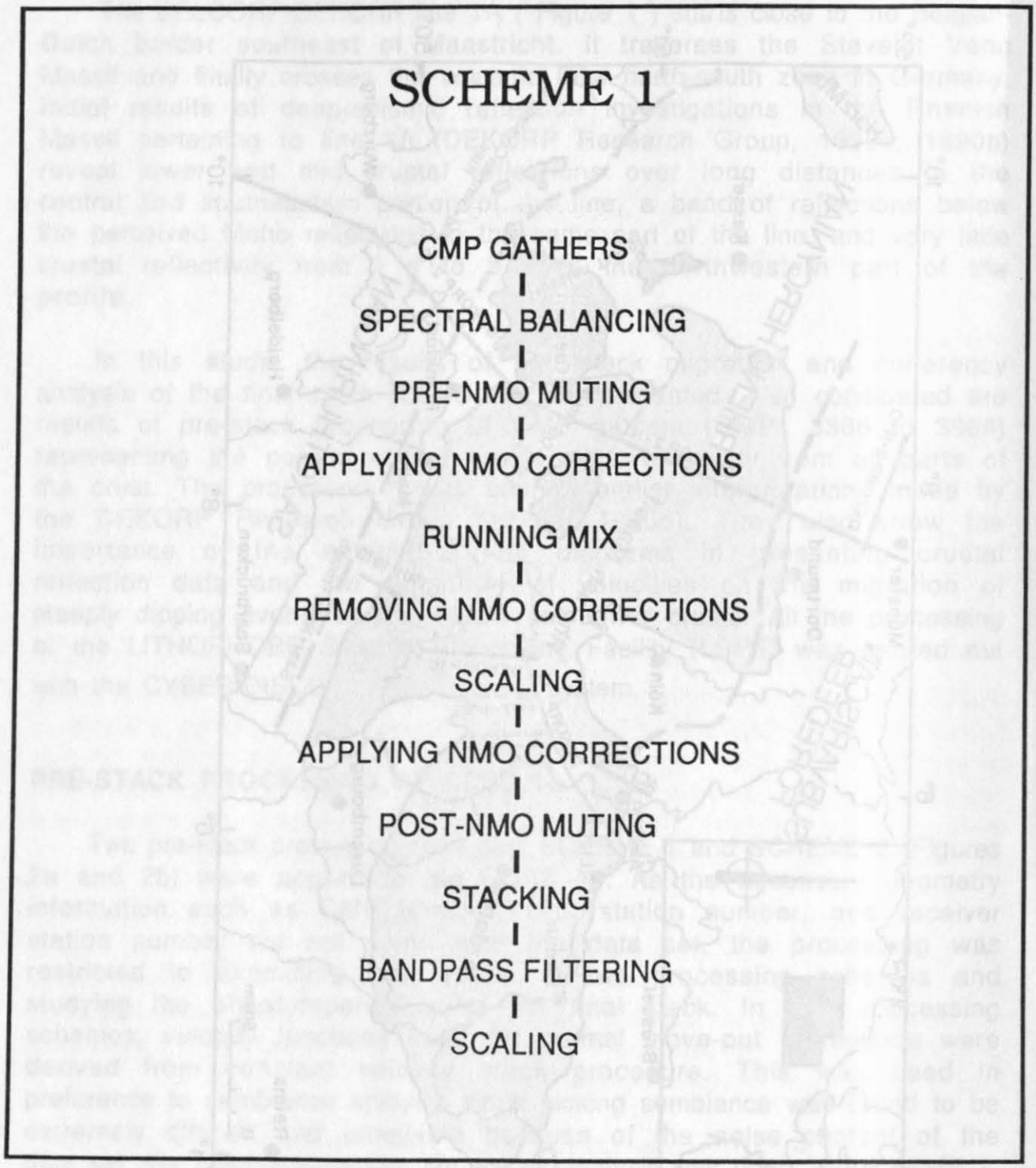

Figure 2a: Processing flowscheme 1 to process the CCSS data set 1c.

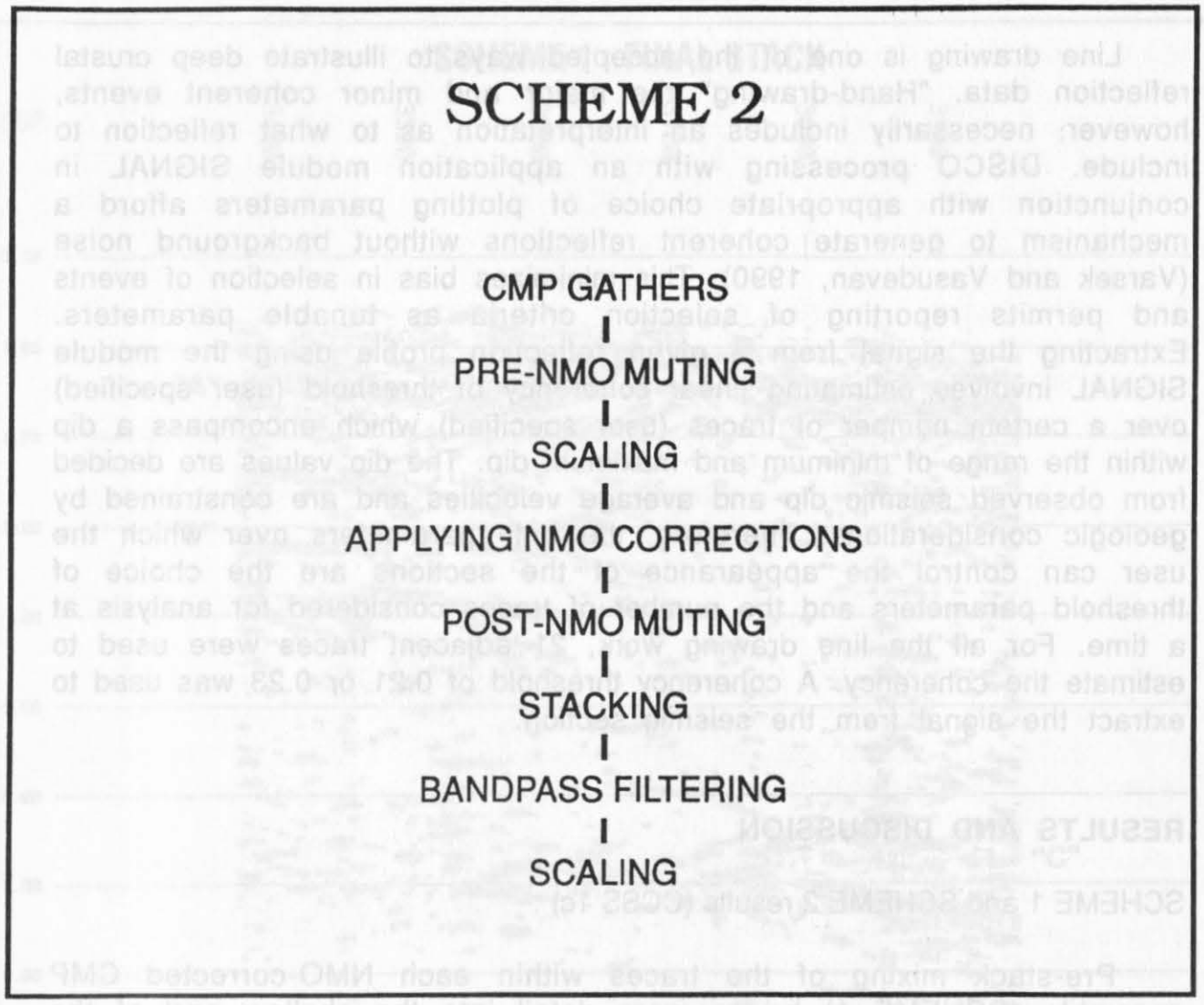

Figure 2b: Processing flowscheme 2 to process the CCSS dataset 1c.

POST-STACK PROCESSING OF CCSS 1b and 1c

Post-stack processing was restricted to applying the finite difference migration to the pre-stack processed result and the DEKORP final stack (CCSS 1b). For migration, a few experiments were carried out with the stacking velocity and model velocity functions. The model velocity function was derived from wide-angle refraction experiments (Mechie et al, 1983; DEKORP Research Group, 1990b). Since there is a certain amount of uncertainty associated with the model velocity function, well-defined variations of the two velocity functions mentioned earlier were allowed in the migration experiments.

COHERENCY FILTERING

Line drawing is one of the accepted ways to illustrate deep crustal reflection data. "Hand-drawing" the major and minor coherent events, however, necessarily includes an interpretation as to what reflection to include. DISCO processing with an application module SIGNAL in conjunction with appropriate choice of plotting parameters afford a mechanism to generate coherent reflections without background noise (Varsek and Vasudevan, 1990). This minimizes bias in selection of events and permits reporting of selection criteria as tunable parameters. Extracting the signal from a given reflection profile using the module SIGNAL involves estimating linear coherency of threshold (user specified) over a certain number of traces (user specified) which encompass a dip within the range of minimum and maximum dip. The dip values are decided from observed seismic dip and average velocities and are constrained by geologic considerations. Therefore, the only parameters over which the user can control the appearance of the sections are the choice of threshold parameters and the number of traces considered for analysis at a time. For all the line drawing work, 21 adjacent traces were used to estimate the coherency. A coherency threshold of 0.21 or 0.23 was used to extract the signal from the seismic section.

RESULTS AND DISCUSSION

SCHEME 1 and SCHEME 2 results (CCSS 1c) :

Pre-stack mixing of the traces within each NMO-corrected CMP ensemble (SCHEME 1) brings more detail into the shallow part of the seismic reflection profile than the SCHEME 2 does (Figures 3 and 4). This result is due to an increase in signal to noise (S/N) ratio with mixing. In SCHEME 1, time invariant, spectral balancing was carried out within the boundaries of the signal bandwidth of the seismic data. Automated gain control-scaling with a window of 1000 ms. was done to the data within the spectral balancing application. The four corner points considered for the signal bandwidth of the seismic data are 10, 12, 45 and 55 Hz. Since NMO-corrections might be significant in the shallow regions of the data, nmoapply was done to the data before running mix.

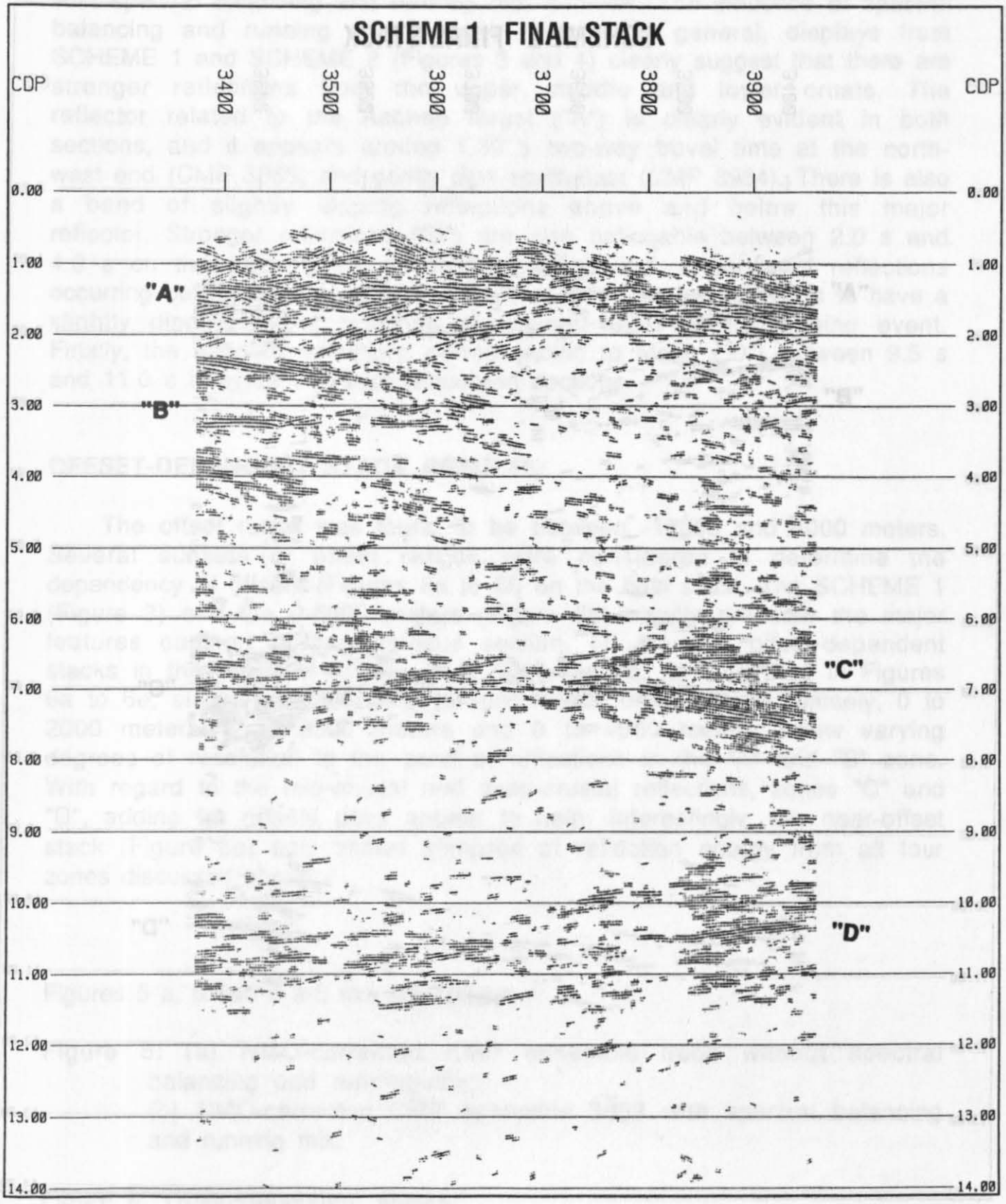

Figure 3: Final coherency stack section - Processing scheme 1 (Plotting direction: left to right corresponds to NW to SE).

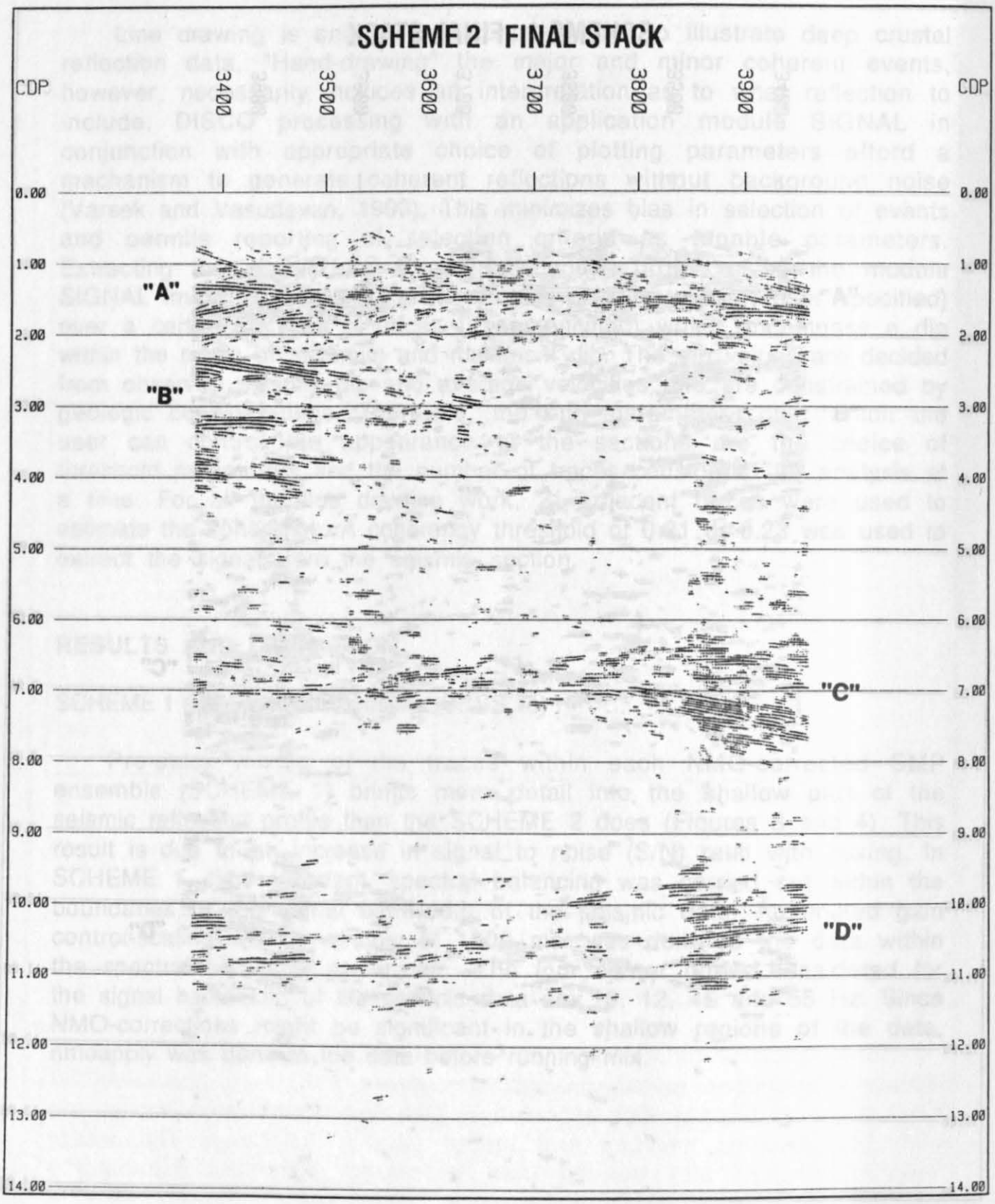

Figure 4: Final coherency stack section - Processing scheme 2 (Plotting direction: left to right corresponds to NW to SE).

In Figure 5, a comparison of results on CMP ensemble 3853 without and with spectral balancing and running mix is made. The influence of spectral balancing and running mix is quite obvious. In general, displays from SCHEME 1 and SCHEME 2 (Figures 3 and 4) clearly suggest that there are stronger reflections from the upper, middle and lower crusts. The reflector related to the Aachen thrust ("A") is clearly evident in both sections, and it appears around 1.30 s two-way travel time at the north-west end (CMP 3366) and gently dips south-east (CMP 3964). There is also a band of slightly dipping reflections above and below this major reflector. Stronger reflections ("B") are also noticeable between 2.0 s and 4.0 s on the western end of the processed line. A series of reflections occurring between 6.0 s and 8.0 s ("C") on the southeast appears to have a slightly dipping event overlying a stronger west-upward dipping event. Finally, the band of reflections corresponding to Moho ("D") between 9.5 s and 11.0 s is evident in both processed sections.

OFFSET-DEPENDENT STACK RESULTS:

The offset range was found to be between -12000 and 4000 meters. Several subsets of offset ranges were considered to determine the dependency of offsets (Figures 6a to 6f) on the final stack. The SCHEME 1 (Figure 3) and the 0-5000 meters (Figure 6e) results preserve the major features outlined in the previous section. Of the five offset-dependent stacks in the range of offsets, 0 to 5000 meters, as illustrated in Figures 6a to 6e, stacks corresponding to intermediate offset ranges, namely, 0 to 2000 meters, 0 to 3000 meters and 0 to 4000 meters, show varying degrees of resolution to the band of reflections in the "A" and "B" zone. With regard to the mid-crustal and deep-crustal reflections, zones "C" and "D", adding far offsets does appear to help. Interestingly, the near-offset stack (Figure 6a) only shows glimpses of reflection energy from all four zones discussed above.

Figures 5 a, b and 6 a-f, see next pages.

Figure 5: (a) NMO-corrected CMP ensemble 3853 without spectral balancing and running-mix;
(b) NMO-corrected CMP ensemble 3853 with spectral balancing and running mix.

Figure 6: Offset-dependent stacks.
(a) 0 - 1000 meters;
(b) 0 - 2000 meters;
(c) 0 - 3000 meters;
(d) 0 - 4000 meters;
(e) 0 - 5000 meters;
(f) > 5000 meters.

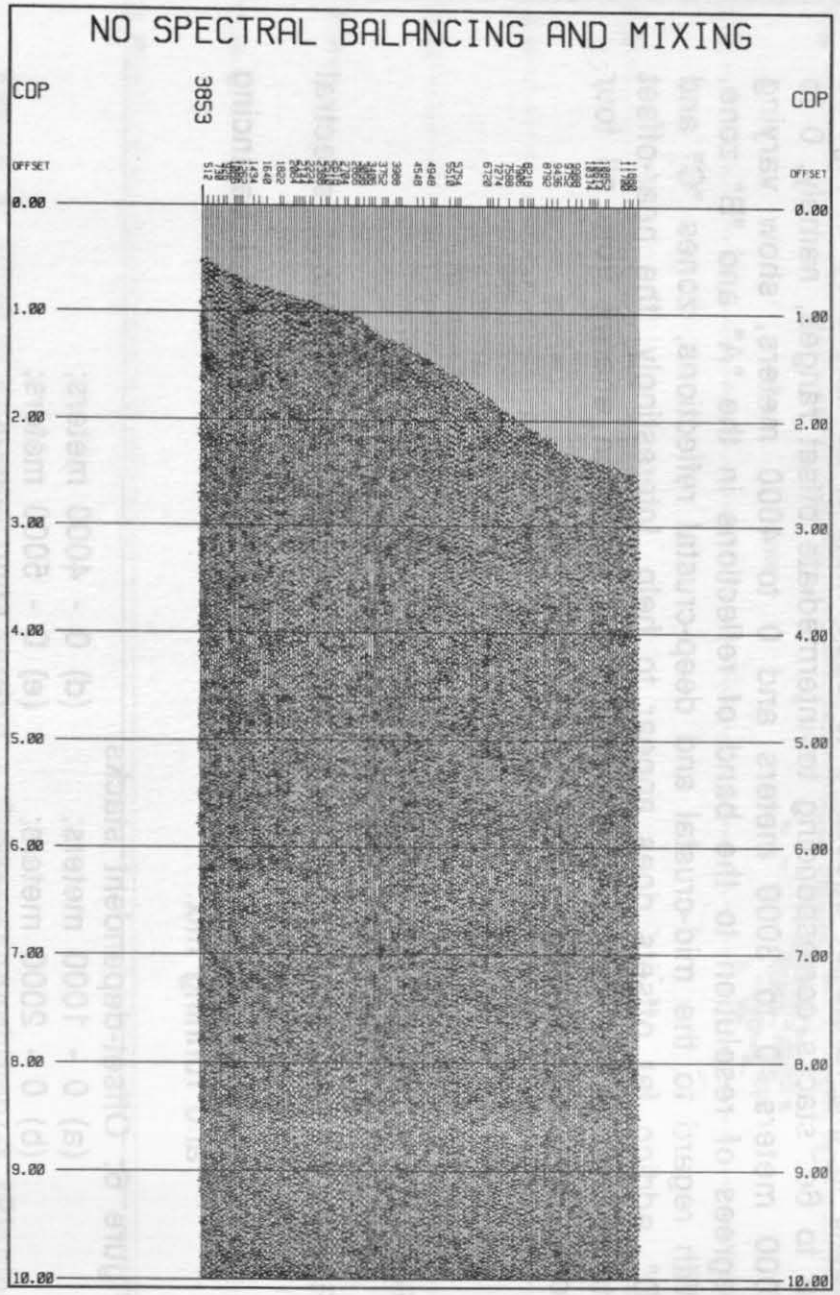

Figure 5a

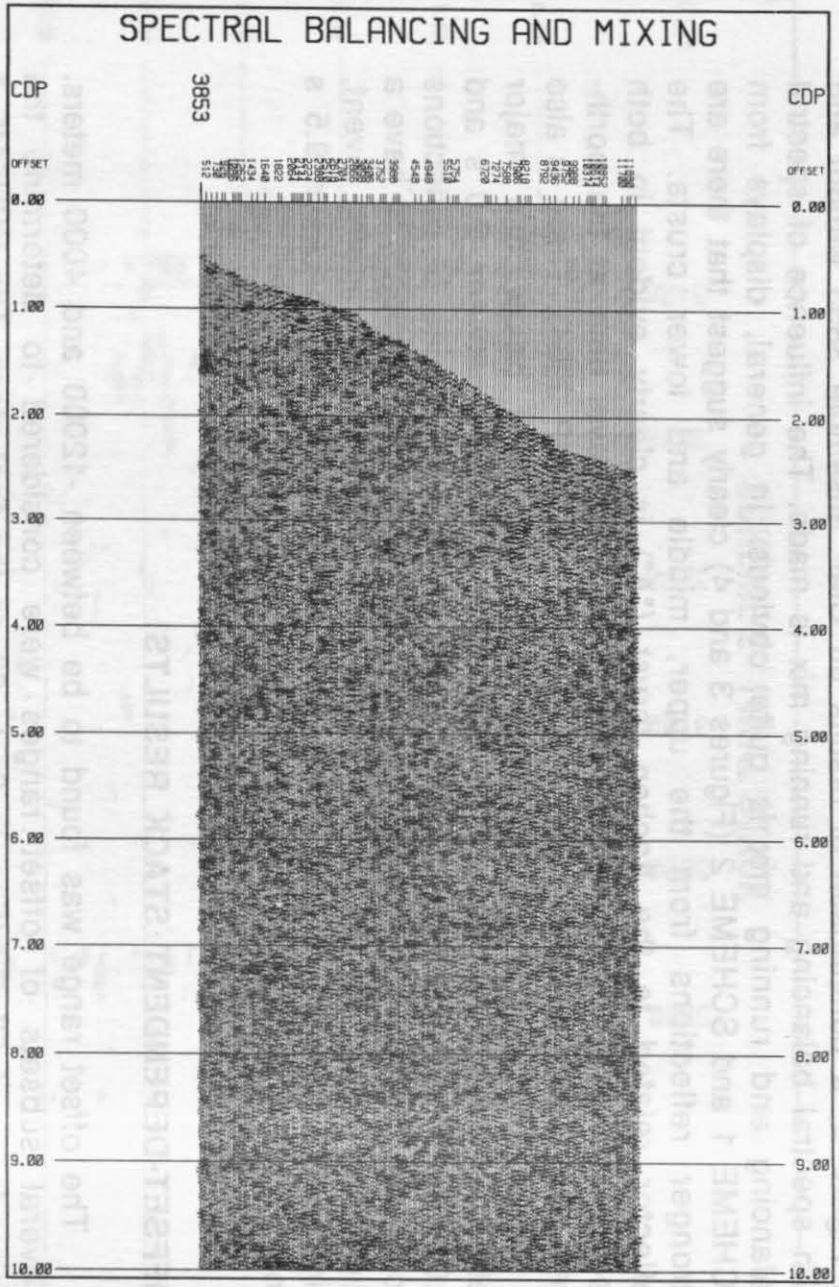

Figure 5b

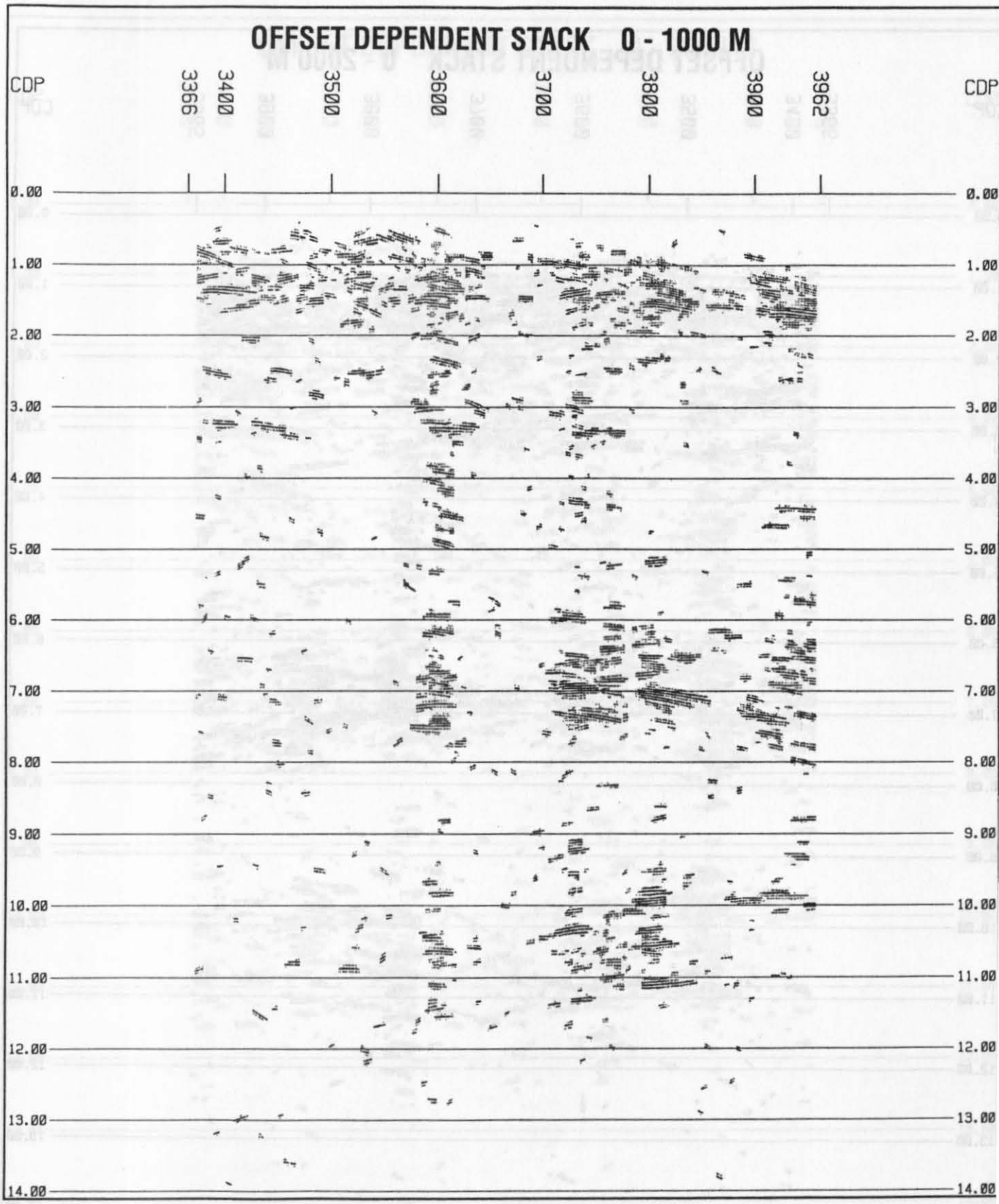
OFFSET DEPENDENT STACK 0 - 1000 M
CDP
3366
3400
3500
3600
3700
3800
3900
3962
CDP
0.00
1.00
2.00
3.00
4.00
5.00
6.00
7.00
8.00
9.00
10.00
11.00
12.00
13.00
14.00

Figure: 6a

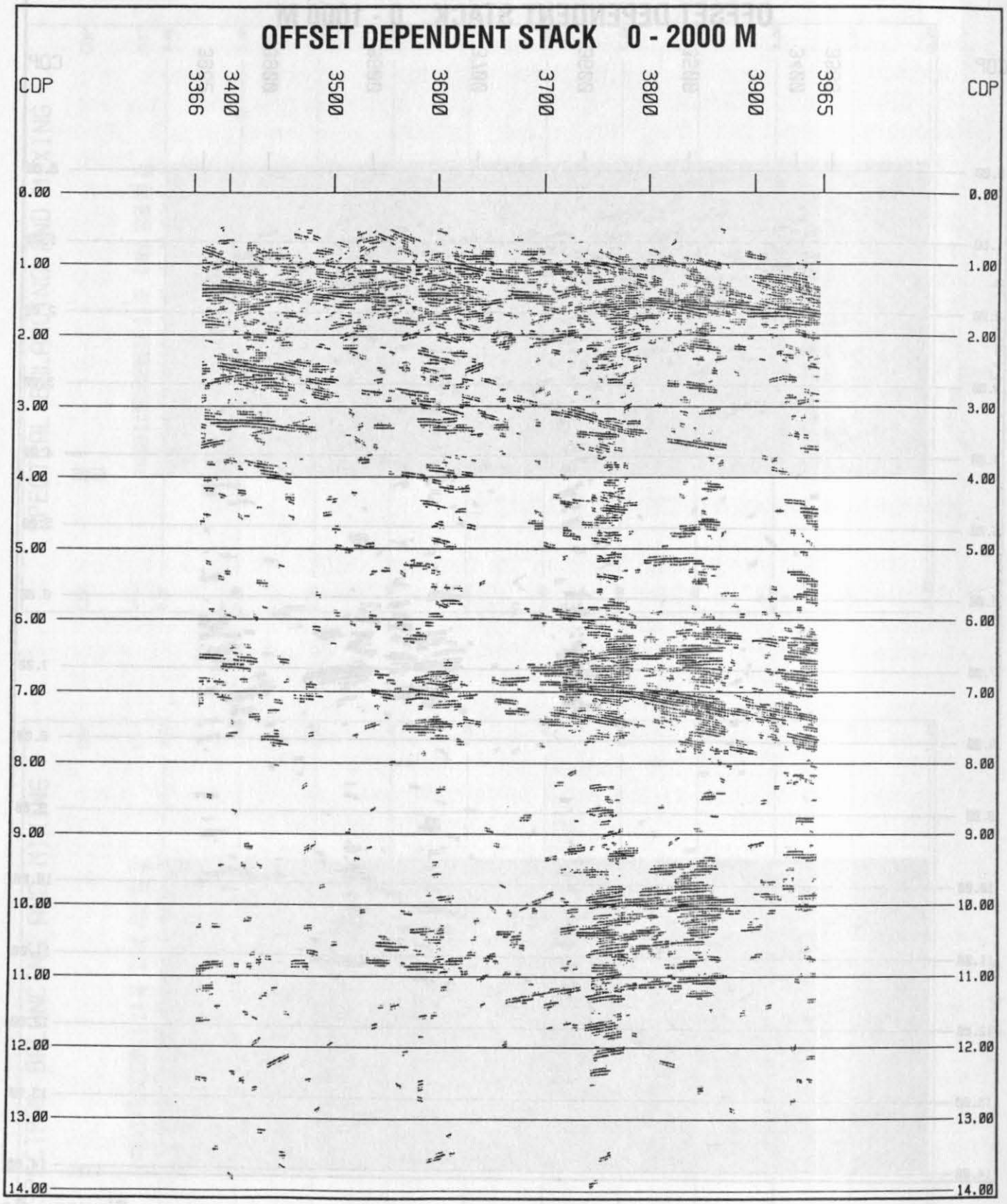
OFFSET DEPENDENT STACK 0 - 2000 M
CDP
3366
3400
3500
3600
3700
3800
3900
3965
CDP
0.00
1.00
2.00
3.00
4.00
5.00
6.00
7.00
8.00
9.00
10.00
11.00
12.00
13.00
14.00

Figure: 6b

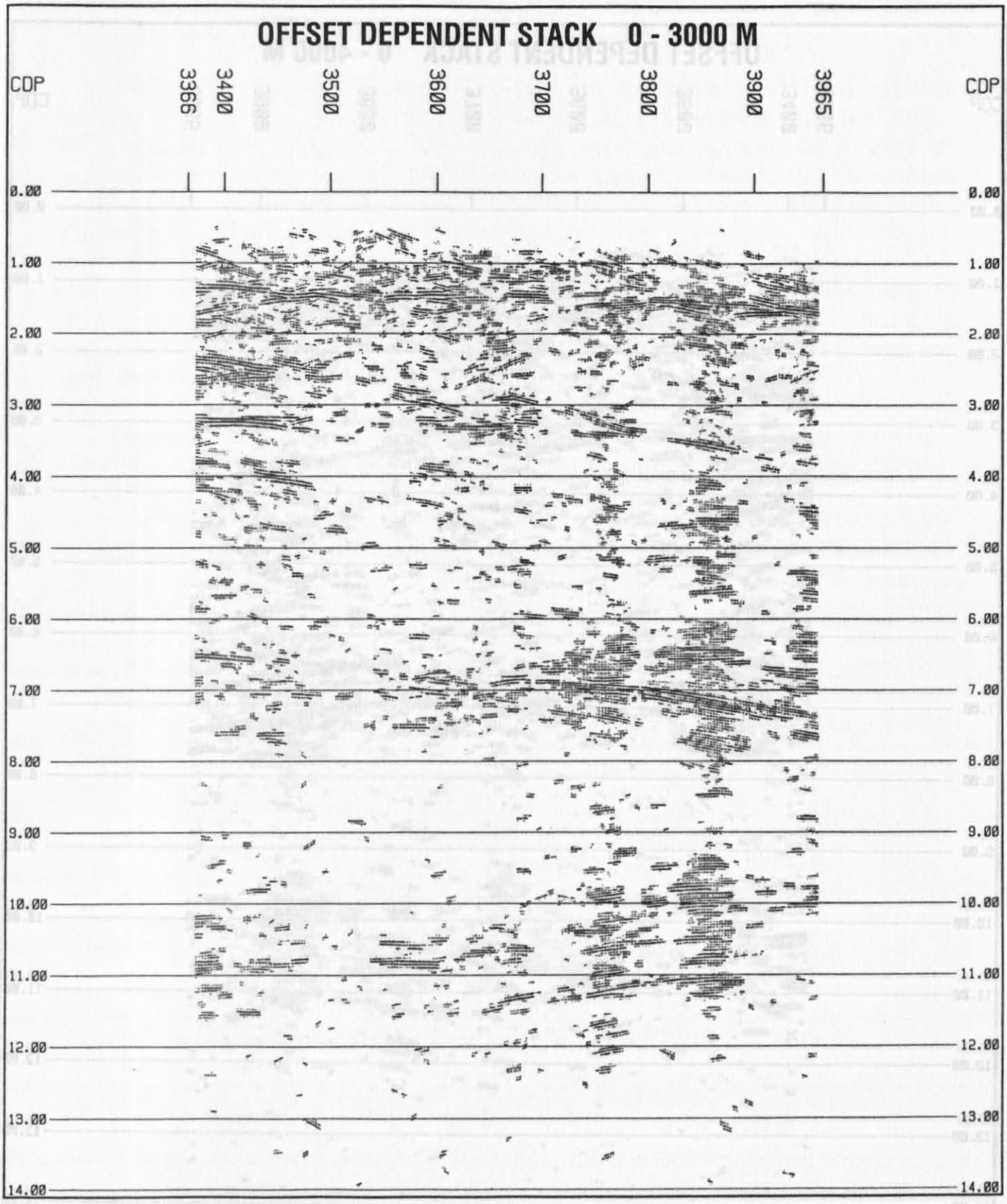
OFFSET DEPENDENT STACK 0 - 3000 M
CDP
3366
3400
3500
3600
3700
3800
3900
3965
CDP
0.00
1.00
2.00
3.00
4.00
5.00
6.00
7.00
8.00
9.00
10.00
11.00
12.00
13.00
14.00

Figure: 6c

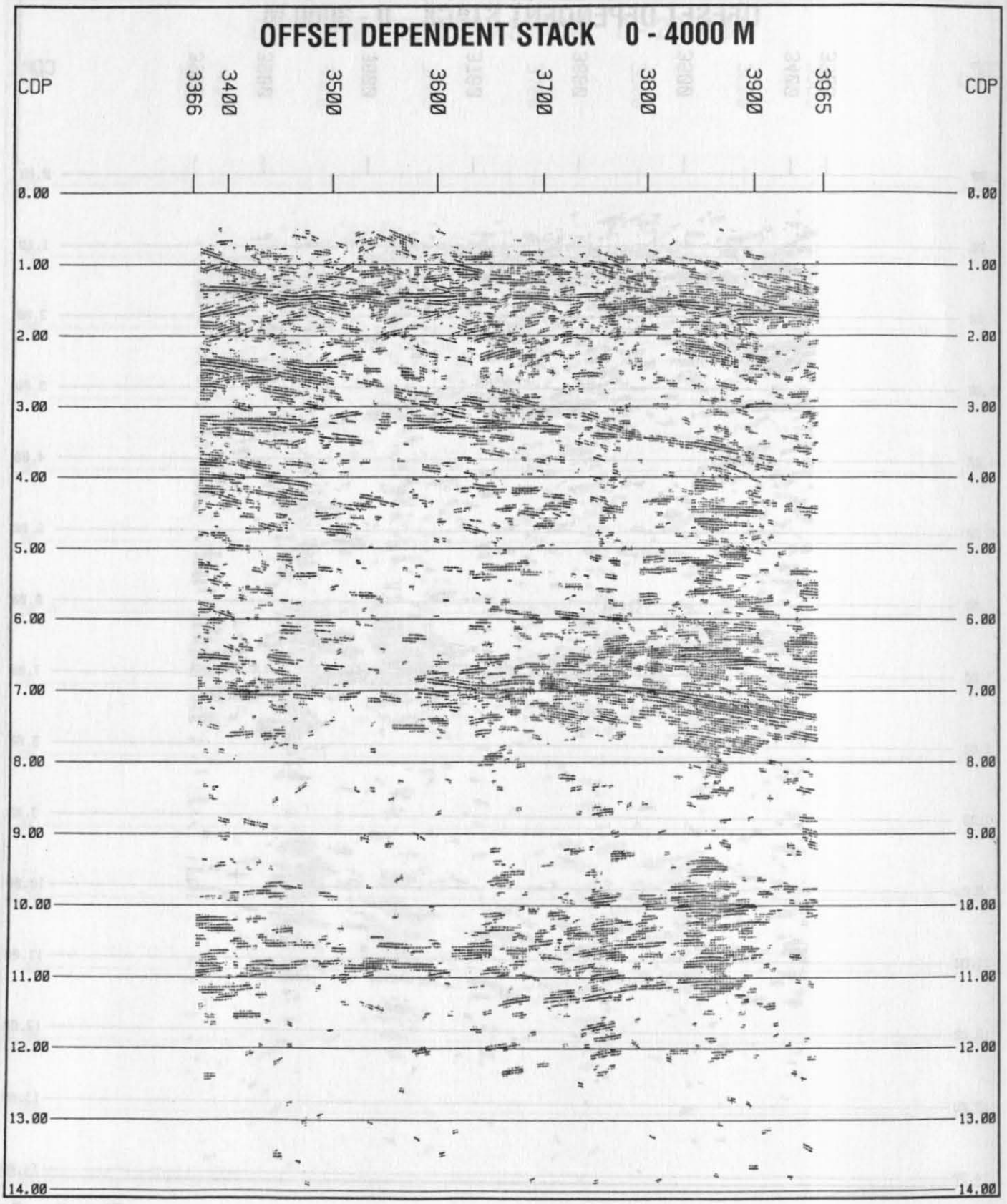
OFFSET DEPENDENT STACK 0 - 4000 M
CDP
3366
3400
3500
3600
3700
3800
3900
3965
CDP
0.00
1.00
2.00
3.00
4.00
5.00
6.00
7.00
8.00
9.00
10.00
11.00
12.00
13.00
14.00

Figure: 6d

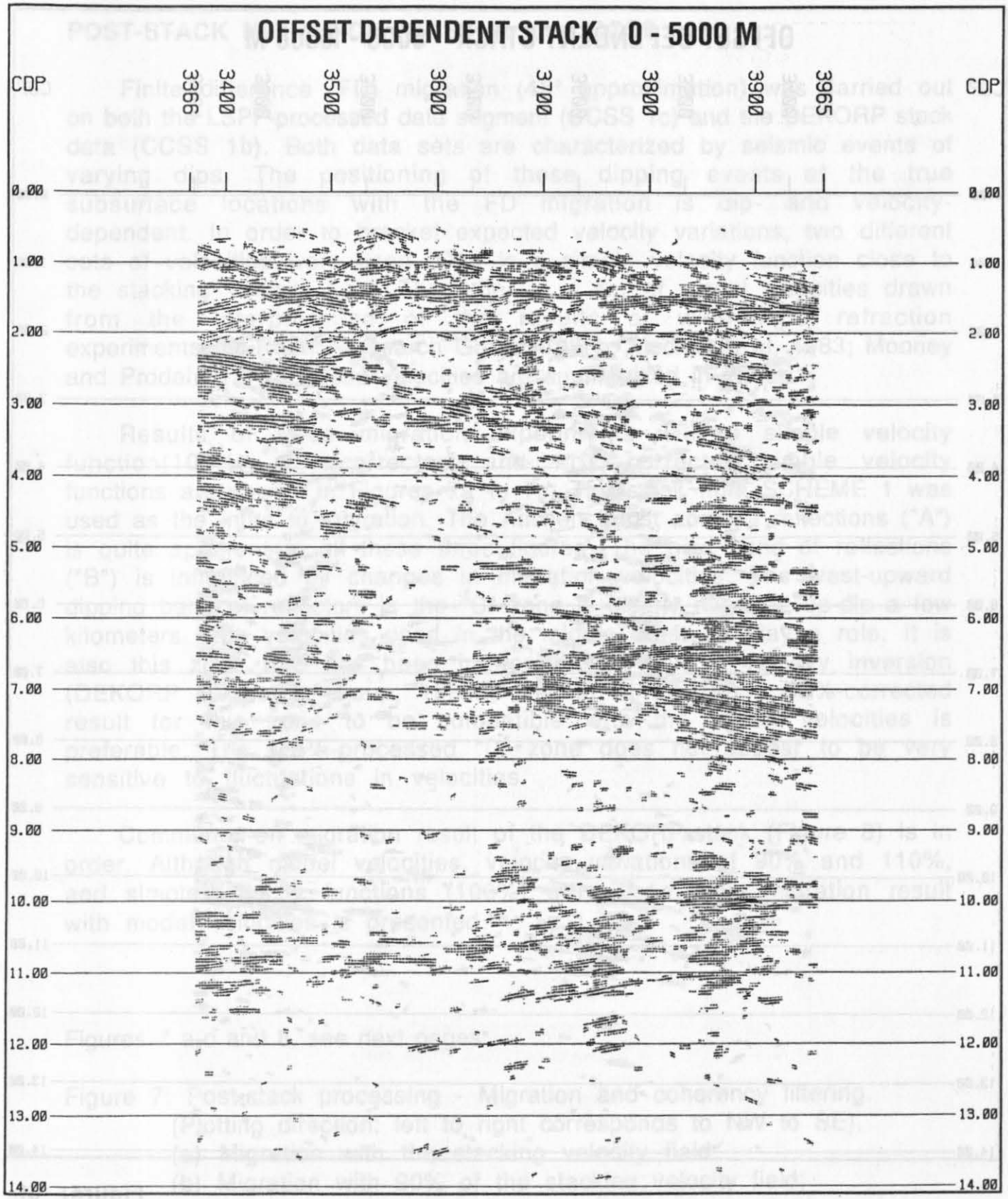
OFFSET DEPENDENT STACK 0 - 5000 M
CDP
3366
3400
3500
3600
3700
3800
3900
3965
CDP
0.00
1.00
2.00
3.00
4.00
5.00
6.00
7.00
8.00
9.00
10.00
11.00
12.00
13.00
14.00

Figure: 6e

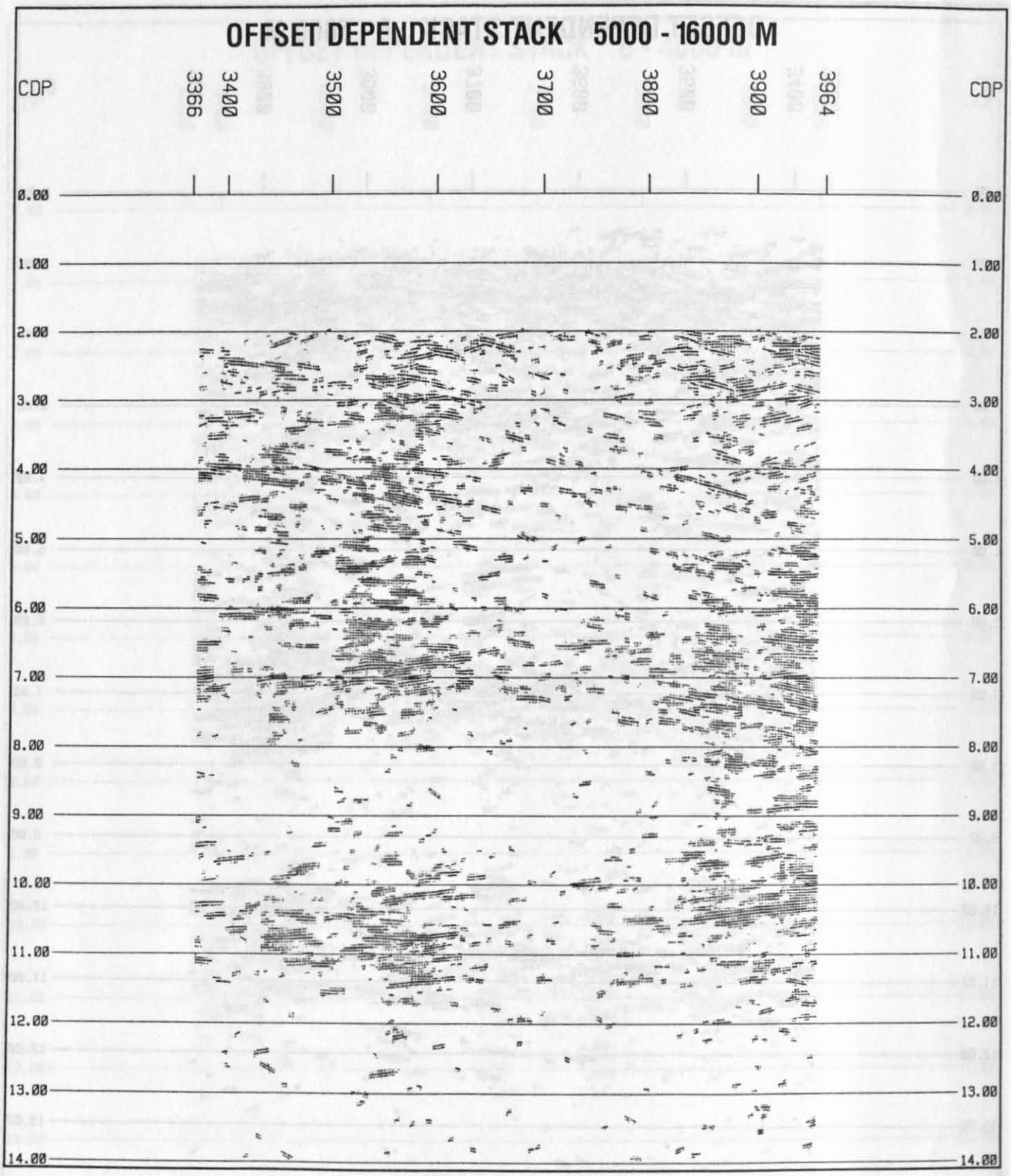
OFFSET DEPENDENT STACK 5000 - 16000 M
CDP
3366
3400
3500
3600
3700
3800
3900
3964
CDP
0.00
1.00
2.00
3.00
4.00
5.00
6.00
7.00
8.00
9.00
10.00
11.00
12.00
13.00
14.00

Figure: 6f

POST-STACK MIGRATION (CCSS 1b and CCSS 1c) :

Finite difference (FD) migration (45° approximation) was carried out on both the LSPF-processed data segment (CCSS 1c) and the DEKORP stack data (CCSS 1b). Both data sets are characterized by seismic events of varying dips. The positioning of these dipping events at the true subsurface locations with the FD migration is dip- and velocity-dependent. In order to bracket expected velocity variations, two different sets of velocities were used. One is a simple velocity function close to the stacking velocity field. The other is a set of model velocities drawn from the interpretation of the results of wide-angle refraction experiments (DEKORP Research Group, 1990b; Mechie et al, 1983; Mooney and Prodehl 1978). These velocities are summarized in Table 1.

Results of three migration experiments with a simple velocity function(100%), 90%-corrected, and 110%-corrected simple velocity functions are shown in Figures 7a to 7c. The stack from SCHEME 1 was used as the input to migration. The Aachen thrust zone of reflections ("A") is quite apparent in all these three figures. The next band of reflections ("B") is influenced by changes in migration velocities. The west-upward dipping band of reflectors in the "C" zone is clearly migrated up-dip a few kilometers. The velocities used in the middle crust do play a role. It is also this zone that has been interpreted to have a velocity inversion (DEKORP Research Group, 1990b; Mechie et al, 1983). 90%-corrected result for this zone to be compatible with the model velocities is preferable. The LSPF-processed "D" zone does not appear to be very sensitive to fluctuations in velocities.

Comments on migration result of the DEKORP-stack (Figure 8) is in order. Although model velocities, velocity variations of 90% and 110%, and simple velocity functions (100%) were used, only migration result with model velocities is presented.

Figures 7 a-c and 8, see next pages.

Figure 7: Post-stack processing - Migration and coherency filtering.
(Plotting direction: left to right corresponds to NW to SE).
(a) Migration with the stacking velocity field;
(b) Migration with 90% of the stacking velocity field;
(c) Migration with 110% of the stacking velocity field.

Figure 8: DEKORP full section - Migration and coherency filtering - migration with the model velocity (Plotting direction: left to right corresponds to NW to SE).

TABLE 1. VELOCITIES USED FOR MIGRATION STUDIES

STACKING VELOCITIES
(Migration of CCSS 1c dataset)

CMP LOCATION 3450		CMP LOCATION 3650		CMP LOCATION 3850	
TIME(S)	VELOCITY(M/S)	TIME(S)	VELOCITY(M/S)	TIME(S)	VELOCITY(M/S)
0.00	4500	0.00	4500	0.00	4500
0.20	4569	0.20	4613	0.40	4612
1.40	5588	1.20	5147	1.00	5530
2.80	6481	2.40	5643	4.40	6444
3.40	6569	3.40	6299	9.80	6444
11.40	6625	7.20	6899	14.00	7750
13.55	7985	10.60	7254	16.00	8200
16.00	8400	16.00	8400		

MODEL VELOCITIES
(Migration of CCSS 1b dataset)

CMP LOCATION 3500		CMP LOCATION 5000	
TIME(S)	VELOCITY(M/S)	TIME(S)	VELOCITY(M/S)
0.00	5000	0.00	5000
1.34	6150	1.34	6200
2.00	6200	2.50	6250
2.34	6400	3.33	5800
3.00	6650	4.00	6400
3.70	6100	5.30	6700
7.30	6100	6.33	6250
8.00	6700	6.67	6300
10.00	6700	9.00	6600
12.00	8100	10.33	8000
16.00	8400	11.33	8100
		16.00	8400

SIMPLE VELOCITY FUNCTION
(Migration of CCSS 1b dataset)

TIME(S)	VELOCITY(M/S)
0	4500
1500	5000
2500	5750
5000	6500
12000	8000
16000	8500

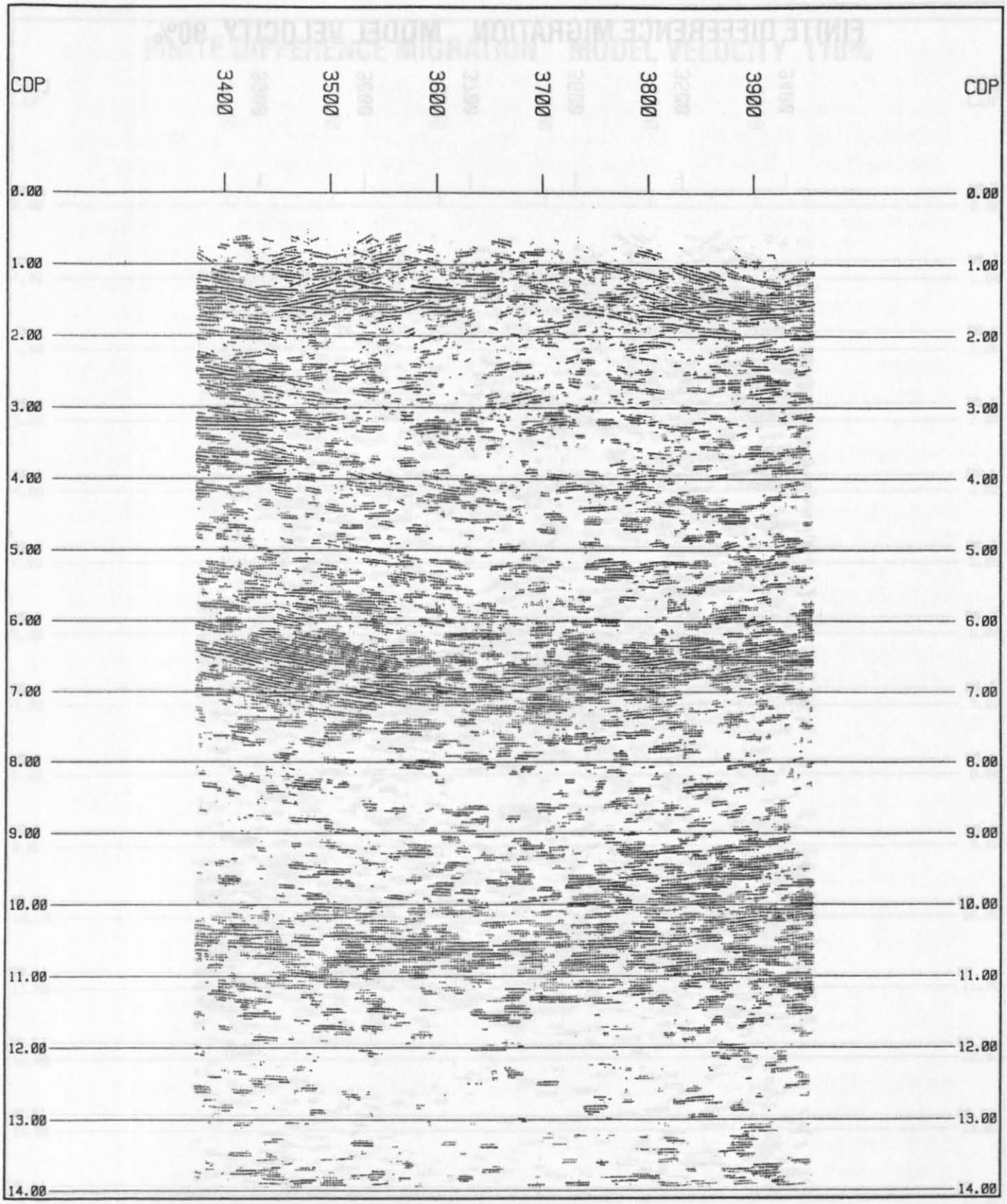
CDP
3400
3500
3600
3700
3800
3900
CDP
0.00
1.00
2.00
3.00
4.00
5.00
6.00
7.00
8.00
9.00
10.00
11.00
12.00
13.00
14.00

Figure: 7a

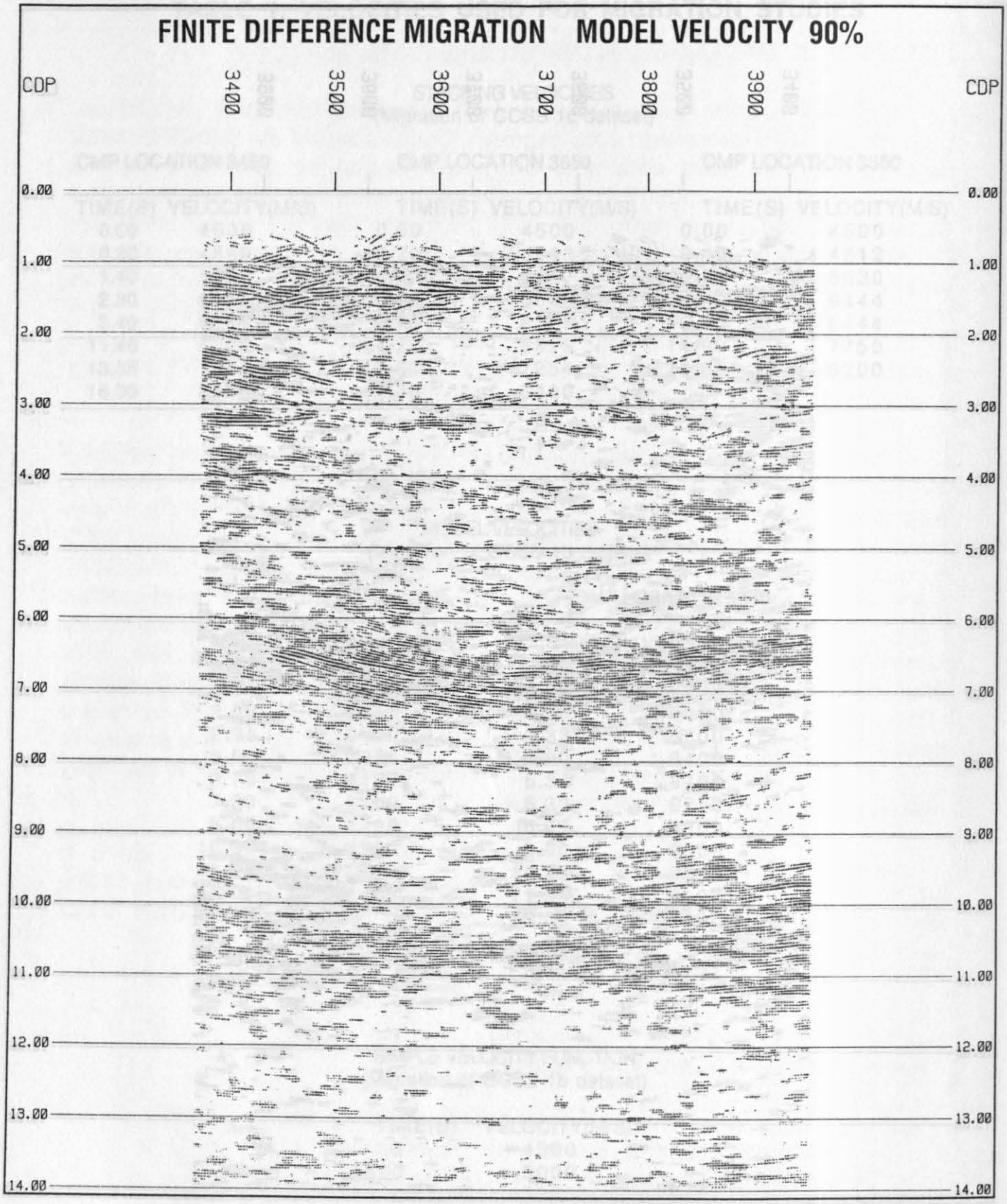
FINITE DIFFERENCE MIGRATION MODEL VELOCITY 90%
CDP
3400
3500
3600
3700
3800
3900
CDP
0.00
1.00
2.00
3.00
4.00
5.00
6.00
7.00
8.00
9.00
10.00
11.00
12.00
13.00
14.00

Figure: 7b

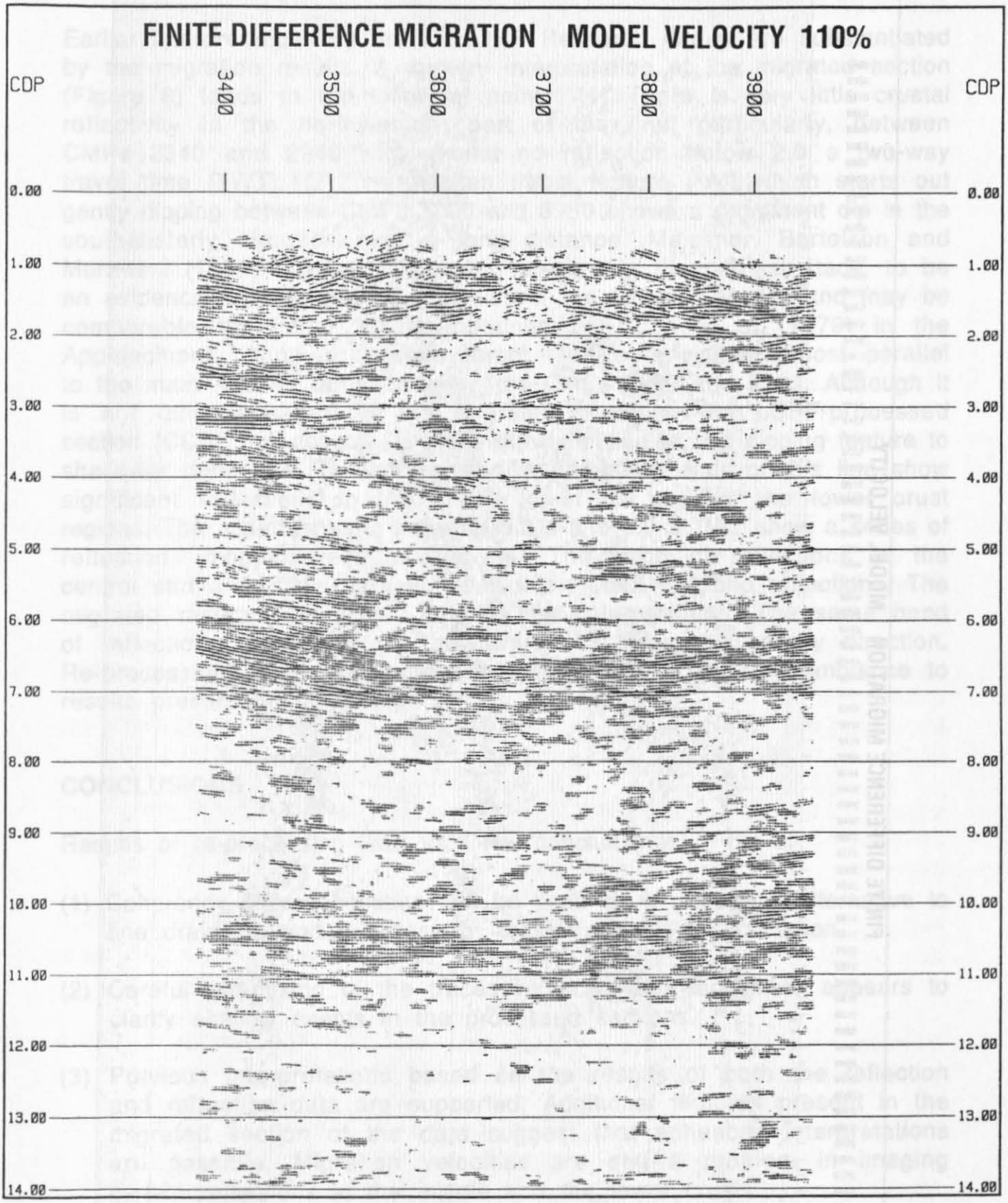
FINITE DIFFERENCE MIGRATION MODEL VELOCITY 110%
CDP
3400
3500
3600
3700
3800
3900
CDP
0.00
1.00
2.00
3.00
4.00
5.00
6.00
7.00
8.00
9.00
10.00
11.00
12.00
13.00
14.00

Figure: 7c

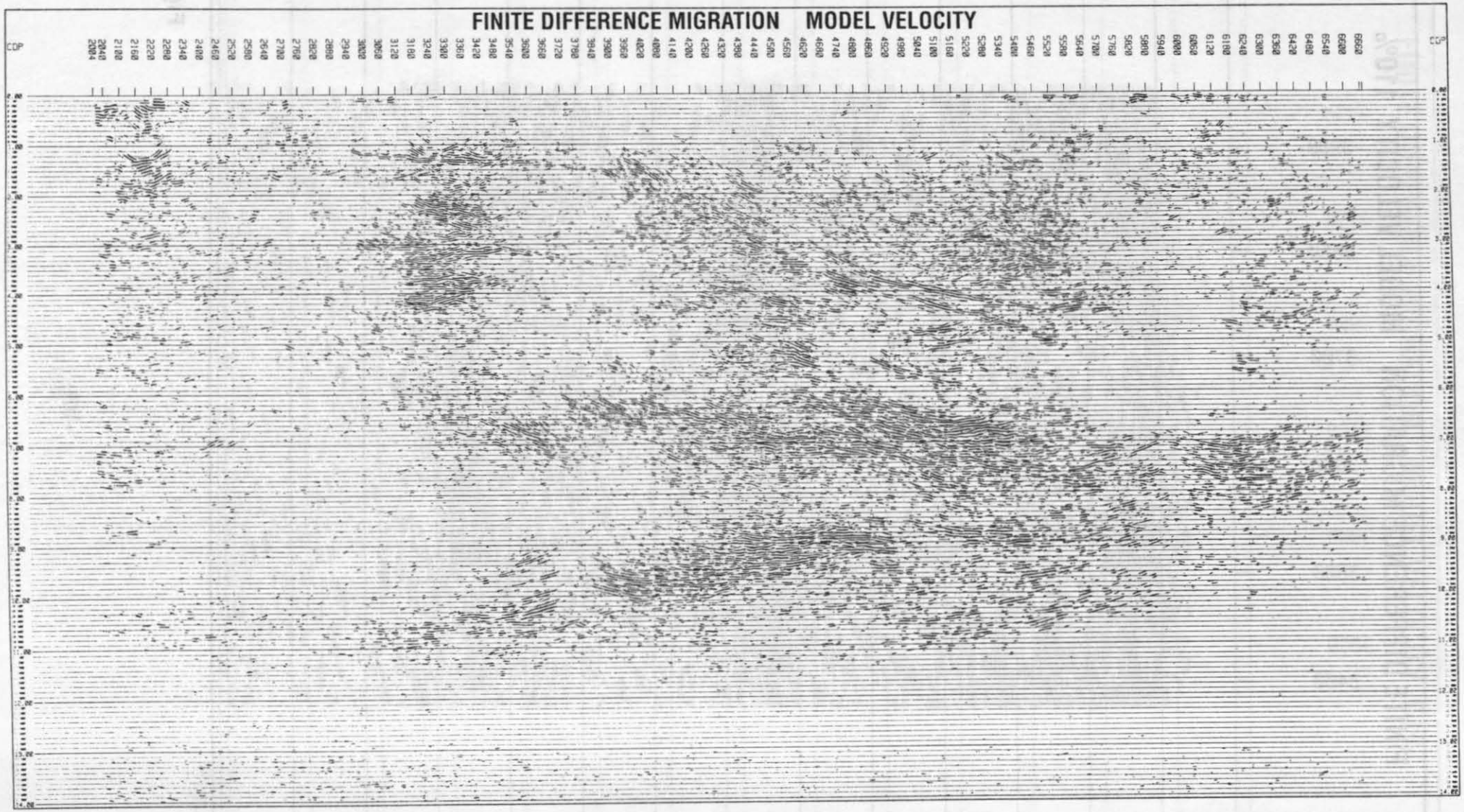

Figure: 8

Earlier interpretations by the DEKORP Research Group are substantiated by the migration results. A cursory interpretation of the migrated section (Figure 8) leads to the following points: (1) There is very little crustal reflectivity in the northwestern part of the line; particularly, between CMPs 2340 and 2940 with almost no reflection below 2.0 s two-way travel time (TWT). (2) The Aachen thrust feature ("A") which starts out gently dipping between CMPs 3000 and 3960 shows a prominent dip in the southeasterly direction over a long distance. Meissner, Bartelson and Murawski (1981) suggest this event, present in the original stack, to be an evidence for thin-skinned tectonics in the Rhenish Massif and may be comparable to similar results obtained by Cook et al (1979) in the Appalachians. Another possible thrust feature is visible almost parallel to the main Aachen thrust between the CMPs 3900 and 5520. Although it is not quite apparent in the migrated sections, the LSPF-processed section (CCSS 1c) appears to show the extension of this dipping feature to shallower depth. (3) The central and southeastern ends of this line show significant reflections in the middle crust as well as the lower crust regions. The mid-crust zone between 5.0 s and 8.0 s TWT show a series of reflections dipping west-upwards. (4) The band of reflections in the central part around 9.0 s have been interpreted as Moho reflections. The migrated results qualitatively support this interpretation. The same band of reflections appear to dip downwards in the northwesterly direction. Re-processing results by Lange and Stiller (1990) bear resemblance to results presented in this report.

CONCLUSIONS

Results of re-processing lead to a few conclusions:

(1) Coherency filtered sections can be used as a preferable alternative to line drawings and are best for crustal seismic interpretation.

(2) Careful pre-mixing of the traces within a CMP ensemble appears to clarify shallow events in the processed sections.

(3) Previous interpretations based on the results of both the reflection and refraction data are supported. Additional features present in the migrated section of the data suggest that enhanced interpretations are possible. Migration velocities are still a problem in imaging certain reflections in the middle and the lower crusts.

ACKNOWLEDGEMENTS

Participation in this processing project would not have been possible without the support and encouragement of Professor Fred Cook. The authors would like to express their sincere thanks to him. One of the authors (K.V.) is grateful to Ernst Flueh of GEOMAR, Kiel, Germany for providing an opportunity to attend the CCSS meeting and for being extremely patient with me towards submitting this article.

REFERENCES

DEKORP Research Group, 1990a: Results of deep-seismic reflection investigations in the Rhenish Massif; Tectonophysics, 173: 507-515.

DEKORP Research Group (represented by Flueh, E.R., Klaeschen, D. and Meissner, R.), 1990b: Wide-angle Vibroseis data from the western Rhenish Massif; Tectonophysics, 173: 83-93.

DEKORP Research Group, 1991: Results of the DEKORP 1 (BELCORP - DEKORP) deep seismic reflection studies in the western part of the Rhenish Massif; Geophys. J. Int., 106, 203-227.

Mechie, J., Prodehl, C., and Fuchs, K., 1983: The long range refraction experiment in the Rhenish Massif; In: K.Fuchs, K.von Gehlen, H. Maelzer,H.Murawaski and A.Semmel (Eds.): Plateau Uplift; Springer-Verlag, Berlin, pp. 260-275.

Varsek, J.L. and Vasudevan, K., 1990: Parameter selection for signal enhancement investigation; LITHOPROBE Seismic Processing Facility Newsletter, Vol. 3, number 1, 25-29.

Mooney, W.D. and Prodehl, C., 1978: Crustal structure of the Rhenish Massif and adjacent areas: a reinterpretation of existing seismic refraction data; J. Geophys., 44, 573-601.

Meissner, R., Bartelsen, H., and Murawski, H., 1981: Thin-skinned tectonics in northern Rhenish Massif; Nature, 290, 399-401.

Cook, F.A., Albough, D.S., Brown, L.D., Kaufman, S., Oliver, J.E., and Hatcher, R.D., 1979: Thin-skinned tectonics in the crystalline Southern Appalachians: COCORP seismic reflection profiling of the Blue Ridge and Piedmont; Geology, 7, 563-567.

Lange, C. and Stiller, P.K., 1990: Re-processing of line BELCORP/DEKORP 1A (CMP 3366 -3965) / CCSS data set 1c - results and findings; Research note presented at the CCSS Workshop, Kiel-Fellhorst, 27-31, August 1990, see this volume.

INTRODUCTION TO DATASET II

Ernst R. Flueh

GEOMAR, Kiel , Germany

Dataset II aimed at a topic that had also been investigated during previous workshops (e.g. Einsiedeln, Switzerland, 1983; Tokyo, 1988), the interpretation of coincident reflection and refraction data. While in previous attempts the two datasets were collected independently, we here used a dataset that was recorded using identical sources, which were a marine airgun array. The data chosen was BIRP's MOBIL 1 line, shot in the North Sea and recorded simultaneously on land by several station, operated by Durham University (Blundell et al., 1991). The data from two of the land stations, on which clear arrivals are seen from 20 to 140 km were distributed as paper record sections. With a shot spacing of 50 km, the data are spatially analyzed and allow detailed phase correlations. In addition, the stacked section of the near-vertical data and a tape containing the raw-stack was made available to the participants. Figure 1 shows a location map of the profile. A detailed description of the experiment and a first interpretation are given by Blundell et al. (1991).

Participants were asked to determine the velocity field along the profile and compare the results of both the near-vertical and wide-angle data. In addition a list of questions and topics of interest was handed out and led to fruitful discussions during the workshop.

Questions were related to topics such as:

- How to process wide-angle data?
- Do wide-angle data make any significant contribution?
- Can we use wide-angle information for an improvement in the reflection data processing?
- Can we compare wide-angle velocity information with stacking velocities?
- Can migration benefit from the wide-angle data?
- Can the data be combined in processing?
- How should future experiments be designed?

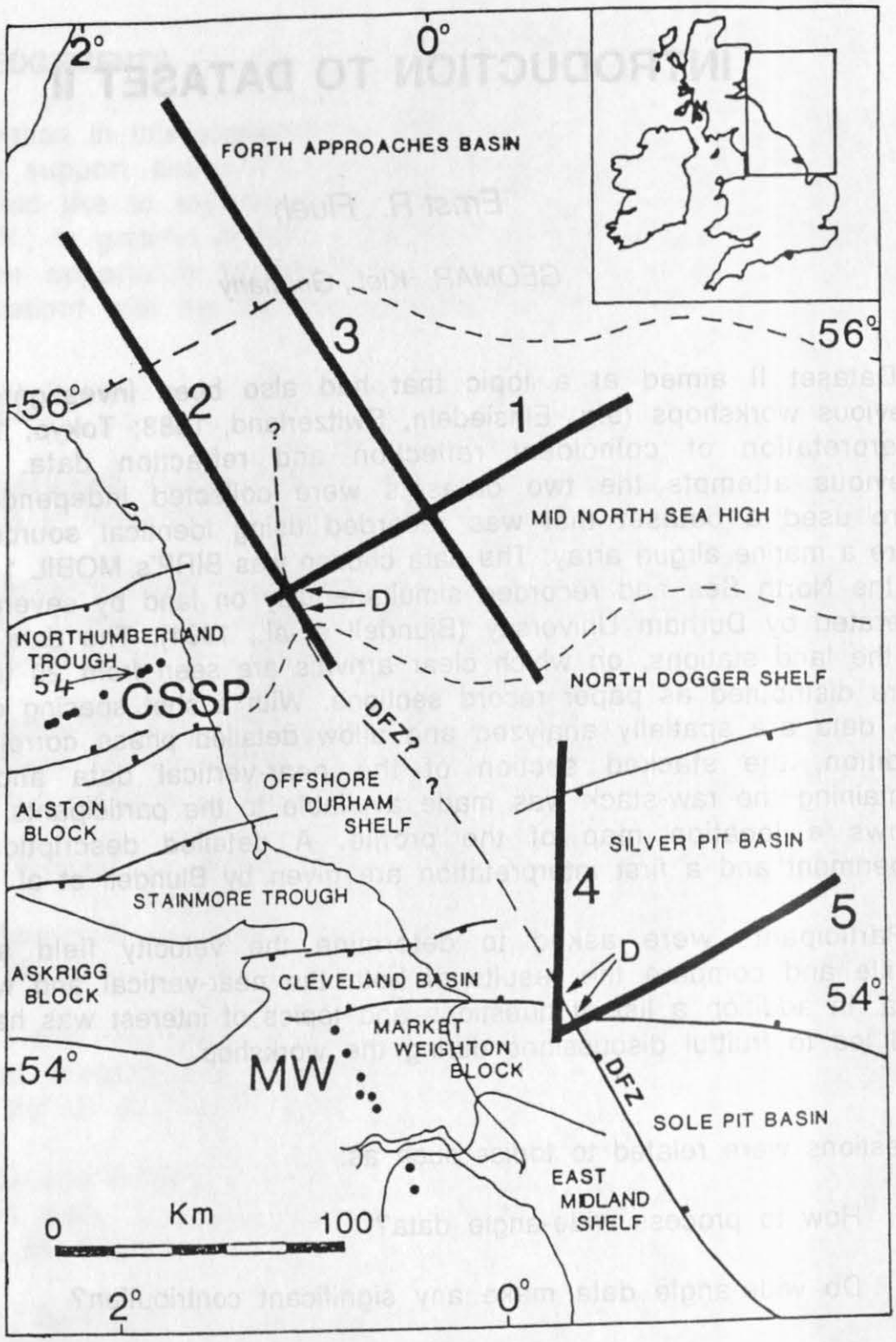

Figure 1: Major geological features of North-East England and the adjacent North Sea region, showing the BIRPS MOBIL normal-incidence seismic profiles (thick black lines) and Durham's WAR recording stations (black dots). DFZ: the Dowsing Fault Zone (the northern extension which cuts lines 1 and 2 is suggested by the MOBIL data). CSSP: Caledonian Suture Seismic Project (Bott et al. 1985) recording stations (across Northumberland) re-occupied during the MOBIL programme. MW: Seismic network located across the Market Weighton gravity anomaly.
From West and Long, this volume.

There was wide agreement in subsequent discussions during the workshop that closely spaced (non-spatially aliazed) wide-angle data and/or full-wavefield records do contain valuable information that complement each other.

Initially this dataset had attracted a large number of investigators. Unfortunately, long after the dataset had been announced, it turned out that the wide-angle data could not be made available in digital form. Much to the organizers and contributors great surprise and disappointment, only large scale paper copies could be supplied to the participants. A number of interested individuals or groups decided not to work on the data and during the workshop only four contributions were presented and summarized here. The contribution by Milkereit et al. focuses on an interpreted processing approach and demonstrates that the available data do not allow to determine a unique velocity model. Holliger applies standard interpretation techniques to the wide-angle data and uses the velocity field for a ray-based depth migration of the near-vertical data. Krishna et al. investigates among other topics a prominent high amplitude "diffraction-like" event seen on the wide-angle data and attributes it to a sub-Moho reflector. West and Long also investigate this event in detail. Their best fitting model attributes this arrival as a diffraction from a step on the Moho.

References

Blundell, D.J., Hobbs, R.W., Klemperer, S.L., Scott-Robinson, R., Long, R.E., West, T.E., and Duin, E. 1991: Crustal structure of the central and southern North Sea from BIRPS deep seismic reflection profiling; J.Geol.Soc.Lond., 148, 445-457.

TRAVEL TIME INTERPRETATION OF DATASET 2: NORMAL INCIDENCE AND CORRESPONDING PIGGY BACK WIDE-ANGLE SEISMIC DATA OF LINE MOBIL1, CENTRAL NORTH SEA

Klaus Holliger

Institute of Geophysics, ETH-Hönggerberg, CH-8093 Zürich, Switzerland

Abstract

In the course of this exercise I have attempted the simultaneous - albeit not synoptic - travel time interpretation of the partially coincident seismic normal incidence reflection data of line MOBIL1 and the corresponding piggy back seismic wide-angle data. The latter were used to derive the velocity information required for the depth migration of the seismic reflection data by classical X^2-T^2 analysis and subsequent verification and refinement by ray tracing. The resulting velocity model is essentially 1-dimensional, does not contain velocity gradients and thus is to be considered as a minimum interpretation of the seismic wide-angle data. Such a minimum velocity model necessarily only represents a crude approximation of the crustal structure but is considered to be not only sufficient but ideal for the purpose of migration. The simultaneous ray-based depth migration of the velocity model and the seismic reflection data leads to an overall good agreement between the interfaces of the velocity model and the most pertinent reflectivity patterns, which may be considered as a possible criterion for successful migration. The results confirm the presence of strong diffractions from the base of the crust inferred by other workers but question their interpretation of the Pg phase as a direct diving wave.

Seismic Wide-Angle Data

Unlike conventional seismic wide-angle data the supplied piggy back recordings of stations 47 and 54 are unaliased, represent the full wave field and have a lateral and vertical resolution comparable to the corresponding normal incidence reflection data of line MOBIL1. Therefore, the "standard" interpretation scheme for seismic wide-angle data consisting of the correlation of the most pertinent wave groups and subsequent forward modelling was considered to be inadequate. Instead line drawings of the two sections were prepared consisting of all phases showing a lateral coherence over at least 5 km, which corresponds approximately to the diameter of the 1st Fresnel zone for this kind of data at lower crustal levels (Figure 1).

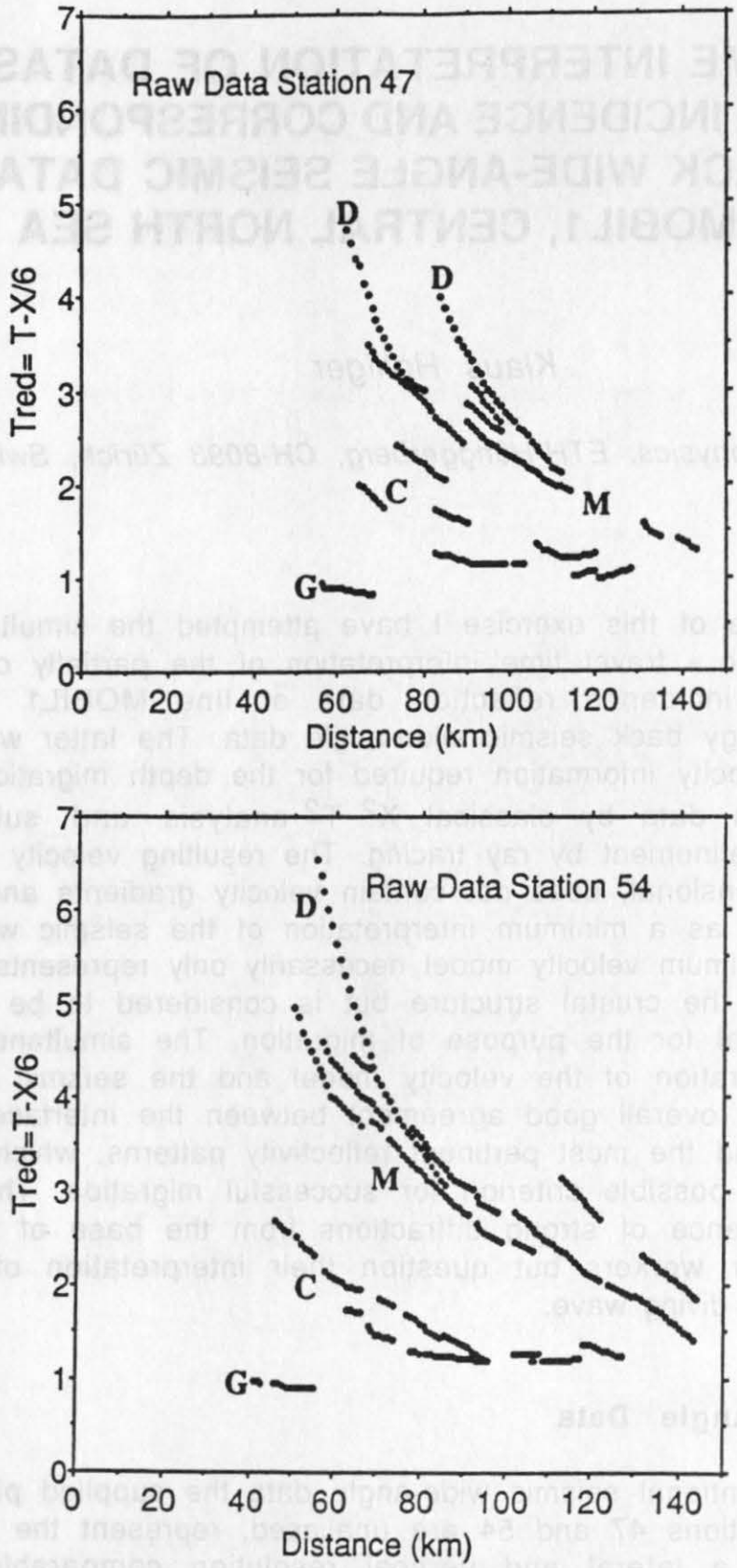

Figure 1: Correlated phases of the seismic wide-angle data recorded at stations 47 (top) and 54 (bottom). Zero distance corresponds to the location of the respective receiver station. G: phase interpreted as the direct diving wave by Blundell et al. (1991), C: reflections from the lower crust, M. reflections from the Moho, D: diffractions.

These line drawings were digitized and plotted after correction for normal move out (NMO) assuming an average velocity of 6.0 km/s (Figure 2) and also in the X^2-T^2 domain (Figure 3).

Correcting the seismic wide-angle data for NMO allows a qualitative comparison with the some westernmost 50 km of line MOBIL1. This display nicely confirmed the existence of a huge diffraction from around Moho depth as postulated by Blundell et al. (1991) (compare "D" on Figures 1, 2 and 3); however, what they interpreted as the Pg phase rather seems to correspond to the prominent shallow reflection pattern around 4 s two-way travel time at the western end of MOBIL1 (compare "G" on Figures 1, 2 and 3). An accurate one-to-one comparison of the two datasets was not attempted because the wide-angle data were available in analogue form only and an accurate positioning was not possible on the basis of the available information.

Plotting the data in the X^2-T^2 domain essentially results in two families of straight lines, one corresponding to reflections from the top of the lower crust labelled "C" in Figure 3, the other to reflections from the Moho labelled "M" in Figure 3. For both receiver stations the extrapolated average slopes and intercept times of these "C" and "M" line families are virtually the same. As to be expected the diffractions identified on the NMO-corrected display show up as curved lines asymptotic to the X^2-T^2 plotted Moho reflections (compare "D" on Figures 2 and 3). The velocity model derived from this X^2-T^2 analysis was subsequently verified and slightly refined by forward ray tracing. Since the data are unreversed every effort was made to keep the velocity structure as simple as possible in order to avoid an overinterpretation of the data. Such an approach necessarily neglects the details of the crustal structure and hence must be considered as minimum interpretation of this dataset. This resulted in the following 1-dimensional velocity model for the crystalline crust and the upper mantle:

- Upper crust (0 to 18 km): 6.0 to 6.1 km/s
- Lower crust (18 to 34 km): 6.5 to 6.6 km/s
- Upper mantle (below 34 km): 8.00 km/s (derived from a short but distinct Pn phase)
- Average crustal velocity (including water layer and sediments): 6.2 to 6.3 km/s

The apparent velocity of the Pg phase on the raw data (see "G" on Figure 1) is as high as the average crustal velocity, which further supports its interpretation as a shallow reflection rather than the direct wave travelling through the upper crust. Apart from the somewhat deeper Moho this velocity structure is in good agreement with the one derived by Bott et al. (1985) using amplitude modelling from a previous nearby experiment with much larger station spacing (approximately 3 km on average).

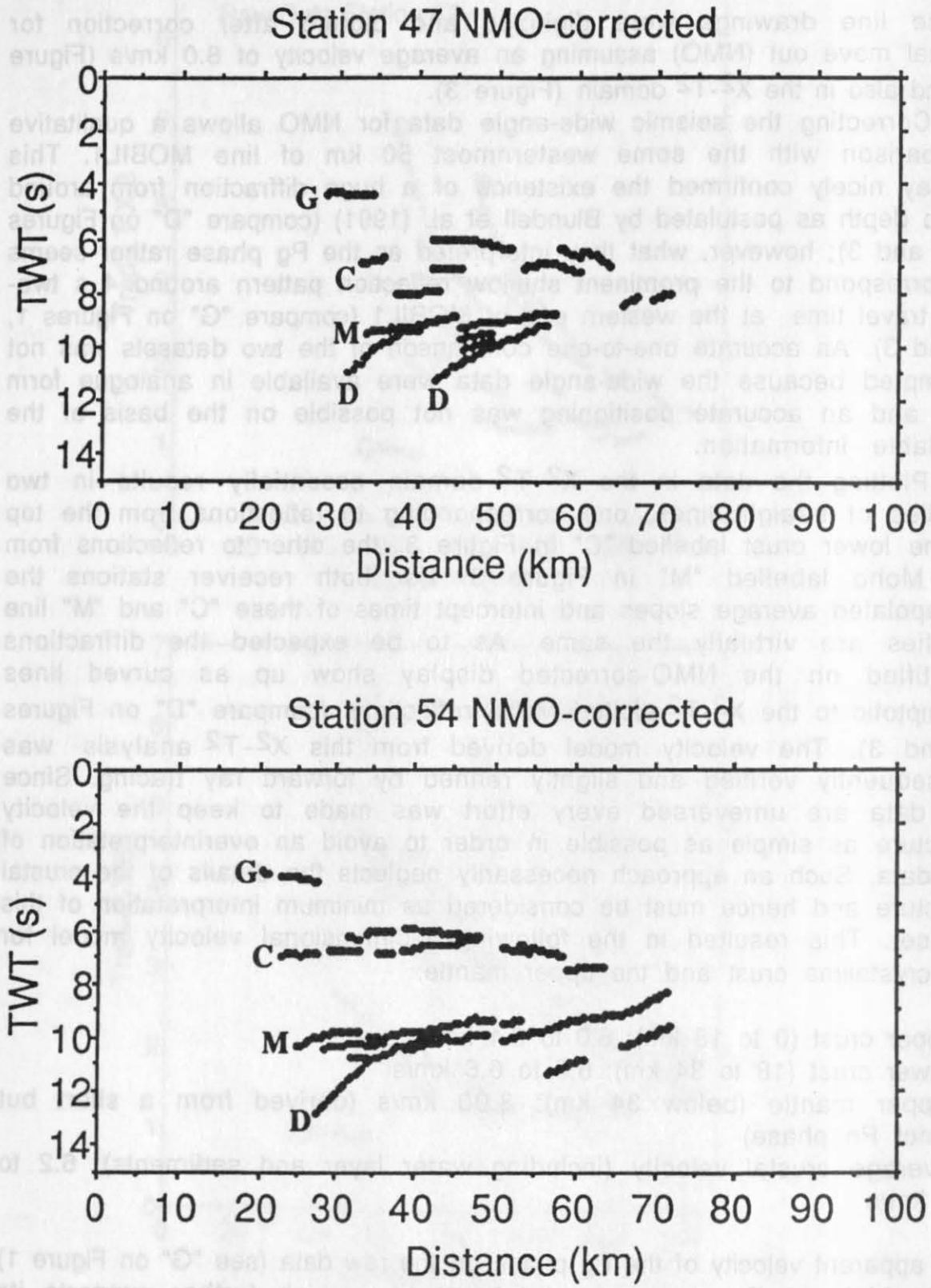

Figure 2: Correlated wide-angle reflections and diffractions recorded at stations 47 (top) and 54 (bottom) after correction for normal moveout with an average velocity of 6.0 km/s. Zero distance corresponds to the location of the respective receiver station. G: phase interpreted as the direct diving wave by Blundell et al. (1991), C: reflections from the lower crust, M. reflections from the Moho, D: diffractions.

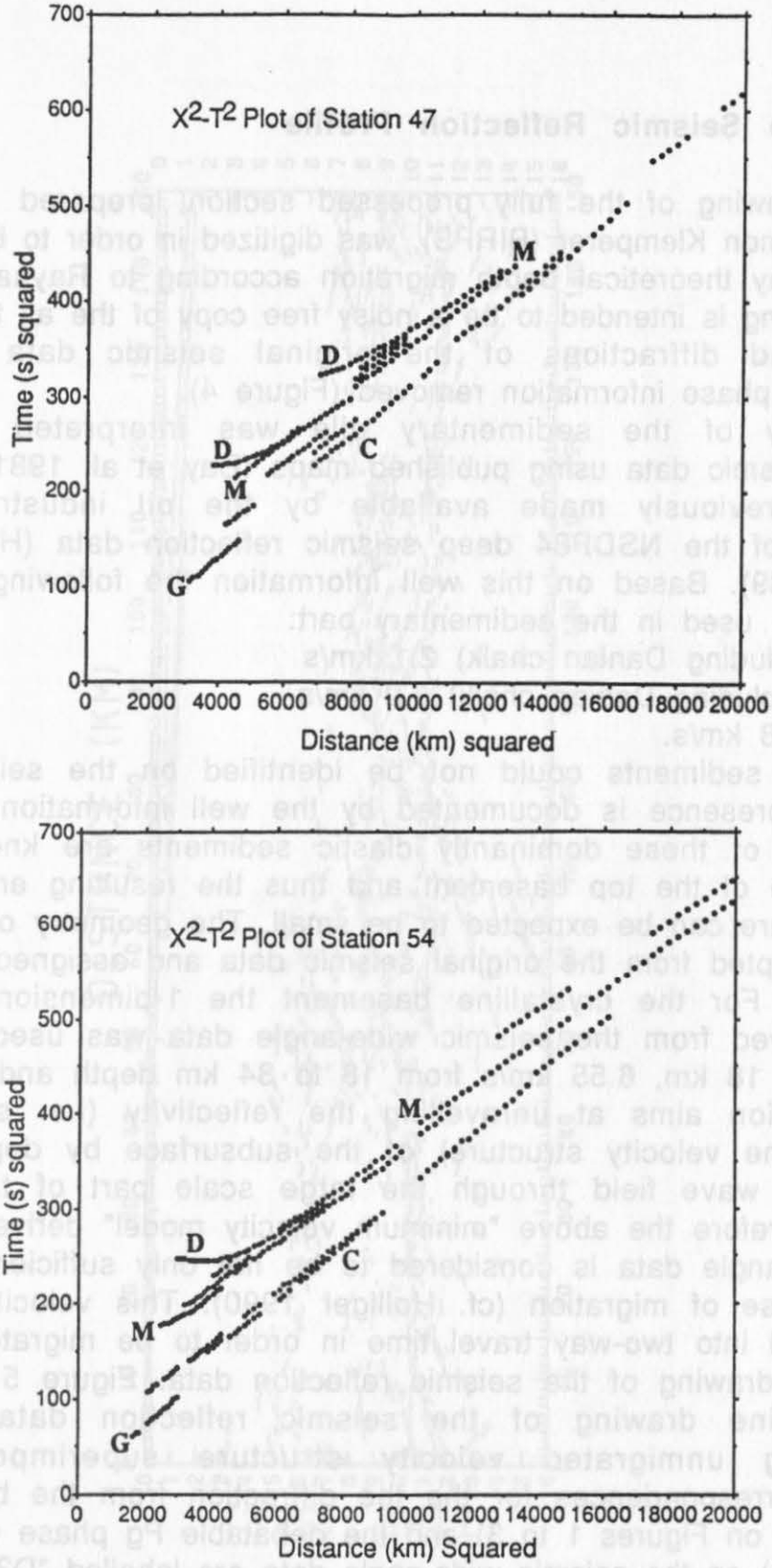

Figure 3: X^2-T^2 plot of the seismic wide-angle data recorded at stations 47 (top) and 54.(bottom).Zero distance corresponds to the location of the respective receiver station. G: phase interpreted as the direct diving wave by Blundell et al. (1991), C: reflections from the lower crust, M. reflections from the Moho, D: diffractions.

MOBIL1 Deep Seismic Reflection Profile

A line drawing of the fully processed section, prepared and kindly supplied by Simon Klemperer (BIRPS), was digitized in order to be used as an input for ray theoretical depth migration according to Raynaud (1988). This line drawing is intended to be a noisy free copy of the all the primary reflections and diffractions of the original seismic data with the amplitude and phase information removed (Figure 4).

The geometry of the sedimentary pile was interpreted from the unmigrated seismic data using published maps (Day et al. 1981) and well information previously made available by the oil industry for the interpretation of the NSDP84 deep seismic reflection data (Holliger and Klemperer 1989). Based on this well information the following migration velocities were used in the sedimentary part:

- Tertiary (excluding Danian chalk) 2.1 km/s
- Mesozoic (including Danian chalk) 3.0 km/s
- Zechstein 4.8 km/s.

Pre-Zechstein sediments could not be identified on the seismic data, though their presence is documented by the well information. However, the velocities of these dominantly clastic sediments are known to be close to those of the top basement and thus the resulting errors in the velocity structure can be expected to be small. The geometry of the water layer was adopted from the original seismic data and assigned a velocity of 1.5 km/s. For the crystalline basement the 1-dimensional velocity structure derived from the seismic wide-angle data was used, i.e. 6.05 km/s down to 18 km, 6.55 km/s from 18 to 34 km depth and 8.00 km/s below. Migration aims at unravelling the reflectivity (i.e. small scale variation of the velocity structure) of the subsurface by depropagating the observed wave field through the large scale part of the velocity structure. Therefore the above "minimum velocity model" derived from the seismic wide-angle data is considered to be not only sufficient but ideal for the purpose of migration (cf. Holliger 1990). This velocity structure was converted into two-way travel time in order to be migrated together with the line drawing of the seismic reflection data. Figure 5 shows the unmigrated line drawing of the seismic reflection data with the corresponding unmigrated velocity structure superimposed. The interpreted correspondences for the the diffraction from the base of the crust (see "D" on Figures 1 to 3) and the debatable Pg phase (see "G" on Figures 1 to 3) on the seismic wide-angle data are labelled "D?" and "G?", respectively (Figure 5). The simultaneous depth migration of the interfaces of the velocity model and the line drawing of the seismic reflection data results in a good focusing of the interpreted diffractions "D?" and an overall excellent agreement between the Moho interpreted from the wide-angle data and the base of the reflective lower crust, whilst the correlation between the "Conrad" and the top of the lower crustal reflectivity is spurious (Figure 6).

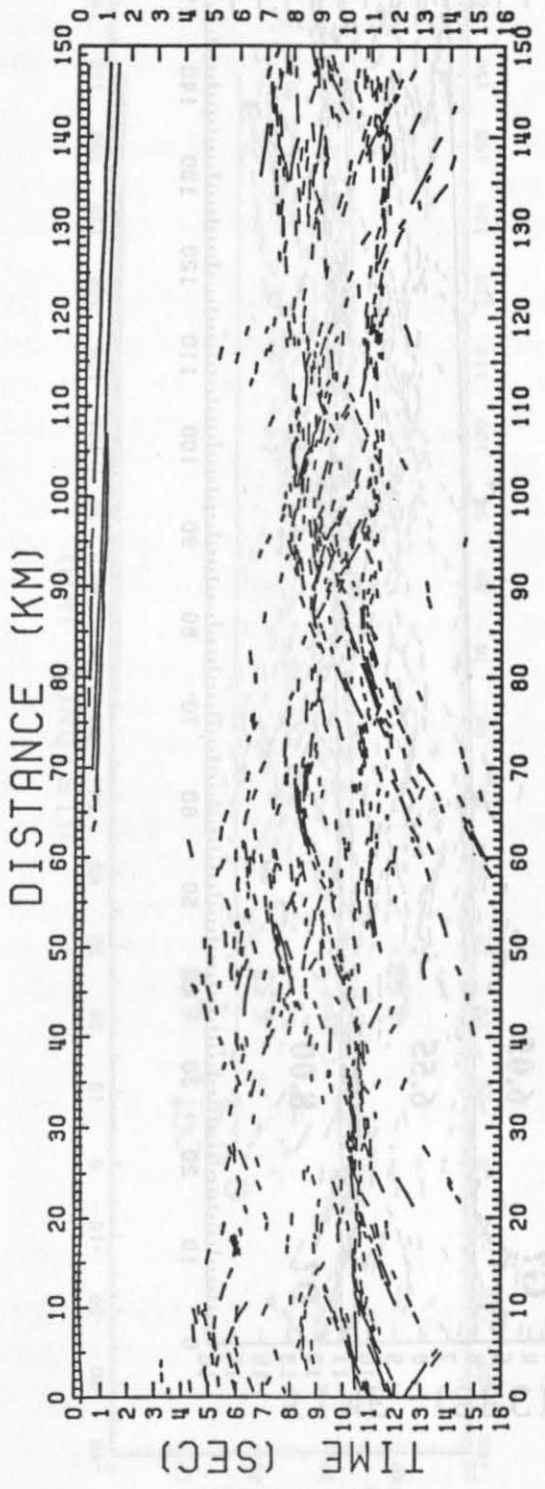

Figure 4: Unmigrated digitized line drawing of the normal incidence seismic reflection data of line MOBIL1 (analogue line drawing courtesy Simon Klemperer). Zero distance corresponds to the westernmost CMP. Horizontal and vertical scales are 1:1 for an average velocity of 6.0 km/s.

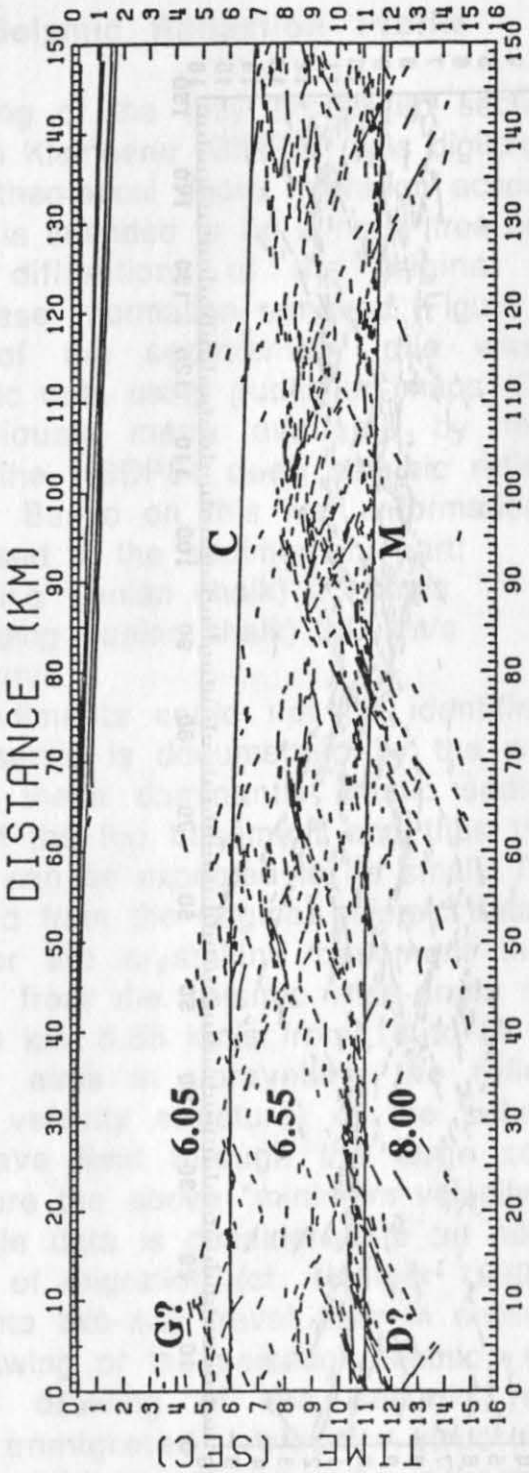

Figure 5: Unmigrated line drawing of line MOBIL1 with the 1-dimensional velocity model derived from the seismic wide-angle data superimposed. The velocity model was converted to two-way travel time in order to be subsequently migrated together with the line drawing of the normal incidence reflection data. Zero distance corresponds to the westernmost CMP. Numerical values are velocities in km/s. G?: interpreted correspondence to G in Figures 1 to 3; D?: interpreted correspondence to D in Figures 1 to 3.

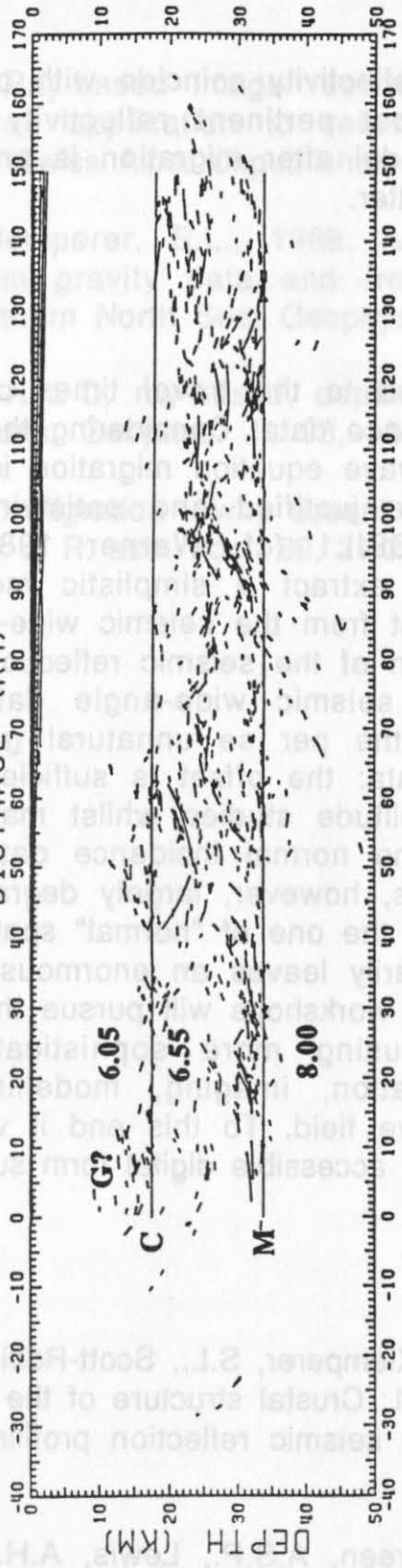

Figure 6: Result of the simultaneous depth migration of the line drawing of MOBIL1 and the velocity structure (cf. Figure 5). Zero distance corresponds to the westernmost CMP. Numerical values are velocities in km/s. G?: interpreted correspondence to G in Figures 1 to 3; the interpreted diffractions D? seem to have been properly focused.

Assuming that changes in reflectivity coincide with changes in lithology the convergence of the most pertinent reflectivity patterns with the interfaces of the velocity model after migration is an important criterion for the correctness of the latter.

Discussion

This study was restricted to the travel times of both the seismic wide-angle and normal incidence data. Considering the inherent problems and limitations of standard wave equation migration in the case of deep data this approach may be justified and satisfying for the seismic reflection data of line MOBIL1 (cf. Warner 1987; Holliger 1990). Furthermore, it allowed to extract a simplistic model of the macro velocity structure of the crust from the seismic wide-angle which in turn allowed an accurate migration of the seismic reflection data.
The piggy back recorded seismic wide-angle data offer to unique possibility to largely close the per se unnatural gap between normal incidence and wide-angle data: the offset is sufficiently big for reliable velocity estimation and amplitude studies whilst maintaining the lateral and vertical resolution of the normal incidence data. An interpretative restriction to the travel times, however, largely degrades the information content of such a dataset to the one of "normal" spatially aliased seismic wide-angle and thus necessarily leaves an enormous potential untapped. Therefore, I hope that future workshops will pursue the study of this kind seismic wide-angle data using more sophisticated interpretational techniques (velocity estimation, imaging, modelling) based on the consideration of the full wave field. To this end it will be necessary to distribute such data in readily accessible digital form such as e.g. SEGY.

References

Blundell, D.J., Hobbs, R.W., Klemperer, S.L., Scott-Robinson, R., Long, R.E., West, T.E., and Duin, E. 1991: Crustal structure of the central and southern North Sea from BIRPS deep seismic reflection profiling; J.Geol.Soc.Lond., 148, 445-457.

Bott, M.H.P., Long, R.E., Green, A.S.P., Lewis, A.H.J., Sinha, M.C. and Stevenson, D.L. 1985: Crustal structure south of the Iapetus suture beneath northern England; Nature, 314, 724-727.

Day, G.A, Cooper, B.A., Andersen, C., Burgers, W.F.J., Rønnevik, H.C.and Schöneich, H., 1981: Regional seismic structure maps of the North Sea; In: Illing, L.V. and Hobson, G.D. (Eds.): Petroleum Geology of the continental shelf of the north-west Europe; Heyden.

Holliger, K., 1990: Ray-based image reconstruction in controlled-source seismology with an application to seismic reflection and refraction data in the central Swiss Alps; Unpublished PhD thesis, ETH Zürich.

Holliger, K. and Klemperer, S.L., 1989: A comparison of the Moho interpreted from gravity data and from deep seismic reflection data in the northern North Sea; Geophysical Journal, 97, 247-258.

Raynaud, B., 1988: A 2-D, ray-based, depth migration method for deep seismic reflections; Geophys. J., 93, 163-171.

Warner, M. R., 1987: Migration - why doesn't it work for deep continental data?; Geophys. J. R. astr. Soc., 89, 21-26.

TOWARDS AN INTEGRATED PROCESSING APPROACH FOR STEEP- AND WIDE-ANGLE DATA: APPLICATION TO THE MOBIL DATA SET

Bernd Milkereit, Carl Spencer, and D.J. White

Geological Survey of Canada, Ottawa, Canada, K1A 0Y3

Summary

We outline a comprehensive approach for the processing and interpretation of coincident steep- and wide-angle reflection data in which both structural complexities and noise are present. Key elements are interactive tomographic travel time inversion for a laterally heterogeneous velocity model.
V(x,z), followed by pre- and post-stack migration schemes which utilize fast ray tracing through the macro velocity model. Examples from the Mobil data set are presented illustrating efficiency and applicability of this approach to steep- and wide-angle reflection data.

Introduction

The determination of the correct velocities for the processing and interpretation of wide-angle and deep seismic data is especially important and presents a number of unique problems:

(i) These data are often recorded in areas of complicated subsurface velocity structures (e.g. continental margins) resulting in the presence of steeply dipping events and large-scale diffraction patterns throughout the seismic section. It is essential for the interpretation that these events be properly imaged.

(ii) The application of conventional velocity analyses to deep crustal steep angle reflection data is often limited by the small move out corrections shown by events from the deeper parts of the section. A tomographic velocity analysis of coincident wide-angle data is a means of obtaining an improved macro velocity model.

(iii) The signal to noise ratios observed in deep crustal data are often low. Processing techniques used to obtain structural information from deep seismic data (for example, migration) must produce reliable results at moderate to significant noise levels.

An ideal flow chart for processing steep- and wide-angle data is shown in Figure 1. Data should be available in digital form, interactive work stations are used for travel time analyses (first breaks and reflected phases), and a 1-D (starting) velocity model may be obtained from waveform data. It is important to determine static corrections, then travel time data can be inverted to obtain a 2-D subsurface velocity model. Fast ray tracing (e.g. bending method) can then be used for further processing both steep- and wide-angle data sets.

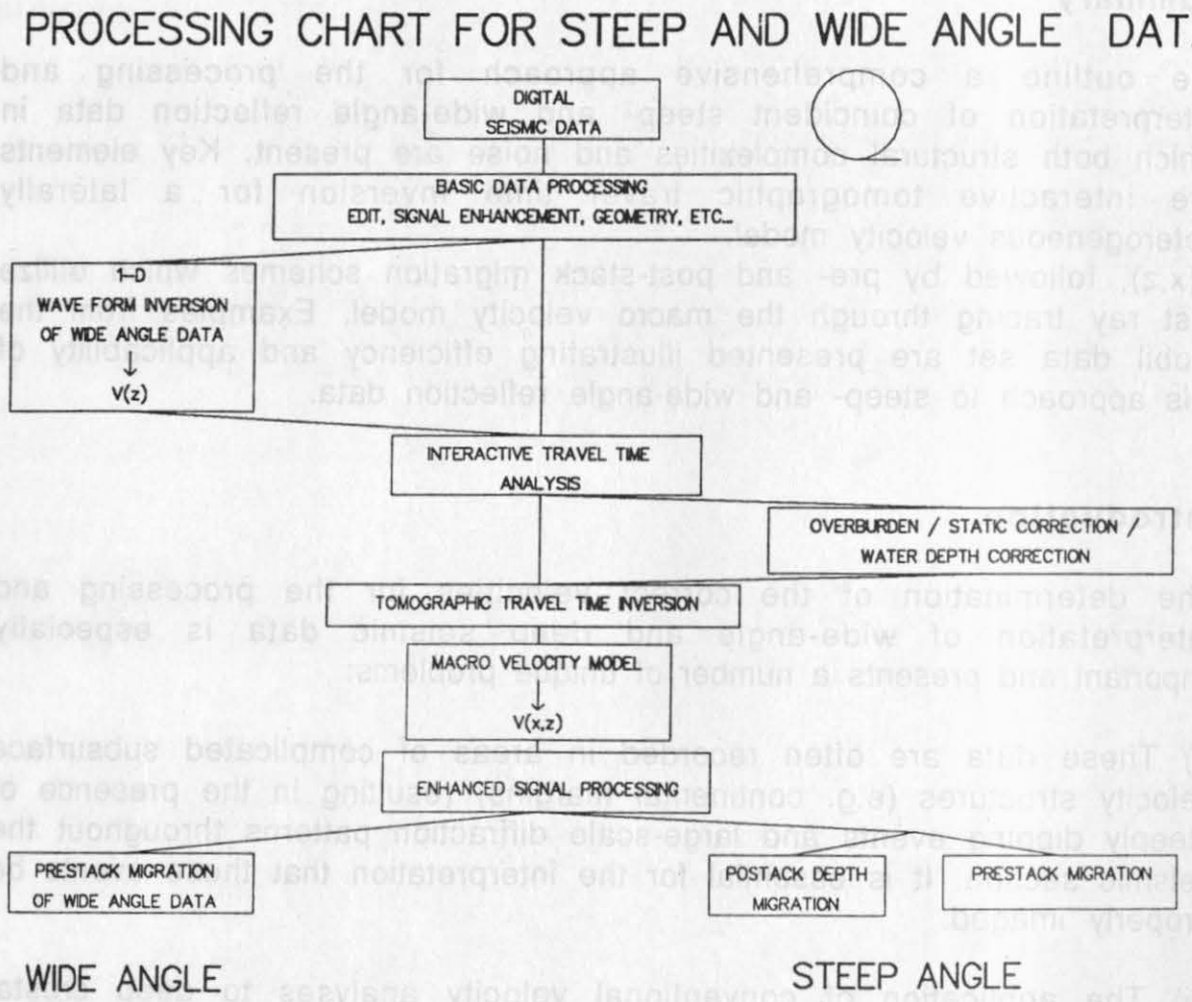

Figure 1: Processing flow for digital steep and wide angle data. Basic processing of wide angle data, followed by tomographic travel time inversion, provides a macro velocity model V(x,z). The macro velocity model can be used for the migration of wide angle data. In addition, V(x,z) can be used for pre- and poststack depth migration of coincident steep angle data.

Application to the Mobil data set

Velocities can be obtained directly from seismic data by travel time tomography (White, 1989). First breaks were picked for stations 54 and 47 (145 first breaks were picked from paper records).

The starting model for the tomographic velocity inversion consists of 3 layers (velocity grid node spacing was; 25 km horizontal, 2.5 km vertical).

Layer 1 with 3.0 km/s and 0.1 s^{-1} vertical velocity gradient,
Layer 2 with 6.0 km/s and 0.01 s^{-1} vertical velocity gradient,
Layer 3 with 8.0 km/s and 0.001 s^{-1} vertical velocity gradient.

In order to constrain the velocity inversion the thickness of the sediments was determined (interpreted) from the stacked section. An example of the interpreted sediment/basement contact (arrow) is shown in Figure 2. The rms-misfit of the staring model was 116 ms.

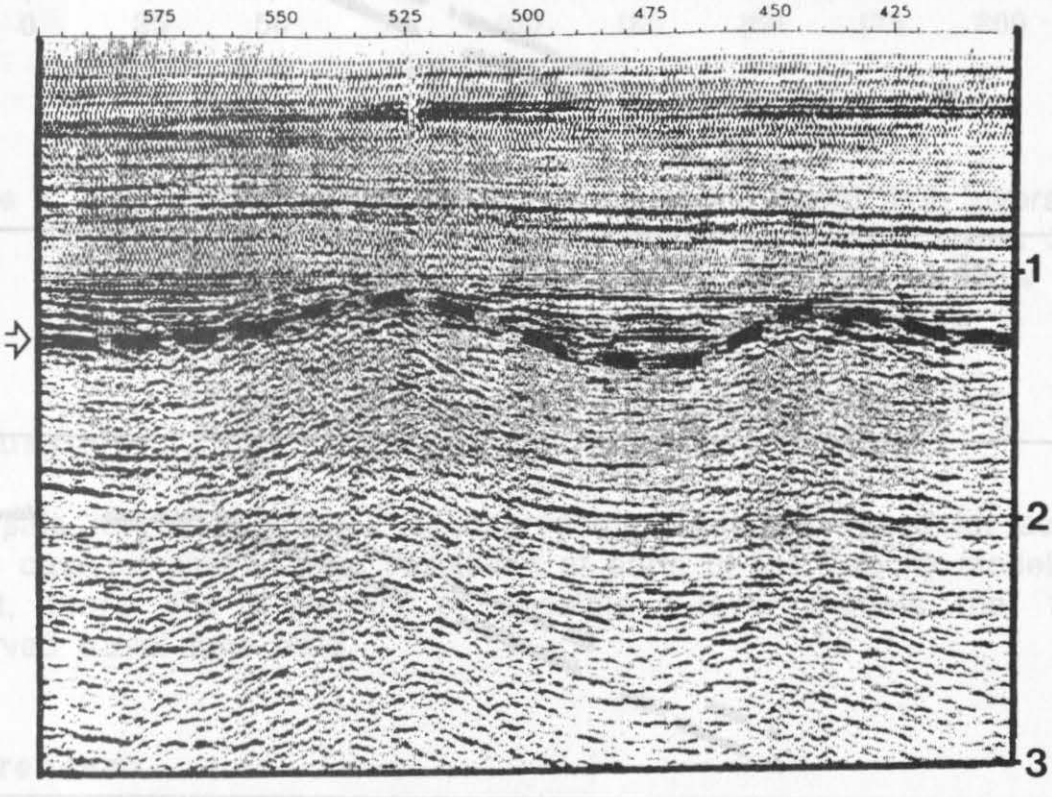

Figure 2: Portion of the Mobil CDP-section with the interpreted sediment/basement contact. The contact was digitized and used to constrain the 2-D travel time inversion of the wide angle data set.

Inversion # 1:
The observed travel time data can be fit by varying only the thickness of layer 1 while maintaining layers 2 & 3 with a horizontal Moho. The observed (I with 50 ms limits) and calculated (triangles) travel times are shown in Figure 3 (top). The rms-misfit is 65 ms. The thickness variations are indicated in Figure 4 (top).

Inversion # 2:
The observed travel time data can be fit by keeping layer 1 fixed and varying the velocity in layer 2 as well as the depth to Moho. The observed (dash) and calculated (triangle) travel times are shown in Figure 3 (bottom). The rms-misfit is 75 ms. The 2-D velocity inversion for a fixed shallow low velocity layer, laterally variable crustal velocities and depth to Moho is shown in Figure 4 (bottom). The velocity model could be used for the pre-stack migration of the wide angle data (Milkereit et al., 1990) or the post-stack depth migration of the Mobil stacked section.

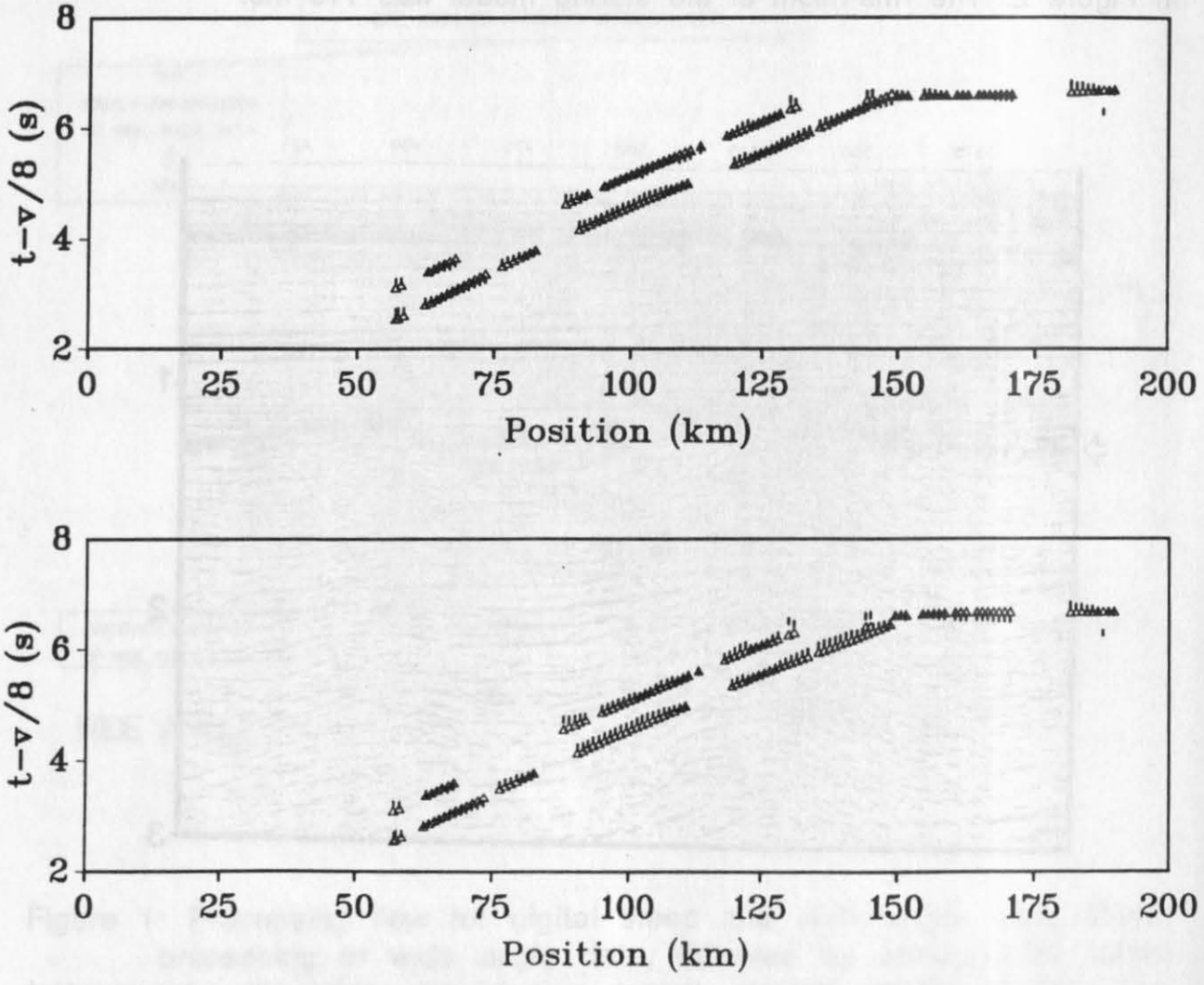

Figure 3: Observed (dash) and calculated (triangles) travel times for inversion schemes #1 (top) and # 2 (bottom).

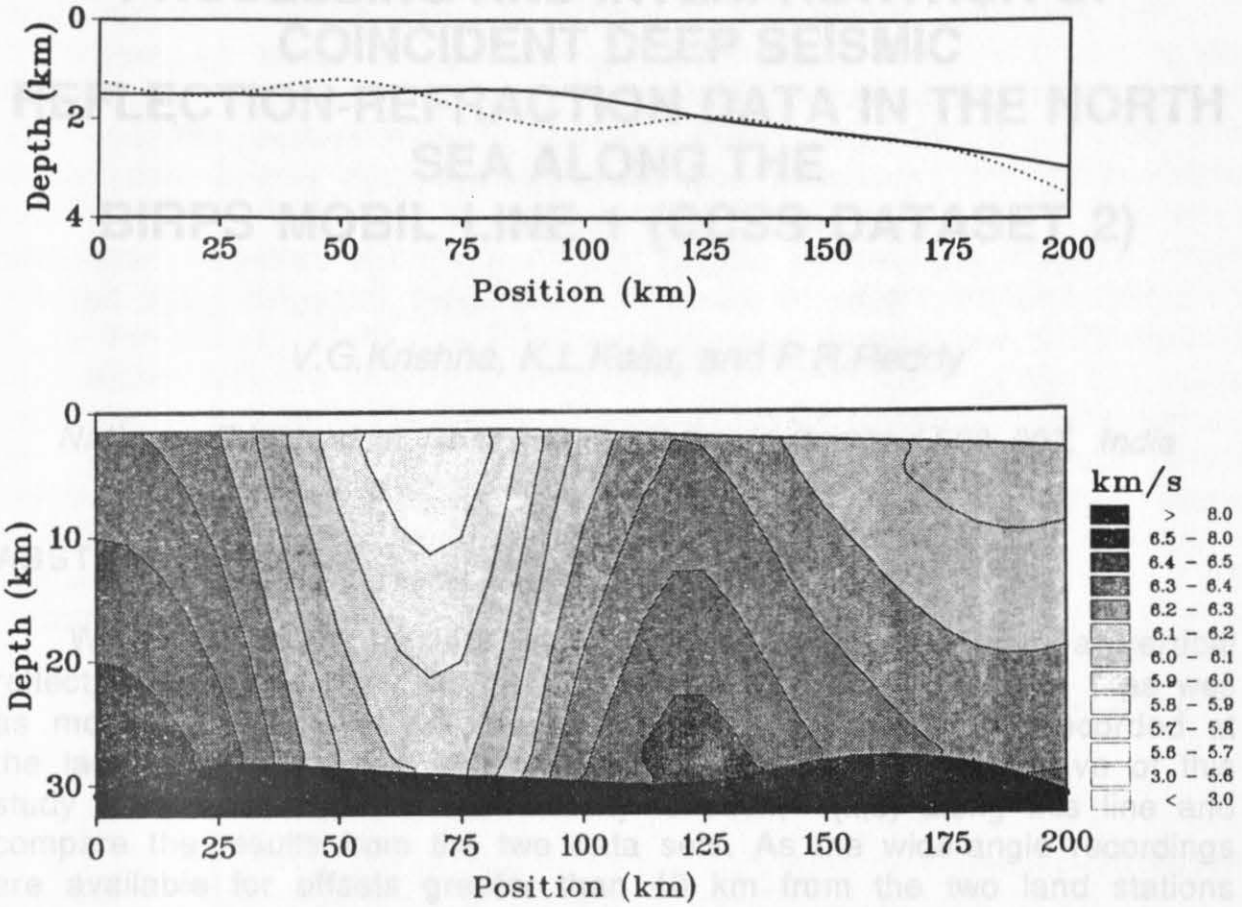

Figure 4: Top: Dotted line shows the result of the travel time inversion by varying the thickness of layer 1 while maintaining layers 2 & 3. Bottom: 2-D velocity inversion for a fixed shallow layer, laterally variable crustal velocities and depth to Moho.

Discussion

It is safe to say that the 2-station recording geometry used for acquiring these data resulted in poor resolution of parts of the velocity model. As a result, there are a variety of possible 3-layer models that fit the observed travel time data.

References:

Milkereit, B., Epili, D., Green A.G., Mereu, R.F. and Morel-a-l'Huissier, P., 1990: Migration of wide-angle data from the Grenville Front in Lake Huron; Journal of Geophysical Reserach, 95, 10987 - 10998.

White, D.J., 1989: Two-dimensional seismic refraction tomography; Geophys.Journal, 97, 223 - 245.

PROCESSING AND INTERPRETATION OF COINCIDENT DEEP SEISMIC REFLECTION-REFRACTION DATA IN THE NORTH SEA ALONG THE BIRPS MOBIL LINE 1 (CCSS DATASET 2)

V.G.Krishna, K.L.Kaila, and P.R.Reddy

National Geophysical Research Institute, Hyderabad-500 007, India

ABSTRACT

We present the results of poststack processing of near-vertical reflection data in the mid-North Sea high along the MOBIL LINE 1 as well as modelling results of coincident wide-angle reflection data recorded at the land seismic stations in northern England. The main objective of this study is to determine the 2-D velocity function, V(x,z) along this line and compare the results from the two data sets. As the wide-angle recordings are available for offsets greater than 40 km from the two land stations 54 and 47, we made use of the results of velocity analyses of the near-vertical reflection data available at 3 km intervals to construct the velocity model V(x,z) for the sedimentary section down to the basement. The two wide-angle record sections consistently reveal five prominent phases P1P, PCP, P2P, PMP and PDP in the later arrivals, identified as reflections from interfaces within the deep crust and the uppermost mantle. The Pg phase of apparent velocity 6.0 km/s (refraction from the basement) is observable out to 60 km offset, and the Pn phase of apparent velocity 7.8 km/s (refraction from the Moho) is observable at offsets greater than 130-140 km in the first arrivals. The PCP and PMP phases, well recorded with high amplitudes, are interpreted as reflections from the interface between the upper and the lower crust at 19-21 km depth (velocity increasing from 6.2 to 6.5 km/s) and the Moho at 27-32 km depth (velocity increasing from 6.6 to 7.8 km/s) respectively.

Modelling of Pn observations reveals a rather high velocity gradient in the uppermost mantle in this region. The 'diffraction-like' PDP phase, characterized by extremely high amplitude and high apparent velocity, is successfully modelled as the reflection from a subcrustal reflector steeply dipping (about 17° dip) towards the west and associated with a velocity increase from 8.2 to 8.7 km/s and a density increase of 0.4 gm/cc. This prominent PDP reflector in the uppermost mantle appears to be related to the Caledonian structures.

The poststack processing sequence of near-vertical reflection data along this line consisted of f-k dip filtering, followed by predictive deconvolution, time variant frequency filtering, amplitude equalization and display of the final stack section. The reflection section thus improved by this processing sequence, displays both vertical and lateral variations of the reflectivity structure along the line. Both the PCP and PMP reflectors appear as bands of discontinuous reflector segments indicating that they may not be sharp boundaries throughout but may be gradational in some parts. The upper crust is essentially transparent up to about 7 s TWT, except on the westernmost 50 km of the line where it is transparent up to only 5-6 s, consistent with the velocity structure. The lower crust is marked by an abrupt increase of the reflectivity in its upper part of 7-8.5 s TWT followed by about a 2 s gap till the Moho reflectivity is again marked by another abrupt increase at about 10.5 s TWT. The PDP reflection, continuous over a 20 km distance on the western end of this reflection section, is associated with high amplitudes consistent with the wide-angle data. We observe a fair agreement between the near-vertical and the wide-angle reflection sections on this line.

INTRODUCTION

As a contribution to the CCSS workshop, the coincident deep seismic reflection-refraction dataset, in the mid-North Sea high along the BIRPS MOBIL LINE 1 (Figure 1), has been processed with an objective to determine the 2-D velocity function, V(x,z) along the line, and compare the results from the reflection and refraction data. In order to test the coincidence of the refraction Moho (defined by the velocity structure) and the reflection Moho (defined as the base of the lower crustal reflective layering), BIRPS acquired deep reflection data along the 151 km long offshore MOBIL LINE 1 coinciding with the line of CSSP (Caledonian Suture Seismic Profile) and complemented by wide-angle recordings of the offshore airgun shots along the same line at land based seismic stations in northern England. This unique sea-to-land coincident deep seismic reflection-refraction line is parallel to the Caledonian strike just south of the supposed surface trace of the Iapetus Suture across northern England (see Figure 1). Earlier deep seismic reflection studies in this region along the NEC profile (Figure 1) proposed that north dipping reflectors imaged on that profile represent the Iapetus Suture (Klemperer and Matthews, 1987). While MOBIL LINE 3 was recorded sufficiently far from NEC to provide a good strike control on reflective structures, MOBIL LINE 2 was selected close enough to image essentially the same structures as on NEC, but was recorded to 24 s TWT in order to establish whether or not any of the reflectors in this area penetrate through the reflection Moho into the mantle.Blundell et al. (1991) found however, that the LINE 2 shows no trace of an extension of the north dipping suture

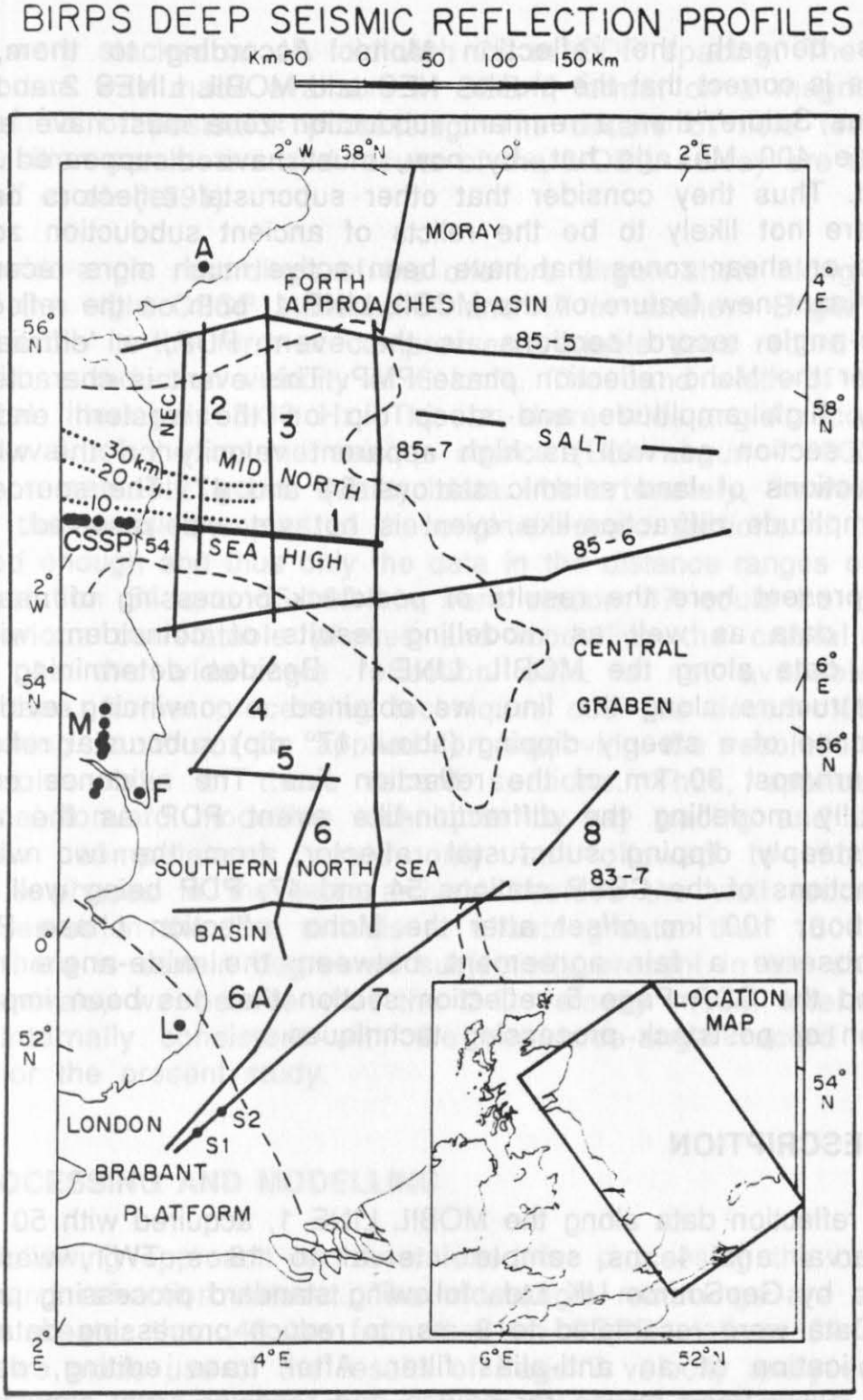

Figure 1: Map of BIRPS deep seismic reflection profiles across central and southern North Sea (after Blundell et al.,1991). Profiles of the MOBIL survey are indicated by numbers with each line. Land recording stations for the MOBIL survey are indicated by filled circles (CSSP: Caledonian Suture Seismic Profile). The contours (10,20 and 30 km) shown by small dots represent the subcrop of the Iapetus Suture interpreted by Klemperer and Matthews (1987).

reflectors beneath the reflection Moho. According to them, if the hypothesis is correct that the profiles NEC and MOBIL LINES 2 and 3 cross the Iapetus Suture, then a remnant subduction zone must have existed in the mantle 400 Ma ago but, by now, must have disappeared or been destroyed. Thus they consider that other subcrustal reflectors on BIRPS profiles are not likely to be the relicts of ancient subduction zones but are faults or shear zones that have been active much more recently. The most dominant new feature on the MOBIL LINE 1, both on the reflection and the wide-angle record sections, is the event PDP, a 'diffraction-like' event after the Moho reflection phase PMP. This event is characterized by extremely high amplitude and steep dip on the western end of the reflection section as well as high apparent velocity on the wide-angle record sections of land seismic stations 54 and 47. The source of this strong amplitude diffraction-like event is not yet well resolved.

We present here the results of poststack processing of near-vertical reflection data as well as modelling results of coincident wide-angle reflection data along the MOBIL LINE 1. Besides determining the 2-D velocity structure along the line, we obtained a convincing evidence for the existence of a steeply dipping (about 17° dip) subcrustal reflector, on the westernmost 30 km of the reflection line. The evidence comes by successfully modelling the diffraction-like event PDP as the reflection from a steeply dipping subcrustal reflector, from the two wide-angle record sections of the CSSP stations 54 and 47, PDP being well recorded out to about 100 km offset after the Moho reflection phase PMP. We further observe a fair agreement between the wide-angle reflection model and the CDP Page 5 reflection section that has been improved by application of poststack processing techniques.

DATA DESCRIPTION

The reflection data along the MOBIL LINE 1, acquired with 50 m airgun shot interval and 4 ms sample interval to 16 s TWT, was initially processed by GeoSource UK Ltd., following standard processing practice of BIRPS. Data were resampled to 8 ms, to reduce processing data volume, with application of an anti-alias filter. After trace editing, data were sorted to allow trace mixing for source and receiver array simulation. The three-trace weighted mix was time variant to maintain resolution in the upper part of the section but build signal amplitude in the lower part. Thus both source and receiver array simulations were made with similar trace mixing. Then a gain function was applied to correct for spherical divergence and the data were CDP sorted for stacking. Time domain deconvolution before stack was designed, to attenuate multiples, using two operators for the shallow and deeper windows. Velocity analyses were made at 3 km intervals. Following application of normal moveout corrections and mutes,

the data were stacked at 45 fold with 25 m CDP spacing. The stacked reflection data was made available in SEG-Y format on a magnetic tape for application of poststack processing. The details of field techniques, data acquisition parameters and results of the MOBIL survey are described by Blundell et al. (1991).

The wide-angle recordings of the offshore airgun shots along the line at two of the eight CSSP stations, 54 and 47 in northern England, were made available in the form of compressed variable area record sections plotted with a reduction velocity of 6 km/s. The band width of this data after digital filtering is 3-30 Hz. This on-shore wide-angle recording at 50 m interval, of the marine seismic source (Bolt airgun - 8500 cu.in.) produced remarkably good quality data. Unfortunately, however, the quality of the supplied copies of the original record sections of this data is not good enough and thus only the data in the distance ranges of 40-180 km from station 54 and 55-160 km from station 47 could be used for picking various correlatable phases and modelling the crustal velocity structure. As the wide-angle reflection data is not available on a magnetic tape, further processing techniques such as deconvolution and digital filtering could not be applied for improving the resolution and/or signal-to-noise ratio of these record sections. Thus, application of conventional forward modelling techniques by ray tracing and synthetic seismogram computations could only be followed to model the correlatable phases in the later arrivals besides the well recorded Pn phase observed in the first arrivals at offsets greater than 130-140 km. Although there is certain degree of subjectivity present in the correlation of later arrivals, we believe that the 2-D velocity model inferred from them is internally consistent with the two wide-angle record sections available for the present study.

DATA PROCESSING AND MODELLING

The following approach has been used for processing the coincident reflection and refraction dataset. The wide-angle recordings are available for offsets greater than 40 km from the two CSSP stations 54 and 47. Therefore we made use of the results of Page 7 velocity analyses of the CDP data along this line, available at 3 km intervals, to construct the 2-D velocity-depth model V(x,z) for the sedimentary section down to the basement of 6.0 km/s velocity. This approach involved conversion of two-way travel times into corresponding depths followed by layer velocity identification and smoothing of various shallow layers along the CDP line. Keeping this sedimentary section down to the basement unchanged, the wide-angle reflection data have been modelled to construct the deeper crustal section along the line. This crustal depth section has finally been converted into a two-way time section in an attempt to compare with the poststack processed CDP reflection time section.

Modelling of wide-angle reflection data

The wide-angle record sections from the two stations, 54 and 47, consistently reveal five prominent phases correlatable in the later arrivals. Due to poor reproduction quality of the copies of the original record sections, we prefer to show here only the travel time picks of the correlated phases in the two record sections. Figures 2 and 6 show the travel time plots of the wide-angle reflection data from stations 54 and 47 respectively. The Pg phase of apparent velocity 6.0 km/s (refraction from the basement) is observable out to only 60 km offset, and the Pn phase (refraction from the Moho) of apparent velocity 7.8 km/s is observable as the first arrival at offsets greater than 130-140 km in the record sections from the two stations. The phases designated as P1P, PCP, P2P, PMP and PDP are modelled as reflection phases as follows. The PCP phase, which is relatively well recorded out to 130-150 km offset with high amplitudes as compared to the P1P and P2P phases, is interpreted as the reflection from an interface between the upper and the lower crust at 19-21 km depth with the velocity increasing from 6.2 to 6.5 km/s. The P1P and P2P phases, which are rather weak but correlatable out to 120 km and 80-100 km offsets, are modelled as reflections from interfaces at 16 km and 23-25 km respectively in the upper and the lower crust, however with smaller velocity contrasts. The phase designated as PMP which is well recorded out to 160-180 km offset with high amplitudes in the two record sections, is modelled as the reflection from the Moho at depths varying from 27-32 km and velocity increasing from 6.6 to 7.8 km/s. The refracted phase Pn from the Moho is found to be consistent with a rather strong velocity increase from 7.8 to 8.2 km/s in the uppermost mantle. The strong amplitude and high apparent velocity PDP phase, after the PMP, is well correlated from 60-100 km offset from station 54 and 80-110 km offset from station 47. This dominant 'diffraction-like' event on these record sections is however interpreted as a reflection from a steep boundary (about 17° dip) at subcrustal depths varying from 43 to 33 km over a distance range of 32 km on the western end of the CDP reflection line. This steep boundary appears to be also characterized by a large velocity and density contrast in order to produce comparable amplitudes of the PDP phase.

The deep crustal and uppermost mantle model along the line has been successively refined by iterative 2-D ray tracing and synthetic seismogram modelling of wide-angle reflection data discussed above, using the SEIS 81 package (Cerveny and Psencik, 1981). The computed travel time curves for various phases, are also shown in Figures 2 and 6 for the two stations along with the correlated travel time picks. The inferred structural model and the ray diagrams for the two stations are shown in Figures 3 and 7. The velocity structure in the sedimentary section above the basement as used for this modelling is shown at three representative locations along this line.

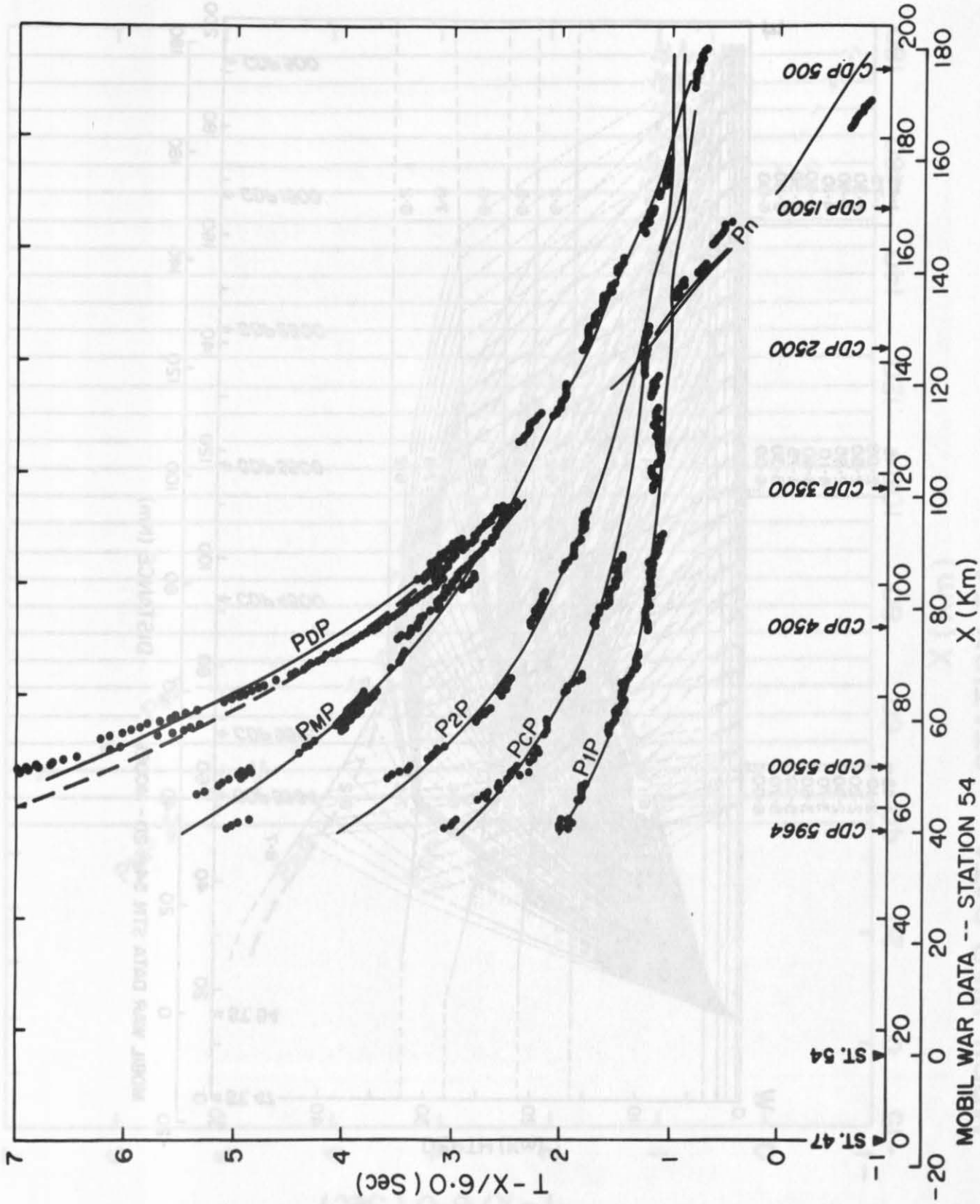

Figure 2: Travel times plot of the wide-angle reflection data correlated from the CSSP station 54 record section. Computed travel time curves for various phases are also shown by continuous curves. The broken curve for the PDP phase is computed for a 2 km shallower depth of the westerly dipping subcrustal reflector shown in Figure 3, indicating that it may be more steeply dipping on the western end.

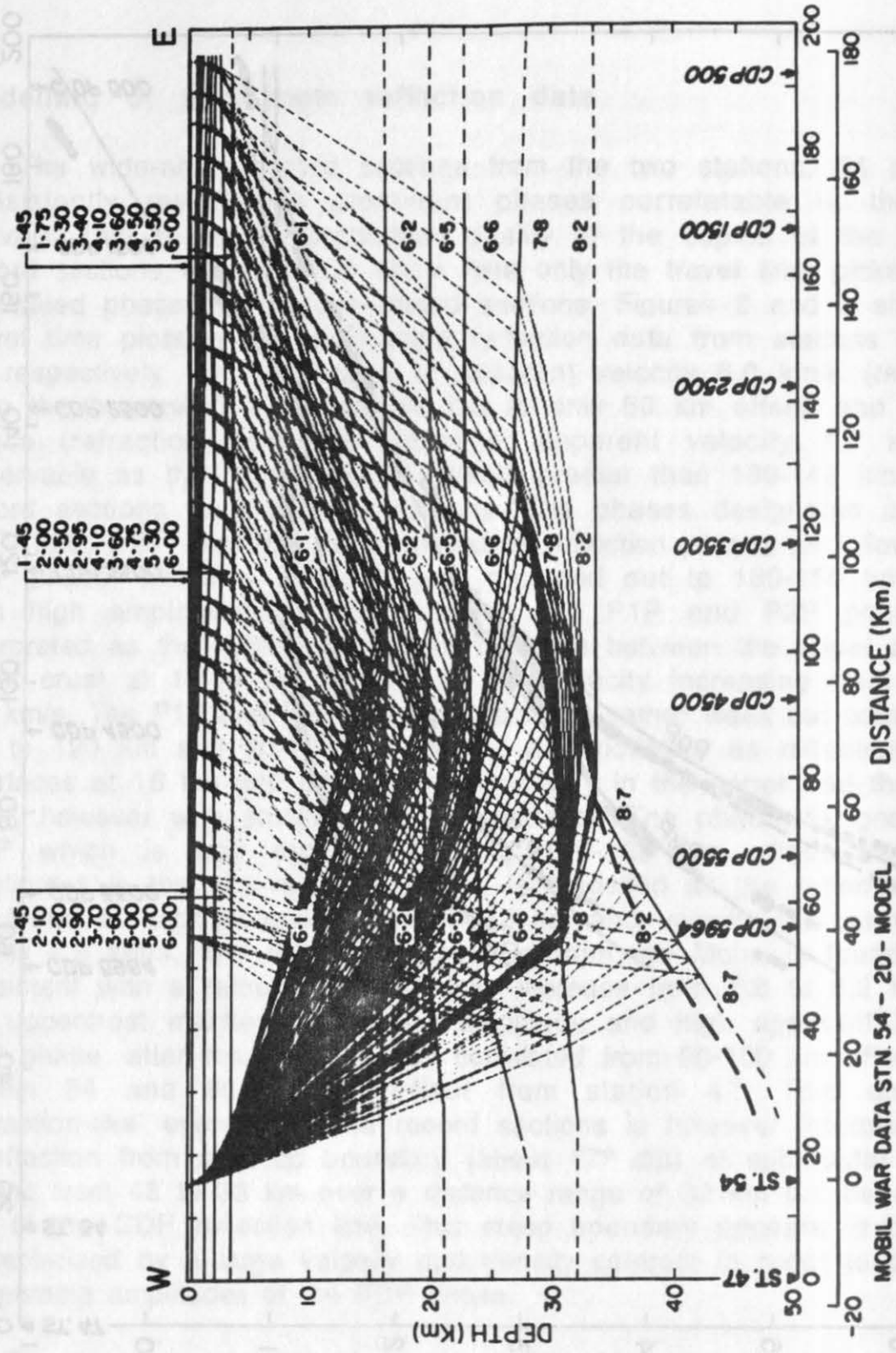

Figure 3: Inferred deep crustal model and the ray trace diagram for the common land seismic station 54. Deep crustal and uppermost mantle P wave velocities in each layer are shown along the profile. The westerly dipping subcrustal reflector is shown in the two depth ranges corresponding to the travel time curves plotted in Figure 2. Velocity models for the Sedimentary section down to the basement, as determined from the CDP reflection data, are shown at three locations on the profile.

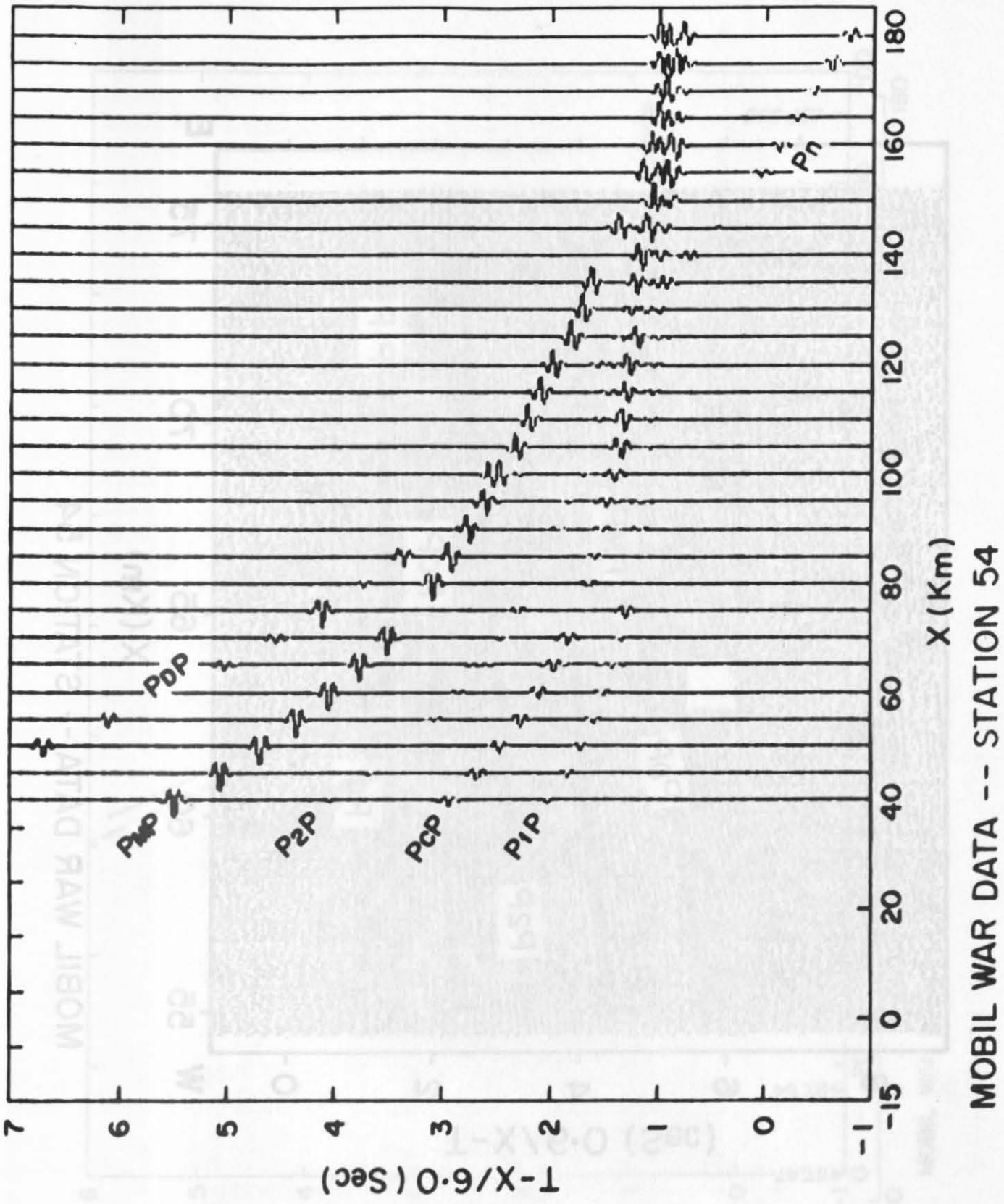

Figure 4: Record section of ray synthetic seismograms computed for the structural model shown in Figure 3 for the common land seismic station 54. Note the relative amplitudes of the PCP, PMP, Pn and the PDP phases matching closely with observations.

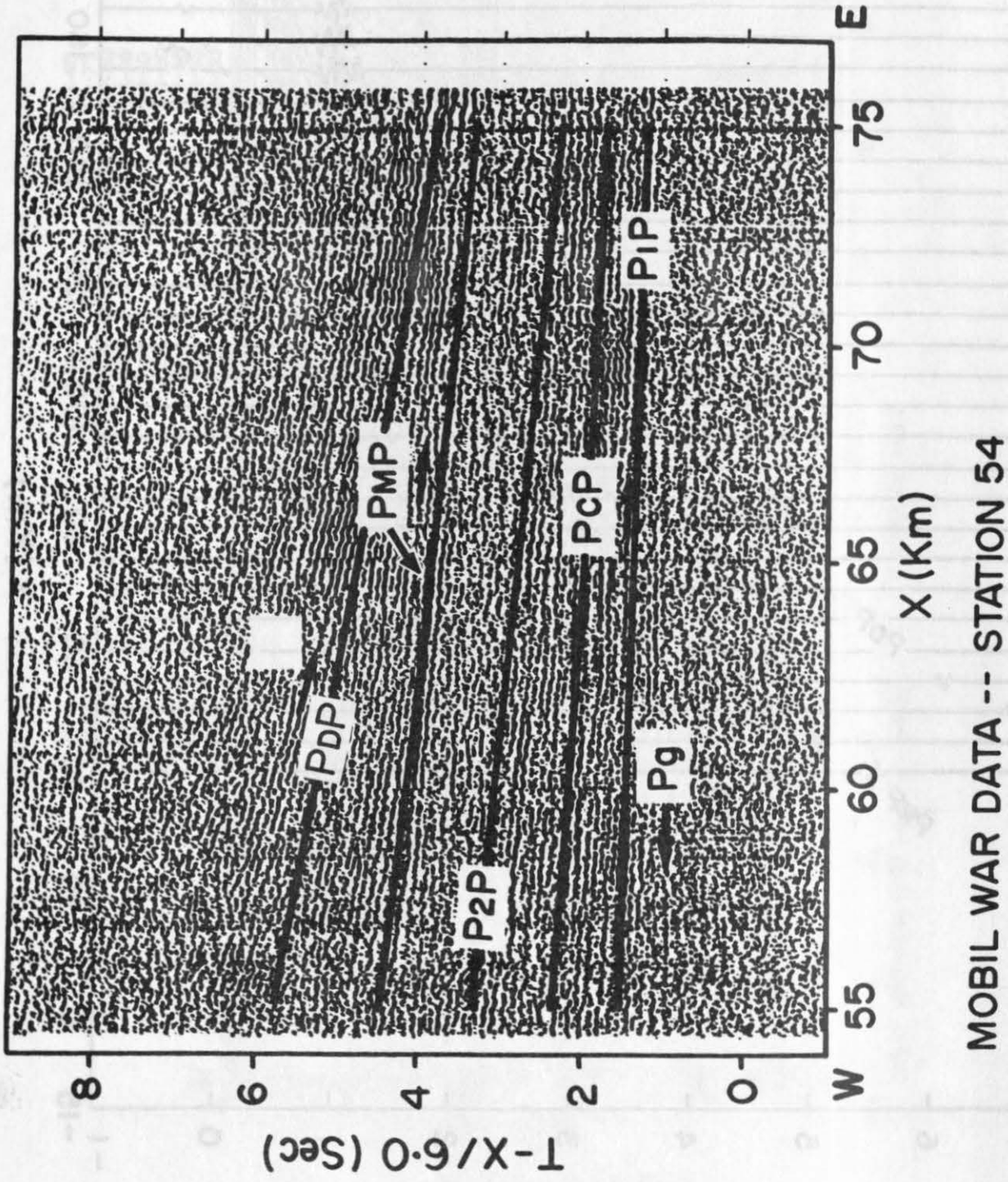

Figure 5: Compressed variable area seismogram section recorded, from airgun shots along MOBIL LINE 1, at the CSSP station 54 in the distance range 55-75 km showing the consistent fit of the P1P, PCP, P2P, PMP and the PDP phases computed for the structural model shown in Figure 3.

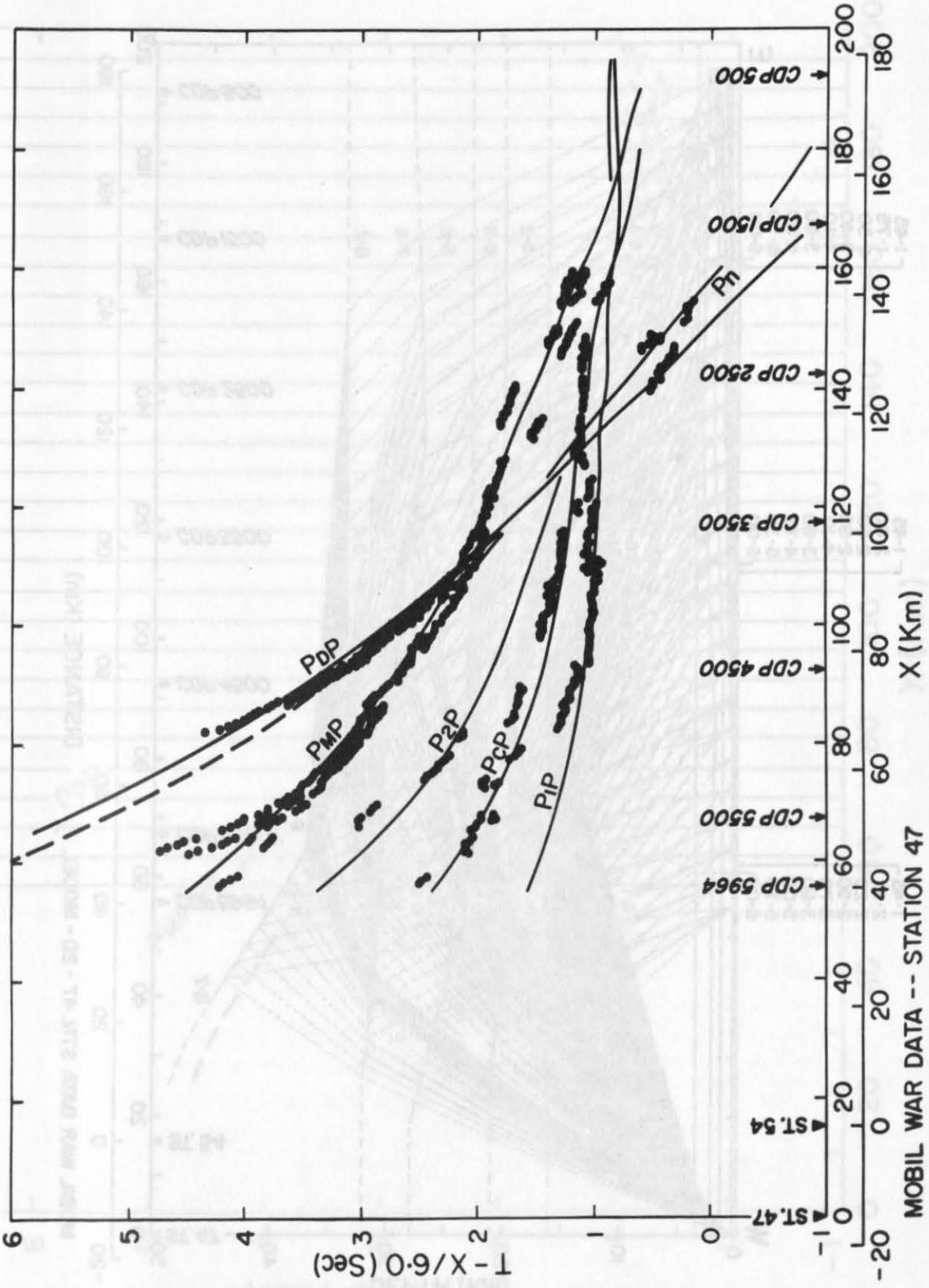

Figure 6: Same as Figure 2 for the CSSP station 47.

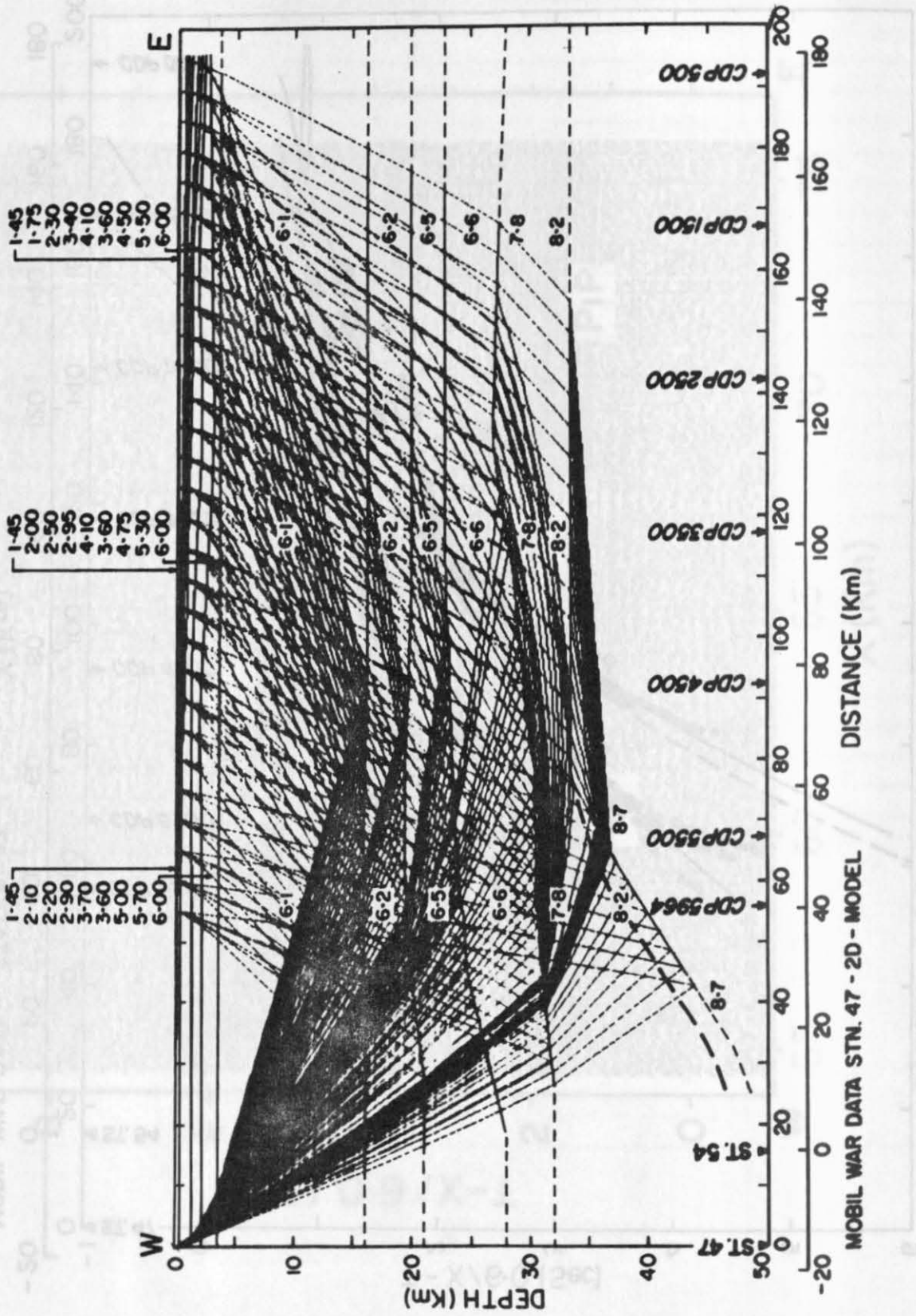

Figure 7: Same as Figure 3 for the CSSP station 47.

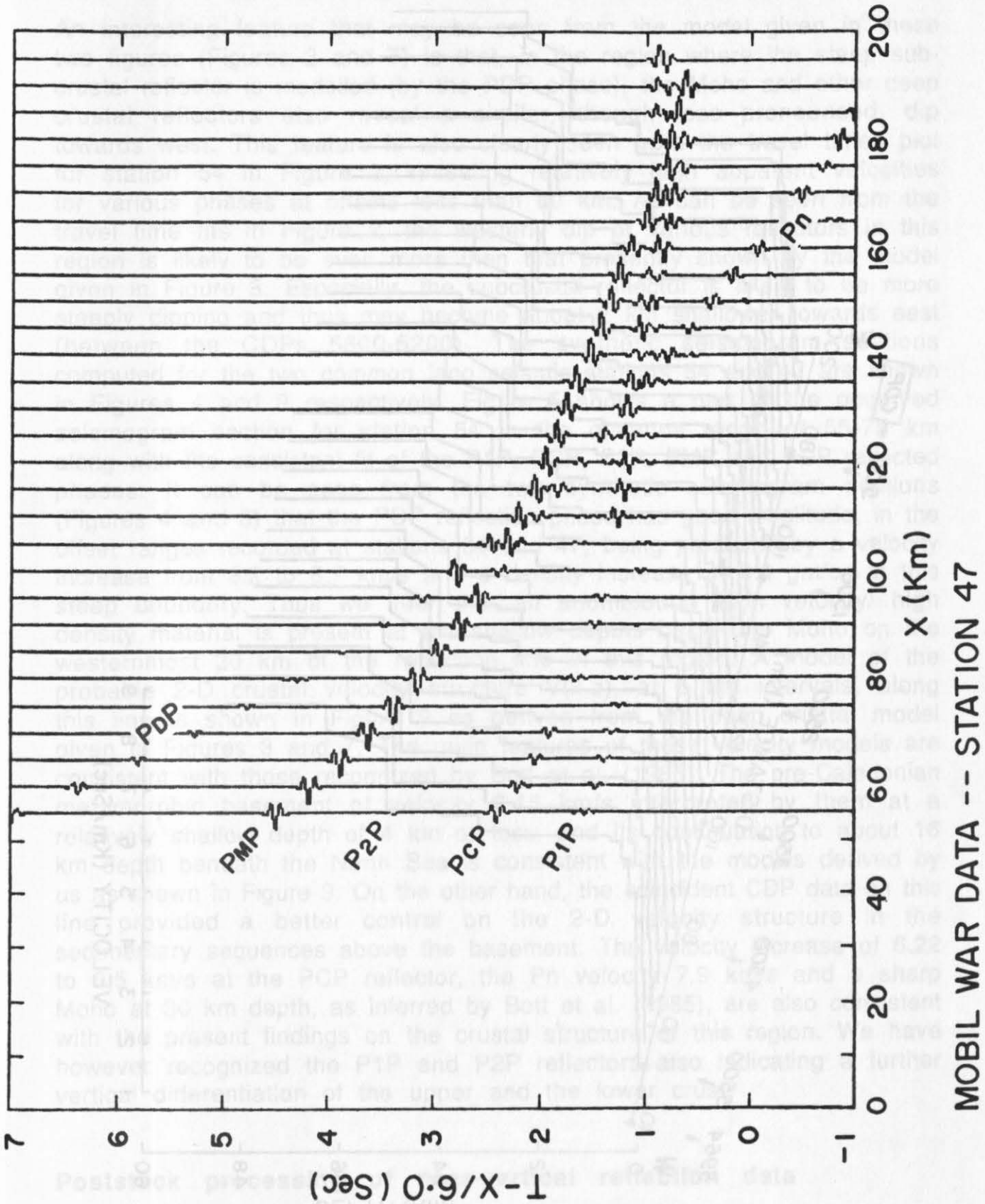

Figure 8: Same as Figure 4 for the CSSP station 47.

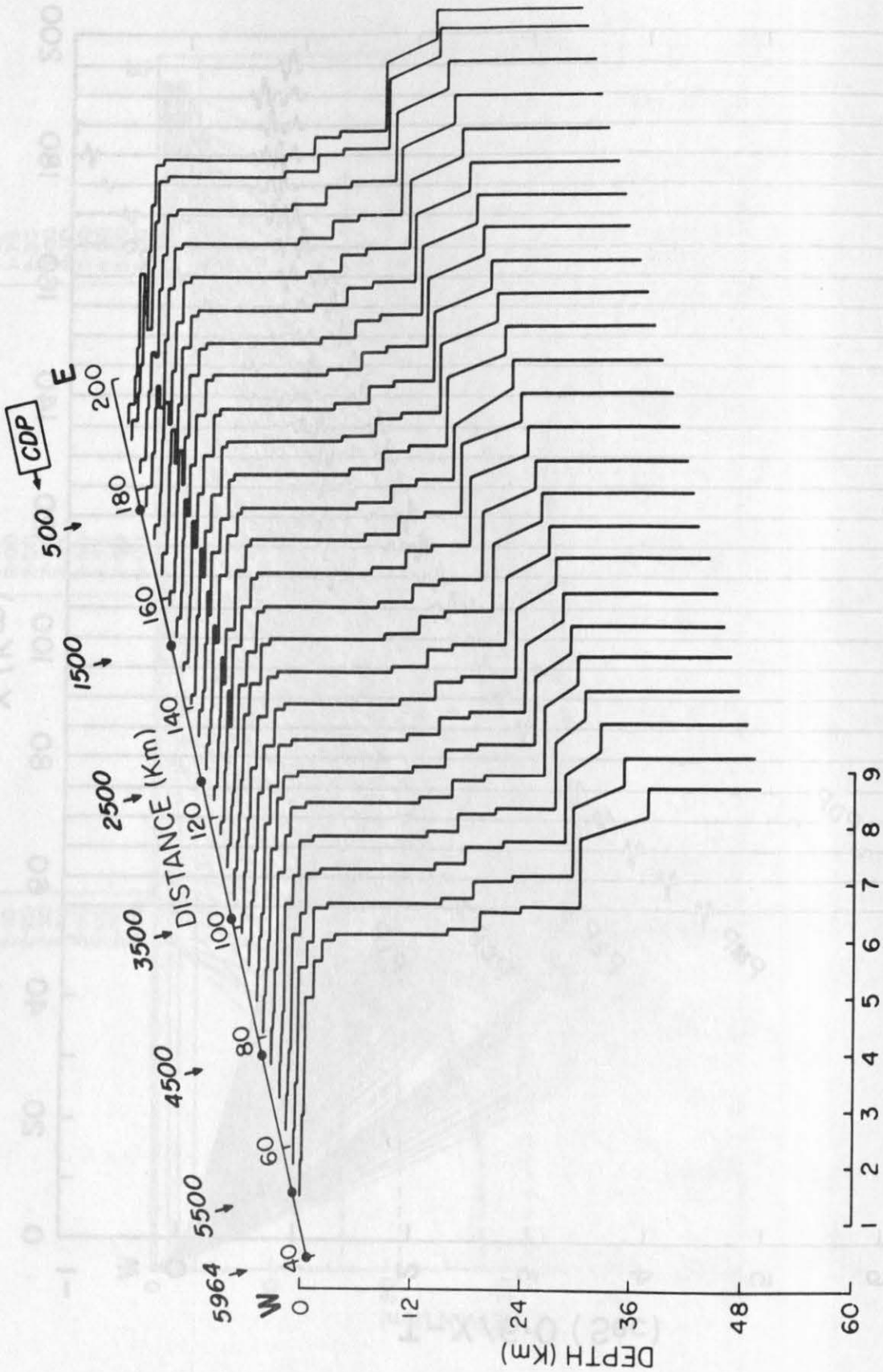

Figure 9: A model of the 2-D velocity function V(x,z) along the MOBIL LINE 1, inferred from coincident reflection/refraction data.

An interesting feature that may be seen from the model given in these two figures (Figures 3 and 7) is that, in the region where the steep subcrustal reflector is modelled (by the PDP phase), the Moho and other deep crustal reflectors also reveal a similar, though less pronounced, dip towards west. This feature is also clearly seen from the travel times plot for station 54 in Figure 2, revealing relatively high apparent velocities for various phases at offsets less than 60 km. As can be seen from the travel time fits in Figure 2, the westerly dip of various reflectors in this region is likely to be even more than that presently shown by the model given in Figure 3. Especially, the subcrustal reflector is likely to be more steeply dipping and thus may become about 2 km shallower towards east (between the CDPs 5600-5200). The synthetic seismogram sections computed for the two common land seismic stations 54 and 47 are shown in Figures 4 and 8 respectively. Figure 5 shows a part of the observed seismogram section for station 54 in the distance range of 55-75 km along with the consistent fit of the P1P, PCP, P2P, PMP and PDP reflected phases. It can be seen from the two synthetic seismogram sections (Figures 4 and 8) that the PDP reflection phase has good amplitude, in the offset ranges recorded at stations 54 and 47, being produced by a velocity increase from 8.2 to 8.7 km/s and a density increase of 0.4 gm/cc at this steep boundary. Thus we infer that an anomalously high velocity/ high density material is present at the shallow depths below the Moho on the westernmost 30 km of the reflection line in this region. A model of the probable 2-D crustal velocity structure V(x,z), at 6 km intervals, along this line is shown in Figure 9 as derived from the deep crustal model given in Figures 3 and 7. The main features of these velocity models are consistent with those recognized by Bott et al. (1985). The pre-Caledonian metamorphic basement of velocity 6.15 km/s interpreted by them at a relatively shallow depth of 4 km or less, and its continuation to about 16 km depth beneath the North Sea is consistent with the models derived by us as shown in Figure 9. On the other hand, the coincident CDP data on this line provided a better control on the 2-D velocity structure in the sedimentary sequences above the basement. The velocity increase of 6.22 to 6.5 km/s at the PCP reflector, the Pn velocity 7.9 km/s and a sharp Moho at 30 km depth, as inferred by Bott et al. (1985), are also consistent with the present findings on the crustal structure of this region. We have however recognized the P1P and P2P reflectors also indicating a further vertical differentiation of the upper and the lower crust.

Poststack processing of near-vertical reflection data

Poststack processing of near-vertical reflection data on the MOBIL LINE 1 has been carried out on the recently established seismic data processing system at the National Geophysical Research Institute, Hyderabad. The hardware configuration of this system consists of a CDC CYBER 180/850A host computer running the dual operating systems NOS

and NOS/VE, a MAP IV array processor, a versatec plotter, large capacity disk storage units, high speed tape drive units and printers. The seismic data processing software package GEOMASTER of the Compagnie Generale de Geophysique, Masse, France, is running with its VOS control system under the NOS operating system. The poststack processing sequence for the MOBIL LINE 1 consisted of attenuating steeply dipping coherent noise by frequency-wavenumber (f-k) dip filtering, suppressing the multiples by predictive deconvolution, time variant band pass frequency filtering to readjust the spectrum, finally the amplitude equalization and display of the final stack section. The only important processing step that has not been carried out in the present processing exercise is that of migration. This is because while processing deep crustal seismic data the main objective is to obtain the final section that is best suitable for interpretation rather than only achieving the highest S/N or resolution. We believe that the final stack section that has been obtained by us meets this requirement and thus is suitable for structural interpretation.

The plot of the raw stack section with only a time variant frequency filtering (10-20/45-60 Hz, 0-500 ms., 5-10/40-55 Hz, 1500-2500 ms., 5-10/35-45 Hz, 3500-4500 ms., 5-8/30-40 Hz, 5500-6500 ms., 5-7/25-32 Hz, 12000-16000 ms) and amplitude equalization is displayed in three parts of the section in Figures 10 a, b, and c. The application of f-k filtering by rejecting signals with dips exceeding +/- 16 ms/trace gives adequate improvement by attenuating the steeper coherent noise and hardly affecting the real reflections. In fact, after f-k filtering, the lateral continuity of various reflections has significantly improved as can be seen from the plot displayed in three parts of the section in Figures 11 a, b, and c. It is further found that predictive deconvolution when applied a second time after stack gives a substantial improvement by suppressing the multiples periodicity significantly.

Figures 10 (a,b,c) and 11 (a,b,c), see next pages.

Figures 10(a,b,c): Raw stack section (Two way time versus CDP locations) plotted with a time variant frequency filtering and amplitude equalization.

Figures 11(a,b,c): Same as Figure 10, after application of the f-k filtering (rejecting slopes exceeding + 16 ms/trace).

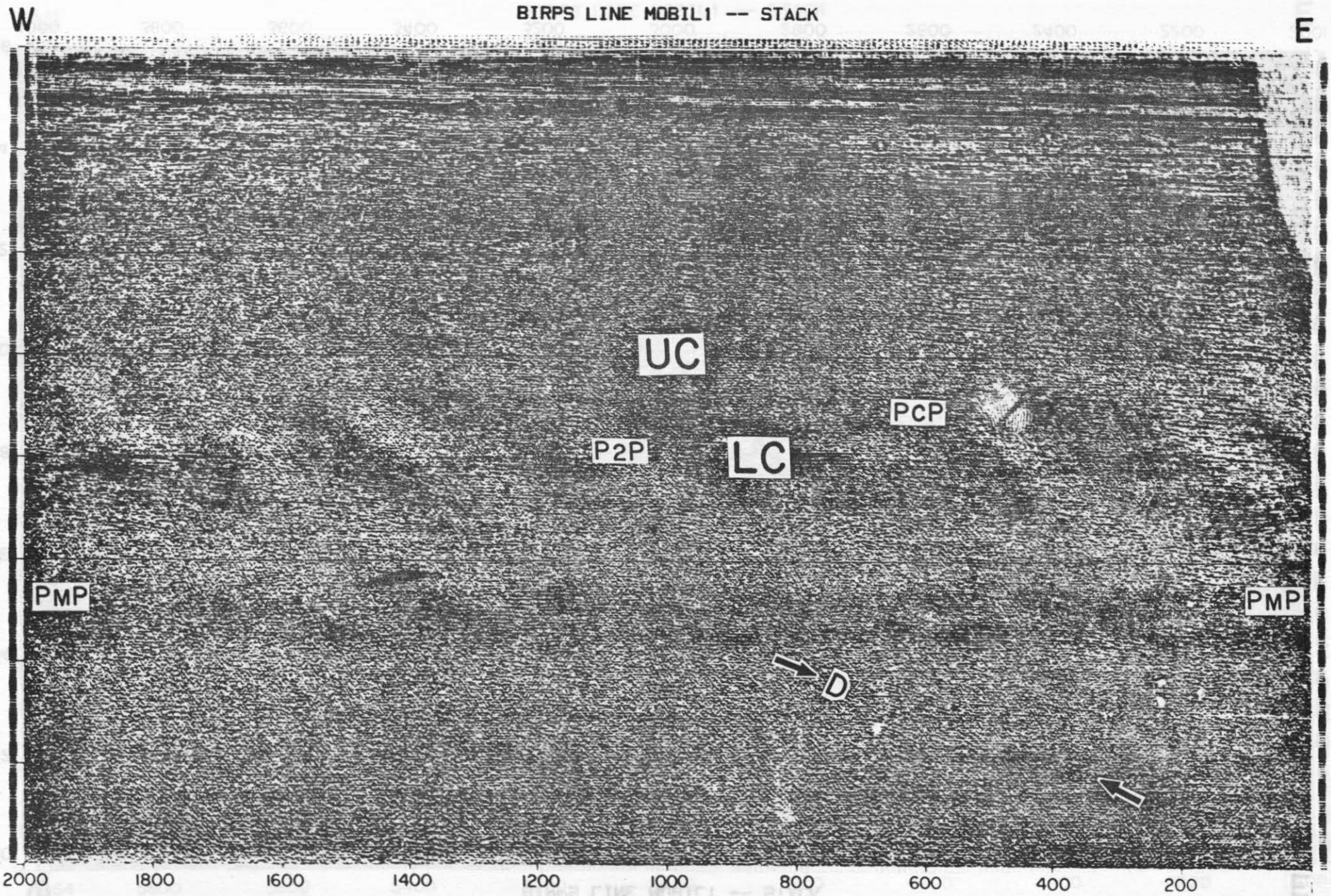
BIRPS LINE MOBIL1 -- STACK
W
E
TWO WAY TIME (Sec)
0
2
4
6
8
10
12
14
16
2000
1800
1600
1400
1200
1000
800
600
400
200
UC
LC
P2P
PcP
PMP
PMP
D

Figure 10a

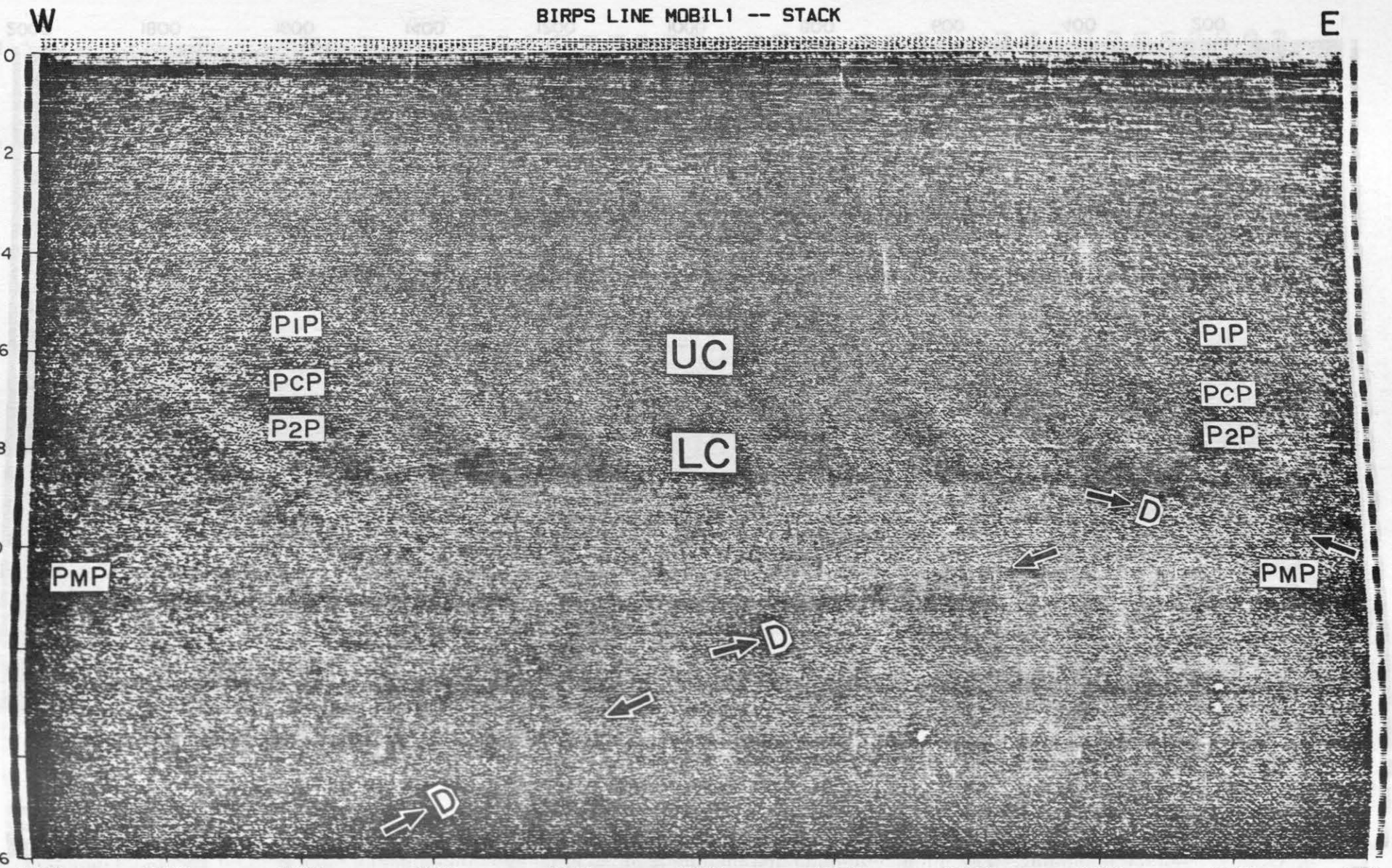
BIRPS LINE MOBIL1 -- STACK
W
E
TWO WAY TIME (Sec)
0
2
4
6
8
10
12
14
16
4000
3800
3600
3400
3200
3000
2800
2600
2400
2200
P1P
PcP
P2P
PMP
UC
LC
D

Figure 10b

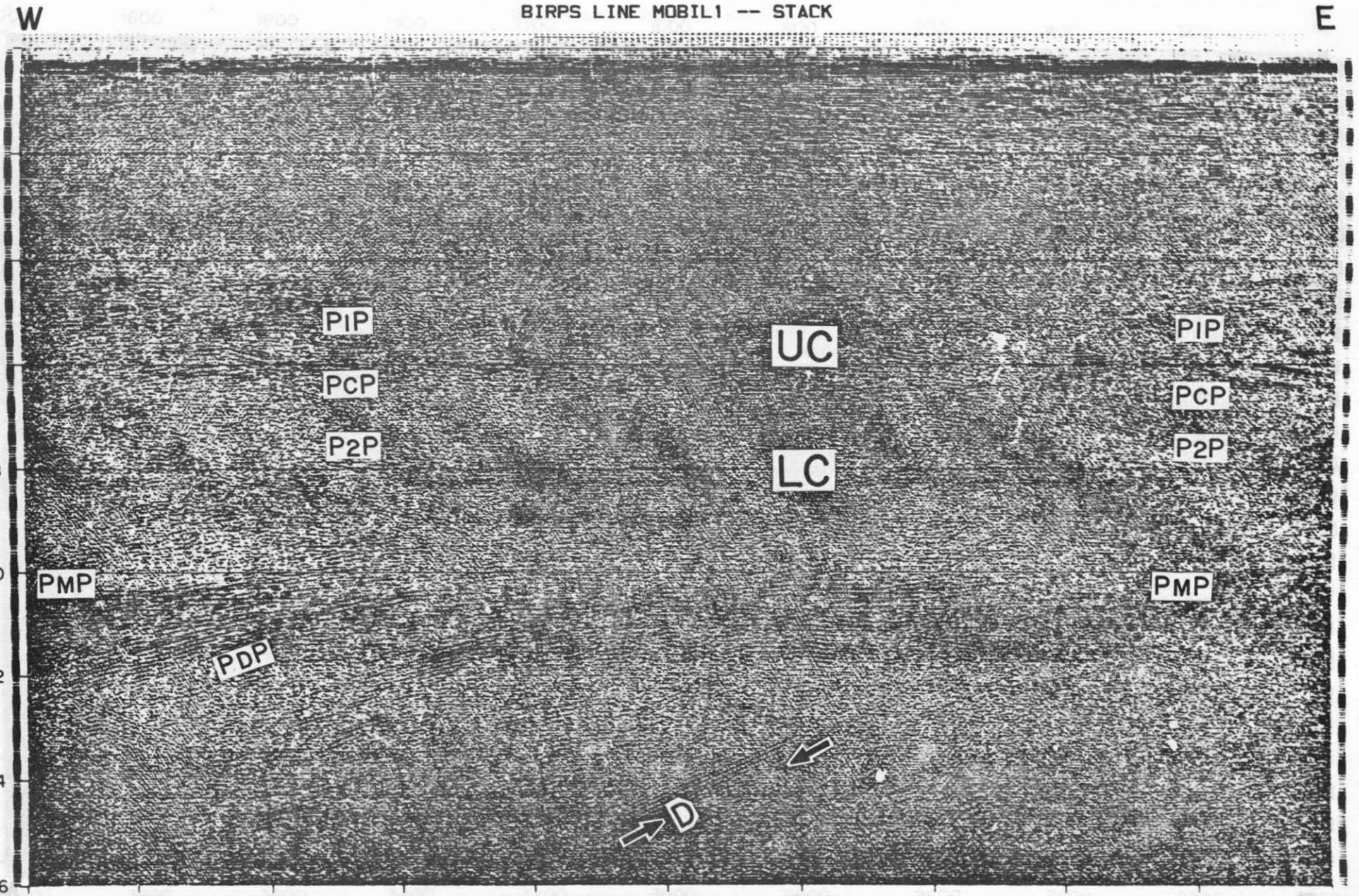
W
BIRPS LINE MOBIL1 -- STACK
E
TWO WAY TIME (Sec)
0
2
4
6
8
10
12
14
16
PIP
PCP
P2P
PMP
PDP
UC
LC
D
PIP
PCP
P2P
PMP
5964
5800
5600
5400
5200
5000
4800
4600
4400
4200

Figure 10c

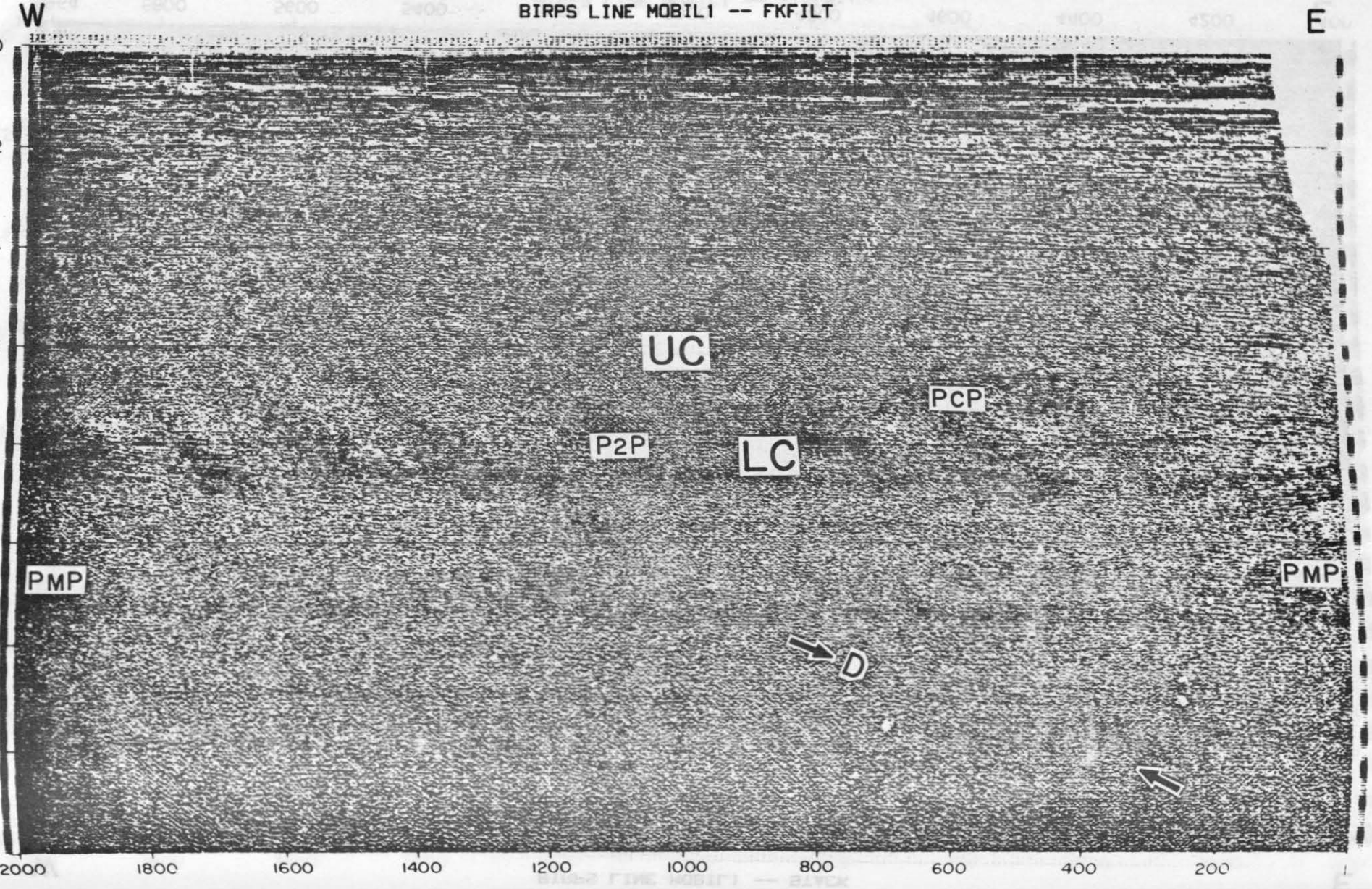
BIRPS LINE MOBIL1 -- FKFILT
W
E
TWO WAY TIME (Sec)
0
2
4
6
8
10
12
14
16
UC
PcP
P2P
LC
PMP
PMP
D
2000
1800
1600
1400
1200
1000
800
600
400
200

Figure 11a

BIRPS LINE MOBIL1 -- FKFILT
W
E
PIP
PCP
P2P
PMP
D
UC
LC
0
2
4
6
8
10
12
14
16
3800
3600
3400
3200
3000
2800
2600
2400
2200
2001
4000
TWO WAY TIME (Sec)

Figure 11b

BIRPS LINE MOBIL1 -- FKFILT
W
E
PIP
PCP
P2P
PMP
UC
LC
PDP
D
TWO WAY TIME (Sec)
0
2
4
6
8
10
12
14
16
5964
5800
5600
5400
5200
5000
4800
4600
4400
4200

Figure 11c

The plot of the final stack, with application of predictive deconvolution (operator length 700 ms, gap 50 ms) on the shallow (600-7000 ms) and deep (5000-10500 ms) design windows, is displayed in three parts of the section in Figures 12 a, b and c. In Figure 12, the two-way time section obtained by converting the 2-D crustal depth section inferred from the wide-angle reflection data, has been superimposed mostly in those parts of the section where a coincident subsurface coverage has been obtained from the two datasets for various reflectors. The CDP reflection data gives a complete coverage of various deep crustal reflectors along this line, while the wide-angle reflection data obviously provides only a limited subsurface coverage. It can be seen from Figure 12 that the agreement between the two datasets is reasonably good within the error limits of phase correlation and their modelling results. It is however inferred from this comparison of various deep crustal reflectors that they have laterally variable reflectivity appearing as bands of discontinuous reflector segments along this line. The possible explanation for this laterally variable reflectivity is that the actual physical contrasts responsible for these reflections may not be sharp throughout but are likely to be more gradational where the reflectors are not obviously visible in the CDP reflection section.

INTERPRETATION AND DISCUSSION

The MOBIL 1 coincident deep seismic reflection/refraction dataset provides a two-dimensional image of the crust and uppermost mantle along the line parallel to the strike of the Iapetus Suture, a fundamental geologic structure (about 400 Ma old) of the Palaeozoic Caledonian orogeny. The shallow section consisting of the Tertiary, the Mesozoic and the Palaeozoic strata has been well delineated by the CDP reflection section. However, the basement reflection is not so continuously observable in the reflection section due to its relatively less reflective nature at near-vertical incidence, possibly being a gradational rather than a sharp boundary. The upper crust in this region is also essentially transparent between 2-3 s to about 7 s TWT, except on the westernmost 50 km of the line where it is transparent up to only 5-6 s. This feature is consistent with the wide-angle data indicating almost a homogeneous upper crustal structure with a nearly constant velocity of 6.1-6.2 km/s

Figures 12 (a,b,c), see next pages.

Figures 12(a,b,c): Same as Figure 11, after predictive deconvolution. The two-way time section, converted from the 2-D crustal P velocity-depth section (given in Figure 3) for various deep crustal reflectors, is shown for comparison. Other symbols in Figures 10-12 are: U C (upper crust), L C (lower crust) and D (Diffractions).

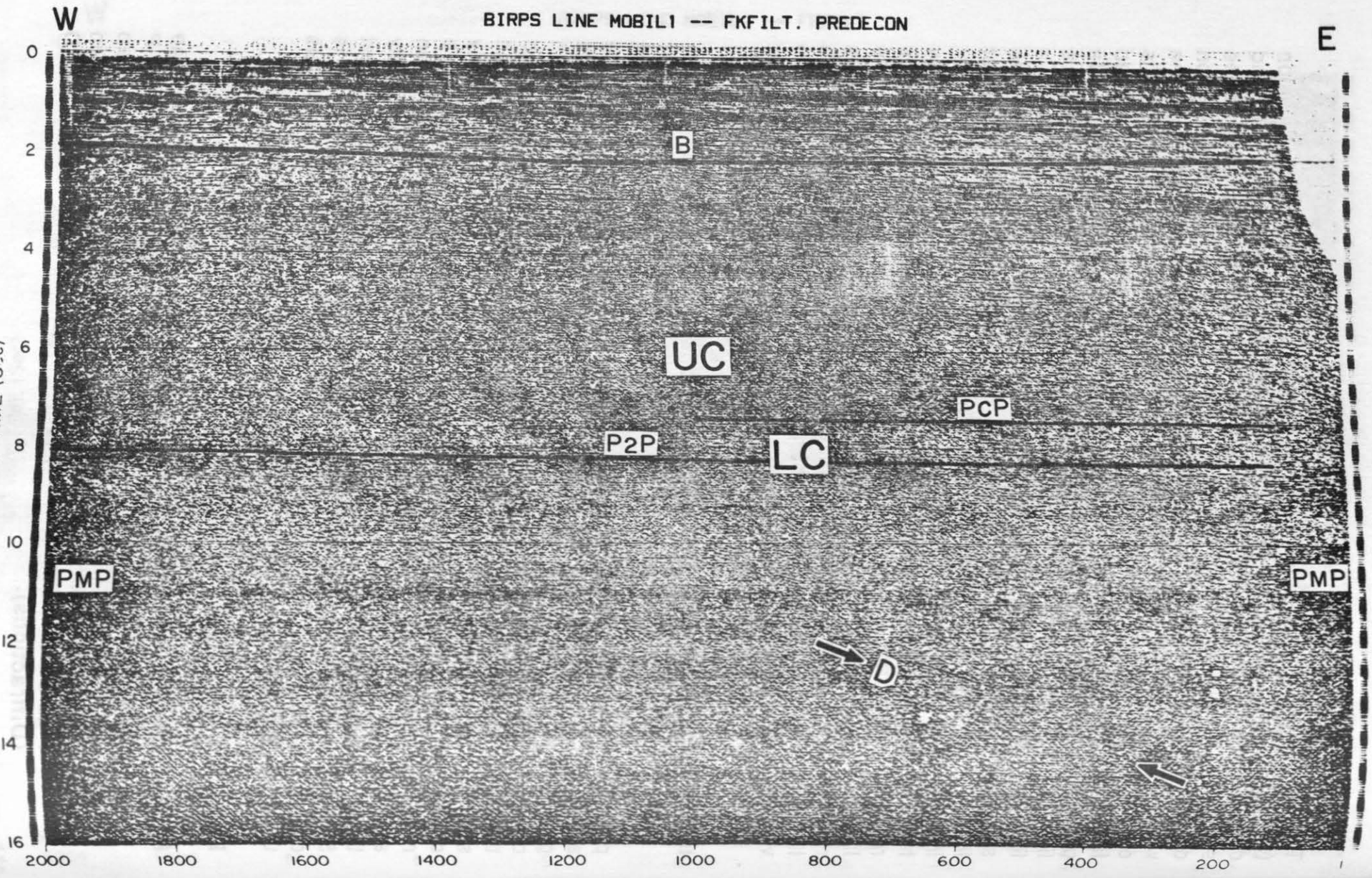
W
BIRPS LINE MOBIL1 -- FKFILT. PREDECON
E
TWO WAY TIME (Sec)
0
2
4
6
8
10
12
14
16
B
UC
PcP
P2P
LC
PMP
PMP
D
2000
1800
1600
1400
1200
1000
800
600
400
200
1

Figure 12a

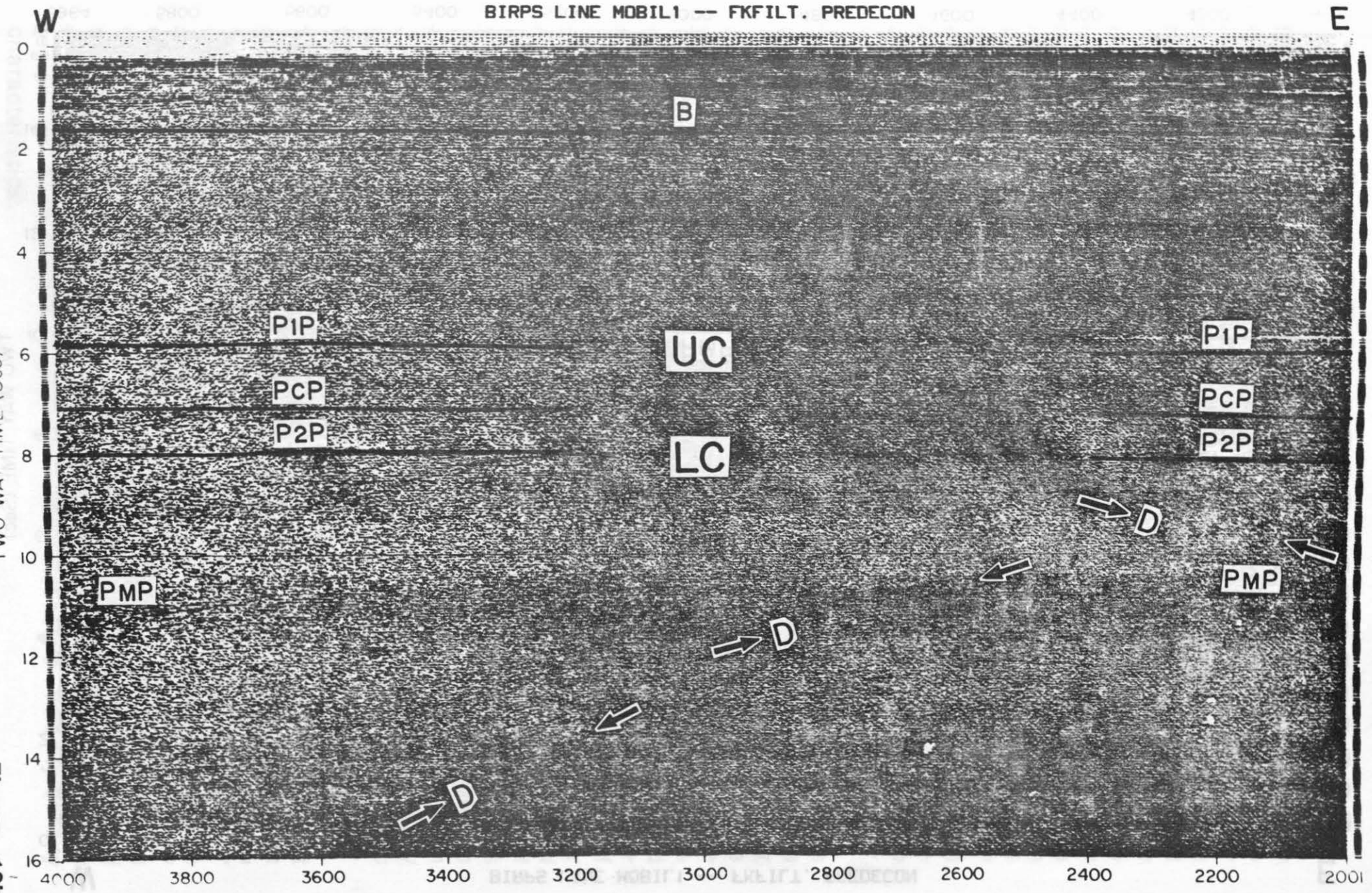
BIRPS LINE MOBIL1 -- FKFILT. PREDECON
W
E
TWO WAY TIME (Sec)
0
2
4
6
8
10
12
14
16
B
P1P
PcP
P2P
UC
LC
PMP
D
4000
3800
3600
3400
3200
3000
2800
2600
2400
2200
2001

Figure 12b

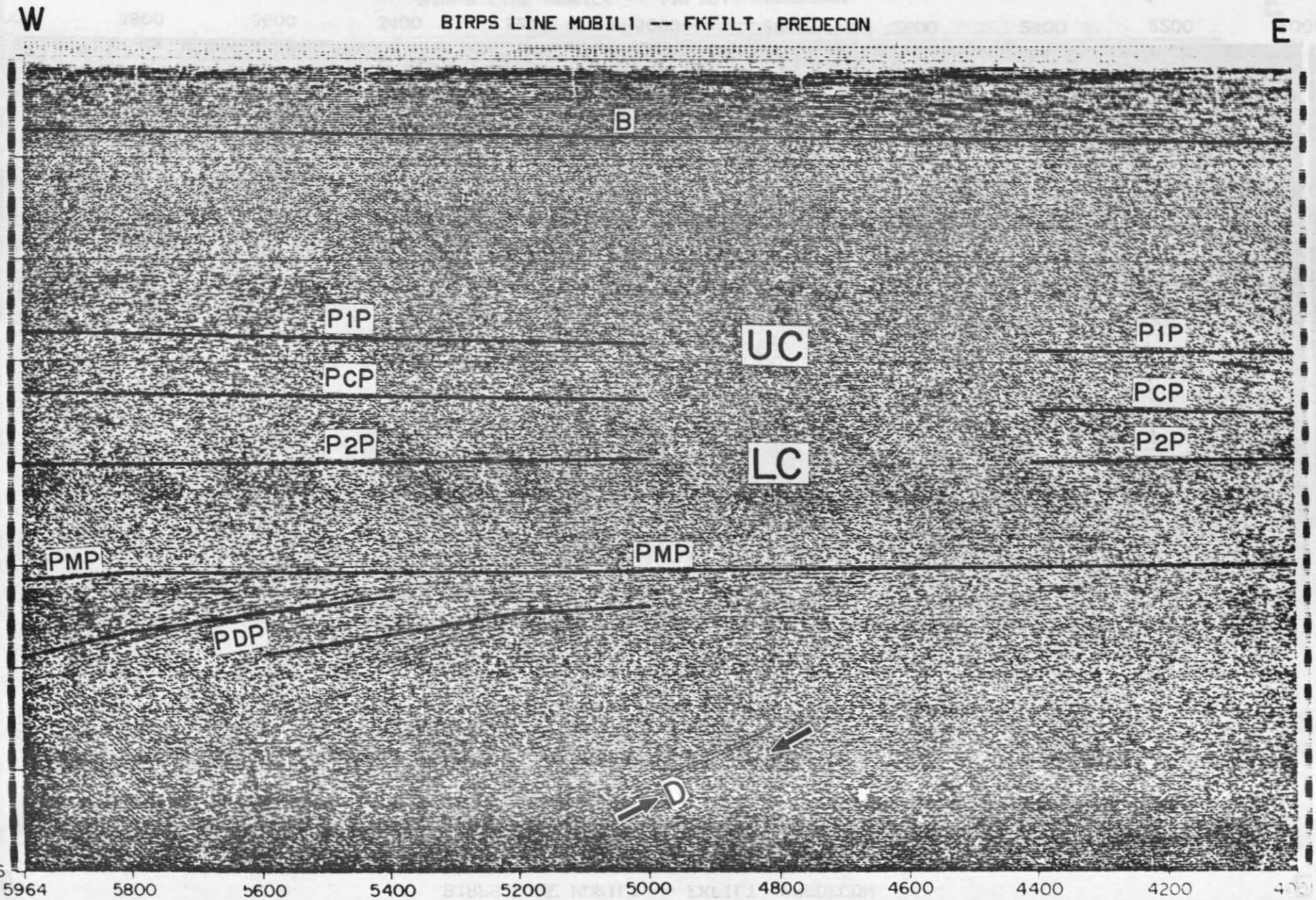
W
BIRPS LINE MOBIL1 -- FKFILT. PREDECON
E
TWO WAY TIME (Sec)
0
2
4
6
8
10
12
14
16
B
P1P
PCP
P2P
UC
LC
PMP
PDP
D
5964
5800
5600
5400
5200
5000
4800
4600
4400
4200

Figure 12c

from 4 km to 19-21 km depth. The lower crustal structure is depicted by a marked increase of the reflectivity at 7-8.5 s TWT corresponding to the PCP and P2P reflectors delineated by the wide-angle data. The lower crust is also not entirely reflective down to the Moho, as can be seen from the CDP reflection sections (Figures 10-12). The Moho reflection at about 10.5 s TWT in these sections is rather well separated by about a 2 s gap in the reflectivity. Both the mid-crustal (PCP) and the Moho (PMP) reflectors also reveal laterally variable reflectivity along this line appearing as bands of discontinuous reflector segments. This may be indicative of the variable nature (sharp or gradational) of the PCP and the PMP reflectors. The wide-angle recordings at the land seismic stations 54 and 47 however reveal high amplitudes for both the PCP and PMP reflections in the entire recording range. The coincidence of the deep crustal and Moho reflectors observed from the near-vertical and wide-angle reflection datasets is well within the error limits of the phase correlations.

Another prominent feature evident from the CDP reflection sections (Figures 10-12) is the presence of a good number of dipping events (marked as D), both in the lower crust and the uppermost mantle. Their amplitude decreases rapidly with increasing TWT. We interpret these events as diffractions which are generated from small scale heterogeneities in the path of the seismic wavefronts. These heterogeneities may represent regions of reflective segments with good acoustic impedance contrasts but with their dimensions equal to or smaller than the Fresnel-zone diameter. At relatively low frequencies of the order of 15 Hz or lower, corresponding to the lower crustal/uppermost mantle depths, the Fresnel-zone diameter would typically be 4-5 km or even larger. The small scale heterogeneities, of these dimensions may represent regions of extensive mixing of rock types with contrasting acoustic properties and originating the diffractions similar to those observed in the reflection section. According to Freeman et al. (1988), one of many geological possibilities to achieve this is by imbrication of continental crust with remnants of subducted oceanic crust.

Contrasting with the diffraction events discussed above, we find that the PDP event has quite different properties, consistently observed both in the near-vertical (between CDPs 5200 and 5964), and the wide-angle (out to 100 km offset) recordings. This strongly curved 'diffraction-like' event has surprisingly high amplitudes which, we believe, cannot be explained by diffracting elements. The remarkable persistence of the PDP event with high amplitudes over about 20 km distance in the near-vertical reflection section, as well as its coincidence on the wide-angle record sections suggest that the source of this reflection should be an anomalous region of considerable dimensions with distinctive velocity/density characteristics.

Following the explanation given by Freeman et al. (1988) for the parallel reflectors P1 and P2 observed on the NEC deep seismic reflection profile in this region, we suggest that the steep reflector (about 17° dip) modelled as the source of the PDP event on the MOBIL 1 line is possibly related to the structures of the Caledonian origin rather than being related to later crustal extension. It may also be interesting here to refer to a recent study of similar 'diffraction-like' events on the DEKORP 2-S deep seismic reflection profile by Kampfmann (1988) who successfully demonstrated by amplitudes modelling that such strong events can be observed due to curved reflectors with dimensions significantly greater than the Fresnel-zone. Due to the similar travel time curves of such strongly curved reflectors and diffractors, they cannot be distinguished from purely kinematic analyses. However, amplitude computations support the hypothesis of curved reflectors as also the results obtained by us from synthetic seismograms modelling of the PDP phase as a subcrustal reflector steeply dipping towards the west on the MOBIL LINE 1. Based on a recent analysis of the common reflection signature within the mantle in the North Sea area on surveys SHET, MOBIL and NSDP, Matthews et al. (1990) found that on the western margin of the North Sea reflectors within the mantle consistently dip towards the west and the southwest. Our inference of the west dipping subcrustal reflector on the MOBIL 1 profile is also quite consistent with their findings. We observe that the reflectivity pattern in the area of present study is controlled by the Caledonian structures.

ACKNOWLEDGEMENTS

We are grateful to the Director, National Geophysical Research Institute, for providing necessary facilities to undertake this study and permission to publish the results. We are also grateful to the organizers of this workshop, especially to Ernst R. Flueh, for providing the necessary datasets for this study and a preprint of Blundell et al., on the MOBIL survey. We thank Messers G.S.P. Rao, G.B.K. Shankar and G.Khandekar of NGRI for their help in computations and Mr. M.Shankaraiah, also of NGRI, for neat drafting of the figures.

REFERENCES

Blundell, D.J., Hobbs, R.W., Klemperer, S.L., Scott-Robinson, R., Long, R.E., West, T.E., and Duin, E. 1991: Crustal structure of the central and southern North Sea from BIRPS deep seismic reflection profiling; J.Geol.Soc.Lond., 148, 445-457.

Bott, M.H.P., Long, R.E., Green, A.S.P., Lewis, A.H.J., Sinha, M.C., and Stevenson, D.L. 1985: Crustal structure south of the Iapetus suture beneath northern England; Nature, 314, 724-727.

Cerveny, V. and Psencik, I. 1981: 2-D seismic ray package; Charles University, Prague.

Freeman, B., Klemperer, S.L., and Hobbs, R.W. 1988: The deep structure of northern England and the Iapetus Suture zone from BIRPS deep seismic reflection profiles; J.Geol.Soc.Lond., 145, 727-740.

Kampfmann, W. 1988: A study of diffraction-like events on DEKORP 2-S by Kirchhoff theory; J.Geophys., 62, 163-174.

Klemperer, S.L. and Matthews, D.H. 1987: Iapetus suture located beneath the North Sea by BIRPS deep seismic reflection profiling; Geology, 15, 195-198.

Matthews, D.H. and THE BIRPS GROUP (Flack, C.A., Hobbs, R.W., Klemperer, S.L., Snyder, D.B., Warner, M.R., and White, N.J.) 1990: Progress in BIRPS deep seismic reflection profiling around the British Isles; Tectonophysics, 173,387-396.

INTERPRETATION OF THE MOBIL LINE 1: WIDE-ANGLE DATASET RECORDED ON LAND FROM MARINE AIRGUN SHOTS

Tracey E. West and Roger E. Long

Department of Geological Sciences,
University of Durham, Science Labs, South Road, Durham DH1 3LE, U.K.

Abstract

The MOBIL wide-angle and normal-incidence seismic dataset was recorded in June 1987, when BIRPS carried out deep normal-incidence profiling off the East coast of England and the University of Durham recorded wide-angle data simultaneously at land-based seismic stations. The resulting wide-angle dataset has excellent resolution in both space and time, revealing unexpected complexity in arrivals. Modelling the principal arrivals indicates a crust about 30 km thick with a change in velocity gradient at 20 km depth and a high velocity of 7 km/s in the bottom 2 km of the crust. There are several wide-angle reflections from mid-crustal depths (between 10 and 20 km depth), but these are not laterally continuous. The most interesting results are that the the upper crustal arrival (Pg) requires a lateral change in velocity at about 40 km offshore to fit the travel times; also that the travel times of a high amplitude arrival ("D") fit those of a diffraction from Moho depths and the cause of this phase seems to be best modelled as a step on the Moho. Collectively these results suggest the presence of a major crustal fault about 40 km offshore. This appears to be borne out by the coincident normal-incidence data section for line 1 and it is suggested that the Dowsing fault, which is recognized as a major structural feature further to the south, continues northward to intersect line 1.

Introduction

Until recently, the spatial resolution of wide-angle seismic surveys has been poor compared to that of normal-incidence surveys on the same scale, in spite of the fact that wide-angle reflection data is a more accurate method of determining the seismic velocity structure. However, during the 1980s, coincident wide angle and normal incidence datasets have become increasingly common (Mooney and Brocher, 1987), often obtaining wide-angle data of almost equal spatial resolution to normal-incidence by using the same source, usually piggy-backing the near-vertical exploration work.

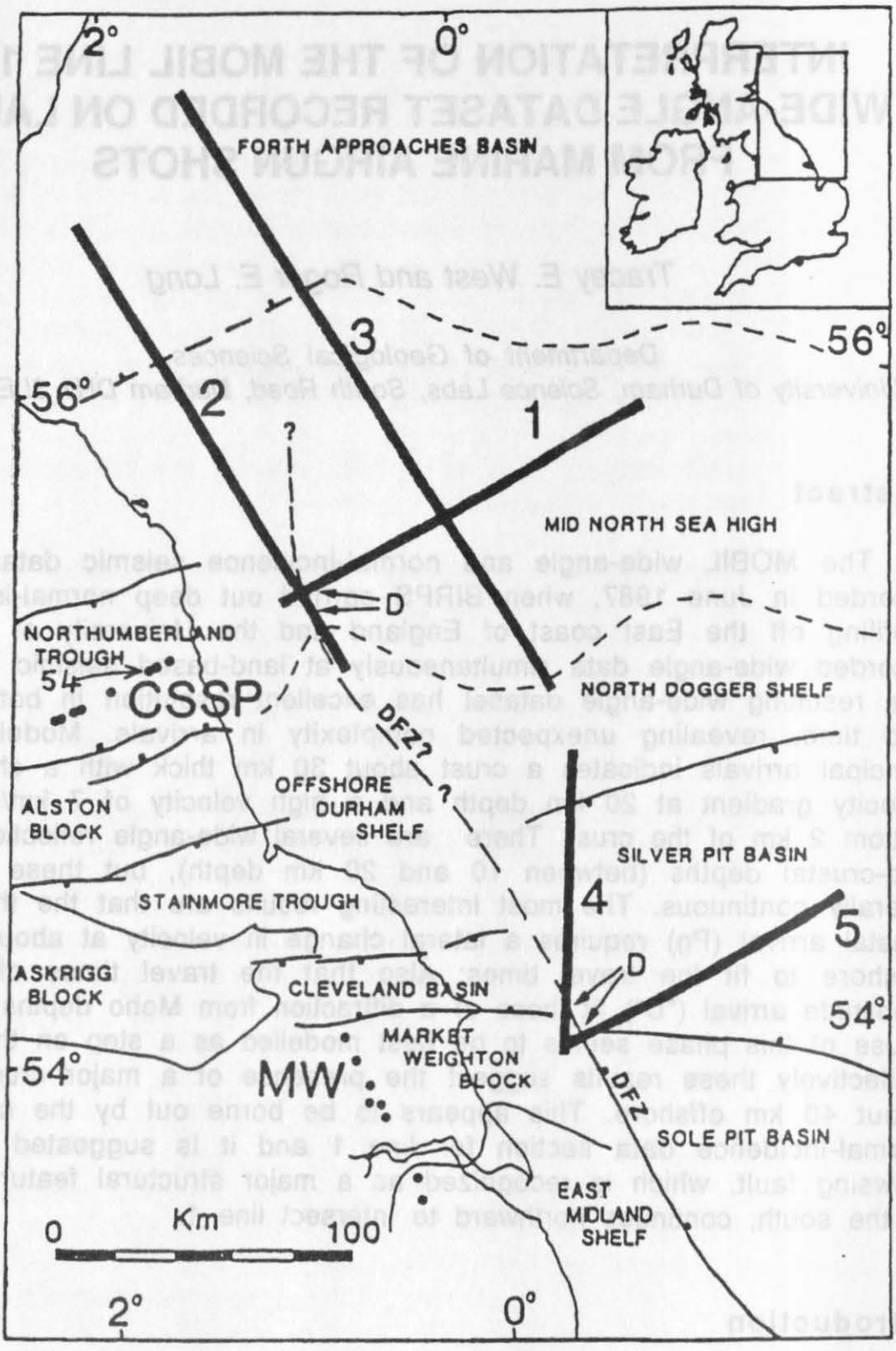

Figure 1: Major geological features of North-East England and the adjacent North Sea region, showing the BIRPS MOBIL normal-incidence seismic profiles (thick black lines) and Durham's WAR recording stations (black dots). DFZ: the Dowsing Fault Zone (the northern extension which cuts lines 1 and 2 is suggested by the MOBIL data). CSSP: Caledonian Suture Seismic Project (Bott et al. 1985) recording stations (across Northumberland) re-occupied during the MOBIL programme. MW: Seismic network located across the Market Weighton gravity anomaly.

The MOBIL dataset, Dataset II of the CCSS workshop, is an example of this kind of experiment. It represents the first successful attempt to record at wide angle on land the shots used in BIRPS normal incidence profiles.

The MOBIL deep crustal normal-incidence profiles were shot off the east coast of Britain and their locations are shown in Figure 1. Lines 1 to 5 were recorded at wide-angle by onshore seismometer arrays operated by the University of Durham. Since line 1 was located along the line of a previous wide-angle seismic experiment, CSSP (Bott et al. 1985), 8 of the CSSP recording sites were re-occupied across Northumberland during the MOBIL survey. Lines 4 and 5 were recorded at wide-angle by a new 80 km linear network, MW, located further south. Dataset II includes the line 1 wide-angle data recorded at two of the Northumberland stations, Stations 54 and 47, and the final stack section of the normal-incidence data from line 1.

Figure 1 also shows the regional geological structure. This reflects the ENE-WSW grain of the early Paleozoic Caledonian orogeny, which determined the pattern of later crustal development of Northern England. The geology is therefore dominated by roughly E-W trending sedimentary basins and structural highs. MOBIL line 1 can be seen to run along the axis of the Northumberland Trough onto the Mid-North Sea High. The onshore basins are known to date from the Carboniferous and the Mid-North Sea high from the Late Palaeozoic (Donato et al.,1983).

The wide-angle seismic data

The complexity of the wide-angle arrivals can be seen in the extract from line 1 sections shown in Figure 2 (from Station 54). Multiples from the water layer and from the relatively strong reflectors in the upper crust add to this complexity. The amplitude of any one arrival can be seen to vary along the section, changing from bright to almost absent within a distance range of only a few tens of kilometers. This makes correlation of arrivals along the record difficult and to some extent subjective. Nevertheless the classical arrivals Pg (the upper crustal diving ray), PcP (from the mid crust), PmP (the Moho reflection or lower crustal diving ray) and Pn (diving ray below the Moho) can all be identified (Figure 3).

At distances of between 100 and 160 km (Figure 3) a triplication can be seen involving PcP, PmP and Pn. This feature is well defined and Pn, which is not normally very obvious as a secondary arrival, is clearly seen here as it interferes with the slower arrivals. Pg does not appear as a continuous arrival over distance, but may be split into a set of arrivals, each occurring over a limited distance range. The amplitude, however, is sufficiently variable to make a formal separation into several separate arrivals questionable. Thus this interpretation assumes a single continuous Pg phase.

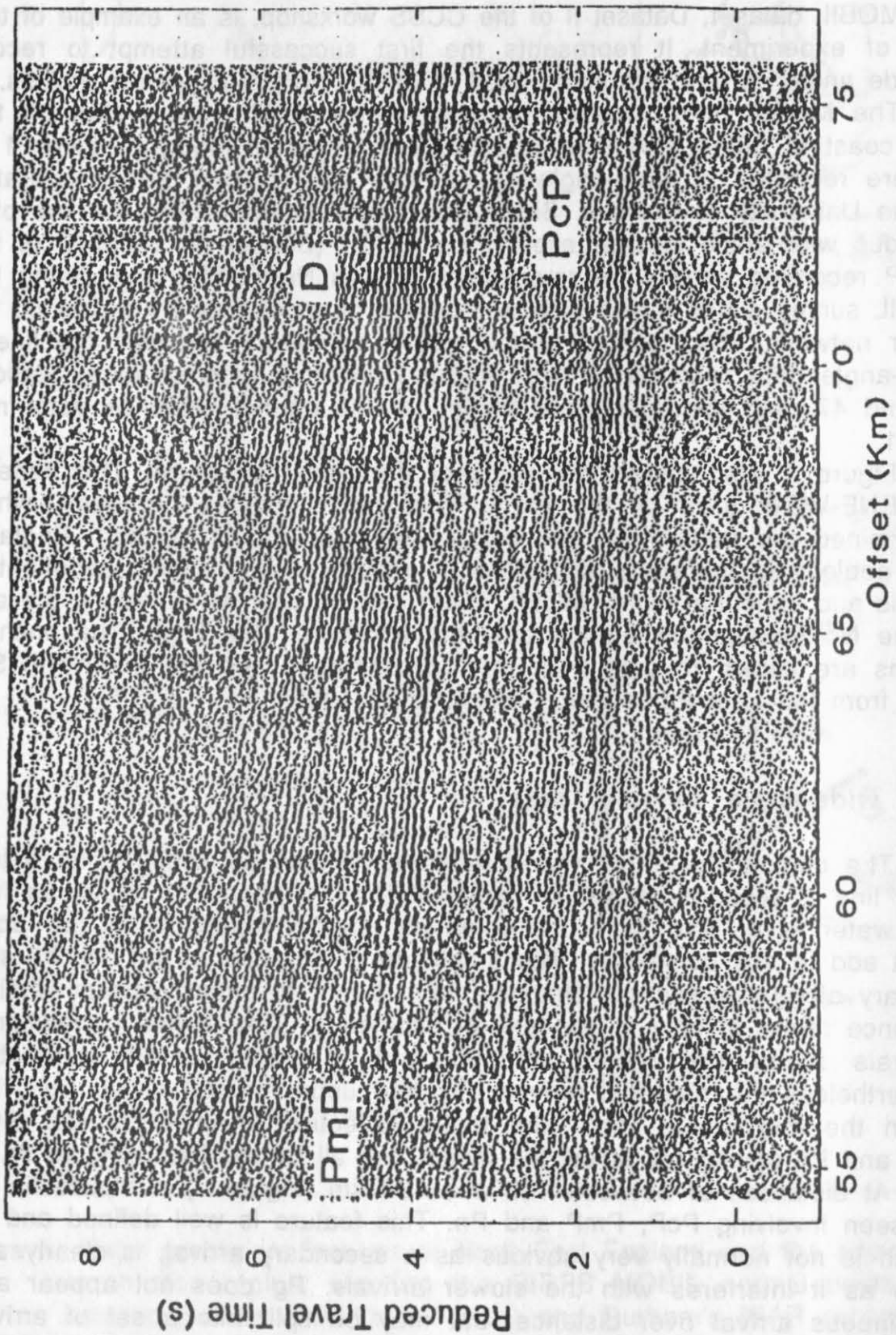

Figure 2: Part of the common station record section of wide-angle seismic data recorded from line 1 at station 54. For key to arrivals, see caption for Figure 3. Note the high amplitude and high apparent velocity of D.

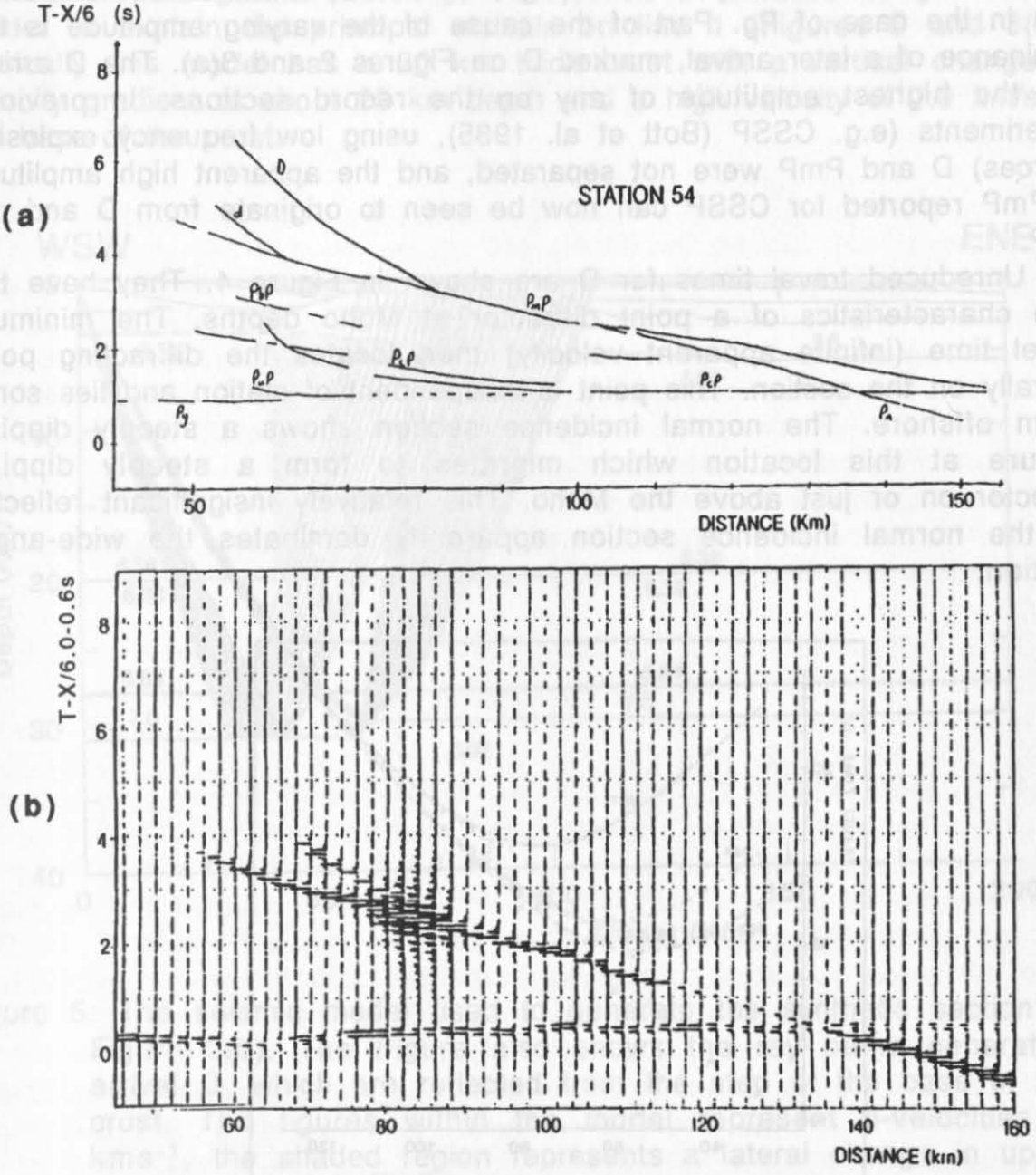

Figure 3(a): Line drawing of Line 1 recorded at station 54 showing the diffraction-type arrivals from the base of the crust, D and d. Pg: upper crustal diving ray; PcP: wide-angle reflection from the mid-crust; PmP: wide-angle reflection from the Mohorovicic discontinuity. PuP and PbP are probably arrivals from the upper and lower crust respectively, and are not modelled here. (b) Synthetic record section generated for line 1 from the model of Figure 5.

The PmP phase is of major interest from the triplication back to shorter distances. Again this appears discontinuous with clear time steps along the record section (Figure 3(a)) and variable amplitude, although at each time step the amplitude is high, so that the truncation is clearer than in the case of Pg. Part of the cause of the varying amplitude is the dominance of a later arrival, marked D on Figures 2 and 3(a). The D arrival has the highest amplitude of any on the record sections. In previous experiments (e.g. CSSP (Bott et al. 1985), using low frequency explosive sources) D and PmP were not separated, and the apparent high amplitude of PmP reported for CSSP can now be seen to originate from D and not PmP.

Unreduced travel times for D are shown in Figure 4. They have the time characteristics of a point diffractor at Moho depths. The minimum travel time (infinite apparent velocity) then locates the diffracting point laterally on the section. This point is independent of station and lies some 40km offshore. The normal incidence section shows a steeply dipping feature at this location which migrates to form a steeply dipping reflector on or just above the Moho. This relatively insignificant reflector on the normal incidence section apparently dominates the wide-angle section.

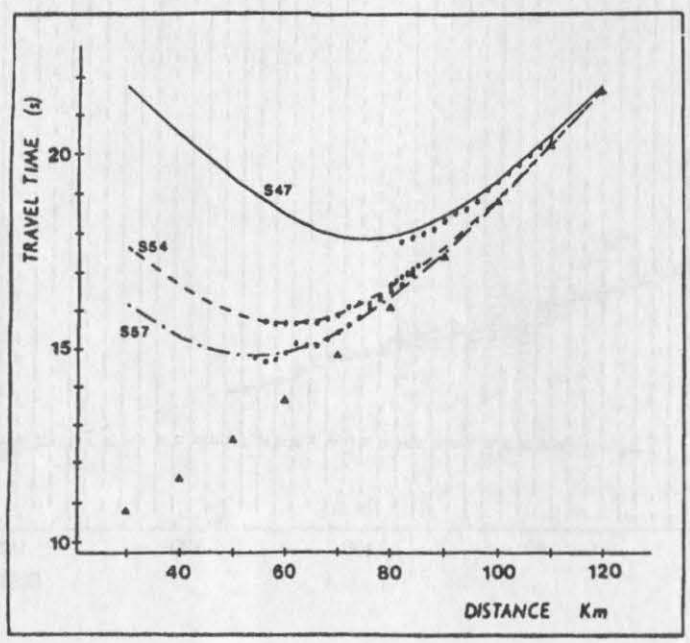

Figure 4: A comparison of the observed travel times of D (dots) with those calculated for a point diffractor at the base of a 30 km thick homogeneous layer (lines). Triangles are the computed times for reflections from the base of the layer; the three dashed lines are for three stations of the CSSP group. The relative offsets of the three minima correspond to the station separation. The minima occur at the same shot point independent of station location, indicating that each station is recording the same diffracting point.

Model

BEAM87, a package which uses the Gaussian beam method to compute synthetic seismograms (Cerveny, 1985), has been used to generate a model to explain the principal arrivals on line 1 (Figures 5 and 3(b)). Basically this model has a 30 km thick crust with a vertical change in velocity gradient at about 20 km depth and a high velocity of 7.0 km/s at the base of the crust.

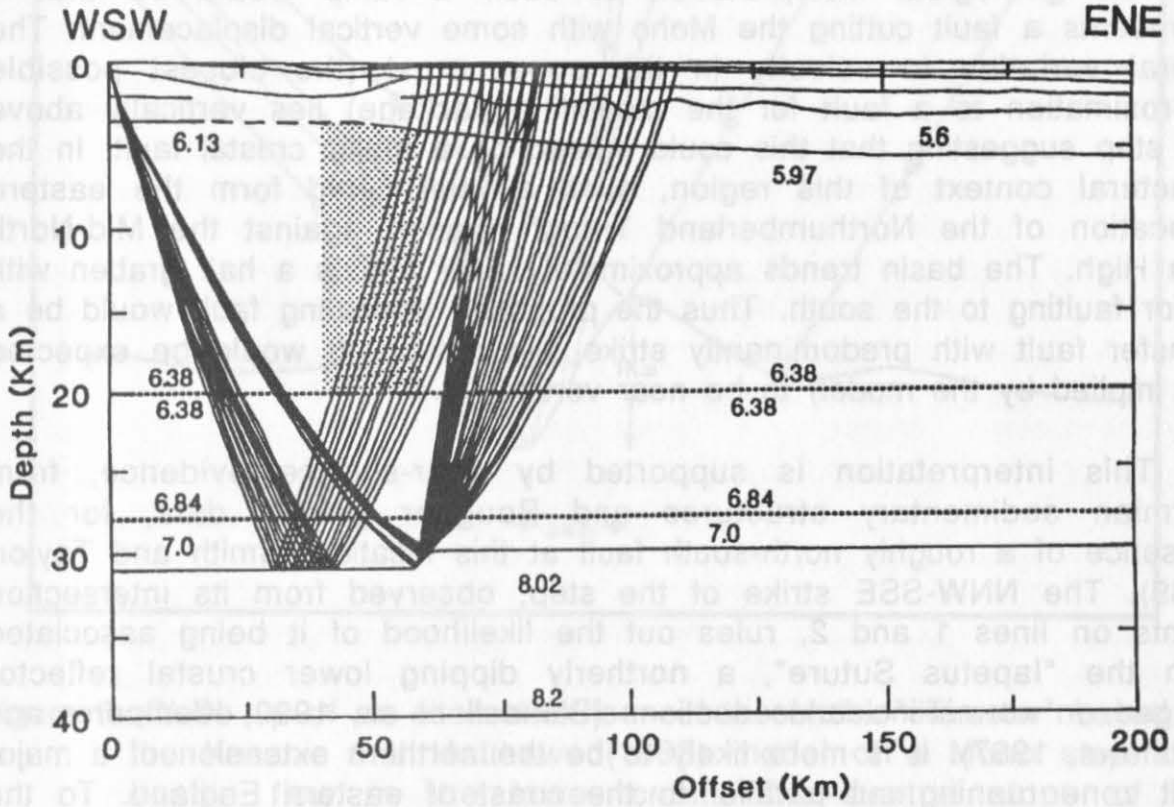

Figure 5: The seismic model used to generate the synthetic section of Figure 3(b). The Figure also shows the ray paths generating arrival D, which are reflected from the step at the base of the crust. The figures within the model represent p-velocities in kms^{-1}, the shaded region represents a lateral change in upper crustal velocity gradient (the nearest possible approximation to a vertical fault) and the dotted lines represent changes in seismic velocity gradient.

Even after allowing for the variation in structure of the top few kilometers of the crust, Pg could not be fitted by a laterally uniform upper crust. The best fit was obtained with a lateral velocity change about 40 km offshore (West, 1990); this lateral change lies approximately above the estimated location of the source of arrival D. The high velocity at the base of the crust is required across the whole model if PmP is to be adequately fitted.

Both the amplitude and travel time of D have been fitted best by modelling the effective "diffractor" as a ramp feature on the Moho. Reflections from the curvature of the ramp give similar travel times to a point diffractor but yield a higher amplitude, closer to that of the observed arrival.

Discussion

The geological interpretation of such a ramp would be that it represents a fault cutting the Moho with some vertical displacement. The lateral variation in velocity in the upper crust (the closest possible approximation to a fault for the modelling package) lies vertically above the step suggesting that this could indeed be a major crustal fault. In the structural context of this region, such a fault could form the eastern truncation of the Northumberland Trough (basin) against the Mid-North Sea High. The basin trends approximately E-W and is a half graben with major faulting to the south. Thus the proposed truncating fault would be a transfer fault with predominantly strike slip motion. It would be expected (as implied by the model) to be near vertical.

This interpretation is supported by near-surface evidence, from Permian sedimentary structures and Bouguer gravity data, for the presence of a roughly north-south fault at this location (Smith and Taylor, 1989). The NNW-SSE strike of the step, observed from its intersection points on lines 1 and 2, rules out the likelihood of it being associated with the "Iapetus Suture", a northerly dipping lower crustal reflector imaged on normal-incidence sections (Blundell et al., 1990, Klemperer and Matthews, 1987). It is more likely to be the northern extension of a major fault zone running sub-parallel to the coast of eastern England. To the south this zone is known as the Dowsing fault zone (Figure 1) which has been associated with extension and inversion of the basins in the south western North Sea. It has never been clear how this zone continues north of the Sole Pit basin, but it is geologically plausible, both structurally and temporally, that it extends north as the truncating fault proposed here (Figure 1).

The last major activation of the Dowsing Fault took place during the second period of inversion of the Sole Pit Basin in the Mid-Tertiary (Van Hoorn, 1987). Since that time, any displacement at the Moho might be expected to have been smoothed out by ductile flow. However, Kusznir and Matthews (1988) have shown that the decay of Moho topography is wavelength dependent, and results in the obliteration of intermediate wavelengths only. The Moho step shown in Figure 6 is based on the theoretical long-term residue (according to Kusznir and Matthews) of a square step. This alternative form of the step provides the curvature necessary to give the high amplitude of D and also fits the observed wide-

angle travel times. It does not require a shallower Moho east of the fault and is therefore more consistent with the Moho reflection observed at normal-incidence.

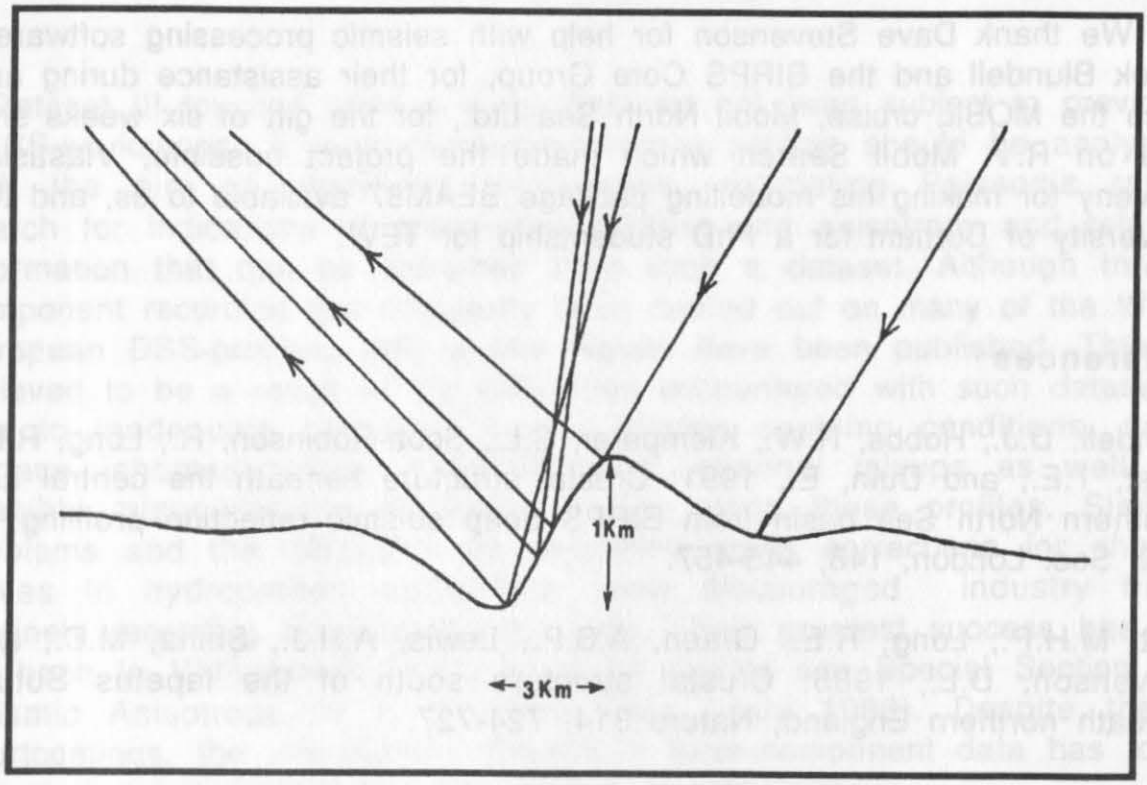

Figure 6: Close up of an alternative form of the Moho "diffractor" based on the Kusznir and Matthews (1988) model of a Moho step after ductile flow in the lower crust. The central slope of the structure reflects rays to generate arrival D.

Concluding remarks

The models of Figures 5 and 6 explain only the major arrivals of the record sections. They ignore the time steps in Pg and PmP, ascribing them to amplitude variation and the interference with D respectively. However these features contain further information on the detail of the boundaries which is worthy of investigation, in addition to the very significant amplitude variations (which do not appear to be shot-dependent).

The arrival D is not the only arrival of its type, but it is the only one modelled. A second arrival with very similar characteristics (d in Figure 3(a)) occurs at shorter distances, implying that the fault zone may be complex and not a single fault, as would be expected of such a major fault. In normal-incidence seismology, it is recognized that the high amplitude of diffractions in normal incidence sections may be caused by

the curvature of layers affected by fault drag. In the models presented here, the "diffraction-type arrivals" such as D have a similar origin.

Acknowledgements

We thank Dave Stevenson for help with seismic processing software, Derek Blundell and the BIRPS Core Group, for their assistance during and since the MOBIL cruise, Mobil North Sea Ltd., for the gift of six weeks ship time on R.V. Mobil Search which made the project possible, Vlastislav Cerveny for making his modelling package BEAM87 available to us, and the University of Durham for a PhD studentship for TEW.

References

Blundell, D.J., Hobbs, R.W., Klemperer, S.L., Scott-Robinson, R., Long, R.E., West, T.E., and Duin, E., 1991: Crustal structure beneath the central and Southern North Sea basin from BIRPS deep seismic reflection profiling; J. geol. Soc. London, 148, 445-457.

Bott, M.H.P., Long, R.E., Green, A.S.P., Lewis, A.H.J., Sinha, M.C., and Stevenson, D.L., 1985: Crustal structure south of the Iapetus Suture beneath northern England; Nature 314, 724-727.

Klemperer, S.L. and Matthews, D.H., 1987: Iapetus Suture located beneath the North Sea by BIRPS deep seismic reflection profiling; Geology 15, 195-198.

Kusznir, N.J. and Matthews, D.H., 1988: Deep seismic reflections and the deformational mechanics of the continental lithosphere; J.Petrology, Special Lithosphere Issue, p. 63-87.

Mooney, W.D. and Brocher, T.M., 1987: Coincident seismic reflection/ refraction studies of the continental lithosphere: a global review; Reviews of Geophysics 25, 723-742.

Smith, D.B. and Taylor, J.C.M., 1989: A North-west passage to the Southern Zechstein basin of the UK North Sea; Proc. Yorks. Geol. Soc. 47, 313-320.

Van Hoorn, B., 1987: Structural evolution, timing and tectonic style of the Sole Pit inversion; In: P.A. Ziegler (Ed.): Compressional Intra-Plate Deformations in the Alpine Foreland; Tectonophysics 137, 239-284.

West, T.E., 1990: A high-resolution, wide-angle seismic study of the crust beneath the Northumberland Trough; Unpublished Ph.D thesis, University of Durham, 123pp.

INTRODUCTION TO DATASET III

Ernst R. Flueh

GEOMAR, Kiel, Germany

Dataset III touches upon a topic that had not been subject to previous CCSS-workshops. A three-component record section should be analyzed with the aim of identifying wave-types, estimating Poisson's ratio, search for indications of shear-wave-splitting and anisotropy and related information that can be extracted from such a dataset. Although three-component recording has frequently been carried out on many of the West European DSS-profiles, only a few results have been published. This is believed to be a result of the difficulties encountered with such datasets, due to inadequate sampling, locally varying coupling conditions, near surface inhomogeneities, miscalibrations, channel mixups as well as possible misorientations of seismometers along these profiles. Similar problems and the difficulties to determine static corrections for shear-waves in hydrocarbon exploration have discouraged industry from routinely recording three-component data. Their greatest success has so far been in VSP-studies (for a thorough review see Special Section on Seismic Anisotropy in J. Geophys. Res., July 1990). Despite these shortcomings, the information inherent in three-component data has long attracted seismologists and exploration geophysicists.

The dataset used for the workshop was an onshore/offshore walkaway profile collected on the continental margin of East Greenland by the GRÖKORT (Grönland-Kolbeinsey Rücken Traverse) Study-Group in summer 1988 (Weigel et al., in prep.). The field work was a joint effort by Hamburg and Kiel Universities` geophysical institutes and the Alfred Wegener Institute for Polar and Marine Research, Bremerhaven. It was supported by the Alfred Wegener Institute and the Deutsche Forschungsgemeinschaft through grant We 690/26.

The data were recorded by a carefully oriented seismometer string comprising six 4.5 Hz three-component seismometers installed on land near Kap Biot. The seismometers were separated by 2 m each and oriented in the field by compass to magnetic north (see Figure 1). The eight channel recording system (MARS 88) enabled the recording of five additional vertical components, which were however not considered for the workshop. The seismic source was a 32 ltr. Bolt airgun, fired at intervals between 150 and 300 m. The way this dataset was collected avoided some of the problems mentioned above. Static and near surface conditions are identical for all records, since the receiver was not changed during the recording period. All shots were fired in water, thus a pure and rather

C C S S dataset 3
L O C A T I O N M A P

3 component recording observation from East Greenland/ Kap Biot

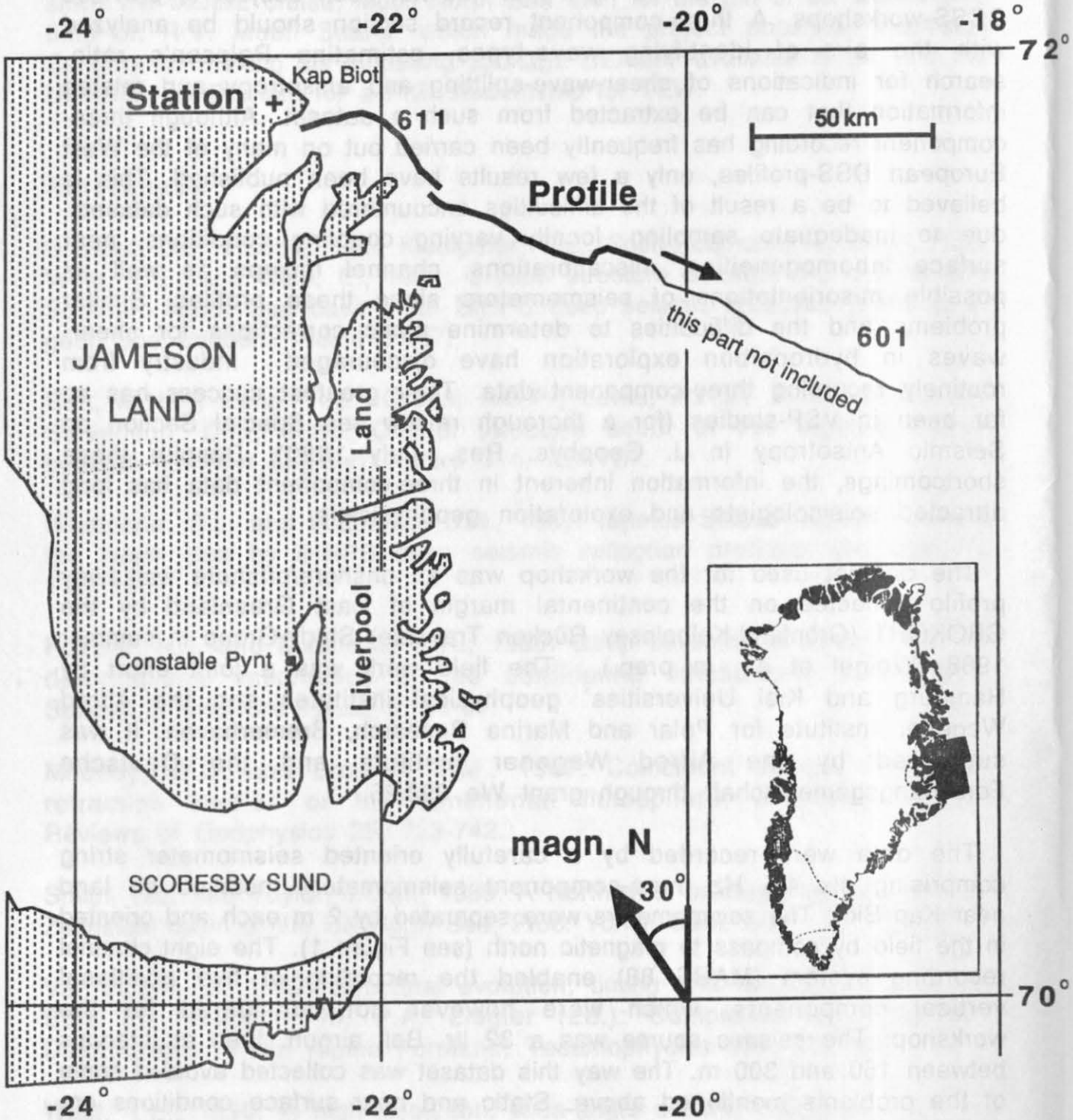

Figure: 1

stable P-wave signal is emitted throughout the section. Water depth, and thus shot statics is rather constant along the parts of the line considered here (~200 ± 20 m).

The package distributed for this dataset contained:

(1) A description of the data and the aim of this exercise, together with a location map of the profile (Figure 1);

(2) Paper copies of the record sections (one for each component) from 10 to 90 km offset, displayed in a reduced time scale (t=t-x/8) and the data stacked into 200 m wide bins (Figures 2-4);

(3) A preliminary P-wave crustal model (Figure 5), and obtained from this and neighboring observations (for details see following contribution by Zhao et al.), and

(4) A SEGY-tape (6250 bpi) of the 454 shots, each record 45 s long, with 5 ms sampling interval, sorted by offset and component.

Clear P-, and S- and converted phases are seen on the record sections and the contributors were asked to identify the phases and investigate Poission's ratio and other topics as mentioned above. Following an introduction to the dataset by E. Flueh (Kiel), with special emphasis on technical aspects of the field operation and the preliminary P-wave model, six contributions were made to this dataset during the workshop. Five of them are presented in this volume.

Most of the interpretations presented and the discussions during the workshop concentrated on a prominent phase between 30 and 60 km offset. In general agreement this phase was interpreted as a P_MS-phase. P-to-S converted Moho reflections are generally not very common, but have also been recognized on other profiles (e.g. Holbrook et al., 1988). However, another striking observation is the fact that this phase has a predominantly transverse motion. Therefore, anisotropy has to be taken into account. Possible models and attempts to quantify the anisotropy are given in the contributions by Minshull and Spencer et al. But the data distributed for the workshop do not allow to uniquely quantify an anisotropic velocity field, because possible 3D-effects cannot be excluded and are unknown. Additional profiles in different azimuths are required to narrow the possible range of models.

In the discussions during the workshop it was felt that three-component data provide valuable information, but require thoughtful planning and proper acquisition parameters to minimize possible ambiguities during the interpretation.

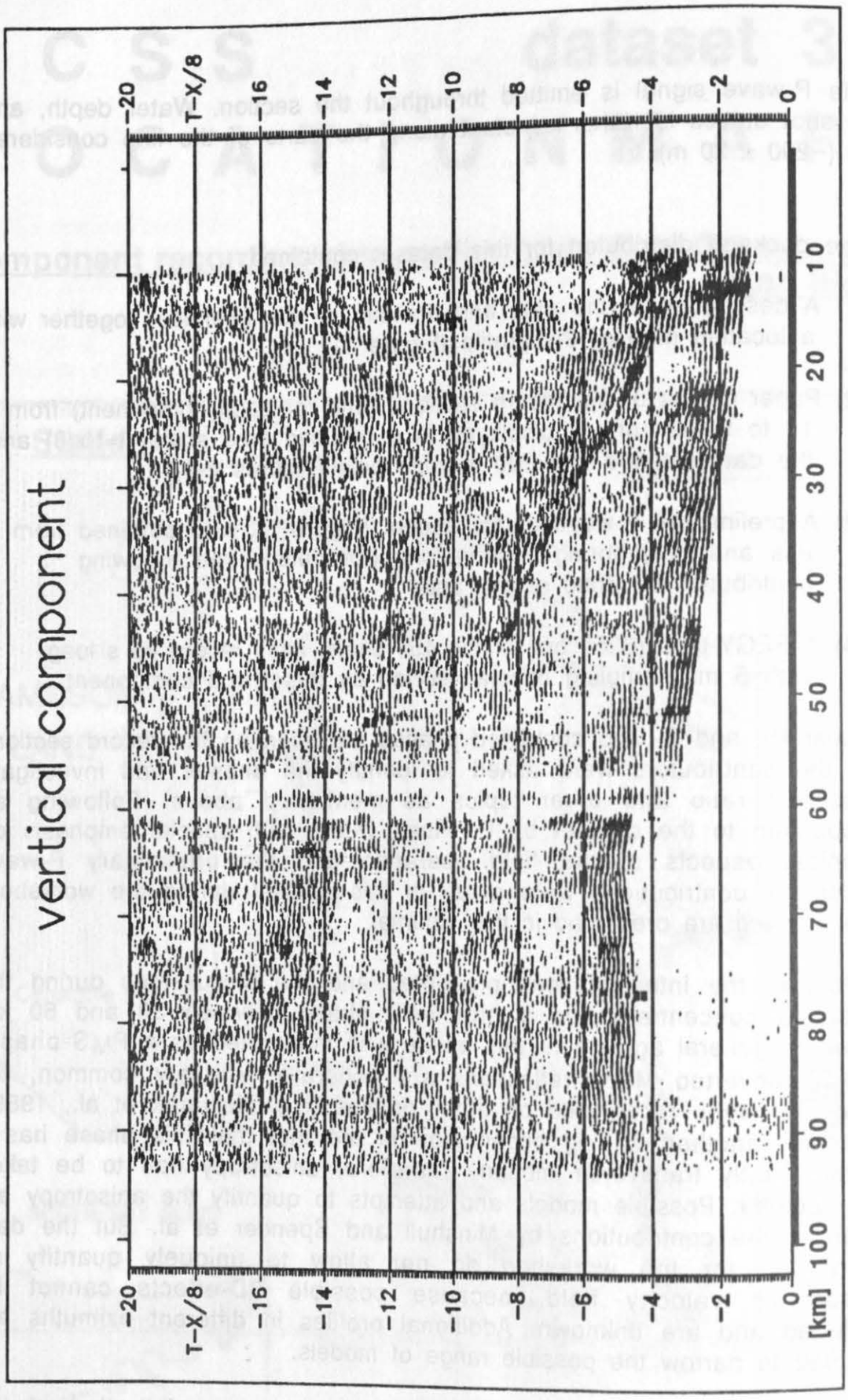

Figure 2: Record section from Kap Biot, 10-90 km offset, filtered 4-25 Hz, stacked into 200 m wide bins, reduced with 8 km/s. Vertical component.

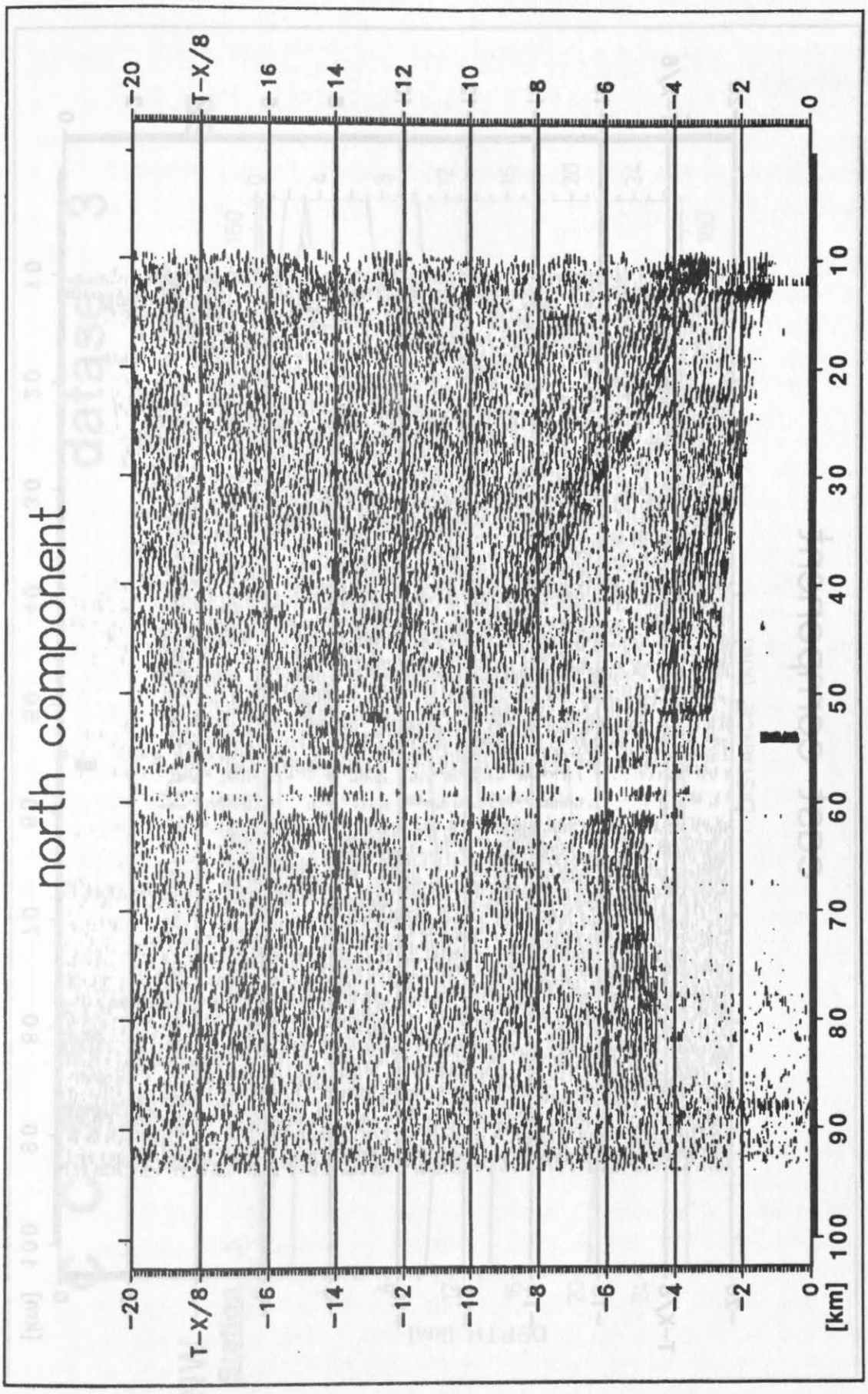

Figure 3: As figure 2, North component.

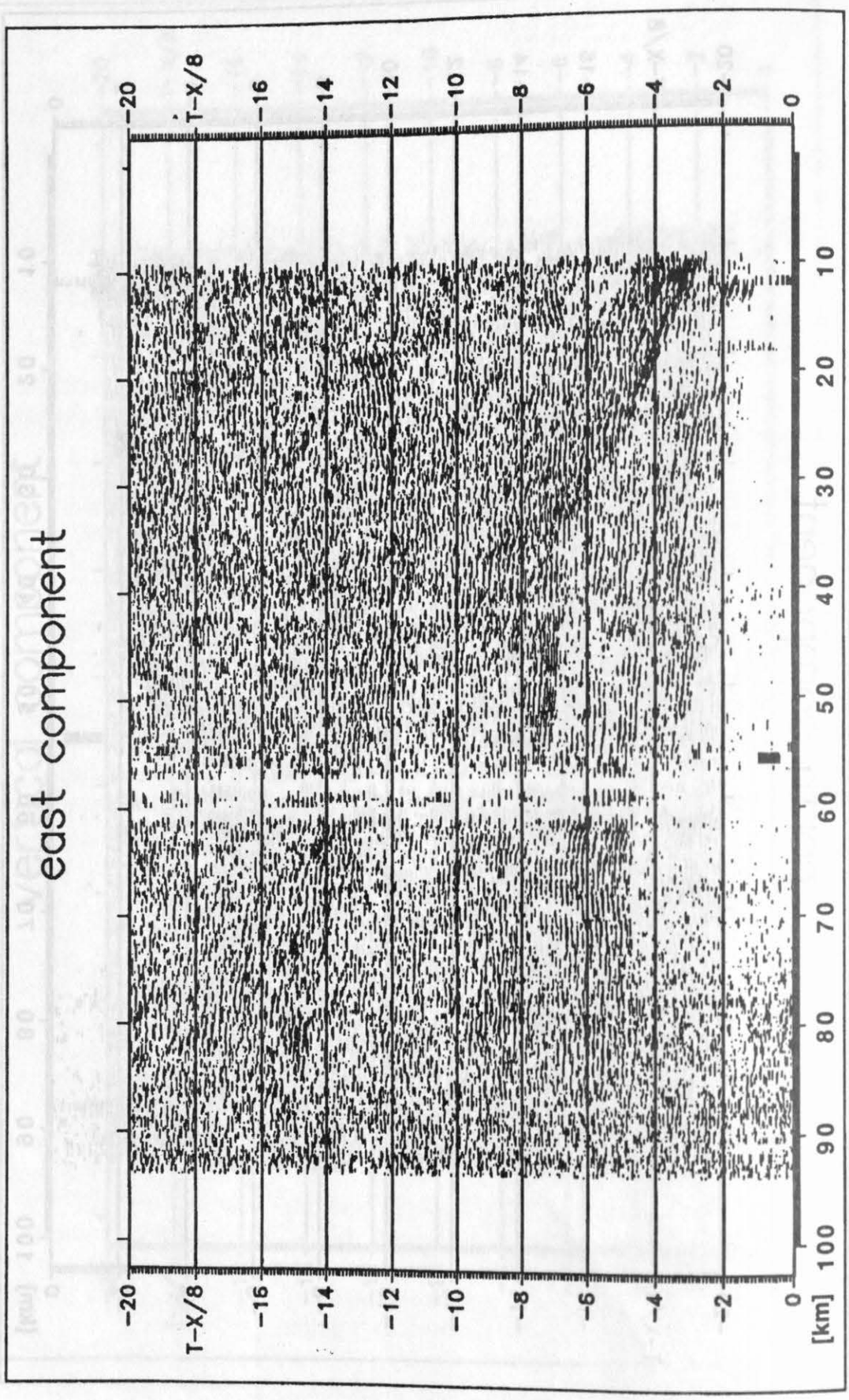

Figure 4: As figure 2, East component.

Figure 5: Preliminary P-wave model for the whole profile, vertical exaggeration 2.5 : 1, from Zhao et al. (this volume).

References

Weigel, W., Miller, H., Flueh, E.R. and the GRÖKORT Study Group: Seismic investigation of the East Greenland continental margin between 70° and 72° N; in preparation.

Holbrook, W.S., Gajewski, D., Krammer, A. and Prodehl, C., 1988: An interpretation of wide-angle compressional and shear wave data in southwest Germany: Poission's ratio and petrological implications; J. Geophys. Res., 93, 12081-12106.

SEISMIC REFRACTION INVESTIGATIONS ACROSS THE EAST GREENLAND MARGIN AT 72°N

Zhu Zhao[1], Ernst R. Flueh[2], Wilfried Jokat[3], and Dirk Klaeschen[2]

[1] *Sichuan Seismological Bureau, Chengdu, Sichuan, People's Republic of China*

[2] *GEOMAR, Kiel, Germany*

[3] *Alfred Wegener Institute for Polar and Marine Research, Bremerhaven, Germany*

Abstract

The P-wave velocity structure along a profile from the mouth of Kong Oscar Fjord across the East Greenland Shelf is investigated using closely spaced airgun shots. The shots were fired at 150 to 300 m intervals along a 150 km long profile and recorded at two land stations and one ocean-bottom-seismometer. On the land stations clear signals are received from the entire profile up to the maximum offset at 165 km. On the OBS the energy of seismic signals is lost in the ambient noise beyond 60 km offset. From clear refracted and reflected arrivals the crust can be divided into four distinct layers. A crustal thinning from 24 km at the coast to 12 km at the foot of the shelf is found. The East Greenland Escarpment is a crustal penetrating fault. In the Inner Liverpool Land basin up to six kilometers of sediments are found. Although due to the limited amount of data available the proposed model is non-unique, it is clear that crustal thinning from the continental realm of East Greenland to the oceanic domain occurs over an at least 100 km wide zone.

Introduction

The East Greenland continental margin is known to have a rather complex tectonic history. Following the closure of the Iapetus Ocean and the Caledonian Orogeny the first rifting and subsequent spreading of the North Atlantic along the Aegir Ridge started at about anomaly 25/24R time (55 ma). As summarized by Larsen (1988), a second rifting phase and subsequent spreading followed at anomaly 6 time along the presently active Kolbeinsey Ridge. During this event the Jan Mayen Ridge was broken off the East Greenland Shelf, and is now found as an isolated continental fragment in the northern Atlantic. Thus, in the region between the Jan Mayen Fracture Zone in the north and the Greenland-Iceland Ridge (or Denmark Strait Ridge) in the south, a rather unique situation is found with respect to the age distribution of the tectonic units. Along an only 400 km long east-west oriented traverse, the Archaean basement of Greenland,

the Caledonian realm of the East Greenland margin, the Miocene continental margin and oceanic crust and the currently active spreading center of the Kolbeinsey Ridge are found in close contact.

In order to better understand the evolution and the tectonic processes involved, a program to investigate the crustal structure was carried out in August 1988. In the so called GROEKORT (Groenland-Kolbeinsey Ridge Traverse) project, several refraction profiles were recorded using both ocean-bottom-seismometers and land stations (Weigel et al., in prep.). A large volume airgun (32 ltr.) was used aboard the icebreaking RV Polarstern as a seismic source, and seismic energy was recorded to maximum offsets of 165 km, thus allowing the investigation of the crust and upper mantle structure. In this paper the data and an interpretation of the P-waves of one of the lines is presented. The profile under investigation starts at the mouth of Kong Oscar Fjord and extends for 165 km in a southeast direction across the shelf. The crustal model and a subset of the data was the subject of dataset III for the Commission on Controlled Source Seismology's (CCSS) workshop held at Fellhorst, Germany, from 27-31 August 1990. The main purpose of this contribution is to provide geological background on the region and explain the crustal model, which was included in the workshop material for dataset III.

Field work

The data were collected during two consecutive nights in August 1988. To avoid interference with nearby land-based exploration work, shooting was only permissible during night hours. The profile is therefore split into two segments, lines 601 and 611 (see Figure 1). The seismic source was a 32 ltr. Bolt airgun, fired at 120 s intervals along line 601 and 60 s along line 611. As the ships speed was 5 knots, the resulting shot spacing was about 300 m for line 601 and about 150 m for line 611. Due to its great weight, the airgun was very suitable for the work in ice covered waters. It was fired at a constant depth of 10 m with a pressure of 2000 psi. At two land stations (L7 on Wegener Halvø and L8 on Kap Biot) and one ocean-bottom-seismometer (OBS 26, see Figure 1) the signals were recorded. A second OBS, located at the end of line 601, was lost due to heavy ice conditions at the scheduled time of recovery. In addition a short (100 m) 24 channel streamer was towed behind the ship and recorded the vertical incidence data. Due to the short streamer length, only a single fold coverage could be obtained, and except for the shelf slope, the records obtained are dominated by multiples and reverberations (see Figure 5). At each of the land stations several recording instruments were operated, using different seismometer types. In this analysis only a small subset of the recordings are considered. From station L7 a single 2 Hz vertical geophone was chosen, while from station L8 an array of six geophone strings with six 4.5 Hz seismometers each was analyzed

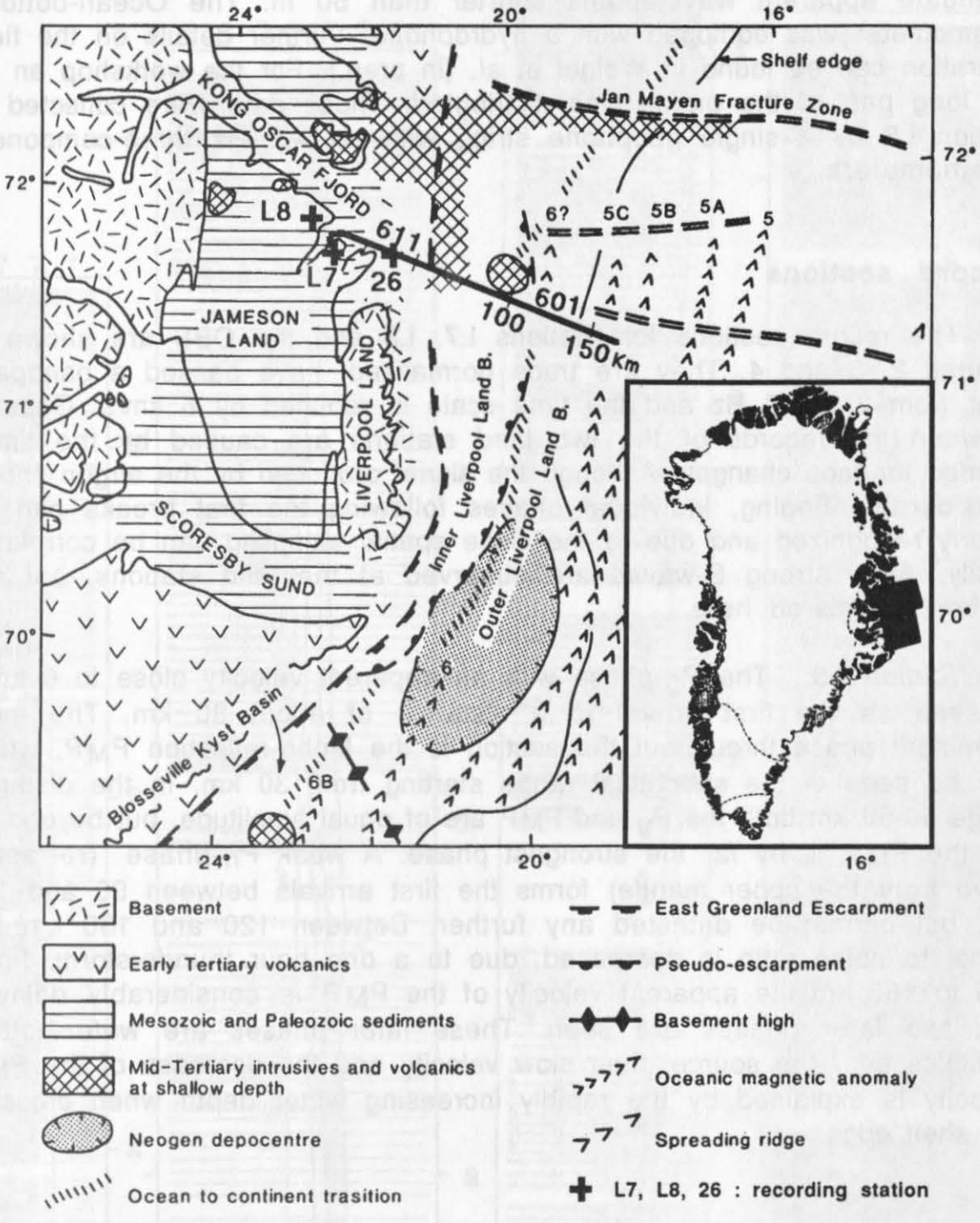

Figure 1: Location map of stations (L7, L8 and OBS 26) and profiles. The thick line marks the position of the airgun shots, with distance labels 100 and 150 km (relative to station L8) added. Modified after Larsen (1990).

(thus signals from 36 seismometers stacked before recording). They were distributed in an areal pattern with a diameter of 50 m, designed to attenuate apparent wavelengths shorter than 50 m. The Ocean-bottom-seismometer was equipped with a hydrophone. Further details on the field operation can be found in Weigel et al. (in prep.). For the workshop an 80 km long part of the profile was distributed. Those data were collected at station L8 by a single geophone string with six 4.5 Hz three-component seismometers.

Record sections

The record sections for Stations L7, L8 and the OBS are shown in Figures 2, 3 and 4. They are trace normalized, have passed a bandpass filter from 2 to 30 Hz and the time scale is reduced by 6 km/s. Gaps in between the records of the two land stations are caused by the times needed for tape changes. Although the signal produced by the airgun shows considerable ringing, individual phases following the first breaks can be clearly recognized and due to the close spatial sampling can be correlated easily. Also, strong S-waves are observed at the land stations, but not further considered here.

Station L8: The P_g-phase with an apparent velocity close to 6 km/s is seen as the first arrival to a distance of about 80 km. The most prominent phase throughout the section is the Moho-reflection P_MP, which can be seen in the subcritical range starting from 30 km. In the distance range 50-60 km both the P_g and P_MP are of equal amplitude, but beyond 60 km the P_MP is by far the strongest phase. A weak P_n-phase (refracted wave from the upper mantle) forms the first arrivals between 80 and 110 km, but cannot be detected any further. Between 120 and 130 km the signal to noise ratio is decreased, due to a one hour thunderstorm. From 145 to 165 km the apparent velocity of the P_MP is considerably delayed and two later phases are seen. These later phases are water-bottom multiples near the source, their slow velocity and the decrease of the P_MP velocity is explained by the rapidly increasing water depth when crossing the shelf edge.

Figure 2., see next page.

Figure 2: Trace normalized record section obtained at station L8, reduced with 6 km/s, filtered 2-30 Hz. An array of six geophone strings with 6 geophones (4.5 Hz) each was used. Phase labelling explained in text.

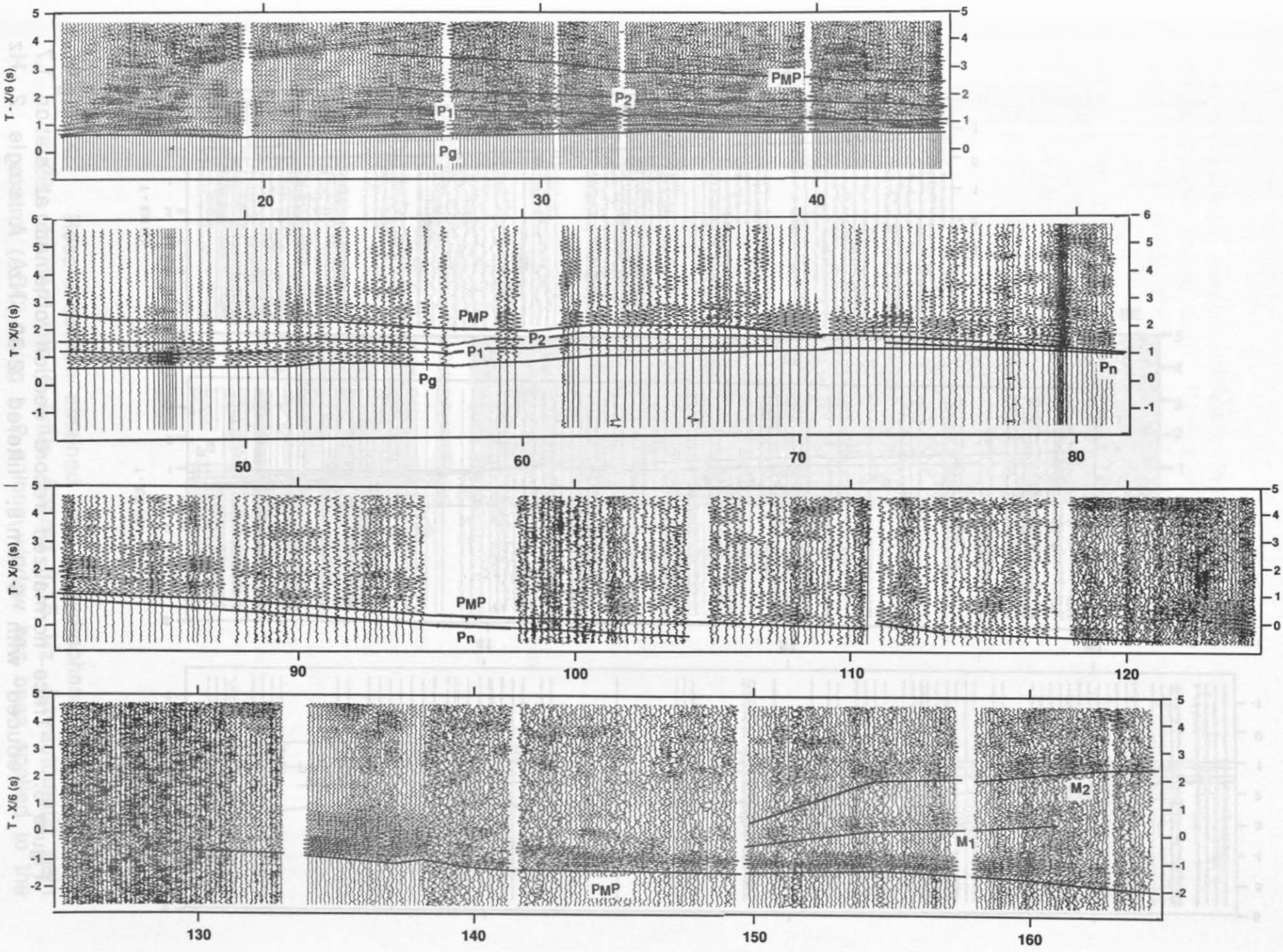
T - X/6 (s)
Pg
P1
P2
PMP
Pn
M1
M2
20
30
40
50
60
70
80
90
100
110
120
130
140
150
160

Figure: 2

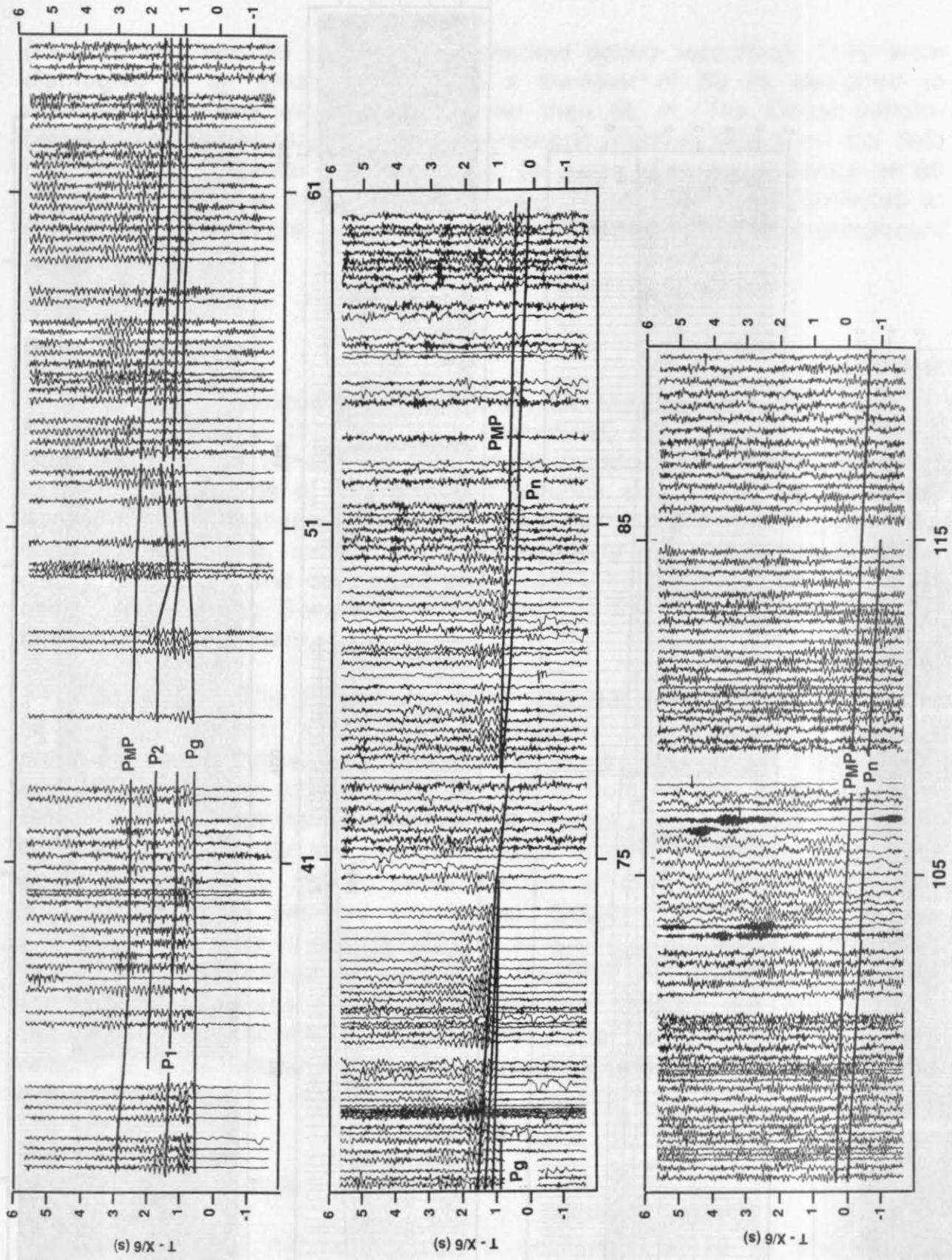

Figure 3: Trace normalized record section obtained at station L7, reduced with 6 km/s, filtered 2-30 Hz. A single 2 Hz seismometer was used. Phase labelling as in Figure 2.

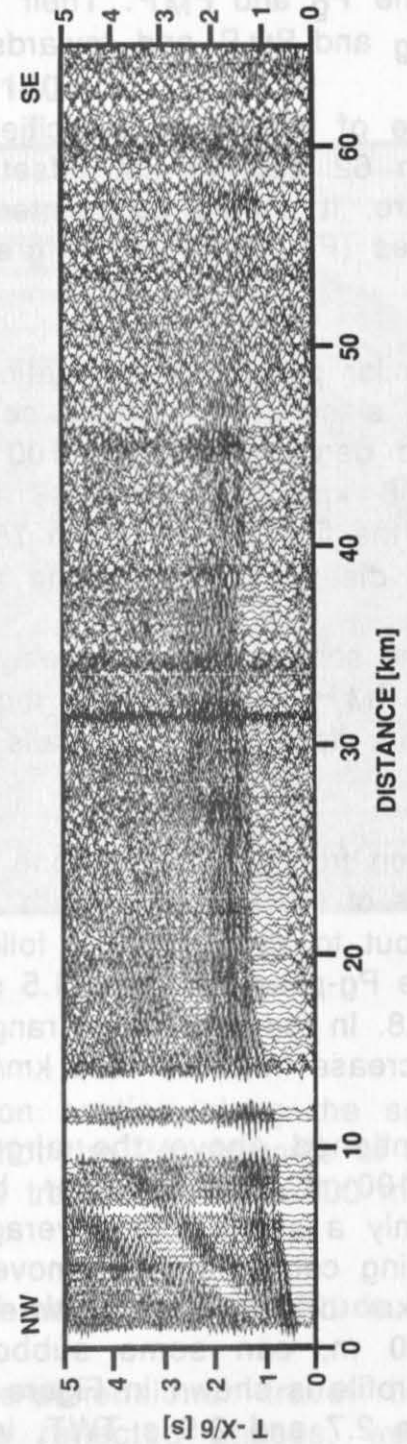

Figure 4: Record section obtained from a hydrophone at station OBS 26, reduced with 6 km/s, filtered 3-15 Hz. An automatic gain control (AGC) using a 2 s long window has been applied to the data.

Between 30 and 70 km offset two intracrustal phases, labelled P_1 and P_2, are observed between the P_g and P_MP. Their phase velocities are intermediate between the P_g and P_MP and towards larger offsets they merge into the P_MP.

A pronounced disturbance of the phase velocities and a clear travel time delay is found between 62 and 65 km offset, indicating a major change in subsurface structure. It should be pointed out that the travel time delay for the later phases (P_1, P_2, P_MP) is greater than for the P_g phase.

Station L7: A rather similar picture as for station L8 is observed on this record section. However, since only a single seismometer was used here, the signal-to-noise ratio degrades beyond 100 km. The P_g-phase stops rather suddenly at 66 km, and from 66 to 75 km the first intracrustal phase P_1 marks the first breaks. From 75 to 90 km the P_n is clearly recognized, but again disappears below the noise towards longer offsets.

Between 50 and 53 km the same travel time delay as mentioned above for station L8 is seen. The P_MP is again the most prominent phase throughout most of the section, its critical point falls between 50 and 60 km.

OBS 26: The record section from the hydrophone at OBS 26 is shown in Figure 4. Weak first arrivals of the P_g-phase with an apparent velocity close to 6.0 km/s are seen out to about 50 km, followed by a reflection (P_1). The intercept time of the Pg-phase is about 1.5 s, thus 1 s later than for the land stations L7 and L8. In the near offset range between 0 and 10 km the velocities observed increase from 3.3 to 6 km/s.

Reflection data: As mentioned above the airgun shots were also recorded by a 24 channel 100 m long streamer, but due to the shot intervals of 150 or 300 m only a single fold coverage can be achieved. Multiples and the source ringing could not be removed. Therefore only in the southeastern most 25 km of the profile, where the water depth increases from 300 to 1500 m, can some subbottom reflections be recognized. This part of the profile is shown in Figure 5. A strong package of reflections is seen between 2.7 and 2.9 s TWT, interpreted to indicate the base of the sediments.

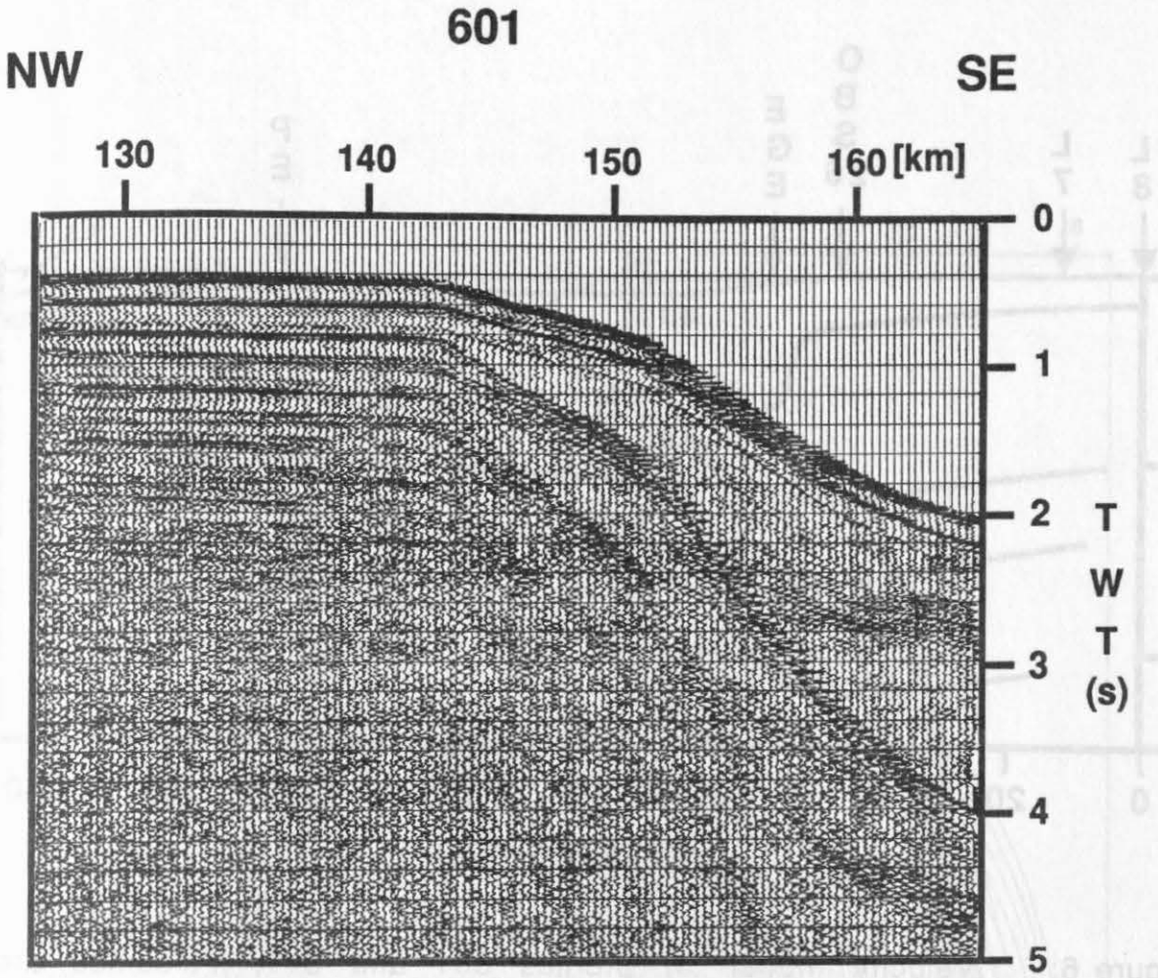

Figure 5: Reflection section along the southeast end of profile 601. For every shot the 24 channels of the 100 m long streamer are stacked. The trace spacing is 300 m, filtered 8-40 Hz.

Modelling of travel time and amplitude data

After initial one-dimensional travel time inversions and X^2-T^2 investigations of the reflected phases, we used a forward modelling approach to derive a velocity cross-section along the profile. The interactive two-dimensional ray-tracing code Ray86 (Luetgert, 1988) was utilized to calculate both the kinematic and dynamic features of the observed wavefield. The final velocity model is shown in Figure 6. In the upper crust a discrete steplike thickening of a layer with velocities ranging from 5.1 to 5.5 km/s is seen 50 km southeast of station L8. This step explains well the observed travel time delays of the P_g-phases from L7 and L8, being refracted through the 6.0-6.2 km/s layer. Also the observed wavefield from OBS 26 is well matched by this structure.

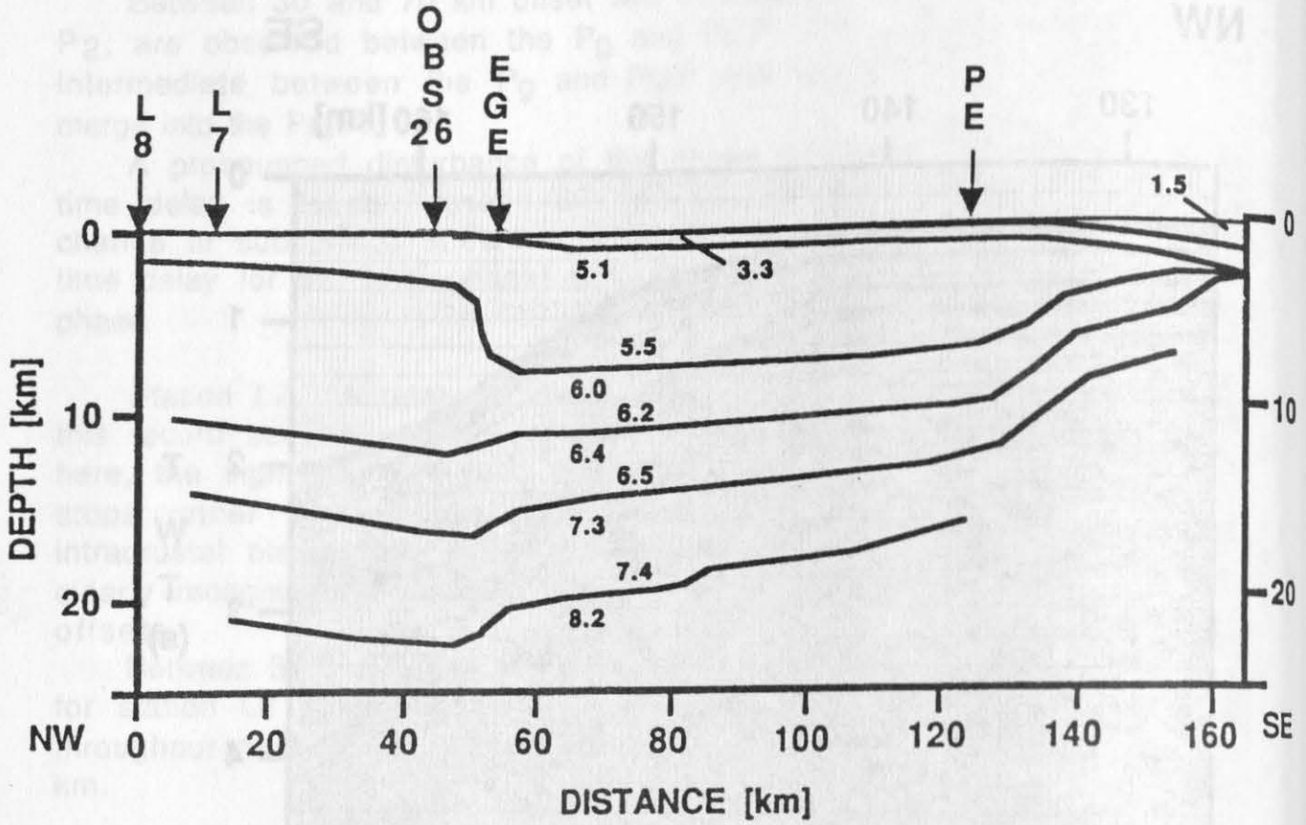

Figure 6: Velocity model for profiles 601 and 611. Velocities are given in km/s, vertical exaggeration 2.5 : 1. EGE and PE indicate the East Greenland Escarpment and the Pseudo Escarpment.

However, the travel time delays observed on the later phases (P1, P2, PMP) are not adequately explained by this change in the upper crustal velocities. In fact, the best fit obtained is by introducing an antistep in the deeper layers at about the same location. The resulting fit between observed and calculated travel times and the corresponding ray diagrams from stations L7 and L8 are shown in Figures 7 and 8.

In order to further test the interpretation synthetic seismograms were calculated for stations L7 and L8 and are shown in Figures 9 and 10. A general agreement between the observed (Figures 2 and 3) and calculated wavefield is found. The largest discrepancy is found between the P_n amplitudes, which are too strong on the synthetic section. This may in part be due to the velocity gradient assumed within the upper mantle (0.05 km/s/km), which however was needed to trace rays back to the surface. Also, no attenuation is included in the calculation of the synthetic seismograms. One should of course keep in mind the limitations of ray-theoretical synthetics before emphasizing these differences. The critical PMP distances are well matched within several km, and the variation of the amplitude ratio between individual phases is also in close agreement with the observed data.

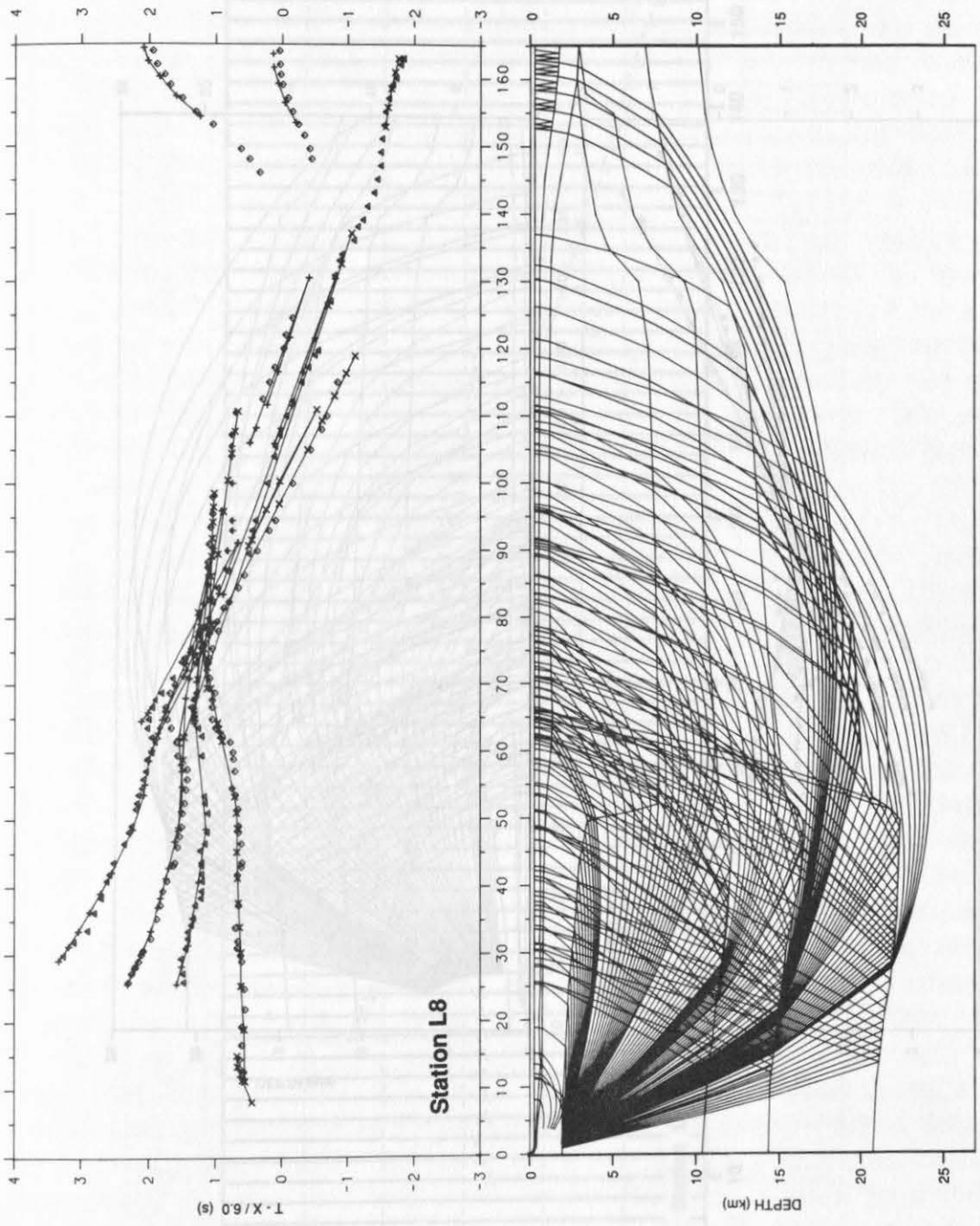

Figure 7: Observed (◊) and calculated (+) travel times for station L8, reduced with 6 km/s. The ray diagram is shown below.

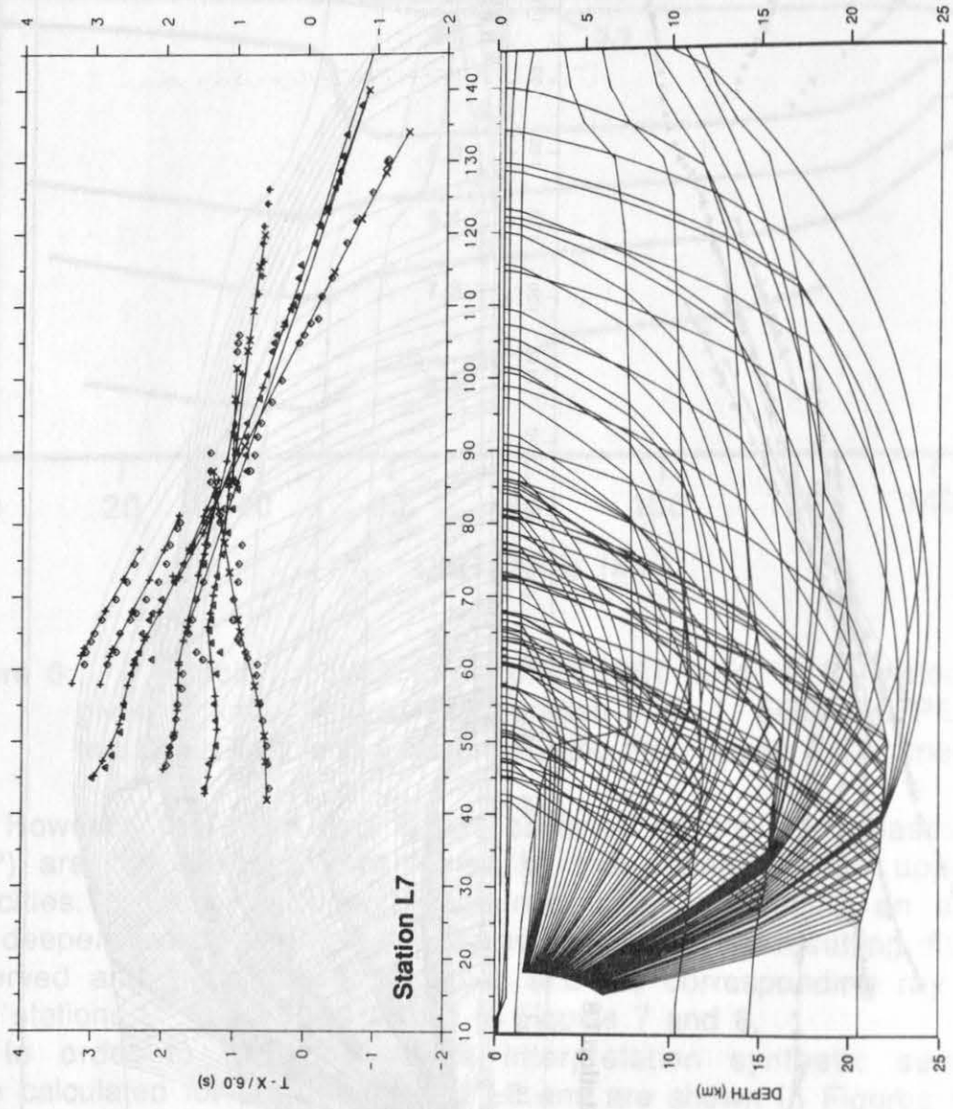

Figure 8: Observed (◊) and calculated (+) travel times for station L7, reduced with 6 km/s. The distance notation refers to that of Figures 5 and 6. The ray diagram is shown below.

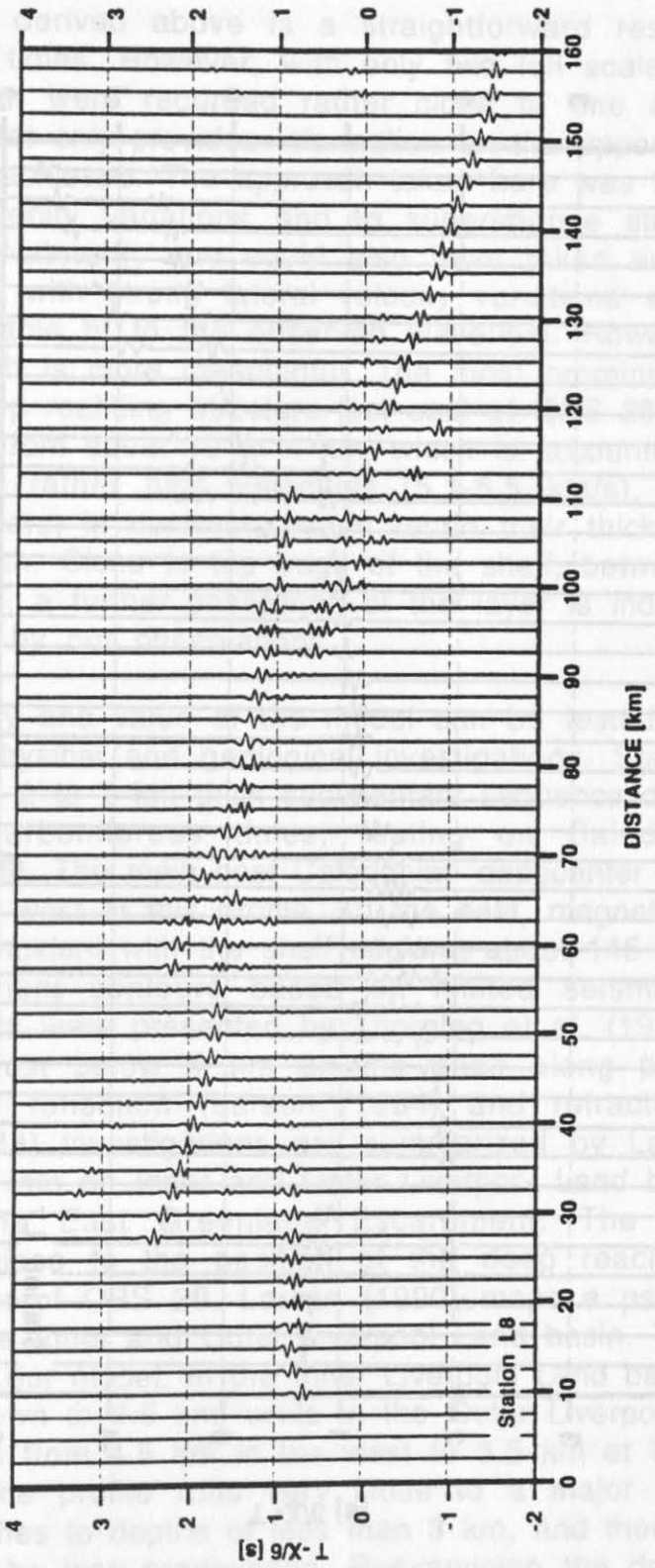

Figure 9: Trace normalized synthetic seismograms for station L8, reduced with 6 km/s.

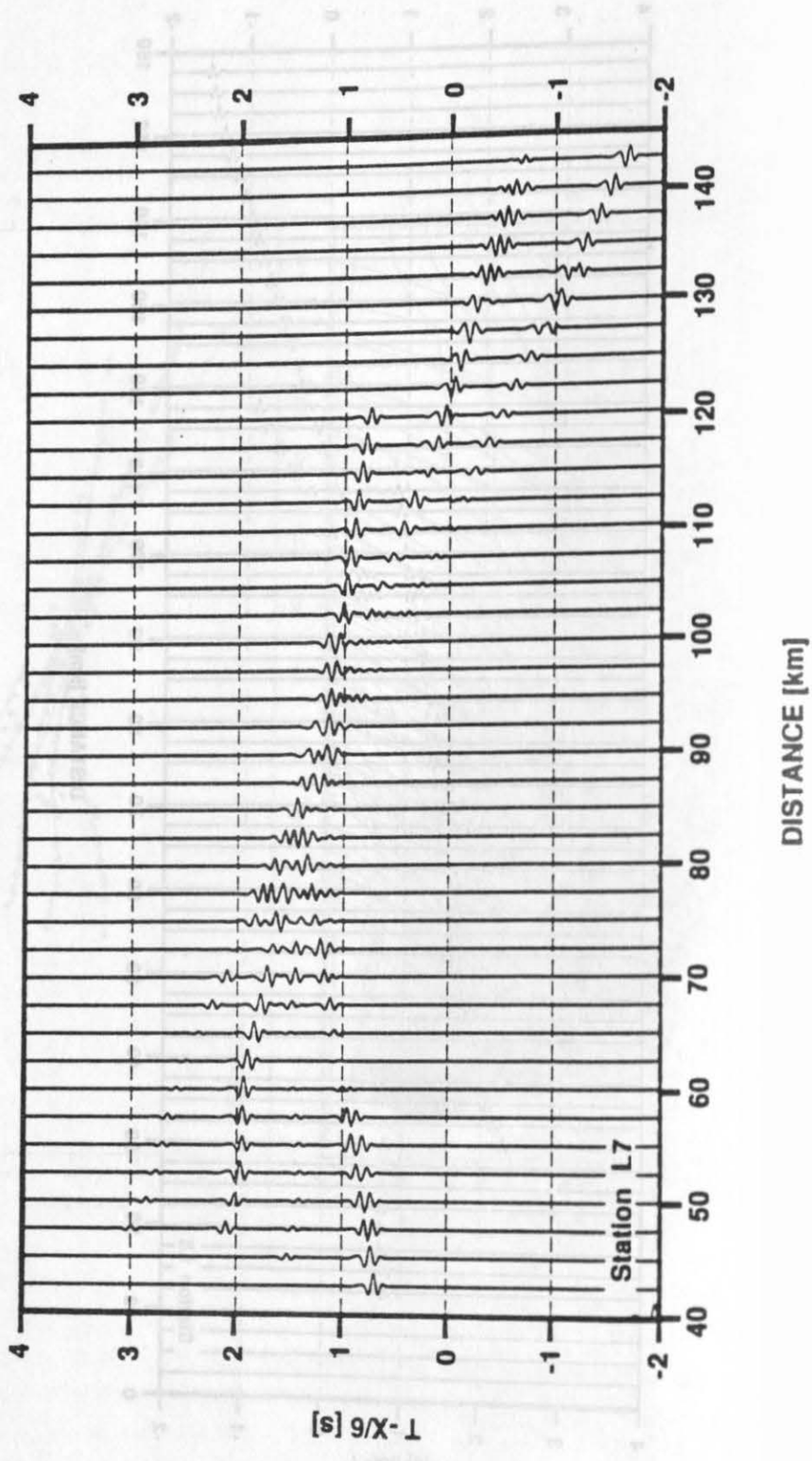

Figure 10: Trace normalized synthetic seismograms for station L7, reduced with 6 km/s. For the distance notation see Figure 8.

Discussion

The model derived above is a straightforward result of fitting the observed travel times. However, with only two full scale record sections, which in addition were recorded rather close to one another, and one record section that only provides information on the upper crust, no unique solution can be achieved. The approach taken here was to use layers with small lateral velocity variations and to superimpose structure to fit the observed data. Naturally, one could also have taken an approach using horizontal layers with strong lateral velocity variations superimposed and derive a reasonable fit to the observed wavefield. However, we felt that the first approach is more meaningful. The most prominent feature of the model is the deep reaching structure just east of OBS 26. Here, the upper crust is thinned from about 10 to 4 km, which is accounted for by a 6 km thick basin with rather high velocities (5.1-5.5 km/s). The middle and lower crustal layers, in contrast, nearly retain their thickness, but appear at shallower depth. Close to the edge of the shelf, between 130 and 165 km of the model, a further shallowing of the layer is indicated, but is not well constrained by our observations.

The reliability and value of the model can be tested when comparing it to other geophysical and geological investigations. Stations L8 and L7 are located on a 2 to 3 km thick sedimentary sequence deposited between Triassic and Carboniferous times, resting on Caledonian basement (Hendriksen, 1986). The main post Caledonian depocenter of Jameson Land is located to the west of this profile. To the east, magnetic anomaly 6 (20 ma) is found coincident with the shelf edge at about 145 km of the model. Depth to basement contours based on limited seismic and intensive aeromagnetic data were presented by Thorning et al. (1982) and show an average depth just below 4 km on the shelf along profile 601. More detailed seismic reflection (Larsen, 1984) and refraction (Larsen and Jakobsdôttir, 1988) investigations are summarized by Larsen (1990). He divides the shelf into an Inner and Outer Liverpool Land basin, bounded to the west by the East Greenland Escarpment. The position of the escarpment is close to the position of the deep reaching fault in our analysis just east of OBS 26. Larsen (1990) maps a pseudo escarpment that separates the Inner and Outer Liverpool Land basin. This is located at about 110 km of our model. In the Inner Liverpool Land basin the basement depth reaches down to 9.5 km, while in the Outer Liverpool Land Basin its depths decreases from 4.5 km in the west to 3.5 km at the end of profile 601. However, the profile runs very close to a major Tertiary intrusive body, which reaches to depths of less than 3 km, and therefore the pseudo escarpment may be less pronounced. Reexamining the data in the 110 to 120 km offset range (with respect to L8), where the pseudo escarpment is crossed, shows that this is the region where the P_n-phase stops. In addition, especially the later phases show some travel time undulation, that we have not attempted to model,

but may well be related to this structure. Starting at 125 km of our model a pronounced decrease of the thickness of the basin is indicated. This is in rather good agreement with the depth found in the analysis of geophysical data as summarized by Larsen (1990). According to his investigations the infill of the basin consists of predominantly rift and post-rift Miocene sediments. The Inner Liverpool Land basin also contains pre-rift sediments of presumed late Paleozoic to Mesozoic age. However, the velocities of 5.1 to 5.5 km/s for the basin fill as assumed for our model are rather high. They are in part constrained by the record from OBS 26. Assuming lower velocities would minimize the disagreement of basements depths between our model and the results presented by Larsen (1990).

Conclusions

The seismic investigation on the East Greenland margin suggests that the shelf offshore Kong Oscar Fjord suffered considerable crustal thinning during the break off of the Jan Mayen Ridge from Liverpool Land in Miocene time (pre anomaly 6). The upper crust, consisting of Archaean to Late Proterozoic gneisses with Middle Proterozoic and Caledonian intrusions, has been considerably thinned, while the lower and middle crust was uplifted due to isostatic adjustment during rifting, when also a 5 to 10 km thick sequence of mainly volcanic deposits was formed. An important observation is the deep penetration of the East Greenland Escarpment into the upper mantle. This crustal offset was previously unknown and may help in better understanding the mechanisms of rifting and extension.

The crustal thickness near the coast at Kap Biot (L8) and Wegener Halvø (L7) is found to be between 20 to 22 km. This is in general agreement with other seismic investigations in Jameson Land (Larsen et al., 1989) and Scoresby Sund (Hepper, 1991), where similar crustal thicknesses are found and interpreted to be the result of a post Caledonian rifting phase.

Acknowledgements

The seismic data presented here are part of the datapool collected by the GROEKORT-Study Group during the cruise ARK V/3 of RV POLARSTERN of the Alfred-Wegener-Institute for Polar and Marine Sciences, Bremerhaven, Germany in August 1988 and supported by the Deutsche Forschungsgemeinschaft (grant We 690/26). Most of the analysis was conducted during a sabbatical leave of Z.Z. to the Institute of Geophysics, University of Kiel.

References

Henriksen, N., 1986: Descriptive text to 1:500.000 sheet 12 Scoresby Sund, Copenhagen; Grønlands Geologiske Unders., 27 pp.

Hepper, J., 1991: Refraktionsseismische Untersuchungen im Scoresby Sund, Ostgrönland; Dipl. Thesis, 120 pp.

Larsen, H.C., 1984: Geology of the East Greenland Shelf. In Norwegian Petroleum Society (Ed.) Petroleum Geology of the North European margin, London; Graham and Trotman, 329-339.

Larsen, H.C., 1988: A multiple and propagating rift model for the NE Atlantic; In: Morton, A.C. and Parson, L.M. (Eds.): Early Tertiary Volcanism and the Opening of the NE-Atlantic; Geological Society Special Publication, 39, 157-158.

Larsen, H.C., 1990: The East Greenland Shelf; In: Grantz, A., Johnson, L., and Sweeny, J.F., (Eds.): The Arctic Ocean region; Boulder, Colorado, Geological Society of America, The Geology of North America, v. 1, 185-210.

Larsen, H.C. and Jakobsdôttir, S.J., 1988: Distribution, crustal properties, and significance of seawards-dipping sub-basement reflectors off E. Greenland; In: Morton, A.C., and Parson, L.M., (Eds.): Early Tertiary Volcanism and the Opening of the NE Atlantic; Geological Society of London Special Publication, 39, 95-114.

Larsen, H.C., Armstrong, G., Marcussen, C., Moore, S., and Stemmerik, L., 1989: Deep Seismic Data from the Jameson Land basin, East Greenland; Terra abstracts, vol 1, 2-3, 29.

Luetgert, J.H., 1988: RAY86/R86PLT - Interactive two-dimensional raytracing/synthetic seismogram package; U.S. Geol. Surv., Open File Rep., 88-238, 55 pp.

Thorning, L., Larsen, H.C. & Jacobsen, N.L., 1982: Project EASTMAR - final report; GGU internal report, 82 pp.

Weigel, W., Miller, H., Flueh, E.R., and the GRÖKORT Study Group: Seismic investigation of the East Greenland continental margin between 70° and 72° N; in preparation.

PROCESSING AND INTERPRETATION OF REFRACTION AND WIDE-ANGLE REFLECTION DATA CCSS-90 DATA SET III, (EAST GREENLAND)

Sanyu Ye and J. Ansorge

Institute of Geophysics, ETH Hoenggerberg, CH-8093 Zürich, Switzerland

Abstract

Data Set III consists of three-component recordings of a large series of airgun shots with an average spacing of 200 m. Due to the relatively low main source frequency of about 6 Hz and the shallow water depth the recorded raw signals appear as reverberating wavetrains which makes it difficult to distinguish any intermediate crustal phases from the first arrivals. The resolution was improved by applying a spiking deconvolution. After the deconvolution a reflected phase from the upper crust can be recognized in addition to the first arrival Pg and the Moho reflection PmP. A sedimentary trough between 55 and 75 km distance on the model scale is introduced to explain the traveltime delay of Pg and PmP. The data do not show evidence for a high velocity layer in the lower crust as proposed in the preliminary model. The observed strong converted wave PmS suggests also that the Moho is a sharp first-order discontinuity. Finally synthetic seismograms are calculated which show good agreement of the general features with the observation.

Introduction

The data consists of an unreversed sequence of seismic signals generated by an airgun source which moved away from the coast of East Greenland (Weigel et al.). The seismograph station was fixed on the coast and recorded three component signals over a distance of 94 km. The mean shot spacing is 200 m. Our goal in this study is to extract as much information as possible from the data by proper processing and to derive a crustal model as a basis for further investigations.

Processing

For the processing, the Phoenix System of Seismograph Service Ltd. installed on a VAX 11/780 at the Institute of Geophysics, ETH Zurich, was used. The data were sorted into three files representing vertical (VR),

north-south (NS magnetic) and east-west (EW magnetic) components. Each file was then edited and despiked. At the same time the data were resampled at 10 ms in order to reduce the time for further processing. Because the data passed a 44 Hz anti-aliasing filter during playback no distortion was caused. Figure 1 shows the vertical component after these initial processing steps. These prepared data were then filtered with a bandpass from 4 to 20 Hz before deconvolution.

To remove signal generated noise like multiples, prediction deconvolution is commonly used. Tests of prediction deconvolution on this dataset did not produce the expected results. The reason is probably the small water depth (around 270 m) and the laterally varying sedimentary structure. Therefore only spiking deconvolution was applied. Two separate correlation windows were chosen for P and S waves, respectively. The operator length was 480 ms. The deconvolution compresses the signals and separates different phases, which facilitates the correlation of arrivals. The improvement is less satisfactory where the signal/noise ratio is poor, for example in the S-wave window. To overcome this, the multichannel deconvolution was applied. This method sums up the autocorrelation of neighbouring traces and derives a common operator which is then applied to these traces individually. Tests with 5 and 25 channels show no significant difference in the result. In general, increasing the number of channels shows a little better phase coherency but loss on characteristics of individual traces. In the final application 10 channels were used.

The processed data were sorted and stacked into 200 m bins and plotted with different reduction velocities. Figure 2 demonstrates the enhancement of the resolution on the vertical component after bandpass filtering and multichannel deconvolution as compared to Figure 1. The wavetrains in Figure 1 consist of several near parallel reverberating phases. The laterally changing pattern of the reverberations indicates a lateral variation of shallow structure beneath the shotpoints.

Figures 1 and 2, see next pages.

Figure 1: First part of partly processed seismic section, vertical component, after resampling and despiking. The reduction velocity is 6.0 km/s.

Figure 2: Same section as Figure 1 after multichannel deconvolution. The improvement of resolution is better in the P-wave window than in the S-wave window. Clearly visible is a reflected phase in the distance range from 17 to 34 km.

Distance (m)
Reduced Traveltime Tred=T - Dist/6.0 (s)
0.0
1.0
2.0
3.0
4.0
5.0
6.0
7.0
10000
11000
12000
13000
14000
15000
16000
17000
18000
19000
20000
21000
22000
23000
24000
25000
26000
27000
28000
29000
30000
31000
32000
33000
34000
35000
36000
37000
38000
39000
40000
41000

Figure: 1

Distance (m)
10000
11000
12000
13000
14000
15000
16000
17000
18000
19000
20000
21000
22000
23000
24000
25000
26000
27000
28000
29000
30000
31000
32000
33000
34000
35000
36000
37000
38000
39000
40000
41000
Ps
Pg
Pi
Pi
Reduced Traveltime Tred=T - Dist/6.0 (s)
0.0
1.0
2.0
3.0
4.0
5.0
6.0
7.0

Figure: 2

Correlation of phases

After processing, several refracted and wide-angle reflected arrivals can be correlated (Figure 2): A sedimentary phase Ps, Pg, a secondary reflected phase Pi from the upper crust between 17 km and 34 km distance, which continues then as first arrival, and the PmP from 50 km onwards (Figure 4a). Figure 3 shows the "transverse" (E-W component) horizontal component with a reduction velocity of 8 km/s after processing as described above. Here, Sg is characterized by a broad band of energy in contrast to the vertical component in Figure 2.

Unlike the clear appearance of PmP, the corresponding Moho reflection SmS produced only a band of scattered energy which is difficult to correlate as a single phase (not shown in the figures). The clear phase between 35 and 55 km in Figure 3 at 7 s reduced time is interpreted as a converted Moho reflection PmS, indicating a sharp jump of velocity at this discontinuity.

Modelling

For an initial structure the model provided with Data Set III (Zhao and Flueh, this volume) was transformed into the format for the 2D raytracing program RAY87 (Luetgert, 1988; Sierro, 1988). Because the initial raytracing did not produce a satisfactory agreement between the observed and the calculated traveltimes at the distance range between 55 and 75 km, doubts rose on the reliability of the initially obtained surficial structure. Eventually GEOMAR provided additional information from a normal-incidence seismic section along the same profile. This allowed a proper control of water depth. Unfortunately, no sedimentary structure can be recognized on this additional unprocessed seismic section. Due to the large offset and the unreversed record section of Data Set III, it is impossible to obtain the detailed information regarding the true surficial sedimentary structure. Therefore, the surficial structure in the model is only modified to fit the first arrivals.

Figures 3 and 4a, see next pages.

Figure 3: First part of processed seismic section of EW component. The reduction velocity is 8.0 km/s. The strong phase between 35 and 55 km with apparent velocity close to 8 km/s is interpreted as converted Moho reflection PmS.

Figure 4a: Seismic section of vertical component with correlation of phases after multichannel deconvolution and bandpass filtering

Figure: 3

Distance (m)
Reduced Traveltime Tred=T - Dist/6.0 (s)
0.0
1.0
2.0
3.0
4.0
5.0
6.0
7.0
8.0
9.0
10.0
P_g
P_i
$P_m P$
S_g

Figure: 4a

It is easy to explain the lateral traveltime delays of the first arrivals and the Moho reflection PmP in the distance range between 55 and 75 km mainly by a trough with sediments. We were also forced to reduce the velocity of the top sediments in a gradient layer to 2.0 km/s at the sea bottom and to 2.5 km/s at the base of this layer. Figure 4b shows the simplified crustal structure that was derived. Contrary to the original preliminary model the abrupt lateral change in depth of the crystalline basement disappears and becomes only a depression. No significant lateral change is needed for the upper crustal interface from 6.05 to 6.4 km/s.

The available data show no evidence for a high-velocity layer in the lower crust as proposed in the preliminary model. The clear and strong PmS in the horizontal components also opposes the existence of such a high-velocity lower crust. 8.2 km/s was assumed for the Pn velocity. The general updip of the Moho to the SE is confirmed.

Because of uncertainties in correlating SmS, no S-wave modelling was done. The only method available to us to model converted waves like PmS is to calculate synthetic seismograms with the reflectivity method (Kind, 1985; Sierro, 1988) for laterally homogeneous 1-D models. Figure 5 shows the radial component of the synthetic seismograms in which a clear PmS is indicated. If one compares Figures 3 and 5, the synthetic seismograms reproduce the observed features rather well, e.g. the reverberating wavetrains running parallel to the first arrivals and the broad band of Sg. Less satisfactory are amplitude ratios between different wave groups, particularly the PmS is weak relative to the first arrivals and Sg. This may be explained by the 1-D model simplification which does not take into account the different structure beneath the receiver and sources.

Conclusion

Similar processing steps designed originally for normal-incidence reflection data can be adapted for densely spaced wide-angle reflection and refraction data. In the case of an offshore airgun source the spiking deconvolution has proved to be a very useful tool to separate different phases and thus extract clear signals from reverberating background noise. This reduces erroneous correlations and interpretations and increases the reliability of resulting structural models. It is very important for a reliable modeling to collect as much additional information as possible about the surficial structure since these data are mostly unreversed observations.

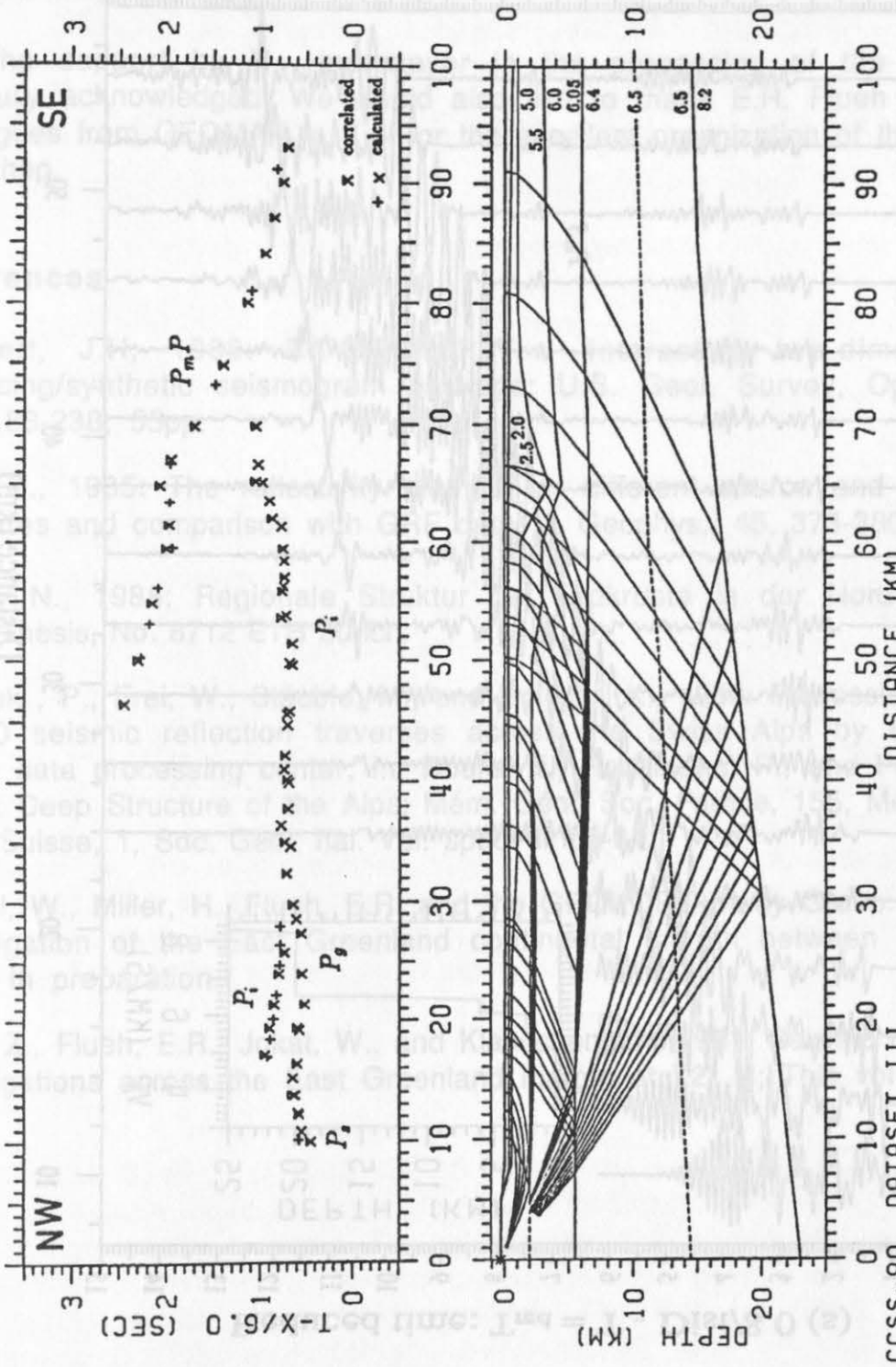

Figure 4b: Model derived from dataset 3. The numbers in the model indicate the P-wave velocity.

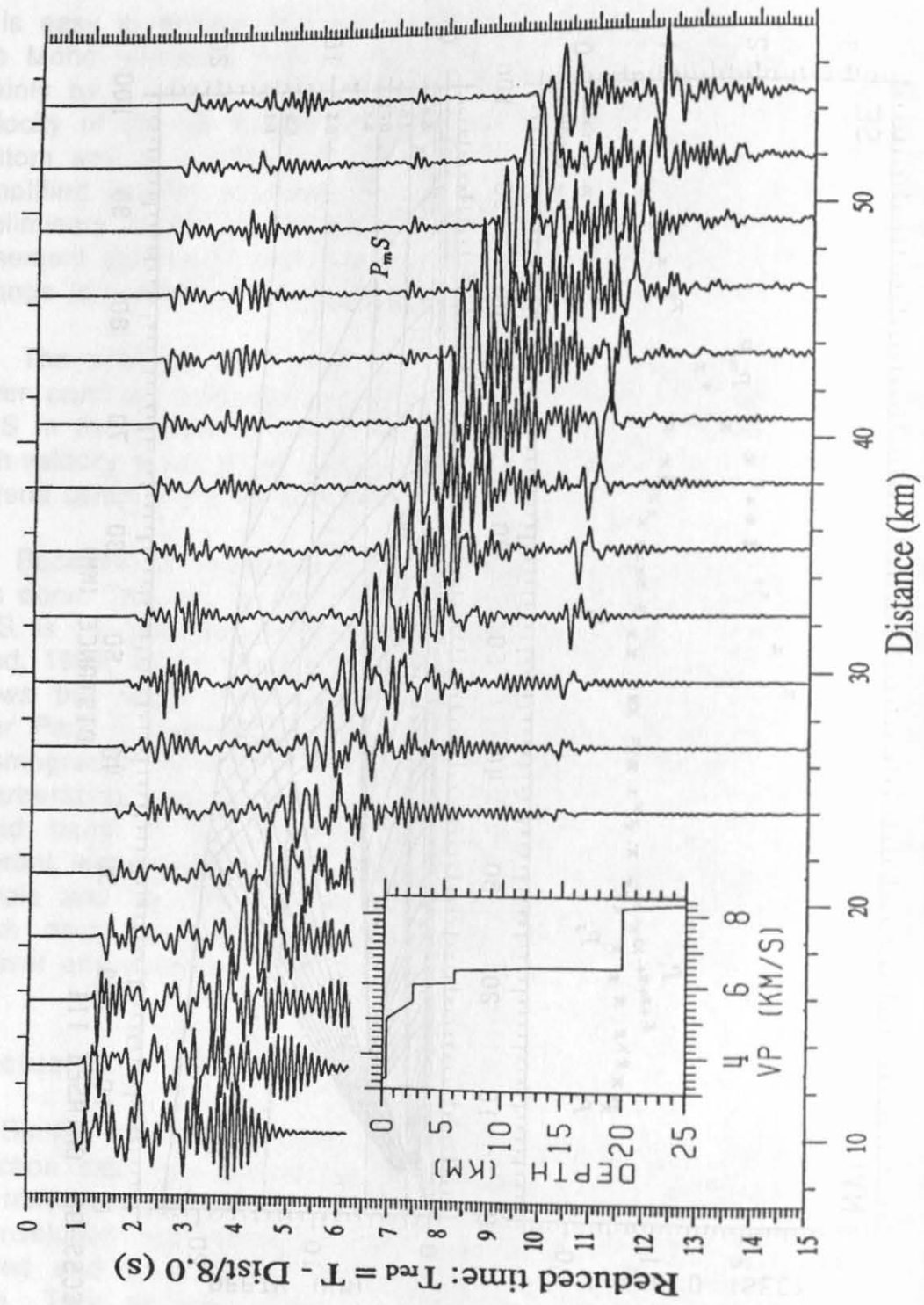

Figure 5: Radial component of the synthetic seismograms calculated with the reflectivity method. The diagram on the left bottom is the corresponding velocity-depth function for P-waves.

Acknowledgements

The support by H. Horstmeyer in the processing of the data is gratefully acknowledged. We would also like to thank E.R. Flueh and the colleagues from GEOMAR in Kiel for the excellent organization of the CCSS Workshop.

References

Luetgert, J.H, 1988: RAY86/R86PLT - Interactive two-dimensional raytracing/synthetic seismogram package; U.S. Geol. Survey, Open File Rept. 88-238, 55pp.

Kind, R., 1985: The reflectivity method for different source and receiver structures and comparison with GRF data; J. Geophys., 45, 373-380.

Sierro, N., 1988: Regionale Struktur der Erdkruste in der Nordschweiz; Ph.D. Thesis, No. 8712 ETH Zürich.

Valasek , P., Frei, W., Stäuble, M., and Holliger, K., 1990: Processing of the NFP20 seismic reflection traverses across the Swiss Alps by the ETH Zürich data processing center; In: Roure, F., Heitzmann, P., and Polino, R. (Eds.): Deep Structure of the Alps; Mém. Géol. Soc. France, 155, Mém. Soc. Géol. Suisse, 1, Soc. Geol. Ital. Vol. spec. 1, 55-64.

Weigel, W., Miller, H., Flueh, E.R. and the GRÖKORT Study Group: Seismic investigation of the East Greenland continental margin between 70° and 72°N; In preparation.

Zhao, Z., Flueh, E.R., Jokat, W., and Klaeschen, D., 1991: Seismic refraction investigations across the East Greenland margin at 72° N; This volume.

EVIDENCE OF SHEAR WAVE SPLITTING FROM A THREE COMPONENT SEISMIC REFRAKTION STUDY OF THE EAST GREENLAND CONTINENTAL MARGIN

Bastian Spaargaren

Department of Geology, Imperial College, London, SW7 2BP, UK

Abstract

The three components of CCSS data set 3 were processed using DISCO and the given P-wave model ray-traced using the SEIS83 package. Comparison of the processed data with the synthetic data showed that the model supplied gave a good fit and that a significant number of phases were identifiable in all three components. A portion of the data with large amplitude S-wave first arrivals in the horizontal components was then analyzed and strong S-wave splitting was found. The fast component is polarized at approximately 20 degrees East of true North and the delay of 150 ms between fast and slow S-wave arrivals is approximately constant with offset in the range studied. The S-wave splitting is interpreted as being indicative of anisotropy in the top 1-2 km of the crust due to vertically aligned cracks perpendicular to the fossil spreading direction. The magnitude of the anisotropy is approximately 4%.

Introduction

Dataset 3 of the 1990 CCSS workshop was a three-component refraction dataset collected over the East Greenland continental margin in 1988 (Weigel et al, in prep.). The source was a single 32 liter airgun and the receiver consisted of six 3-component 4,5 Hz geophones in a 10 m linear array which were field stacked. The data covered a single unreversed profile with offsets between 10 and 94 km heading approximately NW-SE as shown in Figure 1.

Participants were given the raw data and paper sections of the three components as well as a location map of the profile and a preliminary P-wave crustal model. The aim was to concentrate on all information that could be extracted from the two horizontal components as well as the vertical component.

Processing

One immediately noticeable aspect of the data was that it was extremely ringy. Since the source was only a single airgun, and not an array of airguns, the bubble pulse was quite long and dominates the sections. This meant that it was an excellent candidate for predictive (gapped) deconvolution.

Another, less significant, aspect of the data were the straight regular lines at one second intervals crossing the sections at an infinite apparent velocity. These were interpreted as being the reference timing signal which had cross-talked onto all three channels. They started off as being rather insignificant, but after filtering and deconvolution, the data was visibly worsened by their presence. Therefore, an attempt was made to take the timing lines out at the start of the processing sequence.

This was done by slant stacking all of the traces in each component. the resultant trace gave a good indication of the shape of the cross-talked timing signal. A synthetic timing signal was then constructed and subtracted from each data trace. Although this dit not solve the problem completely (as can be seen in the data in Figures 2, 3 and 4), the impact on the final sections was significantly reduced.

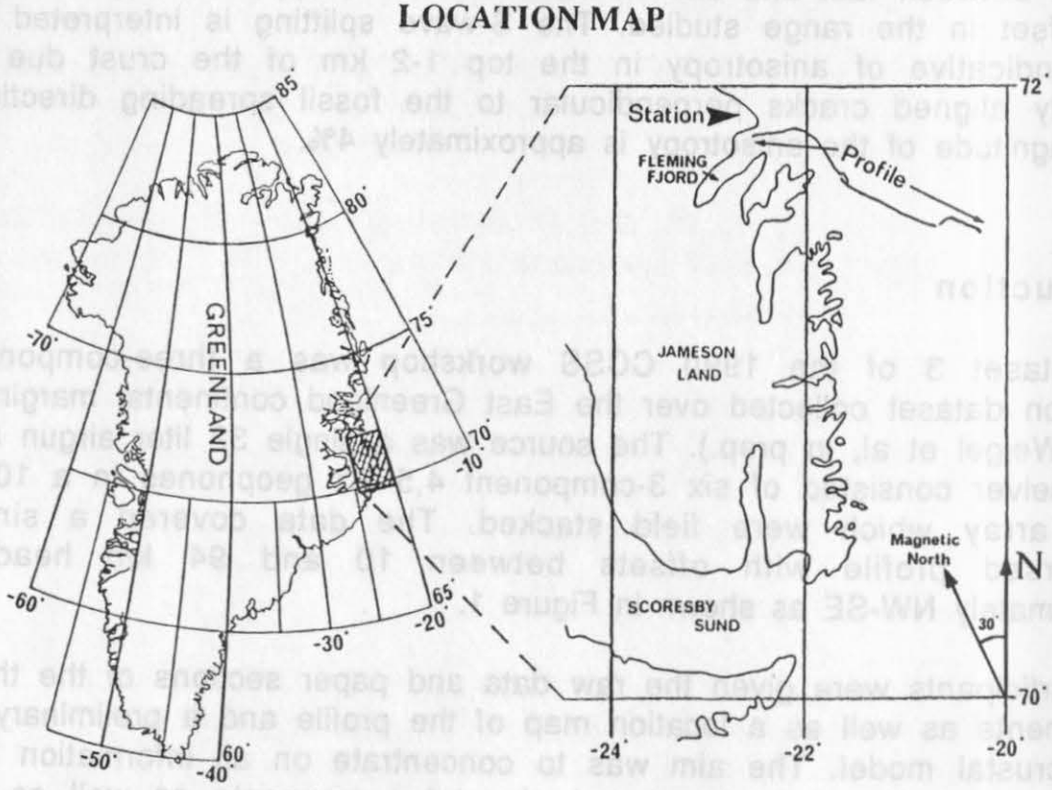

Figure 1: Location map showing position of recording station and direction of refraction profile.

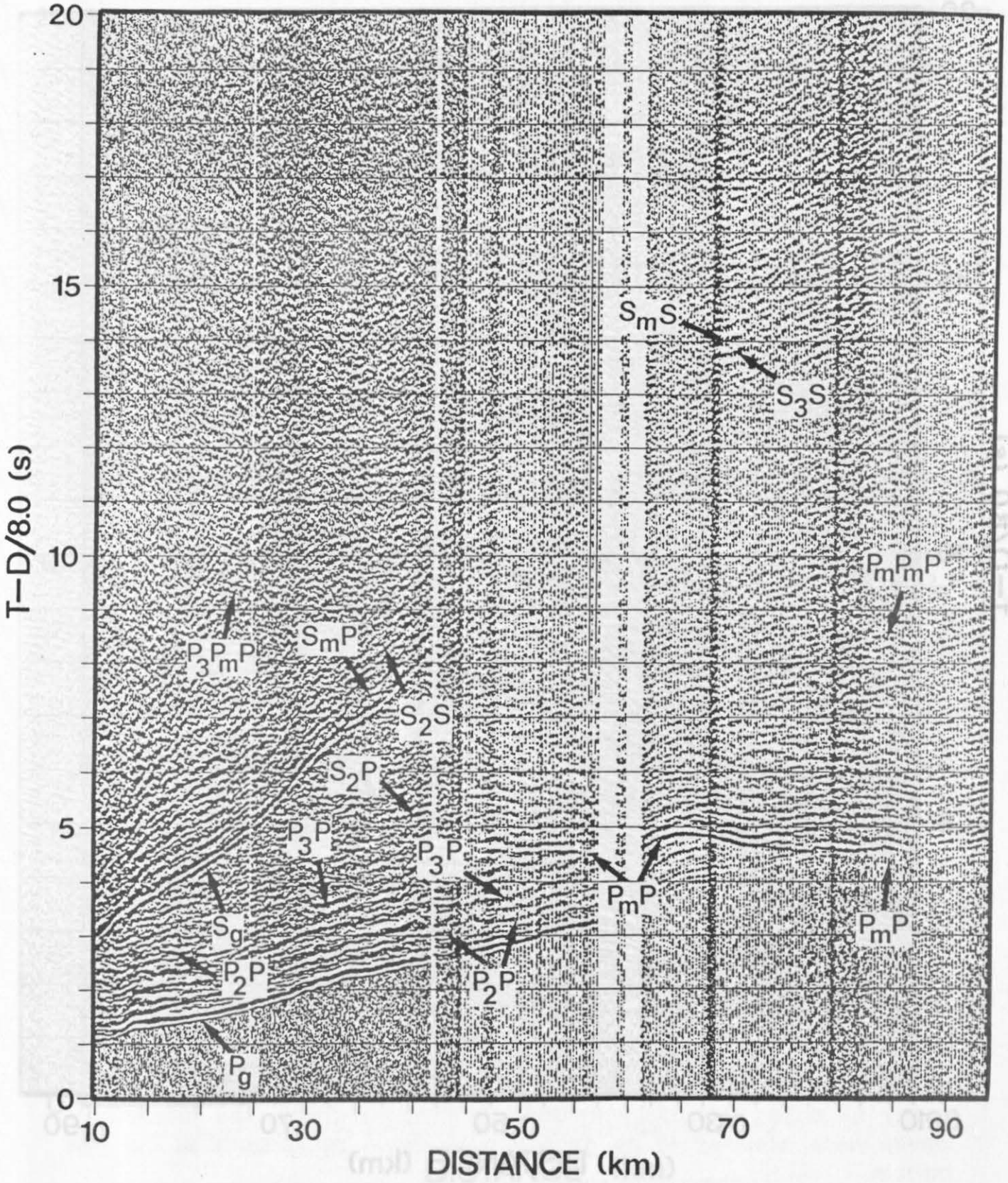

Figure 2: Vertical component processed data showing picked phases.

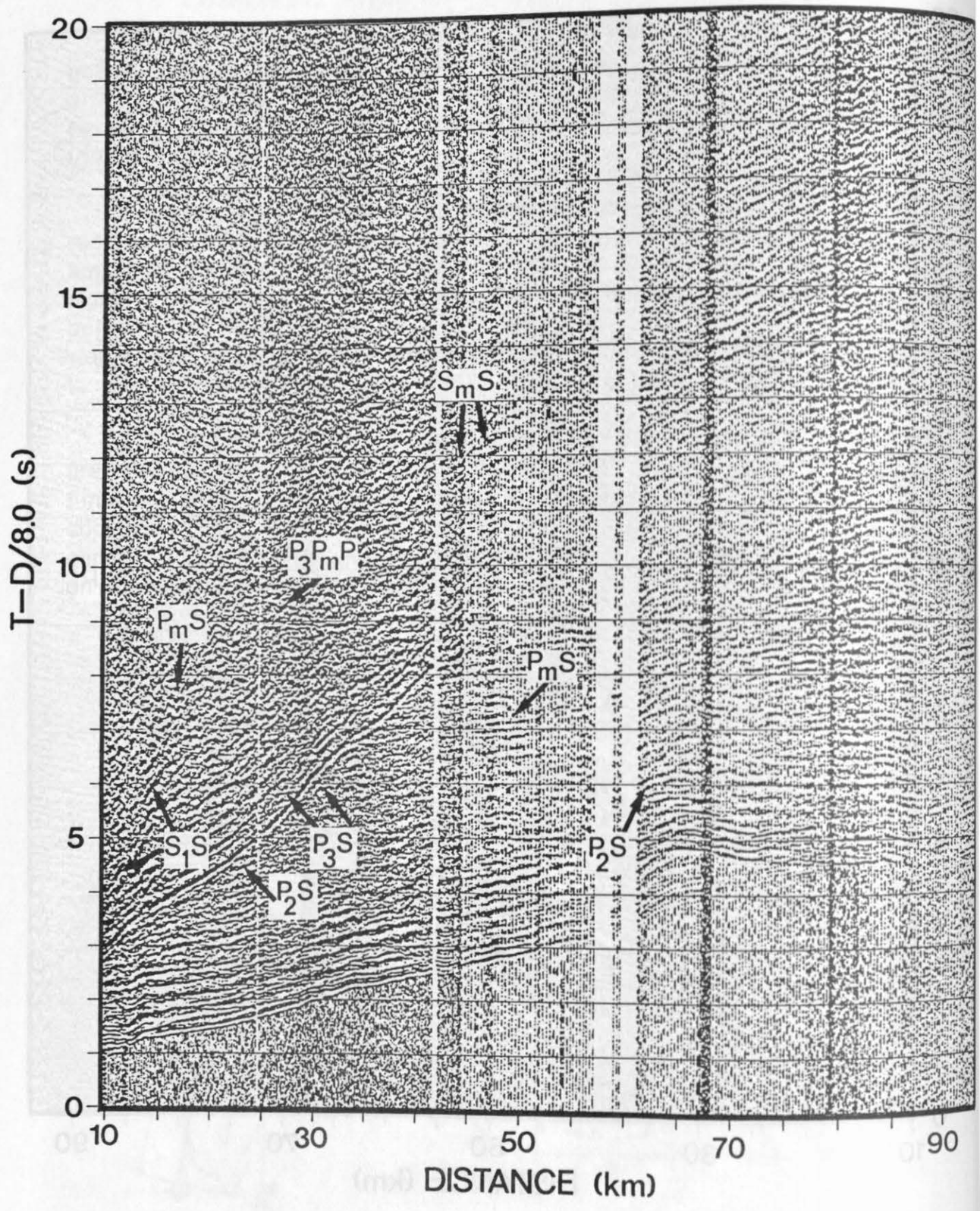

Figure 3: N (magnetic) horizontal component processed data showing picked phases.

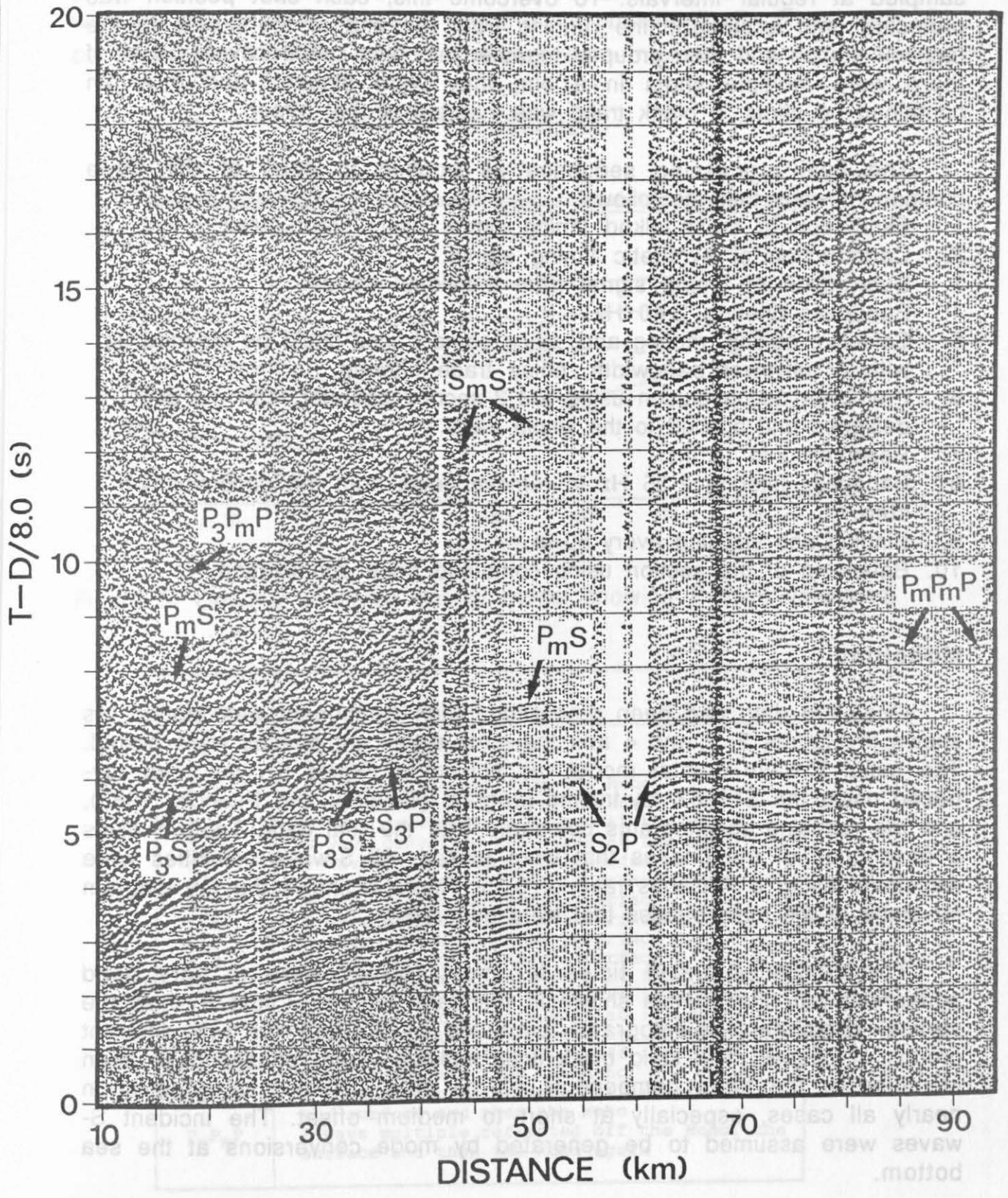

Figure 4: E (magnetic) horizontal component processed data showing picked phases.

As can be seen in Figure 1, the survey was not linear, nor was it sampled at regular intervals. To overcome this, each shot position was projected onto a straight line running from the end of the profile to the receiver station and then grouped together into bins spaced every 50 m. If there were multiple shots in a bin, they were stacked and if a bin contained no shots, a blank trace was inserted at that offset.

The final processing sequence as applied to each of the three components was then as follows.

1. Estimation of cross-talked timing signal using slant stack.
2. Construction of synthetic timing signal.
3. Subtraction of timing signal from individual traces.
4. Bandpass filtering 2-40 Hz.
5. Selective editing, muting and, since some traces could be cleaned up with a narrower bandwidth, noisy trace filtering.
6. Predictive deconvolution using a 1,2 second operator, 150 ms gap designed and applied to the whole trace.
7. Resampling to 10 ms.
8. Bandpass filtering 2-25 Hz to remove noise from the deconvolution step.
9. Binning and stacking every 50 m.
10. Balancing of the section using combined trace equalization.

Modelling

Once the data had been processed, each component was plotted, as shown in Figures 2, 3 and 4 and the most significant phases were picked. The initial P-wave crustal model, as shown in Figure 5, was then ray-traced using the SEIS83 ray-tracing program (Ceverny and Psencik, 1983), and the resulting seismograms compared with the real data. Table 1 gives a description of the phases that were picked. All S-wave velocities were calculated using a Poissons ratio of 0,25. Figure 6 shows the ray diagram for some of the main phases that were generated.

The calculated travel times for most phases were in very good agreement with the phases shown in the data. Figures 7 and 8 show the vertical component seismograms produced by SEIS83 for two different groups of phases. The solid black lines indicate where phases have been identified in the three components of the data. There is a good fit in nearly all cases, especially at short to medium offset. The incident S-waves were assumed to be generated by mode conversions at the sea bottom.

Reflected phases from the intermediate crustal interfaces, labelled 1, 2 and 3 in Figure 5, are visible in the data (Figures 2, 3 and 4) and are labelled P_1P, P_2P,S_3S etc.

Converted phases are also visible, with the most striking being the PmS phase most easily spotted in the E horizontal component. On comparison with the synthetics in Figure 8, two P-wave phases, P_mP_mP and P_3P_mP, corresponding to Moho-seabed multiples were inferred.

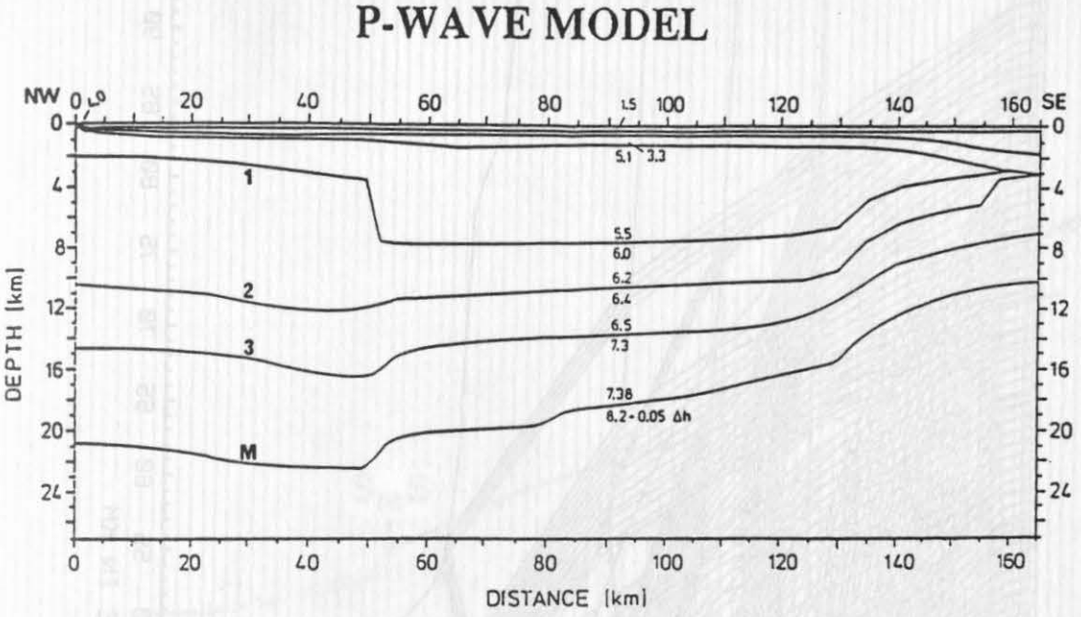

Figure 5: Original unaltered crustal model showing P-wave velocities.

Phase	Description
P_g	Direct refracted P-wave
S_g	Direct refracted S-wave
P_mP	P-wave reflection from the Moho
S_mS	S-wave reflection from the Moho
P_mS	P-wave converted to S-wave at the Moho
S_mP	S-wave converted to P-wave at the Moho
P_1P	P-wave reflection from interface 1
P_2P	P-wave reflection from interface 2
P_3P	P-wave reflection from interface 3
S_1S	S-wave reflection from interface 1
S_2S	S-wave reflection from interface 2
S_3S	S-wave reflection from interface 3
P_2S	P-wave converted to S-wave at interface 2
P_3S	P-wave converted to S-wave at interface 3
S_2P	S-wave converted to P-wave at interface 2
S_3P	S-wave converted to P-wave at interface 3
P_2P_mP	P-wave multiple reflected off interface 2, the surface and then the Moho
P_3P_mP	P-wave multiple reflected off interface 3, the surface and then the Moho
P_mP_mP	P-wave multiple reflected off the Moho, the surface and then the Moho again

Table 1: Description of the main phases picked from the data and ray-traced.

Figure 6: Ray diagram of some of the main arrivals. Arrows indicate the offset range over which S-wave splitting was analyzed.

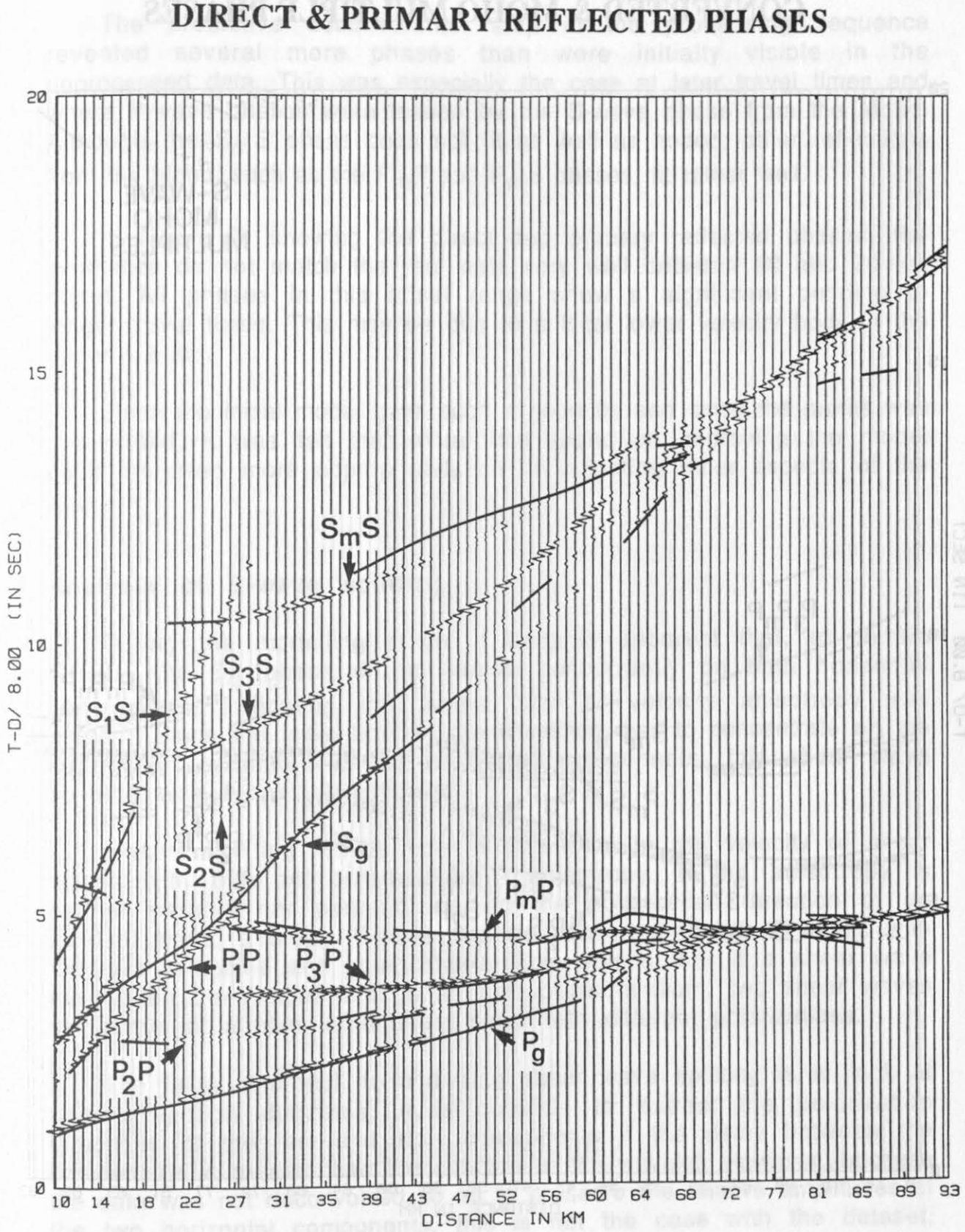

Figure 7: Synthetic seismogram from SEIS83 showing the main direct and primary reflected P and S-wave phases. The black lines indicate where phases have been picked from the real data.

CONVERTED & MOHO MULTIPLE PHASES

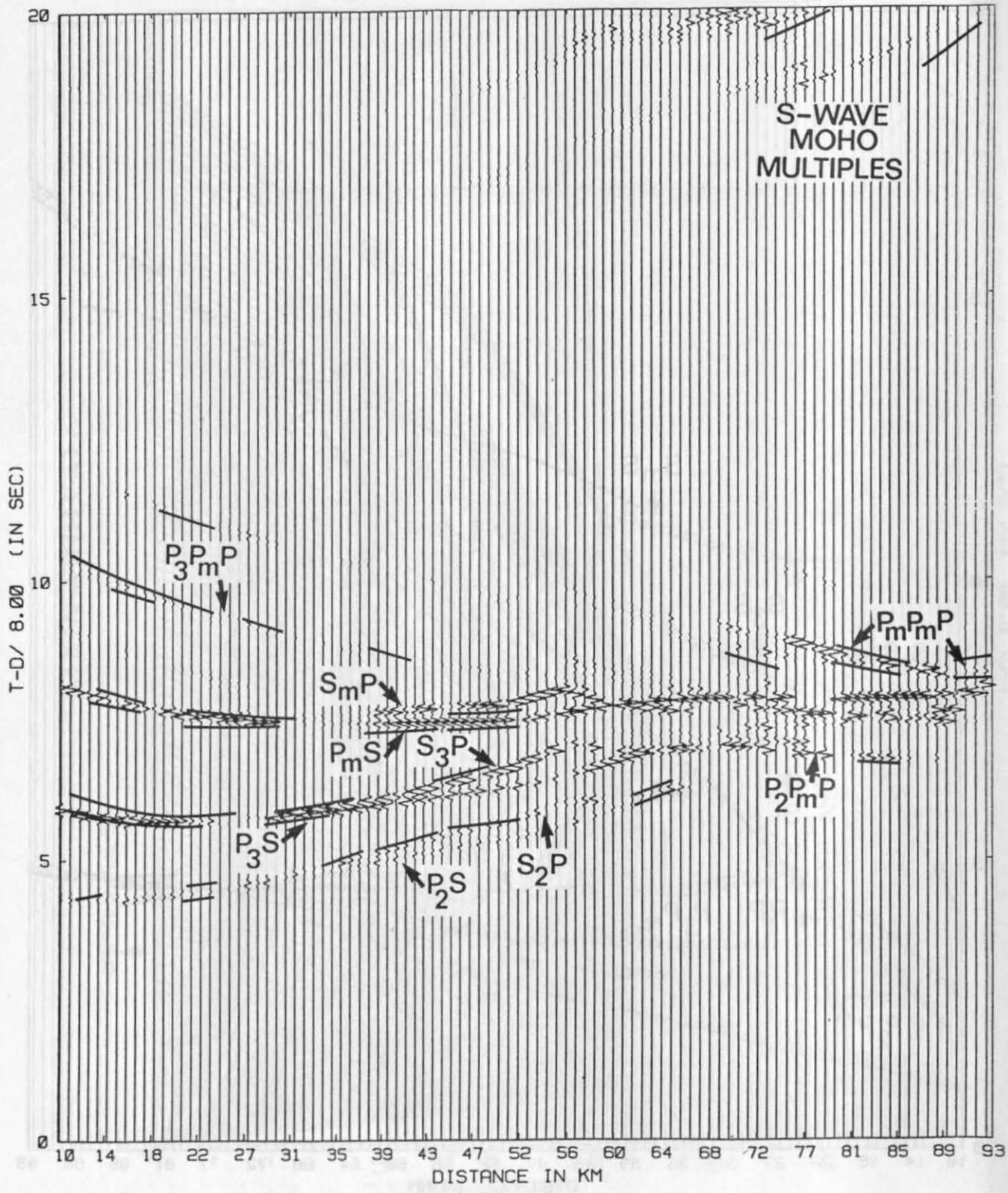

Figure 8: Synthetic seismogram from SEIS83 showing the main converted and Moho multiple P and S-wave phases. The black lines indicate where phases have been picked from the real data.

The predictive deconvolution step in the processing sequence revealed several more phases than were initially visible in the unprocessed data. This was especially the case at later travel times and where P-wave phases were hidden by the S-wave phase from the Moho. Although the S_mS phase does not fit as well as hoped, other reflections from the Moho, such as the P_mP and P_mS phases, fit rather well.

In Figure 7, showing the direct and primary reflected phases, the synthetics do not match the real data very well between 60 and 70 km offset. All phases in this offset range show a significant bending to longer travel times. This may be due to a local lower velocity body in the upper 1-2 km.

Since the initial model gave such a good fit, and since the profile was unreversed, it was felt that extra time spend on improving the model could be used more appropriately on investigating other aspects of the data.

Analysis of S-wave splitting

During the modelling stage, it became apparent that, at certain offsets, the S_g phase dit not arrive concurrently on both horizontal components, indicating that some form of velocity anisotropy was present. Since the initial brief of the workshop was to concentrate on the information contained in the horizontal components, this shear wave splitting was further investigated.

S-wave splitting results from a difference in the velocity of shear waves with different polarizations - anisotropy. If the anisotropy is neither parallel nor perpendicular to the polarization direction of an incident wave, a single S-wave can be converted to two S-waves with different velocities and polarizations. This means that if a shear wave have been transmitted through an anisotropic medium, two shear waves can arrive at a point at different times with different polarizations.

The usual approach to analyzing shear wave splitting is to look at particle motion diagrams. It is possible to extract the polarization directions of the fast and slow components if the delay between the components is greater than the duration of the wavelet. However, because the data was not deconvolved so as to preserve the relative amplitudes of the two horizontal components, this is not the case with the dataset, since the source is strongly reverberant.

A different approach, based on the cross-correlations of the two horizontal components was undertaken. This technique assumes that the two split shear waves have identical wavelets but can be different in amplitude. It also requires that the shear waves arrives at the surface within the "shear wave window" (Crampin, 1984). This means that the angle of incidence must be less than approximately 35 degrees. Although this approach was developed particularly for this study, another similar approach, using cross-correlations for VSP data, has since been brought to my attention (Naville, 1986).

A portion of the unprocessed data showing strong S-wave first arrivals was used as a basis for this study. The S_g arrival between 17 and 23 km offset, which had shown significant differences in travel times in the horizontal components during the modelling, was selected. The modelling had shown that the S-waves must have been generated by conversion at the seabed, so, as long as only one form of anisotropy was present, the split shear waves should have similar waveforms. Also, as can be seen in the ray diagram in Figure 6, the shear waves do seem to arrive within 35 degrees to the vertical, satisfying the second assumption mentioned above.

The approach adopted involved the following steps.

1. Window approximately 1 second of the arrival in both N and E horizontal components.
2. Cross-correlate the two resulting components.
3. Rotate each component by 10 degrees.
4. Repeat steps 2 and 3 until 360 degrees is reached.
5. Plot the resultant cross-correlations in order of angle rotated.

The plot was then analyzed for the following reference points.

1. The angle at which the cross-correlation has the least post-lag energy.
   This gives the direction of polarization of the fast component.

2. At the above polarization direction, the lag at which the maximum peak occurs. This gives the delay between fast and slow components.

Figure 9 explains how the above steps work in a simple case where the source wavelet is a spike and the fast component has an amplitude 4 times that of the slow component.

A. When both fast and slow components are completely separated into their respective polarization directions there is a strong correlation at the lag corresponding to the delay between the components. Note that there is no energy in the post lag.

B. At 5-10 degrees away from the fast direction, there is no longer one spike in the cross-correlation but several, with energy now coming in after zero lag.

C. When the rotation is at 45 degrees to the fast direction, the cross-correlation becomes dominated by the effective auto-correlation of the largest component. The peak at this rotation can be larger than in case A, so one cannot simply look for the largest peak in the plot.

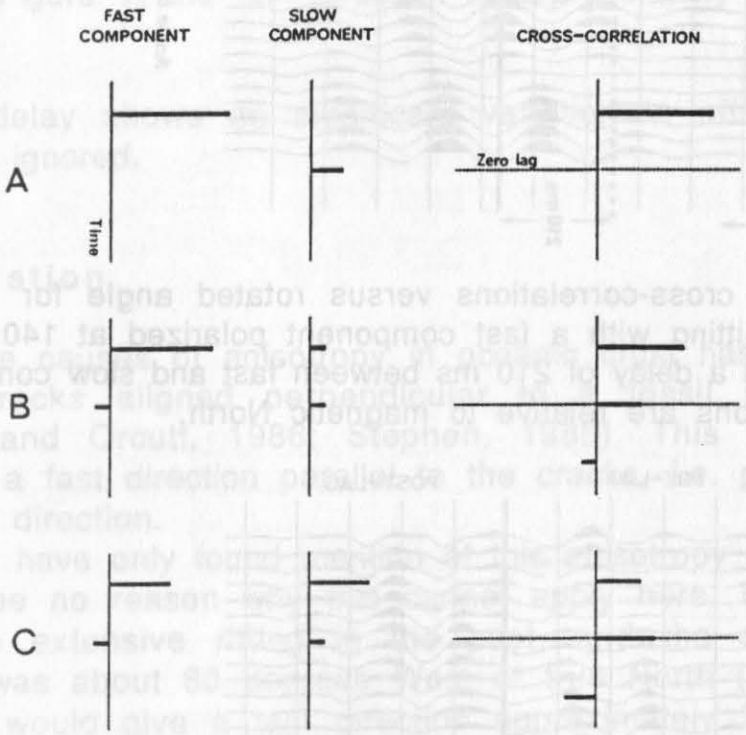

Figure 9: Cartoon showing how rotation of two components in a simple case of S-wave splitting affects the cross-correlations at different rotation angles.

Figures 10 and 11 show plots of cross-correlations against angle of rotation. Figure 10 is a synthetic using a realistic wavelet with a fast direction at 140 degrees and a delay of 210 ms between fast and slow components. Note that both the polarization direction and delay between arrivals can be easily picked using the reference point criteria outlined previously.

Figure 11 is a plot of the real data, and has been analyzed using the same steps. It gave a fast direction of 50 degrees East of magnetic North and a delay of 140 ms.

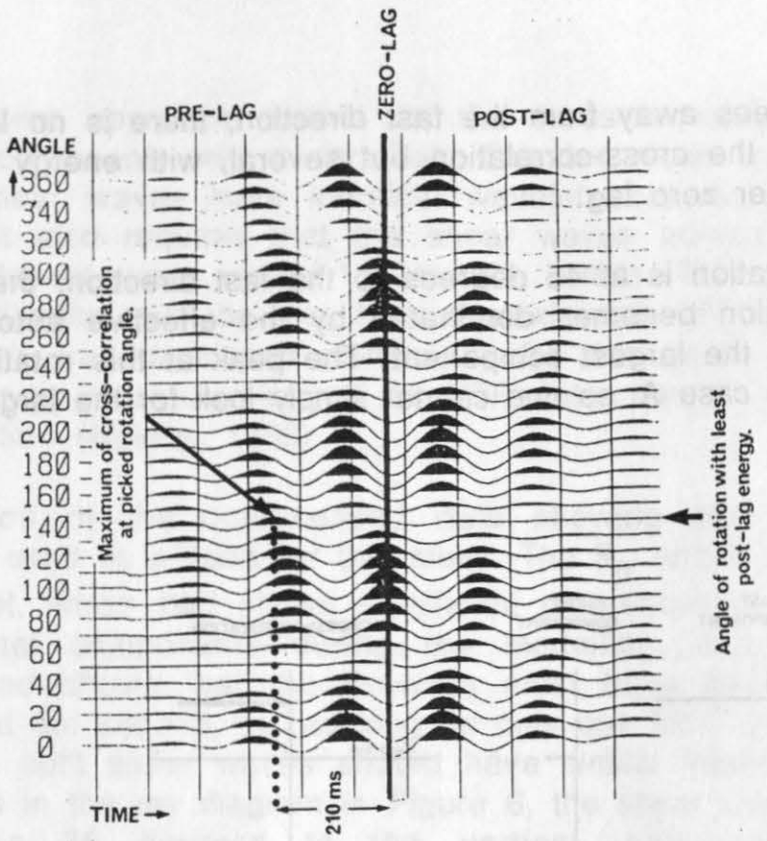

Figure 10: Plot of cross-correlations versus rotated angle for synthetic S-wave splitting with a fast component polarized at 140 degrees E of N and a delay of 210 ms between fast and slow components. The directions are relative to magnetic North.

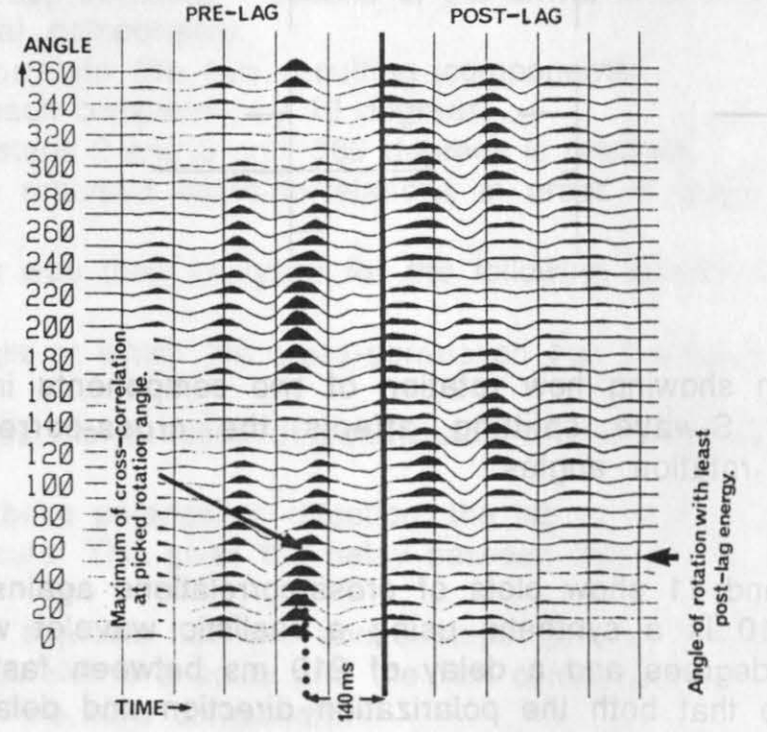

Figure 11: Plot of cross-correlations versus rotated angle for real data showing S-wave splitting with a fast component polarized at 50 degrees E of magnetic N and a delay of 140 ms between fast and slow components.

Results

Plots such as that shown in Figure 11 were made at 34 consecutive traces along the S_g arrival between 17 and 23 km offset. Figures 12 and 13 show how the polarization direction of the fast component and the delay between components vary with offset.

The polarization direction shows no consistent angle to magnetic north until about 19 km. Past that point, the data shows a constant direction of about 50 degrees East of magnetic North. Since magnetic North in the area of the profile is about 30 degrees West of true North, as shown in Figure 1, the fast direction is approximately 20 degrees East of true North.

The delay shows no significant variation in offset if the few wild points are ignored.

Interpretation

One of the causes of anisotropy in oceanic crust has been attributed to vertical cracks aligned perpendicular to a fossil spreading direction (Shearer and Orcutt, 1986; Stephen, 1985). This form of anisotropy results in a fast direction parallel to the cracks, i.e. perpendicular to the spreading direction.
Although I have only found mention of this anisotropy occurring in oceanic crust, I see no reason why this cannot apply here. East Greenland has undergone extensive rifting in the past, and the dominant spreading direction was about 60 degrees West of true North (Ziegler, 1988, plate 11). This would give a fast direction approximately 30 degrees East of North, close to the calculated direction.

If the anisotropy occurred in the upper 1-2 km of the crust, there should be very little variation of delay with offset, since the ray paths through this area at about 20 km offset are roughly the same length and direction (see Figure 6). The ray paths for the chosen arrival are becoming vertical at these depths, and a S-wave oscillating in the sagittal plane could split in the manner described previously.

Conclusions

The original P-wave model given was sufficiently accurate not to warrant any great alterations, especially considering that the profile was not reversed.

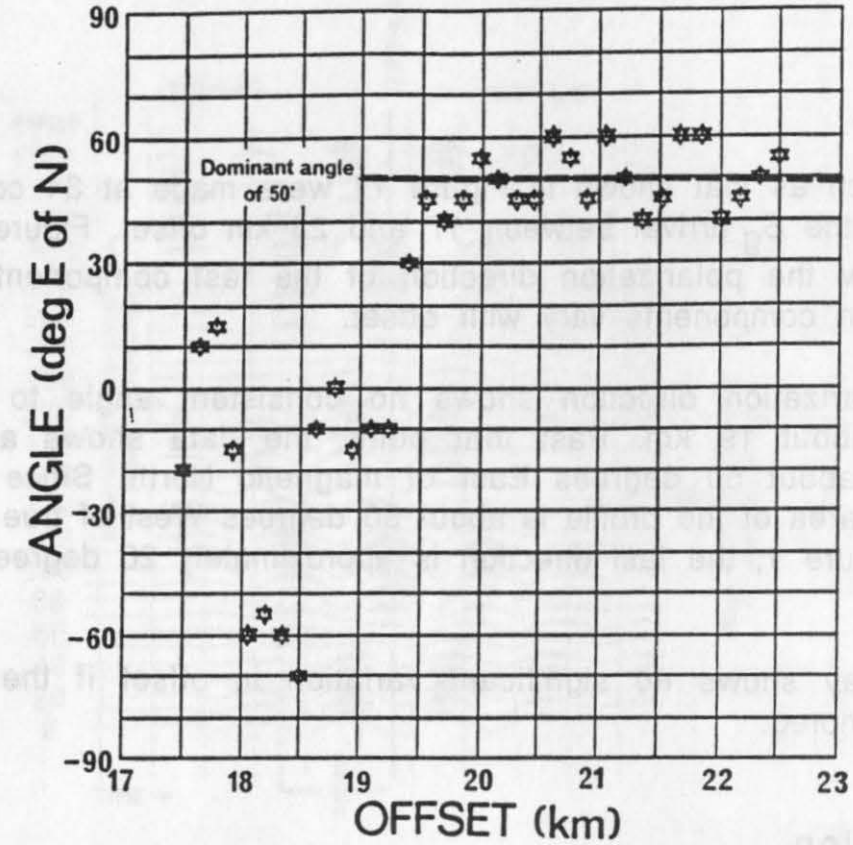

Figure 12: Plot of polarization direction of the fast component (E of magnetic N) against offset. Note that after 19 km offset, the angle is consistently 50 degrees.

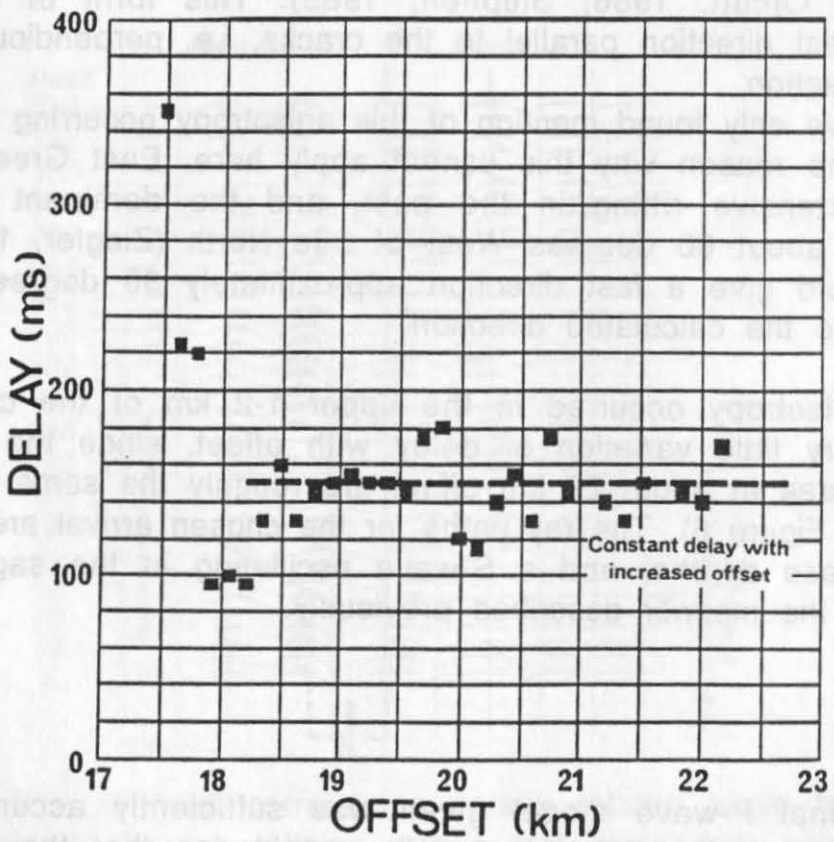

Figure 13: Plot of delay between fast and slow components against offset. Note that there is very little variation in delay with offset.

The pronounced S-wave splitting gave a consistent fast polarization direction within a given offset range, and the delay was approximately constant with offset. The cause of these splitting is interpreted as vertical cracks in the upper 1-2 km of the crust aligned at about 20 degrees East of true North. This direction is close to being perpendicular to the fossil spreading direction which would explain the origin of the vertical cracks.

Since the amount of splitting is 150 ms and the travel time within the upper layers is about 3,5 s, the anisotropy is approximately 4,0%.

Acknowledgements

I would like to thank Shell International Petroleum Company for providing a Ph.D. scholarship and for financing my attendance of the CCSS workshop for which this work was undertaken. Thanks also go to Mike Warner for many useful discussions and to Roland Roberts and an anonymous reviewer for their constructive criticisms.

References

Ceverny, V. and Psencik, I., 1983: Seismic Ray Package, Vydala; Universita Karlova, Prague, Czechoslovakia.

Crampin, S., 1984: Anisotropy in exploration seismics; First Break, March, 19-21.

Naville, C., 1986: Detection of anisotropy using shear wave splitting in VSP surveys: Requirements and applications; Expanded abstract, 56th annual SEG meeting.

Shearer, P.M. and Orcutt, J., 1986: Compressional and shear wave anisotropy in the lithosphere: The Ngendei seismic refraction experiment; Geophys. J.R. astr. Soc., 87, 967-1003.

Stephen, R.A., 1985: Seismic anisotropy in the upper oceanic crust; J. Geophys. Res., 90, 11383-11396.

Weigel, W., Miller, H., Flueh, E.R. and the GRÖKORT Study Group: Seismic investigation of the East Greenland continental margin between 70` and 72` NK; in preparation.

Ziegler, P.A., 1989: Evolution of the Arctic-North Atlantic and the western Tethys; Am. Assoc. Pet. Geol., Mem., 43: 198 pp., 30 plates.

CONTRIBUTION TO DATASET III: COMPLEX TRACE - AND PARTICLE MOTION ANALYSIS

Dirk Klaeschen and Ernst R. Flueh

GEOMAR, Kiel , Germany

Abstract

In this contribution we present some results of complex trace analysis and particle motions on the three-component dataset. Three windows were choosen, two on the P-wave first arrivals at offsets of 37 and 47 km, and a third window also at 47 km offset centered around a prominent phase, interpreted to be a P-to-S conversion at the Moho. For the P-wave arrivals the amplitudes are largest on the vertical and smallest on the east-component. The instantaneous frequencies show that the dominant frequencies are between 6 and 9 Hz for each component, and a slight frequency decrease with increasing offset can be recognized. When investigating the converted phase a number of yet unexplained phenomena are seen. The maximum amplitude is observed on the east - component, and in addition on this component the dominant frequency is nearly doubled, while on the vertical and north component no change of the frequency content with respect to the P-wave first arrivals occurs. The particle motions in this window show that the main movement is on the east component, and the second main axis changes between the north and the vertical component. This observation, together with the apparent increase of the dominant frequency on the east component, is taken as evidence that this phase is made up of several interfering S-waves.

Introduction

Dataset III, as distributed for the Commission´s on Controlled Source Seismology (CCSS) workshop at Fellhorst, Germany from 27. -31.8.1990 consisted of a three-component record section, obtained by land recording of airgun shots on the East Greenland Margin. One of the most prominent features of these data is a phase, that is especially pronounced on the horizontal components and appears to be a P-to-S converted reflection from the Moho. As a contribution to the workshop we have analyzed its instantaneous frequency, amplitude, polarity, and particle motion behavior. To exclude any influence of poor coupling or instrumental failure, these analyses were made in three windows, two on the P-wave first arrivals and one on the P-to-S converted phase.

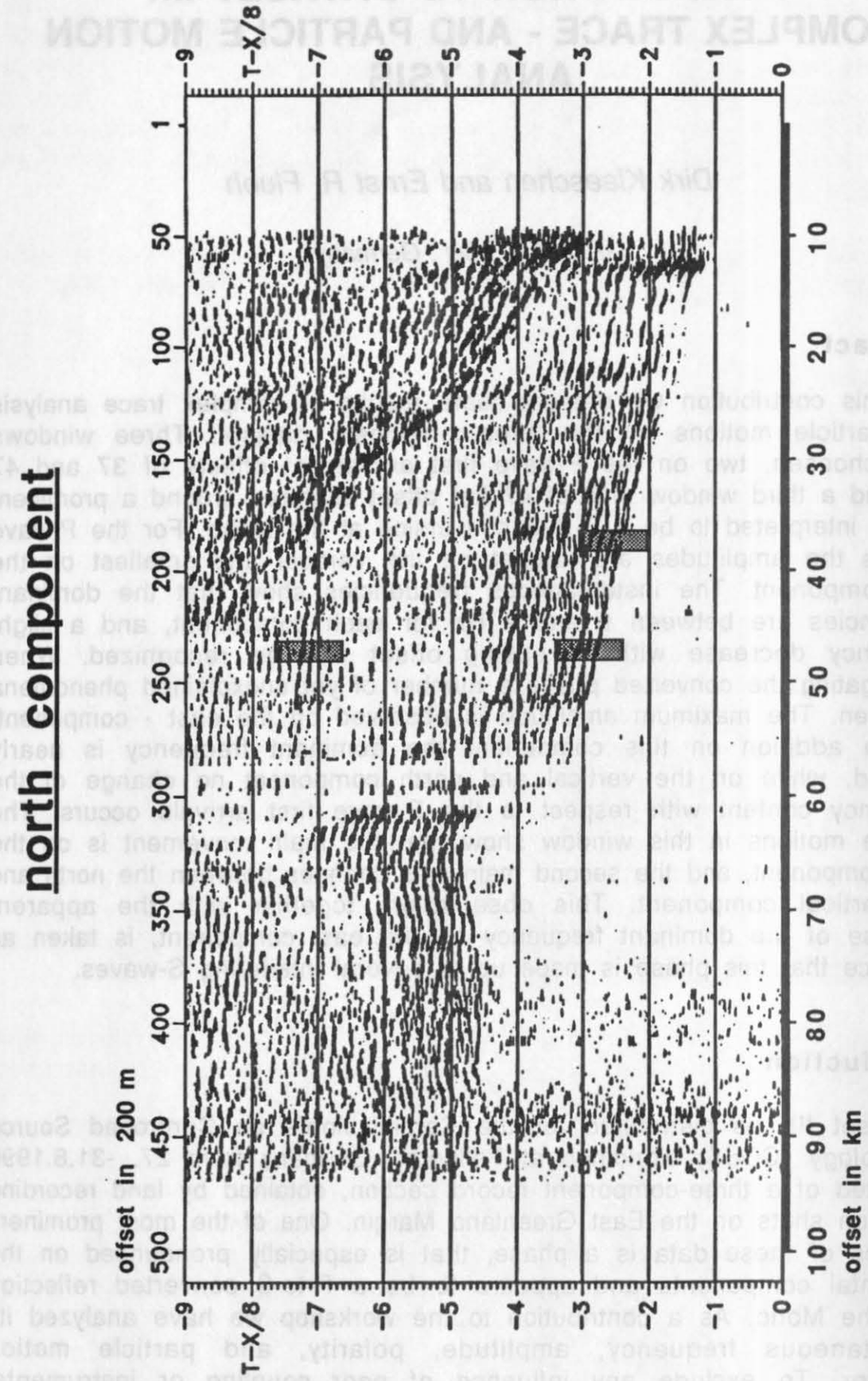

Figure 1: North component of dataset III. The frames indicate the data analyzed in this contribution.

For each window, we compared the amplitudes and polarities, calculated the instantaneous frequencies and analyzed the particle motions. In Figure 1 the record section of the north component is shown and the position of the windows analyzed is indicated.

Complex Trace Analysis

In Figure 2 enlarged plots of the three windows analysed are shown. In the 37 km offset window (traces 180 to 190, left), the maximum amplitude is on the vertical component. The north component (bottom) has an intermediate amplitude, and the same polarity as the vertical component. On the east component (middle) the amplitudes are much decreased, and in addition the polarity is changed. The same observations are true for the 47-km offset P-wave window, as seen in the middle column of Figure 2. However, a totally different picture is seen on the P-to-S converted phase (right column). The maximum amplitudes are seen on the east component, and clear arrivals can be recognised at 6.95 and 7.25 s reduced traveltime. On the north component amplitudes are much reduced and an arrival can be seen at 7.1 s traveltime with opposite polarity. On the vertical component the amplitudes are even further reduced, but weak arrivals may be correlated at 6.95 and 7.25 s.

The instantaneous frequencies for each of the sections from Figure 2 are shown in Figures 3. In the two P-wave windows the dominant frequencies center between 6 and 9 Hz on each component, and a small decrease of the main frequency with offset can be recognized. Similar frequencies are seen on the vertical and north component on the converted phase, but here the east component contains higher frequencies as well, with a peak around 15 Hz. Since for the P-waves the east component does not show any anomaly, instrument or coupling effects can be excluded.

Figures 2 and 3, see next pages.

Figure 2: Left: Display of data in the 36-38 km, 2-3 s window. A constant scaling factor has been used for all traces.
Top: vertical component; Middle: east component; Bottom: north component.
Middle: Display of data in the 46-48 km, 2.4-3.4 s window. Other details as above.
Right: Display of data in the 46-48 km, 6.7-7.7 s window. Other details as above.

Figure 3: Instantaneous frequencies from the data displayed in Figure 2.

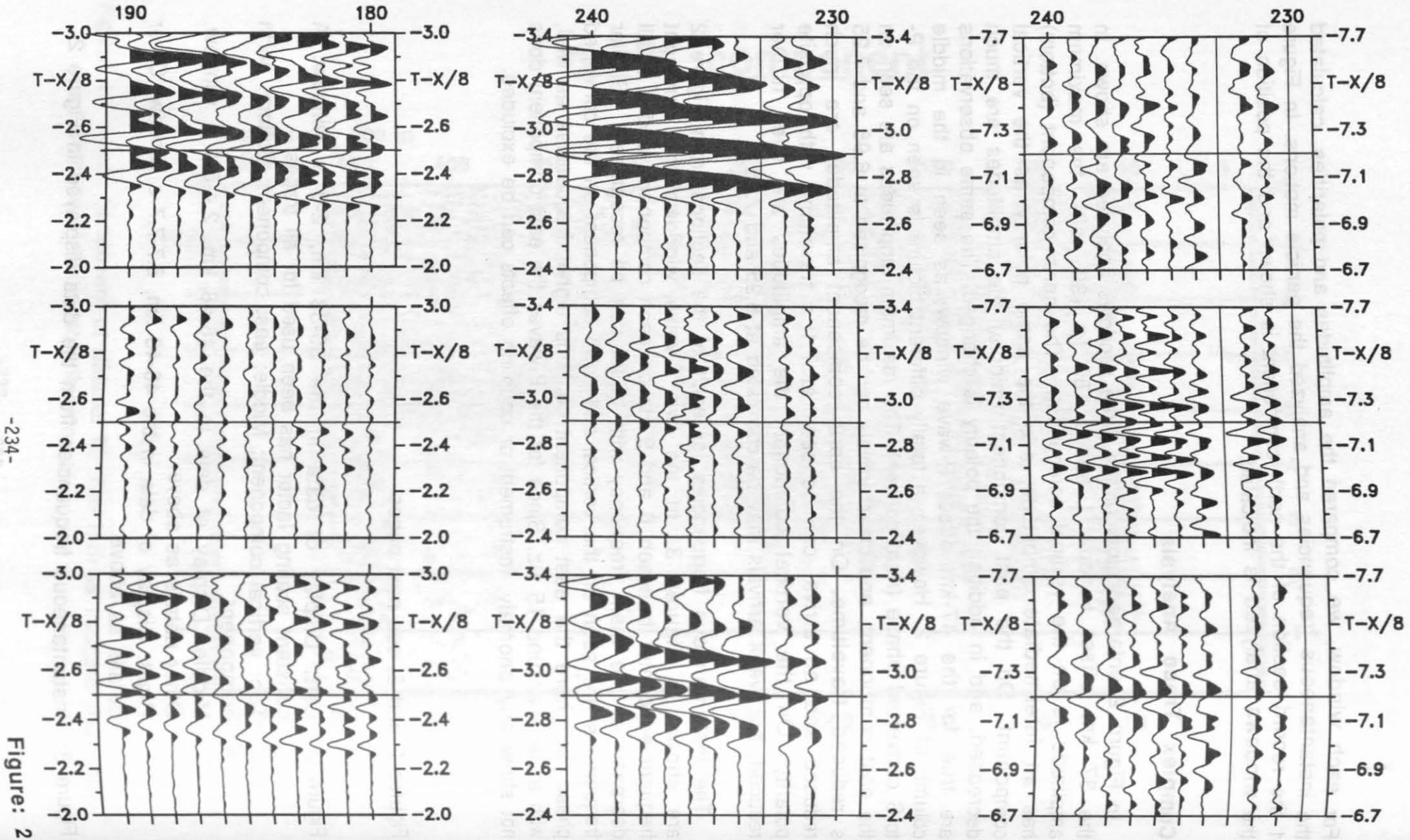

Figure: 2

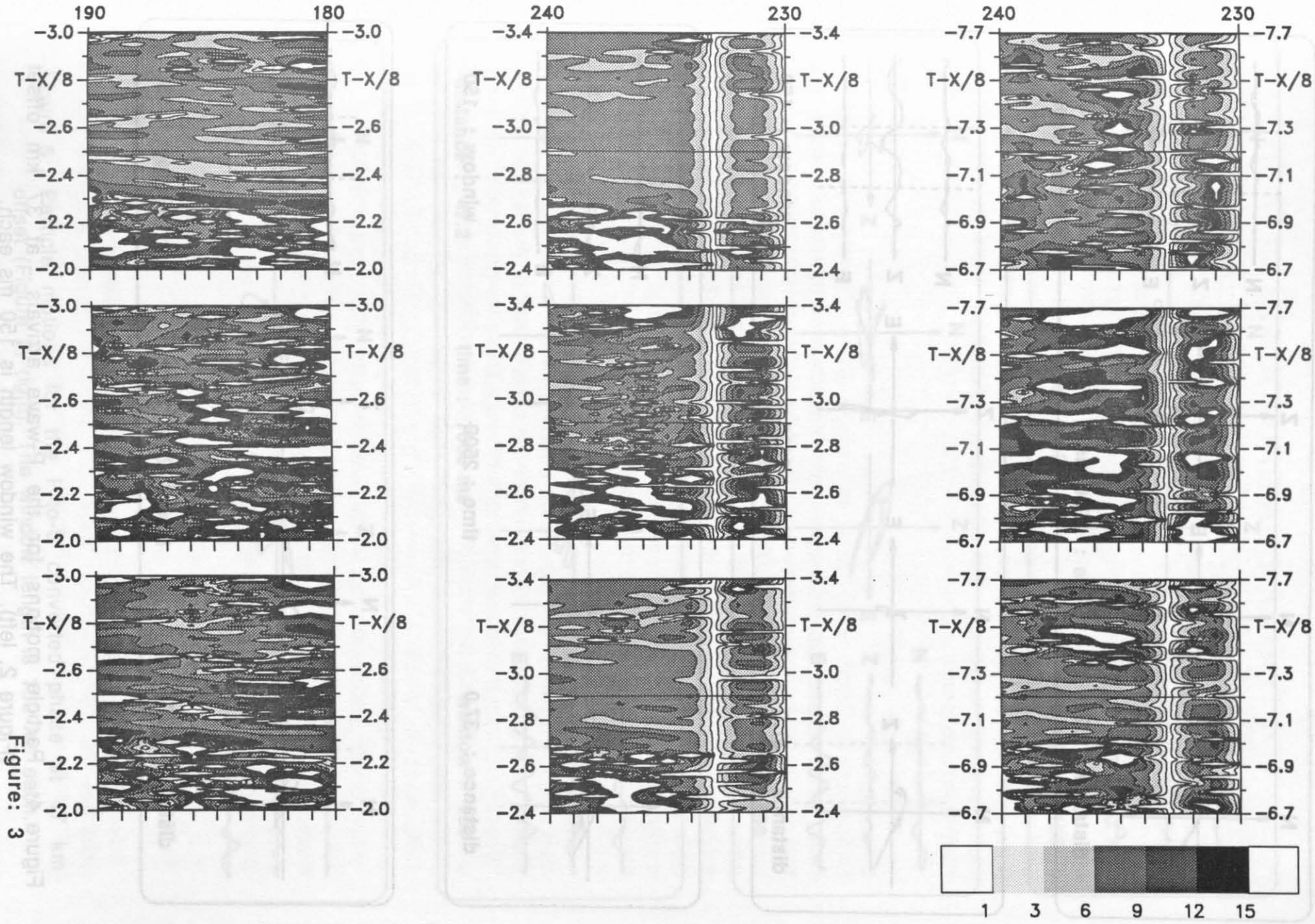
190
180
240
230
240
230
T-X/8
-3.0
-2.6
-2.4
-2.2
-2.0
-3.4
-3.0
-2.8
-2.6
-2.4
-7.7
-7.3
-7.1
-6.9
-6.7
1
3
6
9
12
15

Figure: 3

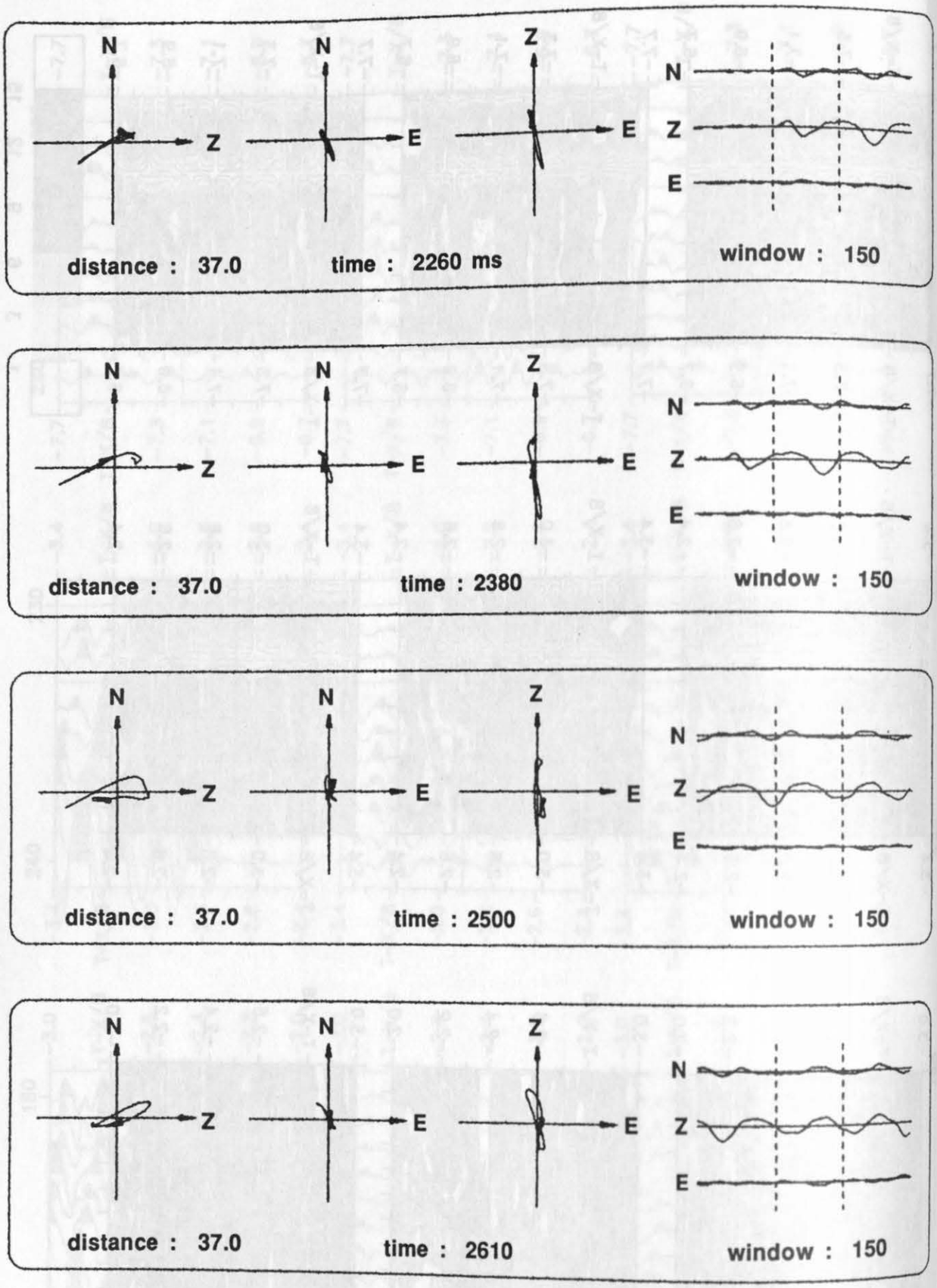

Figure 4: Particle motions for the P-wave arrivals at 37 km offset (Figure 2, left). The window length is 150 ms each.

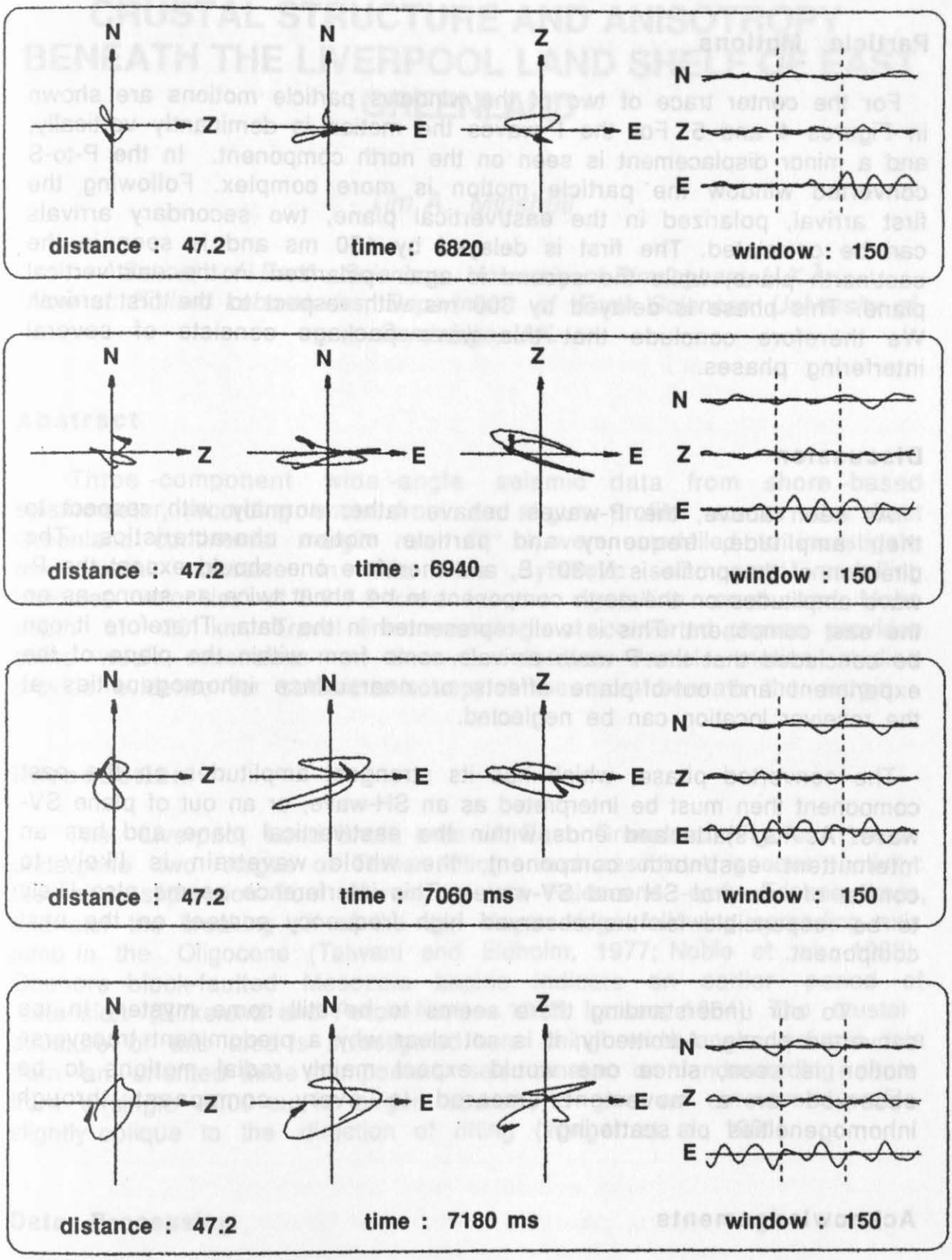

Figure 5: Particle motions for the P-to-S converted phase at 47 km offset (Figure 2, right). The window length is 150 ms each.

Particle Motions

For the center trace of two of the windows particle motions are shown in Figures 4 and 5. For the P-waves the motion is dominantly vertically, and a minor displacement is seen on the north component. In the P-to-S converted window the particle motion is more complex. Following the first arrival, polarized in the east/vertical plane, two secondary arrivals can be correlated. The first is delayed by 150 ms and is seen in the east/north plane, while the second is again polarized in the east/vertical plane. This phase is delayed by 300 ms with respect to the first arrival. We therefore conclude that this wave package consists of several interfering phases.

Discussion

As seen above, the P-waves behave rather normaly with respect to their amplitude, frequency and particle motion characteristics. The direction of the profile is N 30° E, and therefore one should expect the P-wave amplitudes on the north component to be about twice as strong as on the east component. This is well represented in the data. Therefore it can be concluded that the P-wave arrivals come from within the plane of the experiment and out-of-plane effects or nearsurface inhomogeneities at the receiver location can be neglected.

The converted phase, which has its strongest amplitudes on the east component then must be interpreted as an SH-wave, or an out of plane SV-wave. As its starts and ends within the east/vertical plane and has an intermittent east/north component, the whole wavetrain is likely to consist of several SH and SV-waves. This interference seems also likely to be responsible for the observed high frequency content on the east component.

To our understanding there seems to be still some mystery in the converted phase. Admittedly, it is not clear why a predominant transverse motion is seen, since one would expect mainly radial motions to be observed or a movement smeared to every component through inhomogeneities or scattering.

Acknowledgements

We thank W. Rabbel for providing us with his particle motion plotting program.

CRUSTAL STRUCTURE AND ANISOTROPY BENEATH THE LIVERPOOL LAND SHELF OF EAST GREENLAND

Tim A. Minshull

School of Earth Sciences, University of Birmingham, U.K.[1]
[1]*Now at: Bullard Laboratories, Department of Earth Sciences, University of Cambridge, U.K.*

Abstract

Three-component wide-angle seismic data from shore-based seismometer, recording shots from an airgun profile across the East Greenland continental margin near 72° N, were modelled to investigate the crustal structure in this area. Synthetic seismogram modelling indicates velocities of 5.9-6.8 km/s for the crystalline crust and Moho depth of ~ 20 km. Travel-time modelling of converted phases provides some weak constraints on S-wave velocities. Particle motion studies provide evidence for seismic anisotropy in the crust beneath the margin.

Introduction

The Liverpool Land Shelf area of East Greenland (Figure 1) has undergone two stages of Tertiar rifting and associated igneous activity: the initial separation from Norway in late Paleocene-early Eocene times, and later the breaking off of the Jan Mayen ridge following spreading axis jump in the Oligocene (Talwani and Eldholm, 1977; Noble et al., 1988). Onshore block-faulted Mesozoic basins indicate an earlier period of extension (Birkelund and Perch-Nielsen,1975; Larsen; 1984). The crustal structure of this area is investigated here using wide-angle seismic data from an oriented three-component seismometer on landrecording shots from a single 2000 cu. in. airgun source, to give an unreversed profile slightly oblique to the direction of rifting (Weigel et al., 1991).

Data Processing

The seismic data have a dominant frequency of around 6 Hz, and little coherent energy above 20 Hz. Since the water depth beneath the shooting ship was around 300 m along most of the profile, corresponding to a water bottom multiple frequency of around 2.5 Hz, the 6 Hz energy must be attributed to bubble pulse reverberations

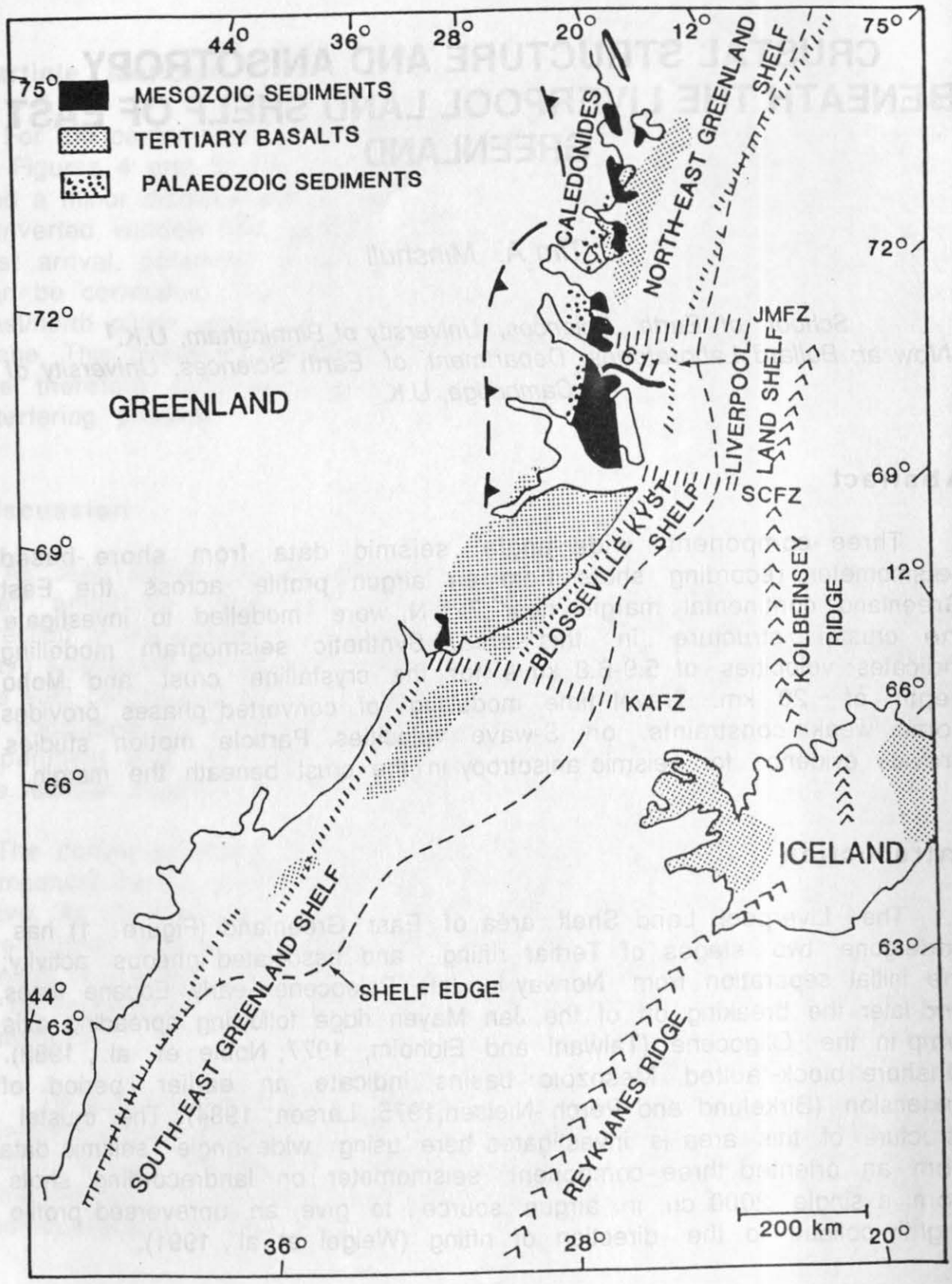

Figure 1: Main structural provinces of the East Greenland margin. Bold line (611) marks profile studied. Hachures mark an inferred continent -ocean boundary. Direction of extension during rifting may be taken as parallel to the fracture zones and hence slightly oblique to the ship´s track. KAFZ is Kangerdluqssuaq Fracture Zone , SCFZ is Scoresby Sund Fracture Zone and JMFZ is Jan Mayen Fracture Zone. Modified from Larsen (1984).

of the large single airgun source. Prior to plotting record sections the data were bandpass filtered (2-20 Hz) and resampled to 10 ms. The filtered data show clear refracted first arrivals out to 70 km range, wide-angle reflections from the Moho at 45-95 km range, and strong converted shear waves out to 40 km range (Figure 2). There are also a large number of interfering wide-angle reflections from within the crust. Deconvolution trials with standard length operators (a few hundred ms) gave little improvement in the section. However, predictive deconvolution with a long (5 s) operator and a delay of 170 ms successfully compressed the long source signature and significantly improved the temporal resolution of the data (Figure 3). This exceptionally long operator was needed to deconvolve high amplitude elements of the source signature with very long delays. In particular, the SmS phase emerged from the background noise in the z-component data, as well as becoming more clearly resolved in the horizontal components.

Synthetic Seismogram Modelling

P-wave travel-times were picked from the z-component data; some mode-converted arrivals were more clearly identified in the horizontal components. Synthetic seismogram modelling was carried out using the Maslov method (Chapman and Drummond, 1982), running on an Apollo DN10000, which allowed raytracing through complex, laterally heterogeneous models in a few seconds of real time. Inhomogeneous layers are divided into triangles with linear velocity gradients and velocities specified at vertices. Efficient use of the program required raytracing from the receiver to the source. This approach is valid for all travel-time modelling, and should be valid, at least approximately, for modelling P-wave amplitudes.

Figures 2, 3 a, b, and c, see next pages.

Figure 2: Bandpass filtered (2-20 Hz) and resampled Z-component data. Data are plotted with a gain proportional to range, but no trace balancing and reduced at 8 km/s.

Figure 3a: Z-component data after predictive deconvolution with a 5 s operator and a gap of 170 ms.

Figure 3b: N-component data after predictive deconvolution.

Figure 3c: E-component data after predictive deconvolution. Note high amplitude of the PmS phase.

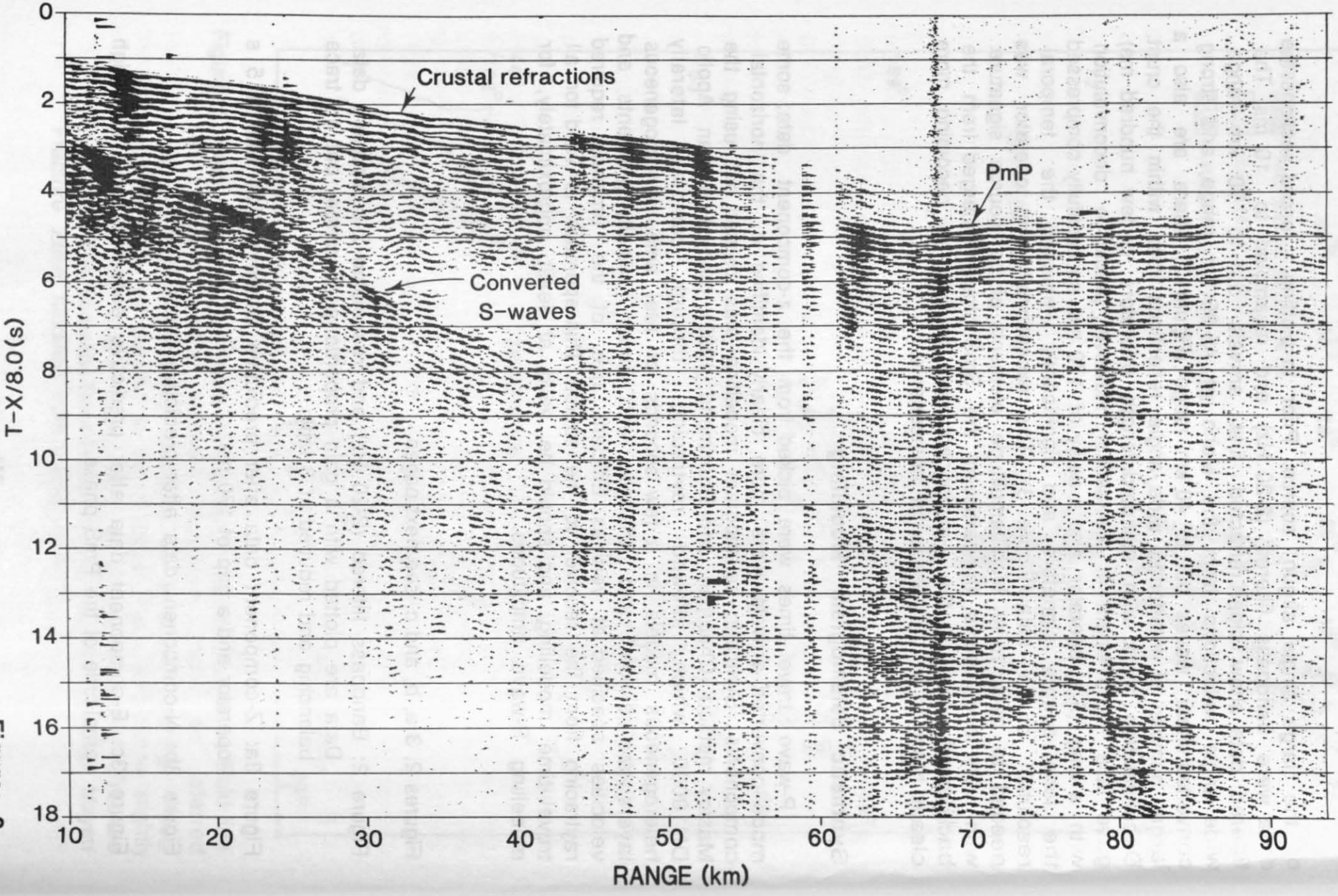
Crustal refractions
PmP
Converted
S-waves
T-X/8.0(s)
RANGE (km)
0
2
4
6
8
10
12
14
16
18
10
20
30
40
50
60
70
80
90

Figure: 2

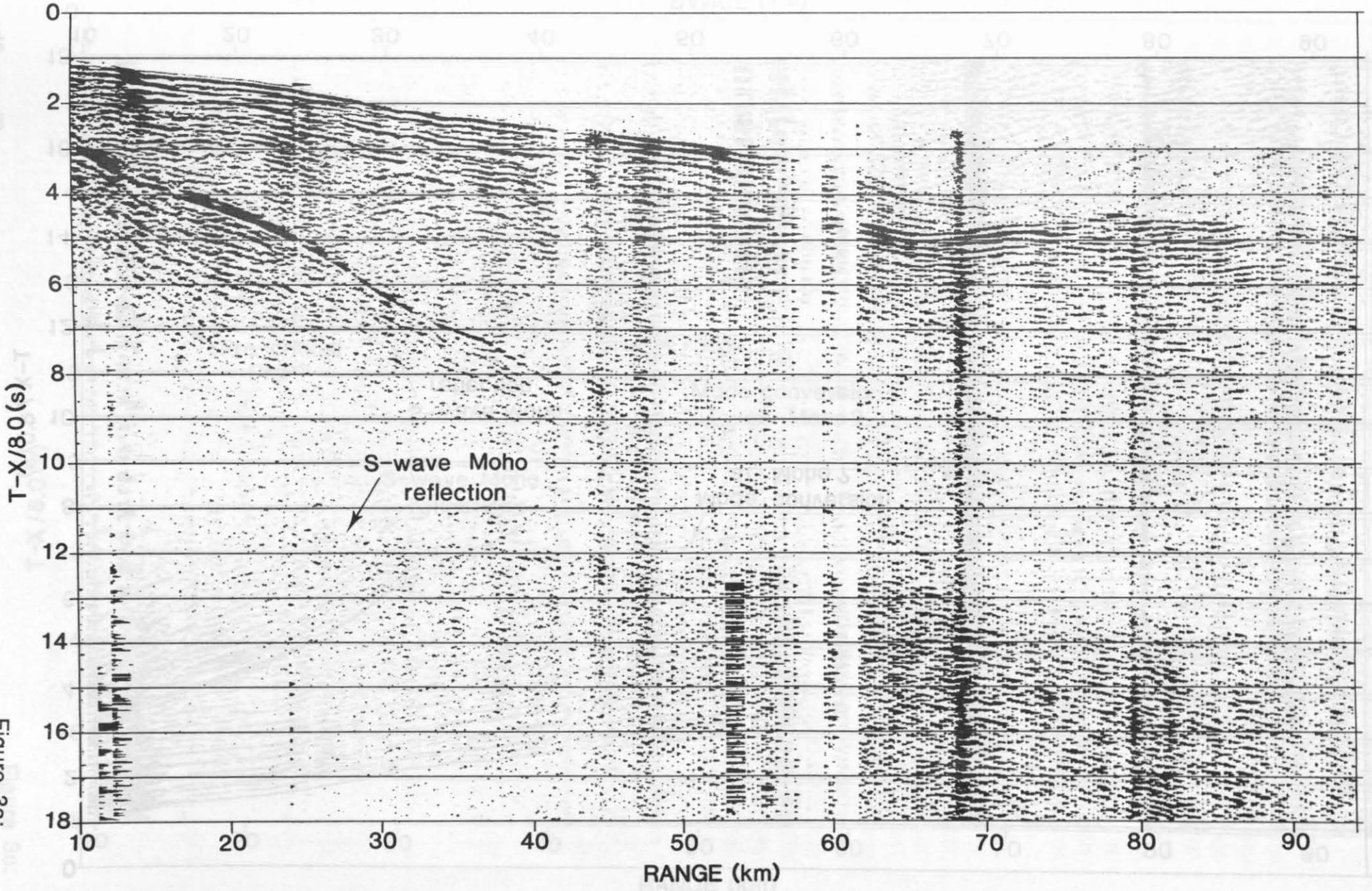
0
2
4
6
8
10
12
14
16
18
T-X/8.0 (s)
S-wave Moho
reflection
10
20
30
40
50
60
70
80
90
RANGE (km)

Figure 3a:

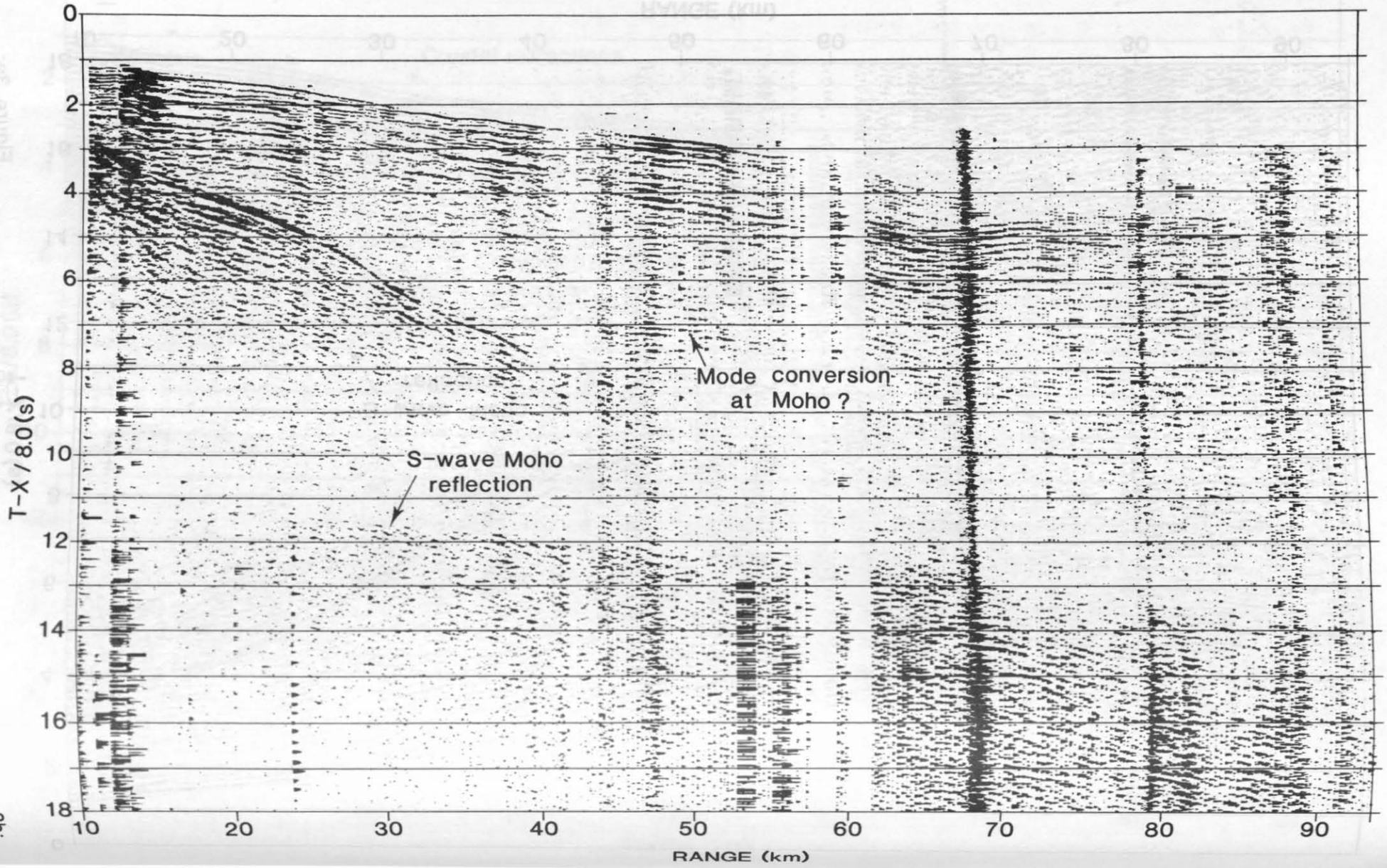
0
2
4
6
8
10
12
14
16
18
T-X / 8.0(s)
10
20
30
40
50
60
70
80
90
RANGE (km)
Mode conversion
at Moho ?
S-wave Moho
reflection

Figure 3b:

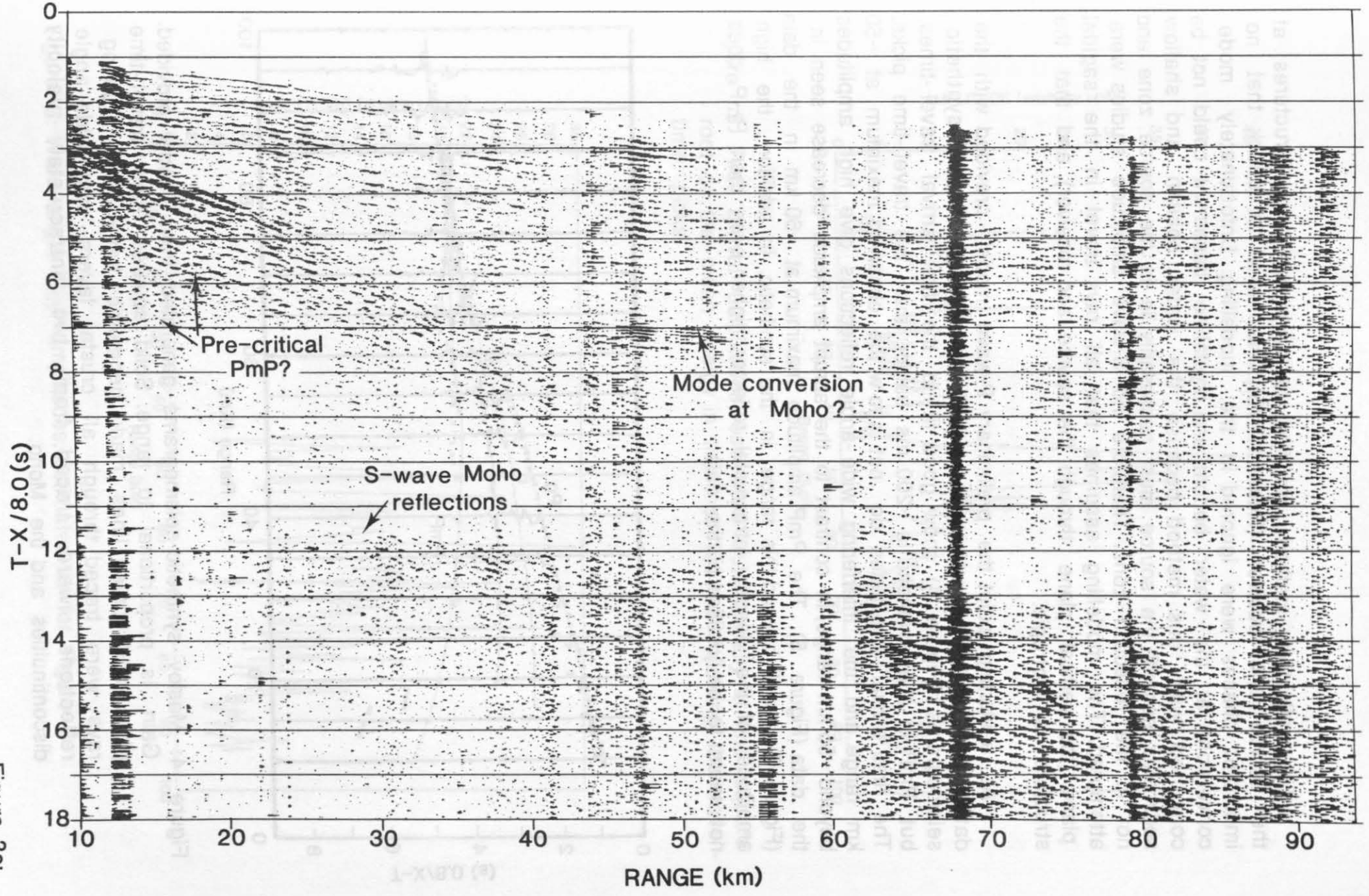
0
2
4
6
8
10
12
14
16
18
T-X/8.0(s)
Pre-critical
PmP?
Mode conversion
at Moho?
S-wave Moho
reflections
10
20
30
40
50
60
70
80
90
RANGE (km)

Figure 3c:

The reflectivity method, modified to allow different structures at the source and receiver (Kennett1975), was used to check that no important phases were ignored in the modelling. Unfortunately mode conversions at the water bottom and crystalline basement could not be computed with this method because the water column and shallow sediments beneath the source must necessarily lie in the source zone and not in the reflection zone. Therefore no S-wave amplitude studies were attempted. The modelling assumes that all rays travel in the sagittal plane (the vertical plane through the source and receiver), and that the structure is isotropic.

At a starting point the preliminary P-wave model provided with the data was digitized and raytraced. The resulting Maslov synthetic seismograms (Figure 4) show good fit to the first arrival travel-times, but PmP in the synthetic is ~200 ms earlier than the travel-time picks. The first arrival amplitudes do not show the observed maximum at ~50 km range and the interfering wide-angle reflections give high amplitudes beyond ~55 km range, in contrast to the abrupt amplitude decrease seen in the data (Figure 5). The PmP amplitude maximum at ~60 km in the data (Figure 6) is well beyond this range in the synthetic. In addition, the high amplitude of the deeper intracrustal reflector, higher even than P_mP, does not seem to be justified by the data.

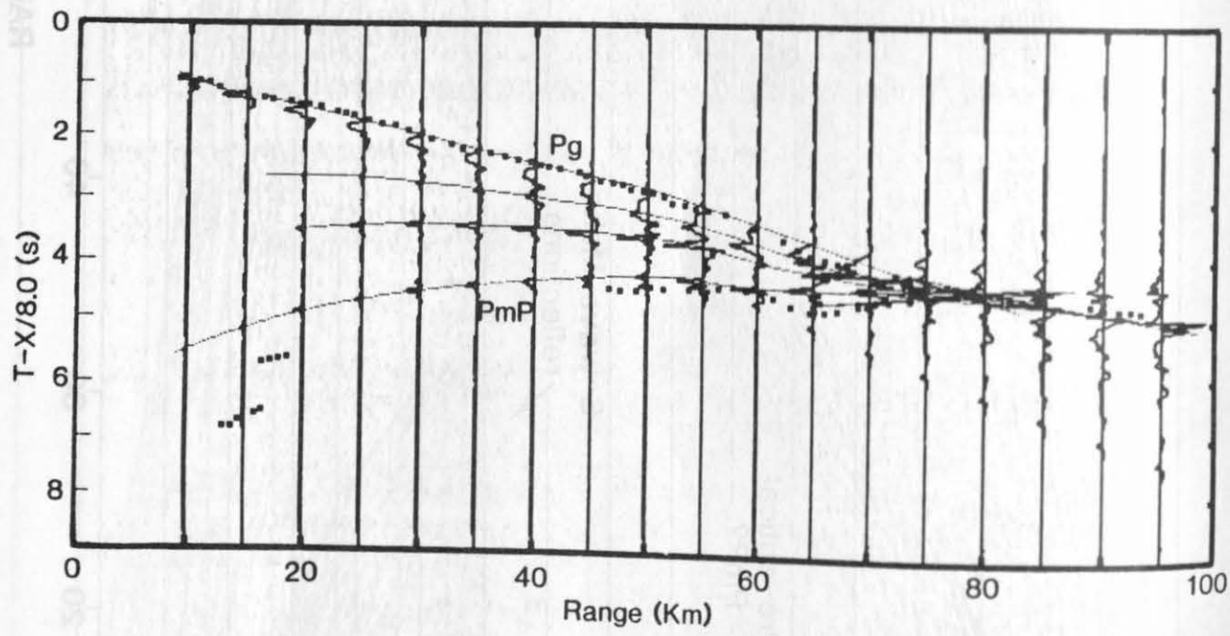

Figure 4: Maslov synthetic seismograms generated from model provided. Gain is proportional to range. Solid squares mark travel-time picks, and curved lines mark geometric travel-times. Turning rays were traced through all crustal layers, and wide-angle reflections were traced from two intracrustal velocity discontinuities and the Moho.

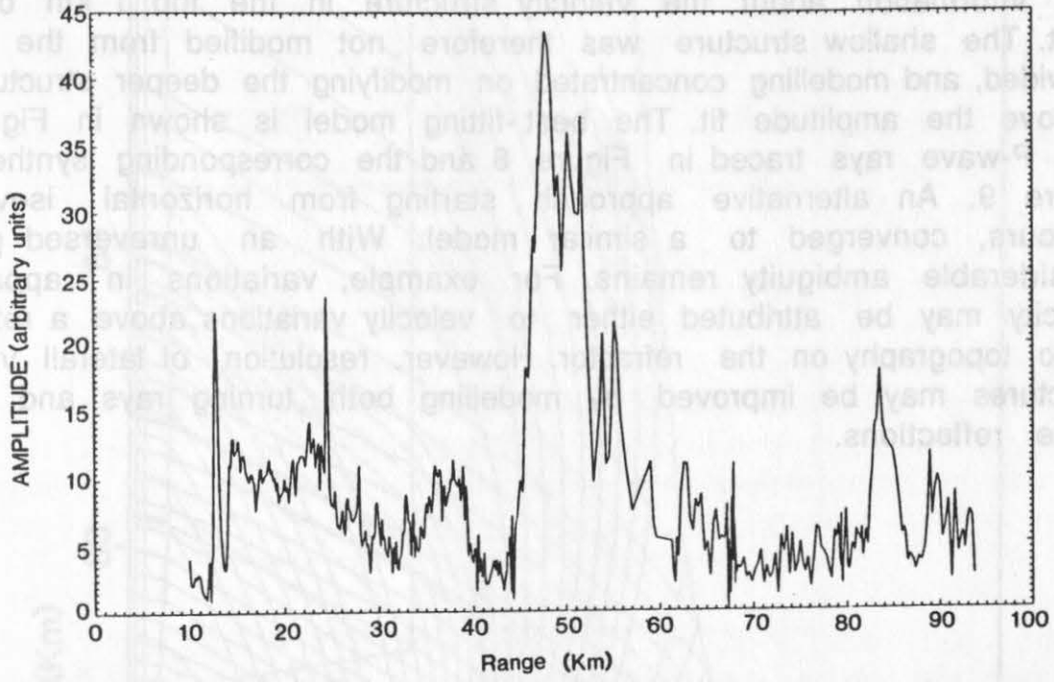

Figure 5: First arrival amplitudes, estimated automatically at the square root of the mean energy in the first 100 ms following the travel-time picks.

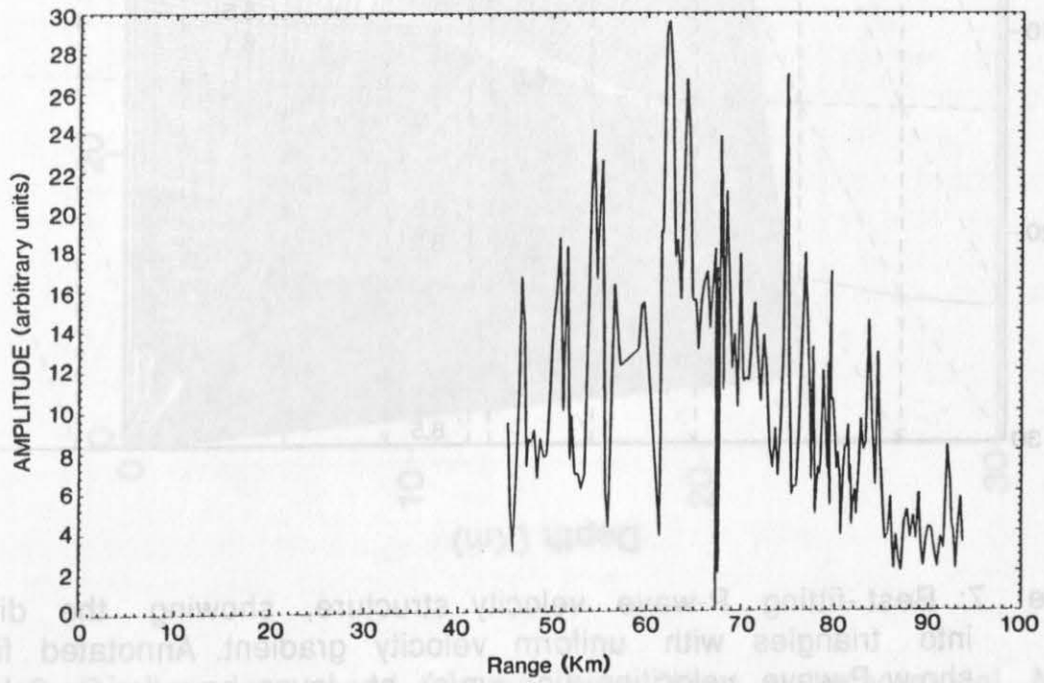

Figure 6: Wide-angle P_mP amplitudes, estimated as for Figure 5.

With a minimum source-receiver offset of ~10 km, the data give little information about the velocity structure in the top 1 km of the crust. The shallow structure was therefore not modified from the model provided, and modelling concentrated on modifying the deeper structure to improve the amplitude fit. The best-fitting model is shown in Figure 7, with P-wave rays traced in Figure 8 and the corresponding synthetic in Figure 9. An alternative approach, starting from horizontal isovelocity contours, converged to a similar model. With an unreversed profile, considerable ambiguity remains. For example, variations in apparent velocity may be attributed either to velocity variations above a refractor or to topography on the refractor. However, resolution of laterall varying structures may be improved by modelling both turning rays and wide-angle reflections.

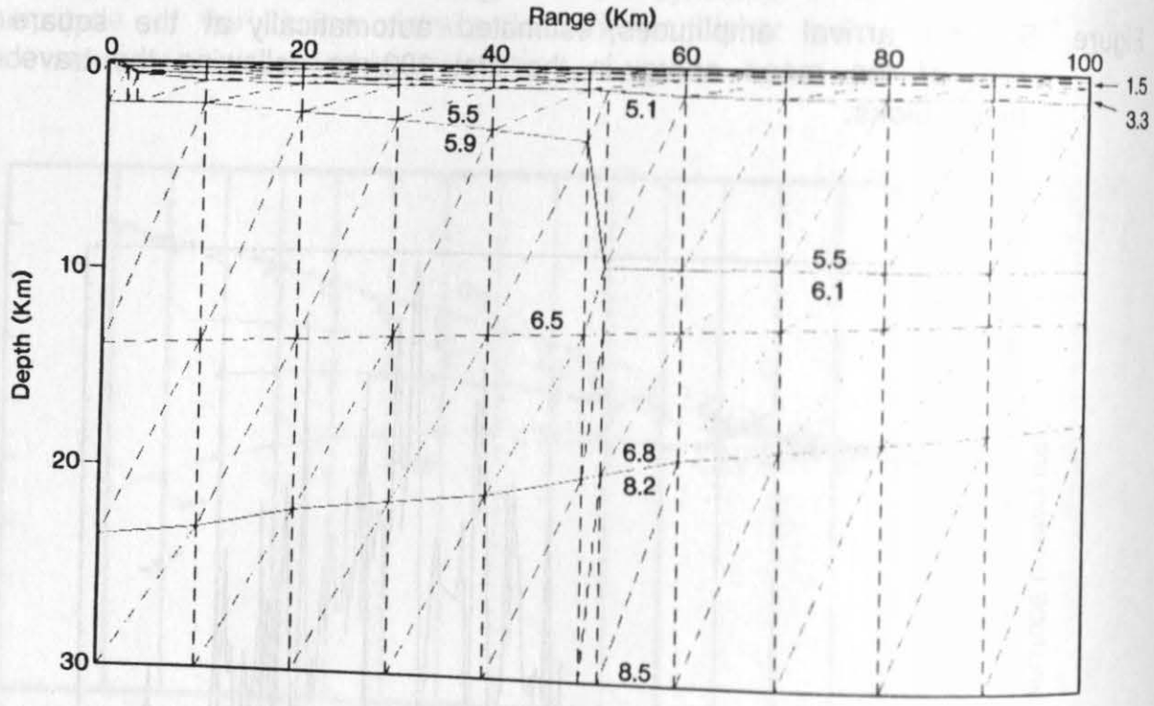

Figure 7: Best-fitting P-wave velocity structure, showing the division into triangles with uniform velocity gradient. Annotated figures show P-wave velocities (in km/s) at layer boundaries; velocities in inhomogeneous layers are linearly interpolated between these values. The main difference from the model provided is the absence of a high velocity basal layer.

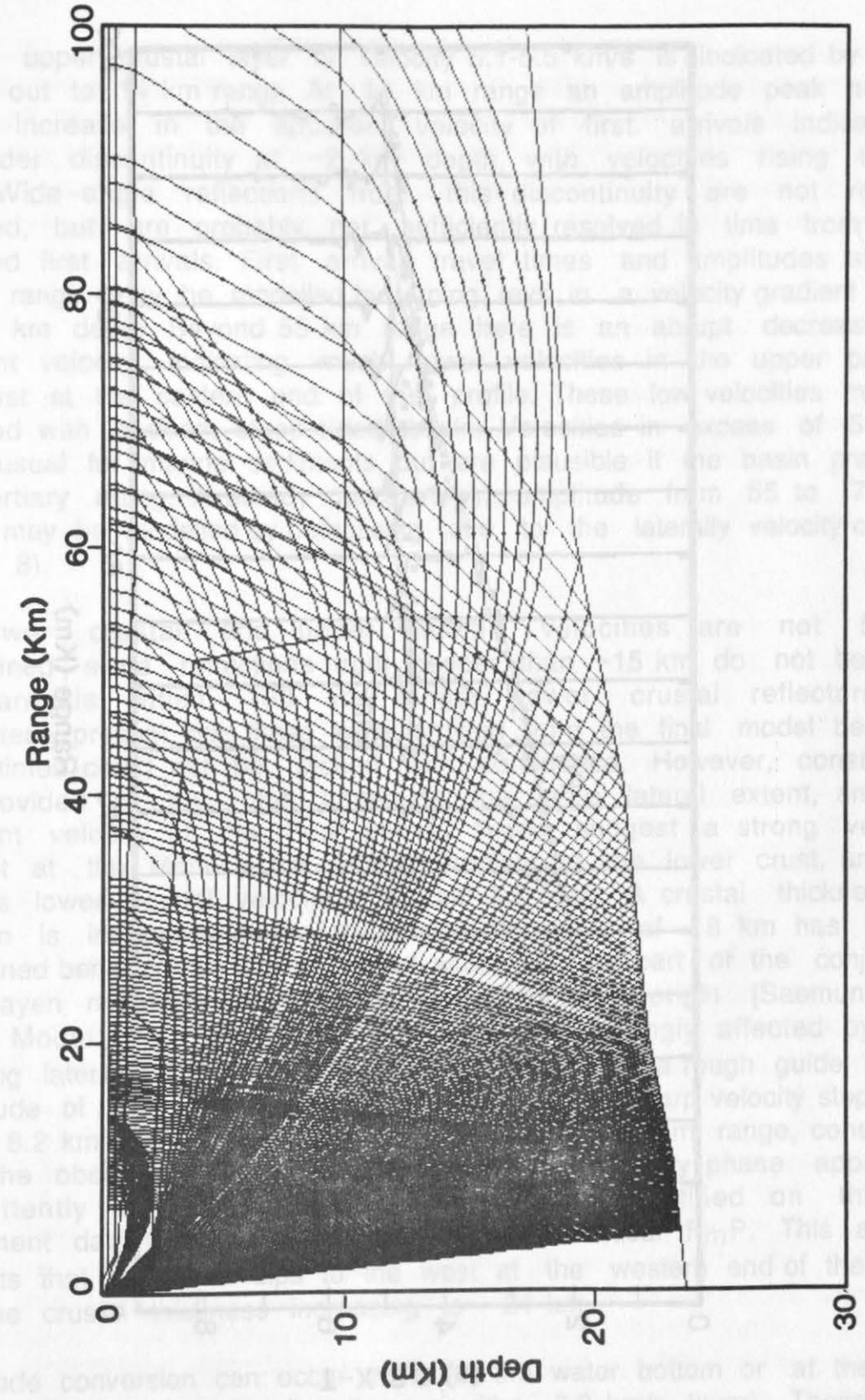

Figure 8: P-waves ray-traced through best-fitting velocity model. Note the defocusing of rays at the edge of the basin. Missing ray at ~35 km range is due to numerical problems close to a triangle vertex.

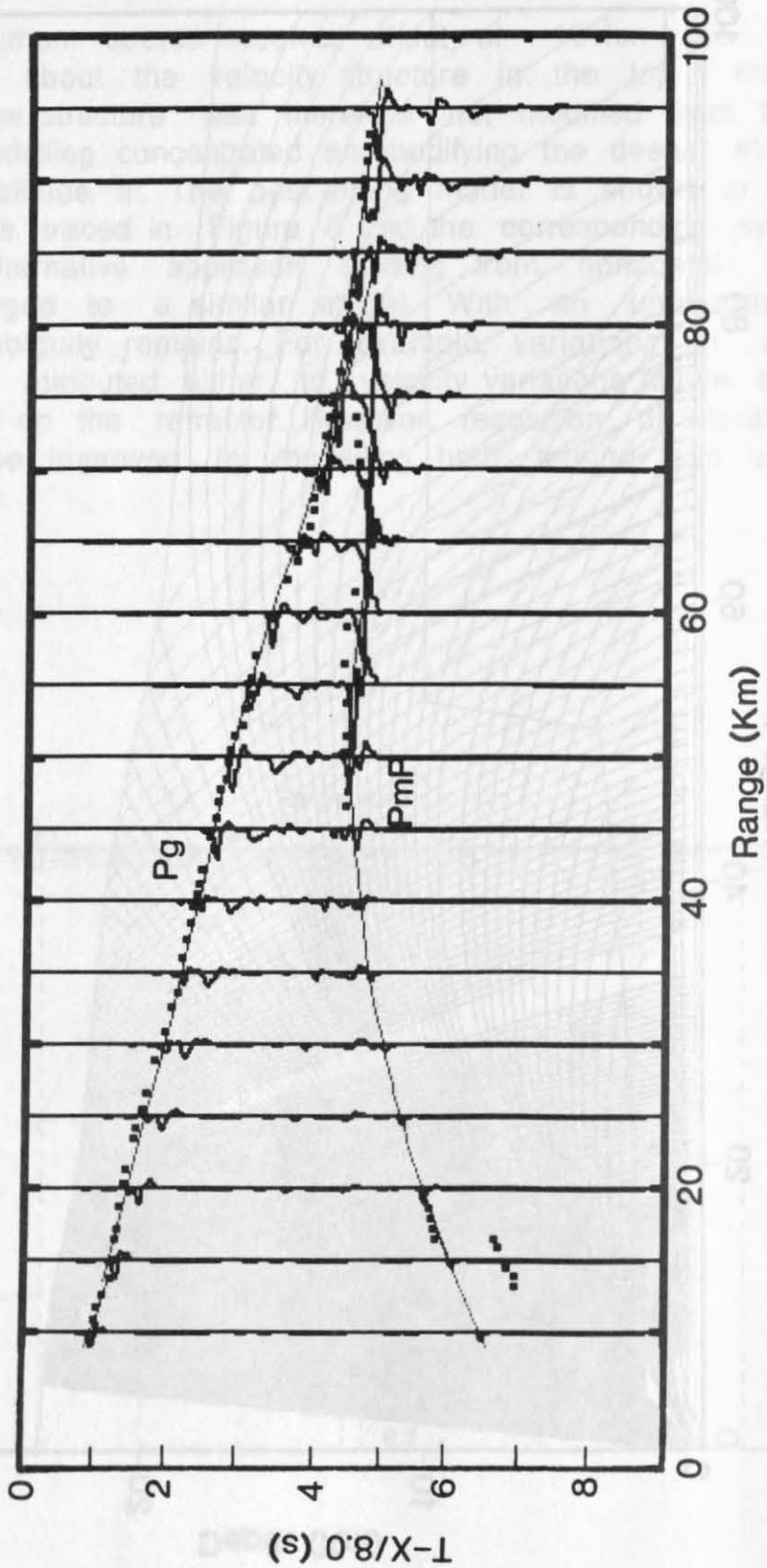

Figure 9: Synthetic seismograms derived from best-fitting model. First arrival amplitude maximum is at the correct range (~50 km) but not as large as the observed maximum (Figure 5). P_mP amplitude maximum is also correctly located.

An upper crustal layer of velocity 5.1-5.5 km/s is indicated by first arrivals out to 14 km range. At 14 km range an amplitude peak and an abrupt increase in the apparent velocity of first arrivals indicates a first-order discontinuity at ~2 km depth, with velocities rising to ~6 km/s. Wide-angle reflections from this discontinuity are not readily identified, but are probably not sufficiently resolved in time from the refracted first arrivals. First arrival travel-times and amplitudes at 14-55 km range may be modelled by turning rays in a velocity gradient down to ~10 km depth. Beyond 55 km range there is an abrupt decrease in apparent velocity, indicating much lower velocities in the upper part of the crust at the eastern end of the profile. These low velocities may be modelled with a deep, steep-sided basin. Velocities in excess of 5 km/s are unusual for marine sediments, but are plausible if the basin predates the Tertiary rifting. A steady decrease in amplitude from 55 to 70 km range may be modelled by defocusing due to the laterally velocity change (Figure 8).

Lower crustal and upper mantle velocities are not tightly constrained, since refractions from deeper than ~15 km do not become first arrivals within 100 km range. Lower crustal reflectors are undoubtedly present, but these were omitted from the final model because travel-times could not be picked with confidence. However, constraints are provided by the high amplitude, the large lateral extent, and the apparent velocity of the PmP phase. These suggest a strong velocity contrast at the Moho, a low velocity gradient in the lower crust, and an average lower crustal velocity of around 6.7 km/s. A crustal thickness of ~20 km is indicated. A similar crustal thickness of 18 km has been determined beneath Jan Mayen island, which may be part of the conjugate Jan Mayen microcontinent, or may be oceanic in origin [Saemundsson, 1986]. Model P_mP amplitude variations are strongly affected by the overlying lateral velocity changes, but can still give a rough guide to the magnitude of the velocity contrast at the Moho. A sharp velocity step from 6.8 to 8.2 km/s gives an amplitude maximum at 60 km range, consistent with the observed location (Figure 6). A high velocity phase appearing intermittently at short ranges, most readily identified on the E-component data (Figure 3c), appears to be precritical P_mP. This arrival suggests that the Moho dips to the west at the western end of the profile with the crustal thickness increasing to ~24 km.

Mode conversion can occur either at the water bottom or at the base of the thin low-velocity sediment cover (the 3.3 km/s layer). These two possibilities cannot be resolved without detailed knowledge of the sediment velocity structure. It is possible that conversion takes place at both interfaces: raytracing both conversions in the correct direction indicates that similar amplitudes arise in both cases. Mode conversion at the water bottom was assumed in raytracing.

Fluctuations in the apparent velocity of the S-wave arrival at ranges where none are seen in the P-wave arrival suggest lateral variations in Poisson's ratio, since the ray-paths of the two arrivals must be very similar. An approximate travel-time fit may be obtained with a value of around 0.25 in the crystalline crust, if values are higher in the two sediment layers (Figure 10).

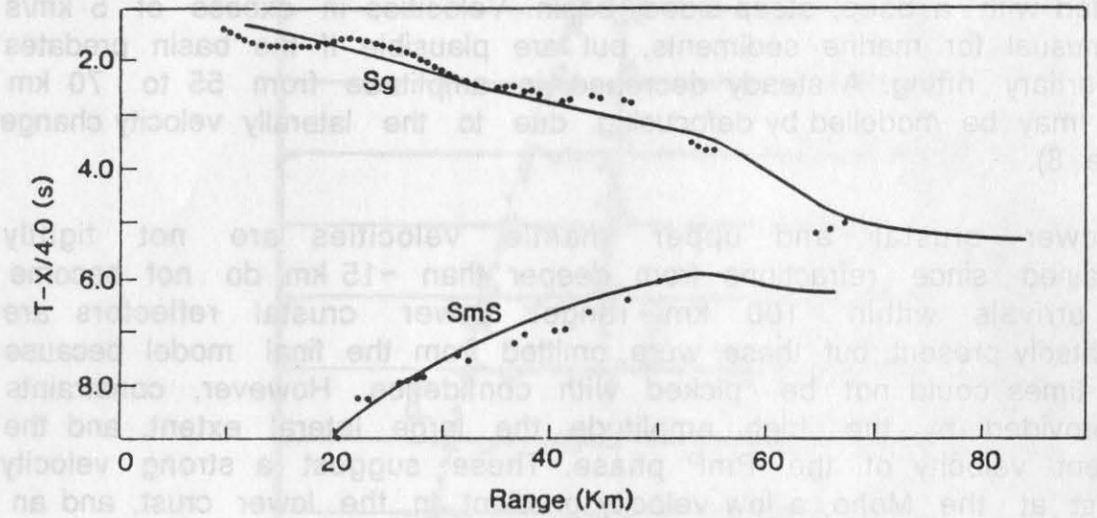

Figure 10: S-wave travel-time fit. Dots mark travel-time picks, and solid line marks geometric travel-times. Model boundaries as for P-waves with Poisson's ratio of 0.33 in the shallow sediments (3.3 km/s layer), 0.305 in the high-velocity sediments, and 0.25 in the crystalline crust.

A phase with apparent velocity close to 8 km/s appears about 4 s after the first arrivals at 45-50 km range, and intermittently at shorter ranges. This phase appears to represent energy which has been mode-converted at the Moho. Synthetic seismogram modelling with the reflectivity program suggests that such energy should be detectable if the Moho is a sharp velocity discontinuity, but the amplitude is unexpectedly high. The phase appears prominently in the horizontal components, but is barely detected in the vertical component, suggesting that the energy travels down through the crust as P-waves and up as S-waves (ie P_mS). Raytracing through the velocity structure derived from P-waves and converted S-waves gives a good fit to the apparent velocity of the phase, but it appears unexpectedly early, requiring, for example, either a 20% higher S-wave velocity throughout the crust, or a substantially shallower Moho reflector (Figure 11). This inconsistency may be an artefact of the

underlying assumption of isotropic velocities, an assumption which is probably not applicable to this area (see below). Alternatively, some or all of the mismatch may arise from Moho topography. The P_mS reflection points are closer to the receiver than those for postcritical P_mP and S_mS, and the modelled Moho topography in this region is based on uncertain travel-time picks for precritical P_mP.

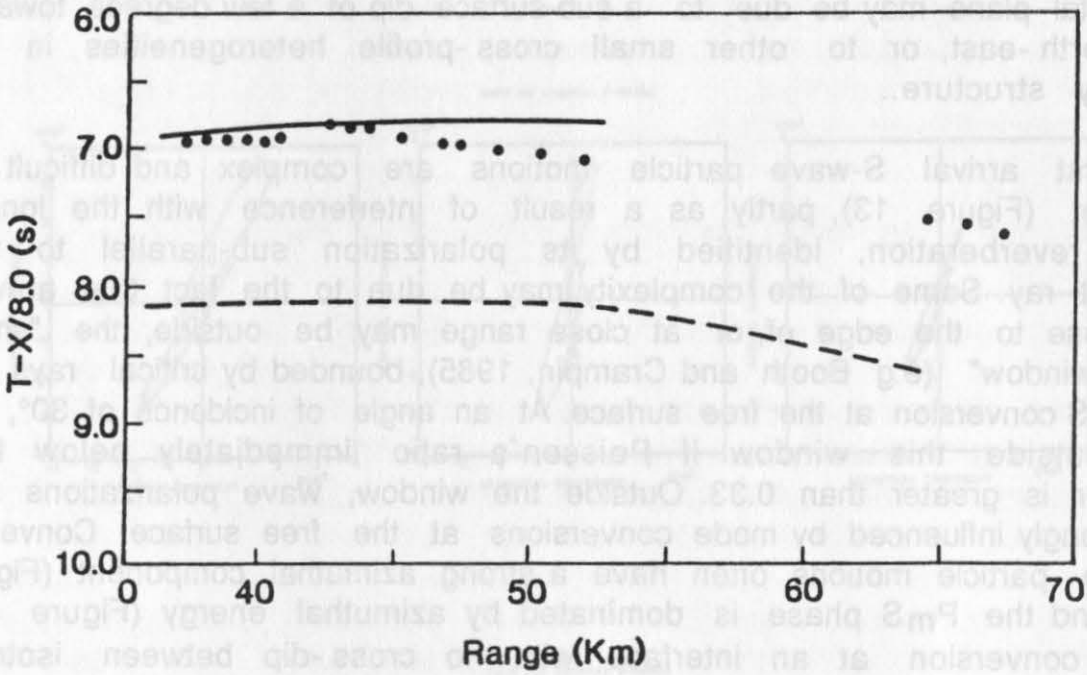

Figure 11: Two attempts to fit P_mS travel-times. Dots mark picks, and lines geometric travel-times. Dashed line corresponds to the velocity model of Figures 7-10. Solid line corresponds to model with S-wave velocities 20% higher (i.e implausibly high); numerical problems prevented raytracing to longer ranges through this model.

Particle Motions

Particle motions were studied using bandpass filtered data without deconvolution, since a statistical deconvolution method was used, and therefore the operators applied to different components cannot be guaranteed to be the same. Horizontal components were resolved into radial (along the source-receiver line, positive away from the source) and azimuthal (positive to the right, as seen from the source) components using the seismometer location and digitized ship's track.

First arrival P-wave particle motions are polarized as an angle around 30° to the vertical and have a very small azimuthal component (Figure 12). The particle motion direction at a free surface results from the combined effects of incident and reflected wavefield, and may be related to the direction of arrival of the incident ray by simple analytic formulae (e.g Aki and Richards, 1980). For typical Poisson's ratios of 0.25-0.35, these two directions differ by no more than a few degrees for an angle of incidence of around 30°, and an angle of incidence of 30° suggests a surface velocity of around 3 km/s , unless there are large near-surface dips. The small azimuthal component of particle motion in the horizontal plane may be due to a sub-surface dip of a few degrees towards the north-east, or to other small cross-profile heterogeneities in the velocity structure..

First arrival S-wave particle motions are complex and difficult to interpret (Figure 13), partly as a result of interference with the long P-wave reverberation, identified by its polarization sub-parallel to the incident ray. Some of the complexity may be due to the fact that arrivals are close to the edge of, or at close range may be outside, the "shear-wave window" (e.g Booth and Crampin, 1985), bounded by critical rays for P to S conversion at the free surface. At an angle of incidence of 30°, rays are outside this window if Poisson's ratio immediately below the receiver is greater than 0.33. Outside the window, wave polarizations may be strongly influenced by mode conversions at the free surface. Converted S-wave particle motions often have a strong azimuthal component (Figure 13) , and the P_mS phase is dominated by azimuthal energy (Figure 14). Mode conversion at an interface with no cross-dip between isotropic media can generate only S-waves polarized in the sagittal plane, and the absence of significant transverse P-wave energy suggests that the azimuthal S-wave energy is not due entirely to out-of-plane effects. Some azimuthal S-wave energy may be generated by twisting of S-wave polarizations in a three-dimensional heterogeneous medium; however, this effect is not large for realistic Earth models (Cormier, 1984). Near-surface scattering may also generate significant azimuthal energy.

Alternatively the azimuthal energy may be attributed to the effects of wave propagation in an anisotropic medium. One possible source of anisotropy in the crystalline crust could be the presence of aligned cracks perpendicular to the direction of extension during the Tertiar rifting episodes. Such a cracked medium has hexagonal symmetry with a horizontal symmetry axis. S-waves split into two components: qSP polarized within the (vertical) symmetry plane, and qSR orthogonal to this plane (e.g Crampin, 1981). Each component has a group velocity dependent on propagation direction. If the line of the profile is close to perpendicular to the cracks, mode conversion at the water bottom will excite mainly the qSR component. In a region of high velocity gradients (~0.5-1.0 s^{-1}) such as the uppermost crust, wave propagation along

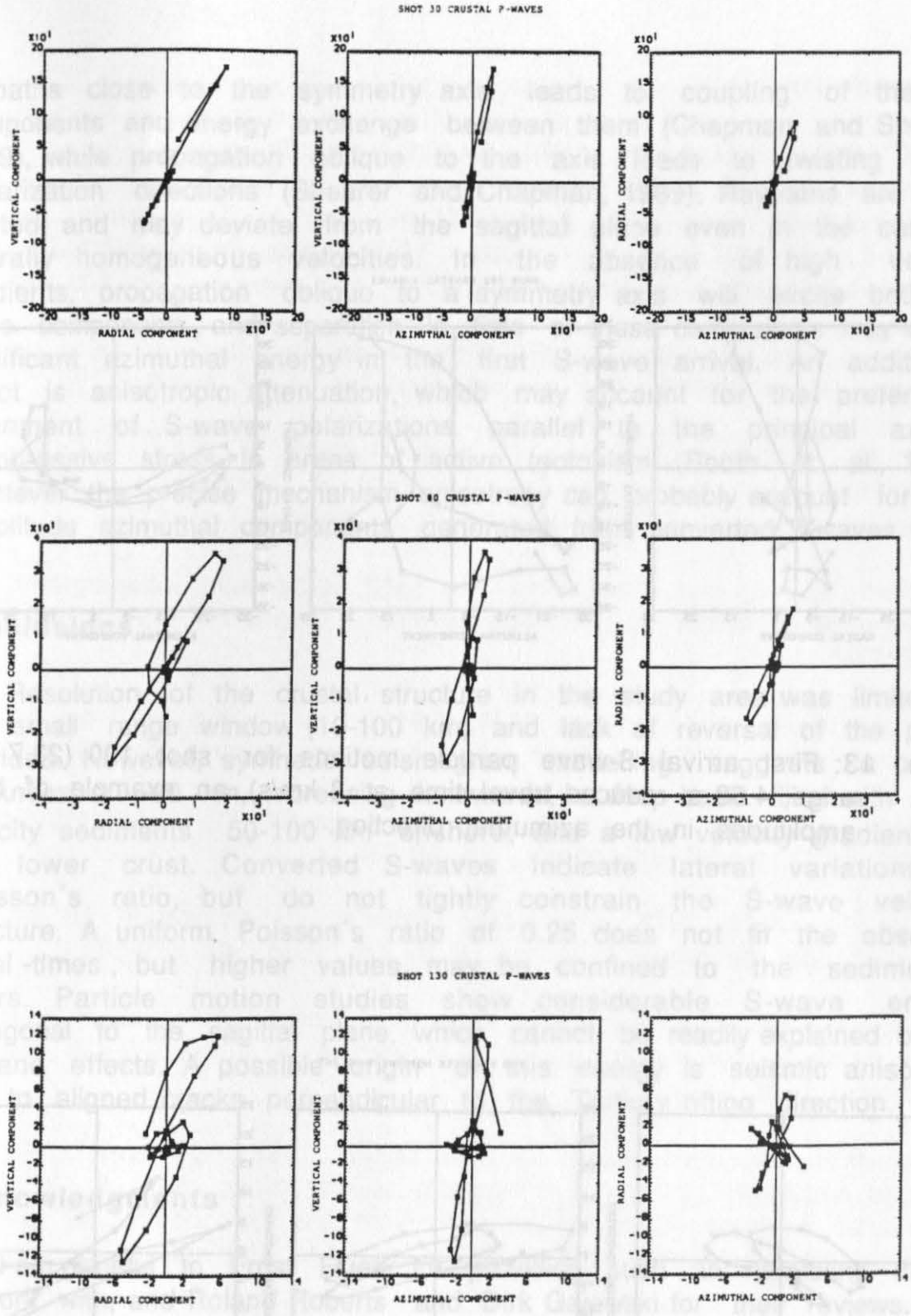

Figure 12: First arrival P-wave particle motions for three selected shots. Thirty samples following the travel-time pick are plotted, with each sample marked. See text for definitions of "radial" and "azimuthal". Ranges and travel-time picks (reduced at 8 km/s) are: 13.6 km and 1.19 s for shot 30, 20.6 km and 1.43 s for shot 80, and 28.0 km and 1.81 s for shot 130. Data are bandpass filtered but otherwise unprocessed. Note that there is little motion in the azimuthal direction.

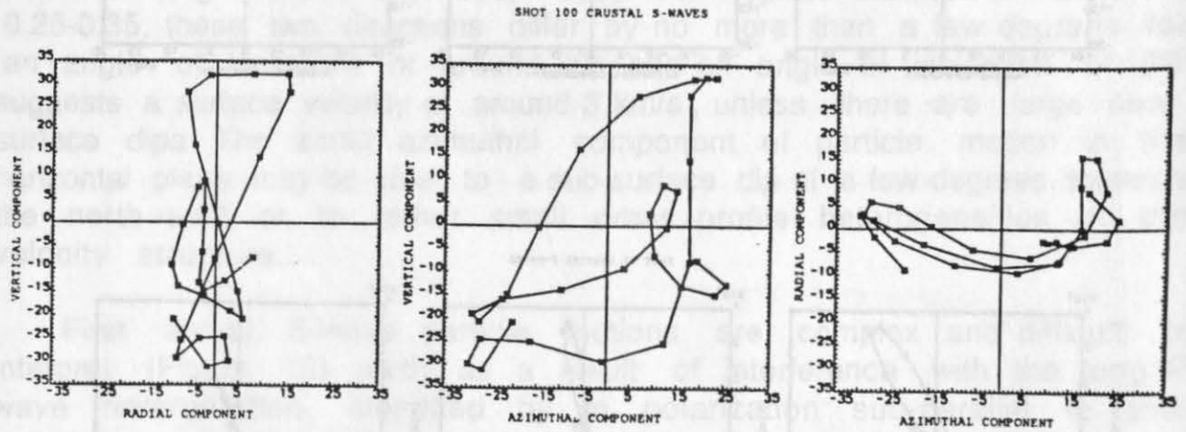

Figure 13: First arrival S-wave particle motions for shot 100 (23.7 km range, 4.68 s reduced travel-time at 8 km/s), an example of high amplitudes in the azimuthal direction.

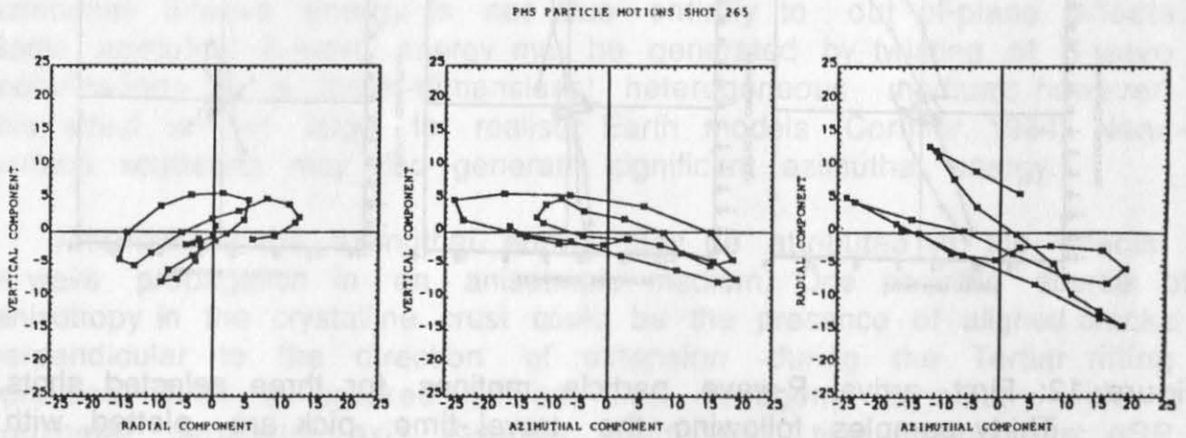

Figure 14: P_mS particle motions at shot 235 (42.2 km range, 6.86 s reduced travel-time at 8 km/s) showing polarization close to the azimuthal direction.

raypaths close to the symmetry axis leads to coupling of the two components and energy exchange between them (Chapman and Shearer, 1989), while propagation oblique to the axis leads to twisting of the polarization directions (Shearer and Chapman, 1989). Raypaths are also twisted, and may deviate from the sagittal plane even in the case of laterally homogeneous velocities. In the absence of high velocity gradients, propagation oblique to a symmetry axis will excite both S-wave components, and separation in time of these components may lead to significant azimuthal energy in the first S-wave arrival. An additional effect is anisotropic attenuation, which may account for the preferential alignment of S-wave polarizations parallel to the principal axis of compressive stress in areas of active tectonism (Booth et al., 1985). Whatever the precise mechanism, anisotropy can probably account for high amplitude azimuthal components generated from converted S-waves.

Conclusions

Resolution of the crustal structure in the study area was limited by the small range window (10-100 km) and lack of reversal of the profile provided. However, synthetic seismogram modelling suggests a crustal thickness of ~20 km, increasing landwards, a deep basin filled with high-velocity sediments 50-100 km offshore, and a low velocity gradient in the lower crust. Converted S-waves indicate lateral variations of Poisson´s ratio, but do not tightly constrain the S-wave velocity structure. A uniform Poisson´s ratio of 0.25 does not fit the observed travel-times, but higher values may be confined to the sedimentary layers. Particle motion studies show considerable S-wave energy orthogonal to the sagittal plane, which cannot be readily explained by out-of-plane effects. A possible origin of this energy is seismic anisotropy due to aligned cracks perpendicular to the Tertiary rifting direction.

Acknowledgments

I am grateful to Ernst Flueh for providing such an interesting dataset to work with, and Roland Roberts and Dirk Gajewski for their reviews. The Maslov code was written and supplied by Chris Chapman and David Lyness. Andy Chambers provided a useful background on Greenland, and Jackie Stokes draughted the figures.

References

Aki, K. and P.G.Richards, 1980: Quantitative Seismology; I, p. 141, W.H.Freeman and Co.

Birkelund , T. and K.Perch -Nielsen , 1975: Late Palaeozoic-Mesozoic evolution of central East Greenland; Geology of Greenland , pp. 303-339.

Booth , D.C. and Crampin, S., 1985: Shear -wave polarizations on a curved wavefront at an isotropic free surface; Geophys. J. R. Astr.Soc., 83, 31-45.

Booth , D. , Crampin, S., Evans, R., and Roberts , R., 1985: Shear -wave polarizations near the North Anatolian fault - I Evidence for anisotropy-induced shear -wave splitting; Geophys.J. R. Astr.Soc., 83, 61-73.

Chapman , C. H. and Drummond , R., 1982: Body-wave seismograms in inhomogeneous media using Maslov asymptotic theory; Bull. Seis. Soc. Am., 72, 5277-5317.

Chapman , C. H. and Shearer, P.M., 1989: Ray tracing in azimuthally anisotropic media -II Quas i-shear wave coupling; Geophys. J. , 96, 65-83.

Cormier ,V.F., 1984: The polarization of S-waves in a heterogeneous isotropic Earth model; J.Geophys., 56, 20-23.

Kennett , B. L. N., 1975 : Theoretical seismogram calculation for laterally varying crustal structures; Geophys. J. R. Astr. Soc., 42, 579-589.

Larsen, H.C., 1984: Geology of the East Greenland Shelf; Petroleum Geology of the North European Margin, (Ed.) A.M.Spencer et al.,pp. 329-339, Graham and Trotman Ltd, London.

Noble , R.H., Macintyre, R.M., and P.E.Brown, 1988: Age constraints on Atlantic evolution: timing of magmatic activity along the E Greenland continental margin in Early Tertiary Volcanism and the opening of the N E Atlantic; (Eds.): A.C.Morton and L. M. Parson, Specl. Publ. Geol. Soc. 39, 201-214.

Saemundsson , K. , 1986: Subaerial volcanism in the western North Atlantic,; In : The Geology of North America, Vol. M ., The Western North Atlantic Region, (Eds.): B.E.Tucholke and P.R. Vogt, pp. 69-86, Geological Society of America, Boulder, Col.

Shearer , P .M. and C.H.Chapman, 1989: Ratracing in azimuthally anisotropic media -I. Results for models of aligned cracks in the upper crust; Geophys.J., 96, 51-64.

Talwani,M. and Eldholm, O., 1977: Evolution of the Norwegian -Greenland Sea; Geol. Soc. Am. Bull., 88, 969-999.

Weigel, W., Miller, H., Flueh, E.R., and the GROKORT Study Group, 1991: Seismic investigation of the East Greenland continental margin between 70° and 72° N; in preparation.

A THREE-COMPONENT SEISMIC INVESTIGATION OF THE EASTERN GREENLAND MARGIN: MODELLING HETEROGENEITY AND ANISOTROPY.

Carl Spencer[1], Sean Guest[2], Mike Kendall[2], and Bernd Milkereit[1]

[1] Geological Survey of Canada,
1 Observatory Cres., Ottawa, CANADA, K1A 0Y3

[2] Department of Geological Sciences, Queen's University,
Kingston, CANADA, K7L 3N6.

Summary

A summary of arrival time and particle motion modelling for dataset 3, collected during a three-component onshore-offshore survey situated off the east coast of Greenland (Weigel et al, 1991) is presented. The principle aim of the modelling is to explain the surprisingly large amount of transverse motion observed in parts of the record section, particularly in S-wave arrivals.

Section 1 contains both a brief review of theoretical results relevant to ray tracing in anisotropic media and the observational evidence for proposing the presence of anisotropy in the region. The results of two dimensional travel-time modelling of the data to obtain a reasonable isotropic velocity model are given in section 2. It is concluded that a strong, horizontally polarized event seen in the data is a P-S conversion at the Moho. Because only a small portion of the data was made available this model contains little detail, but it is useful as a starting point for anisotropic modelling. Models of the S-wave particle motion observations that include crust and mantle azimuthal anisotropy are presented in section 3. The type of anisotropy used is that expected in regions of rifting and extension such as at an ocean ridge. It is concluded that the observations can explained by an azimuthally anisotropic crust with a fast axis at an azimuth of approximately 45° from that of the line of shots.

Particle Motion Observations.

Background Theory: To help understand the particle motion observations and modelling presented in this paper it will be useful to summarize some well known results for the solution of kinematic wave propagation problems in anisotropic media.

More details can be found in Vlaar (1968), Cerveny (1972), Crampin (1981), Shearer & Chapman (1989) and Kendall & Thomson (1989).

Consider a disturbance propagating through a three dimensional space **x** as a wavefront with phase $\tau(x) = t = const.$ Associated with each point on the wavefront are the normal **n**, a phase velocity $\mathbf{v}_n$ and a slowness vector

$$p = \frac{\delta\tau}{\delta x} = \frac{n}{v_n}$$

A three-dimensional array of seismometers may in principle be used to measure **p** by differentiating arrival times with respect to **x.** Particle motions **u**, on the other hand, may be measured from the ground motion at a single receiver. In isotropic media the vectors **p** and **u** are parallel in the case of P-waves and perpendicular in the case of S-waves, but in the case of anisotropic media such relationships do not hold.

Using Hookes law relating the stress σ_{ij} and strain ε_{kl} tensors

$$\sigma_{ij} = c_{ijkl}\,\varepsilon_{kl} = c_{ijkl}\frac{\delta u_k}{\delta x_l}, \qquad (1)$$

where c_{ijkl} is the elastic constant tensor, together with the equation of conservation of momentum

$$\frac{\delta\sigma_{ij}}{\delta x_j} = \rho\ddot{\mathbf{u}}$$

gives the equation for seismic wave motion in an anisotropic medium

$$\frac{\delta}{\delta x_j}\left(c_{ijkl}\frac{\delta u_k}{\delta x_l}\right) = \rho\ddot{\mathbf{u}}_i \qquad (2)$$

Substituting solutions of the form $u(x,t) = U(x)e^{iw\tau}$ in equation 2 gives an equation for the displacement U

$$\Gamma U = v^2{}_n U \qquad (3)$$

where Γ is the 3×3 Christoffel matrix with elements

$$\Gamma_{ij} = \frac{c_{ikjl}\,n_k\,n_l}{\rho}.$$

In other words particle motions are the eigenvectors of the matrix Γ and the normal velocities, v_n, are eigenvalues. In general there will be three such eigenvalues corresponding to one `quasi-P' and two `quasi-S' motions. Equations 3 have a non-trivial solution only if

$$H(p,x) = \det\left|\Gamma_{ij} - v_n{}^2\delta_{ij}\right| = 0 \qquad (4)$$

which, for a given **n** may be solved to give v_n and therefore **p**. The surfaces for **p** traced out as **n** varies are known as slowness surfaces.

Equation 4 can also be be regarded as a first-order partial differential equation involving partial derivatives $\delta\tau / dx$ and in which H is a Hamiltonian, the characteristics of which define three sets of rays. Most ray tracing algorithms proceed by specifying locations and **n** for the start of a ray and then solving the characteristic equations using numerical techniques such as Runge-Kutta.

One of the most important quantities associated with anisotropic wave propagation is the velocity v=dx/dt of an observer moving with the wavefront. Vlaar (1968) shows that **v** is also the velocity of propagation of energy, i.e. the group velocity and has the same direction as rays obtained by solving the characteristic equations. The velocity **v** is called the group, total, or ray velocity by various authors. Differentiating the phase function $\tau(x) = t$ with respect to t gives

$$\frac{d\tau(x)}{dt} = p.v = 1 \qquad (5)$$

thus for a given **p**, vectors **v** define a plane. The total velocity surface is the envelope of these planes as **n** is varied and is usually calculated by solving equation 5 subject to the constraints on slownesses given in equation 4.

The seismograms analyzed in this study are taken from a suite of 454 three component recordings made by a single seismograph on land (Figure 1) of shots at sea, and cover the distance range 10 - 95 km. The source is in a fluid and therefore produces only P-waves, any shear motion incident at the receiver must result from P to S conversions at a discontinuity. Furthermore, if it can be demonstrated that wavefront slownesses predominantly lie in the plane containing both the vertical and the shots, then any transverse[1] motion observed in the seismogram must be a consequence of anisotropy. In such a case it is not necessary to look for S-wave birefringence to differentiate between anisotropy and lateral heterogeneity. Of course it is preferable to support such a conclusion with observations of splitting, but to do so may not always be possible.

In an ideal experiment the result that **p** and **u** are not necessarily parallel could be used to diagnose anisotropy at the receiver. However in this experiment a τ-p analysis would give us **p** at the boat, whereas particle motions provide **u** at the receiver, thus such a diagnosis is impossible. In future experiments it would be preferable to record individual receiver array elements to allow determination of **p**.

[1]For the modelling in this paper we refer to the direction of the line of shots as the x-axis and the vertical as z. we define radial polarizations as those lying in the x-z plane and transverse motions as those parallel to the y axis.

P-wave First Arrivals. Figure 2. contains particle motion diagrams for 6 shots in a 2 s time window spanning the P -wave first arrival. The motion is predominantly vertical, and the small amount of horizontal motion is radial. The importance of this observation is that it indicates that the direct arrivals propagate in the plane containing the vertical and seismic lines and hence ``side-swipe" and other out-of-plane effects are not of great significance for the P -wave onsets. PmP particle motions were also examined and showed a similar redial direction of propagation.

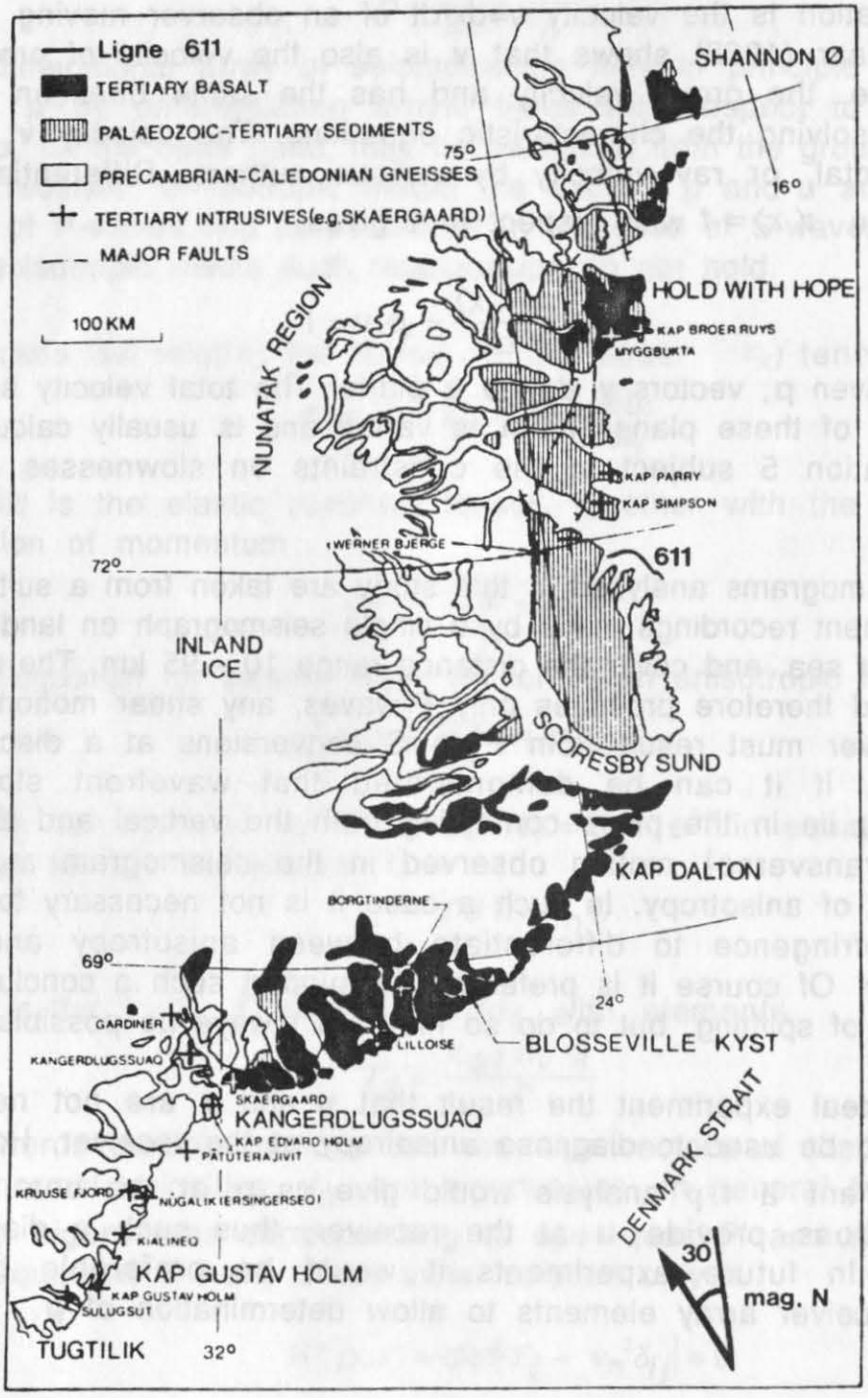

Figure 1: The geology of eastern Greenland (after Brooks (1989), together with the location of seismic line 611. Note that magnetic north is approximately 30° to the northwest of geographic.

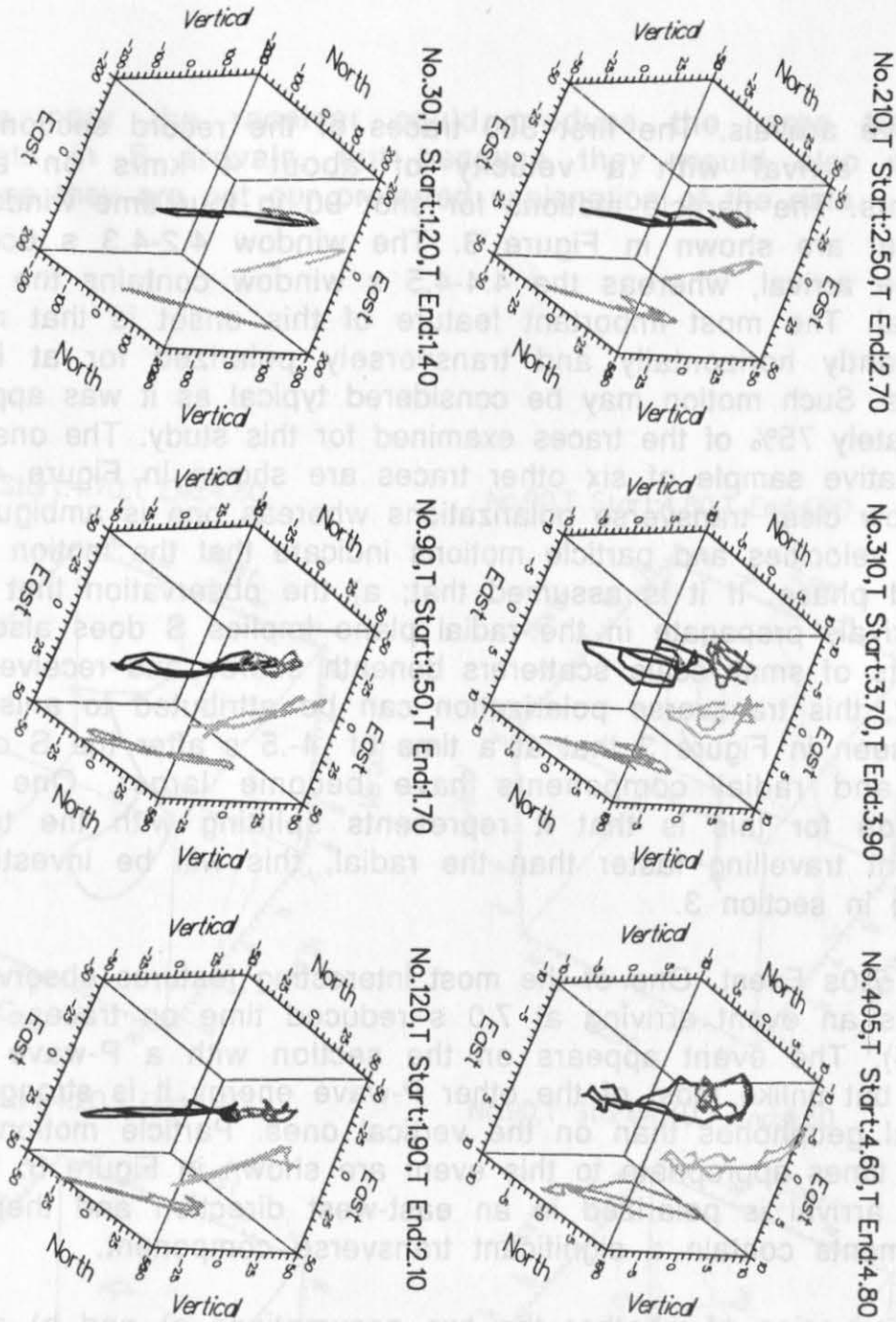

Figure 2: Particle motion plots for six shots spanning the P -wave first arrival window. In these and subsequent figures each particle motion plot consists of four line segments. The first, in black, is the three dimensional particle motion projected onto the diagram using the axis system as shown. In grey are the projections of this motion on the three axial planes. The horizontal component of motion, for example, may be observed by examining the medium-grey trace near the top of each diagram. The viewing angle for the axis system is set at 30° from magnetic north in order that motion in the profile plane appears as a bottom to top line in the diagram whilst transverse motion appears left to right. The axis components refer to magnetic directions and the axis values refer to raw velocities in arbitrary units as recorded on the magnetic tape. The label at the top of each diagram gives the shot number of the record, and the time window in seconds.

S-wave arrivals. The first 300 traces of the record section show a prominent arrival with a velocity of about 4 km/s on all three components. The particle motions for shot 90 in four time windows near this arrival are shown in Figure 3. The window 4.2-4.3 s occurs just before the arrival, whereas the 4.4-4.5 s window contains the onset of the arrival. The most important feature of this onset is that motion is predominantly horizontally and transversely polarized for at least the first 0.2 s. Such motion may be considered typical as it was apparent on approximately 75% of the traces examined for this study. The onsets for a representative sample of six other traces are shown in Figure 4; five of these show clear transverse polarizations whereas one is ambiguous. The apparent velocities and particle motions indicate that the motion is a P-S converted phase. If it is assumed that; a) the observation that P -wave direct arrivals propagate in the radial plane implies S does also, and b) the effects of small scale scatterers beneath source and receiver are not important, this transverse polarization can be attributed to anisotropy. It can be seen in Figure 3 that at a time of .4-.5 s after the S onset, the vertical and radial components have become larger. One possible explanation for this is that it represents splitting with the transverse component travelling faster than the radial, this will be investigated by modelling in section 3.

The 7.0s Event. One of the most interesting features observed in the section is an event arriving at 7.0 s reduced time on traces 150-300 (Figure 5). The event appears on the section with a P-wave apparent velocity, but unlike most of the other P-wave energy it is stronger on the horizontal geophones than on the vertical ones. Particle motions for two shots at times appropriate to this event are shown in Figure 6. It is clear that the arrival is polarized in an east-west direction and therefore the displacements contain a significant transverse component.

A discussion of whether the two assumptions a) and b) above are valid is necessary. Both the particle motions and our a priori geological knowledge would indicate that the problem at hand is predominantly two dimensional. Therefore it would seem unlikely that S phases would contain significantly more out-of-plane propagation than P . The presence of small scale scatterers near the source or receivers is a more serious problem. Scattering near the source, perhaps by the ocean bottom, would produce transversely polarized S arrivals without producing significant transverse motion in P at the receiver, in accordance with the above observations. There are two reasons for thinking this type of scattering is not taking place. Firstly the particle motions of S, and the 7.0 s event are remarkably similar from shot to shot over distances of tens of kilometers, an observation not consistent with the presence of small near-source scatterers. Secondly, and more significantly, we will demonstrate that the 7.0 s event is a P to S conversion that cannot result from scattering near the source.

Scatterers near the receiver could produce the large transverse components in S arrivals, but because they would also affect P polarizations they are not our preferred explanation of the data.

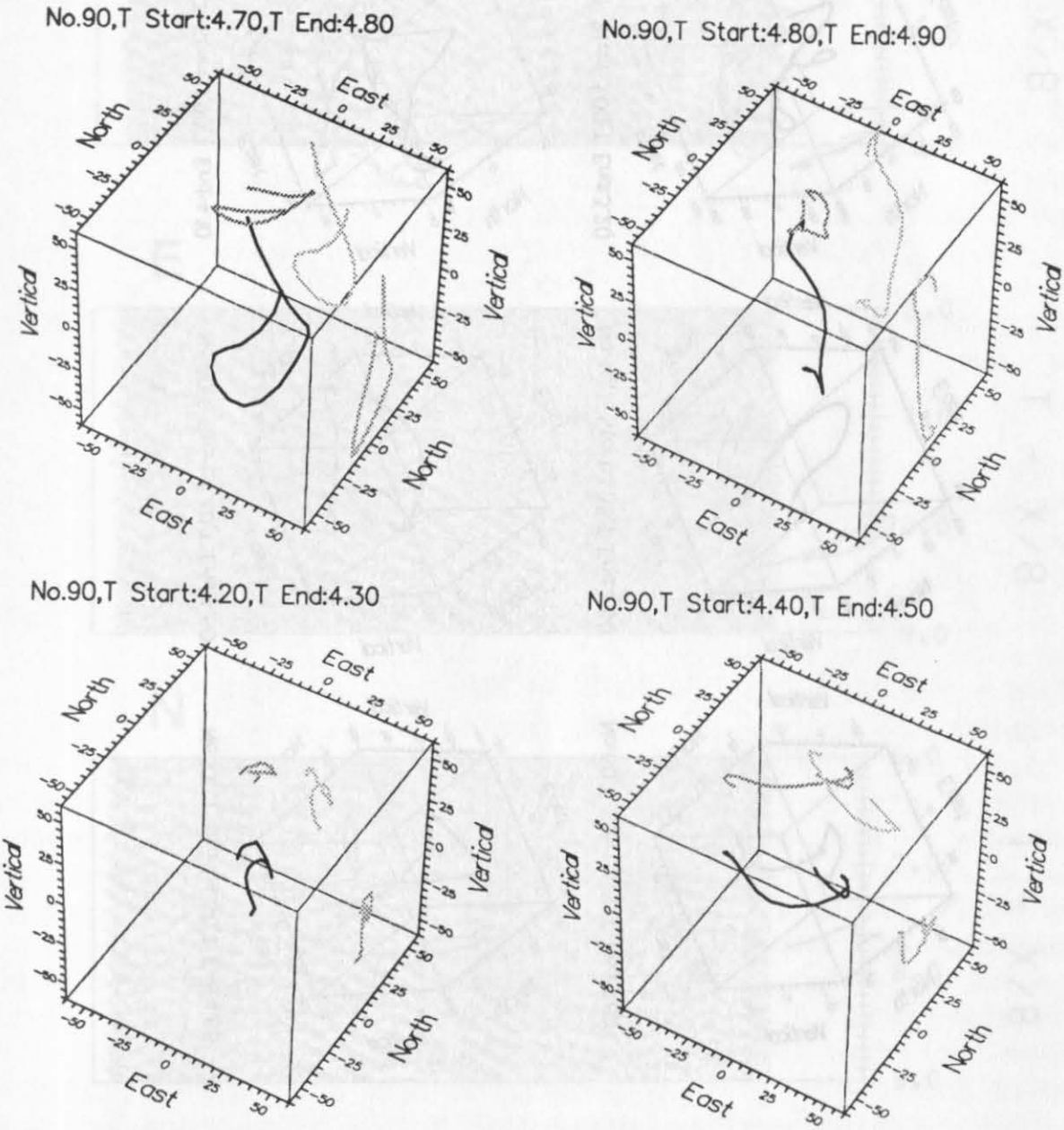

Figure 3: Particle motion plots for shot number 90 in four windows. The window 4.2-4.3 s is immediately before the S onset, 4.4-4.5 s contains the onset. The left-right motion seen in the projection on the North/East plane implies transverse displacements

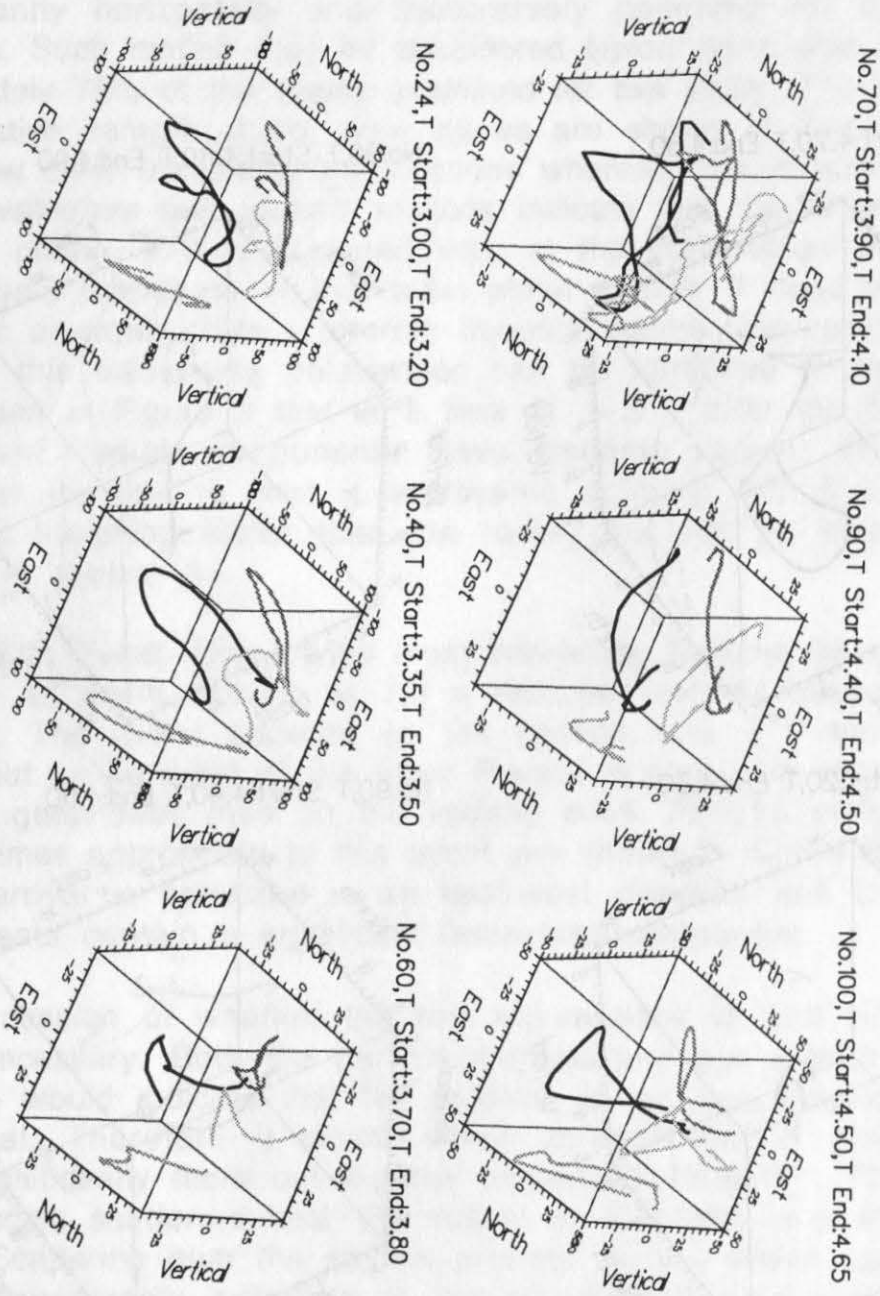

Figure 4: Particle motion plots for six shots in time windows that include the S onset.

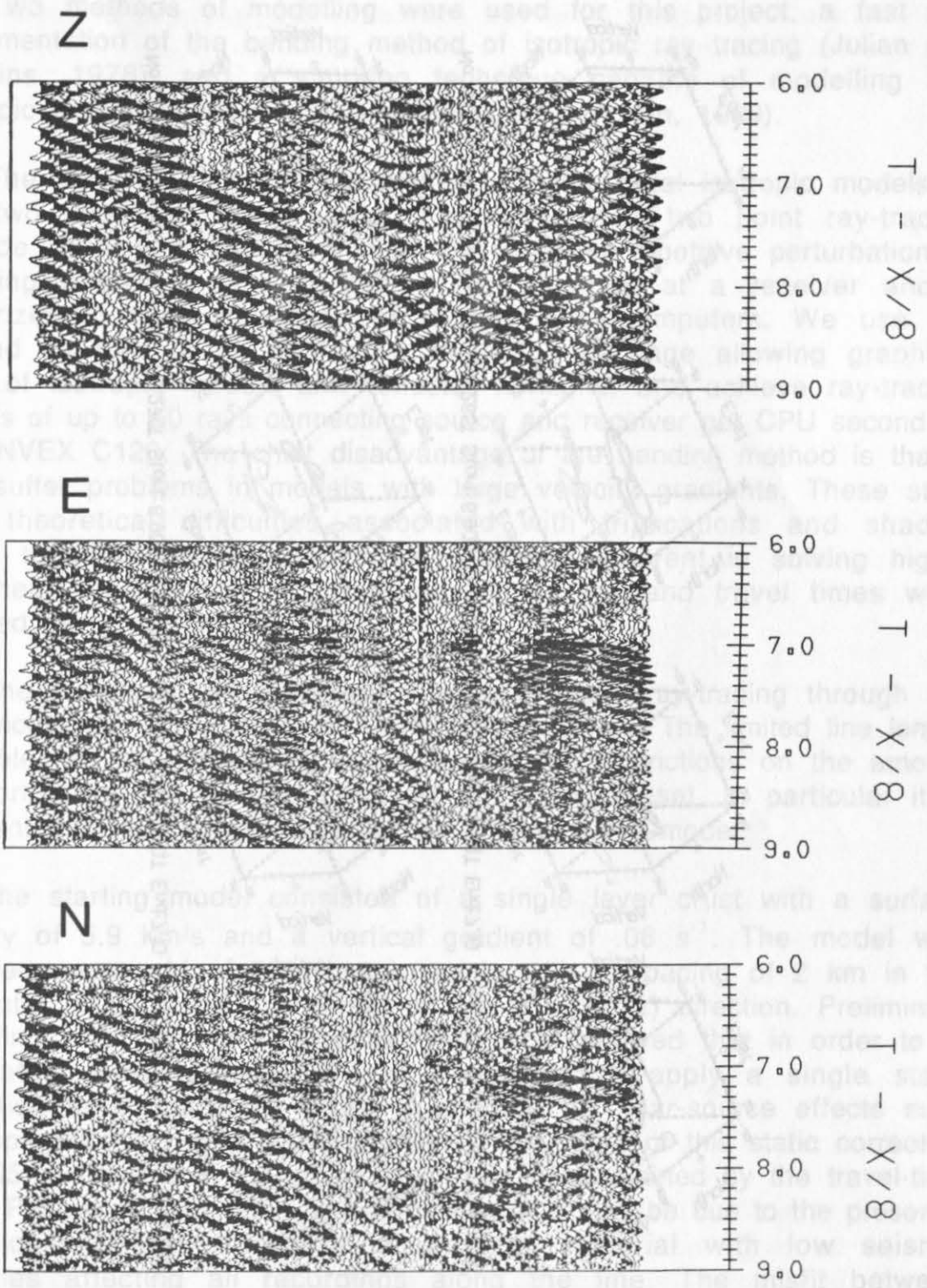

Figure 5: Seismic sections for all three components showing the event at 7 s reduced time referred to in the text.

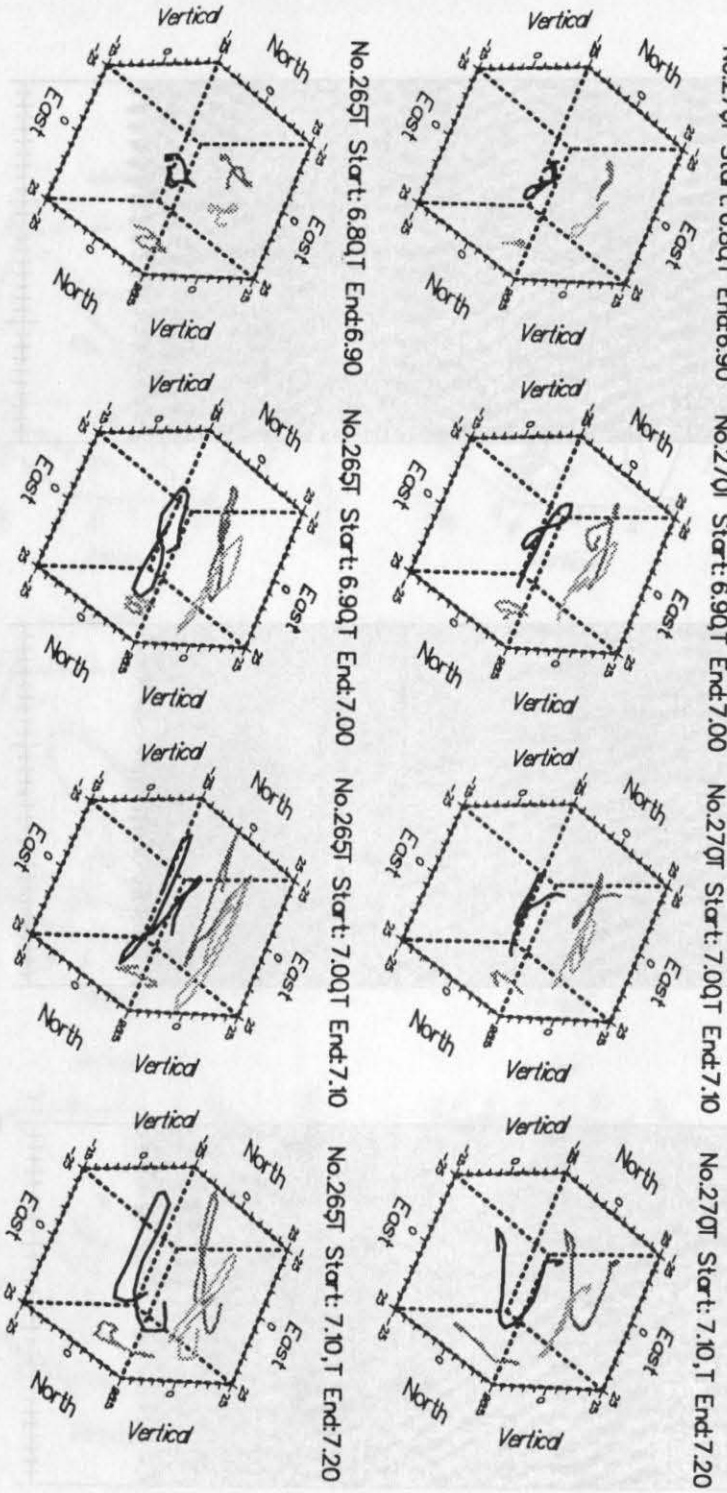

Figure 6: Particle motion diagrams for shot numbers 265 and 270. For each shot four windows are plotted, the first covering the background before the 7 s event and the remainder containing the first .3 s of the event. The shot to receiver distance for these shots is approximately 48 km.

Arrival Time Modelling in Isotropic media.

Two methods of modelling were used for this project, a fast 2-D implementation of the bending method of isotropic ray tracing (Julian and Gubbins, 1976), and a shooting technique capable of modelling 3-D isotropic and anisotropic effects (Kendall & Thomson, 1989).

The bending method was used to provide initial isotropic models. It has two important advantages: It performs true two point ray-tracing (outside shadow zones) eliminating the need for repetitive perturbation of shooting angles to ensure that a ray emerges at a receiver and it vectorizes to take advantage of modern supercomputers. We use the method as part of an interactive modelling package allowing graphical input of isotropic models and reflector horizons, and achieve ray-tracing speeds of up to 50 rays connecting source and receiver per CPU second on a CONVEX C120. The chief disadvantage of the bending method is that it may suffer problems in models with large velocity gradients. These stem from theoretical difficulties associated with triplications and shadow zones together with the numerical problems inherent in solving highly non-linear equations. For this reason final rays and travel times were checked using the shooting method.

The results of bending and shooting P-wave ray-tracing through the final model are shown in Figs 7 and 8 respectively. The limited line length available for the modelling has placed serious restrictions on the amount of information that can be obtained from the dataset, in particular it is apparent that rays sample only the top 10 km of the model.

The starting model consisted of a single layer crust with a surface velocity of 5.9 km/s and a vertical gradient of .08 s^{-1}. The model was specified on a grid of 2091 mesh points with a spacing of 2 km in the horizontal (x) direction and .5 km in the vertical (z) direction. Preliminary modelling with the bending-method ray tracer showed that in order to fit adequately P-wave times it was necessary to apply a single static correction to all traces in order to account for near-source effects such as propagation in water and sediments. The value of this static correction was .65 s about one quarter of which can be explained by the travel-time of the P-wave in sea water. The remaining .4 s may be due to the presence of a considerable thickness of surficial material with low seismic velocities affecting all recordings along the line. The misfit between modelled times and corrected observations was then used to modify the model. The main area of improvement to the model was in the distance range 45 - 95 km where it was necessary to introduce a basin like structure with velocities as low as 4.5 km/s. A depth to basement of 10 km was required to fit a relative delay seen in first arrivals from that portion of the section (Figure 7). All travel times calculated for this final model fit the observed to better than 0.1 s everywhere.

It should be emphasized that not enough data to determine a unique model was used in this study. Although this is important for the interpretation of the travel time data, it is not crucial to the analysis of anisotropic propagation discussed below.

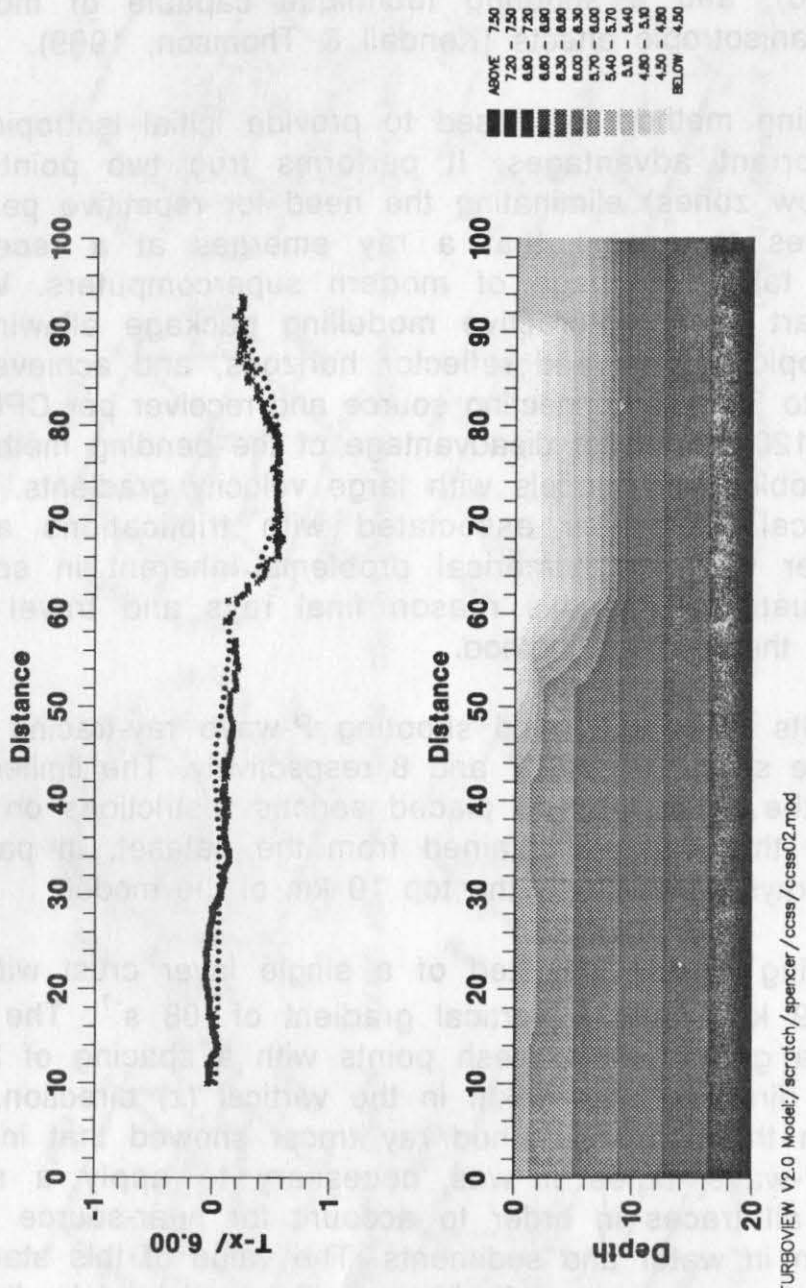

Figure 7: The final model obtained by interactive P-wave fitting using the bending method of travel time calculation. A comparison of observed picks and model times is shown in the top part of the figure where first arrival picks are shown as small crosses and ray-traced times as dots. The velocity scale is in km/s and propagation near the surface has been approximated by the subtraction of a .65 s static correction. Spline interpolation of the model grid was performed before contouring in order that artifacts of interpolation such as oscillation and overshoot are made apparent.

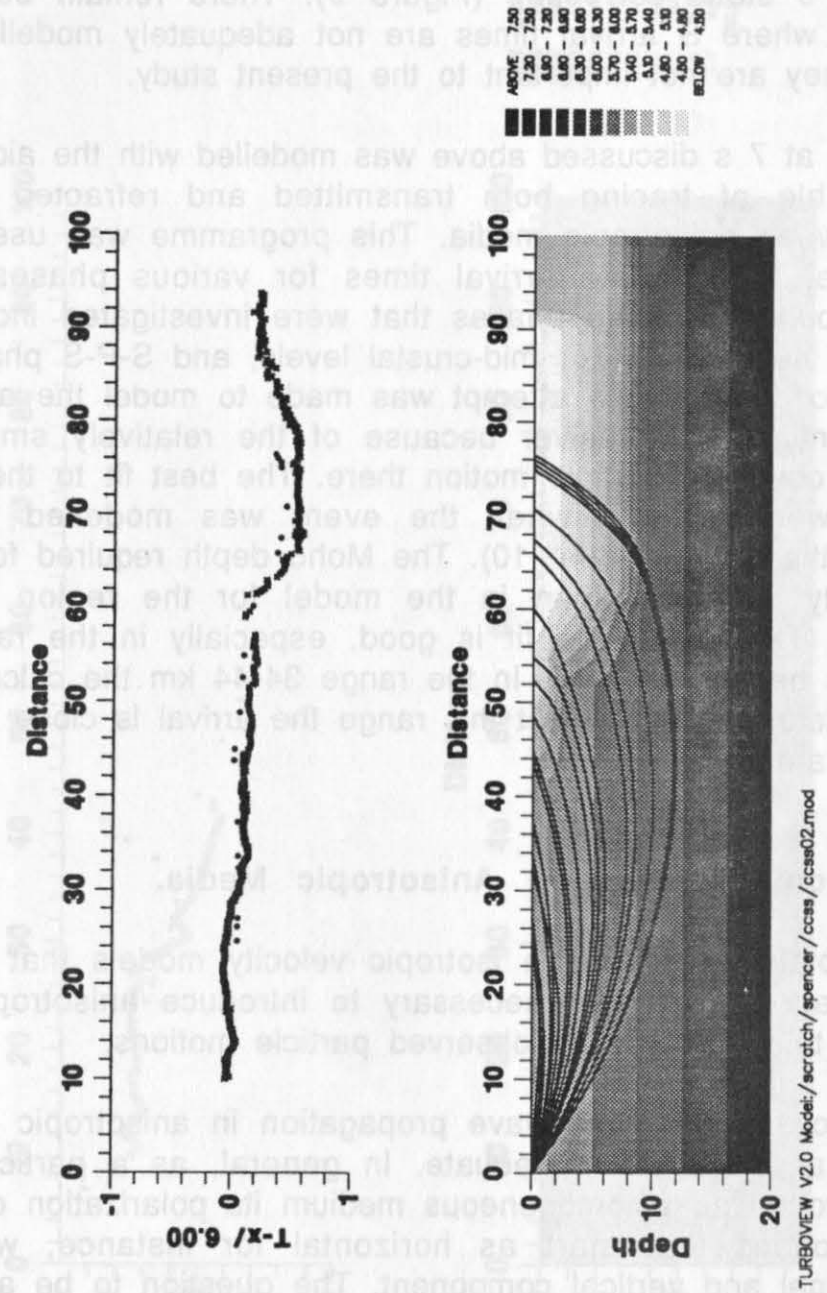

Figure 8: Raypaths and travel times obtained with the shooting method. The annotation of the diagram is the same as in Figure 7.

S-waves resulting from P-S conversions at the ocean bottom are observable in the record sections to a distance of about 50 km. The gross features in the S-wave arrival time curves are adequately reproduced using a model derived from the P model by assuming $V_P/V_S = \sqrt{3}$ and applying a .8 s static correction (Figure 9). There remain some small-scale features where S arrival times are not adequately modelled by this process, but they are not important to the present study.

The event at 7 s discussed above was modelled with the aid of a new program capable of tracing both transmitted and refracted waves at interfaces between anisotropic media. This programme was used with an isotropic model to calculate arrival times for various phases reflected from model boundaries. The phases that were investigated included P-S conversions at near surface or mid-crustal levels, and S-P-S phases along paths similar to direct S. No attempt was made to model the arrival as a P-wave incident at the receiver because of the relatively small vertical component of observed particle motion there. The best fit to the observed travel times was obtained when the event was modelled as a P-S conversion at the Moho (Figure 10). The Moho depth required for this was 19 km, slightly shallower than in the model for the region distributed with the data. The travel-time fit is good, especially in the range 44-60 km where it is better than .1 s. In the range 34-44 km the calculated time is up to .2 s late, but throughout this range the arrival is close to direct S and the picks are uncertain.

Particle Motion Modelling in Anisotropic Media.

Having obtained reasonable isotropic velocity models that match the arrival time data it was then necessary to introduce anisotropy into the models to try to reproduce the observed particle motions.

When discussing seismic wave propagation in anisotropic media, the terms P, SV and SH are inadequate. In general, as a particular phase propagates through an inhomogeneous medium its polarization changes so that wave motions that start as horizontal for instance, will acquire some longitudinal and vertical component. The question to be answered in this section is what anisotropic geometries could reasonably account for the observations discussed above? It should be remembered that anisotropy will affect propagation in three ways. It will affect the reflection and transmission coefficients and polarizations at interfaces. It modifies polarizations and amplitudes during propagation, and finally, it will affect the free surface boundary conditions at the receiver.

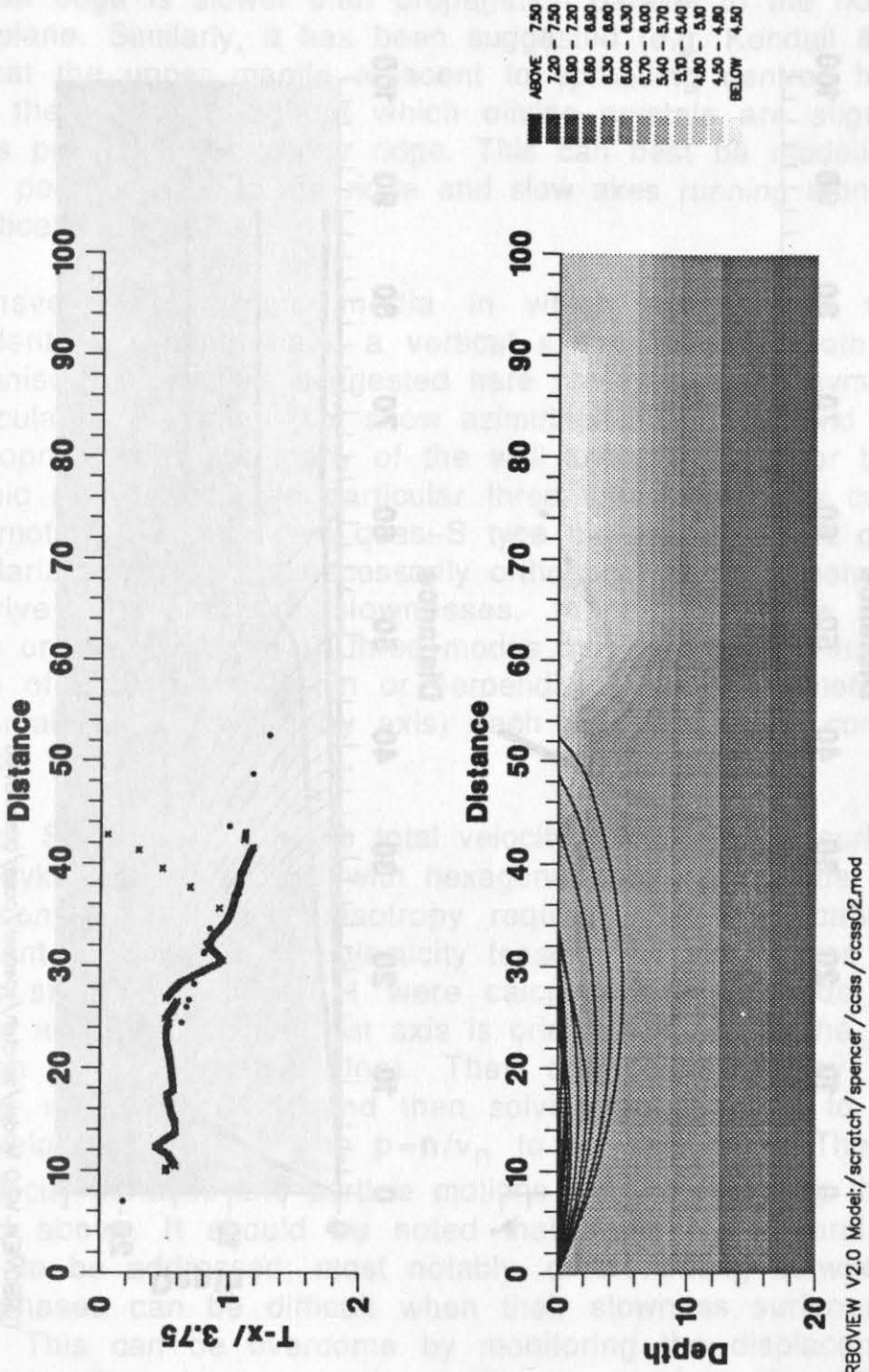

Figure 9: S-wave raypaths and travel times in a model derived from the P-wave model using a Poissons ration of .25. Propagation near the surface has been modelled using a .8s static correction. The annotation of the diagram is the same as in Figure 7.

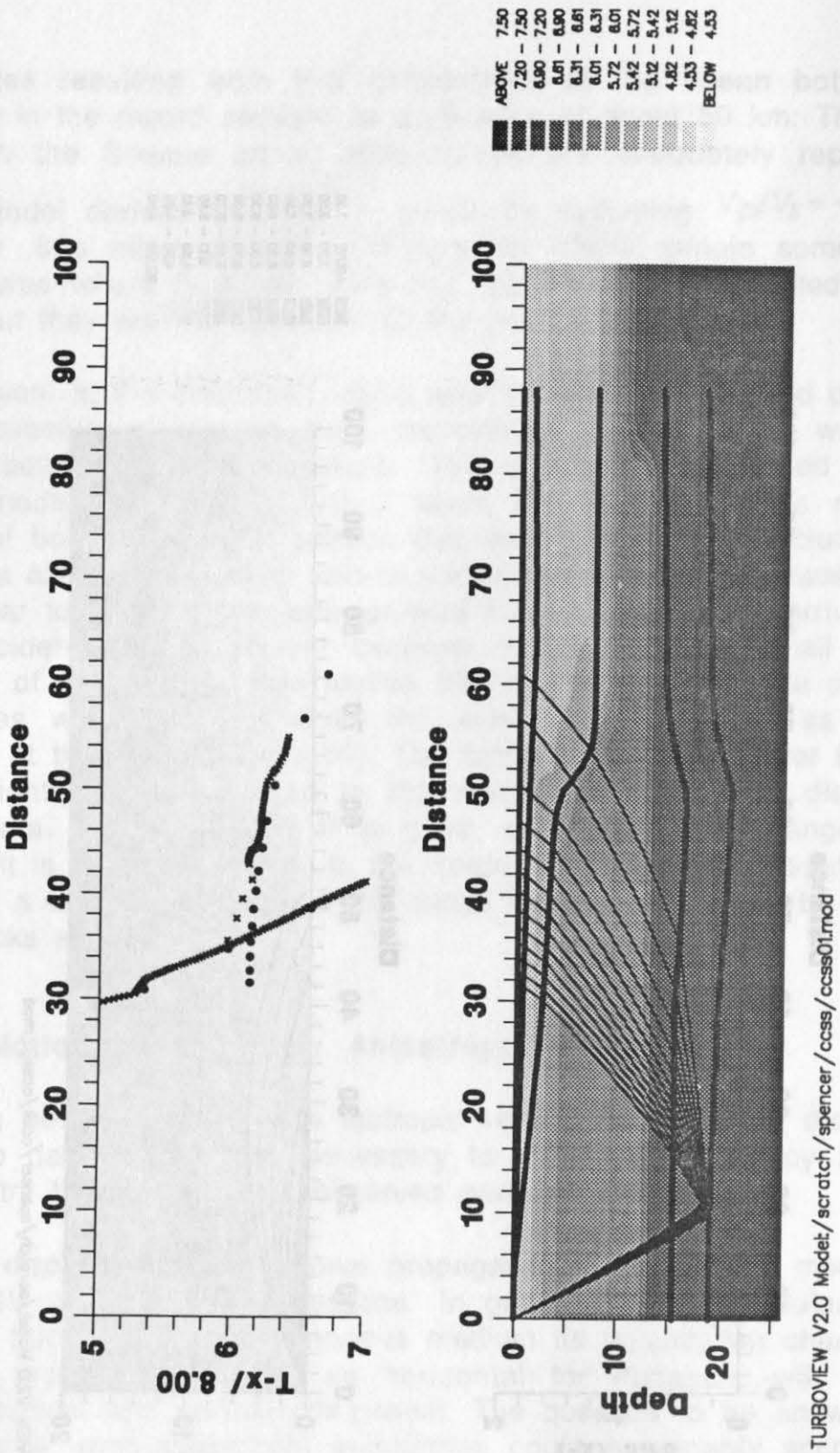

Figure 10: Raypaths and travel time of the P-S converted phase. The velocity model used was similar to that provided to workshop participants and has discontinuities at the locations shown as thick black lines on the model. For graphical purposes the model contoured in this diagram is that used in the previous figures. The steep branch of the observed travel time curve is the direct S arrival.

It would seem reasonable to suggest that the rifting and/or stretching environment of the east coast of Greenland might result in a situation where seismic wave propagation normal to the ridge and continental edge is slower than propagation parallel to the ridge or in a vertical plane. Similarly, it has been suggested (e.g. Kendall & Thomson, 1989) that the upper mantle adjacent to spreading centres has a layer beneath the Moho throughout which olivine crystals are aligned with a long axis perpendicular to the ridge. This can best be modelled using a fast axis perpendicular to the ridge and slow axes running along the ridge and vertically.

Transversely isotropic media in which propagation velocity is independent of azimuth have a vertical symmetry axis. Both crust and mantle anisotropic models suggested here have horizontal symmetry axes perpendicular to the ridge (i.e. show azimuthal anisotropy) and hence with the appropriate rotations many of the well known results for transversely anisotropic media apply. In particular three types of waves can exist; a quasi-P motion (qP), and two quasi-S type motions qSH and qSV. These three polarizations are not necessarily orthogonal at the receiver because they arrive with differing slownesses. In the presence of velocity gradients or discontinuities all three modes may be coupled and except in the case of propagation within or perpendicular to a symmetry plane (a plane containing the symmetry axis) each will have some component of transverse motion.

Direct S. Figure 11 shows total velocity and slowness surfaces for a sheeted dyke type anisotropy with hexagonal symmetry (Model A, Kendall & Thomson, 1989). This anisotropy requires the specification of five independent elements in the elasticity tensor. The slownesses and group velocities shown in Figure 11 were calculated for a model with 10% anisotropy and in which the fast axis is oriented at 45° to the x axis (the orientation of the seismic line). They are calculated by repeatedly specifying ray normals $\mathbf{n}$, and then solving equations 3 to give three normal velocities v_n, allowing $\mathbf{p}=\mathbf{n}/v_n$ to be calculated. Thereafter the group velocity surfaces and particle motions may be found by the methods discussed above. It should be noted that there are several numerical problems to be addressed; most notably, differentiating between the two quasi-S phases can be difficult when their slowness surfaces touch or intersect. This can be overcome by monitoring the displacements near these points. The slowness and velocity curves show the differences in velocities and slownesses of the three phases; note that qSV is the S-wave first arrival. One important feature apparent in Figure 11 is that qSH velocities and slownesses appear to be relatively azimuthally invariant.

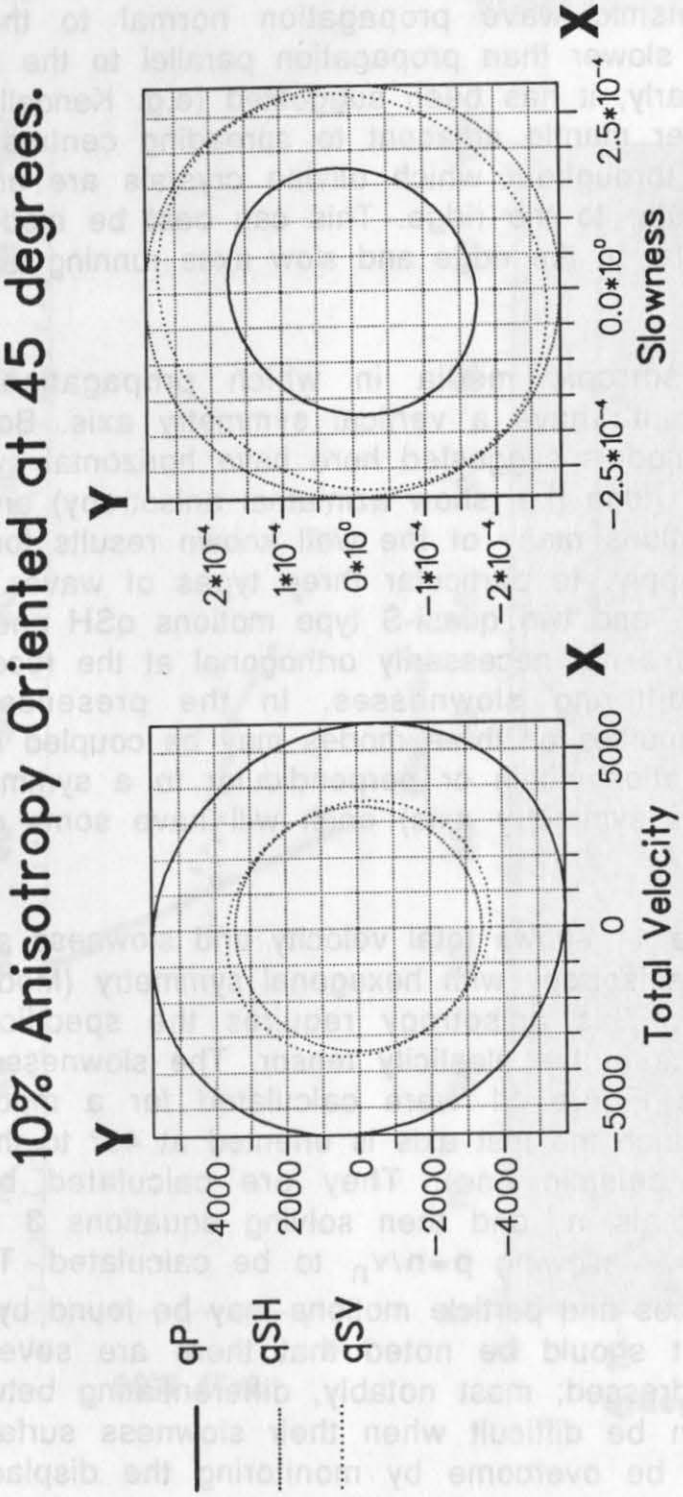

Figure 11: Slowness (p) and group velocity (v) surfaces for anisotropy model A. The slow direction is at 45° to the y axes and the three dimensional surface is rotationally invariant about this direction. The x-axis represents the shot to receiver direction implying a ridge azimuth of 345°.

Varying the relative angle between the propagation direction and the symmetry axis has a strong effect on particle motion directions, not only because of the splitting but also because it affects the out-of plane propagation of the rays. When propagation is at an azimuth 45° to the plane of the experiment (i.e. parallel to the ridge axis) rays travel radially. The same result holds for propagation in the slow direction. At intermediate angles this is not so. Indeed polarizations of the three phases at a receiver are no longer orthogonal because they arrive with differing slownesses. This effect is a maximum when the angle between the ridge and propagation direction is 45°, in which case rotations of about 10° are observed. Nevertheless the rotation due to out of plane propagation is insufficient to explain the observed S-motions as rotated qSV.

Varying the models of anisotropy can affect these results greatly. As an example, slowness and velocity surfaces for a wet crack model (Shearer and Chapman, 1989) with 15% anisotropy (Model B) are shown in Figure 12. In this case points of inflection on the slowness surface produce cusps in the total velocity surface at angles of 0° and 90° to the x axis. As a result, qSH polarizations travel faster than qSV in these directions. This is an extreme example, but smaller amounts of anisotropy can still produce faster qSH than qSV.

The next step in modelling the S arrival was to three-dimensionally trace rays from shot to receiver in the two-dimensional model, fitting travel times with the assumption that elastic coefficients are constant in the y direction. The path consisted of isotropic propagation in the basin, transmission into an anisotropic medium with model A type anisotropy, and propagation to the receiver. Particle motions of qSV and qSH phases for this ray are shown in Figure 13. They demonstrate that conversion at the basin boundary followed by propagation in the anisotropic medium result in a significant transverse component to the qSV wave. It has in effect rotated the qSV polarization into the symmetry plane whereas the qSH motion remained almost purely transverse. The effect of applying free surface boundary conditions at the receiver is also shown in Figure 13. For transverse polarizations the incident and reflected wave interfere constructively producing a doubling in the y component, whilst the vertical component has been reduced. This is very pronounced for rays with a high angle of incidence at the surface. At larger distances, angles of incidence become smaller and the surface effects on qSH and qSV become similar.

The combined result of all these effects is to produce particle motions fitting the observation that the S-wave at the surface is predominantly transverse. Since both qSH and qSV produce surface polarizations that are similar, it will require a more detailed analysis to determine whether the first S arrival is qSH or qSV.

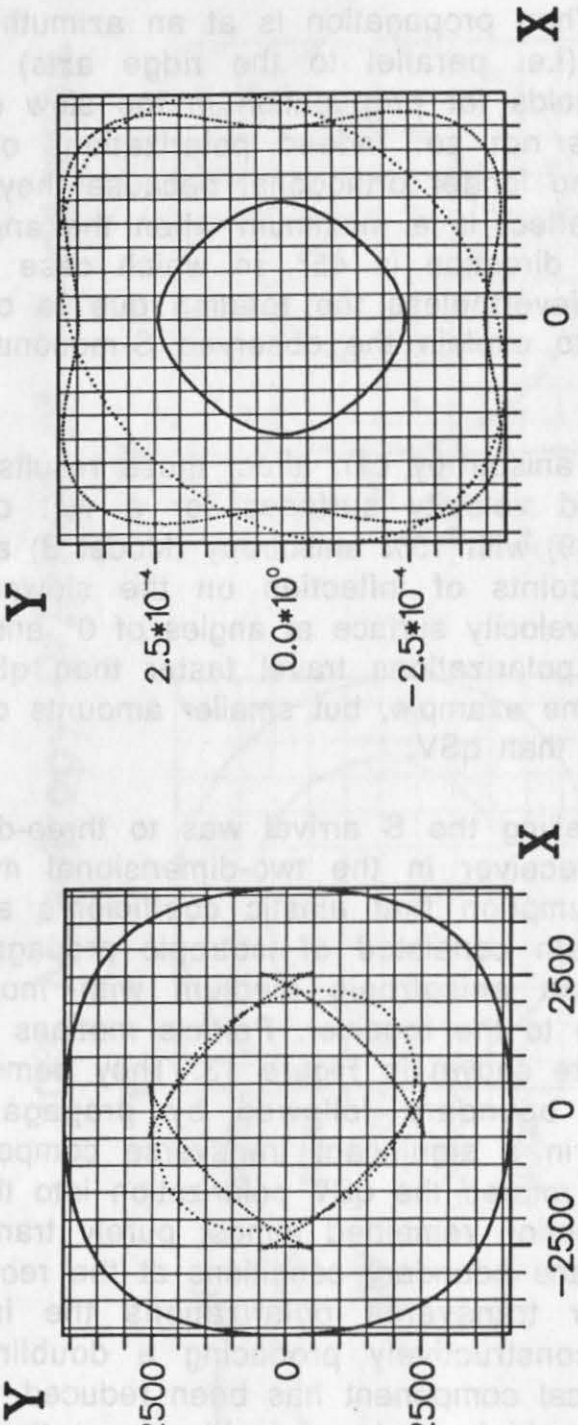

Figure 12: As for Figure 11 using anisotropy model B. Note that in this model propagation in the x direction will result in qSH phases arriving before qSV.

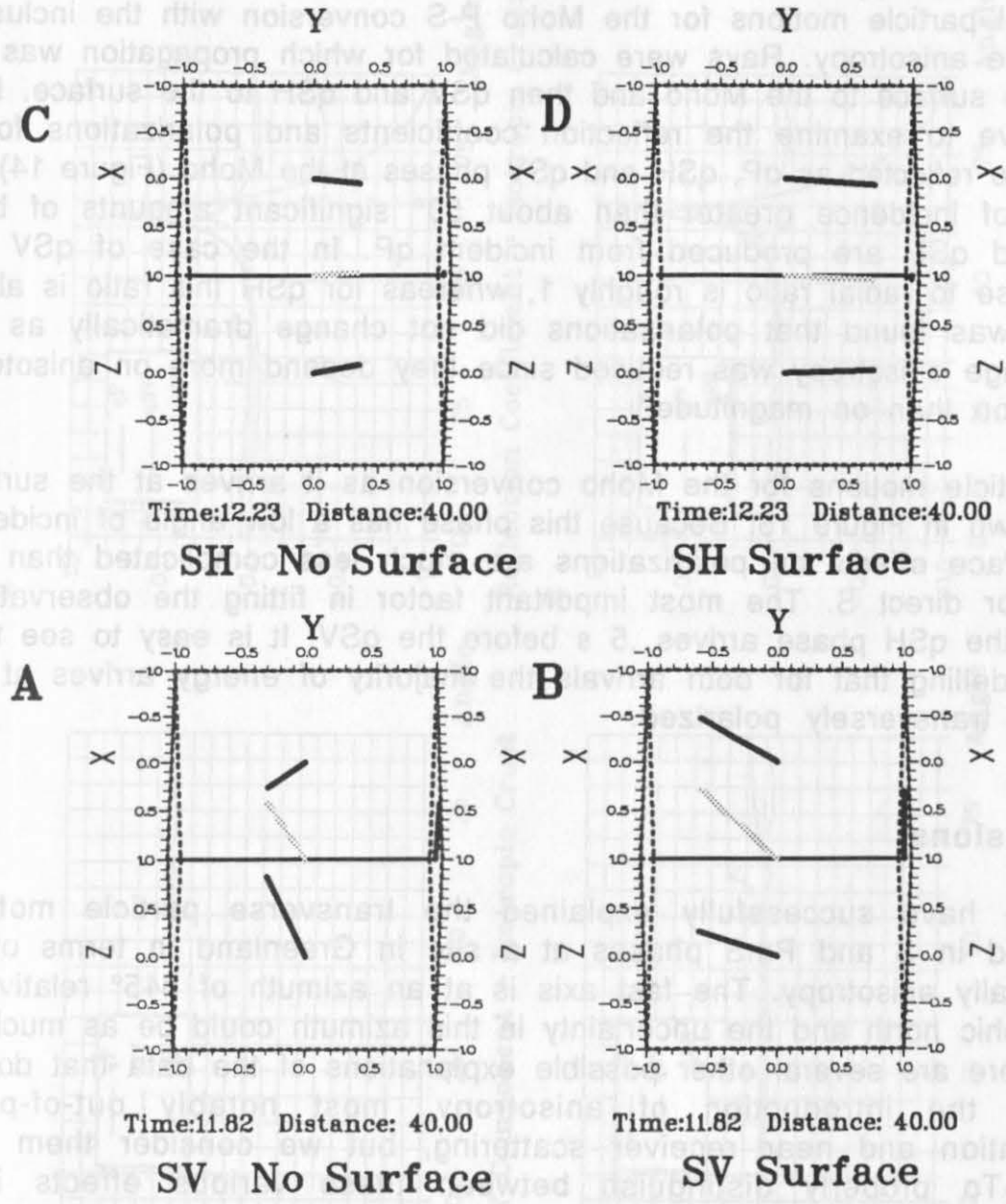

Figure 13: Modelled particle motion diagrams for direct S arrivals. A) qSV polarization with no free surface effect, B) qSV applying free surface boundary conditions, C) qSH polarization with no free surface effects, and D) qSH polarization applying free surface boundary conditions. The light grey lines show the 3-dimensional vector **U** projected on the paper and the solid black lines show the projection of **U** onto the axial planes.

This also implies that it is going to be very difficult to resolve S-wave splitting in this type of model.

P-S conversion modelling. Having determined that the sheeted dyke type of anisotropy of model A is appropriate for the crust it was decided to model particle motions for the Moho P-S conversion with the inclusion of mantle anisotropy. Rays were calculated for which propagation was qP from the surface to the Moho and then qSV and qSH to the surface. It is instructive to examine the reflection coefficients and polarizations for a qP phase reflected as qP, qSH and qSV phases at the Moho (Figure 14). At angles of incidence greater than about 50° significant amounts of both qSV and qSH are produced from incident qP. In the case of qSV the transverse to radial ratio is roughly 1, whereas for qSH this ratio is about 1.5. It was found that polarizations did not change dramatically as the percentage anisotropy was reduced since they depend more on anisotropy orientation than on magnitude.

Particle motions for the Moho conversion as it arrives at the surface are shown in Figure 15. Because this phase has a low angle of incidence the surface effects on polarizations are much less complicated than are those for direct S. The most important factor in fitting the observations is that the qSH phase arrives .5 s before the qSV. It is easy to see from this modelling that for both arrivals the majority of energy arrives at the surface transversely polarized.

Conclusions.

We have successfully explained the transverse particle motions observed in S and PmS phases at a site in Greenland in terms of an azimuthally anisotropy. The fast axis is at an azimuth of 345° relative to geographic north and the uncertainty in this azimuth could be as much as 15° There are several other possible explanations of the data that do not require the introduction of anisotropy, most notably out-of-plane propagation and near receiver scattering, but we consider them less likely. To properly distinguish between these various effects it is necessary to search for S -wave splitting, only hints of which were noticed during this analysis.

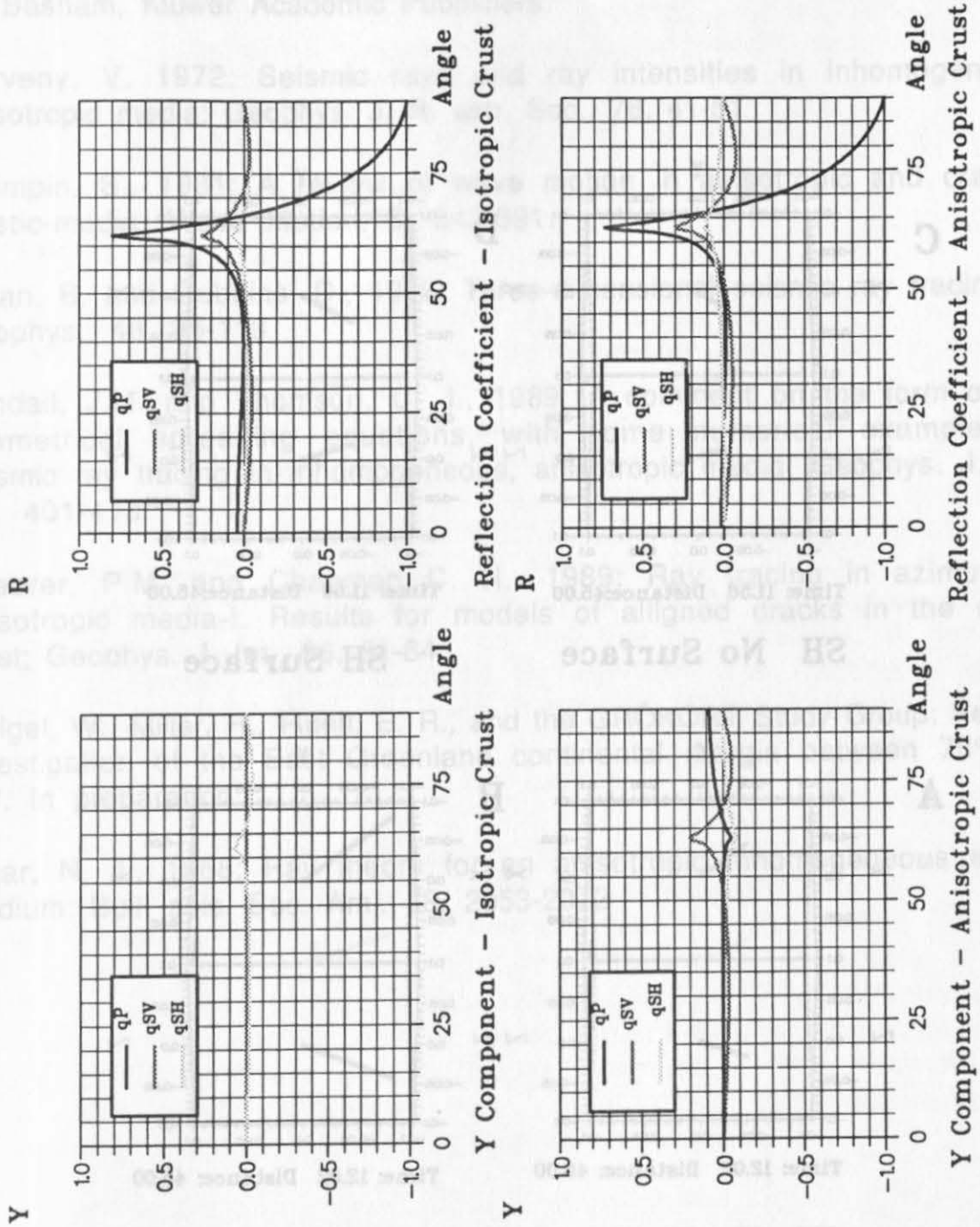

Figure 14: The transverse (Y) component and reflection coefficient (R) for each of the three reflected phases for a P-wave incident at the Moho. Diagrams show these quantities for both an isotropic and anisotropic crust. See text for a discussion of the type of anisotropy used to model the crust and mantle.

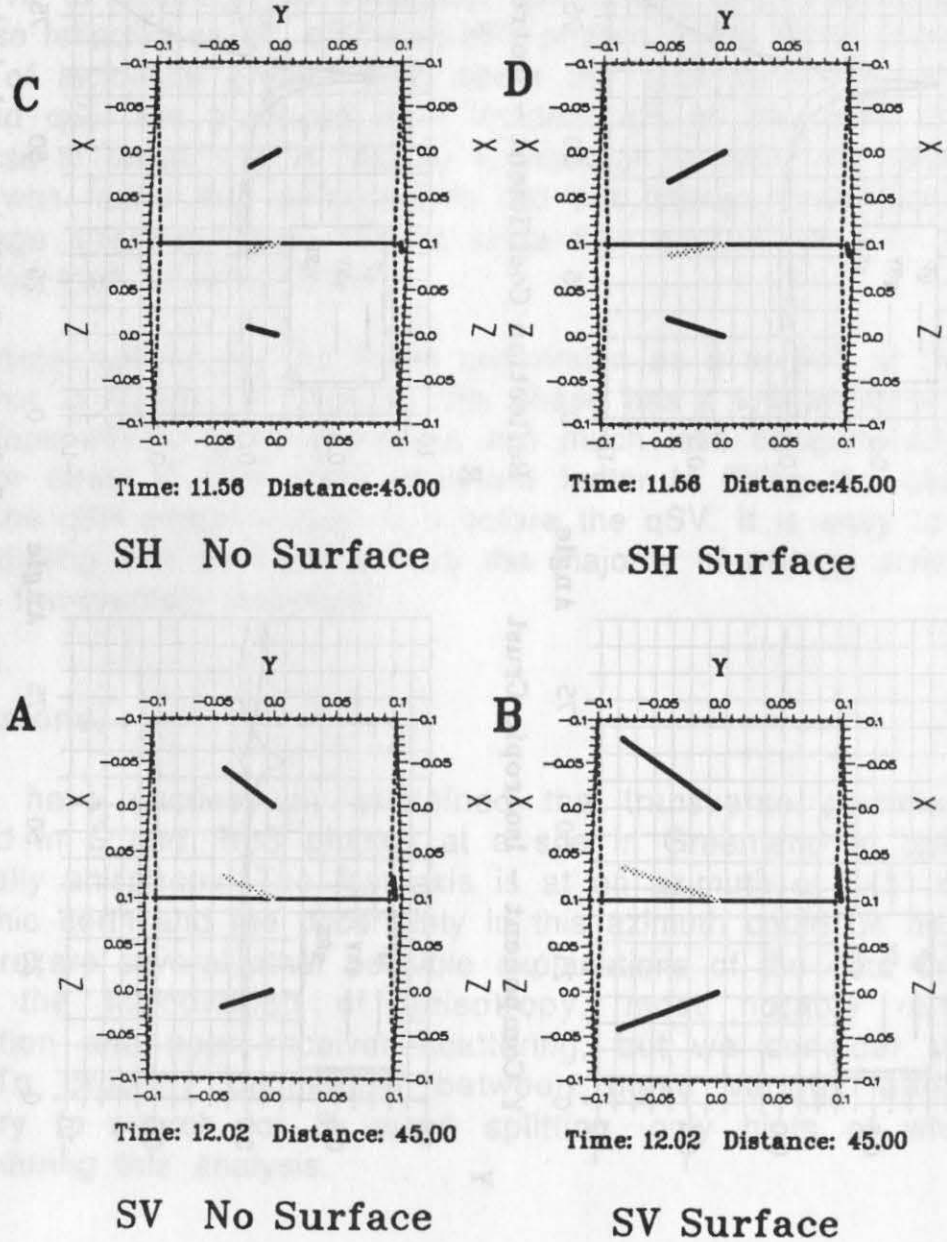

Figure 15: Modelled particle motion diagrams for the P-S Moho converted phase.

References.

Brooks, C. K., 1989: The Geology of the East Greenland Margin, in Earthquakes at North-Atlantic Passive Margins; (Eds.) S. Gregersen and P. W. Basham, Kluwer Academic Publishers.

Cerveny, V, 1972: Seismic rays and ray intensities in inhomogeneous anisotropic media; Geophys. J. R. astr, Soc., 76, 41-51

Crampin, S., 1981: A review of wave motion in anisotropic and cracked elastic-media; Wave Motion, 3, 343-391.

Julian, B. and Gubbins, D., 1976: Three-dimensional seismic ray tracing; J. Geophys., 43, 95-113

Kendall, J.M. and Thomson, C. J., 1989: A comment on the form of the geometrical spreading equations, with some numerical examples of seismic ray tracing in inhomogeneous, anisotropic media; Geophys. J. Int., 99, 401-413

Shearer, P.M. and Chapman C. H., 1989: Ray tracing in azimuthally anisotropic media-I. Results for models of alligned cracks in the upper crust; Geophys. J. Int., 96, 51-64.

Weigel, W., Miller, H., Flueh, E. R., and the GRÖKORT Study Group: Seismic investigation of the East Greenland continental margin between 70° and 72°. In preparation.

Vlaar, N. J., 1968: Ray theory for an anisotropic inhomogeneous elastic medium; Bull. seis. Soc. Am., 58, 2053-2072

A COMPARISON OF THE SYNTHETIC SEISMOGRAM RESULTS FOR THE DATASET 4 MODEL

Robert F. Mereu

Department of Geophysics, University of Western Ontario

Introduction

In recent years both coincident near vertical reflection experiments and wide angle reflection/refraction experiments have been performed over the same line in order that the subsurface structures may be determined from two different perspectives. Each method has its strengths and weaknesses. In the past CCSS Workshops, most of the problems have been on the inverse problem or in other words the interpretation of observed data sets. The forward problem which is to determine synthetic seismograms for a given model has been presented (see for example the 1983 Workshop in Einseideln Switzerland) but has not received the same attention as the inverse problems. A synthetic seismic reflection section provided by Johnson was distributed as an exercise in the 1987 Workshop held at Whistler, British Columbia, Canada. In that interpretational problem the purpose was to obtain the complex model used for the calculation of the section.

The purpose of this workshop's Dataset 4 problem is to compare different methods for calculating synthetic seismograms for the kind of complex crustal models that are now common in the scientific literature. The problem in this workshop differs from that of others in that synthetics for "both" near vertical and wide angle reflection/refraction experiments are computed and compared. Topics of interest include speed, accuracy, completeness of calculations, methods of parameterizing the model and most importantly how useful these calculations are in constraining the interpretations of crustal structure.

The Model and Specification for Synthetics

The model as was presented to the participants of the workshop is shown in Figure 1. A description of the model and instructions and specifications for the synthetics were given by the organizers as follows:

"The model we have chosen is based on the ECORS results across the Pyrenees (ECORS Pyrenees Team, 1988, The deep reflection seismic

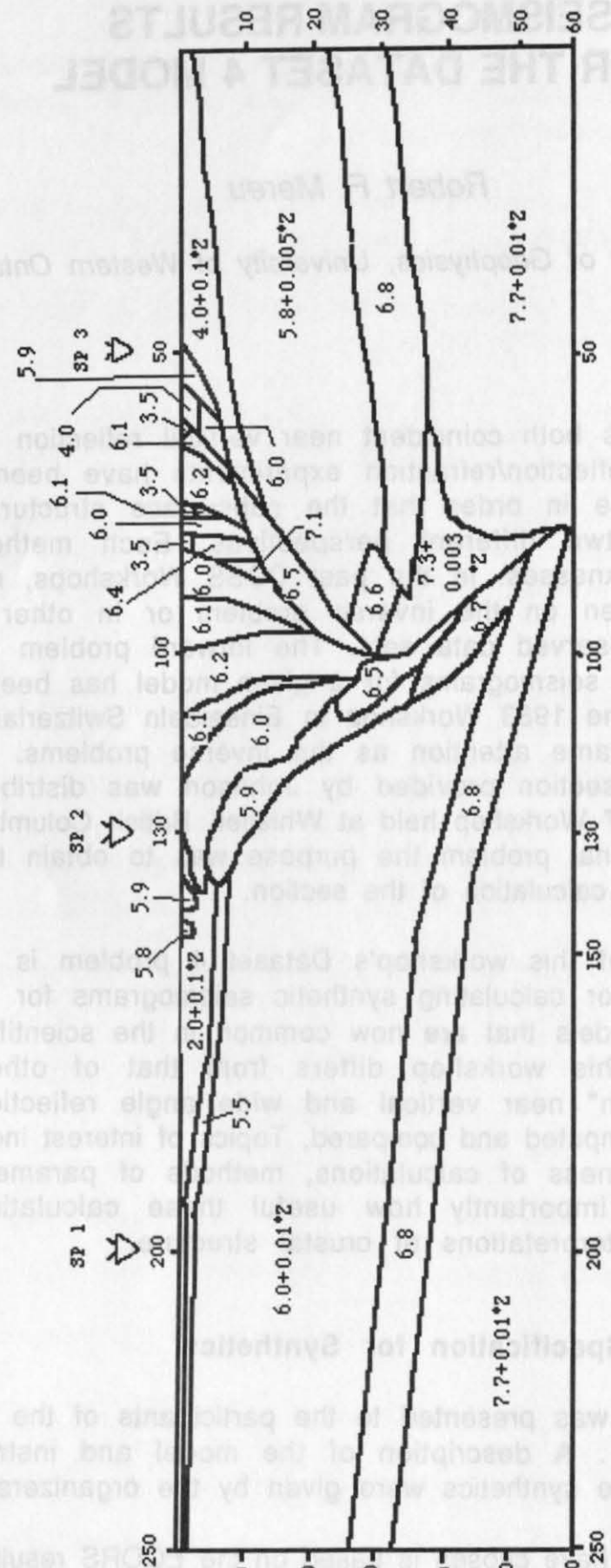
SP 1
SP 2
SP 3
5.9
4.0
6.1
3.5
6.2
6.0
7.1
6.4
6.5
6.6
7.3+
0.003
*2
6.7
6.8
5.8+0.005*2
4.0+0.1*2
7.7+0.01*2
2.0+0.1*2
6.0+0.01*2
5.5
10
20
30
40
50
60
100
130
150
200
250

Figure: 1

survey across the Pyrenees, Nature, 331,508-511). The model is 250 km long and 60 km deep. It is plotted at a scale of 50 cm by 12 cm, and this same scale should be used for the synthetic section. If a larger scale is desired, please double both dimensions. (The use of common scales is critical to meaningfull comparison.) The synthetic should use a simple wavelet with a center frequency of 30 Hz. You want to mix random noise with one plot of the synthetics to make it more realistic. Information regarding velocities and velocity gradients is given on the model.

In addition to a synthetic seismic reflection profile across this model, you are invited to calculate three shot-gathers (seismic refraction record section) from shot points located at 50 km, 130 km and 200 km on this distance scale. These record sections should also be at the same scale as the model (10 km equals 2 cm) and with the same time scale reduced to 6.0 km/s, and 1 second equals 2 cm. Normalized and true-amplitude (scaled by distance to the 1.5 power) plots should be made. The source signal should be a simple wavelet with a center frequency of 15 Hz.

It is understood that the model will have to be approximated in order to calculate reflection and refraction synthetics; how different people make their approximations is the one topic of interest in the comparison."

Summary

Four different research groups each using different techniques attacked the Dataset 4 model. The manner in which the work was done is summarized in Table 1.

TABLE 1 Summary

Research Team	Reflection Synthetics	Refraction Synthetics	Parameterization Method	Analysis Method	Program
1. Jianchun, Chengke and Xuyao	no	yes	Polygonal blocks with constant velocity gradients No. of blocks = ?	Geometrical ray GRT + Maslov asymptotic	Jianchun et al.
2. Mereu	yes	yes	Triangular blocks with constant velocity gradients No. of blocks=355	Geometrical Ray GRT + diffractions and multiples	Mereu
3. Snyder and Hobbs	yes	yes	Layered model No. of layers= 10 Triangular	Geometrical Ray GRT + WKBJ	AIMS (reflection) SIMPLE (refraction)
4. Xiangkang, Chunyong and Liangbao	no	yes	Layered model No of layers=14	ART + Maslov + Maslov	Seis 83-- ART

Parameterization

In order to solve the problem a complex model must first be converted into a set of numbers for input to a computer. This usually involves some simplification steps which can have significant effects on the solution. In this workshop, 5 different techniques were used. Three involved block modelling with constant velocity gradients in each block and two converted the models into a set of layers with variable gradients. Block modelling allows one to incorporate sloping boundaries such as faults etc without any interpolation artifacts. Layered modelling may result in smoother models and hence may avoid some of the spurious events that sometimes occur with block modelling when structures are small and change rapidly. Snyder and Hobbs and Xiangkang et al. also changed the given model by removing steeply dipping boundaries as sources of reflections. Jianchun et al. and Mereu accepted the given model as is in that no boundaries were removed and no velocity values changed from that shown in Figure 1. Program Simple used by Snyder and Hobbs internal specifies triangular blocks from the layers specified. As such it functions much as the block modellers. Sharp lateral velocity contrasts (=foults) occur between triangles but do not produce reflections.

Comparison of Near Vertical Reflection Synthetics

Only two groups Snyder et al. and Mereu attempted the near vertical synthetic solutions. Snyder and Hobbs used a commercial package AIMS in their work while Mereu used a modified version of his triangular block modelling package to compute the zero offset traces. A comparison of their record sections shows good agreement in areas where the model is relatively simple. This can be seen in the distance range 150 km to 200 km where the boundary between the sedimentary rocks and the basement (1 -5 seconds) and the boundaries of the Moho transition zone show up as strong reflectors. Both solutions show the large offset in the Moho at the 140 km distance location. It was not possible to compare the effects at the ends of the model as the Snyder and Hobbs solution does not include the 0-50 km range or the 200-250 km range. Significant differences occur between the 2 solutions in the complex region of the model (50-150 km). There is little doubt that much of this is caused by the fact that the synthetics are very sensitive to the manner in which the model is parameterized. Mereu's second solution show that both diffractions and multiples can contain significant amounts of energy to change the appearance of the sections. An examination of a series of ray trace diagrams to many of the reflectors showed that the shortness and dip of the reflectors made the existence of the zero offset ray path impossible. Both solutions presented at the workshop indicate that conventional CDP stacking methods are really only applicable where the structures are relatively simple and horizontal. In areas of complex geology extreme

care would have to be exercised as to how a proper enhancement of the signal could be achieved. The lack of continuity of reflectors over significant distances may mean that unique identification of the events is not always possible.

Comparison of the Wide Angle Reflection/Refraction Sections

All four research groups computed synthetic seismograms for the three shot points -- SP1 at 200 km , SP2 at 130 km and SP3 at 50 km. A comparison of their results would at first glance give one the impression that the differences are so great that the investigators must have worked on "different" models! A careful examination of the sections do show some agreements. See for example the double reflectors mapped from SP2 in the 190 to 250 km distance range by Mereu and Xiankang et al. There is also good agreement among the researchers for SP2 in the 0-50 km range. The discrepancies which do exist among the solutions result from three different causes:

(i) The plots were not done on the same scale and the same reduced time ranges and distance ranges were not used.
(ii) The plots depend very much on how the models were parameterized.
(iii) The synthetics depend very much on how the different ray groups were chosen.

(i) The plots were not all done in the same manner. Mereu used a conventional reduced time scale of -1 to 7 seconds. This is the region that is normally analyzed in a refraction experiment. Xiankang et al extended the time range from -2 to 20 seconds and used an a different time/distance scale. Their sections thus have an entirely different appearance to those of Mereu. The synthetic sections by Xiankang et al and Mereu are for the complete distance range whereas the other 2 research groups show only the portions of the distance range where they have energy. Snyder and Hobbs plotted their data in an unconventional manner such that a comparison of their record sections with the other groups is not possible. The absence of rays to their surface shot points for SP2 and SP3 is puzzling, but is likely due to shadow zones (see below).

(ii) Mereu accepted the given model as is. This meant that near the surface blocks of high velocity igneous rocks were in place next to sedimentary rocks. This had the effect of introducing huge shadow zones into the sections. Similar shadow zone effects are also seen in the sections of Jianchun et al. The smoothing and removal of near vertical boundaries enabled both Xiankang et al and Snyder and Hobbs to shoot a much more continuous set of rays through the model without having anomalous effects and sharp discontinuities near the source affect the

ray paths. One could easily argue that if one is modelling the real earth then the omission of troublesome boundaries may be an over-simplification. On the other hand ray theory certainly has its limitations in complex structures such that spurious effects can easily occur particularly if the structures are small.It is also difficult to assess how a sharp velocity discontinuity may result from the fault emplacement of two rock types next to one another.

(iii) There are an infinite number of rays which one can shoot through a model to generate synthetics. In practice the number must be reduced to include only those rays which are considered to be significant. A comparison of the ray trace diagrams and corresponding synthetics for all 4 research groups clearly shows that the choice of rays varied greatly from one research group to another. Mereu's program selected all direct rays and all reflected and converted rays including the first two multiples from each of the reflecting boundaries for his synthetics. The manner in which the rays were selected by the other research groups was not stated and hence it is impossible to make further comments on this point. Jianchun et al. produced pairs of synthetics which show very clearly how Maslov asymptotic theory extends the GRT travel-time branches. These effects were also confirmed by Xiankang et al. in the one Maslov synthetic which they produced. Snyder and Hobbs used the SIMPLE program which generates synthetics using the WKBJ approximations. The fact that the solutions obtained by those using the Maslov method show little agreement with each other again indicates that the synthetics are much more sensitive to the method of model parameterization and choice of rays than they are to the second order refinements of asymptotic ray theory.

Conclusions

It is quite clear that much more work on the forward modelling problem must be done to determine how to compute synthetics for the complex models which we expect over tectonically disturbed areas such as that of the Pyrenees. This is a very important point since we all know that the inverse problem which requires proper phase identification is impossible without a good forward modelling approach.

All 4 research groups agree that it would be very difficult to derive a unique complex tectonic structure such as that shown in Figure 1 from an analysis of seismic data obtained over the region. The required resolution of the detailed structure is not possible.

COMPLEX RAYPATHS BENEATH THE PYRENEES

Dave B. Snyder and Richard W. Hobbs

BIRPS, Bullard Laboratories, Madingley Road, Cambridge CB3 0EZ, UK

Abstract

BIRPS concentrated its efforts on the synthetic seismic sections derived from the ECORS model of the Pyrenees. We used AIMS and a 10-layer model with 2D velocity field to calculate a synthetic zero-offset section with 50 m CMP spacing. Parts of the section have as many as 8 phases arriving from primary interfaces within the central part of the Pyrenees model making association of reflection with model layer challenging. A synthetic section, fk-migrated at constant velocity after the addition of random noise, provides a check on the accuracy of the forward modelling. Wide-angle synthetic sections from 3 shotpoints were produced using SIMPLE and the digitized coordinates from the AIMS model. After reformatting and raytracing, synthetic seismograms were computed using both WKBJ and geometric ray theory algorithms. Again, ray paths within the central part of the model produced much multipathing, few diving rays, and generally complex wide-angle reflection raypath tables. Interpretation of the seismograms from this constrained model is thus a confusing and uncertain process.

Introduction

The fourth data set offered for analysis at the Controlled Source Seismology Workshop held at Fellhorst, Germany, was a 2-D velocity model derived from the ECORS interpretation of their deep seismic profile across the Pyrenees (Roure et al., 1989). Data set 4 was intended as the philosophical inverse to data set 5 offered in 1987: here, to determine what seismic section one should expect to observe from a profile across a complex orogenic belt. Whereas the 1987 exercise challenged migration techniques and related assumptions, the present one addresses some basic questions concerning assumptions made in the now common practice of relating a seismic reflection profile to a complex tectonic model. The ECORS Pyrenees Team used migration and geologic inference to develop the tectonic model adapted by the CCSS workshop organizers. The foremost question raised here is the 'robustness' of the ECORS model: is it seismically permissible or definitive?

Additional questions include: can the CMP-gather method ever adequately explore complex orogenies or must all possible seismic energy paths be ray-traced to understand the seismograms properly or will sufficient computational power allow finite-difference or finite-element techniques to compensate for our detailed ignorance about seismic wave paths? Only the first question will be discussed here in any detail.

Model Parameterization

The first step in producing synthetic seismogram from tectonic model is the translation of the geologists' model into numbers for the computer modelling. The CCSS workshop organizers parameterized model seismic velocities into discrete blocks. Some would argue that such blocks introduce too much detail into the model for successful ray tracing and generation of seismograms, others claim that these blocks oversimplify the true velocity distribution and thus guarantee inadequate modelling from the start.

The approach adopted here was a practical one, knowing that near-surface velocity variations were meant to represent changes in metamorphic grade between adjacent thrust nappes within the Pyrenees. Thus, only velocity block boundaries dipping at ~60° or less were made into layer boundaries, steeper velocity boundaries were represented as horizontal velocity gradients similar to the vertical gradients explicitly specified by the CCSS data set. Ten layers were used in the modelling (Figure 1 and Figure 4 for detail). The only non-obvious layer begins at km 200, 4 km depth, is divided into two parts at km 135, and ends at km 80 near 45 km depth (also see Figure 4). Gradients were specified as velocities along the top and bottom of each layer. The primary rationale for this decision was that the CMP method (without pre-stack migration) cannot resolve impedance contrast boundaries dipping more than ~45° as it is based on assumptions of horizontal layers. Second, the layer boundaries were designed to emphasize the major thrusts assumed in the ECORS tectonic model. Clearly many assumptions already bias the results.

The ten layer model was digitized and input to a commercial modelling package, AIMS (Advanced Interactive Modelling System of Geoquest International Inc.), then operating on the Bullard Laboratories' computers in Cambridge, for modelling the zero-offset section. The resulting digital model was then reformatted for input into SIMPLE (Seismic Interactive Modelling Programming Language courtesy of Chris Chapman) for modelling the wide-angle seismograms. The top nine layers have 24, 8, 12, 10, 9, 10, 16, 10, and 11 velocities specified along their upper and lower boundaries, respectively. Each modelling program interpolated these velocity points internally thus modifying the same digitally parameterized model.

Zero-offset synthetic seismograms

A synthetic zero-offset seismic section was produced with AIMS using this digitized model and performing calculations every 50 m along the profile. Here we show a simplified ray diagram in which zero-offset rays were calculated every 2.5 km, using only one in fifty of the stations (Figure 1). The ray diagram illustrates the intricate raypaths caused by the triangular prism in the upper crust of the Pyrenees between kilometers 50 and 125. Some stations near the center of the profile have as many as 8 arrivals from layer boundaries. Note that only a single two-way raypath from station to layer interface is assumed here. The impulse travel-time response was then convolved with a Rickert wavelet centered at 30 Hz to produce a synthetic seismic section without attenuation, scattering, multiples or any noise generated from diffractors (Figure 2).

The synthetic zero-offset seismogram (Figure 2) shows that the upper crustal prism produces a bow-tie pattern between 3 and 14 s travel time and centered at km 100, whereas the dipping slab produces parallel reflections at about 10s travel time that overprint reflections from the model Moho beneath the N. Pyrenean Frontal Thrust and North Pyrenean Zone (Choukroune and ECORS, 1989). The 1-2 second jumps in phases at kilometers 130 and 140 are attributed to vertical discontinuities in the velocity model at the northern edge of the Tremp basin where near-surface velocities change from 2.0 kms^{-1} to 6.0 kms^{-1}. Stacking of synthetic common midpoint gathers was not attempted, but would have resulted in further degradation of signal coherency and amplitude as arrivals vary significantly over typical spread lengths.

Figures 1, 2, and 3, see next pages.

Figure 1: Ray diagram for the zero-offset seismic section showing layers used in the AIMS modelling to represent the tectonic model. One in fifty stations (2.5 km spacing) were raytraced for this figure. No vertical exaggeration in the section, which is not the entire data set 4.

Figure 2: Synthetic zero-offset seismic section derived from the model in figure 1. Some random noise was added, but no multiples or diffractions were calculated. Note that only a partial section is shown (km 80 to 200).

Figure 3: F-k migration of the the synthetic section shown in figure 2 using a constant velocity of 5 kms^{-1} to provide a crude check on the fidelity of the modelling. This checks the original interpretation of the reflection profile, the parameterization of the tectonic model, and the forward modelling done here. Note that the lack of 2D velocity information in the migration does not correct offsets produced by strong, lateral velocity variations in the near-surface at km 130 and 140.

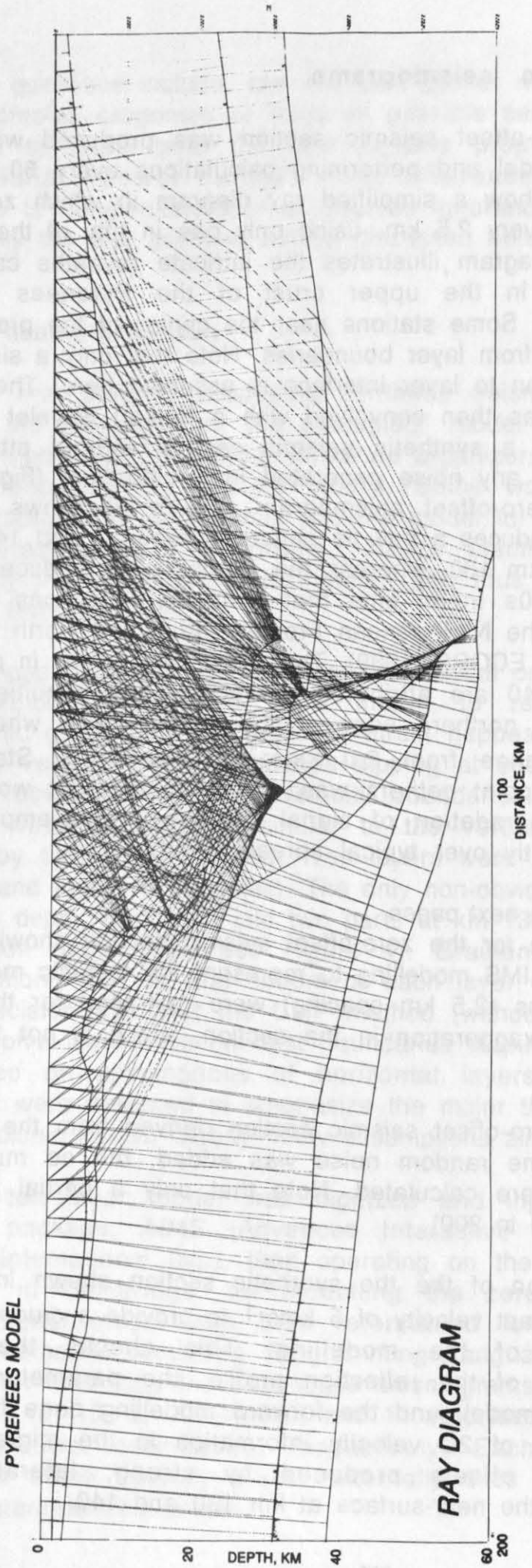
PYRENEES MODEL
RAY DIAGRAM
0
20
DEPTH, KM
40
60
100
200
DISTANCE, KM

Figure: 1

Figure: 2

Figure: 3

A constant velocity (5 kms^{-1}) f-k migration was performed on the synthetics in order to estimate the resolution achievable with this ray-traced forward modelling (Figure 3). The major features such as the upper crustal triangular prism along the central axis of the orogen and the dipping Moho between km 150 and 200 are visible. However, because this was a time-migration and did not include the, at times sharp, velocity variations in the near-surface, reflector offsets are not restored to continuity and instead produce strong over-migration curves. The lower crustal region around km 80 becomes a confused pattern of migration artifacts.

Wide-angle synthetic seismograms

Synthetic seismograms for the same profile using wide-angle reflections and possible diving rays were also calculated for model shots at km 50, 130 and 200 (Figure 4). Such shots were never attempted by the ECORS Pyrenees Team, but these hypothetical sections were anticipated to provide additional constraints or information about the tectonic model or actual earth structure. The ray diagrams (Figure 4) illustrate that few diving rays were successfully traced through the model by the SIMPLE program. This is likely due to the relatively gentle vertical gradients specified throughout the model by the CCSS workshop organizers. As a result, the modelling described here strongly emphasizes the wide-angle reflections.

SIMPLE allows several options to produce synthetic seismograms from the spike arrivals calculated by the travel-time program which traces rays through triangular blocks each with velocity specified at its corners. Here two versions of the synthetic seismograms are shown (Figures 5-9) for each shot point. WKBJ (Maslov) seismograms (Chapman, 1986) produce strong, continuous phases that are easy to trace and thus easier to identify or associate with a layer boundary. Geometric ray theory (GRT) seismograms are equivalent to those of WKBJ except that the theta-phase curve is approximated by parabolas at each stationary point, and phases are truncated beyond where the ray diagram indicates no further successful rays were traced.

Comparison of these seismograms with the ray diagrams and travel-time tables permits identification of the major phases. The relatively simple crustal structure beneath SP1 (Figure 4) produced clear phases from only the near-surface layers, out to ranges of 26 km for layer 1 reflections and diving rays, and out to 20 km ranges for layer 2 reflections (GRT in Figure 5). Amplitudes from the deeper reflections in layer 7 seen on the ray diagram do not appear on either seismogram due to their low amplitude.

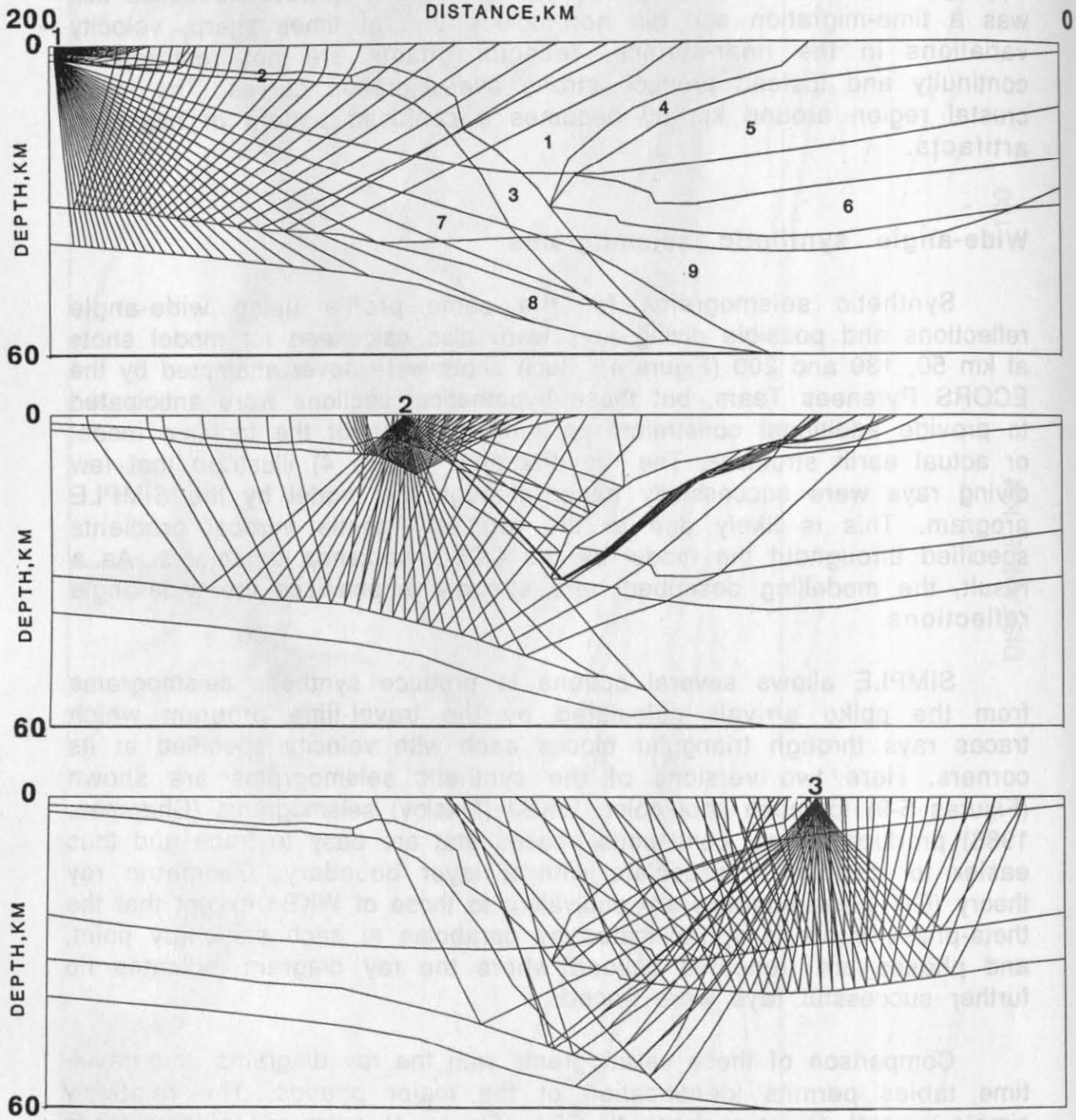

Figure 4: Ray diagrams for the three wide-angle shots. No vertical exaggeration in the sections, numerals in the uppermost model indicate layer numbers used as references in the discussion. Note the general lack of diving rays due to the gentle vertical velocity gradients specified by the organizers.

Shot point 2 North clearly sensed the complex velocity distributions near the center of Pyrenees model. Phases are not linear, nor at all similar between the northern and southern ray directions. To the south, the two topmost layers again produced the largest phases (WKBJ in Figure 6). On the northern gather, reflections from the base of layer 1 indicate the layer's triangular cross section (WKBJ in Figure 7). Reflections from the next deeper boundary, layer 3 (WKBJ in Figures 6 and 7), do not exactly coincide here due to the steep dip of the velocity interface. The brightest phase on the northern gather is from layer 5 and shows numerous branches that converge around km 100 (WKBJ in Figure 7). Layer 7 reflections are of low-amplitude but recognizable both to the north and south.

Shot point 3 sampled the northern half of the orogen. Due to the close proximity of strong velocity changes associated with the North Pyrenean Frontal Thrust, rays sampling either layer 1 or layer 4 have not been successfully identified but may correlate with the numerous bright phases with low velocity seen on the southern gather (WKBJ in Figure 8). Only layers at Moho depths, layers 5 and 6, produced recognizable phases that again show much asymmetry due to curvature of the layers (WKBJ in Figure 9). The general lack of easily identifiable phases on these seismograms is somewhat disappointing.

Figures 5-9, see the next 5 pages.

Figure 5: Synthetic seismograms for shot point 1 (km 200) calculated using both WKBJ and geometric ray theory (GRT) [Chapman, 1986]. Numerals on seismogram indicate interpreted source layer for the phase labelled.

Figure 6: Synthetic seismograms for shot point 2 (km 130) in a southward (toward km 200) direction calculated using both WKBJ and geometric ray theory (GRT). Labels as in figure 5.

Figure 7: Synthetic seismograms for shot point 2 (km 130) in a northward (toward km 0) direction calculated using both WKBJ and geometric ray theory (GRT). Note lack of similarity between the results from the two methods using identical travel-time tables. Labels as in figure 5.

Figure 8: Synthetic seismograms for shot point 3 (km 50) in a southward (toward km 200) direction calculated using both WKBJ and geometric ray theory (GRT). No phases have been confidently identified here.

Figure 9: Synthetic seismograms for shot point 3 (km 50) in a northward (toward km 0) direction calculated using WKBJ theory, GRT produced no phases here. Labels as in figure 5.

Figure: 5

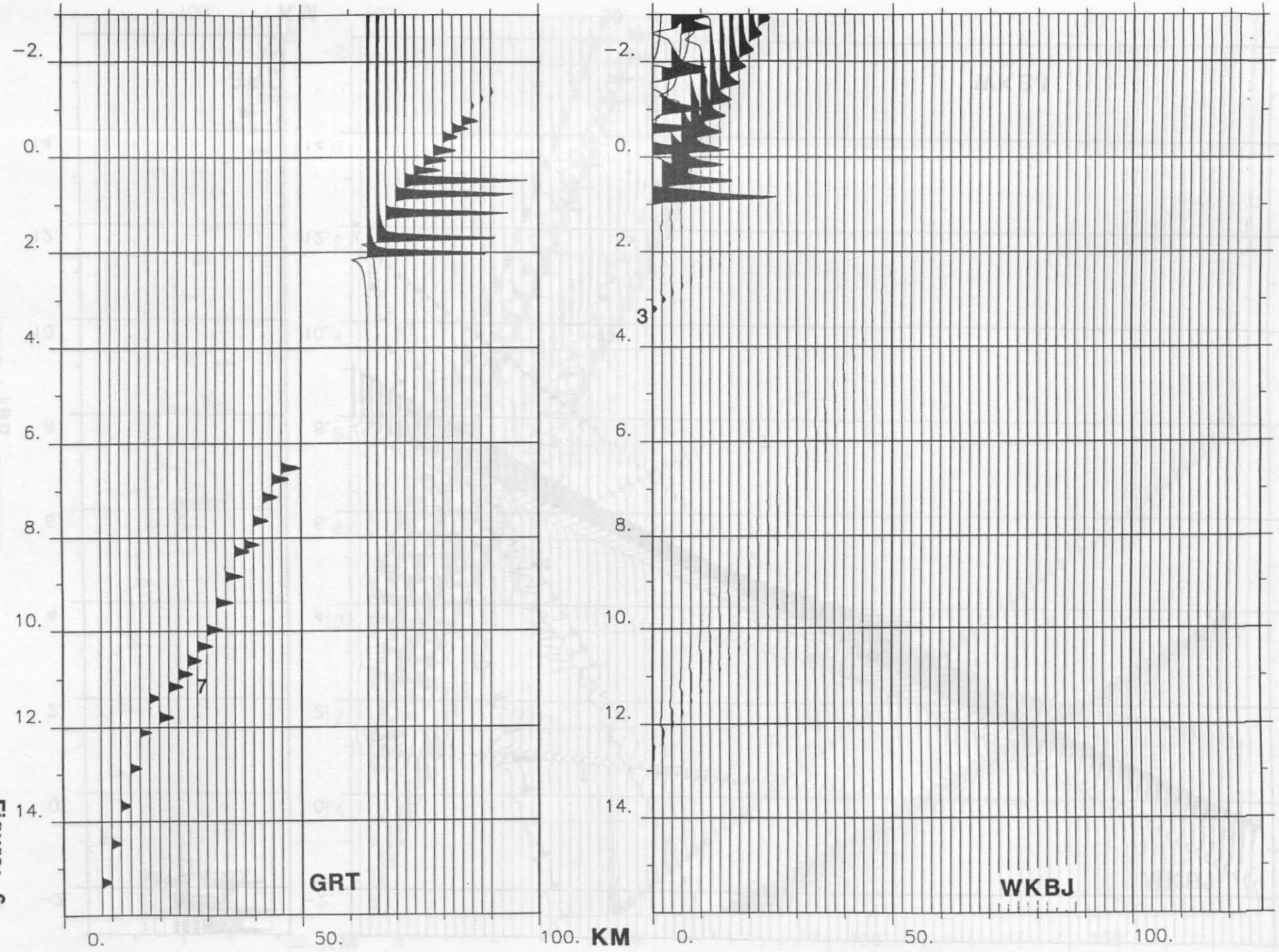

Figure: 6

WKBJ
GRT
KM
0.
50.
100.
150.
100.
-2.
0.
2.
4.
6.
8.
10.
12.
14.
1
2
3
4
5
6
7
TIME(P$_{red}$=0.167),S

Figure: 7

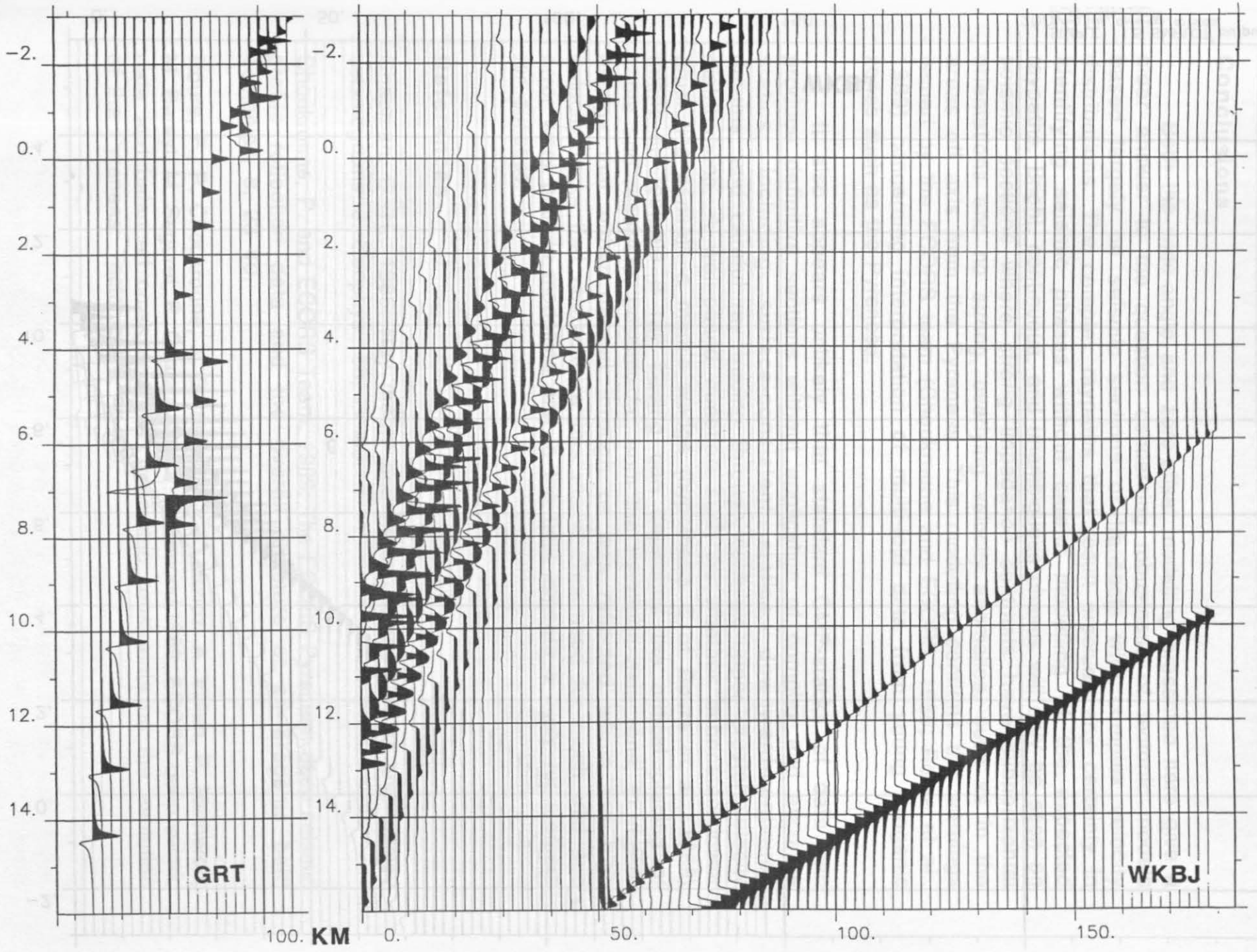

Figure: 8

WKBJ
SIMPLE 1.5 SMPLOT output
TIME(P$_{red}$=0.167),S
-2.
0.
2.
4.
6.
8.
10.
12.
14.
0.
50.
100.
150.
5
6

Figure: 9

Conclusions

Both the wide-angle and zero-offset modelling presented here give a clear answer to the question concerning robustness of tectonic models based largely on seismic sections of transacts with complex velocity distributions. The complex raypaths that result preclude any certainty in identifying seismic phases without careful modelling of the expected raypaths. Bright, continuous, and unambiguous phases will only be seen on seismic sections where strong impedance contrasts have subhorizontal orientations and no strong, overlying velocity anomalies, such as in the areas off axis from the Pyrenees. This modelling confirms the warnings issued by the ECORS team (Choukroune and ECORS, 1989; Roure et al., 1989) concerning interpretation of multi-fold data from young orogenic zones such as the Pyrenees.

It also appears unlikely that standard CMP-stacks of data can produce definitive sections without application of complex and accurate statics, including surface-consistent statics, downward-continued datums, and careful ray tracing through complex upper crustal velocity distributions. A well-posed question such as whether imbricated lower crust lies beneath a mantle wedge (hypothesis C of Roure et al., 1989) might be testable if ray tracing can determine the critical placing of shots and receivers, possibly far from the Pyrenean axis zone, to record energy that either passed through or was reflected within the high velocity rocks that characterize this model. The need for much trial and error work both in modelling and in the field appears a likely requirement for success.

References

Chapman, C. H., 1986: Ray theory and its extensions—WKBJ and Maslov seismograms; J. Geophys., 58, 27–43.

Choukroune, P. and ECORS Team, 1989: The ECORS Pyrenean deep seismic profile reflection data and the overall structure of an orogenic belt; Tectonics, 8, 23–40.

Roure, F., P. Choukroune, X. Berastegui, J. A. Munoz, A. Villien, P. Matheron, M. Bareyt, M. Seguret, P. Camara, and J. Deramond,1989: ECORS deep seimic data and balanced cross sections: geometric constraints on the evolution of the Pyrenees; Tectonics, 8, 41–50.

COMPUTATION OF SYNTHETIC SEISMOGRAM WITH MASLOV'S METHOD FOR A COMPLEX MODEL

Wu Jianchun, Wang Chunyong, and Zhu Lingbao

Institute of Geophysics, SSB, Minzouxueyuan Nanlu Road, Beijing, 100081, P.R.China

Abstract

Maslov's asymptotic method was used for the wave field computation of the given 2-D lateral inhomogeneous model. The velocity structure is parameterized by large polygonal blocks, and within each block the velocity gradient is equal and of arbitrary orientation. A simple, efficient ray trace method presented by Spence (1984) is adopted. To eliminate these singularity effects, we worked out a program to chose the weight factors and filter functions automatically in the computation of the theoretical seismograms.

According to the synthetic seismic sections from three shot points located at 50 km, 130 km and 200 km, the M-discontinuity and the second order discontinuity near 25 km can be sketched. The waveform obtained by Maslov's method near the singular points is well improved compared with the standard ray method. In the non-singular region, the results of both algorithms are basically similar.

Introduction

In the last two decades it has become standard practice to interpret explosive seismic record sections in terms of amplitudes as well as travel-times. The reflectivity method and generalized ray method have obtained relative success for 1-D models. The earth, however, is not composed of a stack of plane layers but more complicated with many seismic parameters and interfaces varying not only vertically but also horizontally. The use of 2-D models to describe the crustal structure more realistically has interest for interpreting seismologists. The most popular method for 2-D inhomogeneous media may be the standard ray method, but it is invalid for singularities (such as caustics, critical points, transitions from illuminated to shadow region etc.). One of the techniques to overcome some of the difficulties in singularities is Maslov's asymptotic method. High efficiency is sought by all algorithms. To reduce computation costs associated with trial and error seismic modelling, a fast ray tracing procedure proposed by Spence (1984) is

adopted in this paper. A program for screen plotting which is much faster than paper plotting has been developed. Liouville's theorem ensures that it is always possible to obtain a uniform asymptotic solution by Maslov's method. But the calculation has to be done carefully because the singular points in X-space and their spatial Fourier transform Y-space may be very close in practice. The choice of weight factors and filter window functions whitch are used to eliminate the singular point effects, are automatically choosen in the program.
In the following, a brief introduction of parameterization and ray tracing will be described. The calculation formula is given directly and a discussion on the synthetic seismograms for data set 4 by standard ray method and Maslov's method will be conducted.

Velocity model and ray tracing

Before a specific ray tracing model is adopted, the main objectives must be brought to mind that the theoretical model must approximate any realistic medium sufficiently, it should be possible to define it by a minimal amount of input parameters,and it must allow a rapid and accurate computation of any type of elementary ray path and the corresponding amplitude.
Considering these points, we think that the velocity structure parameterized by large polygonal blocks is effective in practice. There are two types of block boundary: "model boundary" and "divider boundary". A model boundary used to define velocity in a block is a straight line of arbitrary dip, assigned a constant velocity along its length and a nonzero velocity gradient normal to its length. Only one model boundary is defined in each block. A divider boundary, separates a region with one velocity and gradient from a adjacent region with a different velocity and gradient. Blocks may thus be defined in which the velocity and both the magnitude and the direction of the velocity gradient are arbitrary. According to the given 2-D model, the model boundary of block with the gradient is horizontal, for which the velocity at any point can be calculated from the velocity at the boundary plus the product of gradient by depth Z. A block with constant velocity gives a very small gradient. The ray path within such a given block is a circular arc, for which the travel time and distance traveled may be calculated using very simple analytical expressions.
Figure 1 shows the parameterized model of data set 4.

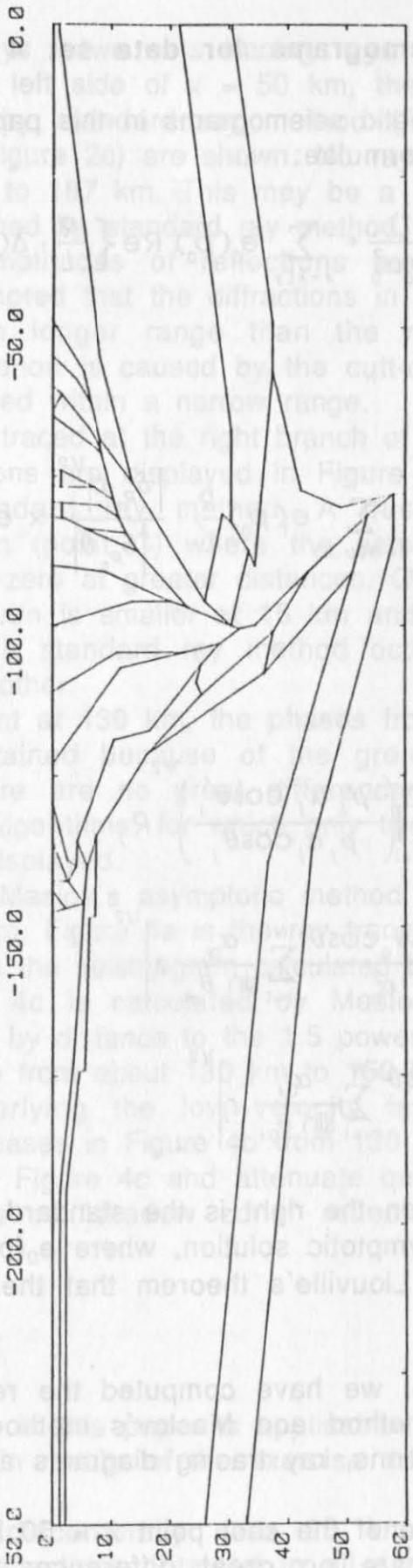

Figure 1: The parameterized model of data set 4.

Synthetic seismograms for data set 4

The synthetic seismograms in this paper are computed according to the following formulae:

$$u(x,t)=\frac{\dot{m}(t)}{4\pi\rho_0\alpha_0^2} * \sum_{x=x(y)} e_0(p_0)\,\mathrm{Re}\left\{\frac{R}{L}\cdot\Delta(t-T(x,x_0))\cdot e^{-i\pi\sigma(x_0,x)/2}\,p\right\}$$

$$-\frac{\dot{m}(t)}{2^{5/2}\pi^2\rho_0\alpha_0^2}$$

$$*\frac{d}{dt}\,\mathrm{Im}\left\{\Lambda(t)\left[\sum_{t=\tau(p,x)} e_1(p_0)\frac{R}{L'}\cdot\frac{\left|\delta_{p_0}p\right|^{1/2}}{\left|\delta_{p_0}\tilde{\theta}\right|}\times e^{-i\pi\sigma(x_0,x)/2-i\pi(1-\mathrm{sgn}(\delta_p x(y_1)))/4}\,p\right]\right\}.$$

Where:

$$y=(p,z)$$

$$R=\left|\frac{\alpha_0\rho_0}{\alpha\rho}\right|^{1/2}\prod_{j=1}^{N}\left(\frac{\rho'_j\alpha'_j\cos\theta'_j}{\rho_j\alpha_j\cos\theta_j}\right)^{1/2}R_j$$

$$L=\left|(\delta_{p_0}x)\,\frac{\cos\theta_0\cos\theta}{\alpha_0^2}\sum_{i=1}^{N}\frac{\alpha_{0i}}{\sin\theta_{oi}}\,r_i\right|^{1/2}$$

$$L'=\left|\frac{\cos\theta_0\cos\theta}{\alpha_0^2}\sum_{i=1}^{N}\frac{\alpha_{0i}}{\sin\theta_{0i}}\,r_i\right|^{1/2}.$$

The first term on the right is the standard ray solution, the second term is Maslov's asymptotic solution, where $e_0(p_0)$, $e_1(p_0)$ are weight factors. It is ensured by Liouville's theorem that there are no singularities in mix space.

For data set 4, we have computed the refraction synthetic sections by standard ray method and Maslov's method respectively for each point. Normalized sections, ray tracing diagrams and travel time curves are also obtained.

At the right side of the shot point x = 50 km, two sets of reflections are traced. There are no great differences between the two algorithms because no singularities exist.

In Figure 2a, five types of rays - two sets tracing rays and three sets reflections - are traced at the left side of x = 50 km, the corresponding synthetic sections calculated by standard ray method (Figure 2b) and Maslov's asymptotic method (Figure 2c) are shown. No rays are observed within the range from 175 km to 187 km. This may be a "shadow zone", where no phases will be obtained by standard ray method, but diffractions appeared clearly and the amplitudes of reflections are smoothed in Maslov's solution. It must be noted that the diffractions in the upper right segment (AB) cover a much longer range than the reflections and attenuate slowly. This phenomenon is caused by the cutt-off error of the integral when the rays are traced within a narrow range.

The most complex phases are traced at the right branch of shot point x = 130 km. Nine sets of reflections are displayed in Figure 3a. Figure 3b shows the result using standard ray method. A cusp appears at approximately 3 s and 15 km (point C) where the amplitudes change abruptly from a large value to zero at greater distances. On the Maslov's section (Figure 3c), the amplitude is smaller at 15 km and is nonzero at greater distances. The cusp in standard ray method occurs when one branch of phases joins with another.

For the left branch of shot point at 130 km, the phases from shallow and middle interfaces are not obtained because of the great abruption of velocity near shot point. There are no great differences between the results calculated by the two algorithms, for which only two sets of deep discontinuity reflections are displayed.

The most successful result of Maslov's asymptotic method is observed at the section of shot point 200 km. Figure 4a is the ray tracing diagram, the response shown in Figure 4b is the seismogram calculated by standard ray method, while that in Figure 4c is calculated by Maslov's asymptotic method. All sections are scaled by distance to the 1.5 power. There are no rays existing between the range from about 130 km to 150 km due to high velocity triangular blocks overlying the low velocity layer. It is not surprising to find the lack of phases in Figure 4b from 130 km to 150 km. The diffractions are observd in Figure 4c and attenuate quickly. The time shift of phases at both sides of "shadow zone" reflects the different velocity structures.

Conclusion

The asymptotic procedure used in this paper is applicable to 2-D laterally inhomogeneous media. The main results of the exercise are concluded as follows:

1. Moho interface and the discontinuity near 25 km can be well constrained by two trains of reflections obtained in all synthetic sections from three shot points. The difference of shallow structures on both sides near 130 km is also reflected from Figure 4, but further detail

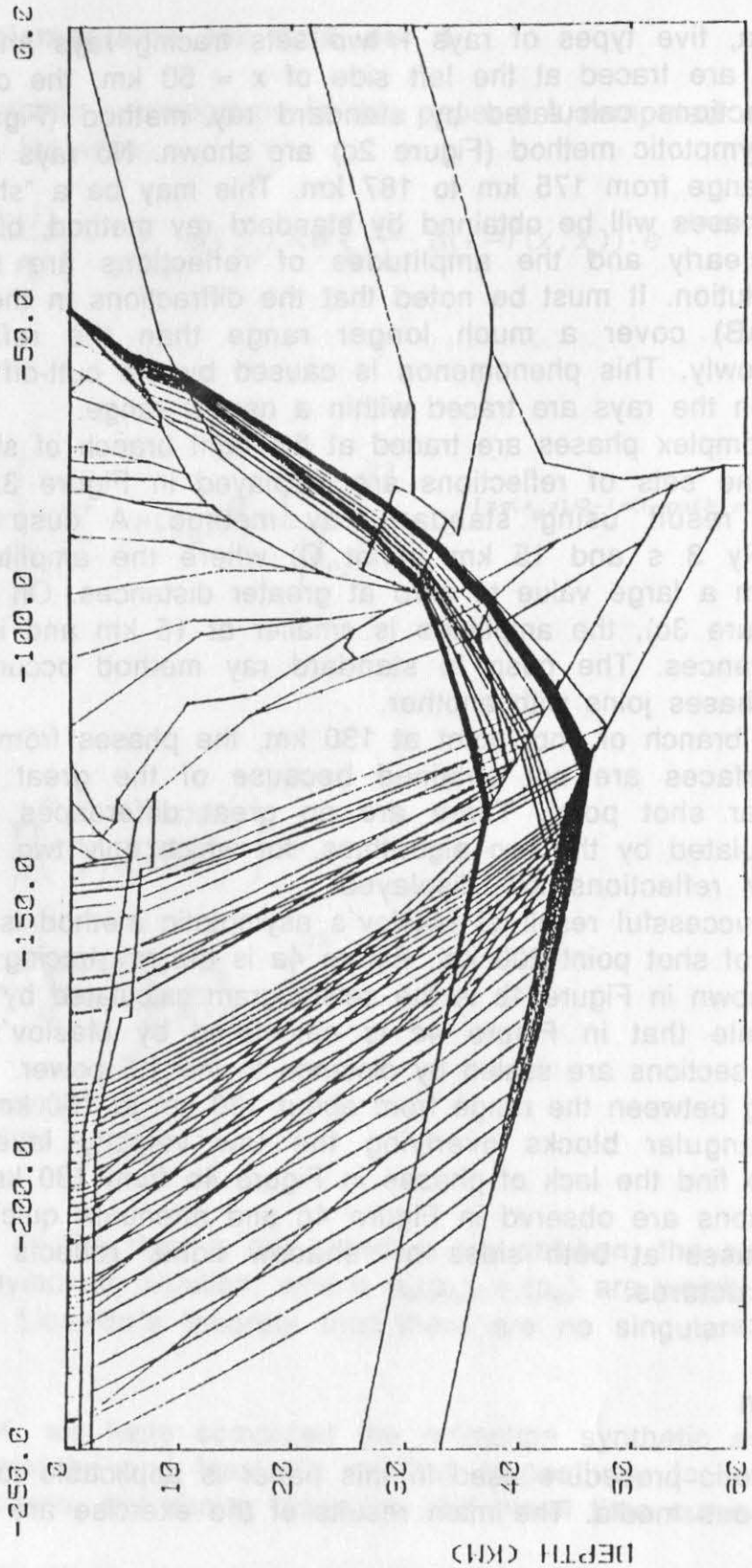

Figure 2a: Ray tracing diagram (x=50 km, left branch)

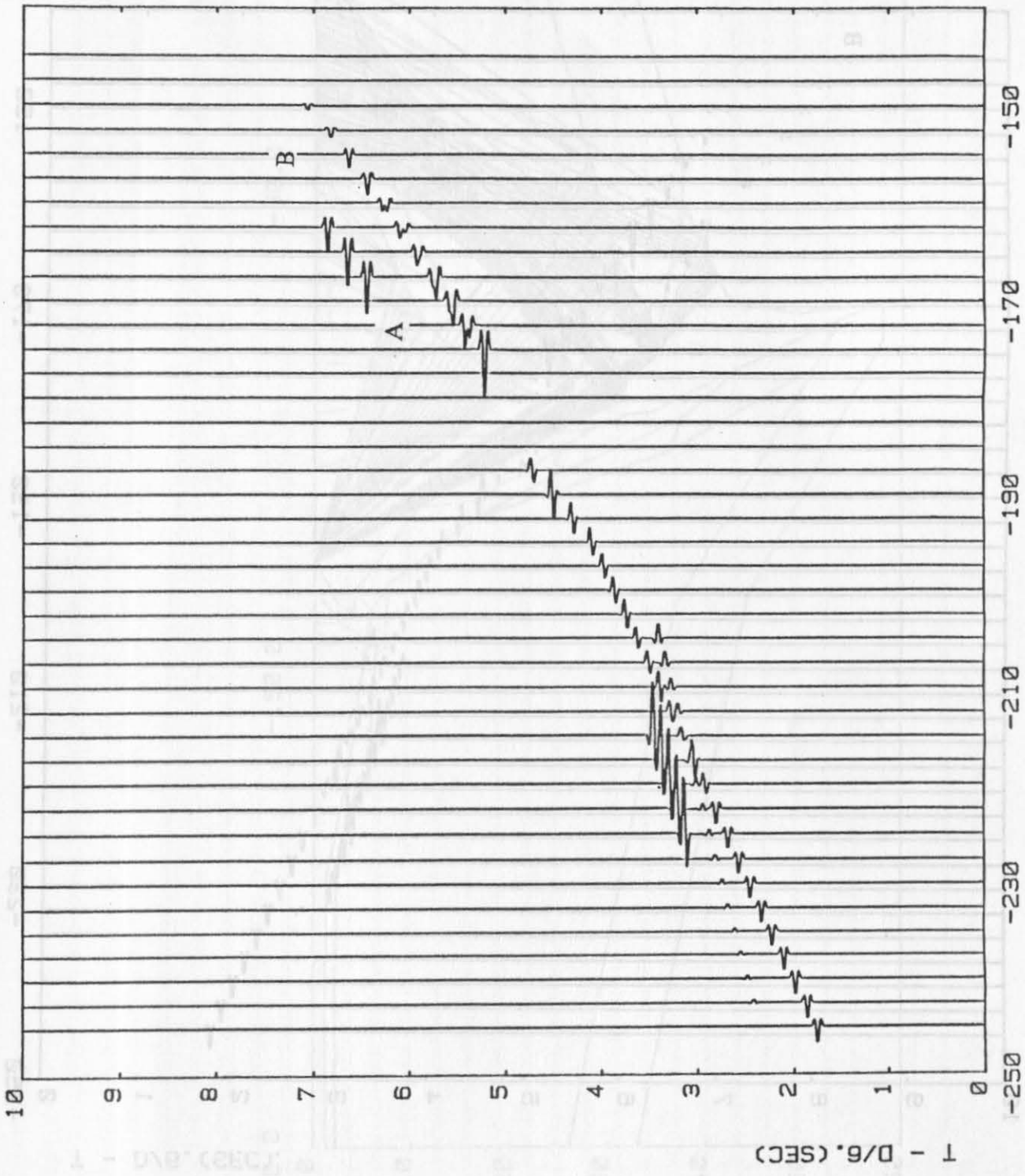

Figure 2b: Synthetic section by standard ray method (x=50 km, left branch)

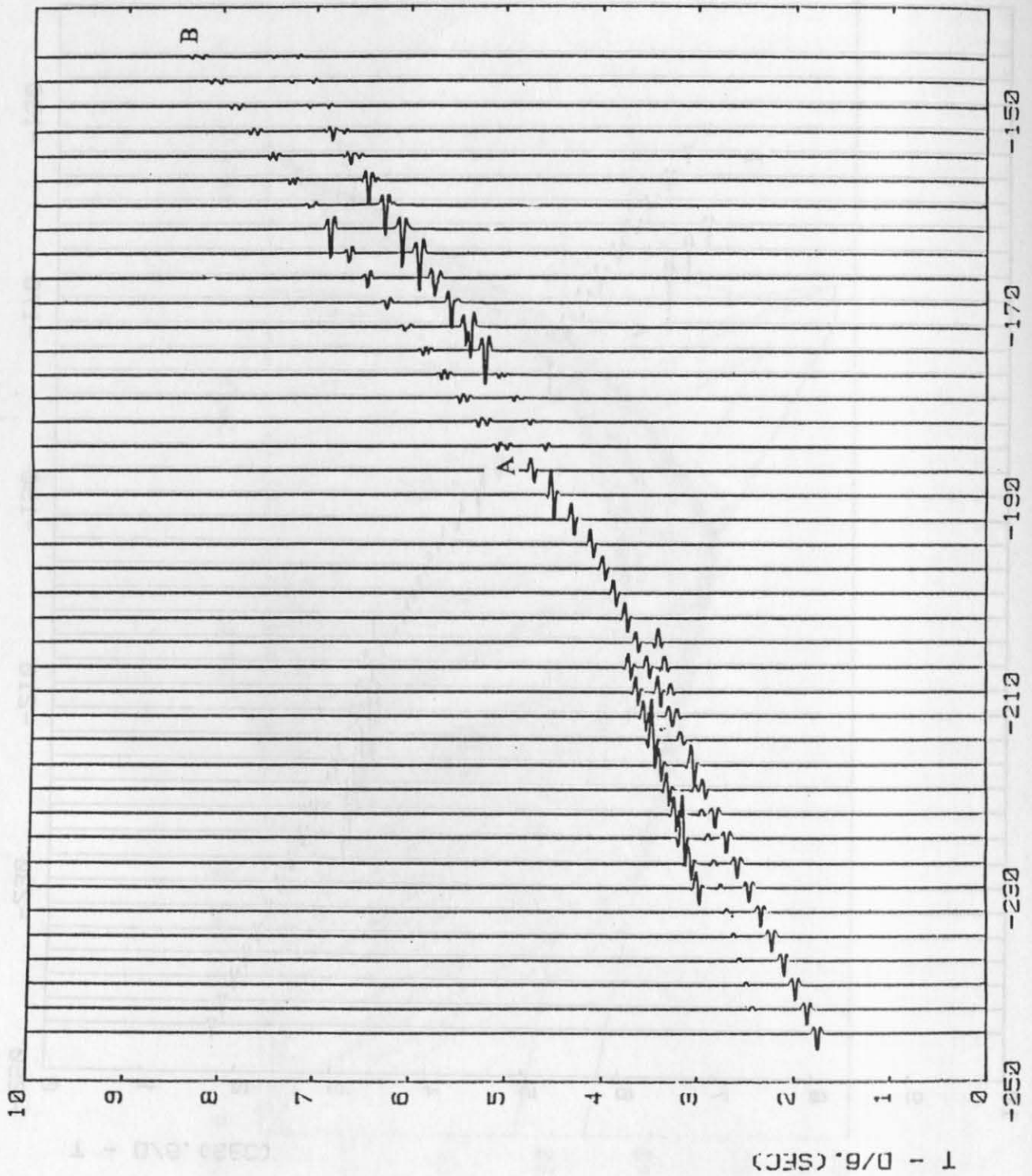

Figure 2c: Synthetic section by Maslov´s asymptotic method (x=50 km, left branch)

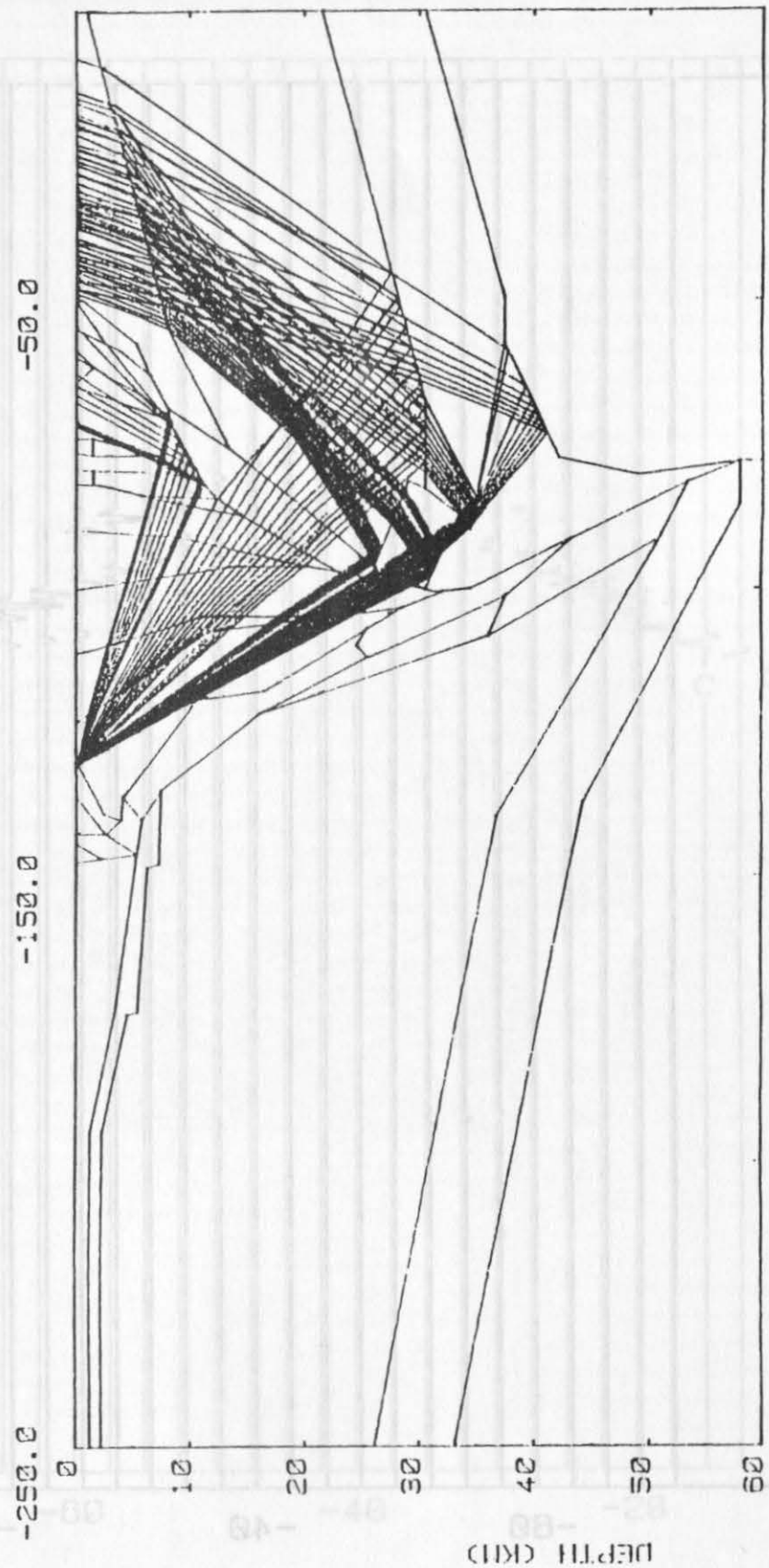

Figure 3a: Ray tracing diagram (x=130 km, right branch)

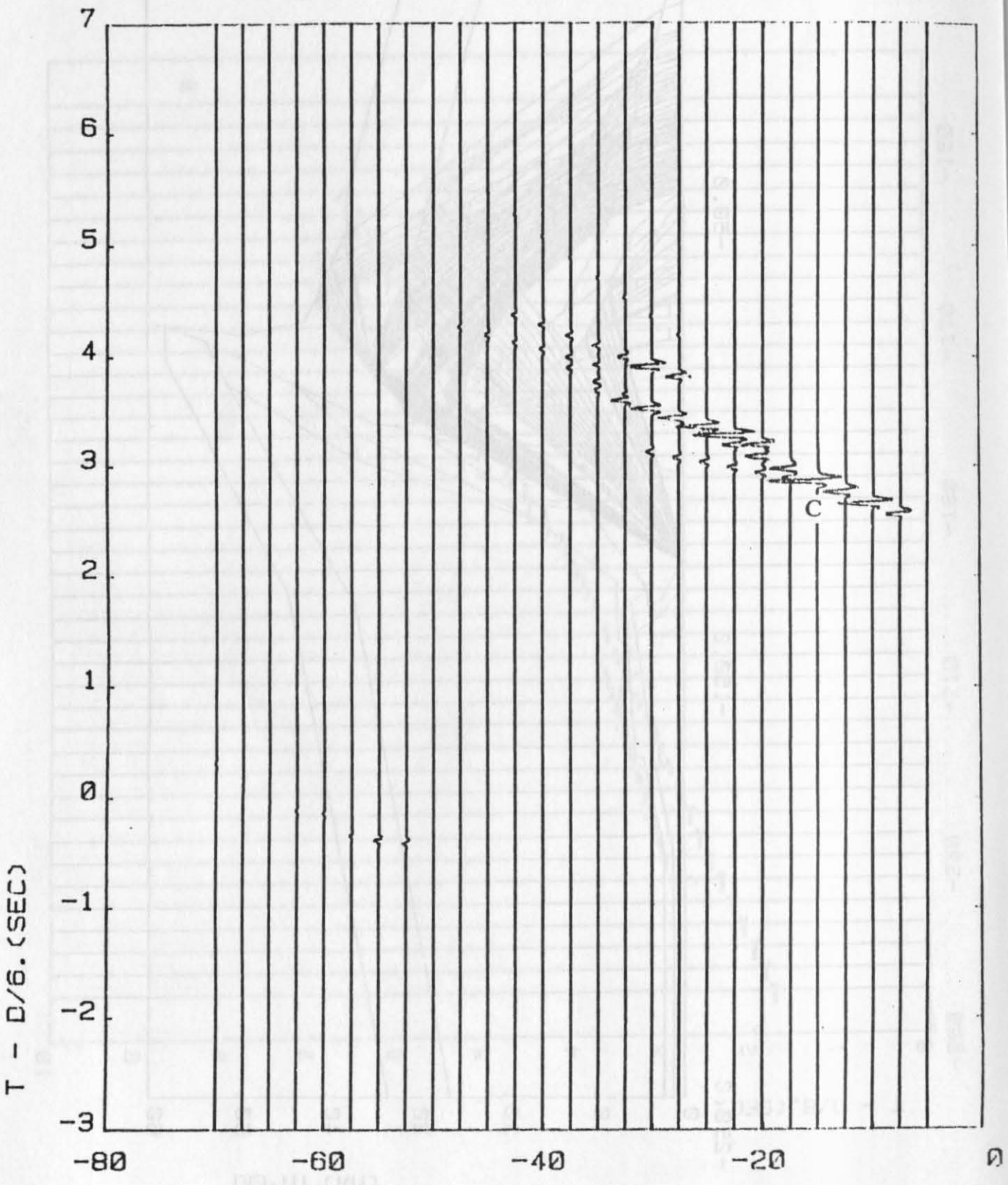

Figure 3b: Synthetic section by standard ray method (x=130 km, right branch)

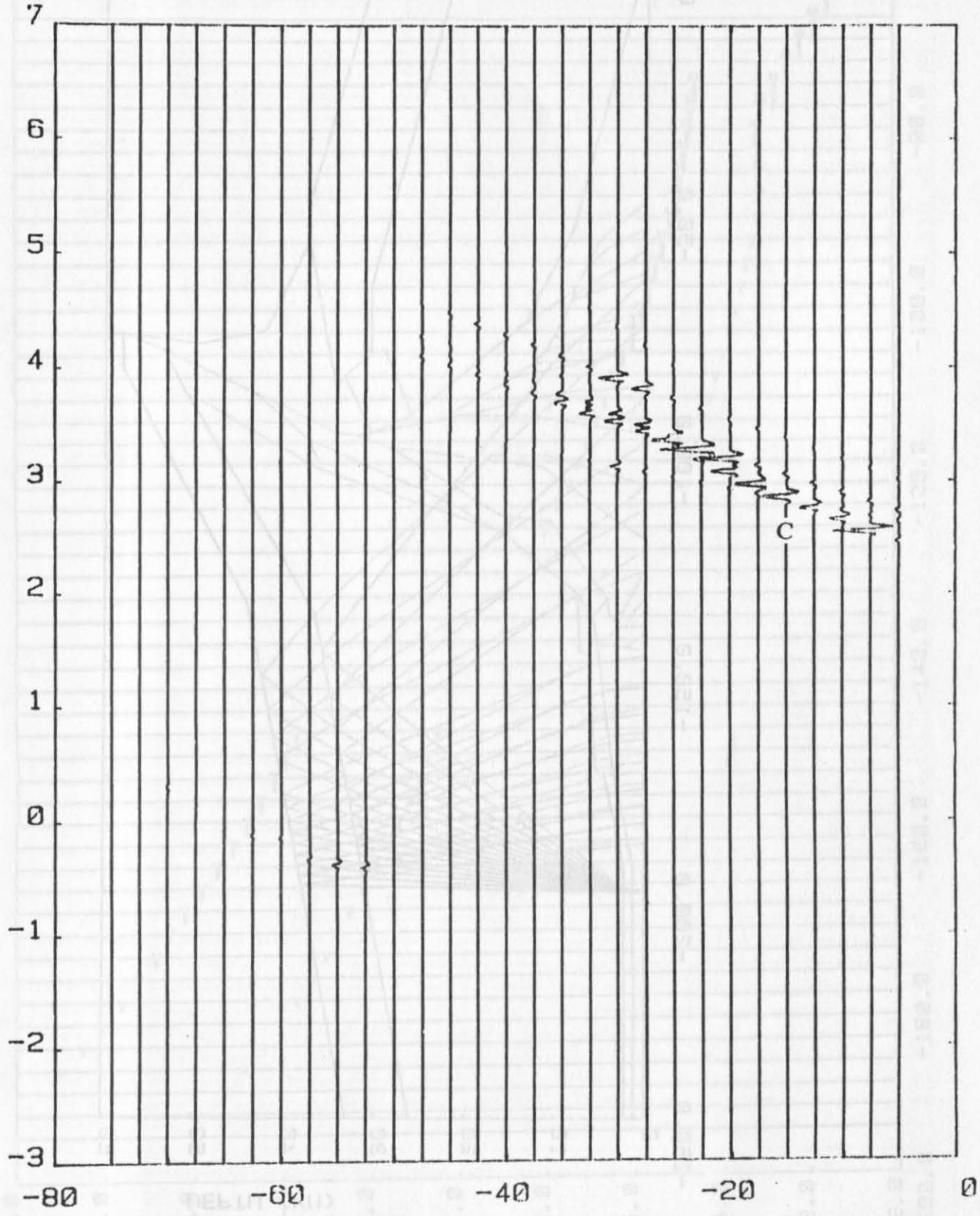

Figure 3c: Synthetic section by Maslov´s asymptotic method (x=130 km, right branch)

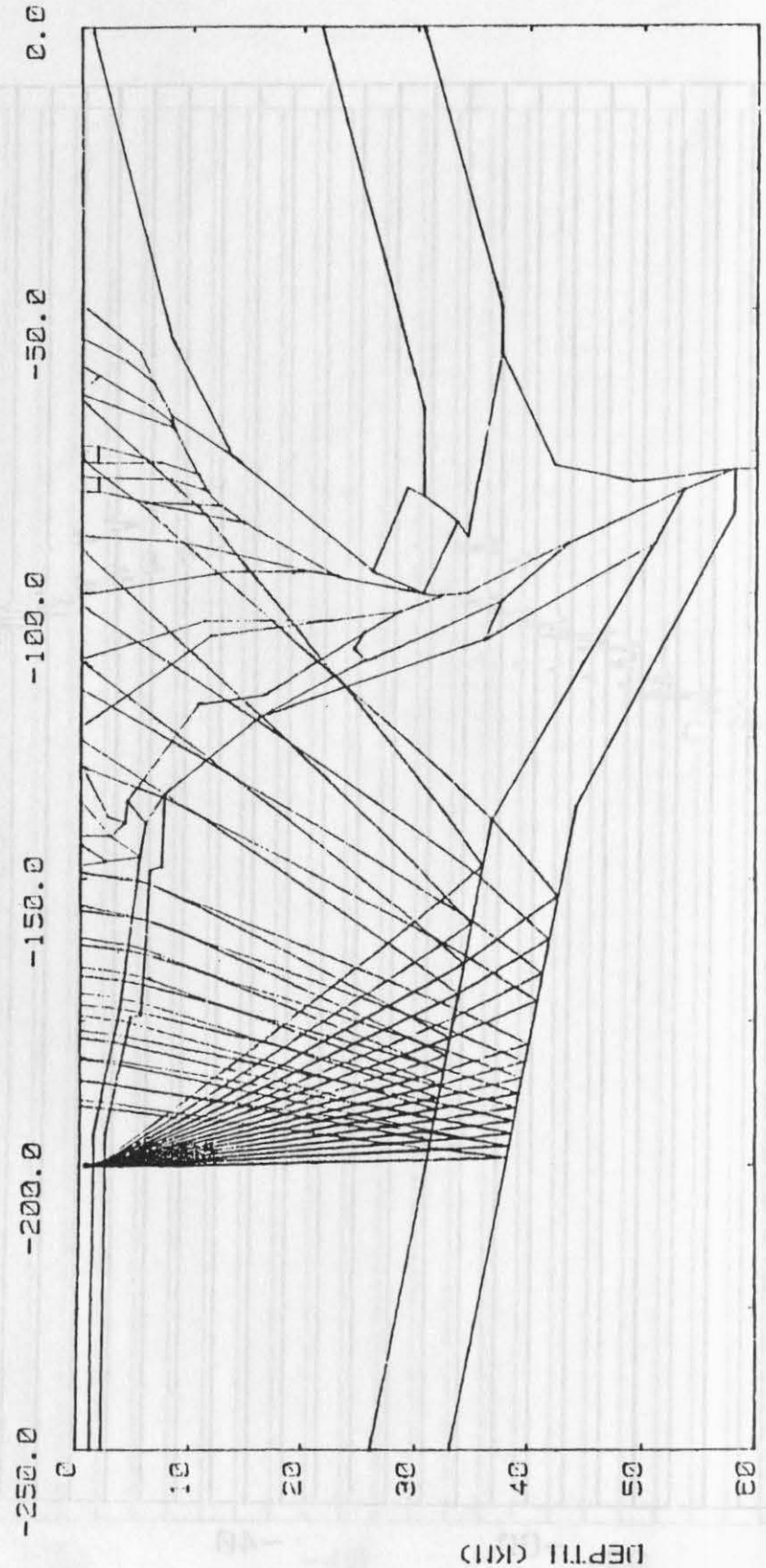

Figure 4a: Ray tracing diagram (x=200 km)

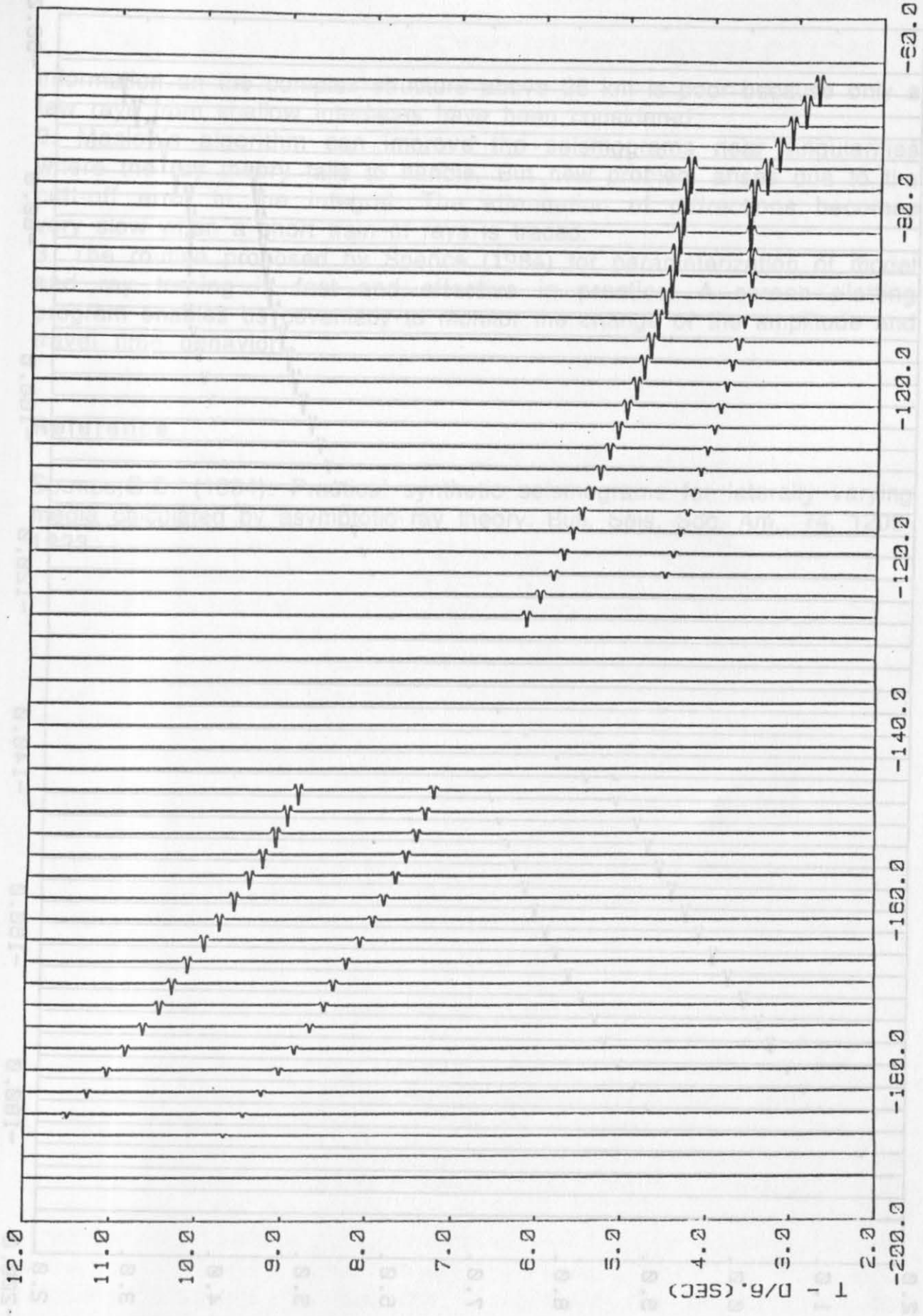

Figure 4b: Synthetic section by standard ray method (x=200 km, right branch)

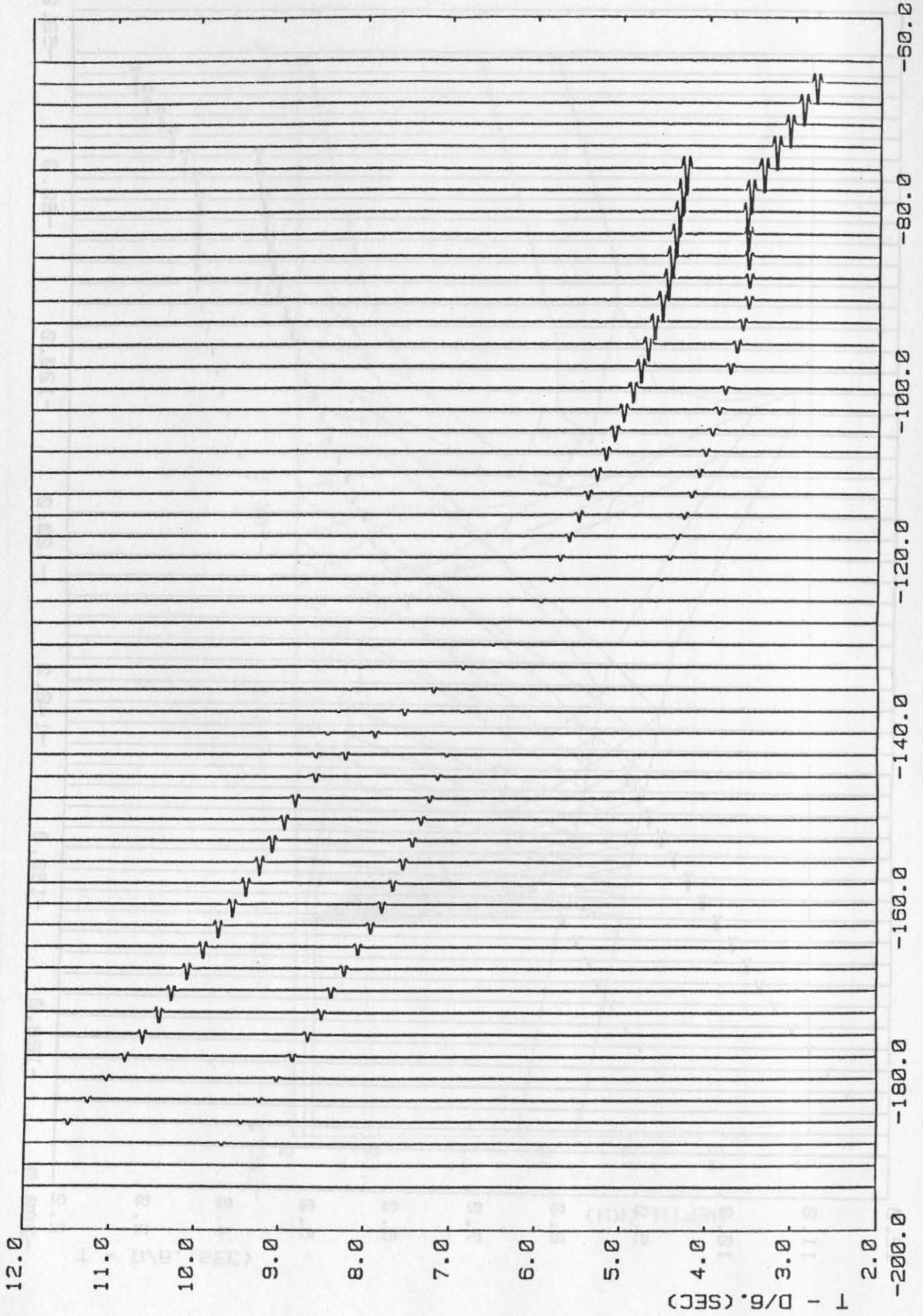

Figure 4c: Synthetic section by Maslov's asymptotic method (x=200 km, right branch)

information on the complex structure above 25 km is poor because only a few rays from shallow interfaces have been considered.
2. Maslov´s algorithm can improve the seismograms near singularities where the ray theory fails to handle. But new problem arises due to the cutt-off error in the integral. The attenuation of diffractions becomes very slow when a short train of rays is traced.
3. The routine proposed by Spence (1984) for parameterization of model and ray tracing is fast and effective in practice. A screen plotting program enables us covenietly to monitor the change of the amplitude and travel time behavior.

Reference

Spence,G.D. (1984): Practical synthetic seismograms for laterally varying media calculated by asymptotic ray theory; Bull. Seis. Soc. Am., 74, 1209-1223.

CALCULATION OF SYNTHETIC REFRACTION PROFILES WITH COMPLEX CRUSTAL STRUCTURES

Zhang Xiankang, Zhang Chengke, Zheng Xuyao

Geophysical Prospecting Brigade, State Seismological Bureau, People Republic of China

Abstract

Based on the crustal model provided by CCSS Fellhorst workshop (data set IV), the synthetic seismic responses are calculated for three specified shot-gathers. ART and Maslov's seismograms are calculated to compare the results given by different methods and to improve the seismic responses in irregular regions. ART seismograms are calculated by use of the program package Seis-83 developed by V. Cerveny and I. Psencik. Since the model is very complex, it must be simplified for the calculation of synthetic seismograms, but the basic features of the model remain. The model for calculation consists of 14 layers and the interfaces are smoothed.

Introduction

Calculations of synthetic seismograms play very an important role in DSS data interpretation. Construction of a reasonable crustal model often benefits from the comparison between synthetic and observed seismograms.

Vertically and laterally inhomogeneous and complex crustal models are often met in seismic study of the crust, therefore, the calculation of seismic responses for very complex structure is interesting. The CCSS workshop at Fellhorst, Kiel, Germany provided such a model (data set IV) as an exercise to comparing different methods for calculation in constraining interpretations of crustal structures. This model is based on the ECORS results across the Pyrenees (Figure 1a), but was simplified to be appropriate for the calculation of synthetic seismic responses. We calculated ART seismograms by use of the program package Seis-83 developed by Cerveny and Psencik (1977). In addition, we have also calculated Maslov's seismograms to compare the results given by different methods.

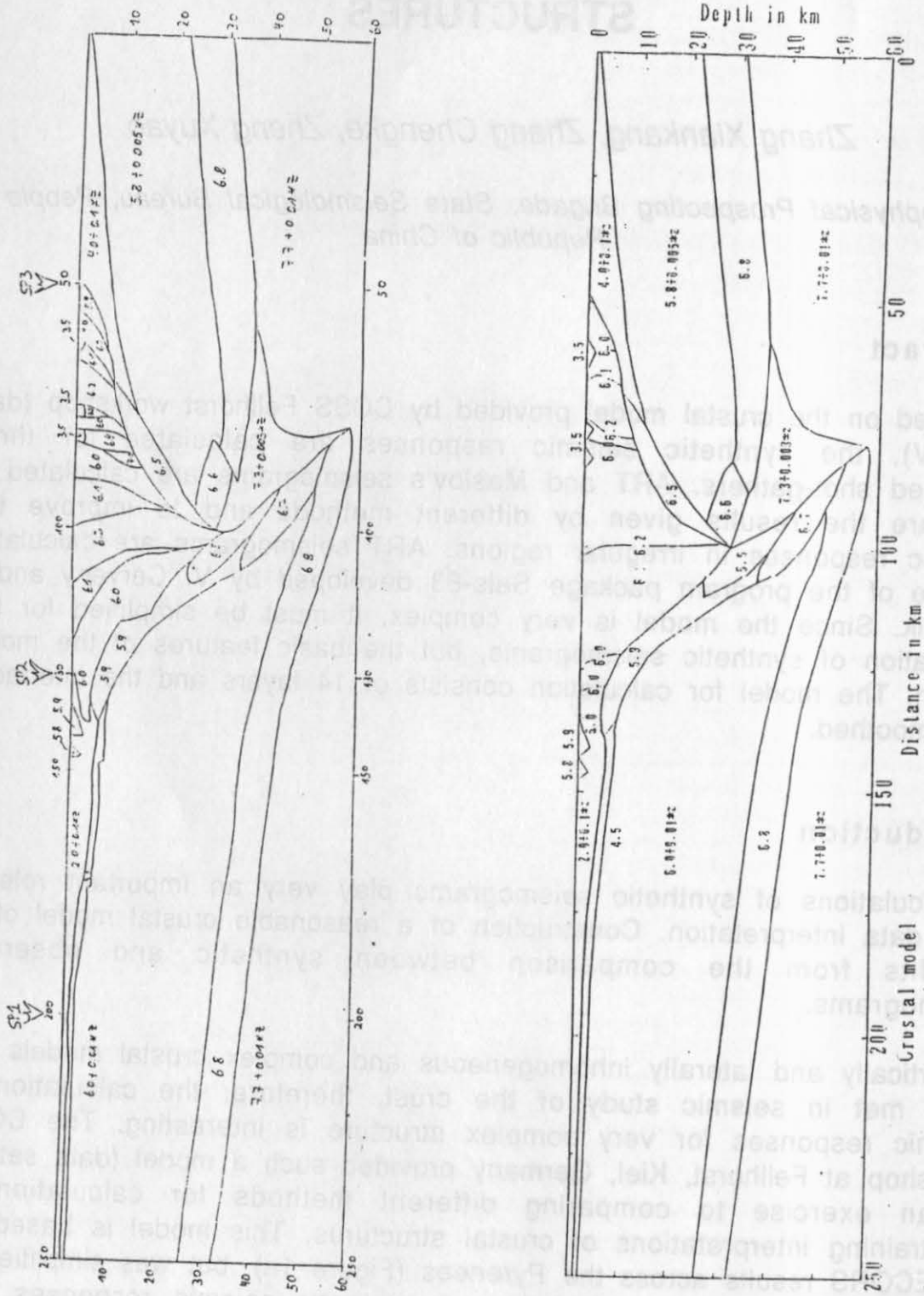

Figure 1a: Crustal model based on ECORS results across the Pyrenees.

Figure 1b: Simplified model, from which synthetic seismograms are calculated.

Simplification and parameterization of the model

Figure 1a shows the original model provided by CCSS Fellhorst workshop. This model is very complex, especially the structures between kilometers 50 and 130. In order to simplify the model, we have omitted some near-vertical interfaces, since their velocity contrasts are not large, and smoothed the interfaces. Figure 1b shows the simplified model, from which synthetic seismic responses are calculated. This model was parameterized by 575 vertical and 77 horizontal lines. The simplified model consists of 14 layers and 15 interfaces. The basic features of the original model remain in the simplified model.

Calculation of synthetic seismic responses

ART synthetic seismograms

Ray method is a very useful tool for calculation of synthetic seismograms in laterally heterogeneous structures. The program package Seis-83 developed by V. Cerveny and I. Psencik (1977) is used to calculate the ART seismograms of this model. The seismic responses for three specified shot-gathers with the shotpoint located at 50, 130, 200 km respectively have been calculated. The spacing of the traces is 2 km.

Maslov's seismograms

Asymptotic ray theory is widely used to describe body waves in inhomogeneous media, but for some special cases, such as caustics, shadows, and critical points, this theory breaks down. Maslov's asymptotic theory provides a method for combining the results of ART with the transform methods in generally inhomogeneous media. It establishes a rigorous basis for the generalization of the WKBJ seismograms method (Chapman, C.H., 1978, 1982; Thomson, C.J. et al., 1985, Zhu Liangbao, 1989).

Two Fourier transforms are used, the first is the Fourier transform with respect to time, t, the second is the Fourier transform with respect to space coordinate, x. Taking these two Fourier transforms of the scalar wave equation sequentially, we can obtain the wave equation in the mixed domain Y(p, y, z). In the X(x, y, z) domain, the wave equation has an asymptotic solution; in the Y domain, it has a similar form solution. Using the solution in the X domain and evaluating the second Fourier transform by the stationary phase method, we have the solution of the wave equation in the mixed domain. In order to obtain Maslov's asymptotic solution in the time-space domain, we must perform the frequency transform first, then complete the slowness integral.

Caustics in ART will occur when

$$\partial poX = O,$$

on the other hand, the amplitude coefficient in the y domain will be singular when

$$\partial pop = O.$$

We have calculated po-x and po-p curves of different shots. Using these curves we can obtain the singular points in two domains. In general, caustics in the x-domain and y-domain do not coincide. In order to eliminate the problems due to the caustics in any domain, Maslov has introduced the weighting function:

$$eo(po) \qquad e1(po)$$

$$eo(po)+e1(po) = 1$$

The weighting functions e1(i=0,1) are chosen to be unity in the regions where the corresponding asymptotic expression (ART or Maslov's) is valid, and zero where it is invalid.

Results

Figure 2a shows the ray graph and reduced travel times for sp.50. No ray arrives at the surface between 150 and 200 km because of the very complex crustal structures in the lower crust near 100 km. Figure 2b shows its corresponding trace-normalized ART seismograms. The trace-normalized Maslov's seismograms of sp.50 are shown in Figure 2c. On it, we can see that some diffracted energy exists between 150 and 200 km, where no seismic energy exists on ART seismograms. However, the diffracted energy does not attenuate rapidly enough.

The ray graphs, reduced traveltimes and ART synthetic seismograms for shotpoints 130 and 200 km are shown by Figure 3a, 3b and Figure 4a, 4b, respectively.

Discussion

From the synthetic seismograms shown above, it can be seen that it will be very difficult to resolve such complicated structures using only the data of three wide angle reflection and refraction shot-gathers. Ray theory is a powerful tool for synthetic seismograms calculations in laterally complicated structures, but ART method will fail in irregular regions of velocity fields, such as in shadow zones and critical regions. Maslov's method improve synthetic seismic responses in irregular regions.

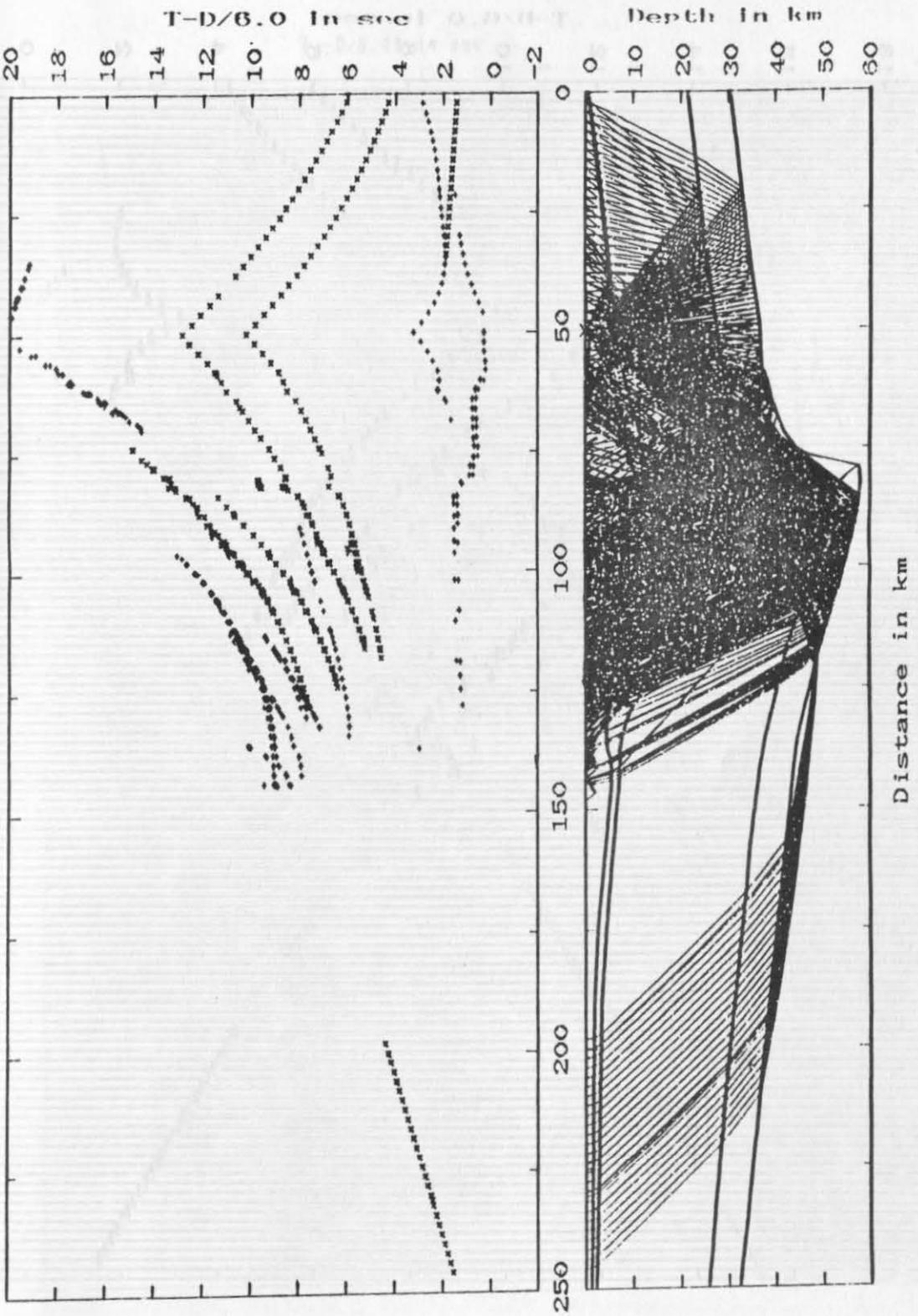

Figure 2a: Ray graph and reduced traveltimes for sp.50.

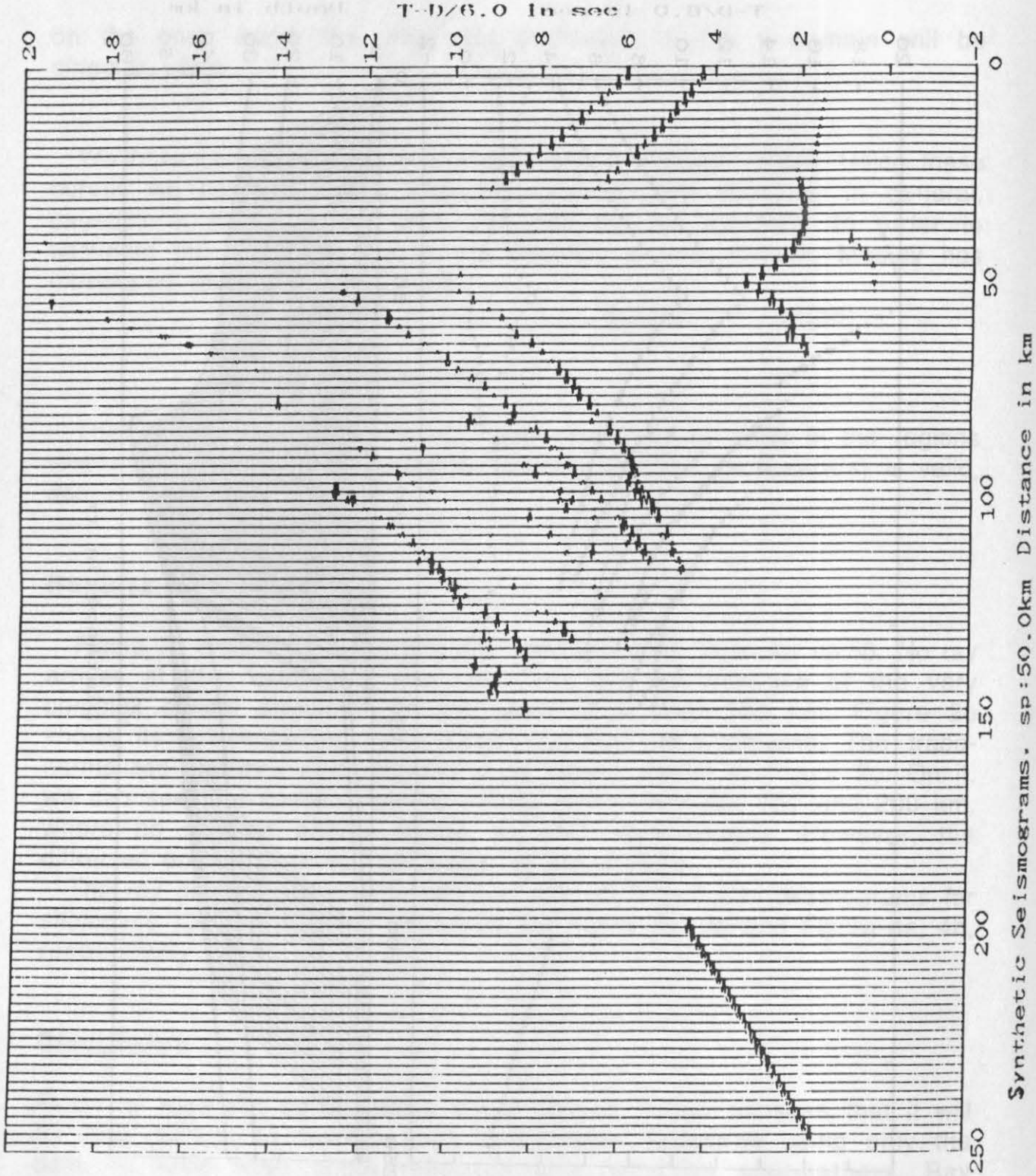

Figure 2b: Trace-normalized ART seismograms for sp.50.

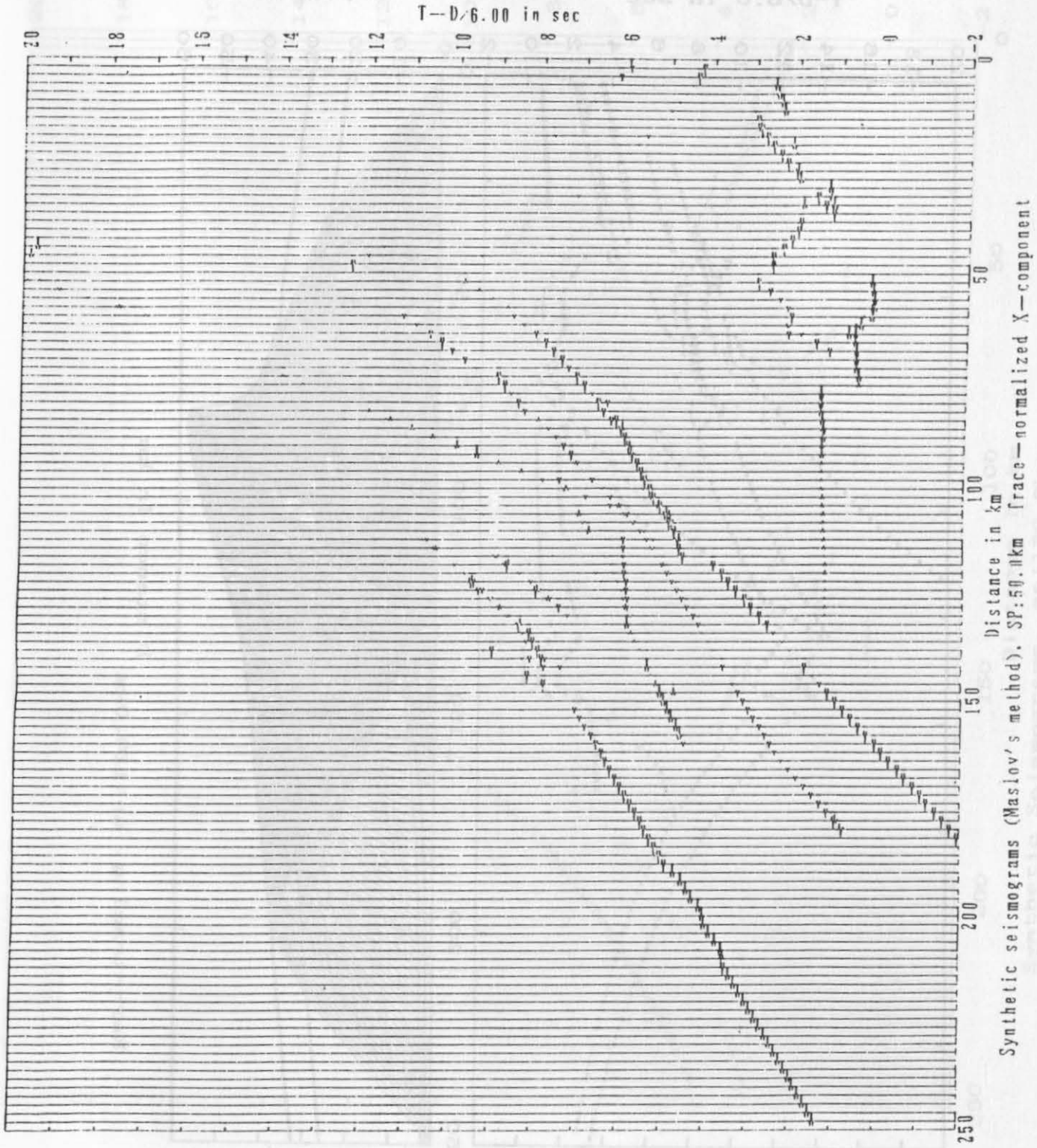

Figure 2c: Trace-normalized Maslov's seismograms for sp.50.

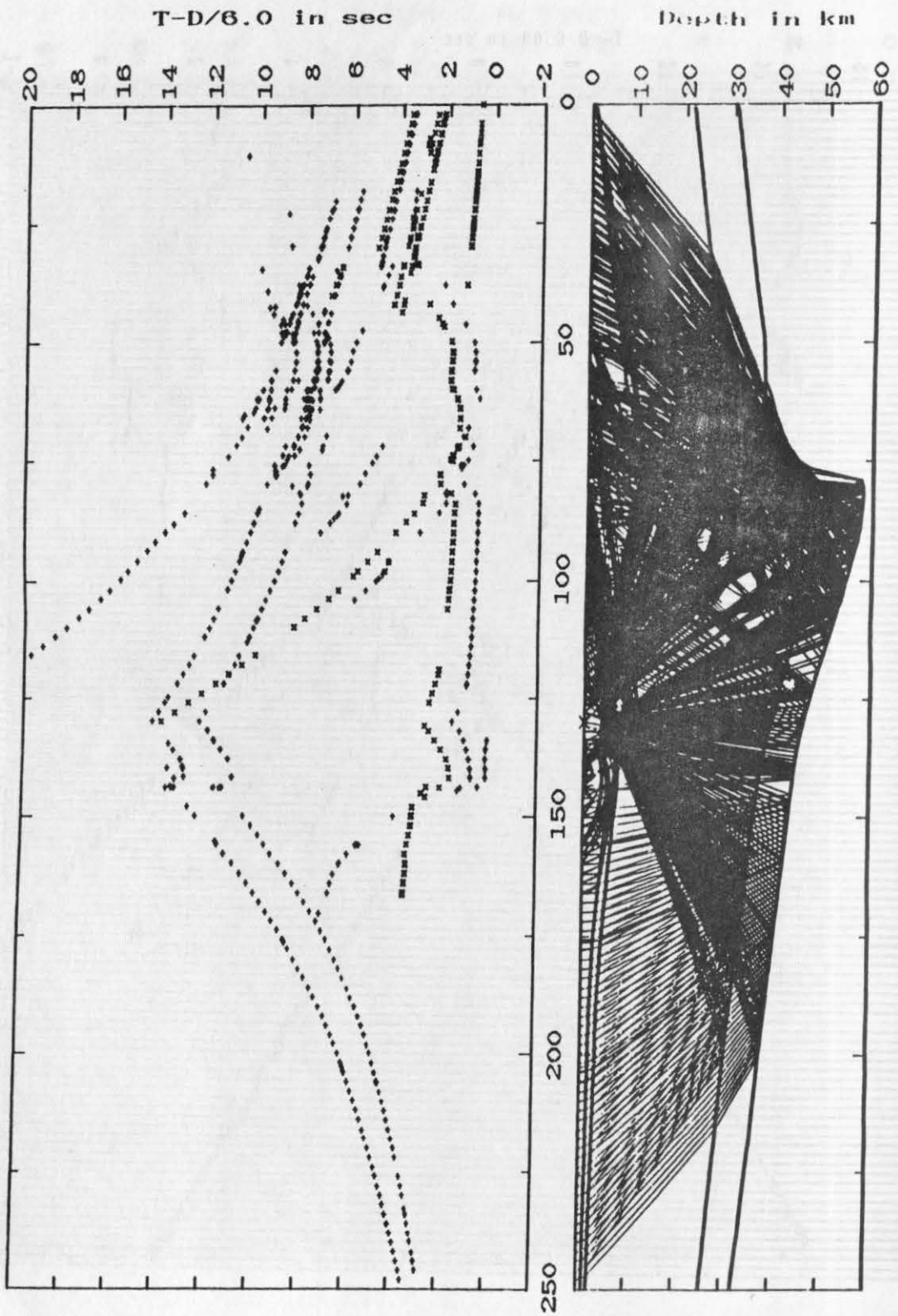

Figure 3a: Ray graph and reduced traveltimes for sp.130.

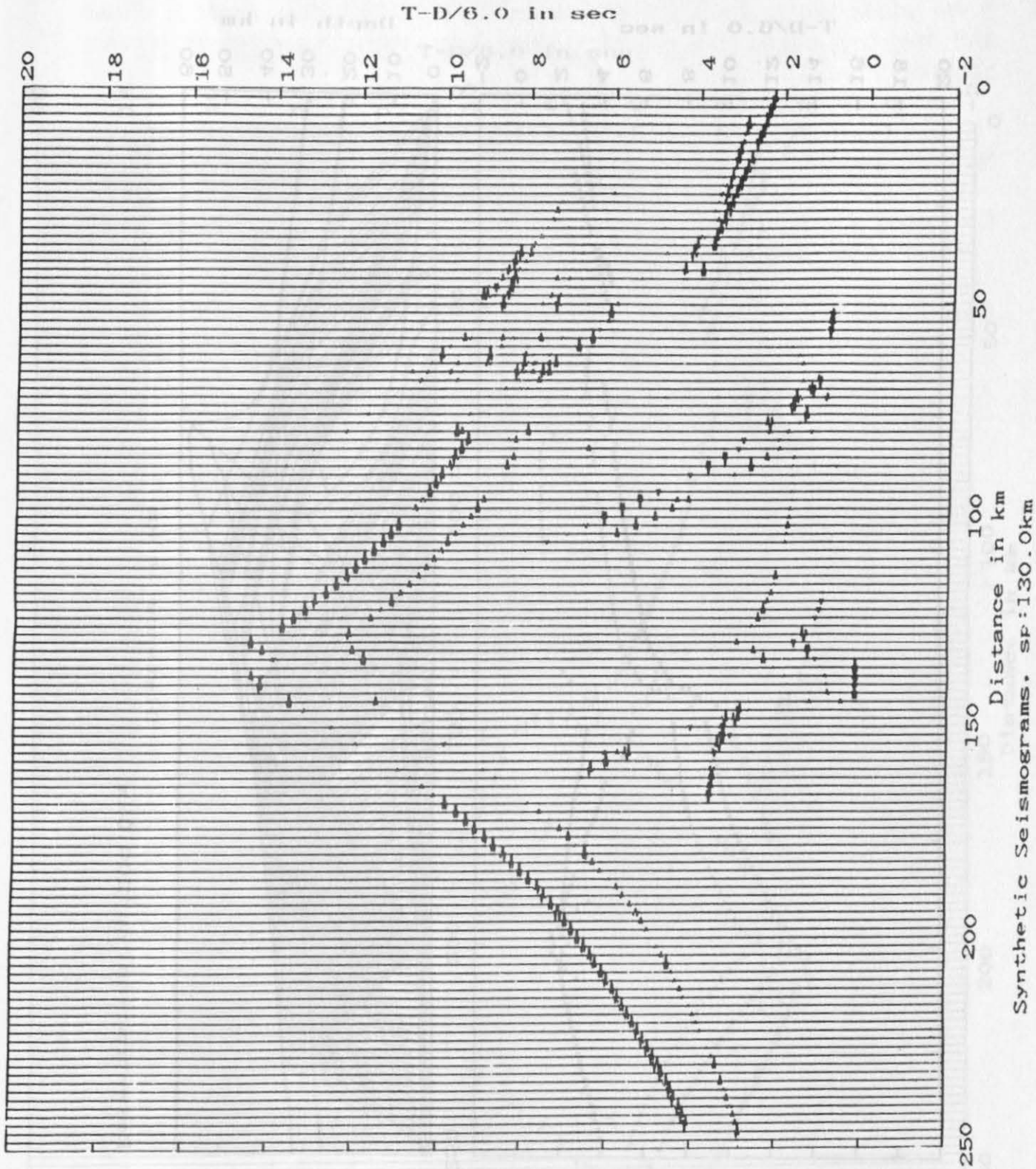

Figure 3b: Trace-normalized ART seismograms for sp.130.

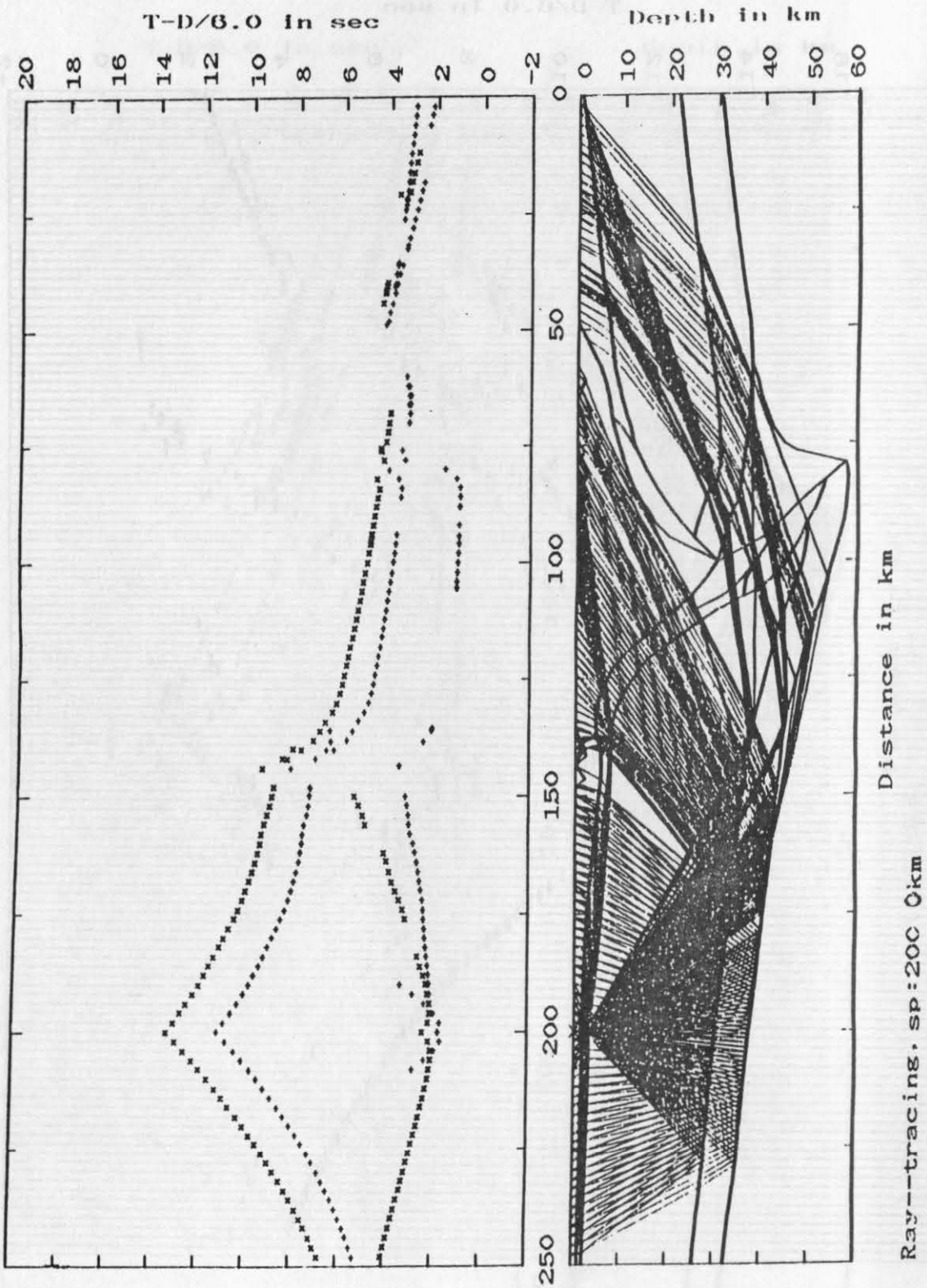

Figure 4a: Ray graph and reduced traveltimes for sp.200.

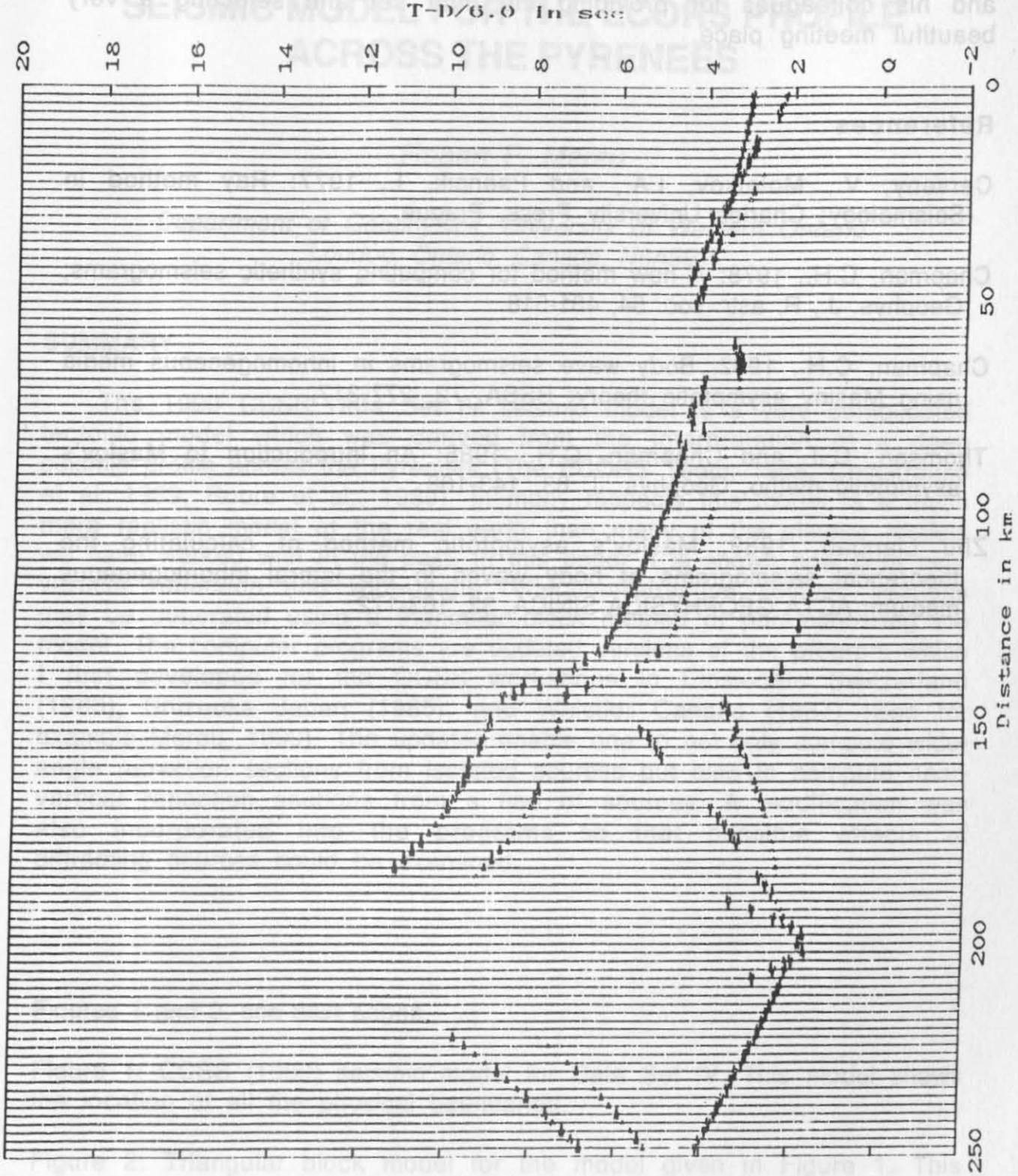

Figure 4b: Trace-normalized ART seismograms for sp.200.

Acknowledgements

We would like to thank the organizers Walter D. Mooney, Ernst R. Flueh and his colleagues for providing the data set and selecting a very beautiful meeting place.

References

Cerveny, V., Molotkov, I.A., and Psencik, I., 1977: Ray method in Seismology; Charles University Press, Prague.

Chapman, C.H., 1978: A new method for computing synthetic seismograms; Geophys. J., R. astr. soc. 54, 481-518.

Chapman, C.H., 1982: Body wave seismograms in inhomogeneous media using Maslov asymptotic theory; BSSA, 72, 277-317.

Thomson, C.J. and Chapman, C.H., 1985: An introduction to Maslov's asymptotic metho; Geophys. J. 83, 143-168.

Zhu Lianbao, 1989: Maslov's asymptotic method of calculating the theoretical seismograms of body waves in the lateral inhomogeneous medium; ACTA GEOPHYSICA SINICA, 32, 163-172.

SYNTHETIC REFRACTION AND REFLECTION SEISMIC SECTIONS FOR THE 1990 CCSS WORKSHOP DATA SET 4. SEISMIC MODEL FOR THE ECORS PROFILE ACROSS THE PYRENEES

Robert F. Mereu

Department of Geophysics, University of Western Ontario
London, Ontario, Canada, N6A5B7

SUMMARY

The 1990 CCSS Data Set IV seismic model is a very complicated tectonic model which was derived from the interpretation of a deep seismic profile across the Pyrenees (The ECORS Team, 1988, Choukroune et al. 1989, Roure et al., 1989). In many respects this model is a much more realistic model of the real earth than many of the simpler models we have worked with in the past. In this paper it is shown how both near vertical reflection and wide-angle reflection/refraction seismic sections may be generated using a triangular block method of paramaterizing the model. The computer programs are updated versions of the program which I first developed for the CCSS workshops in Einsiedeln Switzerland (1983), Shizouka Japan (1985), and Whistler Canada (1987) (See for example Mereu, 1990). The updates enable one to not only compute wide-angle refraction sections from isolated sources but also to compute near-vertical reflection sections from a line of sources. A modification was also incorporated into the programs so that possible effects of diffracting sources could be examined.

Figures 1 and 2, see next pages.

Figure 1: CCSS (1990) seismic model for Data Set IV. This model shows the location of all the physical boundaries.

Figure 2: Triangular block model for the model given in Figure 1. This model has 355 triangles. The velocity function used in each model is of the form: $v(x,z) = ax + bz + c$

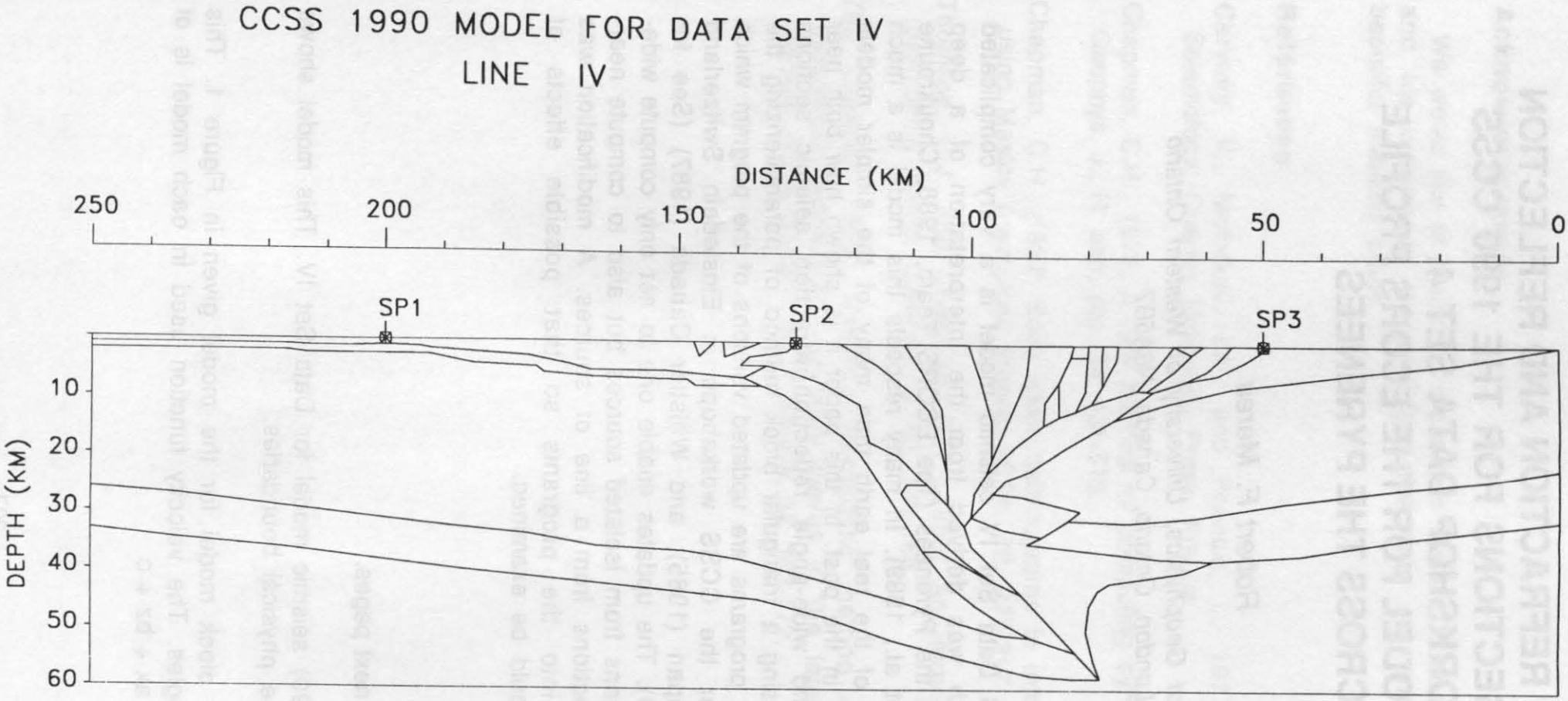
CCSS 1990 MODEL FOR DATA SET IV
LINE IV
DISTANCE (KM)
250
200
150
100
50
0
SP1
SP2
SP3
DEPTH (KM)
10
20
30
40
50
60

Figure: 1

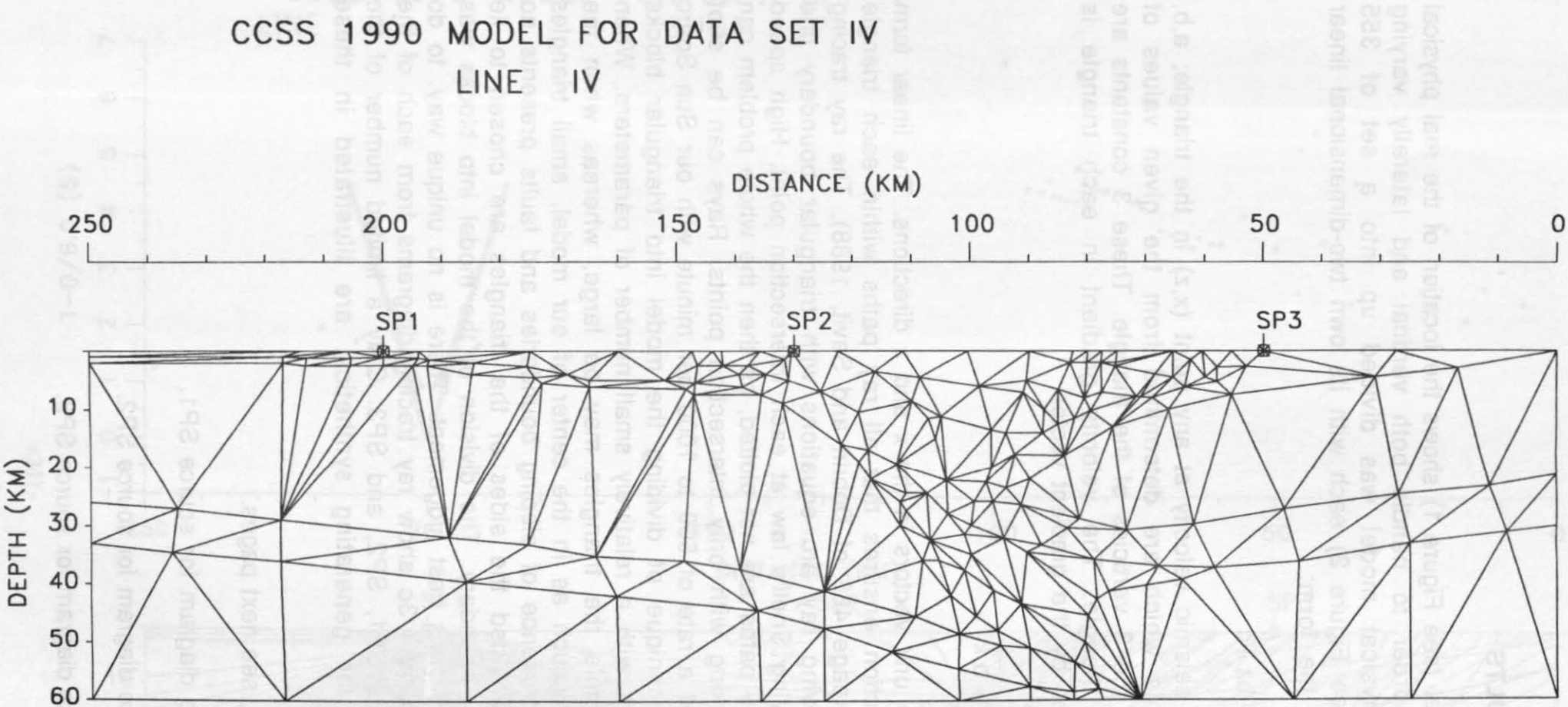
CCSS 1990 MODEL FOR DATA SET IV
LINE IV
DISTANCE (KM)
250
200
150
100
50
0
SP1
SP2
SP3
DEPTH (KM)
10
20
30
40
50
60

Figure: 2

METHOD and RESULTS

The given model (see Figure 1) shows the location of the real physical discontinuities. In order to handle both vertical and laterally varying structures, this physical model was divided up into a set of 355 triangular blocks (see Figure 2) each with its own two-dimensional linear velocity function of the form:

$$v(x,z) = ax + bz + c$$

where v(x,z) is the seismic velocity at any point (x,z) in the triangle; a,b, and c are constants which are determined from the given values of velocity at each of the 3 verticies of the triangle. These 3 constants are different for each triangle. The velocity gradient in each triangle is constant and is given by the gradient vector

$$\text{grad } v = a\,\hat{i} + b\,\hat{k}$$

where $\hat{i}$ and $\hat{k}$ are unit vectors in the x and z directions. The linear form of the velocity function ensures that all ray paths within each triangle are arcs of circles (page 466 of Dobrin and Savit, 1988). The ray tracing is achieved by solving ray arc equations with triangular boundary line equations and applying Snell's law at each intersection point. High speed is obtained if the ray paths are not plotted, as then the whole problem can be handled by working with only intersection points. Rays can be shot through the model at a rate of 500 to 1000 per minute with our Sun Sparc workstation. The technique of dividing the model into triangular blocks enables one to work with a relatively small number of parameters. When the structure is simple the triangles may be large, whereas when the structure is complex such as in the center of our model, small triangles are required. The presence of sloping boundaries and faults presents no inherent difficulty provided the sides of the triangles are chosen to lie along the geological boundary. The division of the model into blocks was done manually using ones best judgement. There is no unique way. to do this. Figures 3a, 3b, and 3c show ray tracing diagrams from each of the refraction shot points SP1, SP2, and SP3. Only a limited number of the actual rays used for generating synthetics, are illustrated in these figures.

Figures 3a, b, and c, see next pages.

Figure 3a: Ray trace diagram for source SP1.

3b: Ray trace diagram for source SP2.

3c: Ray trace diagram for source SP3.

CCSS 1990 MODEL FOR DATA SET IV
LINE IV
SHOT SP1
T-D/6.0 (S)
DISTANCE (KM)
DEPTH (KM)
SP1
SP2
SP3

Figure: 3 a

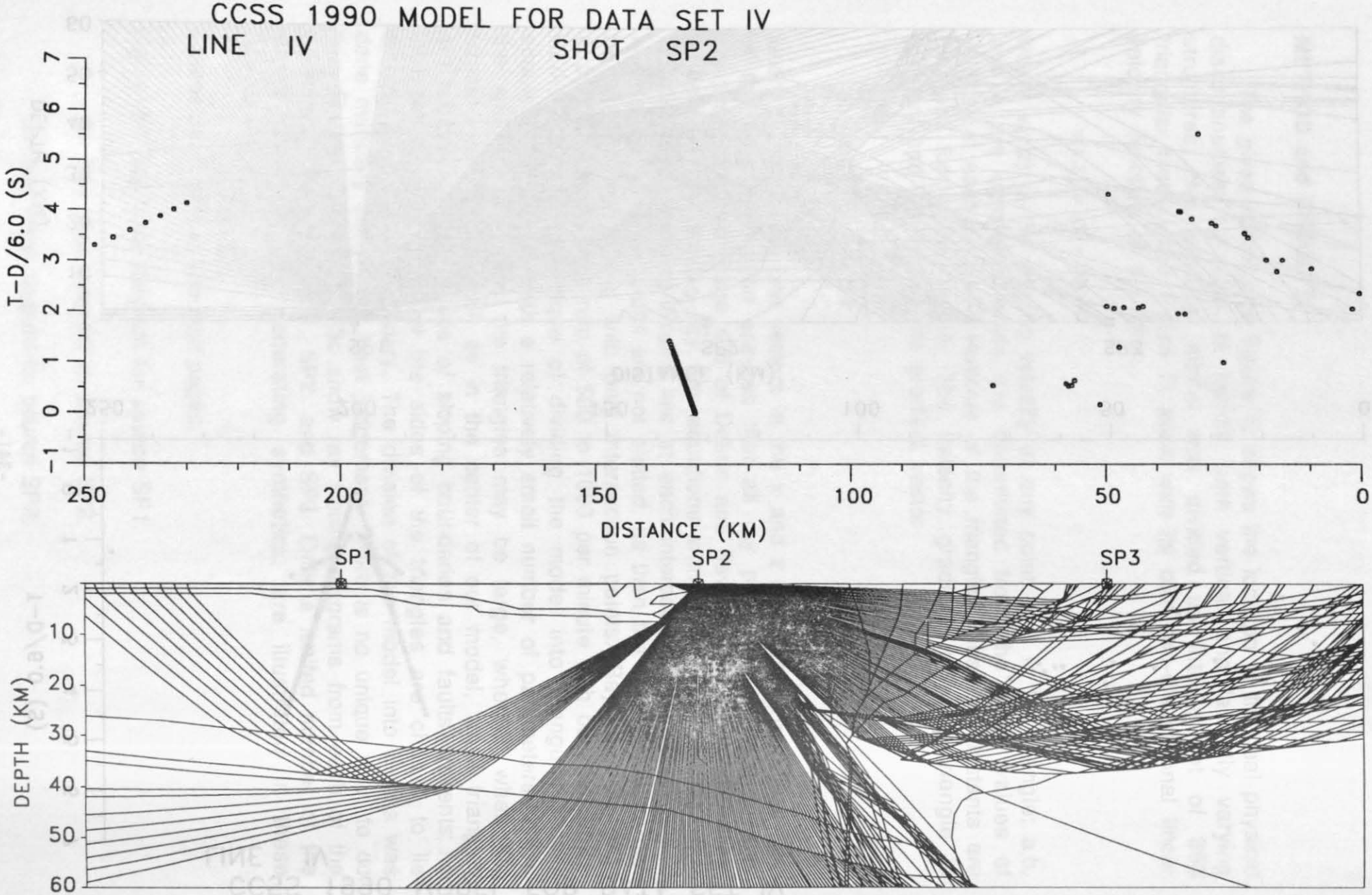
CCSS 1990 MODEL FOR DATA SET IV
LINE IV
SHOT SP2
T-D/6.0 (S)
-1
0
1
2
3
4
5
6
7
250
200
150
100
50
0
DISTANCE (KM)
SP1
SP2
SP3
DEPTH (KM)
10
20
30
40
50
60

Figure: 3 b

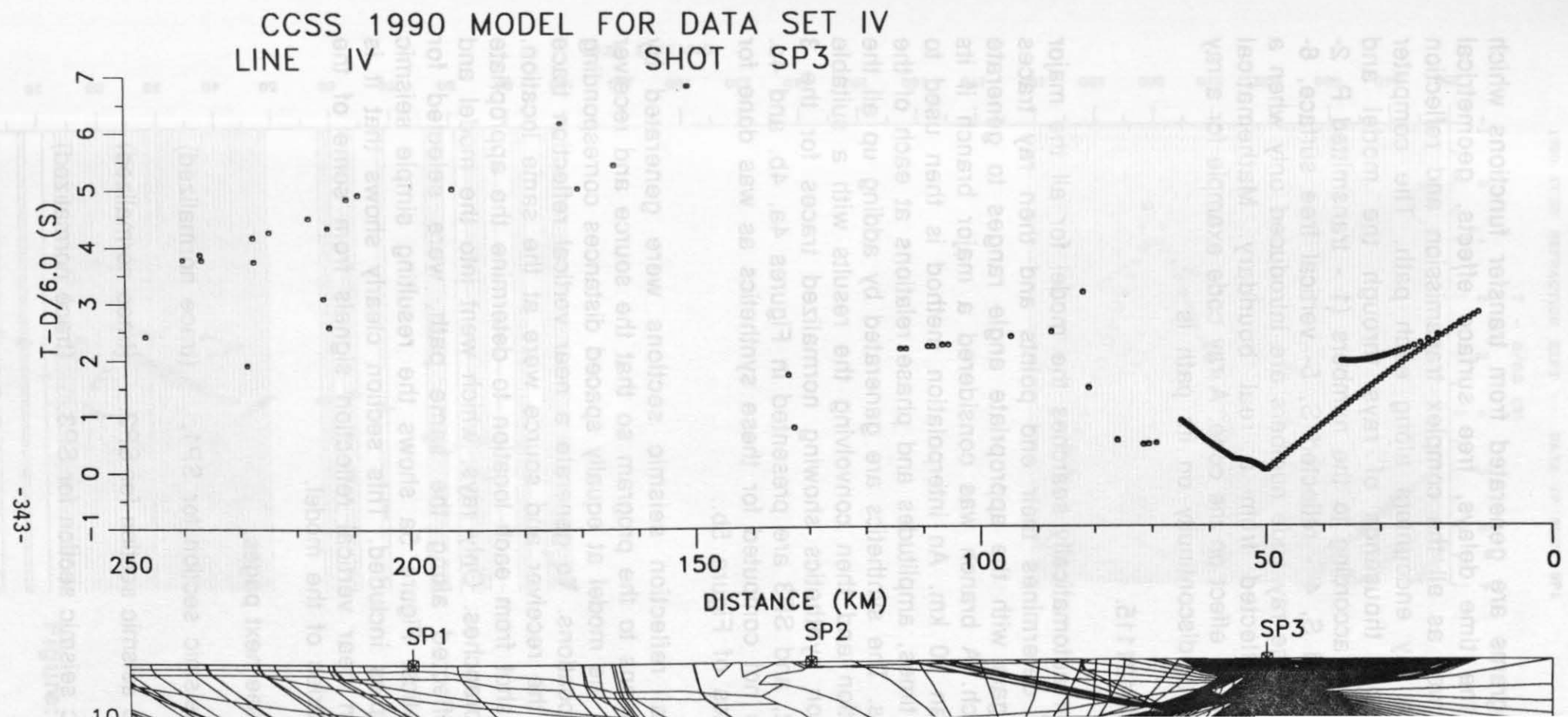
CCSS 1990 MODEL FOR DATA SET IV
LINE IV
SHOT SP3
T-D/6.0 (S)
-1
0
1
2
3
4
5
6
7
250
200
150
100
50
0
DISTANCE (KM)
SP1
SP2
SP3
10

Synthetic seismograms are generated from transfer functions which are computed from the time delays, free surface effects, geometrical spreading effects as well as all the complex transmission and reflection coefficients which the ray encounters along each path. The computer program initially shoots thousands of rays through the model and automatically codes them according to the numbers (1 - transmitted P, 2- reflected P, 3- transmitted S, 4 - reflected S, 5- vertical free surface, 6- horizontal free surface). The ray code numbers are introduced only when a ray traverses or is reflected from a real boundary. Mathematical boundaries do not have an effect on the code. A ray code example for a ray reflected from the fourth discontinuity on its path is

111121115.

The program then automatically searches the model for all the major travel-time branches, determines their end points and then ray traces through the model again with the appropriate angle ranges to generate each significant branch. A branch was considered a major branch if its length was larger than 10 km. An interpolation method is then used to determine the arrival times, amplitudes and phase relations at each of the desired trace locations. The synthetics are generated by adding up all the arrivals at each location and then convolving the results with a suitable wavelet. The refraction synthetics showing normalized traces for the 3 shot points SP1, SP2, and SP3 are presented in Figures 4a, 4b, and 4c. Diffracted energy was not computed for these synthetics as was done for the reflection synthetics of Figure 5b..

The near vertical reflection seismic sections were generated by making some modifications to the program so that the source and receiver could be moved along the model at equally spaced distances corresponding to the desired trace locations. To generate a near vertical reflection trace it was assumed that the receiver and source were at the same location. Numerous rays were shot from each location to determine the appropriate reflection travel-time branches. Only rays, which went into the model and which were then reflected along the same path, were selected for generating the synthetics. Figure 5a shows the resulting simple seismic section with no multiples included. This section clearly shows that it is not possible to obtain near vertical reflection signals from some of the steeply dipping boundaries of the model.

Figures 4 a, b, and c, see next pages.

Figure 4a: Synthetic seismic section for SP1. (trace normalized)

4b: Synthetic seismic section for SP2. (trace normalized)

4c: Synthetic seismic section for SP3. (trace normalized)

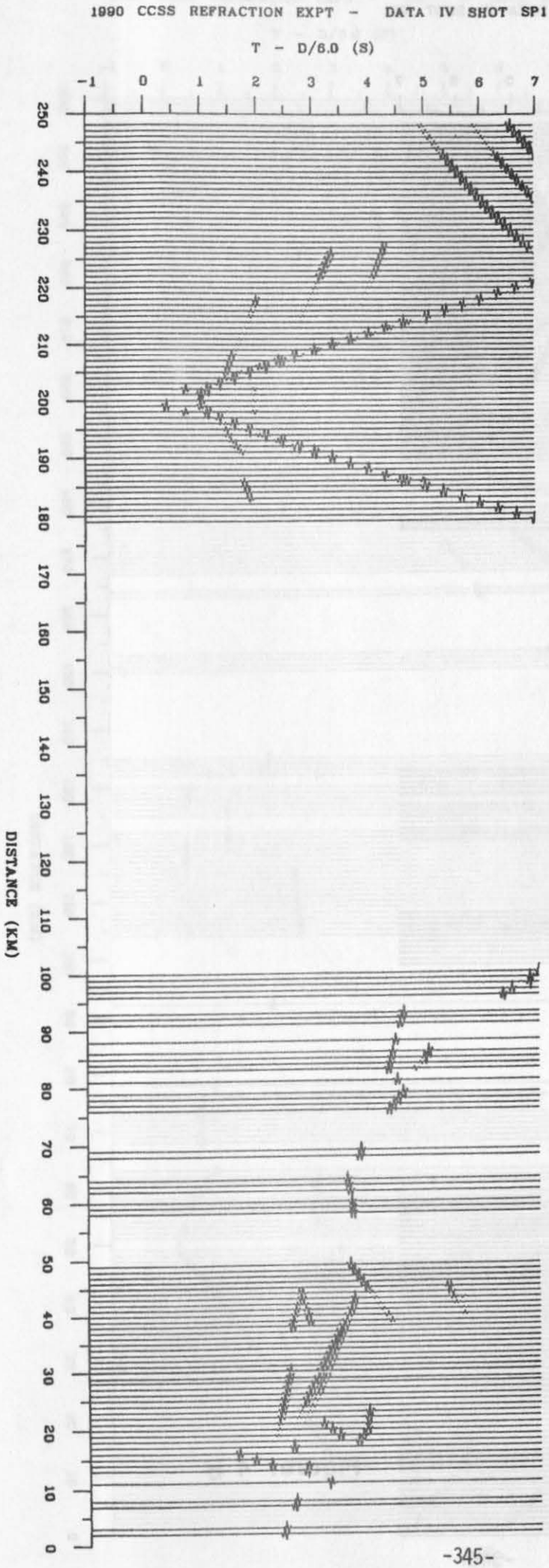
1990 CCSS REFRACTION EXPT - DATA IV SHOT SP1
T - D/6.0 (S)
-1
0
1
2
3
4
5
6
7
DISTANCE (KM)
250
240
230
220
210
200
190
180
170
160
150
140
130
120
110
100
90
80
70
60
50
40
30
20
10
0

Figure: 4 a

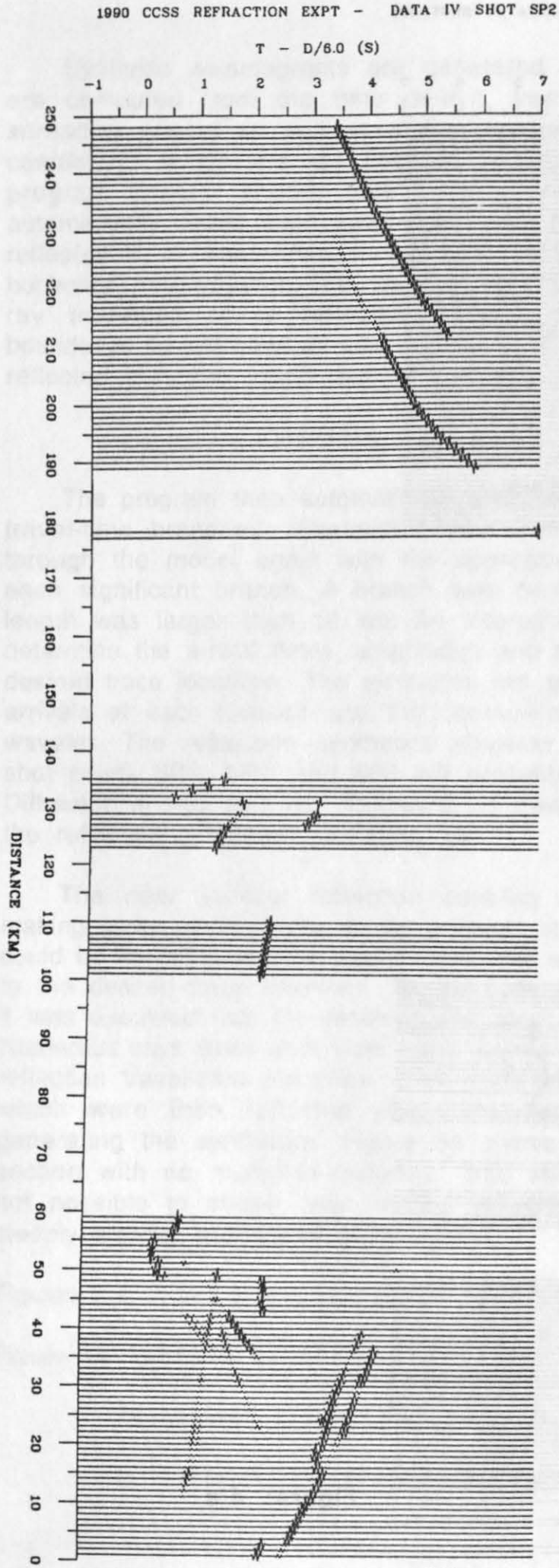
1990 CCSS REFRACTION EXPT - DATA IV SHOT SP2
T - D/6.0 (S)
-1
0
1
2
3
4
5
6
7
DISTANCE (KM)
250
240
230
220
210
200
190
180
170
160
150
140
130
120
110
100
90
80
70
60
50
40
30
20
10
0

Figure: 4 b

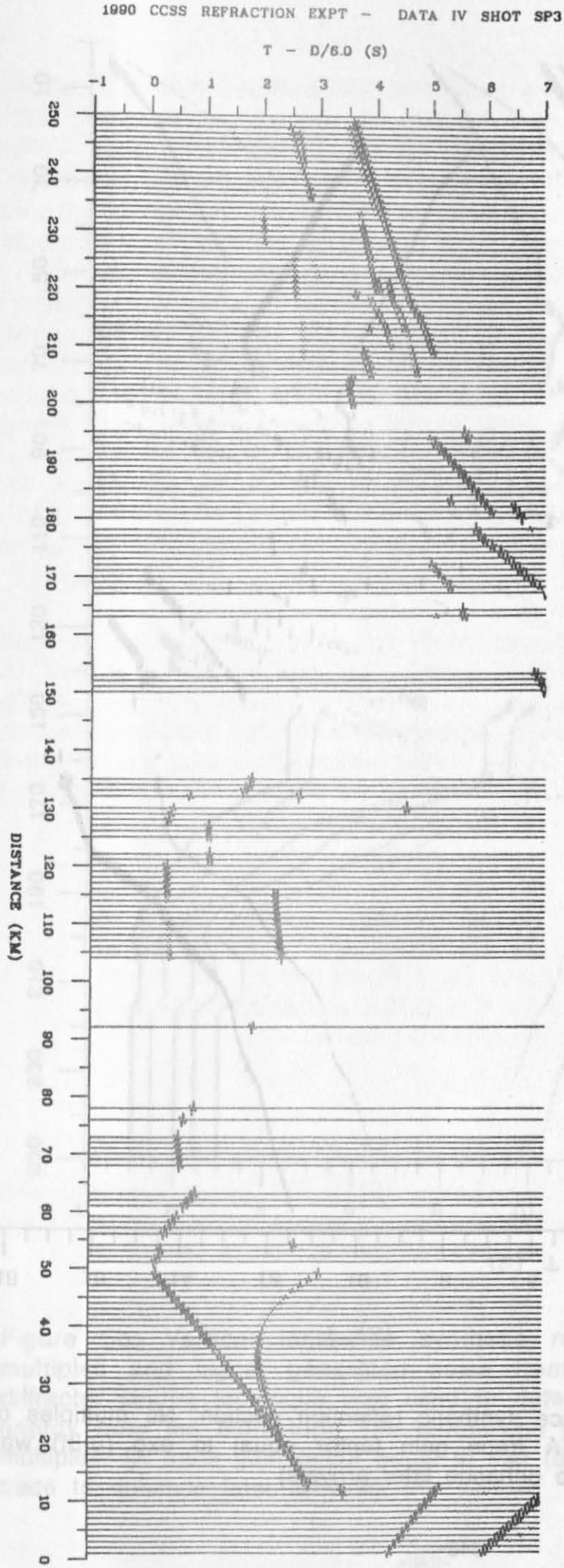
1990 CCSS REFRACTION EXPT - DATA IV SHOT SP3
T - D/6.0 (S)
-1
0
1
2
3
4
5
6
7
DISTANCE (KM)
250
240
230
220
210
200
190
180
170
160
150
140
130
120
110
100
90
80
70
60
50
40
30
20
10
0

Figure: 4 c

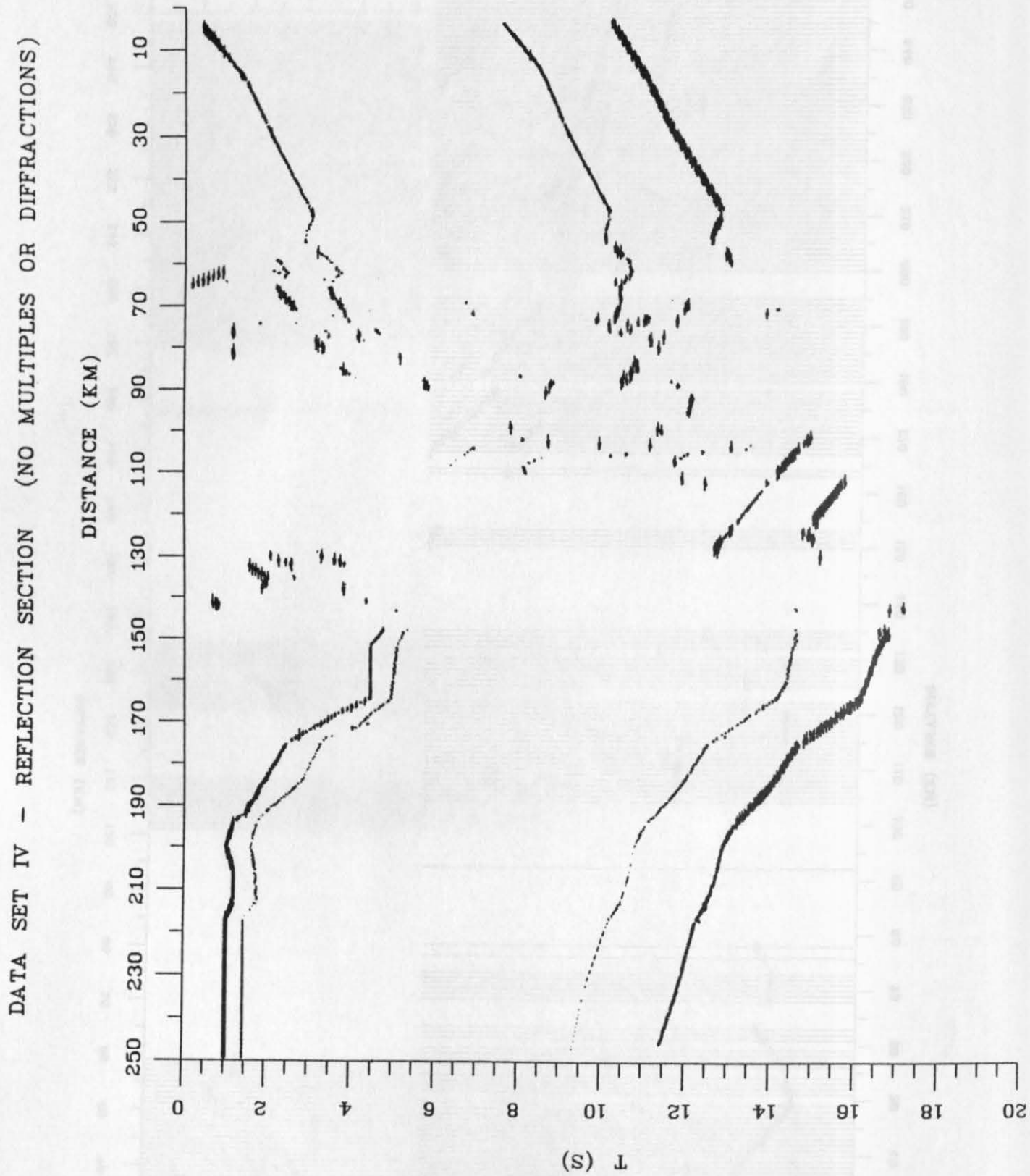

Figure 5a: Vertical incidence synthetic reflection section. No multiples or diffractors are included. (A trace gain factor equal to exp (0.3t) was applied along each trace to enhance later arrivals)

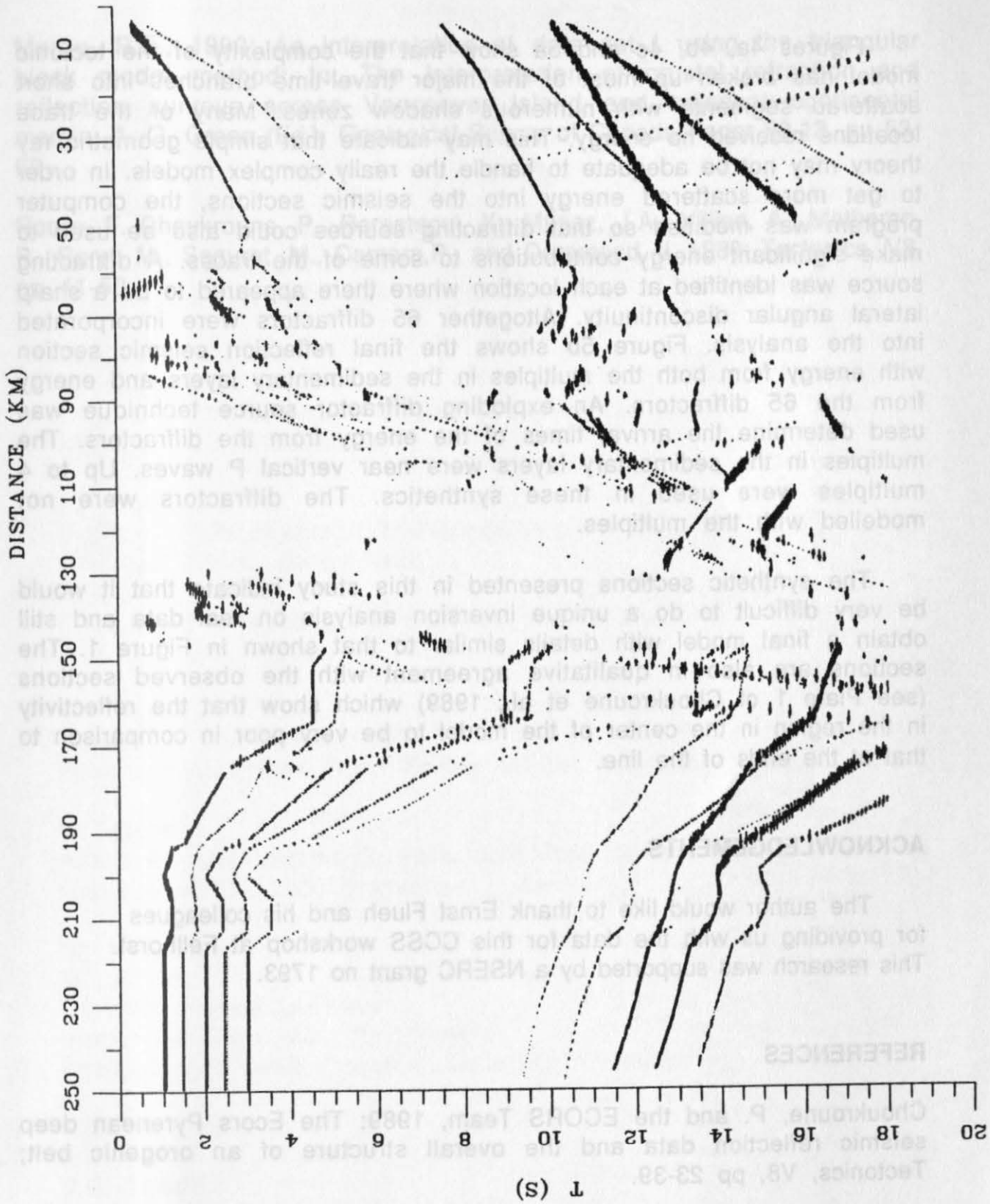

Figure 5b: Vertical incidence synthetic reflection section. Includes multiples and signal generated noise from diffractors. An exploding diffractor source technique was used to determine the arrival times and energy from the diffractors. The diffractions were not modelled with the multiples. (A trace gain factor equal to exp (0.3t) was applied along each trace to enhance later arrivals).

Figures 4a, 4b, 4c and 5a show that the complexity of the tectonic model has broken up most of the major travel-time branches into short scattered segments with numerous shadow zones. Many of the trace locations received no energy. This may indicate that simple geometric ray theory may not be adequate to handle the really complex models. In order to get more scattered energy into the seismic sections, the computer program was modified so that diffracting sources could also be used to make significant energy contributions to some of the traces. A diffracting source was identified at each location where there appeared to be a sharp lateral angular discontinuity. Altogether 65 diffractors were incorporated into the analysis. Figure 5b shows the final reflection seismic section with energy from both the multiples in the sedimentary layers and energy from the 65 diffractors. An exploding diffractor source technique was used determine the arrival times of the energy from the diffractors. The multiples in the sedimentary layers were near vertical P waves. Up to 4 multiples were used in these synthetics. The diffractors were not modelled with the multiples.

The synthetic sections presented in this study indicate that it would be very difficult to do a unique inversion analysis on real data and still obtain a final model with details similar to that shown in Figure 1. The sections are also in qualitative agreement with the observed sections (see Plate 1 of Choukroune et al., 1989) which show that the reflectivity in the region in the center of the model to be very poor in comparison to that at the ends of the line.

ACKNOWLEDGEMENTS

The author would like to thank Ernst Flueh and his colleagues for providing us with the data for this CCSS workshop at Fellhorst. This research was supported by a NSERC grant no 1793.

REFERENCES

Choukroune, P. and the ECORS Team, 1989: The Ecors Pyrenean deep seismic reflection data and the overall structure of an orogenic belt; Tectonics, V8, pp 23-39.

Dobrin, M.B. and Savit, C.H., 1988: Introduction to Geophysical Prospecting; McGraw-Hill.

ECORS Pyrenees Team, 1988: The Ecors deep reflection seismic survey across the Pyrenees; Nature, 331, pp 508-511.

Mereu, R.F., 1990: An interpretation of data set I using the triangular block model method; In: The interpretation of crustal refraction and reflection surveys across Vancouver Island and adjacent continental margin; A. G. Green (Ed.), Geological Survey of Canada Paper 89-13, pp 53-63.

Roure, F. Choukroune, P., Berastegui, X., Munoz, J.A., Villian, A., Matheron, P., Baryt, M., Seguret, M., Camara,P., and Deramond, J. 1989: Tectonics, V8, pp 41-50.

APPENDICES

ADRESSES OF THE AUTHORS

E.R. Flueh
D. Klaeschen
Forschungszentrum für marine Geowissenschaften der
Christian Albrechts Universität zu Kiel, GEOMAR,
Wischhofstr. 1-3, 2300 Kiel 14, Germany.

S. Guest
M. Kendall
Department of Geological Sciences, Queens University,
Kingston, K7L 3N6, Canada.

K. Holliger
Institute of Geophysics, ETH-Hönggerberg,
CH-8093 Zürich, Switzerland.
Now at:
Department of Geology and Geophysics, Rice University,
P.O. Box 1892, Houston, TX 77251, U.S.A.

W. Jianchun
Institute of Geophysics, SSB,
Minzouxueyuan Nanlu Road, Beijing, 100081, P.R.China.

W. Jokat
Alfred Wegener Institut für Polar und Meeresforschung
Columbusstraße, 2850 Bremerhaven, Germany.

M. Klöckner
M. Stiller
DEKORP Processing Center
Institut für Geophysik, TU Clausthal,
Postfach 230, 3392 Clausthal- Zellerfeld, Germany.

V.G. Krishna
K.L. Kaila
P.R. Reddy
National Geophysical Research Institute,
Uppal Road, Hyderabad-500 007, India.

C.W. Lange
P.K. Stiller
Peussag AG, Leibnitz- Rechenzentrum,
Karl Wichert Allee 4, 3000 Hannover 1, Germany.

R.F. Mereu
Dept. of Geophysics, University of Western Ontario,
London Ontario, N6A 5B7, Canada.

T.A. Minshull
School of Earth Sciences, University of Birmingham,
Birmingham, BI5 2TT, U.K.
Now at:
Bullard Laboratories, Department of Earth Sciences,
University of Cambridge, U.K.

D.B. Snyder
R.W. Hobbs
BIRPS,
Madingley Rise, Madingley Road, Cambridge, CB3 OEZ, U.K.

B. Spargaaren
Department of Geology, Imperial College,
Prince Consort Road, London, SW7 2BP, U.K.

C. Spencer
B. Milkereit
D.J. White
Geological Survey of Canada,
1 Observatory Crescent, Ottawa, Ontario, K1A OY3, Canada.

K. Vasudevan
T. Clark
Lithoprobe Seismic Processing Facility,
Department of Geology and Geophysics, The University of Calgary,
Calgary, Alberia, T2N 1N4, Canada.

T.E. West
R.E. Long
University of Durham, Dept. of Geological Science, Science Laboratories,
South Road, Durham, DHL 3LE, U.K.

Z. Xiankang
Z. Chengke
Z. Xuyao
Geophysicals Prospecting Brigade, State Seismological Bureau,
104 Wenhua Road, Zhengzou, Henan, P.R.China.

S. Ye
J. Ansorge
Institut für Geophysik, ETH- Hönggerberg,
CH-8093 Zürich, Switzerland.

Z. Zhao
Sichuan Seismological Bureau,
Chengdu, Sichuan, P.R.China.

LIST OF PARTICIPANTS

I. Azbel, Kola Science Center, Apatity, U.S.S.R.
A. Egorkin, NPO Neftegeophysica, Moscow, U.S.S.R.
E. R. Flueh, GEOMAR, Kiel, Germany
K. Holliger, ETH-Hönggerberg, Zürich, Switzerland
W. Jianchun, SSB, Beijing, P.R.China
K. L. Kaila, Geophysical Research Institute, Hyderabat, India
D. Klaeschen, GEOMAR, Kiel, Germany
M. Klöckner, DEKORP Processing Center, Clausthal-Zellerfeld, Germany
R. Meissner, Christian Albrechts Universität, Kiel, Germany
R. F. Mereu, University of Western Ontario, London, Ontario, Canada
B. Milkereit, Geological Survey of Canada, Ottawa, Ontario, Canada
T. A. Minshull, University of Birmingham, Birmingham, U.K.
R. Mjelde, University of Bergen, Bergen, Norway
W. D. Mooney, United States Geological Survey, Menlo Park, California, U.S.A
N. Pavlenkova, Institute of Physics of the Earth, Moscow, U.S.S.R.
W. Rabbel, Christian Albrechts Universität, Kiel, Germany
D. Snyder, BIRPS, Cambridge, U.K.
B. Spaargaren, Imperial College, London, U.K.
C. Spencer, Geological Survey of Canada, Ottawa, Ontario, Canada
M. Stiller, DEKORP Processing Center, Clausthal-Zellerfeld, Germany
P. Stiller, PREUSSAG Erdöl und Erdgas GmbH, Hannover, Germany
K. Vasudevan, LITHOPROBE, University of Calgary, Calgary, Alberta, Canada
R. von Huene, GEOMAR, Kiel, Germany
T. E. West, Science Laboratories, Durham, U.K.
J. A. Wright, Memorial University, St. John´s, NF, Canada
Z. Xiankang, Geophysicals Prospecting Brigade, Zhengzhou, Henan, P.R.China
S. Ye, ETH-Hönggerberg, Zürich, Switzerland
Y. Zhou, British Geological Survey, Edinburgh, U.K.

CCSS-PUBLICATIONS

Compilation of papers presented at the workshop in Leningrad, USSR, 28. August- 2. September 1968:
Kosminskaya, I.P., Sollogub, V.B., and Pavlenkova, N.I., (Eds.) 1969: Transactions- "The International Conference of Experts on Explosion Seismology", Leningrad, 1968, (in Russian); Academy of sciences of the USSR, Soviet Geophysical Committee, Publisher Nauka, Kiev, 242 pp.

Summary paper on the workshop in Karlsruhe, Federal Republic of Germany, 1- 16 August 1977:
Ansorge, J., Prodehl, C., and Bamford, D. 1982: Comparative Interpretation of Explosion Seismic Data; J. Geophys., 51, 69-84.

Compilation of papers presented at the CCSS Workshop in Yalta, USSR, 5-12 Mai 1978:
Pavlenkova, N.I. (Ed.) 1980: Investigation of the Lithosphere and Asthenosphere by Long-Range Profiles (in Russian); Academy of Sciences of the USSR; Schmit-Institute of Geophysics, Publishers Nauka, Moskow, 250 pp.

Summary paper on the workshop in Park City, Utah, 11- 17 August 1980:
Mooney, W.D. and the IASPEI Workshop 1981: Seismic Modelling of Laterally Varying Structures; EOS, Transact. AGU, 62, p. 19.

Kosminskaya, I.P and Pavlenkova, N.I. 1981: Chronicle, Commission on Contolled Source Seismology (CCSS) and its regular workshop meeting in the USA in 1980 (in Russian); Academy of Sciences USSR, Physics of the Earth, 7, 109-111.

Ansorge, J. and Mereu, R.F. (Eds.) 1983: Probing the Earth´s Lithosphere by Controlled Source Seismology. Proc. of Symposium C7 by the Commission on controlled Source Seismology at the 21st IASPEI General Assembly, London, Ontario, Canada, July 1981; Physics of the Earth and Planetary Interiors, 31, 4 (Special Issue), 277- 383.

Mooney, W.D. and Prodehl, C., (Eds.) 1984: Proceedings of the 1980 Workshop of the International Association of Seismology and Physics of the Earth´s Interior on the Seismic Modelling of Laterally Varying Structures: Contributions based on data from the 1978 Saudi Arabian Refraction Profile; U.S. Geological Survey Circular 937, 158 pp.

Summary report on the workshop in Einsiedeln, Switzerland, 7-12 August 1983:
Finlayson, D.M. and Ansorge, J. (Eds.) 1984: Workshop Proceedings: Interpretation of Seismic Wave Propagation in Laterally Heterogeneous Structures; Bureau of Mineral Resources, Geology and Geophysics, Australian Government Publishing Service, Canberra, Report 258, 207 pp.

Internal Reports of the Commission on Controlled Source Seismology:
a) Meyer, R.P. and Mereu, R.F. (Convenors) 1983: Proceedings of the Workshop on Portable Digital Seismograph Development; Los Altos, California, 212 pp.
b) Meyer, R.P. (Compiler) 1984: Reports on Portable Digital Seismograph Development; Engeneering Notes 1, Dept. of Geology and Geophysics, University of Wisconsin- Madison, WI 53706, USA, 94 pp.

Commission on Controlled Source Seismology (CCSS): Interpretation of the SJ-6 seismic reflection refraction profile, south- central California, US; Walter, A.W. and Mooney, W.D. (Eds.) 1987: Proc. of the 1985 Workshop on Interpretation of Seismic Wave Propagation in Laterally Heterogeneous Terranes; Susono Shizuoka, Japan, 15-18 August, 1985; USGS Menlo Park, Open-file Report 87- 73, 132 pp.

Asano, S. and Mooney, W.D. 1987: Seismic Studies of Continental Lithosphere. Selected Papers of the same Symposium convened by CCSS at the IASPEI Congress, Tokyo, August 1985; Tectonophysics (spec. Issue), 140, 1- 220.

Buchbinder, G.G.R., Ansorge, J., and Crampin, S. (Eds.) 1989: Fine Structure and Anisotropy of the Lithosphere. Proc. of Symposium S7 by the Commission on Controlled Source Seismology at the XIX IUGG General Assembly, Vancouver, Canada, August 1987 (5 Papers); Tectonophysics, 165, Special Section, 269- 338.

Summary report of the workshop in Whistler, British Columbia, Canada, 2-7 August 1987:
Green, A.G. (Ed.) 1990: Studies of Latrally Heterogeneous Structures using Seismic Refraction and Reflection Data; Geological Survey of Canada, Paper 89-13, 224 pp.

CCSS-WORKSHOPS

Leningrad, USSR, 1968
Menlo Park, California, USA, 1971
Paris, France, 1975
Karlsruhe, FRG, 1977
Yalta, USSR, 1978
Park City, Utah, USA, 1980
Einsiedeln, Switzerland, 1983
Susono-Shizuoka, Japan, 1985
Whistler, British Columbia, Canada, 1987
Kiel-Fellhorst, FRG, 1990

Forthcoming workshop:
St. Petersburg, USSR, 1993